



Missouri University of Science and Technology  
**Scholars' Mine**

---

International Specialty Conference on Cold-Formed Steel Structures

(2008) - 19th International Specialty Conference on Cold-Formed Steel Structures

---

Oct 14th, 12:00 AM - Oct 15th, 12:00 AM

## 19th International Specialty Conference: Recent Research and Developments in Cold-Formed Steel Structures

Wei-Wen Yu Center for Cold-Formed Steel Structures

Follow this and additional works at: <https://scholarsmine.mst.edu/isccss>



Part of the [Structural Engineering Commons](#)

---

### Recommended Citation

Wei-Wen Yu Center for Cold-Formed Steel Structures, "19th International Specialty Conference: Recent Research and Developments in Cold-Formed Steel Structures" (2008). *International Specialty Conference on Cold-Formed Steel Structures*. 1.

<https://scholarsmine.mst.edu/isccss/19iccfss/info/1>

This Conference proceedings is brought to you for free and open access by Scholars' Mine. It has been accepted for inclusion in International Specialty Conference on Cold-Formed Steel Structures by an authorized administrator of Scholars' Mine. This work is protected by U. S. Copyright Law. Unauthorized use including reproduction for redistribution requires the permission of the copyright holder. For more information, please contact [scholarsmine@mst.edu](mailto:scholarsmine@mst.edu).

Continuing Education

Nineteenth International Specialty Conference on  
Cold-Formed Steel Structures

RECENT RESEARCH AND DEVELOPMENTS IN  
COLD-FORMED STEEL  
DESIGN AND CONSTRUCTION

Held in St. Louis, Missouri  
October 14 & 15, 2008

Edited by  
Roger A. LaBoube and Wei-Wen Yu

Department of Civil, Architectural & Environmental Engineering  
Missouri University of Science & Technology  
Rolla, Missouri



**Presented by**

Department of Civil, Architectural & Environmental Engineering  
Wei-Wen Yu Center for Cold-Formed Steel Structures  
Missouri University of Science & Technology

**Sponsored by**

American Iron and Steel Institute  
Cold-Formed Steel Engineers Institute of the Steel Framing Alliance  
Metal Building Manufacturers Association  
Metal Construction Association  
Rack Manufacturers Institute  
Steel Deck Institute  
Steel Stud Manufacturers Association  
Missouri University of Science & Technology

**In Cooperation with**

ASCE Committee on Cold-Formed Members  
Canadian Sheet Steel Building Institute, Canada  
SSRC Task Group on Thin-Walled Metal Construction  
University of Strathclyde, Scotland, UK  
Centre for Advanced Structural Engineering  
of the University of Sydney, Australia

**Conference Directors**

Roger A. LaBoube, Director  
Wei-Wen Yu, Founding Director  
of the Wei-Wen Yu Center for Cold-Formed Steel Structures,  
Missouri University of Science & Technology

**Planning Committee**

D. Allen – Representative of SSMA  
R.L. Brockenbrough - R.L. Brockenbrough & Associates, Inc.  
H.H. Chen - Representative of the American Iron and Steel Institute  
J. Crews – Unarco Material Handling Inc.; Representative of RMI  
W.S. Easterling – Virginia Tech  
S.R. Fox- Representative of CSSBI, Canada  
G.J. Hancock - Representative of the University of Sydney, Australia  
R.B. Haws - NUCONSTEEL  
D.L. Johnson - Consultant  
R.A. LaBoube –Missouri S&T; Conference Director  
J.W. Larson – Representative of the American Iron and Steel Institute  
J. A. Mattingly –CMC Joist and Deck; Representative of MCA  
T.B. Pekoz - Cornell University  
J. Rhodes - Representative of the University of Strathclyde, Scotland, UK  
B.W. Schafer – Johns Hopkins University; Representative of  
SSRC Task Group on Thin-Walled Metal Construction  
W.E. Schultz – Nucor Research and Development;  
P.A. Seaburg – Southern Illinois University - Edwardsville  
W.L. Shoemaker - Representative of MBMA  
T. Sputo – Representative of SDI;  
W.W. Yu – Missouri S&T; Conference Co-Director; Representative of  
the Wei-Wen Yu Center for Cold-Formed Steel Structures



# CONTENTS

Preface.....	v
Program.....	vi

## TECHNICAL SESSION No. 1

### Elements and Cross-Section Behavior

Floor System Design for Distortional Buckling Including Sheathing Restraint B.W. Schafer, R.H. Sangree, and Y. Guan .....	1
Simplified Methods for Predicting Elastic Buckling of Cold-Formed Steel Structural Members with Holes C.D. Moen and B.W. Schafer .....	17
Generalized Beam Theory Formulation Able to Capture Load Application and Localized Web Buckling Effects N.M.F. Silva, D. Camotim, and N. Silvestre .....	33
GBTUL – A Code for the Buckling Analysis of Cold-Formed Steel Members R. Bebbiano, N. Silvestre, and D. Camotim .....	61

## TECHNICAL SESSION NO. 2

### Compression Members

Impact of Global Flexural Imperfections on the Cold-Formed Steel Column Curve B.W. Schafer and V. M. Zeinoddini .....	81
Computed Flexural Buckling Stress for Cold-Formed Stainless Steel Columns S.H. Lin, C.L. Pan and C.P. Yu .....	97
Stability of Cold-Formed Steel Simple and Lipped Angles under Compression W.R. Maia, J.M. Neto and M. Malite .....	111
Structural Analysis of Scaffolding with Plank and Anchor Rod during Construction J.L. Peng., C.L. Pan, K.H. Chen, and S.L. Chan .....	127

## TECHNICAL SESSION NO. 3

### Design Standards and Guides Development

What's New in the 2007 Edition of the North American Cold-Formed Steel Specification? R. Brockenbrough, R. Schuster, R. LaBoube, and H. Chen .....	147
---	-----

An Update on AISI Standards for Cold-Formed Steel Framing	
J. Larson .....	159
Overview of the Standard for Seismic Design of Cold-Formed Steel Structural Systems – Special Bolted Moment Frames	
H. Chen, C.M. Uang, R. Bjorhovde, and B. Manley .....	175

#### **TECHNICAL SESSION NO. 4**

##### **Flexural Members**

Buckling Studies of Thin-Walled Channel Sections under Combined Bending and Shear	
C.H. Pham, G.J. Hancock .....	185
Experimental Study on Web Crippling of Lapped Cold-Formed Steel Channels Subjected to Interior Two-Flange Loading	
Q. Rahman, K. Sennah, and S. Fox .....	205
Simplified Models for Cross-Section Stress Demands on C-Section Purlins in Uplift	
L.C.M. Vieira, M. Malite, and B.W. Schafer .....	219
Flexural Resistance of Cold-Formed Steel Built-Up Box Sections Subjected to Eccentric Loading	
L. Xu and P. Sultana .....	235
Web Crippling Behaviour of Thin-Walled Lipped Channel Beams Subjected to EOF and ETF Loading	
M. Macdonald, M.A. Heiyantuduwa, and J. Rhodes .....	251

#### **TECHNICAL SESSION NO. 5**

##### **Rack Systems and Panel and Deck Assemblies**

Simplified Consideration of Down-Isle Stability in Pallet Racking	
J. Rhodes and M. Macdonald .....	265
Response of Metal Roofs to Uniform Static and True Hurricane Wind Loads	
R. R. Sinno .....	281
State of the Art Report on Thin-Walled Cold-formed Profiled Steel Decking	
N.A. Hedao, L.M. Gupta, G.N. Ronghe, and S.K. Parikh .....	307

## **TECHNICAL SESSION NO. 6**

### **Floor Joists and Floor Joist Assemblies**

Vibration Performance of Lightweight Floor Systems Supported by Cold-Formed Steel Joists B.W. Davis, R. Parnell, and L. Xu.....	325
Innovative Composite Cold-Formed Steel Floor Joist System D.M. Fox, R.M. Schuster, and M. Strickland .....	341
Flexural Behaviour and Design of the New Built-Up LiteSteel Beams S. Jeyaragan and M. Mahendran.....	357
Experimental and Numerical Studies of the Shear Behaviour of LiteSteel Beams P. Keerthan and M. Mahendran .....	377

## **TECHNICAL SESSION NO. 7**

### **Shear Wall Assemblies**

Inelastic Performance and Design of CFS Walls Braced with Straps Having Reduced Width Fuses K. Velchev, G. Comeau, N. Balh, and C.A. Rogers .....	391
Pilot Research on Cold-Formed Steel Framed Shear Wall Assemblies with Corrugated Sheet Steel Sheathing H. Vora and C. Yu .....	409
Structural Testing of Corrugated Sheet Steel Shear Walls B. Stojadinovic and S. Tipping .....	425
Shear Resistance of Cold-Formed Steel Framed Shear Wall Assemblies with 0.027-, 0.030-, 0.033-inch Sheet Steel Sheathing C. Yu.....	441
Estimating the Effective Yield Strength of Cold-Formed Steel Light-Frame Shear Walls R. Serrette .....	457

## **TECHNICAL SESSION NO. 8**

### **Wall Studs and Stud Assemblies**

Effect of Varied Imperfections on Bracing Demand of Cold-Formed Steel Stud Walls T. Sputo, K. Beery, and E. Wong .....	471
Finite Element Analytical Investigation of Torsional Bracing Requirements for Cold-Formed Steel C-Shaped Studs J. Tovar, T. Helwig, and T. Sputo.....	485



Strength of Cold-Formed Steel Jamb Stud-to-Track Connections	
A.V. Lewis, S.R. Fox, and R.M. Schuster .....	501
Thermal Performance of Plasterboard Lined Steel Stud Walls	
P. Kolarkar and M. Mahendran .....	517
Testing and Evaluation of CFS L-Headers	
J. Pauls, L.Xu, and S. Fox.....	531

### TECHNICAL SESSION NO. 9

#### Connections

Effects of Elevated Temperatures on Ultimate Moment Capacity of Bolted Moment-Connections between Cold-formed Steel Members	
J. B.P. Lim and Ben Young .....	547
Cold-Formed Steel Special Bolted Moment Frames: Cyclic Testing and Numerical Modeling of Moment Connections	
C.M. Uang, J.K. Hong, A. Sato, and K. Wood.....	563
Cold-Formed Steel Special Bolted Moment Frames: Capacity Designed Requirements	
A. Sato and C.M. Uang.....	577
Cold-Formed Steel Portal Frame Joints: A Review	
A.M. Wrzesien and J.B.P. Lim.....	591
Strength of Arc-Spot Welds Made in Single and Multiple Steel Sheets	
G.L. Snow and W.S. Easterling .....	607
Cold-Formed Steel Bolted Connections without Washers on Oversized Holes: Shear and Bearing Failures in Sheets	
C. Yu and I. Sheerah.....	623
Experimental Response of Connections Between Cold-Formed Steel Profile and Cement-Based Panel	
L. Fiorino, O. Iuorio, and R. Landolfo.....	639
Test Standard for Joist Connectors Attached to Cold-Formed Steel Framing	
G. Greenlee.....	655
New Test Standard for Hold-downs Attached to Cold-Formed Steel Structural Framing	
J. Ellis .....	661
Behavior of Arc Spot Weld Connections Subjected to Combined Shear and Tension Forces	
L.K. Stirneman and R.A. LaBoube.....	681

## PREFACE

Cold-formed steel members are used in virtually every area of construction. In order to review the research findings and the design methods developed in this field, 19 International Specialty Conferences on Cold-Formed Steel Structures have been held since 1971.

In recent years, significant progress has been made in the development of design standards and in research studies of cold-formed steel members and structural systems throughout the world. The Nineteenth International Specialty Conference on Cold-Formed Steel Structures was held in St. Louis, Missouri on October 14 & 15, 2008. It was sponsored by the American Iron and Steel Institute (AISI), Cold-Formed Steel Engineers Institute of the Steel Framing Alliance (CFSEI), Metal Building Manufacturers Association (MBMA), Metal Construction Association (MCA), Rack Manufacturers Institute (RMI), Steel Deck Institute (SDI), Steel Stud Manufacturers Association (SSMA), and the Missouri University of Science & Technology (formerly University of Missouri-Rolla) in cooperation with the American Society of Civil Engineers Committee on Cold-Formed Members, Canadian Sheet Steel Building Institute, Structural Stability Research Council Task Group on Thin-Walled Metal Construction, the University of Strathclyde in Scotland and the Centre for Advanced Structural Engineering of the University of Sydney in Australia.

This publication contains 43 papers that were presented at the conference. These papers not only report the results of recent research but also discuss the technical developments in cold-formed steel design and construction.

As Directors of the Conference, we are very grateful to all the sponsors and supporting organizations for their financial and technical support and to all authors for their contributions in the field of cold-formed steel structures. Appreciation is also due to members of the Planning Committee (D. Allen, R.L. Brockenbrough, H.H. Chen, J. Crews, W.S. Easterling, S.R. Fox, G.J. Hancock, R.B. Haws, D.L. Johnson, R.A. LaBoube, J.W. Larson, J.A. Mattingly, T.B. Pekoz, J. Rhodes, B.W. Schafer, W.E. Schultz, P.A. Seaburg, W.L. Shoemaker, T. Sputo and W.W. Yu) for review and selection of papers and their advice in preparation of the conference. We would also like to thank all of the session chairpersons listed in the program for their time and effort.

Special thanks are extended to Mrs. Christina Stratman and Ms. Kristin Imm for their assistance in preparing this publication.

Roger A. LaBoube

Wei-Wen Yu

## **PROGRAM**

**Monday, October 13, 2008**

**6-9 p.m. Registration**

**Tuesday, October 14, 2008**

**7 a.m. – 4 p.m. Registration**

**8:00 a.m. Welcoming Remarks**

R.A. LaBoube, Missouri University of Science & Technology

Presentation of 2008 AISI Market Development Industry Leadership Award to Dr. J.M. Fisher, Computerized Structural Design, Milwaukee, WI,

**8:10 a.m. Technical Session No. 1**

**Elements and Cross-Section Behavior**

**Chairpersons:**

W.S. Easterling, Virginia Tech, Blacksburg, VA, USA

D.L. Johnson, Maus Engineering, Wolfeboro, NH, USA

**“Floor System Design for Distortional Buckling Including Sheathing Restraint;”**

B.W. Schafer, R.H. Sangree, Y. Guan, Johns Hopkins University, Baltimore, MD, USA

**“Simplified Methods for Predicting Elastic Buckling of Cold-Formed Steel Structural Members with Holes;”**

C.D. Moen, Virginia Tech, Blacksburg, VA, USA, and B.W. Schafer, Johns Hopkins University, Baltimore, MD, USA

**“Generalized Beam Theory Formulation Able to Capture Load Application and Localized Web Buckling Effects;”**

N.M.F. Silva, D. Camotim, N. Silvestre, Technical University of Lisbon, Lisbon, Portugal

**“GBTUL – A Code for the Buckling Analysis of Cold-Formed Steel Members,”**

R. Bebbiano, N. Silvestre, D. Camotim, Technical University of Lisbon, Lisbon, Portugal

**9:30 a.m. Break**

**9:50 a.m. Technical Session No. 2**

**Compression Members**

**Chairpersons:**

J. Rhodes, University of Strathclyde, Glasgow, Scotland

W.L. Shoemaker, Metal Building Manufacturers Association, Cleveland, OH, USA

**“Impact of Global Flexural Imperfections on the Cold-Formed Steel Column Curve;”**

B.W. Schafer, V. M. Zeinoddini, Johns Hopkins University, Baltimore, MD, USA

**“Computed Flexural Buckling Stress for Cold-Formed Stainless Steel Columns;”**

S.H. Lin, Minghsin University of Science & Technology, Taiwan, R.O.C., C.L. Pan and C.P. Yu, Chaoyang University of Technology, Taiwan, R.O.C.

**“Stability of Cold-Formed Steel Simple and Lipped Angles under Compression;”**

W.R. Maia, J.M. Neto and M. Malite, University of Sao Paulo, Sao Carlos, Brazil

**“Structural Analysis of Scaffolding with Plank and Anchor Rod during Construction;”**

J.L. Peng, Yunlin University of Science & Technology, Taiwan, R.O.C., C.L. Pan, Chaoyang University of Technology, Taiwan, R.O.C., K.H. Chen, National Science Council, Taiwan, R.O.C., S.L. Chan, Hong Kong polytechnic University, Hong Kong, China

**11:10 a.m. Technical Session No. 3**

**Design Standards and Guides Development**

**Chairpersons:**

R.L. Brockenbrough, R.L. Brockenbrough and Associates, Pittsburgh, PA, USA

W.W. Yu, Missouri University of Science & Technology, Rolla, MO, USA

**“What's New in the 2007 Edition of the North American Cold-Formed Steel Specification?;”**

R. Brockenbrough, R.L. Brockenbrough and Associates, Pittsburgh, PA, R. Schuster, University of Waterloo, Waterloo, Ontario, Canada, R. LaBoube, Missouri University of Science & Technology, Rolla, MO, H. Chen, American Iron and Steel Institute, Washington, D.C.

**“An Update on AISI Standards for Cold-Formed Steel Framing;”**

J. Larson, American Iron and Steel Institute, Washington, D.C.

**“Overview of the Standard for Seismic Design of Cold-Formed Steel Structural Systems - Special Bolted Moment Frames;”**

H. Chen, American Iron and Steel Institute, Washington, D.C., C.M. Uang, University of California – San Diego, La Jolla, CA, R. Bjorhovde, The Bjorhovde Group, Tucson, AZ, B. Manley, American Iron and Steel Institute, Washington, D.C.

**12:10 p.m. Lunch**

**1:10 p.m. Technical Session No. 4**  
**Flexural Members**

**Chairpersons:**

R.M. Schuster, University of Waterloo, Ontario, Canada  
T. Sputo, Steel Deck Institute, Gainesville, FL USA

**“Buckling Studies of Thin-Walled Channel Sections under Combined Bending and Shear;”**

C.H. Pham, G.J. Hancock, University of Sydney, Sydney, Australia

**“Experimental Study on Web Crippling of Lapped Cold-Formed Steel Channels Subjected to Interior Two-Flange Loading;”**

Q. Rahman, Ryerson University, Toronto, Ontario, Canada, K. Sennah, Ryerson University, Toronto, Ontario, Canada, S. Fox, Canadian Sheet Steel Building Institute, Cambridge, Ontario, Canada

**“Simplified Models for Cross-section Stress Demands on C-Section Purlins in Uplift;”**

L.C.M. Vieira, Johns Hopkins University, Baltimore, MD, USA, M. Malite, University of Sao Paulo, Sa Carlos, Brazil, B.W. Schafer, Johns Hopkins University, Baltimore, MD, USA

**“Flexural Resistance of Cold-Formed Steel Built-Up Box Sections Subjected to Eccentric Loading;”**

L. Xu, P. Sultana, University of Waterloo, Waterloo, Ontario, Canada

**“Web Crippling Behaviour of Thin-Walled Lipped Channel Beams Subjected to EOF and ETF Loading;”**

M. Macdonald, Glasgow Caledonian University, Glasgow, Scotland, M.A. Heiyantuduwa, Glasgow Caledonian University, Glasgow, Scotland, J. Rhodes, University of Strathclyde, Glasgow, Scotland

**2:50 p.m. Break**

**3:10 p.m. Technical Session No. 5**  
**Rack Systems and Panel and Deck Assemblies**

**Chairpersons:**

B.W. Schafer, Johns Hopkins University, Baltimore, MD  
J. Crews, Unarco Material Handling, Springfield, TN USA

**“Simplified Consideration of Down-isle Stability in Pallet Racking;”**

J. Rhodes, University of Strathclyde, Glasgow, Scotland and M. Macdonald, Glasgow Caledonian University, Glasgow, Scotland

**“Response of Metal Roofs to Uniform Static and True Hurricane Wind Loads;”**

R. R. Sinno, Mississippi State University, Mississippi

**“State of the Art Report on Thin-walled Cold-formed Profiled Steel Decking;”**

N.A. Hedao, College of Engineering, Pune, India, L.M. Gupta, Viseesearaya National Institute of Technology, Nagpur, India, G.N. Ronghe, Viseesearaya National Institute of Technology, Nagpur, India, S.K. Parikh, College of Engineering, Pune, India

**4:10 p.m. Technical Session No. 6**

**Floor Joists and Floor Joist Assemblies**

**Chairpersons:**

M. Macdonald, Glasgow Caledonian University, Glasgow, Scotland  
R.B. Haws, NUCONSTEEL, Denton, TX, USA

**“Vibration Performance of Lightweight Floor Systems Supported by Cold-Formed Steel Joists;”**

B.W. Davis, R. Parnell, L. Xu, University of Waterloo, Waterloo, Ontario, Canada

**“Innovative Composite Cold-Formed Steel Floor Joist System;”**

D.M. Fox, iSPAN Technologies, Richmond Hill, Ontario, Canada, R.M. Schuster, University of Waterloo, Waterloo, Ontario, Canada, M. Strickland, iSPAN Technologies, Richmond Hill, Ontario, Canada

**“Flexural Behaviour and Design of the New Built-up LiteSteel Beams;”**

S. Jeyaragan, M. Mahendran, Queensland University of Technology, Brisbane, Australia

**“Experimental and Numerical Studies of the Shear Behaviour of LiteSteel Beams;”**

P. Keerthan, M. Mahendran, Queensland University of Technology, Brisbane, Australia

**5:30 p.m. Adjourn**

**6:00-7:00 pm. Reception**

**Sponsored by:**

**American Iron and Steel Institute**  
**Cold-Formed Steel Engineers Institute of Steel Framing Alliance**  
**Metal Building Manufacturers Association**  
**Metal Construction Association**  
**Rack Manufacturers Institute**  
**Steel Deck Institute**  
**Steel Stud Manufacturers Association**

**Wednesday, October 15, 2008**

**8:00 a.m Technical Session No. 7  
Shear Wall Assemblies**

**Chairpersons:**

S.R. Fox, Canadian Sheet Steel Building Institute, Cambridge, Ontario, Canada  
J.W. Larson, American Iron and Steel Institute, Washington, D.C., USA

**“Inelastic Performance and Design of CFS Walls Braced with Straps Having Reduced Width Fuses;”**

K. Velchev, G. Comeau, N. Balh, C.A. Rogers, McGill University, Montreal, Canada

**“Pilot Research on Cold-Formed Steel Framed Shear Wall Assemblies with Corrugated Sheet Steel Sheathing;”**

H. Vora, C. Yu, University of North Texas, Denton, TX

**“Structural Testing of Corrugated Sheet Steel Shear Walls,”**

B. Stojadinovic, University of California at Berkeley, CA, USA, S. Tipping, Tipping Mar + Associates, Berkeley, CA, USA

**“Shear Resistance of Cold-Formed Steel Framed Shear Wall Assemblies with 0.027-, 0.030-, 0.033-inch Sheet Steel Sheathing;”**

C. Yu, University of North Texas, Denton, TX, USA

**“Estimating the Effective Yield Strength of Cold-Formed Steel Light-Frame Shear Walls;”**

R. Serrette, Santa Clara University, Santa Clara, CA, USA

**9:40 a.m. Break**

**10:00 a.m. Technical Session No. 8  
Wall Stud and Wall Stud Assemblies**

**Chairpersons:**

D. Allen, Steel Stud Manufacturers Association, Washington, D.C., USA  
P.A. Seaburg, Consultant, Edwardsville, IL, USA

**“Effect of Varied Imperfections on Bracing Demand of Cold-Formed Steel Stud Walls;”**

T. Sputo, K. Beery, E. Wong, University of Florida, Gainesville, FL, USA

**“Finite Element Analytical Investigation of Torsional Bracing Requirements for Cold-Formed Steel C-Shaped Studs;”**

J. Tovar, Schwab Structural Engineering, New Braunfels, TX, T. Helwig, University of Texas, Austin, TX, T. Sputo, University of Florida, Gainesville, TX, USA

**“Strength of Cold-Formed Steel Jamb Stud-to-Track Connections;”**

A.V. Lewis, University of Waterloo, Waterloo, Ontario, Canada, S.R. Fox, Canadian Sheet Steel Building Institute, Cambridge, Ontario, Canada, R.M. Schuster, University of Waterloo, Waterloo, Ontario, Canada

**“Thermal Performance of Plasterboard Lined Steel Stud Walls;”**

P. Kolarkar, M. Mahendran, Queensland University of Technology, Brisbane, Australia

**“Testing and Evaluation of CFS L-Headers;”**

J. Pauls, University of Waterloo, Waterloo, Ontario, Canada, L.Xu, University of Waterloo, Waterloo, Ontario, Canada, S. Fox, Canadian Sheet Steel Building Institute, Cambridge, Ontario, Canada

**11:40 a.m. Lunch**

**1:00 p.m. Technical Session No. 9  
Connections**

**Chairpersons:**

J. Mattingly, CMC Joist & Deck, Summit, NJ, USA

H. Chen, American Iron and Steel Institute, Washington, D.C., USA

**“Effects of Elevated Temperatures on Ultimate Moment Capacity of Bolted Moment-Connections between Cold-formed Steel Members;”**

J. B.P. Lim, University of Strathclyde, Glasgow, Scotland, Ben Young, University of Hong Kong, Hong Kong

**“Cold-Formed Steel Special Bolted Moment Frames: Cyclic Testing and Numerical Modeling of Moment Connections;”**

C.M. Uang, University of California, San Diego, La Jolla, CA, USA, J.K. Hong, Myers, Houghton & Partners, Long Beach, CA, USA, A. Sato, Kyoto University, Kyoto, Japan, K. Wood, KL Wood Engineering, Colorado Springs, CO, USA

**“Cold-Formed Steel Special Bolted Moment Frames: Capacity Designed Requirements;”**

A. Sato, Kyoto University, Kyoto, Japan, C.M. Uang, University of California, San Diego, La Jolla, CA, USA

**“Cold-Formed Steel Portal Frame Joints: A Review;”**

A. Wrzesien, J.B.P. Lim, University of Strathclyde, Glasgow, Scotland

**2:20 p.m. Break**



**2:30 p.m. Technical Session No. 9 (cont.)**

**“Strength of Arc-Spot Welds Made in Single and Multiple Steel Sheets;”**

G. Snow, W.S. Easterling, Virginia Tech, Blacksburg, VA, USA

**“Cold-Formed Steel Bolted Connections Without Washers on Oversized Holes: Shear and Bearing Failures in Sheets,”**

C. Yu and I. Sheerah, University of North Texas, Denton, TX

**“Experimental response of connections between cold-formed steel profile and cement-based panel;”**

L. Fiorino, O. Iuorio, R. Landolfo, University of Naples “FedericoII”, Naples, Italy

**“Test Standard for Joist Hangers and Similar Devices Attached to Cold-Formed Steel Framing;”**

G. Greenlee, USP Structural Connectors, Burnsville, MN, USA

**“New Test Standard for Hold-downs Attached to Cold-Formed Steel Structural Framing”**

J. Ellis, Simpson-Strong Tie, Pleasanton, CA, USA

**“Behavior of Arc Spot Weld Connections Subjected to Combined Shear and Tension Forces;”**

L.K. Stirneman, R.A. LaBoube, Missouri University of Science & Technology, Rolla, MO, USA

**4:30 p.m. Closing Remarks and Adjournment**





## **Floor system design for distortional buckling including sheathing restraint**

Schafer, B.W.<sup>1</sup>, Sangree, R.H.<sup>2</sup>, Guan, Y.<sup>3</sup>

### **ABSTRACT**

The objective of this paper is to describe how to include the beneficial rotational restraint, provided by sheathing to the compression flange of a cold-formed steel floor joist, to partially or fully retard the formation of distortional buckling. The design method for checking distortional buckling adopted in the 2007 AISI Specification (AISI-S100-07) provides a means to include a rotational restraint term,  $k_\phi$ , to account for sheathing restraint. A series of cantilever tests were conducted to determine the rotational stiffness,  $k_\phi$ , between a joist and attached sheathing. Tests were conducted for different joist thicknesses, depths, and flange widths, two fastener types, and plywood, oriented strand board, and gypsum board sheathing. The testing lead to (a) the development of a proposed design method, and (b) improvements to the AISI test standard for cantilever tests; both of which are presented herein. The focus of the design method and the improvements to the test standard are the separation of the rotational stiffness,  $k_\phi$ , into contributions from the sheathing and from the local fastener (connector) deformations. It is shown that the sheathing stiffness is well correlated with tabled bending rigidity values, and the connector stiffness is primarily derived from the thickness of the flange. The developed recommendations have been proposed for the next edition of AISI standards and are presented in an Appendix.

---

<sup>1</sup> Assoc. Prof., Civil Engineering, Johns Hopkins University, [schafer@jhu.edu](mailto:schafer@jhu.edu)

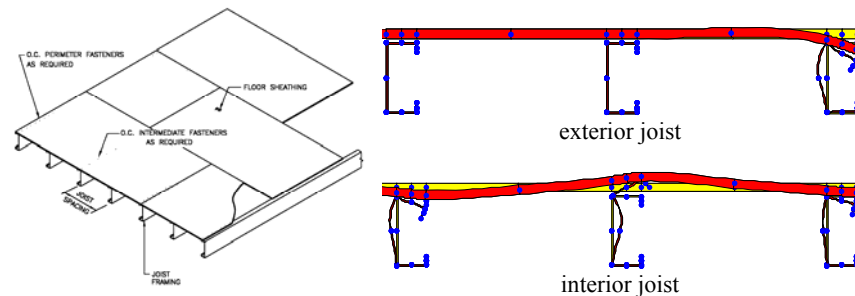
<sup>2</sup> Post-doctoral Res., Civil Eng., Johns Hopkins University, [sangree@jhu.edu](mailto:sangree@jhu.edu)

<sup>3</sup> Undergrad. Res. Asst., Civil Eng., Johns Hopkins University [yguan@jhu.edu](mailto:yguan@jhu.edu)

## INTRODUCTION

Lateral-torsional buckling, local buckling, and distortional buckling are the three key member instabilities that may limit the ultimate strength of a floor joist. The most common concern is lateral-torsional buckling of the joist; blocking and bridging combined with fastened sheathing is employed to stabilize the joist from the global translation and twist associated with lateral-torsional buckling, as shown in Figure 1a. Local buckling, where the strength and rigidity of portions of the member are partially lost due to plate buckling, must also be accounted for. The strength in local buckling is largely independent of the floor framing details as the instability occurs over a short length of the joist.

The final member instability of concern is distortional buckling (Figure 1b); distortional buckling may be conceptualized as an instability driven by flexural-torsional buckling of the compression flange, involving large rotations of the flange and large plate bending deformations in the web. The floor sheathing provides a beneficial restraint for the joist against distortional buckling, but the magnitude of this restraint is poorly understood. This paper summarizes recent testing which characterizes the rotational restraint from sheathing and a related procedure which allows this restraint to be included in design.



(a) typical floor system (SFA 2000) (b) distortional buckling of a sheathed floor joist  
Figure 1 Floor system and distortional buckling

An investigation into the restraint that sheathing provides against distortional buckling is timely as new provisions to account for distortional buckling have recently been adopted in the cold-formed steel specification: AISI-S100-07 (AISI 2007). These provisions, section C3.1.4 of AISI-S100-7, were developed through a series of 4-point bending tests conducted by Yu and Schafer (2003, 2006) which examined distortional and local buckling of bending members. The distortional buckling tests, as shown in Figure 2, did not include any compression flange restraint and resulted in distortional buckling failures (Figure 2b). When the metal panel shown in the shear spans of Figure 2a was

extended into the center region and fastened to the compression flange with pairs of fasteners, the failure mode changed to local buckling. In these latter tests the metal panel was engaged and distortional buckling was restricted. The rotational restraint provided by the metal deck was the key to avoiding distortional buckling. The new provisions for distortional buckling in C3.1.4 of AISI-S100-07 include a stiffness term,  $k_\phi$ , which increases the distortional buckling capacity as a function of available rotational restraint (stiffness).



(a) unrestrained distortional buckling test setup of Yu and Schafer (2006)



(b) unrestrained 800S200-054 C exhibiting distortional buckling

Figure 2 Tests on distortional buckling of C-sections

In the early 1980's the Metal Building Manufacturer's Association (MBMA) examined available rotational restraint in their systems: purlins fastened through insulation to metal deck. MBMA developed the "F" test (MRI 1981, Hausler and Pabers 1973) which later was formalized as AISI TS-1-02 (AISI 2002). The test uses a small cantilevered segment of panel with a purlin attached, and pulls on the free flange of the purlin such that a moment and rotation is induced at the panel-purlin connection. This test provides an estimate of the panel-purlin rotational restraint,  $k_\phi$ . The  $k_\phi$  results are critically dependent on purlin thickness (LaBoube 1986). The important role of thickness in the conducted tests (as opposed to purlin depth, deck thickness, insulation, etc.) suggests that the panel-purlin connection flexibility, and local flange deformations at the connection, played a dominant role in the behavior.

The restraint provided by metal deck was further explored in Yu's thesis (Yu 2005) and the existing MBMA tests were found to provide a conservative prediction of developed restraint and suggested for use as  $k_\phi$  in the distortional buckling (Section C3.1.4) commentary of AISI-S100. However, no equivalent data for cold-formed steel framing systems, such as floor joists, is available. The work summarized herein uses an augmented version of the AISI-TS-1-02 tests to examine cold-formed steel framing systems: steel joists sheathed with plywood and OSB, as well as steel joists sheathed with gypsum board as might exist in walls and ceilings.

## CHARACTERIZING SHEATHING RESTRAINT

The basic test setup for measuring the sheathing rotational restraint is shown in Figure 2. The setup is similar to that used in AISI TS-1-02 (AISI 2002) but has been modified and expanded to reflect the specific needs of this testing program. Based on the measured load,  $P$ , the moment, per unit width is:

$$M = (P/w)h_o \quad (1)$$

This definition for  $M$  is exact only for the undeformed state. The total rotation,  $\theta_2$ , of the sheathing-connector-joist assembly considers only  $\Delta_v$  and  $h_o$  where:

$$\theta_2 = \tan^{-1}(\Delta_v/h_o) \quad (2)$$

Based on these definitions for  $M$  and  $\theta$  the rotational stiffness is defined as

$$k_{\phi_2} = M/\theta_2 \quad (3)$$

where  $k_{\phi_2}$  has units of (force-distance/length)/radian or simply force/radian.

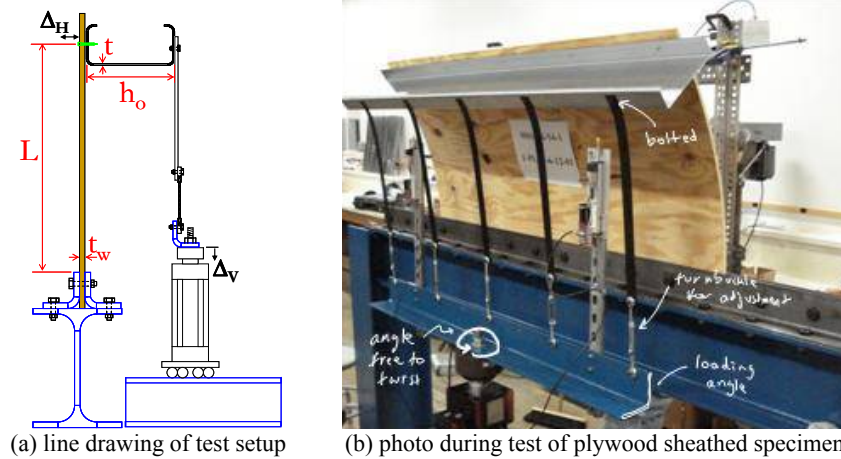


Figure 3 Test setup for rotational restraint,  $k_{\phi}$ , measurement

### Component stiffness calculations

AISI-TS-1-02 only considers  $k_{\phi}$  of Eq. 3, but due to the large variability in the stiffness of typical sheathing, the methodology was expanded to separate the rotation into sheathing and connection components. The rotation due to the sheathing,  $\theta_w$ , may be removed from the total rotation by assuming a simple beam theory model for the sheathing and measuring the horizontal displacement,  $\Delta_h$ . The lateral deflection at the point of moment application in the linear elastic range assuming standard beam theory for the sheathing deformation is:

$$\Delta_h = ML^2/(2EI_w) \quad (4)$$

and the rotation at the point of moment application is

$$\theta_w(\text{at } \Delta_h) = ML / (EI_w) \quad (5)$$

Using Eq. 4 and 5 the sheathing rotation is defined as

$$\theta_w = 2\Delta_h / L$$

The rotational stiffness of the sheathing (wood) may then be determined via:

$$k_{\phi_w} = M / \theta_w = M / (2\Delta_h / L) \quad (6)$$

The simplest definition of the connector rotation,  $\theta_{c2}$ , assumes that only the sheathing rotation should be removed from the total rotation, i.e.:

$$\theta_{c2} = \theta_2 - \theta_w \quad (7)$$

which results in a connector stiffness of:

$$k_{\phi_{c2}} = M / \theta_{c2} = M / (\theta_2 - \theta_w) \quad (8)$$

Note, this definition of the connector stiffness includes flexibilities from bending of the joist and the loading apparatus. This component model is consistent with a spring in series model, thus:

$$k_{\phi_2} = (1 / (1/k_{\phi_{c2}} + 1/k_{\phi_w})) \quad (9)$$

## EXPERIMENTAL RESULTS

The measured rotational restraint from the tests ( $k_{\phi_2}$ ) is reported in Table 1 for the 36 tests conducted (which covered 24 different sets of parameters, due to multiple tests for some parameter sets). To provide an overview of the conducted experiments, results for tests on an 800S200-54 joist with #6 fasteners spaced 12 in. on-center attached to OSB, plywood, and gypsum sheathing (24 in. long, 54 in. wide) are provided in Figure 4. The stiffness results (slope of the M- $\theta$  lines) indicates that OSB provides the most robust response, plywood can undergo significant rotation, but is much more flexible than OSB, and gypsum provides a stiff response, but with low rotation capacity.

Table 1 Parameters of conducted rotational restraint tests

Sheathing -->	$k_{\phi_2}$ (lbf-in./in./rad)									
	Plywood					OSB		Gypsum		
	12"		24"		24"		12"		24"	
	6	10	6	10	6	10	6	10	6	10
Fastener # -->	6"		12"		12"		12"		12"	
Fastener Spacing -->	6"	12"	6"	12"	12"	12"	12"	12"	12"	12"
362S162-33	40						75			
362S162-68	42						94			
800S200-54	41	34	33	18	57	44	76	60	53	58
800S250-54	53		43							
800S200-97			47 44				66		58	
1200S200-54	34				44					
1200S200-97			59				75			

(joist designation, e.g., 362S162-33, in SSMA nomenclature, [www.ssma.com](http://www.ssma.com), 1 in. = 25.4 mm)

(1) average values reported when multiple tests conducted

(2) re-tests of specimens not included in average value calculations (only original test)

As presented (Table 1, Figure 4), the rotational restraint includes deformations from the sheathing and connector. Figure 5 provides the M- $\theta$  relations for the



isolated sheathing and connector components for the same three tests as given in Figure 4. Figure 5 shows that the difference between the plywood sheathed specimens and the OSB and gypsum sheathed specimens is due to the plywood, not the connection. In fact, the connection stiffness for all three specimens (slope of the  $M-\theta_{c2}$ ), which have nominally the same joist dimension, joist thickness, fastener size, and fastener spacing are quite similar despite varying attached sheathing types. Complete experimental results for all testing conducted are provided in Schafer et al. (2007).

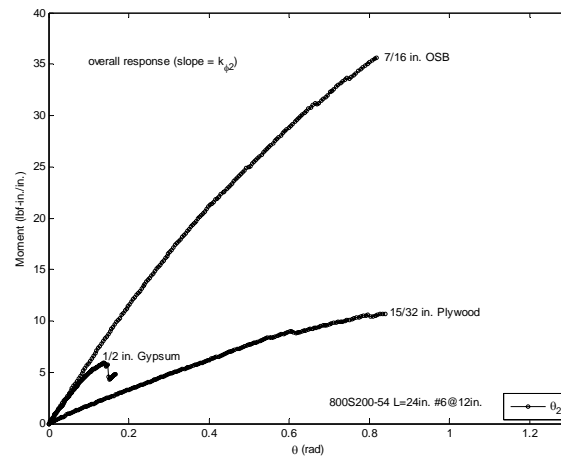


Figure 4 Typical moment-rotation results for overall stiffness (1 lbf = 4.448 N)

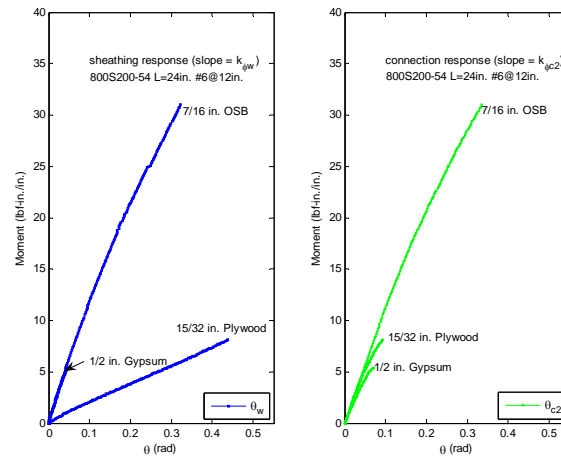
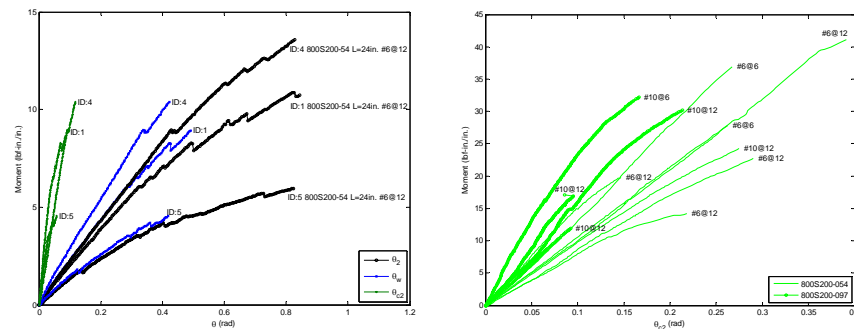


Figure 5 Typical moment-rotation results for sheathing and connection stiffness

## Plywood Sheathing

Significant variability was observed in the sheathing stiffness in the plywood sheathed specimens. For example, Figure 6a provides the results for the three plywood sheathed specimens nominally identical to that of Figure 4. Interestingly, the variability derives from variation in the sheathing stiffness, not the connection stiffness (compare  $M-\theta_w$  with  $M-\theta_{c2}$  in Figure 6a).

An example of the comparisons provided in Schafer et al. (2007) for the plywood sheathed specimens is provided in Figure 6b, which shows the influence of joist thickness and fastener details on the observed connection response of 800S200 joists (slope of the lines is  $k_{\phi c2}$ ). Careful study shows that joist thickness is a more significant variable than fastener size or spacing. However, close spacing does provide an improved (stiffer) connection response.



(a) response of 3 nominally identical plywood sheathed joists

(b) Connector  $M-\theta_{c2}$  for 800S200 joists with varied thickness and fastener details

Figure 6 Moment rotation response of plywood sheathed specimens

## OSB Sheathing

Overall moment-rotation response, and hence stiffness (slope of the  $M-\theta_2$  curve in Figure 7a), shows significant variation in OSB sheathed joists. However, the observed variability is primarily attributed to connection and joist details, not the OSB – which generally provides a consistent response. In addition, in one of the OSB sheathed specimens a pull-through failure was observed, thus indicating the possibility of this failure mode in OSB. However, the observed pull-through failure did not occur until approximately 0.5 rad (29 deg.), which is well beyond the anticipated rotational demands in distortional buckling up to and including collapse. See Schafer et al. (2007) for further discussion.

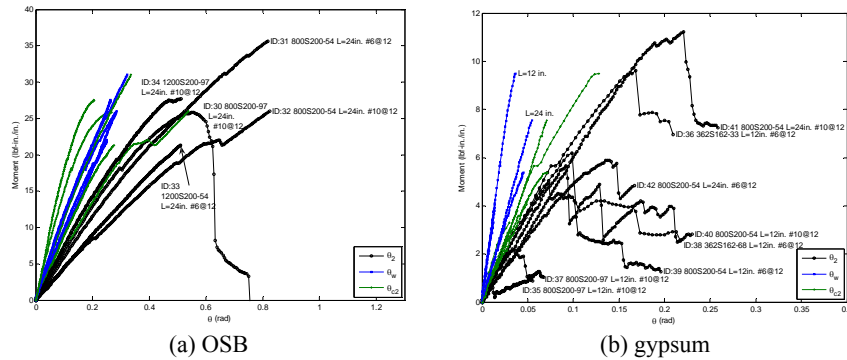


Figure 7 Moment rotation response of OSB and gypsum sheathed specimens

### Gypsum Sheathing

The response of the joists sheathed with gypsum was significantly different than the OSB or plywood sheathed specimens: at low rotations the fasteners pulled-through the gypsum board and failed the specimens (Figure 7b and Figure 8). Figure 7b provides the moment-rotation results for the gypsum sheathed specimens. As the joist thickness increases, the rotation capacity decreases. The observed behavior suggests that while gypsum board may be able to resist distortional buckling of walls and ceilings at service loads, it is unreliable at ultimate strength levels as it has inadequate rotation capacity.



(a) large separation between joist and gypsum board

(b) pull-through failure and fracture of gypsum board

Figure 8 Response of 800S200-54 joist sheathed to gypsum board with #10s @ 12 in.

Significantly more detail for all of the testing conducted is provided in Schafer et al. (2007). Utilization of the tested rotational stiffness in design is the focus of the remaining sections of this paper.

## DEVELOPMENT OF DESIGN MODEL

It is proposed that the total rotational restraint,  $k_{\phi}$ , needed for the distortional buckling calculation in AISI-S100 C3.1.4 be found using  $k_{\phi 2}$  of Eq. 9. Thus, requirements for design are the sheathing rotational stiffness,  $k_{\phi w}$ , and the connection rotational stiffness,  $k_{\phi c 2}$ . Based on the experiments reported herein, it is determined (below) that industry provided sheathing stiffness values are conservative for determining  $k_{\phi w}$ , and that a simplified empirical expression may be used for the connection stiffness,  $k_{\phi c 2}$ .

### Sheathing stiffness compared with industry tables values

Employing Eq. 4, the displacement,  $\Delta_h$ , and the load,  $P$ , may be used to back-calculate the experimentally observed sheathing bending rigidity  $EI_w$ . The observed  $EI_w$  are compared to industry provided values in Table 2. The results indicate that the measured values are generally consistent with industry provided values, but industry provided values are typically more conservative than the average measured response. The relationship between the bending rigidity ( $EI_w$ ) and the sheathing rotational stiffness ( $k_{\phi w}$ ) is depicted in Figure 9 where it is shown to be a function of joist spacing and location. The expressions for interior and exterior joists given in Figure 9 are recommended for design.

Table 2 Sheathing bending rigidity  
(a) sheathing stiffness determined from testing

	$EI_w$ (lbf-in. <sup>2</sup> /ft of panel width)			
	mean	C.O.V.	n	min max
Plywood*	9000	0.3	27	4000 14000
OSB*	31000	0.1	5	26000 35000
Gypsum	41000	0.1	7	37000 43000

\*stress perpendicular to strength axis

(b) sheathing stiffness available from standards

	$EI_w$ (lbf-in. <sup>2</sup> /ft of panel width)	
	mean	source
32/16 Plywood*	8100	APA, Panel Design Spec. (2004)
24/16 OSB*	16000	APA, Panel Design Spec. (2004)
32/16 OSB*	25000	APA, Panel Design Spec. (2004)
Gypsum (min)	18000	Gypsum Assoc. GA-235-01, (2001)
Gypsum (max)	48000	Gypsum Assoc. GA-235-01, (2001)

\*stress perpendicular to strength axis

$$(1 \text{ lbf-in.}^2/\text{ft} = 9.476 \text{ kN-mm}^2/\text{m})$$

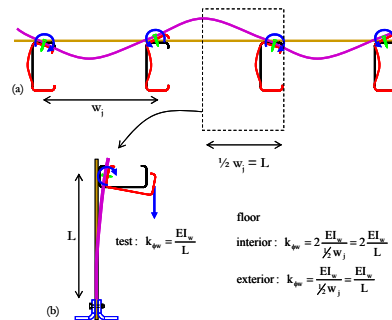


Figure 9 Sheathing stiffness for interior and exterior joists and comparison to conducted tests

### Connection stiffness and design simplification

The average connection stiffness using Eq. 8, measured in the testing reported here, is provided in Table 3. The two parameters found to have the most influence on the connection rotational stiffness are joist thickness and fastener

spacing (see Schafer et al. 2007 for additional analysis and discussion on this point). From a practical standpoint industry has shown a reluctance to move towards fastener spacing less than 12 in. on center, so the focus of the results are on the 12 in. on-center tests. For those tests, joist thickness is varied from 0.033 in. to 0.097 in. and the resulting measured connection rotational stiffness is reported in Figure 10.

Table 3 Average measured connection rotational stiffness

Sheathing --> Cantilever (L) --> Fastener # --> Fastener Spacing -->	$k_{\phi c2}$ (lbf-in./in./rad)										
	Plywood				OSB			Gypsum			
	12"		24"		24"			12"		24"	
	6	10	6	12"	6	10	12"	6	10	6	10
362S162-33		81					100				
362S162-68		102					137				
800S200-54	116	109		97	137	113	77	103	77	91	99
800S250-54		116		124							
800S200-97			269	167			159		144		
1200S200-54		78				85					
1200S200-97				215			195				

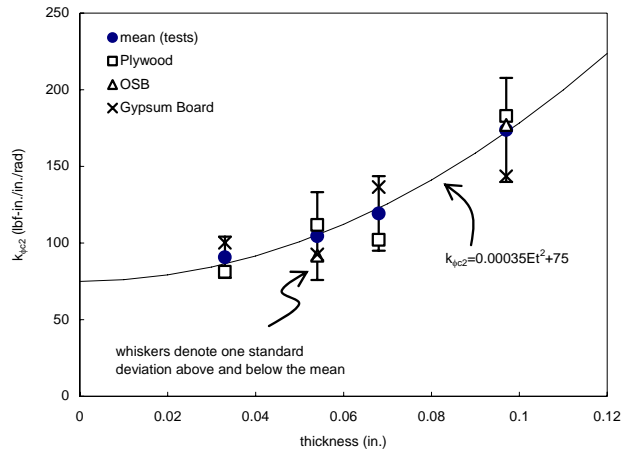


Figure 10 Connection rotational stiffness as a function of joist thickness

Figure 10 shows that an empirical relationship exists between the joist thickness and the connection rotational stiffness, largely independent of sheathing type (sheathing influence is captured through  $k_{\phi w}$ ), in Imperial units:

$$k_{\phi c2} = 0.00035Et^2 + 75 \tag{10}$$

where:  $k_{\phi w}$  = sheathing rotational stiffness in units of lbf-in./in. width / radian,  $E = 29,500,000$  psi, and  $t =$  nominal joist thickness in inches. Eq. 10 has no mechanical basis, and is merely a mathematical convenience. To date, simple

dimensionally consistent mechanical models that have been investigated (see Schafer et al. 2007) have lead to poor correlation with the data.

Comparison of the design method with the measured total rotational stiffness is provided in Table 4. Use of average tested values for the sheathing material leads to relatively high standard deviations for the plywood, but given the variability of plywood this seems acceptable. Simplification of the connection stiffness to values based on the thickness of the joist increases the variability of the predictive method for OSB and gypsum, but leaves the average test-to-predicted values within acceptable ranges. Use of Eq. 10 for  $k_{\phi c2}$  is statistically equivalent to using the average tabled values for connection stiffness. Use of design values for the sheathing bending rigidity (i.e., based on APA or GA tables) introduces conservatism and increases variability of the predictive method, but is nonetheless recommended for design practice at this time.

Table 4 Test-to-predicted ratio for total rotational stiffness  $k_{\phi 2}$

$k_{\phi w}$	$k_{\phi c2}$	plywood		OSB		gypsum board	
		ave.	st. dev.	ave.	st. dev.	ave.	st. dev.
Table 2a	tested values	0.97	0.21	1.00	0.06	1.00	0.02
Table 2a	thickness only*	0.98	0.22	0.97	0.14	0.92	0.16
Table 2a	Eq. 10	0.98	0.22	0.97	0.14	0.92	0.16
Table 2b, min values	Eq. 10	1.03	0.23	1.47	0.26	1.30	0.21

\*  $k_{\phi c2}$  is determined from the average tested values for a given joist thickness

The developed design model, in Specification language, is provided in the Appendix to this paper.

## DISCUSSION AND DESIGN GUIDANCE

From the standpoint of simplifying design, the desired rotational restraint is the  $k_{\phi}$  that will eliminate the distortional buckling limit state. For the sections tested in this experimental program, the  $k_{\phi}$  such that  $M_n$  for distortional buckling per C3.1.4(b) of AISI-S100 (2007) is always greater than  $M_n$  for a fully laterally braced ( $L_b=0$ ) section is determined and reported in Table 5. Comparison with Table 1 indicates the provided  $k_{\phi}$  in floor systems is typically not high enough to completely eliminate the distortional buckling limit state from consideration.

At longer unbraced lengths, lateral-torsional buckling will control and distortional buckling will not matter even if  $k_{\phi}=0$ , thus Table 5 also reports the unbraced length  $L_b$  at which  $M_n$  for distortional buckling per C3.1.4(b) of AISI-

S100 (2007) is greater than  $M_n$  (per C3.1.2) for lateral-torsional buckling (LTB). The length at which distortional buckling does not control is relatively short, so if blocking or bracing is spaced at lengths greater than  $L_b$  of Table 5 and that length is used for the LTB strength, then distortional buckling can be ignored.

Table 5 Minimum  $k_\phi$  and  $L_b$  to avoid distortional buckling for example sections  
avoid distortional buckling via

<b>Section</b>	<b><math>k_\phi</math></b> (lbf-in./in./rad)	<b><math>L_b</math></b> (ft)
362S162-33	36	4.4
362S162-33 (50ksi)	76	4.2
362S162-68	<i>DB never controls</i>	<i>DB never controls</i>
362S162-68 (50ksi)	<i>DB never controls</i>	<i>DB never controls</i>
800S200-33	31	6.6
800S200-33 (50ksi)	30	5.3
800S162-54	92	4.1
800S162-54 (50ksi)	190	4.1
800S200-54	300	6.1
800S200-54 (50ksi)	326	6.0
800S250-54	190	7.8
800S250-54 (50ksi)	233	7.1
800S200-97	<i>DB never controls</i>	<i>DB never controls</i>
800S200-97 (50ksi)	400	3.8
1200S200-54	128	5.9
1200S200-54 (50ksi)	123	5.6
1200S200-97	118	4.1
1200S200-97 (50ksi)	770	4.4

Finally, the first author of this paper recently completed a Technical Note for the Cold-Formed Steel Engineers Institute that provides additional tables, design aids, and extensive example calculations for distortional buckling. Designers and interested readers are referred to that document, as of this writing it is currently in press (complete and approved, but not yet printed) but should be available at [www.cfsei.org](http://www.cfsei.org) by the time of the conference.

## CONCLUSIONS

Distortional buckling of cold-formed steel members in bending can be significantly retarded, or even altogether precluded, depending on the rotational restraint provided by sheathing or other attachments to the compression flange. A series of cantilever tests on sheathed joists was conducted to assess the rotational stiffness provided by plywood, OSB, and gypsum board sheathing to typical cold-formed steel joists in use in North America. The tests indicate that plywood and OSB can provide beneficial restraint, but gypsum has inadequate rotational capacity due to a pull-through failure which occurs at low strength and rotation. The traditional cantilever testing protocol (AISI TS-1-02) was

successfully extended to include additional displacement measurements which were then used to separate the rotational stiffness into a sheathing component and a connection component. Evaluation of the connection stiffness indicated that joist thickness and fastener spacing are the most influential variables for predicting the available stiffness. A simple design method for predicting the component stiffness values was developed and shown to provide reasonable and conservative agreement with the conducted tests. This design method is recommended for use in the design of cold-formed steel framing systems where sheathing partially restrains distortional buckling.

#### ACKNOWLEDGMENTS

The authors of this study would like to acknowledge the American Iron and Steel Institute – Committee on Framing Standards for providing the gift that lead to this research. In addition we would like to acknowledge Johns Hopkins University undergraduate Eric Deuser who worked in the lab on the testing conducted herein, as well as lab technician Nickolay Logvinovsky who was invaluable in developing the test setup and conducting the testing. In addition, Simpson Strong-Tie donated the fasteners along with their QuikDrive system and screw guns for installation of the fasteners.

#### REFERENCES

- AISI (2002) “Rotational-Lateral Stiffness Test Method for Beam-to-Panel Assemblies” AISI TS-1-02, AISI Cold-Formed Steel Design Manual, 2002 Edition
- AISI-S100 (2007). North American Specification for the Design of Cold-Formed Steel Structural Members. American Iron and Steel Institute, Washington, D.C.
- APA (2004) Panel Design Specification, APA – The Engineered Wood Association.
- GA (2001) Gypsum Board Typical Mechanical and Physical Properties, Gypsum Association, Washington, D.C., GA-235-01.
- Hausler, R.W., Pabera, R.F. (1973). “Connection strength in thin metal roof structures.” Proc. of the 2<sup>nd</sup> Int’l. Spec. Conf. on Cold-Formed Steel Struct.. St Louis, Missouri.
- LaBoube, R.A. (1986). "Roof Panel to Purlin Connections: Rotational Restraint Factor", Proc. IABSE Colloq. on Thin-Walled Metal Struct. in Blds., Stockholm, Sweden.
- MRI (1981). “Determination of Rotational Restraint Factor ‘F’ for Panel to Purlin Connection Rigidity”. Observer’s Report: MRI Project No. 7105-G. Midwest Research Institute, Kansas City, Missouri.
- SFA (2000) Low-rise residential construction details, Steel Framing Alliance, Washington, D.C.
- Yu, C. (2005). “Distortional Buckling of Cold-Formed Steel Members in Bending”, PhD Thesis, Johns Hopkins University, Baltimore, MD.
- Yu, C., Schafer, B.W. (2003). “Local Buckling Tests on Cold-Formed Steel Beams.” ASCE, Journal of Structural Engineering. 129 (12) 1596-1606.
- Yu, C., Schafer, B.W. (2006). “Distortional buckling tests on cold-formed steel beams.” ASCE, Journal of Structural Engineering. 132 (4) 515-528.



## APPENDIX: PROPOSED DESIGN MODEL

Based on the results presented herein, this Appendix provides a method for calculating the rotational stiffness for use in distortional buckling calculations in “proposed” Specification language:

Calculation of the nominal distortional buckling strength in flexure per C3.1.4 of AISI S100, or per Appendix 1 of AISI S100 may utilize the beneficial system affect of sheathing fastened to the compression flange of *floor joists, ceiling joists, roof rafters, or wall studs* through the calculation of the rotational stiffness provided to the bending member,  $k_{\phi}$ .

Calculation of the nominal distortional buckling strength in compression per C4.2 of AISI S100, or per Appendix 1 of AISI S100 may utilize the beneficial system affect of sheathing fastened to both flanges of *floor joists, ceiling joists, roof rafters, or wall studs* through the calculation of the rotational stiffness provided to the bending member,  $k_{\phi}$ .

The rotational stiffness  $k_{\phi}$  shall be determined via

$$k_{\phi} = (1/k_{\phi w} + 1/k_{\phi c})^{-1} \quad (A1)$$

where the sheathing rotational restraint  $k_{\phi w}$  is calculated

for interior members (joists or rafters) with sheathing fastened on both sides as

$$k_{\phi w} = EI_w/L_1 + EI_w/L_2 \quad (A2)$$

for exterior members, or members with sheathing fastened on one side as

$$k_{\phi w} = EI_w/L_1 \quad (A3)$$

and:

$EI_w$  = sheathing bending rigidity,

for plywood and OSB use APA (2004) as given in Table A1(a),

for gypsum board use min values of GA (2001) as given in Table A1(b);

**note**, gypsum may be used for serviceability, but not for strength

$L_1, L_2$  = one half the joist spacing to the first and second sides respectively, as illustrated in Figure A2

where the connection rotational restraint  $k_{\phi c}$  is calculated for fasteners spaced 12 in. o.c. or closer in plywood, OSB, or gypsum

$$k_{\phi c} = \text{values per Table 2} \quad (A4)$$

Table A1 Sheathing Bending Rigidity  
 (a) Plywood and OSB bending rigidity per APA, Panel Design Spec. (2004)  
 divide table values by 12 to convert to lbf-in.<sup>2</sup>/in. of panel width

Span Rating	Stress Parallel to Strength Axis				Stress Perpendicular to Strength Axis			
	Plywood				Plywood			
	3-ply	4-ply	5-ply	OSB	3-ply	4-ply	5-ply	OSB
<b>PANEL BENDING STIFFNESS, EI (lb.-in.<sup>2</sup>/ft of panel width)</b>								
24/0	66,000	66,000	66,000	60,000	3,600	7,900	11,000	11,000
24/16	86,000	86,000	86,000	78,000	5,200	11,500	16,000	16,000
32/16	125,000	125,000	125,000	115,000	8,100	18,000	25,000	25,000
40/20	250,000	250,000	250,000	225,000	18,000	39,500	56,000	56,000
48/24	440,000	440,000	440,000	400,000	29,500	65,000	91,500	91,500
16oc	165,000	165,000	165,000	150,000	11,000	24,000	34,000	34,000
20oc	230,000	230,000	230,000	210,000	13,000	28,500	40,500	40,500
24oc	330,000	330,000	330,000	300,000	26,000	57,000	80,500	80,500
32oc	715,000	715,000	715,000	650,000	75,000	165,000	235,000	235,000
48oc	1,265,000	1,265,000	1,265,000	1,150,000	160,000	350,000	495,000	495,000

(b) Gypsum board bending rigidity (modified to APA units) Gypsum Assoc., GA-235-01 (2001)

Effective Stiffness (EI)* (typical range)		
Board Thickness (in.)	Lb-in <sup>2</sup> /in of width	N-mm <sup>2</sup> /mm of width
1/2	1500 to 4000	220,000 to 580,000
5/8	3000 to 8000	440,000 to 1,160,000

\* EI is dependent on board density, relative humidity, type of board, paper type, direction of board during testing and the amount of handling prior to measurement. In general the value of EI follows the following relationships:  
 Type X Gypsum Board > Regular Gypsum Board  
 Denser Gypsum Board > Less Dense Gypsum Board  
 Machine Direction > Cross Direction  
 Low Relative Humidity > High Relative Humidity

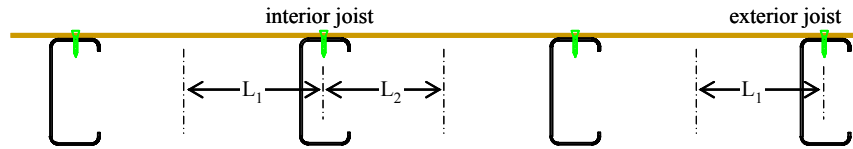


Figure A2 Illustration of L<sub>1</sub>, L<sub>2</sub> for sheathing rotational restraint

Table A2 Connection Rotational Restraint

t (mils)	t (in.)	k <sub>φc</sub> (lbf-in./in./rad)	k <sub>φc</sub> (N-mm/mm/rad)
18	0.018	78	348
27	0.027	83	367
30	0.03	84	375
33	0.033	86	384
43	0.043	94	419
54	0.054	105	468
68	0.068	123	546
97	0.097	172	766

- (1) fasteners spaced 12 in. o.c. or less
- (2) values based on  $k_{\phi c} = 0.00035Et^2 + 75$   
 with E in psi, t in in., k<sub>φc</sub> in lbf-in./in./rad



## **Simplified Methods for Predicting Elastic Buckling of Cold-Formed Steel Structural Members with Holes**

Cristopher D. Moen<sup>1</sup>, B.W. Schafer<sup>2</sup>

### **Abstract**

Simplified methods for approximating the local, distortional, and global critical elastic buckling loads of cold-formed steel columns and beams with holes are developed and summarized. These methods are central to the extension of the Direct Strength Method (DSM) to members with holes, as DSM employs elastic buckling properties to predict ultimate strength. The simplified methods are developed as a convenient alternative to shell finite element eigenbuckling analysis, which requires commercial software not always accessible to the engineering community. A variety of simplified methods are pursued including (a) hand methods founded primarily on classical plate stability approximations and (b) empirical extensions to the semi-analytical finite strip method (i.e., modifying and using the freely available, open source software, CUFSM). The proposed methods are verified with shell finite element eigenbuckling studies. The developed simplified methods are intended to be general enough to accommodate the range of hole shapes, locations, and spacings common in industry, while at the same time also defining regimes where explicit use of shell finite element analyses are still needed for adequate accuracy.

### **Introduction**

The forthcoming implementation of the Direct Strength Method (AISI-S100 2007; Schafer 2008) for cold-formed steel structural members with holes may be aided greatly by approximate methods for predicting elastic buckling behavior. Early research evaluated the influence of a single hole on the elastic buckling of

---

<sup>1</sup> Graduate Research Asst, Johns Hopkins University, Baltimore, MD, 21218, USA. (moen@jhu.edu)

<sup>2</sup> Associate Professor, Johns Hopkins University, Baltimore, MD, 21218, USA. (schafer@jhu.edu)

a thin square plate (Kumai 1952; Schlack Jr. 1964; Yoshiki and Fujita 1967). Holes were observed to reduce bending stiffness and concentrate the axial stress in the plate strips adjacent to the hole. This research led to a useful approximation of elastic buckling stress for plates with holes, based on assuming the strips adjacent to the hole act as unstiffened elements in compression (Kawai and Ohtsubo 1968). This approximation laid the groundwork for the development of the Specification's "unstiffened strip" approach, where elastic buckling of the plate strips are used to predict ultimate strength with the effective width method (Vann 1971; Yu and Davis 1973; Miller and Peköz 1994).

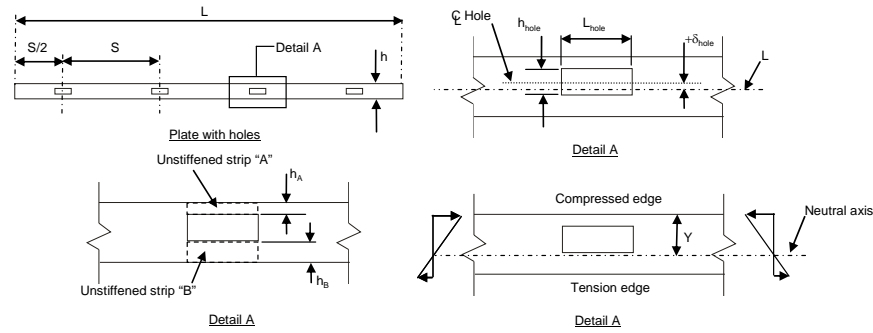
More recent thin shell finite element research on the elastic buckling of rectangular plates with multiple holes has demonstrated that the presence of holes can either increase or decrease the critical elastic buckling stress and change the length and quantity of the buckled half-waves, depending upon the quantity of hole material removed relative to the size of the plate (Brown and Yettram 2000; El-Sawy and Nazmy 2001; Moen and Schafer 2006). Research on an approximate method for calculating the critical elastic buckling loads of cold-formed steel columns with holes using the semi-analytical finite strip method has shown promise (Tovar and Sposito 2005). Progress on predicting the local, distortional, and global buckling of cold-formed steel rack posts with arrays of small holes has also been achieved (Kesti 2000; Sarawit 2003). The work presented here focuses on holes common in cold-formed steel framing, where multiple holes may exist along the length, but typically only a single hole exists in any one element (i.e., web or flange).

To facilitate the use of DSM for members with holes, approximate (and conservative) methods for calculating the elastic buckling of cold-formed steel members with holes are presented in this paper. The simplified approaches can be used in lieu of a full finite element eigenbuckling analysis. Elastic buckling approximations based on classical plate stability equations are presented for stiffened and unstiffened elements with holes. Finite strip approximations for local and distortional buckling of full cold-formed steel members with holes are introduced, and modifications to the classical column and beam stability equations are proposed for global buckling of members with holes. The simplified methods are intended to be general enough to accommodate the range of hole shapes, sizes, and spacings common in industry.

### **Elastic buckling of elements with holes**

Approximate elastic buckling prediction methods are presented here for two common element types in a thin-walled cross-section, stiffened elements (e.g.,

flange or web of a C-section) and unstiffened elements (e.g., flange lip of a C-section). In design, a stiffened element is approximated as a simply-supported plate and an unstiffened element is treated as a plate simply-supported on three sides and free on the fourth edge parallel to the application of load. Element and hole dimension notation for the prediction methods are summarized in Figure 1. The strips of plate between a hole and the plate edges are referred to as unstiffened strip “A” and unstiffened strip “B”. For stiffened elements in bending, the neutral axis location  $Y$  is measured from the compressed edge of the plate. Finally,  $\delta_{hole}$  is the transverse offset distance of a hole measured from the centerline of the plate.



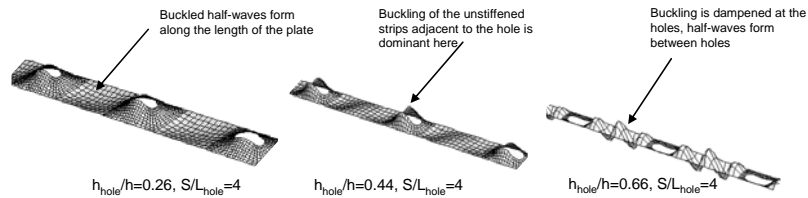
**Figure 1 Element and hole dimension definitions**

The viability of the element prediction methods has been verified within the following geometric limits (Moen 2008):

$$\frac{L_{hole}}{h_A} \leq 10, \frac{L_{hole}}{h_B} \leq 10, \frac{h_{hole}}{h} \leq 0.50, \frac{S}{L_{hole}} \geq 2, \frac{S}{h} \geq 1.5. \quad (1)$$

#### *Stiffened element in uniaxial compression*

This approximate method predicts the critical elastic buckling stress of stiffened elements with holes under uniaxial compression considering two potential elastic buckling states: buckling of the plate without influence from the hole(s), or buckling of the unstiffened strips adjacent to a hole, as shown in Figure 2.



**Figure 2 Buckled mode shapes for a stiffened element with holes**

The elastic buckling stress of a stiffened element with holes is approximated as

$$f_{crf} = \min[f_{cr}, f_{crh}] \quad (2)$$

The critical elastic buckling stress for plate buckling (without hole influence) is

$$f_{cr} = k \frac{\pi^2 E}{12(1-\nu^2)} \left(\frac{t}{h}\right)^2, \quad (3)$$

where  $k$  is commonly taken equal to 4 when considering long rectangular plates ( $L/h > 4$ ). When elastic buckling of the stiffened element is governed by the buckling of an unstiffened strip adjacent to the hole, the critical elastic buckling stress of the governing unstiffened strip is:

$$f_{crh,net} = \min[f_{crA}, f_{crB}] \quad (4)$$

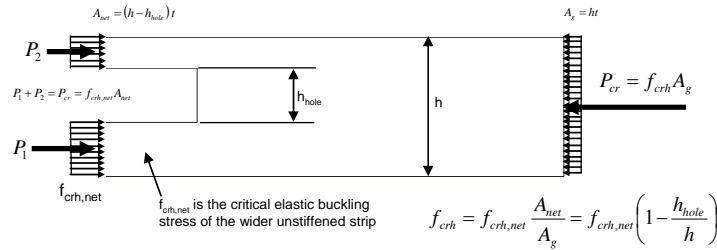
$$f_{cri} = k_i \frac{\pi^2 E}{12(1-\nu^2)} \left(\frac{t}{h_i}\right)^2 \text{ and } i = A \text{ or } B \quad (5)$$

The plate buckling coefficient  $k_i$  for unstiffened strips A and B are approximated by (Yu and Schafer 2007):

$$\text{for } L_{hole}/h_i \geq 1, \quad k_i = 0.425 + \frac{0.2}{(L_{hole}/h_i)^{0.95} - 0.6}, \quad (6)$$

$$\text{for } L_{hole}/h_i < 1, \quad k_i = 0.925, \text{ and } i = A \text{ or } B. \quad (7)$$

Eq. (6) accounts for the length of the unstiffened strip, as hole length shortens relative to the unstiffened strip width,  $k_i$  increases. This is an improvement over AISI-S100 which conservatively assumes the lowerbound  $k=0.425$  regardless of hole length. When  $L_{hole}/h_i$  is less than 1,  $k$  may be conservatively assumed equal to 0.925 via Eq. (7) or calculated directly by solving the classical stability equations for an unstiffened element (Timoshenko 1961).



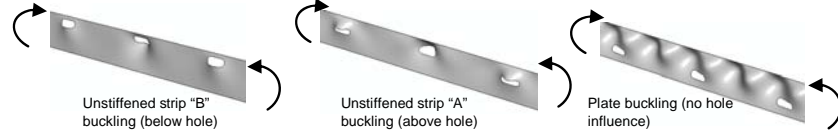
**Figure 3 Unstiffened strip elastic buckling stress conversion from the net to the gross section**

To compare the buckling stress from the unstiffened strip ( $f_{crh,net}$ ) to that of the entire plate ( $f_{cr}$ ) equilibrium between the net and gross section must be considered, as shown in Figure 3 and provided in the following:

$$f_{crh} = f_{crh,net} \left(1 - \frac{h_{hole}}{h}\right). \quad (8)$$

### Stiffened element in bending

Similar to the stiffened element in uniaxial compression, a stiffened element in bending must consider buckling of the unstiffened strips on either side of the hole, or buckling of the stiffened element independent of the holes, as illustrated in Figure 4. Either buckling of the unstiffened strip between the hole and the compressed edge of the plate (unstiffened strip “A”) or the tension edge of the plate (unstiffened strip “B”) may occur depending upon the transverse location of the hole in the plate, the width of the hole ( $h_{hole}$ ) relative to the depth of the plate ( $h$ ), and the location of the plate neutral axis ( $Y$ ). If the hole is completely contained within the tension region of the plate then the hole has a minimal influence on elastic buckling.



**Figure 4 Buckled mode shapes for a stiffened element in bending**

The critical elastic buckling stress of a stiffened element with holes in bending is approximated as:

$$f_{cr\ell} = \min[f_{cr}, f_{crh}] \quad (9)$$

The critical elastic buckling stress for a stiffened element in bending (without the influence of holes),  $f_{cr}$ , may be determined with Eq. (3), where the buckling coefficient  $k$  is calculated with AISI-S100-07 Eq. B2.3-2 (AISI-S100 2007):

$$k = 4 + 2(1 + \psi)^3 + 2(1 + \psi) \quad (10)$$

and  $\psi$  is the absolute value of the ratio of tensile stress to compressive stress applied to the stiffened element, i.e.:

$$\psi = |f_2 / f_1| = (h - Y) / Y \quad (11)$$

When elastic buckling of the stiffened element is governed by the buckling of an unstiffened strip adjacent to a hole, the critical elastic buckling stress is:

$$f_{crh,net} = \min[f_{crA}, f_{crB}] \quad (12)$$

Consideration of unstiffened strip “A” is required only if  $h_A < Y$ , i.e., at least a portion of the hole must lie in the compression region of the stiffened element. If that condition is met the elastic buckling stress for strip “A” is:

$$f_{crA} = k_A \frac{\pi^2 E}{12(1 - \nu^2)} \left( \frac{t}{h_A} \right)^2 \quad (13)$$

The plate buckling coefficient for the unstiffened strip “A” is approximated as



$$k_A = \frac{0.578}{\psi_A + 0.34} + \frac{2.70 - 1.76\psi_A}{0.024\psi_A + 0.035 + (L_{hole}/h_A)^2}, \text{ and } \psi_A = \frac{Y - h_A}{Y} \quad (14)$$

Eq. (14) is a modification of AISI-S100-07 Eq. B3.3-2 (AISI-S100 2007). This expression accounts for the gradient of the compressive stress distribution and the aspect ratio of the unstiffened strip (Moen 2008).

Consideration of unstiffened strip “B” is required only if  $h_A + h_{hole} < Y$ , i.e., only when the entire hole lies within the compressed region of the plate. For this case the buckling stress of the unstiffened strip, converted to a stress at the compressed edge is found as:

$$f_{crB} = k_B \frac{\pi^2 E}{12(1-\nu^2)} \left( \frac{t}{h_B} \right)^2 \left( \frac{Y}{Y - h_A - h_{hole}} \right) \quad (15)$$

Where the final term in Eq. (15) converts the buckling stress from the edge of unstiffened strip “B” to the edge of unstiffened strip “A” so that the two stresses ( $f_{crA}$  and  $f_{crB}$ ) may be compared in Eq. (12) to determine the minimum. The plate buckling coefficient for the unstiffened strip “B” is approximated as:

for  $L_{hole}/h_B \geq 0.75$

$$k_B = 0.340\psi_B^2 + 0.100\psi_B + 0.573, \quad (16)$$

for  $L_{hole}/h_B < 0.75$

$$k_B = 0.340\psi_B^2 + 0.100\psi_B + 0.573 + 15(0.75 - L_{hole}/h_B), \quad (17)$$

and the ratio of tension to compressive stresses is:

$$\psi_B = \frac{h - Y}{Y - h_A - h_{hole}}, \quad 0 \leq \psi_B \leq 10. \quad (18)$$

The plate buckling coefficient  $k_B$  is developed based on AISI-S100-07 Eq. B3.2-5 (AISI-S100 2007), but is modified to be applicable over a larger range of  $\psi_B$  and to account for the increase in  $k_B$  as the unstiffened strip aspect ratio tends to zero (i.e., a wide, short strip resulting from a small hole) (Moen 2008).

Conversion to the gross section for the comparison of stresses required in Eq. (9) requires that:

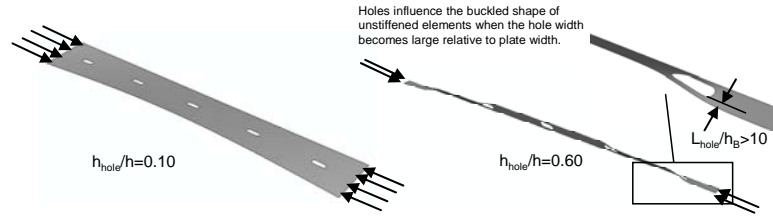
$$\text{for } h_A + h_{hole} \geq Y, \quad f_{crh} = f_{crh,net} \left( 1 + \psi_A \right) \frac{h_A}{Y}, \quad (19)$$

$$\text{for } h_A + h_{hole} < Y, \quad f_{crh} = f_{crh,net} \left[ 1 - \frac{h_{hole}}{Y} \left( 2\psi_A - \frac{h_{hole}}{Y} \right) \right]. \quad (20)$$

The conversion from  $f_{crh,net}$  at the net section of the plate to  $f_{crh}$  on the gross cross-section is obtained with a similar method to that described in Figure 3 for stiffened elements in uniaxial compression; the total compressive force at the net and gross cross-sections are assumed in equilibrium (Moen 2008).

#### *Unstiffened element in uniaxial compression*

For an unstiffened element in compression with hole(s), the approximation considers buckling of the entire unstiffened element without holes, buckling of the entire unstiffened element with holes shown in Figure 5a, and buckling of the unstiffened strip adjacent to the hole at the simply-supported edge. The plate strip adjacent to the hole and the free edge exhibits Euler buckling as shown in Figure 5b as its aspect ratio increases, which is not predicted by this method, motivating the  $L_{hole}/h_B \leq 10$  limit in Eq. (1).



**Figure 5 (a) Buckled mode shape of an unstiffened element with holes and (b) Euler buckling of the unstiffened strip at the free edge**

The elastic buckling stress of an unstiffened element in compression with holes is thus approximated as:

$$f_{crl} = \min[f_{cr}, f_{crh}]. \quad (21)$$

The critical elastic buckling stress prediction for plate buckling of the unstiffened element without holes ( $f_{cr}$ ) is calculated with Eq. (3), where  $k=0.425$  when considering long rectangular plates ( $L/h > 4$ ). The minimum critical elastic buckling stress of the unstiffened element with holes,  $f_{crh}$ , coincides with either buckling of the entire unstiffened element with holes or buckling of the unstiffened strip “A” adjacent to the hole and the simply supported edge, or:

$$f_{crh} = \min \left[ k \frac{\pi^2 E}{12(1-\nu^2)} \left( \frac{t}{h} \right)^2, f_{crA} \left( 1 - \frac{h_{hole}}{h} \right) \right] \quad (22)$$

where  $k$  is an empirical plate buckling coefficient derived from finite element eigenbuckling studies which reflect the reduced axial stiffness of an unstiffened element with holes (Moen 2008):

$$k = 0.425 \left( 1 - 0.062 \frac{L_{hole}}{h_A} \right). \quad (23)$$

$f_{crA}$  is calculated with Eq. (5) and modified by the factor  $(1 - h_{hole}/h)$  to convert the stress on the unstiffened strip “A” to the stress at the end of the plate so that it can be compared to the buckling stress of the unstiffened element.  $f_{crh}$  will always be predicted as less than or equal to  $f_{cr}$  with this method.

### Elastic buckling of members with holes

The element-based methods introduced in the previous section can be used as the first step for element-based effective width methods, or to approximate the (local) elastic buckling stress of cold-formed steel beams and columns. However, beam and column stability predictions determined from the element-based expressions are typically too conservative for use in DSM because they ignore beneficial inter-element interaction in the cross-section. Elastic buckling approximations are now presented for full cold-formed steel structural members with holes. The finite strip method is employed to predict local and distortional elastic buckling, and modifications to the classical column and beam stability equations are proposed for global buckling of cold-formed steel structural members with holes. Examples are presented which demonstrate the viability of the methods. Complete verification studies have also recently been completed and are provided in Moen (2008).

#### *Local buckling*

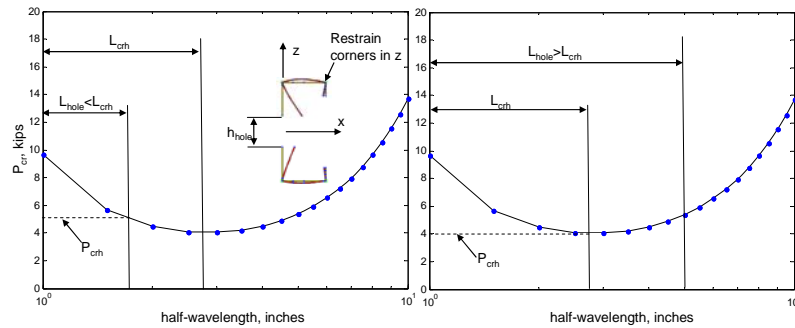
The approximate method for predicting the local elastic buckling behavior of cold-formed steel members with holes, presented here, is an extension of the element-based approximations, where local buckling is assumed to occur as either plate buckling of the entire cross-section or unstiffened strip buckling at the location of the hole. The use of the finite strip method allows for a more realistic prediction of  $P_{cr}$  (and  $M_{cr}$  in beams) including the interaction of the cross-section with the unstiffened strip.

The local critical elastic buckling load  $P_{cr}$  is approximated for a cold-formed steel column with holes as

$$P_{cr} = \min(P_{cr}, P_{crh}). \quad (24)$$

The calculation of the local critical elastic buckling load on the gross cross-section,  $P_{cr}$ , is performed using standard procedures defined in Appendix 1 of AISI-S100-07 (AISI-S100 2007).  $P_{crh}$  is calculated with the finite strip software CUFSM (Schafer and Adany 2006) using the net cross-section shown in Figure 6. The corners of the cross-section are restrained in the  $z$ -direction in the finite strip model to isolate local buckling from distortional buckling of the cross

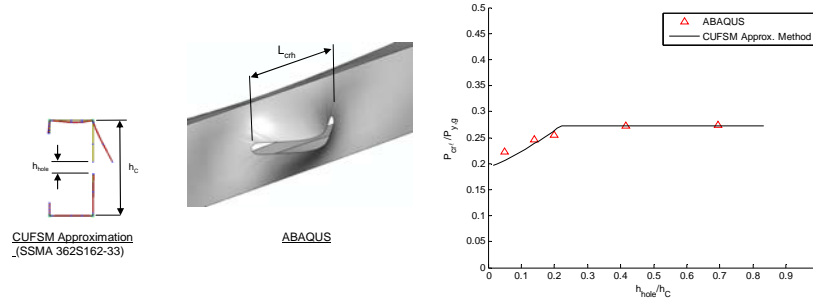
section. (This method of isolating local buckling is viable for C-section columns or beams with web holes. For other cross-section shapes and hole locations, fixity in the  $x$ -direction or both the  $x$ - and  $z$ -directions may be required.) An eigenbuckling analysis is performed with this net cross-section, and an elastic buckling curve is generated. The half-wavelength corresponding to the minimum buckling load is identified as  $L_{crh}$ . When  $L_{hole} < L_{crh}$ , as shown in Figure 6a,  $P_{crh}$  is equal to the buckling load at the length of the hole (FE and experimental studies support that buckling in the unstiffened strip occurs over the length of the hole). If  $L_{hole} \geq L_{crh}$  as shown in Figure 6b,  $P_{crh}$  is obtained at the minimum on the buckling curve (as in this case the hole is long enough to allow the natural wavelength of the unstiffened strip to form). Determining elastic buckling loads at specific half-wavelengths is a new and fundamentally different use of the finite strip method when compared to its primary application within DSM, which is calculating the lowest fundamental elastic buckling modes of cold-formed steel members. This method can also be implemented in its current form to predict  $M_{crf}$  for beams with holes.



**Figure 6** Local elastic buckling curve of net cross-section when (a) hole length is less than  $L_{crh}$  and (b) when hole length is greater than  $L_{crh}$

An example is now presented where the approximate method is employed to calculate  $P_{crf}$  for a 100 in. (2540 mm) long column with an SSMA 362S162-33 cross section and evenly spaced slotted web holes where  $S=20$  in. (508 mm) (SSMA 2001). Figure 7a compares the finite strip and ABAQUS mode shapes for  $h_{hole}/h_C=0.14$ , where  $h_C$  is the C-section web depth measured from the flange centerlines. The CUFSM approximate method predictions are plotted for a range of  $h_{hole}/h_C$  and compared with ABAQUS eigenbuckling predictions in Figure 7b. For this example, smaller hole widths lead to the largest reductions in  $P_{crf}$ . This counterintuitive result occurs because for small holes unstiffened strip buckling controls the local buckling behavior and for large holes, local buckling occurs between the holes. (One must keep in mind that for strength the net section in

yielding, as well as the elastic buckling load, ultimately determine the capacity, not just  $P_{crf}$ .)



**Figure 7 Comparison of CUFSM approximate method and ABAQUS local buckling (a) modes and (b) critical elastic buckling loads**

### *Distortional buckling*

An approximate method utilizing the finite strip method is introduced here for predicting the distortional critical elastic buckling load,  $P_{crdb}$  of cold-formed steel columns with holes. The method simulates the loss in bending stiffness of a C-section from the presence of a web hole within a distortional buckling half-wave by modifying the cross-section thickness in the finite strip method. The thickness of the entire web is reduced based on the relationship between web bending stiffness (derived with observations from ABAQUS thin shell elastic FE analyses) and the bending stiffness matrix terms of a finite strip element (Moen 2008). The distortional half-wavelength of the cross-section,  $L_{crdb}$  without holes is determined first using the gross section of the column in CUFSM to generate an elastic buckling curve. Half-wavelength  $L_{crd}$  is defined by the location of the distortional minimum, as shown in Figure 8. The web thickness is then modified in the finite strip method to account for the lost stiffness due to the holes via:

$$t_{web,hole} = \left(1 - \frac{L_{hole}}{L_{crd}}\right)^{1/3} t, \quad (25)$$

where  $t$  is the cross-section thickness. A similar modification to  $t$  has been proposed for web-slotted thermal structural studs (Kesti 2000). Finally, an additional finite strip analysis is performed and the elastic buckling curve is generated for the modified cross-section and  $P_{crd}$  (including the presence of the hole) is determined as the elastic buckling load occurring at  $L_{crd}$  as shown in Figure 8. Actually, only a single analysis at  $L_{crd}$  is required, but a range of  $L$ 's are shown in Figure 8 to illustrate the concept.

To demonstrate the method, the distortional critical elastic buckling load  $P_{crd}$  is approximated for a long column ( $L=100$  in. or 2540 mm) with an SSMA 250S162-68 cross-section and five evenly spaced slotted web holes where  $S=20$  in. (508 mm) and  $L_{hole}=4$  in. (102 mm). The width of the hole is varied relative to the web width, and ABAQUS eigenbuckling results are used to evaluate the viability of the method.  $P_{y,g}$  is the squash load of the column calculated with the gross cross-sectional area and assuming  $F_y=50$  ksi (345 MPa). The ABAQUS distortional buckling mode shape is provided in Figure 8b, when  $h_{hole}/h=0.63$ . Nine distortional half-waves form along the member in ABAQUS, with every other half-wave containing one slotted hole. The CUFSM prediction method is compared over a range of  $h_{hole}/h$  to ABAQUS eigenbuckling results in Figure 8b, demonstrating that the CUFSM approximation is a viable predictor of  $P_{crd}$ . This approximate method has also been implemented successfully for C-section beams with web holes (Moen 2008).

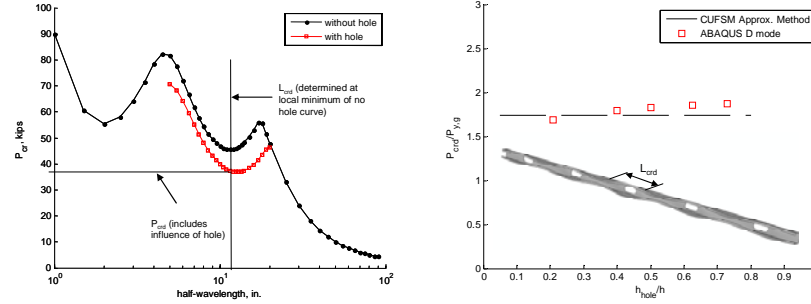


Figure 8 Distortional buckling (a) approximating  $P_{crd}$  for an SSMA 250S162-68 cross-section with holes and (b) comparing the approximate method to ABAQUS predictions

### Global buckling

The exact solution for the global (flexural only) critical elastic buckling load  $P_{cre}$  of a column with holes symmetrically spaced about the longitudinal midline can be derived using energy methods based on classical expressions (Timoshenko 1961) modified to account for holes (Moen 2008):

$$P_{cre} = \frac{\pi^2 EI_{avg}}{L^2}, \quad (26)$$

where

$$I_{avg} = \left( \frac{I_g L_{NH} + I_{net} L_H}{L} \right). \quad (27)$$

$I_g$  is the moment of inertia of the gross cross-section,  $I_{net}$  is the moment of inertia of the net cross-section,  $L_{NH}$  is the length of column without holes and  $L_H$  is the

length of column with holes (note that  $L_{NH} + L_H = L$ ).  $I_{avg}$  is the weighted average of the gross and net cross section moment of inertia along the column length.

An approximate method for calculating  $P_{cre}$  is proposed here which extends this “weighted properties” methodology in Eq. (27) to all of the cross-section properties of the column required to solve the classical cubic buckling equation for columns (Chajes 1974):

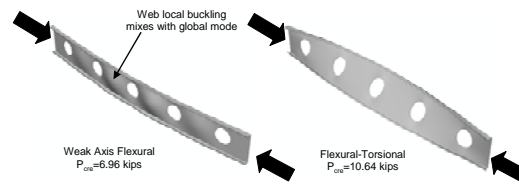
$$\left(P_{cre,y} - P\right)\left(P_{cre,x} - P\right)\left(P_{cre,\phi} - P\right) - \left(P_{cre,y} - P\right)\frac{P^2 x_o^2}{r_o^2} - \left(P_{cre,x} - P\right)\frac{P^2 y_o^2}{r_o^2} = 0, \quad (28)$$

including the cross-sectional area  $A$ , moment of inertia  $I_x$  and  $I_y$ , St. Venant torsional constant  $J$ , and shear center location. The computer program CUTWP solves Eq. (28) for any general cross-section and is freely available (Sarawit 2006). The net section properties can be calculated in CUFSM (or CUTWP) by reducing the sheet strip thickness to zero at the location of the hole. The net section warping torsion constant  $C_{w,net}$  is not as clearly defined though. If cross-section continuity at the hole is assumed,  $C_{w,net}$  is calculated assuming the full cross-section is resistant to warping (i.e., the line integral used to solve for the warping function is continuous around the cross-section). This approach leads to unconservative (stiffer) predictions of the actual average  $C_w$  derived from thin shell FE analysis (Moen 2008). Research is ongoing in this area, but for now it is recommended to conservatively assume  $C_{w,net}=0$  when calculating  $C_{w,avg}$  for use in Eq. (28). In addition to the approximate method proposed here for evenly spaced holes along the member length, global buckling approximations for columns with a single hole or irregularly spaced holes have also been recently developed (Moen 2008).

ABAQUS global eigenbuckling results are compared to the “weighted properties” approximation for an SSMA 1200S162-68 long column with evenly spaced circular holes. The length of the column  $L=100$  in. (2540 mm), the hole spacing  $S=20$  in. (508 mm), and the diameter of the circular hole is varied from  $h_{hole}/H=0.10$  to  $0.90$  where  $H$  is the out-to-out depth of the cross-section. Figure 9 provides the weak-axis flexural and flexural-torsional buckling modes when  $h_{hole}/H=0.50$ . Note that thin shell FE predicts local buckling mixing with the weak-axis flexural mode when  $h_{hole}/H>0.50$  because  $P_{cre}$  is reduced by the presence of holes to a magnitude similar to the local critical elastic buckling load  $P_{cr}=6.69$ kips (29.8 kN).

The gross cross-section properties  $A_g$ ,  $I_{x,g}$ ,  $I_{y,g}$ ,  $J_{y,g}$ ,  $C_{w,g}$  and the gross centroid and shear center locations of the SSMA 1200S162-68 cross section are

calculated in CUFSM. The net section properties  $A_{net}$ ,  $I_{x,net}$ ,  $I_{y,net}$ ,  $J_{y,net}$ , net centroid and shear center locations are then calculated in CUFSM assuming zero thickness at the hole.  $C_{w,net}$  is conservatively assumed equal to zero. Eq. (27) is employed to obtain the average cross-section properties of the column, which are then used in the cubic column buckling equation of Eq. (28) (or equivalently CUTWP) to arrive at the approximate weak-axis flexural and flexural-torsional critical elastic buckling loads.

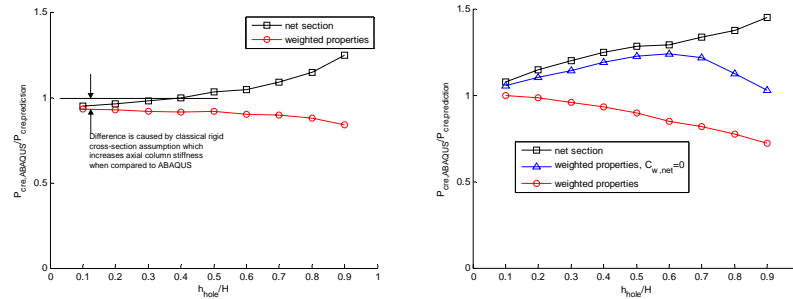


**Figure 9 Weak-axis flexural and flexural-torsional global buckling modes for an SSMA 1200S162-68 column with evenly spaced circular holes**

Figure 10a compares the weak-axis flexural critical elastic buckling load of the 1200S162-68 column calculated with the “weighted properties” prediction methods to ABAQUS eigenbuckling results. The ABAQUS calculation of  $P_{cre}$  is systematically 10% lower than the prediction method (even for a column without holes), which results from the assumption of a rigid cross-section in the classical stability equations. (The reduction in  $P_{cre}$  was confirmed in CUFSM, which like ABAQUS, accounts for plate-type deformations in elastic buckling calculations.) The approximate method is an accurate predictor of the weak-axis flexural  $P_{cre}$ , even when hole width becomes larger relative to web depth. The prediction of  $P_{cre}$  using just the net section properties is also plotted in Figure 10a as a conservative baseline.

Figure 10b compares the “weighted properties” methods to ABAQUS results for the second global mode, flexural-torsional column buckling. The accuracy of the prediction methods decrease with increase  $h_{hole}/H$  confirming that  $C_{w,avg}$  calculated with  $C_{w,net}$  assuming zero thickness at the hole, but otherwise continuous, overpredicts the average warping torsion stiffness of the column, especially as  $h_{hole}/H$  becomes large. Using  $C_{w,net}=0$  in the “weighted properties” approach is shown to be a conservative predictor of  $P_{cre}$ , although work is ongoing to improve the accuracy of the method for modes involving torsional buckling. The “weighted properties” method can also be employed for predicting the global buckling of beams with evenly spaced holes (Moen 2008).





**Figure 10 Comparison of “weighted properties” predictions to ABAQUS results for an SSMA 1200S162-68 column in (a) weak-axis flexural and (b) flexural-torsional buckling**

## Conclusions

Viable, conservative, approximate methods for predicting elastic buckling of cold-formed steel structural members with holes are presented here, both for elements and the entire member. The element-based approximations primarily rely on improvements to the unstiffened strip approach to account for hole length and stress gradients in the partially supported plates adjacent to the holes. Member-based approximations for local and distortional buckling of cold-formed steel rely on empirical modifications to the finite strip method to account for the new buckling modes introduced by the hole(s). For global buckling a “weighted properties” approach is proposed for cold-formed steel columns and beams with regularly spaced holes. Taken together the approximate methods provide a basic building block for needed improvements in both the element-based effective width method, and the member-based Direct Strength Method for the design of cold-formed steel structural members with holes.

## Acknowledgements

This research was conducted under the generous sponsorship of the American Iron and Steel Institute (AISI) and reflects insightful contributions from the dedicated members of the AISI Committee on Specifications.

## References

- AISI-S100. (2007). *North American Specification for the Design of Cold-Formed Steel Structural Members*, American Iron and Steel Institute, Washington, D.C.
- Brown, C.J., and Yettram, A.L. (2000). "Factors influencing the elastic stability of orthotropic plates containing a rectangular cut-out." *Journal of Strain Analysis for Engineering Design*, 35(6), 445-458.
- Chajes, A. (1974). *Principles of Structural Stability*, Prentice Hall College Div, Englewood Cliffs, NJ.
- El-Sawy, K.M., and Nazmy, A.S. (2001). "Effect of aspect ratio on the elastic buckling of uniaxially loaded plates with eccentric holes." *Thin-Walled Structures*, 39(12), 983-998.
- Kawai, T., and Ohtsubo, H. (1968). "A Method of Solution for the Complicated Buckling Problems of Elastic Plates with Combined Use of Rayleigh-Ritz's Procedure in the Finite Element Method." *Proceedings of the Second Conference on Matrix Methods in Structural Mechanics*, AFFDL-TR-68-150, Wright-Patterson Air Force Base, Ohio, 967-994.
- Kesti, J. (2000). "Local and Distortional Buckling of Perforated Steel Wall Studs," Dissertation/Thesis, Helsinki University of Technology, Espoo, Finland.
- Kumai, T. (1952). "Elastic stability of the square plate with a central circular hole under edge thrust." *Reports of Research Institute for Applied Mechanics*, 1(2).
- Miller, T.H., and Peköz, T. (1994). "Unstiffened strip approach for perforated wall studs." *ASCE Journal of Structural Engineering*, 120(2), 410-421.
- Moen, C.D. (2008). "Direct Strength Design for Cold-Formed Steel Members with Perforations," Ph.D. Thesis, Johns Hopkins University, Baltimore.
- Moen, C.D., and Schafer, B.W. (2006). "Impact of holes on the elastic buckling of cold-formed steel columns with applications to the Direct Strength Method." *Eighteenth International Specialty Conference on Cold-Formed Steel Structures*, Orlando, FL, 269-283.
- NAS. (2007). *Supplement to the North American Specification for the Design of Cold-Formed Steel Structural Members, Appendix 1*, American Iron and Steel Institute, Washington, D.C.
- Sarawit, A. (2003). "Cold-Formed Steel Frame and Beam-Column Design," Ph.D. Thesis, Cornell University, Ithaca.
- Sarawit, A. (2006). "CUTWP Thin-walled section properties, December 2006 update <[www.ce.jhu.edu/bschafer/cutwp](http://www.ce.jhu.edu/bschafer/cutwp)> ", accessed January 2008.
- Schafer, B.W. (2008). "Review: The Direct Strength Method of cold-formed steel member design." *Journal of Constructional Research*, 64(7/8), 766-778.
- Schafer, B.W., Adany, S. (2006). "Buckling analysis of cold-formed steel members using CUFSM: conventional and constrained finite strip methods." *Eighteenth International Specialty Conference on Cold-Formed Steel Structures*, Orlando, FL.
- Schlack Jr., A.L. (1964). "Elastic stability of pierced square plates." *Experimental Mechanics*, 4(6), 167-172.
- SSMA. (2001). "Product Technical Information, ICBO ER-4943P." Steel Stud Manufacturers Association, [www.ssma.com](http://www.ssma.com).
- Timoshenko, S.P., Gere, James M. (1961). *Theory of Elastic Stability*, McGraw-Hill, New York.
- Tovar, J., and Spoto, T. (2005). "Application of direct strength method to axially loaded perforated cold-formed steel studs: Distortional and local buckling." *Thin-Walled Structures*, 43(12), 1882-1912.
- Vann, P.W. (1971). "Compressive buckling of perforated plate elements." *First Specialty Conference on Cold-formed Structures*, Rolla, Missouri, 58-64.
- Yoshiki, M., and Fujita, Y. (1967). "On the Buckling Strength of Perforated Plates (1)." *Proceedings of the Society of Naval Architects of Japan*, No. 122.
- Yu, C., and Schafer, B.W. (2007). "Effect of Longitudinal Stress Gradients on Elastic Buckling of Thin Plates." *ASCE Journal of Structural Engineering*, 133(4), 452-463.
- Yu, W.W., and Davis, C.S. (1973). "Cold-formed steel members with perforated elements." *ASCE J Struct Div*, 99(ST10), 2061-2077.



## **Generalized Beam Theory Formulation Able to Capture Load Application and Localized Web Buckling Effects**

Nuno M.F. Silva<sup>1</sup>, Dinar Camotim<sup>2</sup> and Nuno Silvestre<sup>3</sup>

### **Abstract**

This paper presents the formulation and illustrates the application of a novel Generalized Beam Theory (GBT) formulation able to handle the influence of localized effects on the buckling behavior of prismatic thin-walled members (*e.g.*, cold-formed steel profiles) – for instance, this formulation accounts for effects stemming from (i) the position of transverse loads (with respect to cross-section shear centers) or (ii) the occurrence of web buckling phenomena (*e.g.*, web crippling). In order to achieve this goal, the GBT formulation traditionally employed in buckling analyses must be enhanced by including specific (i) non-linear terms and (ii) transverse extension modes. Due to its unique modal nature and computational efficiency, this GBT formulation/implementation is a very advantageous alternative to shell finite element analyses – at present, the only available method to capture the above localized effects rigorously. In order to illustrate the application and capabilities of the proposed GBT formulation-implementation, one presents and discusses numerical results concerning the buckling behavior of (i) hat and I-section cantilevers acted by transverse tip point loads applied at various cross-section points, and (ii) I-section simply supported beams under top-flange distributed and point loads – one also assesses how end support transverse web stiffeners improve the beam buckling behavior. For validation, the GBT results are compared with values reported in the literature and/or yielded by ABAQUS shell finite element analyses.

---

<sup>1</sup>Ph.D. Student, <sup>2</sup>Associate Professor and <sup>3</sup>Assistant Professor, Department of Civil Engineering and Architecture, IST/ICIST, Technical University of Lisbon, Portugal.

## Introduction

Due to the growing demand for structural configurations that are progressively more efficient and/or “architecturally daring” (*i.e.*, leaving a lasting aesthetic impression), steel designers have been frequently led to solutions involving extremely slender thin-walled members (*e.g.*, cold-formed steel profiles). However, optimizing the geometry of a member, thus minimizing the material expenditure and/or maximizing the visual impact, invariably renders it highly susceptible to several types of instability: global, local and *localized* buckling phenomena – the latter, which receive particular attention in this work, often stem from the existence of very slender walls (usually webs) and/or from the presence of transverse loads, which may act at different cross-section points.

It is well known that the lateral-torsional buckling behavior of thin-walled metal or FRP composite beams is strongly affected by the locations of the points of application of transversal loads acting on them – the relevant quantity is the vertical distance to the cross-section shear centers. While this effect has been properly quantified in steel beams for decades (*e.g.*, Trahair 1993), the same is not true in the case of FRP composite beams – for instance, it was only a dozen years ago that Turvey (1996) addressed this issue: he conducted an experimental, analytical and numerical investigation on the lateral-torsional buckling behavior of I-section pultruded cantilevers acted by tip point loads applied in the top flange, bottom flange and shear center. However, concerning the influence of the transverse load position on the member local-plate, distortional and/or localized buckling phenomena<sup>2</sup> (*i.e.*, those involving cross-section in-plane deformations), the amount of available research work is much more scarce, a statement that is particularly true for distortional buckling – to the authors best knowledge, this topic has only been addressed by (i) Gonçalves & Camotim (2004) and Gonçalves (2007), who only studied a specific problem (hat-section cantilever under acted by a tip load) using an approximate one-dimensional model, and (ii) Samanta & Kumar (2006) and Kumar & Samanta (2006), who used shell finite elements to investigate the “distortional buckling”<sup>3</sup> of singly symmetric I-section beams acted by transverse loads applied at their top and bottom flanges.

---

<sup>2</sup> Note that local-plate and distortional buckling are sometimes grouped under the designation “local buckling”, characterized by the fact that the member axis remains undeformed. On the other hand, local-plate buckling is often termed “local buckling”. As for distortional buckling, it may occur in members with end-stiffened lipped flanges (*e.g.*, lipped channel, hat-section or rack-section profiles) and always involves rigid body rotations of member wall assemblies – *e.g.*, a compressed flange-lip assembly rotating about the corresponding web-flange longitudinal edge).

<sup>3</sup> It is important to mention that this “distortional buckling” phenomenon is not the same that was described in the previous footnote (which cannot occur in I-section beams with no lipped flanges). Indeed, it is triggered by the (lateral) transverse bending and has been originally designated as “lateral-distortional buckling” by Bradford (1992) – this designation was subsequently also used by Pi and Trahair (1997). Very recently, Dinis *et al.* (2008) proposed “lateral-torsional-distortional buckling”, a wording that, in their opinion, reflects more closely the mechanics of this phenomenon.

Concerning the localized buckling phenomena that stem from the high slenderness of the member walls (usually webs), they may arise in several practical applications – for instance, industrial crane girders and large-span steel or composite (steel-concrete) bridges. In both cases, the beams have virtually always very slender webs and, when acted by top-flange point loads, often experience web localized buckling phenomena, such as web crippling or shear buckling. Unlike lateral-torsional and local-plate buckling, which are rather well studied and understood phenomena, is it fair to say that there are practically no simplified (one-dimensional) models to assess, with reasonable accuracy, instabilities stemming from transverse normal and/or shear stresses – indeed, the few available models either (i) are of a semi-empirical nature and exhibit a low and somewhat unpredictable accuracy (*e.g.*, the design formulae and methodologies prescribed by most of the current steel codes, such as the very recently published Part 1-5 of Eurocode 3 – CEN 2006), or (ii) have a limited range of application (*e.g.*, cannot handle buckling mode coupling effects). Therefore, it is not surprising that nearly all the works reported on localized buckling phenomena in thin-walled members (mostly involving I-beam webs) concern experimental and/or shell finite element numerical simulations. In this context, it is worth mentioning two recent publications: (i) the experimental study carried out by Lucic & Scepanovic (2004), dealing with web crippling of transversally stiffened I-section beams acted by transverse loads applied eccentrically with respect to the web plane, and (ii) the numerical investigation conducted by Topkaya (2006), who analyzed the buckling behavior of simply supported I-beams with laterally restrained compression flanges. The latter provided evidence that such I-beams may exhibit a critical buckling mode that combines lateral-torsional and web local-plate buckling features – moreover, the author (i) performed a parametric study and, on the basis of the results obtained, (ii) developed semi-empirical formulae to estimate the critical loads/stresses associated with this “mixed” buckling mode.

Despite the fairly intense research activity currently going on in this area, steel designers are not yet equipped with numerical tools allowing them to assess efficiently and rigorously the localized web buckling behavior in thin-walled members with arbitrary loadings and support conditions. Indeed, they must either (i) use the semi-empirical design formulae and methodologies prescribed by the steel codes or (ii) resort to rather complex shell finite element analyses – this last option is very time consuming (besides the computational needs, one must not also forget the laborious data input and result interpretation) and clearly incompatible with the current design office practice in routine applications.

Recently, a novel approach to analyze the local and global buckling behavior of prismatic thin-walled members has been explored and shown to constitute a very attractive/advantageous alternative to the shell finite element modeling – this approach is based on the Generalized Beam Theory (GBT), which may be seen as a beam (one-dimensional) theory that (i) incorporates local (in-plane cross-section) deformations

and (ii) exhibits very convenient modal features. By expressing the member deformed configuration (or buckling mode shape) as a combination of *deformation modes* with clear structural meanings (local-plate, distortional and global modes), GBT provides elegant, rigorous and computationally efficient solutions for several structural problems concerning prismatic thin-walled members (*e.g.*, Camotim *et al.* 2004, 2006a, 2006b, and Bebbiano *et al.* 2007) – these solutions include the majority of the (geometrically) linear and non-linear effects captured by the shell finite element analyses, but at a much lower computational cost.

The aim of this paper is (i) to present main steps involved in the formulation and implementation, and (ii) illustrate the application of a GBT-based beam finite element that incorporates non-linear terms stemming from the presence of pre-buckling normal (longitudinal and transverse) and shear stresses. This makes it possible to capture (i) the influence of the location of a transverse load point of application<sup>4</sup> and also (ii) localized wall (web) buckling effects. The illustrative numerical results presented and discussed concern the buckling behavior of (i) hat and I-section cantilevers acted by transverse tip point loads applied at various cross-section points, and (ii) I-section simply supported beams under top-flange distributed and point loads (*i.e.*, highly prone to web crippling) – one also assesses how the inclusion of end support transverse web stiffeners improve the beam buckling behaviour. In order to provide validation for the proposed approach and, at the same time, offer a better grasp of its capabilities, the GBT-based results are compared with values yielded by shell finite element analyses carried out in the code ABAQUS (HKS 2002).

### Fundamental GBT Equations

Consider the arbitrary thin-walled prismatic member shown in figure 1, where  $x$ ,  $s$  and  $z$  are local coordinates along the longitudinal direction (member axis), cross-section mid-line and the wall thickness –  $u(x,s)$ ,  $v(x,s)$  and  $w(x,s)$  are the corresponding member mid-surface displacement fields. The key GBT feature is the fact that these displacement components are expressed by means of a linear combination of *cross-section deformation modes* – *i.e.*, one has

$$u(x,s) = u_k(s)\phi_{k,x}(x) \quad v(x,s) = v_k(s)\phi_k(x) \quad w(x,s) = w_k(s)\phi_k(x) \quad , \quad (1)$$

---

<sup>4</sup> As mentioned earlier, Gonçalves & Camotim (2004) and Gonçalves (2007) also used GBT to study the influence of the location of a tip transverse load point of application point on the distortional and lateral-torsional buckling behaviour of hat-section cantilevers. Although the approximate methodology adopted by these authors proved to be adequate to analyse this particular problem (as far as anti-symmetric distortional and lateral-torsional buckling are concerned), it lacks generality – *e.g.*, the symmetrical distortional and local-plate buckling behaviours of these same hat-section cantilevers are not handled properly (the web in-plane rotations are no longer rigid-body ones, due to significant transversal bending).

where  $u_k(s)$ ,  $v_k(s)$  and  $w_k(s)$  ( $k=1,\dots,n$ ) are deformation mode shapes and  $\phi_k(x)$  functions providing the longitudinal variation of their amplitudes. The cross-section deformation modes may be either (i) global (axial extension, major/minor axis bending and torsion), (ii) local (distortional and local-plate), (iii) (warping) shear or (iv) transversal extension ones – moreover, they are determined by means of a GBT “trademark”

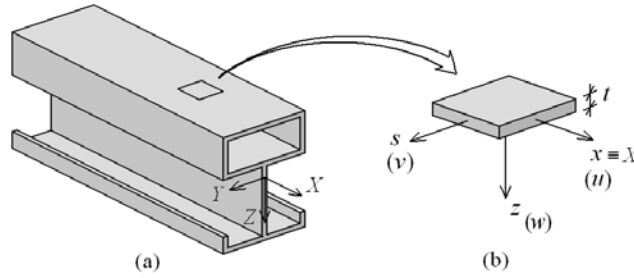


Fig. 1: (a) Geometry and (b) local coordinate system and corresponding displacement field and local of an arbitrary thin-walled cross-section

procedure termed *cross-section analysis*. The concepts and operations involved in this procedure, which are not addressed here, can be found in a very recent paper by the authors (Silva *et al.* 2008) – similar (but not identical) procedures have also been proposed by other authors, namely Silvestre & Camotim (2002) and Gonçalves (2007).

Assuming that the member is made of a material with linear elastic constitutive law, it is possible to derive the GBT equations governing its first order and buckling behaviors – they are given by

$$C_{ik}\phi_{k,xxxx} + (E_{ik} + E_{ki} - D_{ik})\phi_{k,xx} + B_{ik}\phi_k - \lambda \left( C_{jik}(\phi_{j,xx}^0 \phi_{k,x})_{,x} + D_{jik}(\phi_{j,x}^0 \phi_k)_{,x} - D_{jki}\phi_{j,x}^0 \phi_{k,x} - B_{jik}\phi_j^0 \phi_k \right) - q_i = 0 \quad , \quad (2)$$

where (i) the second-order tensors (matrices)  $C_{ik}$ ,  $B_{ik}$ ,  $D_{ik}$  and  $E_{ik}$  account for the linear stiffness values associated with (i<sub>1</sub>) longitudinal extensions, (i<sub>2</sub>) transverse extensions, (i<sub>3</sub>) shear strains and (i<sub>4</sub>) coupling between longitudinal and transverse extensions due to Poisson effects<sup>5</sup>, and (ii) the third-order tensors  $C_{jik}$ ,  $B_{jik}$  and  $D_{jik}$  take into consideration the member geometric stiffness and concern the works done by the (ii<sub>1</sub>) longitudinal normal, (ii<sub>2</sub>) transverse normal and (ii<sub>3</sub>) shear stresses, corresponding to the non-linear terms of the longitudinal extensions  $\epsilon_{xx}^{NL} = (v_{,x}^2 + w_{,x}^2)/2$ , transverse extensions ( $\epsilon_{ss}^{NL} = w_{,s}^2/2$ ) and shear strains ( $\gamma_{ss}^{NL} = w_{,x}w_{,s}$ ). The components of these second and third-order tensors are given by the expressions

<sup>5</sup> The tensor components  $E_{ik}$  should not be confused with the material Young's modulus  $E$ .



$$\begin{aligned}
C_{ik} &= \frac{E}{1-\nu^2} \int_b \left( t u_i u_k + \frac{1}{12} t^3 w_i w_k \right) ds \\
B_{ik} &= \frac{E}{1-\nu^2} \int_b \left( t v_{i,s} v_{k,s} + \frac{1}{12} t^3 w_{i,ss} w_{k,ss} \right) ds \\
D_{ik} &= G \int_b \left( t (u_{i,s} + v_i)(u_{k,s} + v_k) + \frac{1}{3} t^3 w_{i,s} w_{k,s} \right) ds \\
E_{ik} &= \frac{\nu E}{1-\nu^2} \int_b \left( t u_i v_{k,s} + \frac{1}{12} t^3 w_i w_{k,ss} \right) ds
\end{aligned} \tag{3}$$

$$\begin{aligned}
C_{jik} &= \frac{E}{1-\nu^2} \int_b \int_t (u_j - z w_j)(v_i v_k + w_i w_k) dz ds \\
B_{jik} &= \frac{E}{1-\nu^2} \int_b \int_t (v_{j,s} - z w_{j,ss}) w_{i,s} w_{k,s} dz ds \\
D_{jik} &= G \int_b \int_t (u_{j,s} + v_j - 2z w_{j,s}) w_i w_{k,s} dz ds
\end{aligned} \tag{4}$$

Finally, a vector  $q_i$  component represents the work per unit length done by a distributed load having components  $q_x$ ,  $q_s$  and  $q_z$  (deemed to be applied at the wall mid-surfaces) and associated with deformation mode  $i$  – thus, one has

$$q_i = \int_b (q_s v_i + q_z w_i - q_{x,x} u_i) ds \tag{5}$$

As mentioned above, system (2) provides the equilibrium equations governing the member first-order and buckling behaviors – they are obtained by assigning null values to either (i) the load parameter  $\lambda$  (first-order behavior) or (ii) the vector  $q_i$  components (buckling behavior). One should still mention that, when calculating the third-order tensor (geometric stiffness) components, the inclusion of the pre-buckling stresses and deformations effects is accomplished by means of the modal amplitude functions  $\phi_j^0$  (see (2)). These pre-buckling stresses (i) are the solution of the member first-order analysis under a reference loading profile (loading profile multiplying the load parameter  $\lambda$  in buckling analyses), and (ii) include the transverse normal stresses that appear when the loads are not applied at the cross-section shear center<sup>6</sup> – they may be compressive or tensile, depending on whether the load is applied above or below this shear center.

---

<sup>6</sup> Indeed, this is precisely the effect that this work aims at investigating.

### GBT-Based Finite Element Solutions

The member first-order and buckling analyses are performed by means of GBT-based beam finite element formulations, which are similar to the one originally developed by Silvestre & Camotim (2003), in the context of the buckling analysis of pultruded FRP columns. The following strategy is adopted to approximate (discretize) the modal amplitude functions  $\phi(x)$ : (i) the functions concerning deformation modes involving non-null transverse displacements  $v_i(s)$  and/or  $w_i(s)$  are approximated by means of Hermite cubic polynomials, and (ii) those related with deformation modes involving only axial displacements  $u_i(s)$  (*i.e.*, the axial extension and shear modes) are approximated using linear Lagrange polynomials. The corresponding element linear and geometric stiffness matrices are given by

$$K_{ik\alpha\beta}^e = C_{ik} \int_{L_e} \psi_{\alpha,xx} \psi_{\beta,xx} dx + B_{ik} \int_{L_e} \psi_{\alpha} \psi_{\beta} dx + D_{ik} \int_{L_e} \psi_{\alpha,x} \psi_{\beta,x} dx + E_{ik} \int_{L_e} \psi_{\alpha,xx} \psi_{\beta} dx + E_{ki} \int_{L_e} \psi_{\alpha} \psi_{\beta,xx} dx \quad (6)$$

$$G_{ik\alpha\beta}^e = \left( C_{jik} \int_{L_e} \psi_{\eta,xx} \psi_{\alpha,x} \psi_{\beta,x} dx + B_{jki} \int_{L_e} \psi_{\eta} \psi_{\alpha} \psi_{\beta} dx + D_{jik} \int_{L_e} \psi_{\eta,x} \psi_{\alpha,x} \psi_{\beta} dx + D_{jki} \int_{L_e} \psi_{\eta,x} \psi_{\alpha} \psi_{\beta,x} dx \right) d_{j\eta}^0 \quad (7)$$

where (i) subscripts  $i, j, k$  identify the deformation modes, (ii) subscripts  $\alpha, \beta$  concern the  $\phi(x)$  approximation nature (Hermite/Lagrange polynomials) and (iii)  $d_{j\eta}^0$  are the pre-buckling generalized displacement components – the latter are obtained through the finite element solution of the first-order problem

$$\mathbf{d}^0 = \mathbf{K}^{-1} \mathbf{f}^0 \quad (8)$$

where  $\mathbf{K}$  and  $\mathbf{f}^0$  are the member overall linear stiffness matrix and load vector. Finally, a member buckling analysis involves solving the eigenvalue problem

$$(\mathbf{K} - \lambda \mathbf{G}) \mathbf{d} = 0 \quad (9)$$

where vector  $\mathbf{d}$  assembles the (discretized) degrees of freedom.

It is still worth pointing out that the GBT analyses required to solve the above first-order and buckling problems do not necessarily have to involve the same sets of deformation modes. For instance, very often one does not need to include shear and transverse extension modes in the buckling analyses. On the other hand, the inclusion of such deformation modes in the first-order analyses is absolutely crucial to obtain precise pre-buckling generalized displacement components  $d_{j\eta}^0$  – they are then used to

evaluate “exact” pre-buckling stresses, which play a key role in determining accurate geometric stiffness values.

### Illustrative Examples

In this section one presents and discusses numerical results that illustrate the application and potential of the developed GBT formulation – all are elastic buckling problems. The first two problems concern simply supported I-beams with slender webs are intended to (i) illustrate the various types of buckling phenomena that may occur in the presence of transverse loadings (applied at the top flange), (ii) assess the (beneficial) effect of adding end support transverse web stiffeners and (iii) validate the proposed GBT model, by comparing its results with ABAQUS shell finite element values. The last two problems concern the effect of the position of the load point of application point on the buckling behavior of I-section and hat-section cantilevers – in this case, the GBT-based results are validated through the comparison with values (i) reported by Bebiano *et al.* (2007), for the I-section cantilevers, and (ii) again yielded by ABAQUS shell finite element analyses, for the hat-section cantilevers.

**Simply Supported I-Beams.** The first two illustrative examples concern simply supported beams<sup>7</sup> made of S460 steel ( $E=210\text{ GPa}$ ,  $\nu=0.3$ ,  $f_{yk}=460\text{ MPa}$ ) and exhibiting the I-section geometry depicted in figure 2(a). They are acted by two transverse loadings applied at the top flange: either (i) two point loads (*i.e.*, distributed over a very small area, to be more precise) or (ii) a uniformly distributed load along the whole beam span. It is worth noting that, due to the high web slenderness, this cross-section is classified as “Class 4” according to Eurocode 3 (CEN 2005) – this implies that the beam ultimate strengths are strongly influenced by the occurrence of web-triggered local and/or localized buckling phenomena. For the discretization shown in figure 2(b), the GBT cross-section analysis leads to 30 deformation modes: global (1-4), local-plate (5-12), shear (13-21) and transverse extension (22-30) modes<sup>8</sup> – the main features of the most relevant of them are displayed in figure 3<sup>9</sup>.

First, one analyzes the beam schematically depicted in figure 4, (i) with length  $L=200\text{ cm}$ , (ii) with the simple supports located in the bottom flange and (iii) acted by two symmetric vertical point loads applied at the top flange and in

<sup>7</sup> The end cross-sections can deform freely, since only the web-flange corner displacements are restrained – they are strictly necessary to avoid cross-section rigid-body motions (global modes).

<sup>8</sup> All deformation modes are normalized to exhibit unit maximum displacement components – either (i)  $v$  or  $w$  (if they are not both null) or (ii)  $u$  (if  $v$  and  $w$  are both null).

<sup>9</sup> Recall that the shear and transverse extension deformation modes only have to be included in the member first-order analyses.

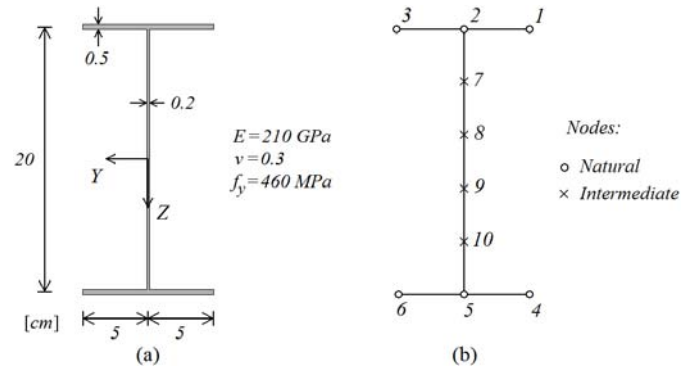


Fig. 2: I-section (a) geometry and dimensions, and (b) GBT nodal discretization

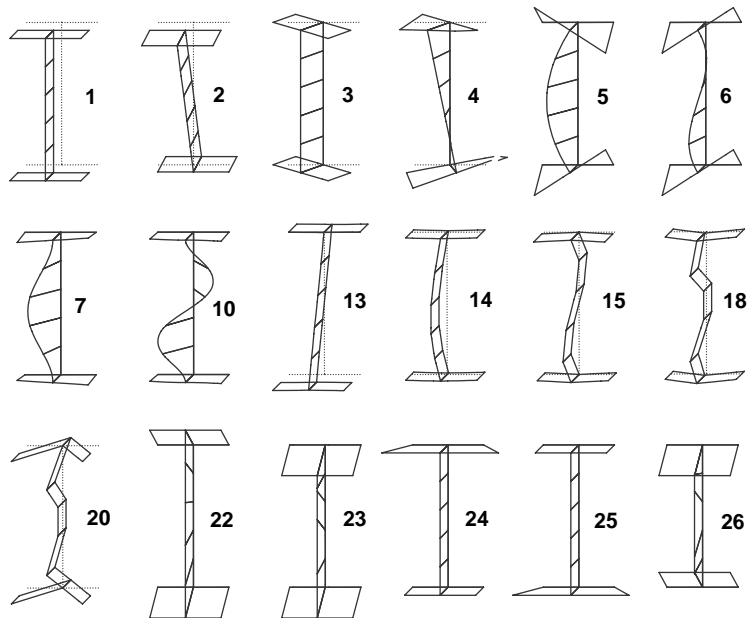


Fig. 3: Main features of the most relevant I-section deformation modes: global (1-4), local-plate (5-12), shear (13-21) and transverse extension (22-30)

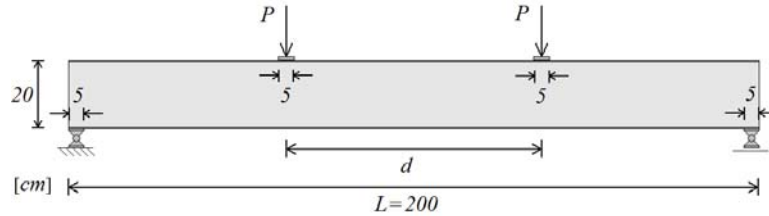


Fig. 4: Simply supported I-section beam acted by two symmetric point loads

the plane of web – their points of application are a (variable) distance  $d$  apart. One assumes that (i) the point loads are effectively uniformly distributed over a length  $s=5\text{ cm}$  (see fig. 4) (ii) the beam is only laterally restrained at the top and bottom flanges of the end cross-sections (supports), and (iii) the flange displacements are free along the whole beam length. Concerning the presence of web transverse stiffeners, one addresses two cases: (i) no stiffeners and (ii) stiffeners only at the beam end cross-sections – each stiffener is formed by two steel plates of thickness  $t_s=5\text{ mm}$ , normal to the web and connecting the two flanges along their full widths.

GBT-based analyses are employed to assess the variation of the critical loadings  $P_{cr}$  with the parameter  $d/L$  (normalized distance between the two point loads), both for beams with and without web transverse stiffeners at the supports – all 30 deformation modes are included in the analyses<sup>10</sup> and the beams are discretized into 22 finite elements with different lengths (smaller in the vicinity of the supports, as can be seen in figs. 7(a) and 7(c)), which corresponds to a total of 1143 degrees of freedom (d.o.f.). For validation purposes, one also performs shell finite element analyses in the code ABAQUS – the beams are discretized into fine meshes involving 1280 S9R5 elements (9-node shell elements with 5 d.o.f. per node and reduced integration), which corresponds to an overall amount of about 27000 d.o.f.. The numerical results are presented in figures 5, 6(a)-(b) and 7(a)-(d): (i)  $P_{cr}$  vs.  $d/L$  curves, yielded by the GBT and ABAQUS analyses, (ii) GBT modal participation diagrams providing the variation, with  $d/L$ , of the deformation mode contributions to the beam critical buckling modes and (iii) the GBT and ABAQUS critical buckling mode shapes concerning the beams with  $d/L=0.3$ . The observation of these results prompts the following comments:

- (i) As expected, the unstiffened beam instability is always triggered by the buckling of the web near the supports (see fig. 7(a)), due to the combined action of shear and transverse normal stresses. Obviously, this means that  $P_{cr}$  does not depend on  $d/L$  (provided that the loads are not applied in the close vicinity of the

<sup>10</sup>As mentioned earlier, it will be shown that the shear and transverse extension deformation modes do not participate in the beams critical buckling modes, which means that they can be omitted from the buckling analyses. Their role is restricted to the first-order analyses.

supports) – therefore, it is not surprising that the critical load remains practically constant ( $P_{cr} \approx 17 \text{ kN}$ ) up to  $d/L=0.8$ , and then gradually decreases to about half that value ( $P_{cr}=8.46 \text{ kN}$  for  $d/L=1$ ). For  $d/L=0.3$  ( $P_{cr}=16.98 \text{ kN}$ ) all the contributions to the beam critical buckling mode come from local-plate and global deformation modes: **7** (50%), **5** (30.6%), **4** (8%), **10** (5.6%), **6** (3.5%) and **3** (1.9%)<sup>11</sup>.

- (ii) Again as expected, the stiffened beam instability is also triggered by the buckling of the web, but now in the regions where the loads are applied (see fig. 7(c)). This explains why  $P_{cr}$  decreases monotonically as the two

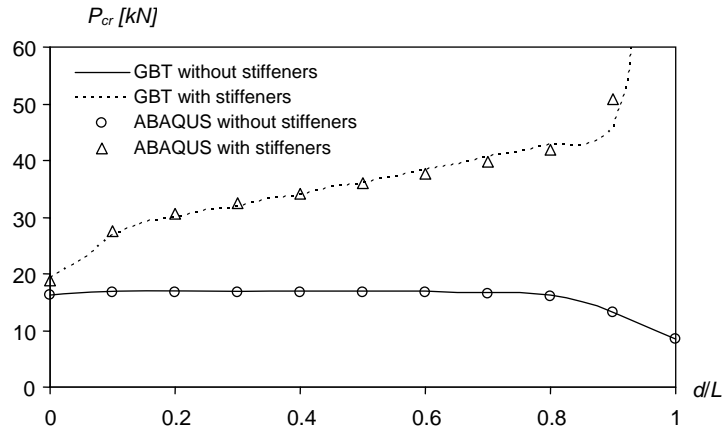


Fig. 5:  $P_{cr}$  vs.  $d/L$  curves for the unstiffened and stiffened I-beams

<sup>11</sup> The participations of the GBT deformation modes in the beam critical buckling mode are obtained from the maximum values, along the beam length, of the various modal amplitude functions (e.g., Silva *et al.* 2008) – thus, each deformation mode contribution is expressed as a percentage value  $p_i$ . To have all deformation mode amplitudes with the same dimensions, the torsion mode one corresponds to the maximum displacement component causes by it (like for all other modes) – note that the “usual” torsion mode amplitude corresponds to a rotation value.

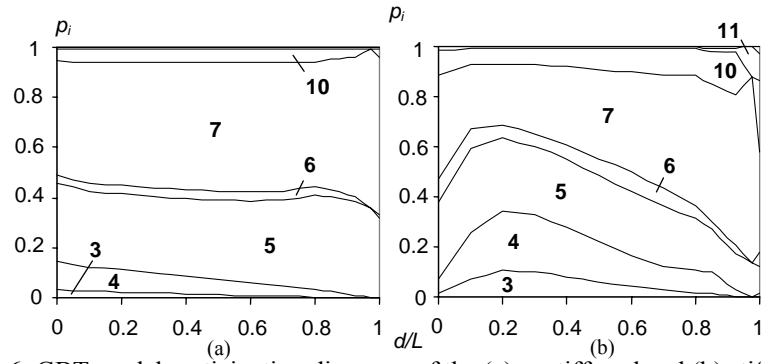


Fig. 6: GBT modal participation diagrams of the (a) unstiffened and (b) stiffened I-beams

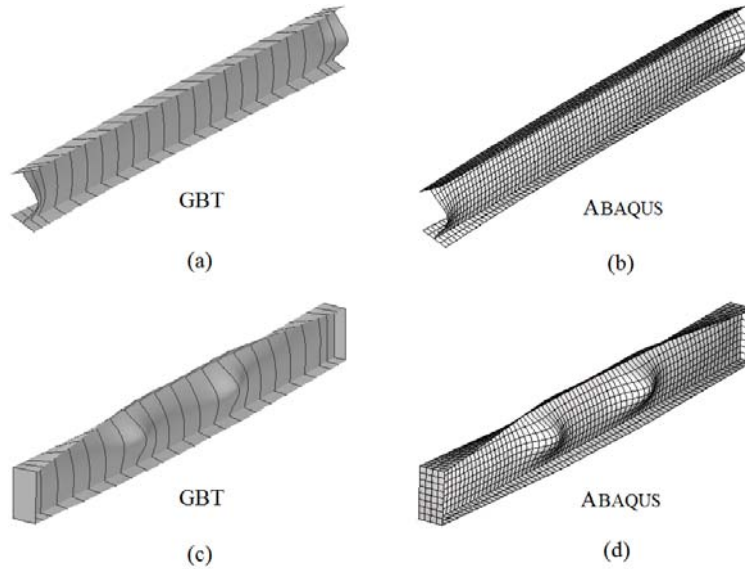


Fig. 7: Critical buckling mode shapes provided by the GBT and ABAQUS analyses for the (a+b) unstiffened and (c+d) stiffened beams with  $d/L=0.3$

loads get closer (*i.e.*, as  $d/L$  decreases) – the lower and higher values are  $19.67 \text{ kN}$  (mid-span loading) and  $170.28 \text{ kN}$  (support loading). For  $d/L=0.3$  ( $P_{cr}=32.01 \text{ kN}$ ), the critical buckling mode combines relevant participations

from local-plate and global deformation modes: **5** (27.5%), **7** (27.5%), **4** (22.8%), **3** (9.9%), **10** (6.3%) and **6** (5%)<sup>12</sup>.

- (iii) The presence of the end web stiffeners obviously improves the beam buckling behavior – this improvement becomes more relevant as the loads get closer to the supports (unlike in the unstiffened beams, the stiffened beam  $P_{cr}$  value grows exponentially as  $d/L$  tends to 1). The percentage difference between the critical buckling loads of the two beam (iii<sub>1</sub>) is of 18% for  $d/L=0$  and (iii<sub>2</sub>) increases rapidly with  $d/L$  – e.g., for  $d/L=0.3$  this difference is already equal to 89%.
- (iv) The GBT modal participation diagrams shown in figures 6(a)-(b) provide in-depth insight into the beam buckling behavior. For instance, they readily reveal that (iv<sub>1</sub>) the global deformation modes **3** and **4** are much more important in the stiffened beams than in the unstiffened ones, (iv<sub>2</sub>) the local-plate deformation modes **5** and **7** always prevail (regardless of the load position), particularly in the unstiffened beams, and (iv<sub>3</sub>) the maximum global (flexural-torsional) contribution to the critical buckling mode occurs for the stiffened beam with  $d/L=0.2$ .
- (v) Finally, note the very good agreement between the GBT and ABAQUS results – as clearly shown in figures 5 and 7, there is a virtually perfect match between both the critical load values and the buckling mode shapes, as long as one has  $d/L \leq 0.8$ . Indeed, the  $P_{cr}$  differences never reach either 1.2% (unstiffened beams) or 3.0%, (stiffened beams). For  $d/L > 0.8$ , on the other hand, these differences may be as high as 10%, which is due to the GBT web stiffener modeling<sup>13</sup>. In order to illustrate the above statements, one presents next some critical load values provided by the ABAQUS and GBT analyses for the unstiffened and stiffened beams with  $d/L=0.3$ : (v<sub>1</sub>)  $P_{cr.GBT}=32.01 \text{ kN}$  and  $P_{cr.ABQ}=32.40 \text{ kN}$  (stiffened beam) and (v<sub>2</sub>)  $P_{cr.GBT}=16.97 \text{ kN}$  and  $P_{cr.ABQ}=16.79 \text{ kN}$  (unstiffened beam).

The second beam analyzed differs from the first one (depicted in fig. 4) in the fact that the loading consists now of a uniformly distributed load spanning the whole member length and applied at the beam top flange (in the plane of the web) – its value is  $p=2P/L$ , which leads to support reactions equal to  $P$ . The GBT and ABAQUS critical buckling loads of the unstiffened and stiffened beams are given in table 1. In order to assess the relevance of including the non-linear term of the transverse extensions ( $\varepsilon_{ss}^{NL} = w_{,s}^2/2$  – see  $B_{jik}$  in (4)) in the buckling analysis of beams with slender

<sup>12</sup>The participation of the global modes are now much more relevant, since the cross-sections that are most involved in the beam critical buckling mode critical are located far away from the supports – thus, they exhibit a considerably smaller “global stiffness”.

<sup>13</sup>In GBT, the web stiffeners are modeled by restraining the local-plate and transverse extension mode amplitudes in the beam end cross-sections – this corresponds to assuming that the stiffening plates are fully rigid in their own-planes and completely flexible out of them, which does not correspond to the ABAQUS shell finite element modeling. Additionally, GBT does not take into account the stresses developing in the stiffeners, thus making it impossible to capture their own (localized) buckling behaviors.



webs acted by transverse loads, table 1 also contains  $P_{cr}$  values obtained from GBT analyses that neglect this term. As for figures 8(a)-(d), they show the two beam critical buckling mode shapes yielded by GBT and ABAQUS analyses. Finally, figure 9 displays the pre-buckling shear and transverse normal stresses obtained from first-order analyses carried out in ABAQUS. After observing these results, one is led to the following conclusions:

- (i) As before, the unstiffened beam instability is triggered by the buckling of the web near the supports (see fig. 8(a)). It occurs for  $P_{cr}=16.16\text{ kN}$ , *i.e.*, practically the same critical buckling load of the beam acted by point loads applied far away from the supports – this is not surprising, since the critical buckling load is governed by the support reaction value, which is the same in both cases. Concerning the beam critical buckling mode, the participations of the various GBT deformation modes also attest the enormous similarity with the previous one, easily confirmed by looking at figures 8(a) and 7(a) – indeed, the main contributions come from modes **7** (52.6%), **5** (32.4%), **10** (5.3%), **4** (4.8%), **6** (3.6%) and **3** (0.8%), *i.e.*, practically the same as before.
- (ii) When the transverse extension non-linear term is neglected, the GBT analysis of the unstiffened beam yields  $P_{cr}=64.73\text{ kN}$ , a value four times higher than the correct one. Moreover, the participations of global modes in the beam critical buckling mode become considerably higher – the main contributions come are now from modes **7** (27.3%), **4** (22.8%), **5** (18.8%), **3** (14.2%), **10** (8.3%), **6** (7.4%) and **11** (0.9%).
- (iii) Localized web buckling no longer occurs in the stiffened beam, given the absence of point loads – buckling now takes place in a mode that (iii<sub>1</sub>) combines global deformation modes (minor axis bending and torsion) with web-governed local-plate ones, and (iii<sub>2</sub>) extends throughout the

Table 1:  $P_{cr}$  values of the I-beams acted by uniformly distributed loads

Beam	$P_{cr.ABQ}$ [kN]	$P_{cr.GBT}$ [kN]	$\Delta$ (%)	$P_{cr.GBT}$ without $\epsilon_{ss}^{NL}$ [kN]	$\Delta$ (%)
without stiffeners	15.98	16.16	+1.1	64.73	+305.1
with stiffeners	55.88	53.69	-3.9%	84.40	+51.0

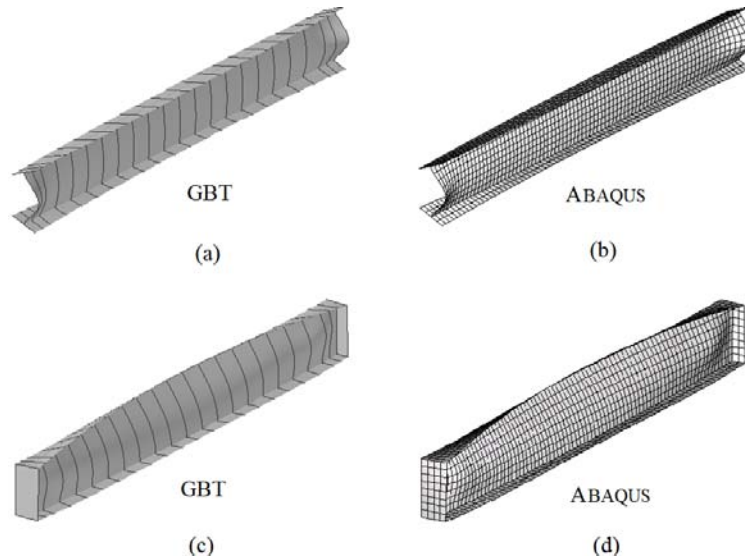


Fig. 8: GBT and ABAQUS critical buckling mode shapes for the (a+b) unstiffened and (c+d) stiffened beams under uniformly distributed loads

whole beam length (see fig. 8(c)). One has  $P_{cr}=53.69\text{ kN}$  and the most relevant critical buckling mode contributions come from deformation modes **4** (40.7%), **3** (20.8%), **7** (16%), **5** (15.7%), **10** (3.5%) and **6** (2.7%).

- (iv) When the transverse extension non-linear term is neglected, the GBT analysis of the stiffened beam yields  $P_{cr}=84.40\text{ kN}$ , which corresponds to a 57% increase with respect to the correct value. As for the deformation mode contributions to the beam critical buckling mode, they also change

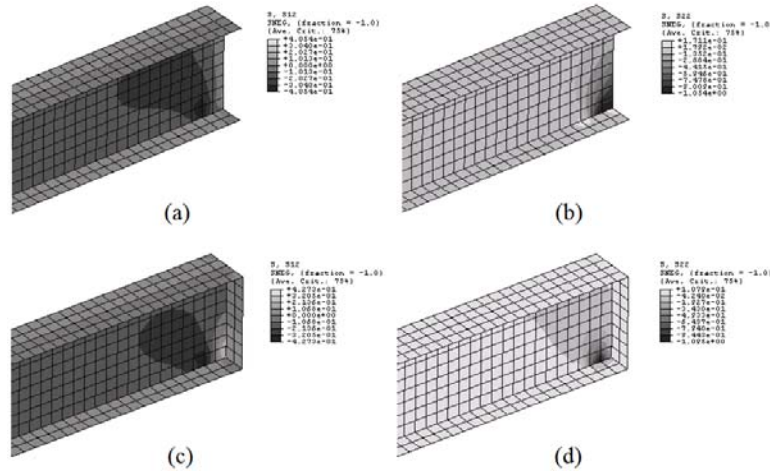


Fig. 9: (a+c) Shear and (b+d) transverse normal stress distributions near the supports of the unstiffened and stiffened beams (uniformly distributed load)

considerably – the main ones concern modes **7** (31.4%), **4** (24.9%), **3** (20.2%), **10** (9.7%), **5** (7.3%), **6** (4.4%) and **11** (1.8%).

- (v) As shown above, the transverse extension non-linear term plays a pivotal role, as far as assessing the web-triggered instability of beams acted by transverse loads not applied at the cross-section shear center is concerned. Therefore, GBT models not incorporating this term (to the authors' best knowledge, all the ones developed up to now) may lead to considerably erroneous results when adopted to analyze this type of problems.
- (vi) There is again very good agreement between the GBT and ABAQUS critical buckling loads (table 1) and mode shapes (figs. 8(a)-(d)). The  $P_{cr}$  differences values are equal to either 1.1% (unstiffened beam) or 3.9% (stiffened beam) – concerning the latter, the stiffener modeling explains again the lower value yielded by the GBT analysis.
- (vii) Obviously, the support reactions are transmitted distinctly in the stiffened and unstiffened beams. In the latter case, higher and more widespread (vii<sub>1</sub>) shear and (vii<sub>2</sub>) compressive transverse normal stresses develop in the web – this can be readily attested by comparing figures 9(a+b) and 9(c+d). Naturally, these stress distributions render the unstiffened beam much more prone to undergo web localized buckling (or web crippling).

**I-Section Cantilevers.** One analyses now an I-section cantilever (i) with the cross-section and material properties indicated in figure 10(a) and (ii) acted by a tip transverse point load  $Q$  causing major axis bending and applied at either the end cross-

section (i) top flange, (ii) shear center or (iii) bottom flange – no nodal displacement and/or rotations is allowed at the fixed end cross-section. Adopting the cross-section discretization shown in figure 10(b), the GBT cross-section analysis leads to a set of 39 deformation modes – the 18 most relevant for the analyses under consideration are displayed in figure 11. As for the longitudinal discretization, it involves 12 finite elements, thus corresponding to a total of 780 degrees of freedom.

First, recall once again that it is essential to include the shear and transverse extension deformation modes in the first-order analysis aimed at determining accurately the pre-buckling stresses, thus capturing all relevant geometrically non-linear effects. Figure 12 shows curves that provide the variation of the cantilever critical buckling moment ( $M_{cr} = Q_{cr}L$ ) with its length ( $L$ ), for the three tip transverse load locations mentioned above – the modal participation diagrams of the corresponding critical buckling modes are displayed in figure 13. As for figure 14, it depicts the GBT-based critical buckling mode shapes of cantilevers with various lengths and the three tip load locations. The observation of these buckling results prompts the following comments:

- (i) The cantilever critical buckling mode may be either lateral-torsional or local-plate (see fig. 14) – the latter may be triggered by the compressed flange (near the fixed end) or the web (near the load application region).

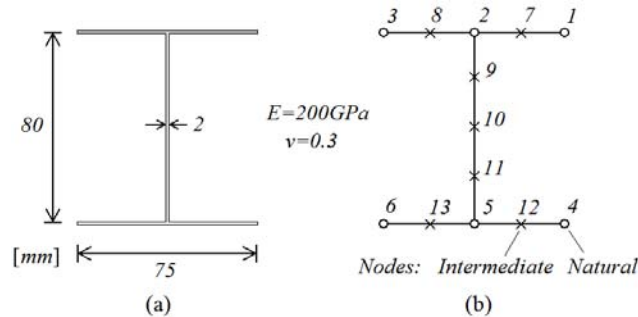


Fig. 10: Cantilever I-section (a) geometry and dimensions and elastic constants, and (b) GBT nodal discretization

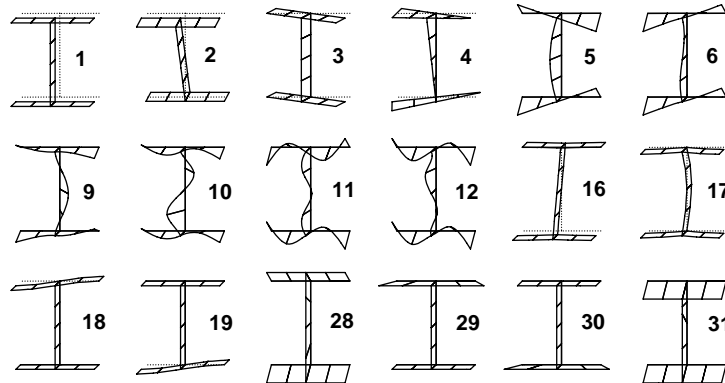


Fig. 11: Most relevant cantilever I-section deformation modes: global (1-4), local-plate (5-12), shear (13-21) and transverse extension (22-30)

- (ii) The flange-triggered local-plate buckling is not affected by the load position. Conversely, the lateral-torsional and web-triggered local-plate buckling phenomena are strongly influenced by this parameter.
- (iii) As far as lateral-torsional buckling is concerned, an upward motion of the load point of application (iii<sub>1</sub>) leads to a  $M_{cr}$  decrease and (iii<sub>2</sub>) causes

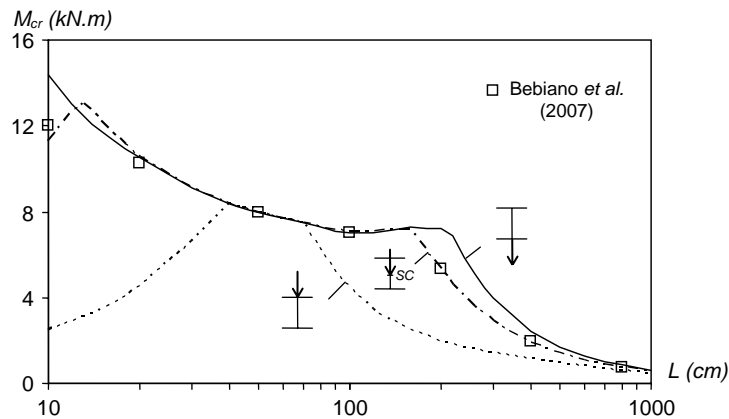


Fig. 12: I-section cantilevers:  $M_{cr}(L)$  buckling curves concerning the three positions of the tip point transverse load

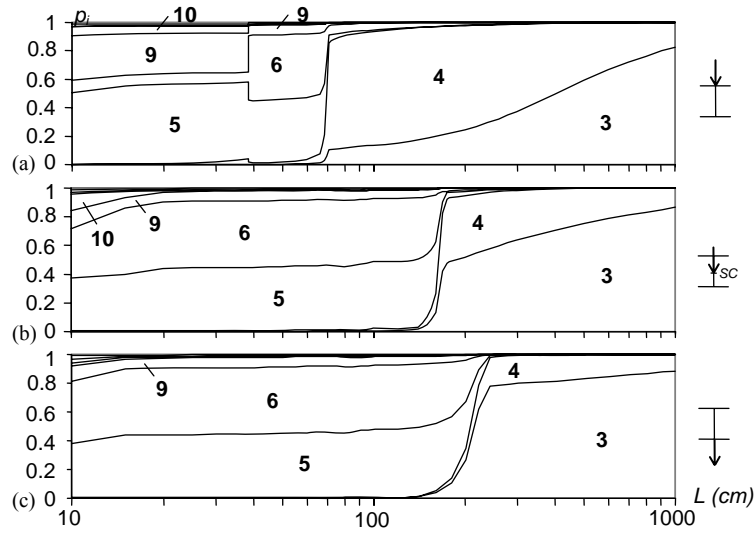


Fig. 13: GBT modal participation diagrams of I-section cantilevers under tip point loads acting at the (a) top flange, (b) shear center and (c) bottom flange

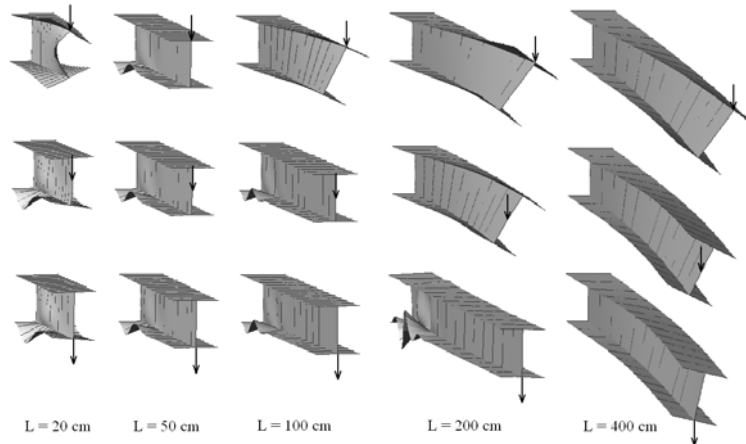


Fig. 14: I-section cantilever: GBT-based critical buckling mode shapes for various lengths and the three load positions under consideration

this buckling phenomenon to be critical for shorter cantilevers. Moreover, the GBT modal participation diagrams presented in figures 13(a)-(c) show clearly that the torsion mode **4** contribution to the lateral-torsional buckling mode decreases as (iii<sub>1</sub>)  $L$  increases (for a given load position) and (iii<sub>2</sub>) the load position moves downwards (for a given  $L$ ).

- (iv) Besides the expected contributions from the global deformation modes **3** and **4**, the cantilever so-called “lateral-torsional buckling modes” also exhibit small participations from local-plate modes – however, they decrease as the cantilevers become longer (see figs. 13 (a)-(c)). For instance, consider the  $L=200\text{ cm}$  cantilever subjected to shear center loading, for which one has  $M_{cr}=5.30\text{ kN.m}$  and a critical buckling mode combining deformation modes **3** (51.9%), **4** (42.9%), **5** (3%), **9** (1.3%) and **6** (0.8%) – for top flange loading,  $M_{cr}$  drops to  $1.99\text{ kN.m}$  and the modal participations (iv<sub>1</sub>) increase for modes **4** (73.6%) and **6** (1.9%), and (iv<sub>1</sub>) decrease for modes **3** (24.3%) and **5** (0.2%) and **9** (0%).
- (v) In cantilevers with lengths comprised between  $40\text{ cm}$  and  $70\text{ cm}$ , the local-plate critical buckling mode is always triggered by the compressed flange near the fixed end, regardless of the load position – since it is applied far away from the region where the instability occurs, the  $M_{cr}$  values are exactly the same for the three load positions. For instance, the  $L=50\text{ cm}$  cantilever has  $M_{cr}=7.96\text{ kN.m}$  and a critical buckling mode combining of mostly the local-plate deformations modes **6** (45.7%), **5** (44.2%) and **9** (6.9%) – figures 13 (a)-(c) show clearly that the modal participations do not vary within the  $40\text{-}70\text{ cm}$  length range (note that, in the shear center and bottom flange loading cases, the modal participations are exactly the same for  $L=40\text{-}160\text{ cm}$ ).
- (vi) The cantilevers with  $L < 40\text{ cm}$  and subjected to top flange loading buckle in local-plate triggered by the web zone close to the cantilever free end (see fig. 14 –  $L=20\text{ cm}$ ). Within this length range,  $M_{cr}$  increases with  $L$ , because the length increase overshadows the (logical) drop in the critical buckling load  $Q_{cr}$  (the cantilever becomes more flexible). For  $L=20\text{ cm}$ , one has  $Q_{cr}=22.4\text{ kN}$  ( $M_{cr}=4.48\text{ kN.m}$ ) and the critical buckling mode has (vi<sub>1</sub>) predominant contributions from the symmetric local-plate modes **5** (55.6%) and **9** (28.2%), and (vi<sub>2</sub>) lesser participations from modes **6** (7.6%), **10** (5.2%), **12** (1.4%) and **4** (0.8%).
- (vii) As expected, the  $M_{cr}$  (or  $Q_{cr}$ ) values associated with the shear center loading virtually replicate those recently published by Bebiano *et al.* (2007). Note, however, that the model developed by these authors only includes non-linear terms of the works done by the longitudinal normal and shear stresses, as there is no such term concerning the work done by the transverse normal stresses – this absence precludes the capture of all effects stemming from the load position with respect to the shear center.

**Hat-Section Cantilevers.** The last illustrative example concerns the buckling behavior of hat-section cantilevers (i) with the geometry and elastic constants given in figure 15(a) and (ii) acted by two identical tip transverse point loads applied at either the web-flange or web-lip corners – the value of each of them is  $Q/2$  (*i.e.*,  $Q$  is the total applied load). The adopted GBT cross-section discretization, depicted in figure 15(b), leads to 39 deformation modes – the 18 most relevant ones are displayed in figure 16. Moreover, the longitudinal discretization always involves 8 beam finite elements, leading to a total of 520 degrees of freedom. For validation purposes, one also performs ABAQUS shell finite element analyses – as before (simply supported I-beams), these cantilevers are discretized into fine S9R5 element meshes.

The main objective is to assess the influence of the load position on the cantilever critical buckling moment ( $M_{cr} = Q_{cr} L$ ) and mode shape. Figures 17, 18 and 19 present, for the two loadings considered, (i)  $M_{cr}(L)$  buckling curves, (ii) the corresponding GBT modal participations diagrams and (iii) the GBT-based critical buckling mode shapes of cantilevers with four lengths. The observation of these buckling results leads to the following conclusions:

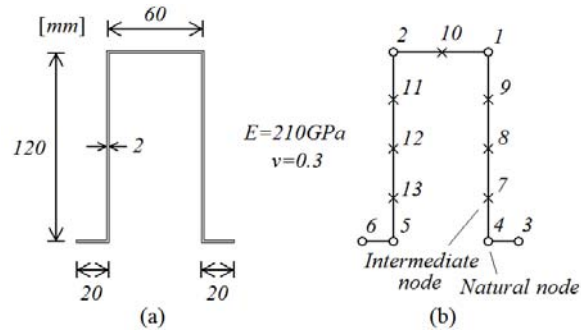


Fig 15: Cantilever hat-section (a) geometry, dimensions and elastic constants, and (b) GBT nodal discretization



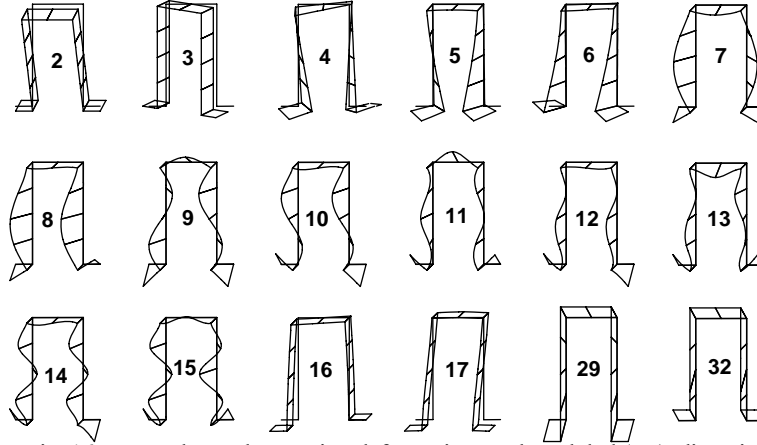


Fig. 16: Most relevant hat-section deformation modes: global (1-4), distortional (5-6), local-plate (7-15), shear (16-19) and transverse extension (28-32)

- (i) There is a very visible difference between the cantilever critical buckling behaviors associated with the two loadings (loads applied at the web-flange and web-lip corners, *i.e.*, top and bottom loading) –  $M_{cr}$  values and mode shapes. Concerning the critical buckling moments, the values corresponding to top loading may be more than 40% lower than their bottom loading counterparts (see fig. 17). In both cases, the critical buckling modes include relevant contributions from global, distortional and local-plate deformation modes, as clearly shown in figures 18 (a)-(b) – they combine (i<sub>1</sub>) symmetric distortional (5) and local-plate (7, 9, 11, 13, 15) modes, for  $L < 55$  cm, or (i<sub>2</sub>) anti-symmetric global (3, 4), distortional (6) and local-plate (8, 10) modes, for  $L < 55$  cm.
- (ii) In order to illustrate the statements made in the previous item, consider the  $L=50$  cm and  $L=100$  cm cantilevers, associated with the two critical buckling mode types. In the first case, one has (ii<sub>1</sub>)  $M_{cr}=14.26$  kN.m and critical buckling mode participations from deformation modes 5 (66.2%), 7 (21.9%), 9 (7.3%), 11 (2%), 13 (1.7%) and 15 (0.9%), for top loading, and (ii<sub>2</sub>)  $M_{cr}=24.65$  kN.m and contributions from modes 7 (41.6%), 5 (27.6%), 9 (18.6%), 13 (6%), 11 (3.0%) and 15 (2.5%), for bottom loading – note the 73% critical moment increase. In the second case, one has (ii<sub>1</sub>)  $M_{cr}=10.67$  kN.m and contributions to the critical buckling mode from deformation modes 4 (80.2%), 6 (15.9%), 3 (2.4%),

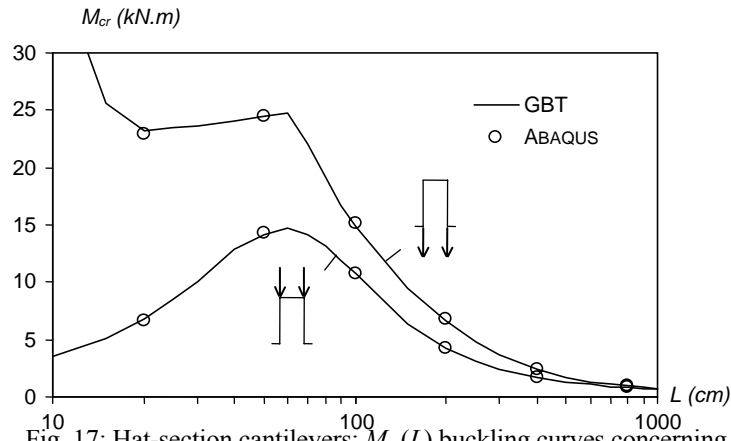


Fig. 17: Hat-section cantilevers:  $M_{cr}(L)$  buckling curves concerning the two positions of the tip point loads

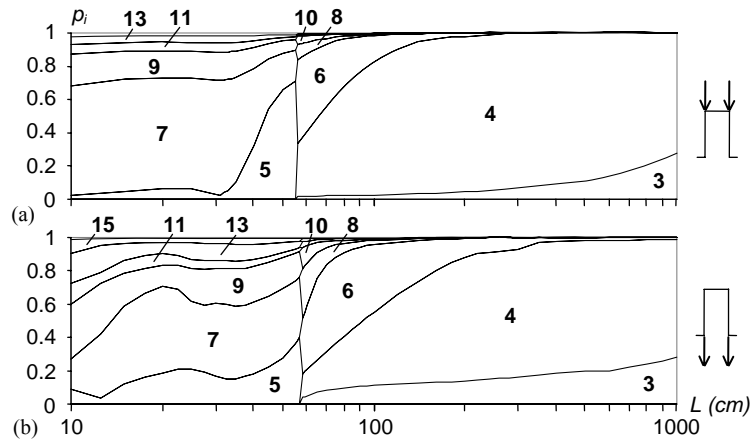


Fig. 18: GBT modal participation diagrams of hat -section cantilevers under (a) top (web-flange corners) and (b) bottom (web-lip corners) tip loading

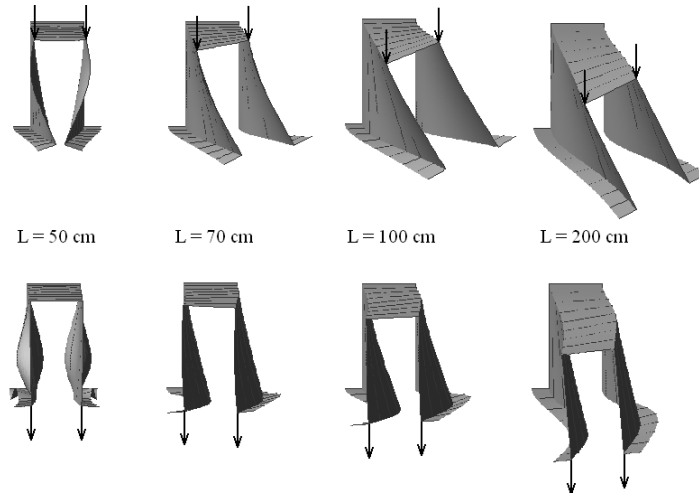


Fig. 19: Hat-section cantilevers: GBT-based critical buckling mode shapes for four lengths and the two loadings under consideration

**8** (0.7%) and **10** (0.5%), for top loading, and (ii)<sub>2</sub>  $M_{cr}=14.84$  kN.m and participations from modes **4** (43.9%), **6** (40.5%), **3** (11.2%), **8** (2.7%), **10** (0.6%) and **12** (0.5%), for bottom loading – now, besides the 39% critical moment increase, the participation of mode **4** (torsion) decreases, while those of modes **3** (bending) and **6** (distortion) increase (see figs. 18(a)-(b)).

- (iii) The comparison between the critical buckling moment provided by the GBT and ABAQUS analyses showed an excellent agreement for all cantilever lengths, as can be readily attested by looking at figure 17 – the differences never exceed 4%, thus confirming the great accuracy of the GBT analyses (in spite of the small number of d.o.f. involved)<sup>14</sup>.

## Conclusion

This paper presented a novel GBT formulation that includes a non-linear transverse extension term, thus making it possible to handle rigorously the influence of localized effects on the local (local-plate or distortional) and global buckling behavior of prismatic thin-walled members – in particular, this formulation accounts for effects stemming from (i) the position of transverse loads (with respect to cross-section shear centers) or (ii) the occurrence of localized web buckling phenomena. In order to illustrate the application and potential of the developed and implemented

<sup>14</sup>The adopted shell finite element discretizations involve between 120 and 12000 elements (depending on the cantilever length), corresponding to 1250 to 125000 degrees of freedom.

GBT formulation, one presented and discussed numerical results concerning the buckling behavior of (i) hat and I-section cantilevers acted by transverse tip point loads applied at various cross-section points, and (ii) I-section simply supported beams under top-flange distributed and point loads – one also assessed how end support transverse web stiffeners improve the beam buckling behavior. The GBT-based buckling results were validated through the comparison with values yielded by ABAQUS shell finite element analyses (most cases) or reported in the literature. Among the various conclusions drawn from the performance of this work, the following ones deserve a special mention:

- (i) The proposed GBT formulation/implementation was shown to provide accurate buckling results and also to be computationally very efficient (its application always requires a fairly small number of degrees of freedom) – it requires sequentially performing first-order and buckling analyses. Moreover, an excellent agreement was consistently found between the critical buckling loads/moments and mode shapes provided by the GBT and ABAQUS (shell finite element) analyses.
- (ii) It is essential to include the transversal extension non-linear term in the GBT analyses intended to study global, local and/or localized wall buckling phenomena caused by transverse loads – the influence of this term becomes particularly noticeable when the load (or support reaction) point of application does not coincide with the cross-section shear center, thus entailing the development of significant (membrane) transverse normal stresses. In one illustrative example addressed in this work, omitting the transverse extension non-linear term from the analyses led to an overestimation of the critical buckling loads/moments that reached 50% (end stiffened beams) or 300% (unstiffened beams).
- (iii) As expected, the numerical results confirmed the relevance of including web transverse stiffeners at the simply supported I-beam end supports – critical buckling load/moment increases of up to 250% were observed.
- (iv) The GBT modal nature made it possible to acquire more in-depth insight on the mechanics underlying the thin-walled member buckling behavior (through the analysis of the corresponding modal participation diagrams).

### **Acknowledgements**

The first author gratefully acknowledges the financial support provided by *Fundação para a Ciência e Tecnologia* (FCT – Portugal), through the doctoral scholarship n° SFRH/BD/21439/2005.

### **References**

Bradford M.A. (1992). Lateral distortional buckling of steel I-section members, *Journal of Constructional Steel Research*, **23**(1-3), 97-116.

- Bebiano R., Silvestre N. and Camotim D. (2007). GBT formulation to analyze the buckling behaviour of thin-walled members under non-uniform bending, *International Journal of Structural Stability and Dynamics*, **7**(1), 23-54.
- Camotim D., Silvestre N., Gonçalves R. and Dinis P.B. (2004). GBT analysis of thin-walled members: new formulations and applications, *Thin-Walled Structures: Recent Advances and Future Trends in Thin-Walled Structures Technology* (Loughborough, 25/6), J. Loughlan (ed.), Canopus Publishing Ltd., Bath, 137-168.
- Camotim D., Silvestre N., Gonçalves R. and Dinis P.B. (2006a). GBT-based structural analysis of thin-walled members: overview, recent progress and future developments, *Advances in Engineering Structures, Mechanics and Construction* (SMCD 2006 – Waterloo, 14-17/5), M. Pandey, W.C. Xie, L. Xu (eds.), Springer, 187-204.
- Camotim D., Silvestre N., Dinis P.B., Bebiano R. and Basaglia C. (2006b). Recent progress in the numerical analysis of thin-walled steel members and frames, *Proceedings of International Symposium on Innovative Design of Steel Structures* (Hong Kong, 10/11), B. Young (ed.), 63-104.
- CEN (Comité Européen de Normalisation) (2005), *Eurocode 3: Design of Steel Structures - Part 1.1: General Rules and Rules for Buildings* (EN 1993-1-1), Brussels.
- CEN (Comité Européen de Normalisation) (2006), *Eurocode 3: Design of Steel Structures - Part 1.5: Plated Structural Elements* (EN 1993-1-5), Brussels.
- Dinis P.B., Gonçalves R. and Camotim D. (2008). On the local and global buckling behaviour of cold-formed steel hollow-flange channel beams, *Proceedings of Fifth International Conference on Thin-Walled Structures* (ICTWS 2008 – Brisbane, 18-20/6). (in press)
- Gonçalves R. and Camotim D. (2004). Application of generalised beam theory (GBT) to investigate the local and global stability of cold-formed steel beams, *Computational Methods in Engineering* (CMCE – Lisboa, 31/5-2/6), C.M. Soares *et al.* (eds.), 191. (full paper in CD-ROM Proceedings) (Portuguese)
- Gonçalves R. (2007). *Analysis of Thin-Walled Beams with Deformable Cross-Sections: New Formulations and Applications*, PhD thesis in Civil Engineering, IST, Technical University of Lisbon, 2007. (Portuguese)
- HKS (Hibbit, Karlsson & Sorensen Inc.) (2002). *Abaqus Standard* (vrs. 6.3-1).
- Kumar A. and Samanta A. (2006). Distortional buckling in monosymmetric I-beams: reverse-curvature bending, *Thin-Walled Structures*, **44**(7), 721-725.
- Lucic D. and Scepanovic B. (2004). Experimental investigation on locally pressed I-beams subjected to eccentric patch loading, *Journal of Constructional Steel Research*, **60**(3-5), 525-534.
- Pi Y.L. and Trahair N.S. (1997). Lateral-distortional buckling of hollow flange beams, *Journal of Structural Engineering* (ASCE), **123**(6), 695-702.

- Samanta A. and Kumar A. (2006). Distortional buckling in monosymmetric I-beams, *Thin-Walled Structures*, **44**(1), 51-56.
- Silva N.M.F., Camotim D. and Silvestre N. (2008). GBT cross-section analysis of thin-walled members with arbitrary cross-sections: a novel approach, *Proceedings of Fifth International Conference on Thin-Walled Structures (ICTWS 2008 – Brisbane, 18-20/6)*. (in press)
- Silvestre N. and Camotim D. (2002). First order generalised beam theory for arbitrary orthotropic materials, *Thin-Walled Structures*, **40**(9), 755-789.
- Silvestre N. and Camotim D. (2003). GBT buckling analysis of pultruded FRP lipped channel members, *Computers and Structures*, **81**(18-19), 1889-1904.
- Topkaya C. (2006). A numerical study on linear bifurcation web buckling of steel I-beams in the sidesway mode, *Engineering Structures*, **28**(7), 1028-1037.
- Trahair N.S. (1993). *Flexural-Torsional Buckling of Structures*, E & FN Spon (Chapman & Hall), London.
- Turvey G.J. (1996). Effects of load position on the lateral buckling response of pultruded GRP cantilevers – comparisons between theory and experiment, *Composite Structures*, **35**(1), 33-47.



## **GBTUL – A Code for the Buckling Analysis of Cold-Formed Steel Members**

Rui Bebiano<sup>1</sup>, Nuno Silvestre<sup>2</sup> and Dinar Camotim<sup>3</sup>

### **Abstract**

This paper presents GBTUL 1.0 $\beta$ , a code to perform buckling and vibration analyses of open-section cold-formed members that is now available online as freeware. This code, developed at the Department of Civil Engineering and Architecture of the Technical University of Lisbon (ICIST/IST – UTL), constitutes the numerical implementation of a recent Generalized Beam Theory (GBT) formulation – GBT is a thin-walled beam theory that incorporates local deformation and discretizes a member deformed configuration (*e.g.*, a buckling or vibration mode shape) into a linear combination of *cross-section deformation modes* with longitudinally varying amplitudes. After presenting a very brief overview of the GBT formulation, one addresses the GBTUL 1.0 $\beta$  graphic user interface and describes its main commands. Finally, the paper closes with an illustrative example: the application of the code to analyze the buckling behavior of a lipped channel cantilever beam – particular attention is paid to the quality of the code graphic outputs (2D and 3D mode shape representations).

### **Introduction**

Most thin-walled members exhibit high global and local slenderness values, a feature responsible for a rather complex structural behaviour, strongly affected by various instability phenomena, such as local-plate, distortional and global (Euler – flexural, torsional or flexural-torsional) buckling. In the particular case of cold-formed steel members, a considerable amount of research work has been recently devoted to the development of safe and economic design rules, notably in Australia and the USA (*e.g.*, Hancock *et al.* 2001). One of the main fruits of this intense research activity was the

---

<sup>1</sup> Ph.D. Student, Assistant Professor<sup>2</sup> and Associate Professor<sup>3</sup>, Department of Civil Engineering and Architecture, IST/ICIST, Technical University of Lisbon, Portugal.



Direct Strength Method (DSM – *e.g.* Schafer 2005, 2008), which can handle the combined effect of local-plate, distortional and global buckling, and has already been included in the current North American (AISI 2004) and Australian/New Zealander (SA-SNZ 2005) specifications for cold-formed steel member design. Since the application of the DSM provisions, as well as virtually all other existing design rules concerning the buckling ultimate limit states of cold-formed steel members (*e.g.*, Eurocode 3 – CEN 2005), requires knowing the member buckling stresses and mode nature, it is indispensable for practitioners to have wide access to accurate and easy-to-use tools to obtain this information. Bearing this in mind, researchers from the University of Sydney (under the leadership of Greg Hancock) and Ben Schafer (first at the University of Cornell and later at Johns Hopkins University) developed the codes THIN-WALL (Papangelis & Hancock 1998) and CUFSM (Schafer 2007), both based on the semi-analytical finite strip method (SAFSM – *e.g.*, Cheung & Tham 1998) – note that the latest CUFSM version already includes the so-called “constrained finite strip method” (*e.g.*, Ádány & Schafer 2006). However, the SAFSM codes currently available can only be applied to simply supported members (end sections locally/globally pinned and free to warp) acted by uniform applied internal force and/or moment diagrams – for instance, non-uniform bending problems are excluded. Then, the assessment of the local and global buckling behavior of thin-walled members with other loading and/or end support conditions is only possible through shell finite element analyses, usually performed in powerful commercial codes (*e.g.*, ABAQUS, ANSYS or ADINA).

Generalised Beam Theory (GBT) may be viewed as either (i) a *bar theory* that incorporates cross-section in-plane and out-of-plane deformations or (ii) a *folded-plate theory* that includes plate rigid-body motions (*e.g.*, Schardt 1989 or Camotim *et al.* 2004, 2007). By expressing the member buckling/vibration modes or deformed configurations as linear combinations of longitudinally varying cross-section *deformation modes*, which account for cross-section rigid-body motions and deformations, GBT provides a general and elegant approach to obtain accurate solutions for several structural problems involving prismatic thin-walled members – moreover, one also obtains the contributions of each deformation mode, a feature enabling a much clearer interpretation of the structural response under consideration. In recent years, Camotim and his co-workers at the Technical University of Lisbon developed and implemented GBT formulations to perform (i) first-order, buckling and post-buckling analyses, and (ii) vibration and dynamic analyses of *isotropic* and *orthotropic* thin-walled members (*e.g.*, Camotim *et al.* 2004, 2006a,b, 2007). However, an important limitation to a more widespread use of GBT analyses has been the lack of an accessible and easy-to-use computer code to perform them.

The aim of this paper is to report on the development and capabilities of the code GBTUL 1.0 $\beta$  (acronym for “GBT at the TU Lisbon” – Bebbiano *et al.* 2008), which is intended to fill the aforementioned gap and implements a recent GBT formulation

developed by Bebiano *et al.* (2007). It is available online at <http://www.civil.ist.utl.pt/gbt> (as *freeware*) and performs elastic buckling and vibration analyses of thin-walled members (i) with open cross-sections, (ii) with several end support and/or loading conditions, and (iii) made of isotropic or special orthotropic materials – since the member walls may exhibit different properties, hybrid steel profiles and composite steel-concrete members can also be handled. The code features include (i) the modal decomposition and identification (local-plate, distortional, global) of the member buckling or vibration mode, (ii) the possibility of performing analyses involving any number of selected deformation modes, (iii) 3D high-quality visualisation effects and (iv) user-friendly data input and output.

### Generalized Beam Theory: A Brief Overview

The main distinctive feature of GBT is the approximation of the cross-section displacement field by a linear combination of deformation modes with a clear structural meaning. Any GBT-based (buckling or vibration) analysis involves the sequential procedure depicted in fig. 1.

For given material properties and cross-section geometry, one begins by performing the *cross-section analysis*, which leads to the identification of its deformation modes and the evaluation of the corresponding modal mechanical properties. In order to provide a brief illustration of this step, consider the lipped channel beam (longitudinal axis  $X$ ) shown in fig. 2(a) – in each wall, one defines local axes  $x$ - $s$ - $z$ , associated with the displacement components  $u$ ,  $v$  and  $w$ . The beam is made of steel ( $E=210\text{ GPa}$ ,  $\nu=0.3$ ,  $\rho=7.800\text{ kg/m}^3$ ), and its cross-section geometry and discretization are depicted in figs. 2(b)-(c) – the number and nature of the deformation modes obtained depends on the cross-section discretization into

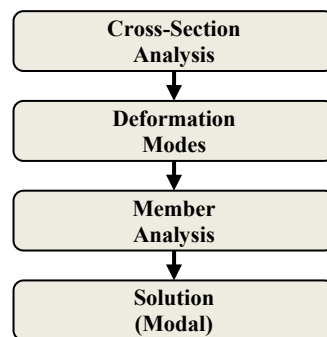


Fig. 1: GBT-based analysis procedure

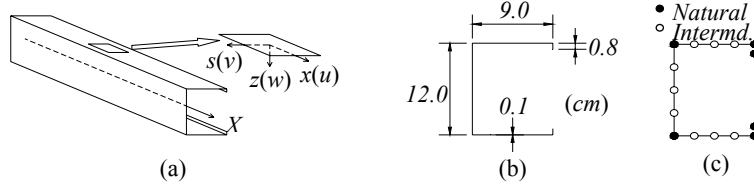


Fig. 2: Lipped channel member: (a) overall view an local axes, and cross-section (b) geometry and (c) GBT discretization

*natural nodes* (all wall ends) and *intermediate nodes* (within the walls – selected by the user to obtain the desired accuracy).

The modal representation of the member displacement field can be expressed as

$$u(x, s) = u_k(s)\phi_{k,x}(x) \quad v(x, s) = v_k(s)\phi_k(x) \quad w(x, s) = w_k(s)\phi_k(x) \quad , \quad (1)$$

where (i)  $u_k(s)$ ,  $v_k(s)$  and  $w_k(s)$  are the modal displacement profiles (defined along the cross-section mid-line) and (ii)  $\phi_k(x)$  are their longitudinal amplitude functions (the summation convention applies to subscript  $k$ ).

In this case, the cross-section discretization adopted (see fig. 2(c)) leads to a set of  $N_d=17$  deformation modes – fig. 3 depicts the in-plane deformed shapes of the 12 most relevant ones (mode 1 involves no in-plane motions – axial extension). In order to solve a given problem, one may choose to include any subset of  $n_d$  ( $1 \leq n_d \leq N_d$ ) deformation modes in the buckling/vibration analysis.

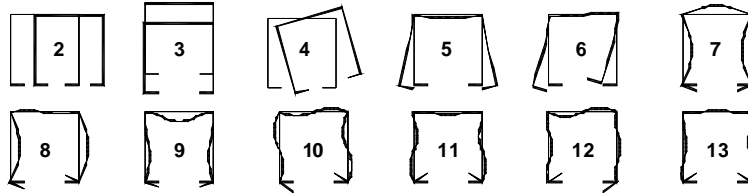


Fig. 3: In-plane configurations of the cross-section deformation modes 2-13

Then, the *member analysis* yields the solution of the buckling or vibration problem, namely the corresponding eigenvalues (buckling loads or natural frequencies and eigenvectors (buckling or vibration mode shapes) – the latter provide the coefficients of the modal amplitude functions  $\phi_k(x)$ ). In buckling analyses, the system to be solved reads where (i)  $C_{ik}$ ,  $D_{ik}$ ,  $B_{ik}$  are the cross-section linear stiffness matrices,

$$C_{ik}\phi_{k,xxxx} - D_{ik}\phi_{k,xx} + B_{ik}\phi_k - \lambda \left[ X_{jik} \left( W_j^0 \phi_{k,x} \right)_{,x} - X_{jki}^T \left( W_{j,x}^0 \phi_k \right)_{,x} + W_{j,x}^0 X_{jik}^T \phi_{k,x} \right] = 0 \quad , \quad (2)$$

(ii)  $X_{jik}$ ,  $X_{jik}^c$  are geometrical stiffness matrices (concerning normal and shear stresses), and (iii)  $\phi_k(x)$  are the longitudinal amplitude functions of the deformation modes. Vector  $W_j^0$  ( $W_j^0(x)$ , with  $j=1\dots 4$ ) contains the resultants of the pre-buckling applied stresses, namely (i) axial force ( $W_1^0(x)\equiv N(x)$ ), (ii) major and minor bending moments ( $W_2^0(x)\equiv M_1(x)$ ,  $W_3^0(x)\equiv M_2(x)$ ), and (iii) bimoment ( $W_4^0\equiv B$ ).

The solution of (2), which yields the buckling load parameters  $\lambda$  and mode shapes  $\phi(x)$ , may be obtained either (i) *analytically* (simply supported members acted by longitudinally uniform stress resultants – sinusoidal  $\phi_k(x)$  functions) or (ii) *numerically* (any members, by means of a longitudinal discretization into GBT-based beam finite elements). These procedures are addressed in the next sub-sections.

**Analytical Solution.** For members acted by loads that cause longitudinally uniform stress resultants (*i.e.*,  $W_j^0(x)\equiv W_j^0$ ), system (2) becomes

$$C_{ik}\phi_{k,xxxx} - D_{ik}\phi_{k,xx} + B_{ik}\phi_k - \lambda X_{jik}W_j^0\phi_{k,xx} = 0 \quad . \quad (3)$$

For simply supported members, this system has exact solutions ( $k=1\dots n_d$ )

$$\phi_k(x) = A_k \sin\left(\frac{n_k\pi x}{L}\right) \quad . \quad (4)$$

Introducing (4) into (3), one defines a system whose solution provides the sought eigenvalues  $\lambda$  and eigenvectors  $A_k$ . Since the dimension of this system ( $n_d \times n_d$ ) is fairly low, only a small computational effort is required to obtain the solution – this is why an analytical solution is always preferable to a numerical one (computationally much more involved).

**Numerical Solution – GBT-Based Finite Element.** The GBT-based beam finite element is derived on the basis of the variational (or weak) form of the equilibrium equation system. Within the finite element length  $L_e$ , the amplitude functions  $\phi_k(x)$  are approximated by means of linear combinations of Hermite cubic polynomials, *i.e.*,

$$\phi_k(x) = d_{k,1}^e \Psi_1(\tilde{x}) + d_{k,2}^e \Psi_2(\tilde{x}) + d_{k,3}^e \Psi_3(\tilde{x}) + d_{k,4}^e \Psi_4(\tilde{x}) \quad , \quad (5)$$

where  $d_{k,1}^e = \phi_{k,x}(0)$ ,  $d_{k,2}^e = \phi_k(0)$ ,  $d_{k,3}^e = \phi_{k,x}(1)$ ,  $d_{k,4}^e = \phi_k(1)$ ,  $\tilde{x} = x/L_e$  and

$$\begin{aligned} \Psi_1 &= L_e(\tilde{x}^3 - 2\tilde{x}^2 + \tilde{x}) & \Psi_2 &= 2\tilde{x}^3 - 3\tilde{x}^2 + 1 \\ \Psi_3 &= L_e(\tilde{x}^3 - \tilde{x}^2) & \Psi_4 &= -2\tilde{x}^3 + 3\tilde{x}^2 \end{aligned} \quad , \quad (6)$$

which means that each finite element has 4 degrees of freedom per mode, hence a total of  $4 \times n_d$ . If the member is discretized into  $n_e$  such finite elements, the total number of degrees of freedom is approximately equal to  $2 \times n_d \times (n_e + 1)$ .

When a numerical solution is carried out, the GBT modal nature makes it possible to consider distinct boundary conditions for different deformation modes. Standard

boundary conditions, *i.e.* those involving the full restraint of displacements ( $\phi_k=0$ ) and/or its derivatives ( $\phi_{k,x}=0$ ), are easily taken into account when assembling the member equilibrium eigensystem. GBTUL 1.0 $\beta$  offers the possibility of assigning 4 different support conditions, namely (i) simply supported (“S-S”), (ii) clamped-free (or cantilever, “C-F”), (iii) clamped-clamped (“C-C”) and (iv) clamped-pinned (“C-S”) – see table 1.

Table 1: The 4 member end support conditions available in GBTUL1.0 $\beta$

End Support Conditions	
S-S	$\phi_k(0)=\phi_k(L)=0$
C-F	$\phi_k(L)=\phi_{k,x}(L)=0$
C-C	$\phi_k(0)=\phi_{k,x}(0)=\phi_k(L)=\phi_{k,x}(L)=0$
C-S	$\phi_k(0)=\phi_{k,x}(0)=\phi_k(L)=0$

These four types of support conditions can be applied independently to the following deformation modes are: (i) mode **2** (major axis bending), (ii) mode **3** (minor axis bending), (iii) modes **4+D** (torsion and distortional modes), and (iv) modes **LP** (local-plate modes).

**Modal Participation Factors.** In order to assess the contribution of a given deformation mode to a member buckling or vibration mode, one provides the value of its *participation factor*  $P_i$ , given by

$$P_i = \int_L |\phi_i(x)| dx / \sum_{k=1}^{n_d} \int_L |\phi_k(x)| dx \times 100\% \quad , \quad (7)$$

where  $L$  is the member length. It corresponds to the ratio between (i) the total area limited by the mode amplitude function  $\phi_i(x)$  and (ii) the sum of the areas limited by all the modal amplitude functions ( $i=1..n_d$ ) –  $P_i$  quantifies the relative importance of deformation mode  $i$  to the buckling or vibration solution.

### Code GBTUL: Scope and Structure

**Scope.** The code GBTUL (more specifically, its 1.0 $\beta$  version) performs elastic buckling (bifurcation) or vibration analyses of thin-walled members with arbitrary open cross-sections (*i.e.*, excluding cross-sections with *closed cells*). The member walls can be made by one or several *isotropic* or *specialty orthotropic* materials (the latter include, for instance, pultruded FRP profiles) – this means that *heterogeneous* members (*e.g.*, hybrid steel or composite steel-concrete members) can also be handled. In order to enable the user to benefit from the GBT modal features, a tool making it possible to visualize and select the deformation modes is included in the code.

As mentioned earlier, the code covers four types of member end support conditions: (i) simply supported (pinned-pinned), (ii) fixed-free (cantilever), (iii) fixed-fixed and (iv) fixed-pinned – moreover, recall that it is also possible to specify different support conditions for the various deformation modes (*e.g.*, bending and torsion). On the other hand, the (pre-buckling) applied stresses may stem from arbitrary combinations of (i) end bending moments, (ii) axial or transverse point loads (acting at any cross-section along the span), (iii) axial or transverse uniformly distributed loads and (iv) uniform bimoments – however, the transverse loads must act on a plane containing the shear centre.

The user may indicate an arbitrarily long list of member lengths ( $L$  values), so that the code produces a curve describing the variation of  $\lambda_b$  (buckling load parameter) or  $\omega$  (natural frequency) with  $L$  as well as the corresponding modal participation diagrams  $P_i$  vs  $L$  – in either case, the plot scale and limit values are freely chosen by the user. The buckling or vibration modes are represented by means of either (i) 3D deformed configurations of the entire member, combined with interactive visualization tools, or (ii) 2D deformed configurations of any cross-section – it is always possible (i) to select the deformation modes employed to obtain the representation (out of the  $n_d$  included in the analysis, selected after performing the cross-section analysis) and (ii) to specify the displacement scale. Finally, the code output is also saved in formatted text files, thus making the task of processing it by means of spreadsheet applications (*e.g.*, Microsoft Excel) very easy and straight forward.

The GBTUL interface was conceived to minimize the amount of data inputs and also the occurrence of the most common mistakes (some inputs are controlled to detect them). Moreover, “help buttons” associated with most input/output commands are also available.

**Structure.** The GBTUL code executable program is written in FORTRAN 90 and linked to a graphic user interface developed in VB.NET, and has its 3D representations created in the VRML graphic environment – this graphic user interface involves the sequence of *four screens* shown in fig. 4(b): while the first three deal with data input, the fourth one is related to the result output. This sequence is closely related to the performance of a GBT analysis (see fig. 4(a)): (i) Screens 1, 2 and 3 concern the inputs associated with the cross-section analysis, deformation mode selection and member analysis, and (ii) Screen 4 displays the sought buckling or vibration solution.

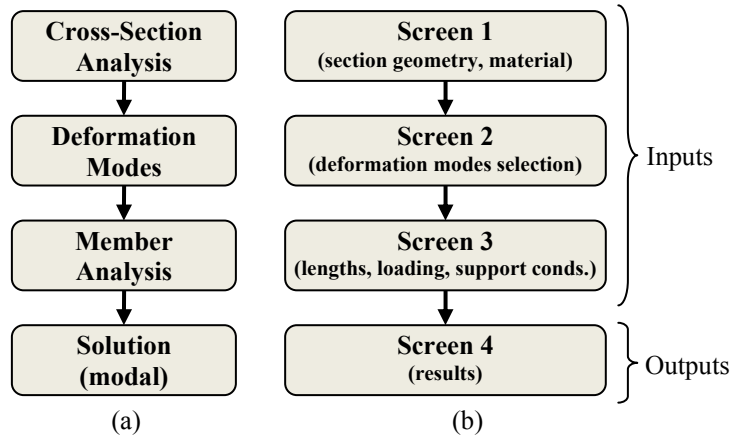


Fig. 4: Comparison between (a) the steps involved in a GBT-based analysis and (b) the sequential procedures of the GBTUL graphical user interface.

### Input Data

The first three screens ask for the data required to perform the desired analysis – button `Next`, located at the bottom right corner of each of them, directs the user to the subsequent screen. In the next subsections, one provides a brief description of the main commands associated with each screen. Moreover, one illustrates the application of GBTUL to perform the buckling analysis of (i) lipped channel steel cantilevers with the cross-section dimensions and GBT discretization given in figs. 2(b)-(c) and acted by a uniformly distributed transverse load acting along the shear center axis (see fig. 5). One obtains  $\lambda_b$  vs.  $L$  curves concerning the first three buckling modes and the length range  $10 \leq L \leq 1000$  cm – all the 17 deformation modes yielded by the GBT cross-section analysis are included in the buckling analyses.

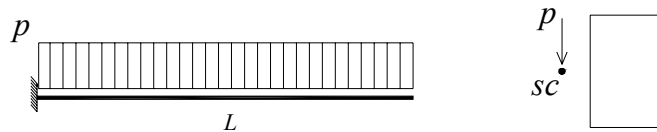


Fig. 5: Illustrative example: lipped channel cantilever beam acted by an uniformly distributed transverse load applied along the shear center axis

**Cross-Section Analysis.** The first screen, shown in fig. 6, contains (i) several data inputs and (ii) a graphic representation window with a few associated commands. In the `Material Model` field, one introduces the elastic constants of the member

material (or materials) – for isotropic members (e.g., the cantilever of the illustrative example), one uses the template associated with button `Isotropic` (see fig. 7(a)) and only the values of  $E$ ,  $\nu$  and  $\rho$  are required (the unit system is arbitrary – in this case, one uses  $[kN, cm, s]$ ). The next field asks for the cross-section wall characterization: the (i) end node coordinates, (ii) material, (iii) thickness and (iii) number of intermediate nodes. For the commonly used cross-section geometries, such as C, U, “Rack”, Z, I, T and L (and also a single plate), pre-defined templates

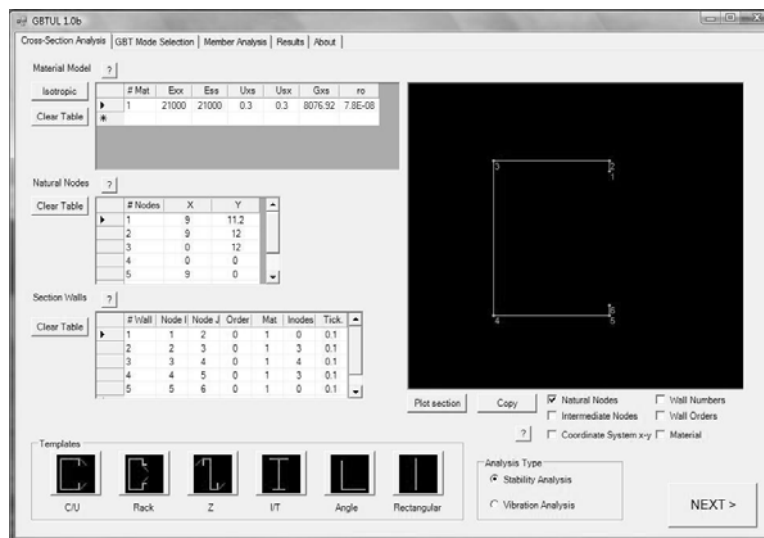


Fig. 6: GBTUL – general view of Screen 1

are available to minimize the amount of input data. In the illustrative example, button `C/U` activates the window shown in fig. 7(b), which requires the cross-section dimensions – note that, as shown in fig. 2(c), 3 intermediate nodes (`Inodes`) are considered both in the lipped channel web and flanges.

The cross-section geometry is visualized in the representation window. Using the check boxes shown below, one may choose to represent several additional features, like the intermediate nodes or the wall material references – the illustrative lipped channel section representation is shown in fig. 6. Finally, the type of analysis is selected through button `Analysis Mode`: either buckling (`Stability Analysis`) or free vibration (`Vibration Analysis`).



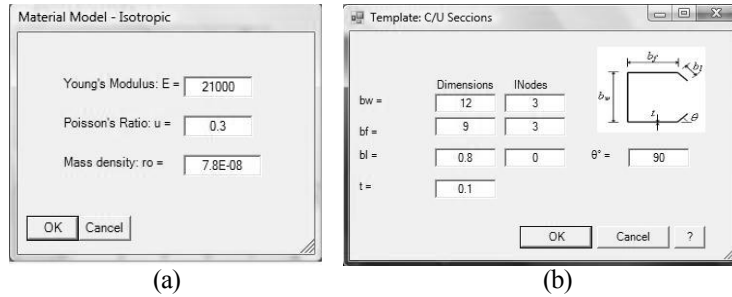


Fig. 7: Screen 1: (a) isotropic material and (b) “C/U” cross-section templates

**Screen 2: Deformation Mode Selection.** The second screen, depicted in fig. 8, (i) displays the output of the *cross-section analysis* and (ii) asks the user to select the deformation modes to be included in the subsequent *member analysis*. Several cross-section features are presented on the left side: the (i) geometrical properties (*e.g.*, cross-section area, major/minor moments of inertia or warping constant), and (ii) stiffness and mass matrices – they are shown upon a click on the corresponding buttons.

The representation window, located on the right side, makes it possible to visualize each individual cross-section deformation mode – both the in-plane deformed configuration (in-plane displacements –  $v_k(s)$  and  $w_k(s)$ ) and the warping profile (warping displacements –  $u_k(s)$ ). The  $n_d$  deformation modes to be included in the analysis can be selected in three different ways: (i) button `Pick Mode`, which adds the mode currently displayed, (ii) button `Pick Mode`, which adds the mode currently displayed, (ii) button `Pick All`, which selects all available modes ( $n_d=N_d$ ) or (iii) the text field `Mode Selection`, where the selected mode numbers can be entered directly.

In the illustrative example, one presents the displacement field associated with deformation mode 4 (torsion): in-plane deformed configuration (fig. 9(a) –  $v_4$  and  $w_4$ ) and warping profile (fig. 9(b) –  $u_4$ ). Since all the deformation modes are to be included in the buckling analysis, one clicks `Pick All`.

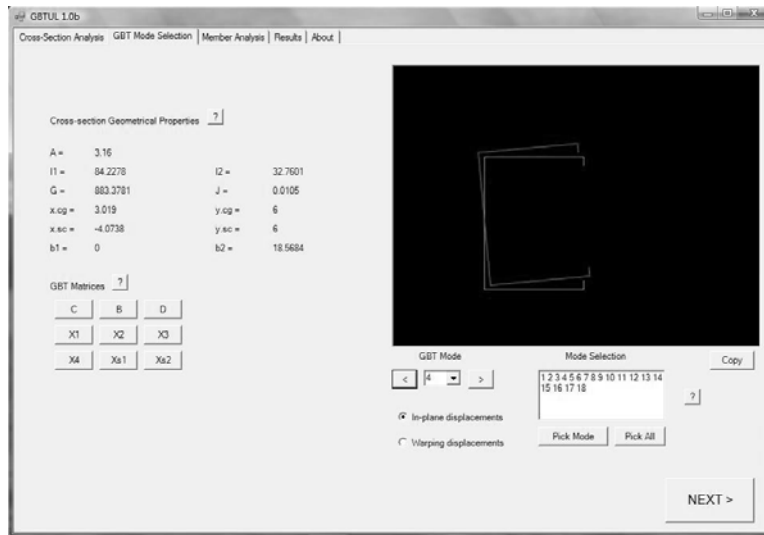


Fig. 8: GBTUL – general view of Screen 2.

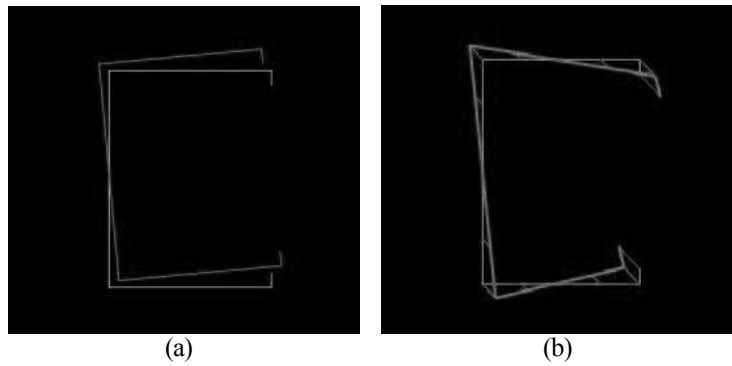


Fig. 9: Screen 2: (a) in-plane deformed configuration and (b) warping profile of mode 4

**Screen 3: Member Analysis.** In the third screen of GBTUL (see fig. 10), the user (i) chooses the type of solution (analytical or numerical) and (ii) specifies the member length, loading and end support conditions. On the left side, there are the tabs Analytical Solution (fig. 11(a)) and Numerical Solution (fig. 11(b)), which indicate that the equilibrium equations are to be solved analytically (sinusoidal  $\phi_k(x)$ ) or numerically (beam finite elements). Since the illustrative example corresponds to cantilever beams, the numerical solution is the only that can be adopted – moreover, the cantilevers are subjected to non-uniform bending moment diagrams.

When adopting the analytical solution (fig. 11(a)), always computationally more efficient (whenever applicable), the user must provide (i) the parameters defining the acting (uniform) internal force, moments and bimoment (*i.e.*,  $N$ ,  $M_y$ ,  $M_z$  and  $B$ ), (ii) the Number of half-waves (*i.e.*, the maximum number of longitudinal half-waves exhibited by the buckling/vibration mode) and (iii) the Number of intervals – this number is important for the graphical representations appearing in Screen 4 and addressed further ahead.

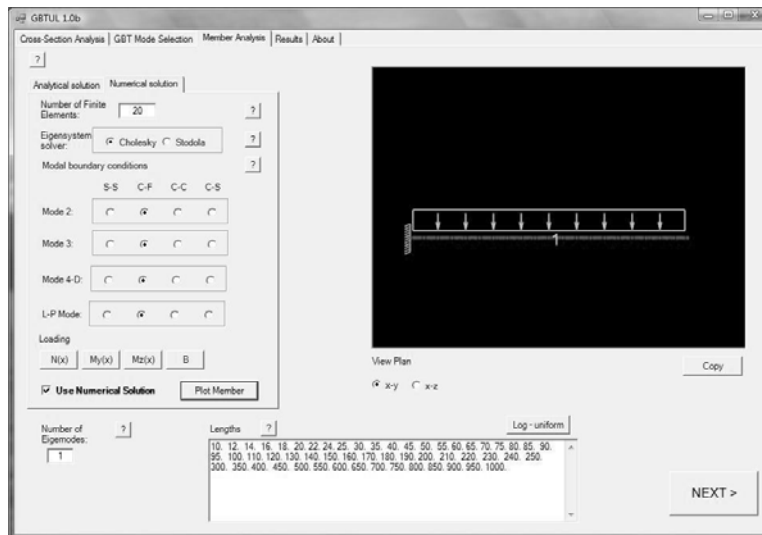


Fig. 10: GBTUL – general view of Screen 3

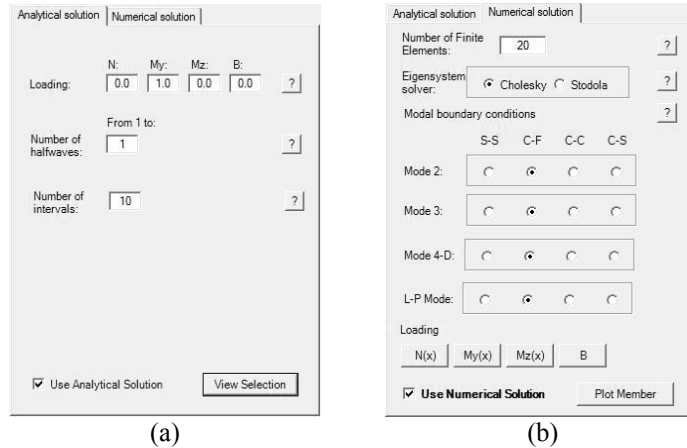


Fig. 11: Screen 3: (a) analytical solution and (b) numerical solution tabs

On the other hand, if the numerical solution is adopted (Numerical Solution tab in fig. 11(b)), the user first indicates the desired Number of Finite Elements – 20 in the illustrative example. Then, he must choose the eigenvalue problem solver between (i) Cholesky’s factorization method (the one adopted by default) and (ii) Stodola’s method. Next, the four rows of buttons Modal Boundary Conditions allow for the specification of the member boundary conditions. This can be made independently for (i) mode 2, (ii) mode 3, (iii) modes 4+D (modes 4, 5 and 6 in the illustrative example), and (iv) modes LP (modes 7-17 in the illustrative example) – concerning mode 1 (axial extension), it is always fully restrained at the member left end section and completely free at the right one. In the illustrative cantilever beam, it suffices to select C-F in the four button rows. Finally, the buttons  $N(x)$ ,  $M_Y(x)$ ,  $M_Z(x)$  and B concern the definition of the loading pattern (buckling analysis only), which may involve stress gradients associated with the axial force and bending moments – fig. 12 shows the illustrative example dialogue box concerning  $M_Y(x)$  – an unitary value has been assigned to the distributed load parameter  $p_Y$ . The window on the right makes it possible to visualize and check the correctness of the loading and support conditions specified in the tabs.

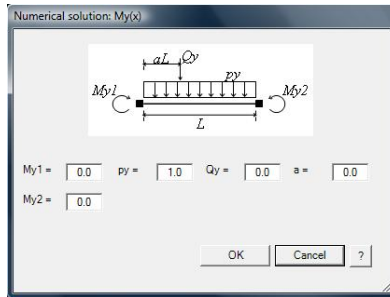


Fig. 12: GBTUL –Screen 3: “My(x) dialogue box”

Lastly, the fields `Number of Eigenmodes` and `Lengths` ask the user to specify (i) the highest order of the buckling or vibration modes sought and (ii) the lengths of the members to be analysed. In the illustrative example, one asks for the 3 first buckling modes of cantilevers with lengths in the interval  $10 \leq L \leq 1000\text{cm}$  – a 63-value length list comprised in that range appears by default in the `Lengths` field (alternatively, the `Log-uniform` button makes it possible to indicate a length list uniformly spaced in a logarithmic scale).

### Output Data

The results of the analyses performed are presented graphically in Screen 4 as (i) buckling or vibration curve plots, which provide the variation of the buckling load parameter or natural frequency with the member length  $L$ , (ii) modal participation diagrams, and (iii) 2D or 3D representations of the member buckling or vibration modes – these data are also recorded in formatted text files, making it very easy to further process them. In the next subsections, one describes these result outputs.

**Screen 4: Graphic Outputs.** Fig. 13 provides a general overview of Screen 4. While the buckling ( $\lambda_b$  vs.  $L$ ) or vibration ( $\omega$  vs.  $L$ ) curves are depicted at the upper right side, the modal participation diagrams ( $P_i$  vs.  $L$ ) are plotted in the bottom right side. On the left side there are some commands concerning the selection of options associated with the plots presented.

While both plots displayed in fig. 13 correspond to the length range indicated, (i) the results appearing above the upper plot and (ii) the 2D and 3D deformed configurations concern the buckling or vibration mode of a beam with a

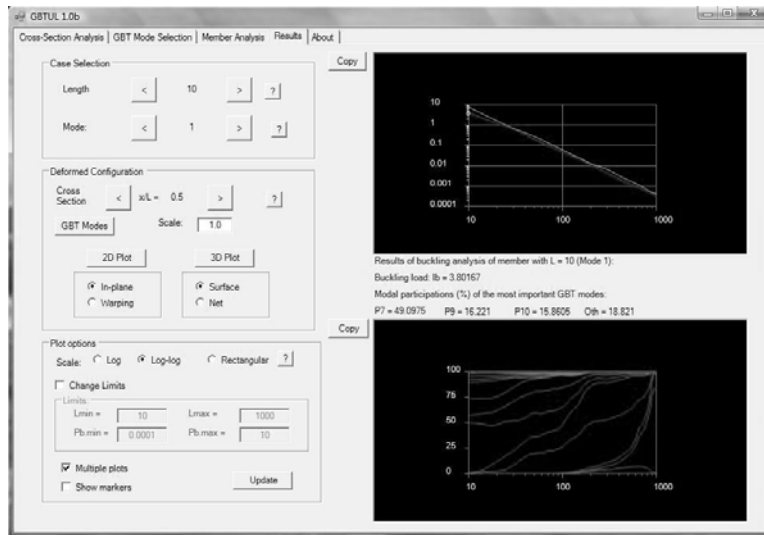


Fig. 13: GBTUL – general view of Screen 4

particular length  $L$  – the selection of this beam is made through the commands `Length` and `Mode`, located on the screen top left side. The results displayed are the bifurcation parameter value  $\lambda_b$  ( $\lambda_b$ ) and the most important deformation mode contributions to the buckling or vibration mode ( $P_i$ ). On the other hand, the “location” of that specific member on the two above plots is identified by (i) a small “ball” (lying on top of the  $\lambda_b$  vs.  $L$  or  $\omega$  vs.  $L$  curve under consideration) and (ii) a vertical line (crossing the modal participation diagram at that  $L$  value).

By using the `Plot Options`, located at the screen bottom left side, one is able to change some features associated with the visualization of the two plots, namely (i) the scales of the axes, which may be either logarithmic (`Log`), bi-logarithmic (`Log-Log`) or rectangular, (ii) the scale limits (`Limits`), (iii) the number of curves shown (one or more) (`Multiple Plots`), and (iv) the option of showing or hiding the points defining the buckling/vibration curves (`Show Markers`).

Finally, the commands pertaining to the 2D or 3D representations are located at mid-height on the left side – they concern the specific member under consideration and are displayed in separate windows after one clicks on buttons `2D Plot` or `3D Plot`. In the 2D configurations, one (i) uses the command `Cross-Section`, in order to select the sought cross-section (*i.e.*, its  $x$  coordinate value), and (ii) selects either `In-plane` (see fig. 14(a)) or `Warping` (see fig. 14(b)) displacements. As for the 3D configurations, the member buckling or vibration mode shape can be plotted either (i) with opaque surfaces (`Surface` – see fig. 15(a)) or (ii) with a line network (`Net` – see fig. 15(b)). In either case, the user may still specify

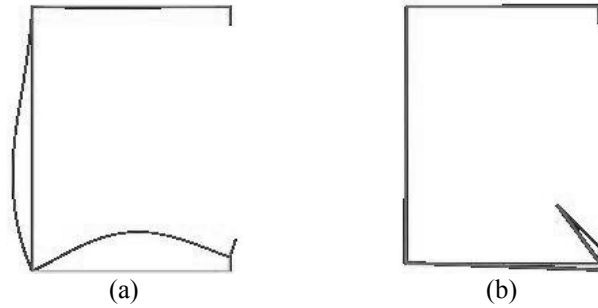


Fig. 14: GBTUL -Screen 4: (a) In-plane and (b) Warping buckling mode shape representations ( $L=50\text{ cm}$ ,  $x/L=0.25$ )

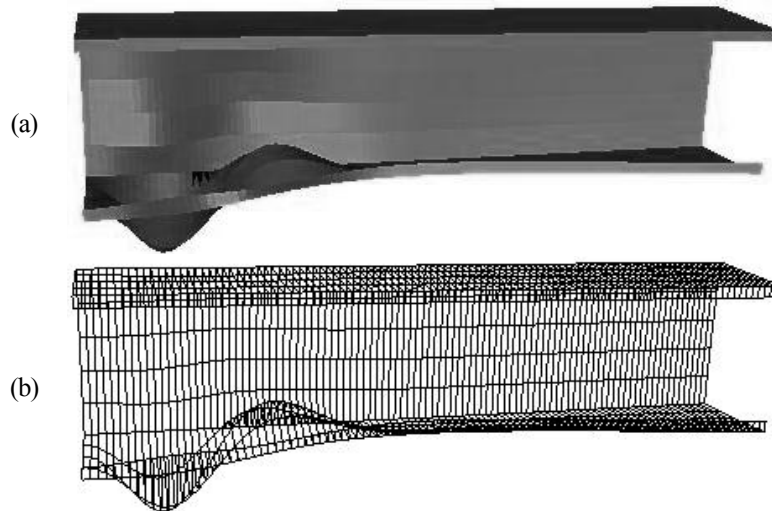


Fig. 15: Screen 4: (a) Surface and (b) Net 3D buckling mode shape representations ( $L=50\text{ cm}$ )

(i) the subset of the deformation modes included in the analysis (those selected in Screen 2) on which to base the representation, and also (ii) a displacement scale factor.

With respect to the illustrative example, fig. 13 shows (i) the  $\lambda_b$  vs.  $L$  curves corresponding to the three first 3 buckling modes (in bi-logarithmic scale) and (ii) the  $P_i$  vs.  $L$  modal participation diagram associated with the first (critical) buckling mode. As

for figs. 14 and 15, they show 2D and 3D representations of the  $L=50\text{ cm}$  cantilever first buckling mode (for which  $\lambda_b \equiv p_b = 19.26\text{ kN/m}$ ).

**Text Files.** All the results are saved into three formatted text files, which can be opened and used as input to most data processing applications. These files, created in the folder `GBTUL\calc\Output_Files\`, are the following:

- (i) `Matrices.txt` – contains (i<sub>1</sub>) the displacement values ( $u_i$ ,  $v_i$  and  $w_i$ ) at each cross-section node, for each deformation mode, and (i<sub>2</sub>) the components of the GBT matrices.
- (ii) `Results.txt` – includes (ii<sub>1</sub>) a list of the eigenvalues (buckling load parameters or natural frequencies) associated with every member length and eigenvector (buckling or vibration mode), as well as (ii<sub>2</sub>) the corresponding modal participation factors and (ii<sub>3</sub>) the number of half-waves they exhibit (only in the case of the analytical solutions).
- (iii) `Mafuncs.txt` – contains the longitudinal amplitude functions ( $\phi_k(x)$ ) and their derivatives ( $\phi_{k,x}(x)$ ) associated with every deformation mode included in the analysis, for all member lengths and buckling or vibration modes determined. These functions are defined by their values at a selected (finite) set of cross-sections located along the member length.

## Conclusion

This paper presented the code `GBTUL 1.0β`, which performs buckling or vibration analyses of prismatic thin-walled members with open cross-sections. The code is based on Generalized Beam Theory (GBT) and is available *online* as *freeware*. Initially, a very brief overview of the performance of a GBT structural analysis was provided, focusing on its unique modal features. Then, the sequential procedure involved in using `GBTUL 1.0β` was addressed – it consisted of going through its four interactive screens, explaining and illustrating, by means of the buckling analysis of a cantilever acted by an uniformly distributed transverse load (non-uniform bending), all the steps and the options associated with the performance of a specific member buckling or vibration analysis.

Finally, one last word to mention that the code and its documentation, including user manuals and tutorials, are available for free download on the website <http://www.civil.ist.utl.pt/gbt>.

## Acknowledgements

The first author gratefully acknowledges the financial support provided by *FCT – Fundação para a Ciência e Tecnologia* (Portugal), through the doctoral scholarship n° SFRH/BD/18289/2004.



## References

- Ádány S. and Schafer B.W. (2006). “Buckling mode decomposition of single-branched open cross-section members via finite strip method: derivation”. *Thin-Walled Structures*, 44(5), 563-584.
- AISI (American Iron and Steel Institute) (2004). *Appendix I of the North American Specification (NAS) for the Design of Cold-Formed Steel Structural Members: Design of Cold-Formed Steel Structural Members with the Direct Strength Method*, Washington DC.
- Bebiano R., Pina P., Silvestre N. and Camotim D. (2008). *GBTUL 1.0 $\beta$ – Buckling and Vibration Analysis of Thin-Walled Members*, DECivil/IST, Technical University of Lisbon (<http://www.civil.ist.utl.pt/gbt>).
- Bebiano R., Silvestre N. and Camotim D. (2007). “GBT formulation to analyze the buckling behavior of thin-walled members under non-uniform bending”, *International Journal of Structural Stability and Dynamics*, 7(1), 23-54.
- Camotim D., Silvestre N., Gonçalves R. and Dinis P.B. (2004). “GBT analysis of thin-walled members: new formulations and applications”, *Thin-Walled Structures: Recent Advances and Future Trends in Thin-Walled Structures Technology* (Loughborough, 25/6) J. Loughlan (ed.), Canopus Publishing, Bath, 137-168.
- Camotim D., Silvestre N., Gonçalves R. and Dinis P.B. (2006a). “GBT-based structural analysis of thin-walled members: overview, recent progress and future developments”, *Advances in Engineering Structures, Mechanics and Construction* (SMCD 2006 – Waterloo, 14-17/5) M. Pandey, W.-C. Xie, L. Xu (eds.), Springer, Dordrecht, 187-204.
- Camotim D., Silvestre N., Dinis P.B., Bebiano R. and Basaglia C. (2006b). “Recent progress in the numerical analysis of thin-walled steel members and Frames”, *Proceedings of International Symposium on Innovative Design of Steel Structures* (Hong Kong, 10/11) B. Young (ed.), 63-104.
- Camotim D., Silvestre N. and Bebiano R. (2007). “GBT local and global vibration analysis of thin-walled members”, *Dynamics of Plated Structures: Analysis and Design*, N.E. Shanmugam and C.M. Wang (eds.), Woodhead Publishing Ltd., Cambridge, 36-76.
- Cheung Y.K. and Tham L.G. (1998). *The Finite Strip Method*, CRC Press, Boca Raton.
- CEN (Comité Européen de Normalisation) (2005). *Eurocode 3: Design of Steel Structures - Part 1.3: General Rules and Supplementary Rules for Cold-formed Members and Sheeting*, Brussels.
- Hancock G.J., Murray, T. and Ellifritt D. (2001). *Cold-Formed Steel Structures to the AISI Specification*, Marcel Dekker, New York.

- Papangelis J.P. and Hancock G.J. (1998). *THIN-WALL 2.0*, Center for Advanced Structural Engineering, School of Civil and Mining Engineering, University of Sydney.
- SA-SNZ (Standards of Australia and Standards of New Zealand) (2005). *Australian/New Zealand Standard on Cold-Formed Steel Structures – AS/NZS 4600* (2<sup>nd</sup> edition), Sydney-Wellington.
- Schafer B.W. (2005), *Direct Strength Method Design Guide*, American Iron & Steel Institute (AISI), Washington DC.
- Schafer B.W. (2008). “Review: the Direct Strength Method of cold-formed steel member design”, *Journal of Constructional Steel Research*, **64**(7-8), 776-778.
- Schafer B.W. (2007). *CUFSM 3.12 – Finite Strip Buckling Analysis of Thin-Walled Members*, Department of Civil Engineering, Johns Hopkins University (<http://www.ce.jhu.edu/bschafer>).
- Schardt R. (1989). *Verallgemeinerte Technische Biegetheorie*, Springer-Verlag, Berlin, 1989. (German)



## **Impact of global flexural imperfections on the cold-formed steel column curve**

Schafer, B.W.<sup>1</sup>, Zeinoddini, V.M.<sup>2</sup>.

### **ABSTRACT**

Due to inherent complications in manufacturing and installation global out-of-straightness imperfections in cold-formed steel columns may sometimes be greater than  $L/960$ , which is the maximum amount assumed in North American cold-formed steel design specifications. The correction that should be applied to currently used column design curves to account for imperfections larger than  $L/960$  is unknown. To find this correction the strength of typical cold-formed steel columns with explicit imperfections is determined using a geometric and material nonlinear beam finite element solution, and a closed-form solution. The closed-form solution is shown to agree well with the finite element solution and accurately recreates the current design specification column curves at the  $L/960$  imperfection level. The closed-form solution is used as the basis for predicting reductions in the nominal column stress for columns with imperfections that are greater than  $L/960$ . The developed solution is recommended in design for those situations in which large out-of-straightness imperfections are encountered.

### **INTRODUCTION**

Cold-formed steel columns, like all columns, are sensitive to geometric imperfections, such as out-of-straightness. Under axial load, imperfections ( $\delta_o$ ) lead to lateral deformations ( $\delta$ ) which create bending demand on the columns, known as  $P-\delta$  moments. As a result of imperfections, even a column with

---

<sup>1</sup> Associate Professor, Department of Civil Engineering, Johns Hopkins University, Baltimore, MD 21218

<sup>2</sup> Graduate Student, Department of Civil Engineering, Johns Hopkins University, Baltimore, MD 21218

perfectly aligned axial load undergoes compression and bending. However, it is inconvenient to consider every column as a beam-column, thus the effect of P- $\delta$  moments occurring due to  $\delta_o$  imperfections are empirically buried into column curves used in design.

For hot-rolled steel the AISC column curve (i.e., AISC 2005) assumes an out-of-straightness imperfection,  $\delta_o$ , of  $L/960$ , where  $L$  is the column length (Galambos 1998). The column curve for cold-formed steel was determined based on comparing test data to the AISC column curve, with appropriate reductions for local buckling. This comparison led to the adoption of the AISC column curve in cold-formed steel design (i.e., AISI-S100 2007). As a result, the maximum assumed out-of-straightness in a cold-formed steel column curve is also  $L/960$ .

Production of a cold-formed steel column involves the potential for larger out-of-straightness imperfections than a typical hot-rolled steel column. Therefore, this paper investigates the implication of considering larger  $\delta_o$  imperfections in cold-formed steel and the impact of these larger  $\delta_o$  imperfections on cold-formed steel column capacity and the cold-formed steel column design curve.

#### **AISI-COFS Stud Preliminary Out-of-Straightness Study Request**

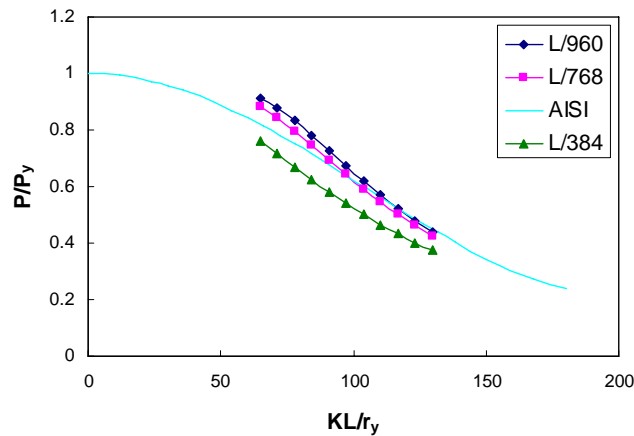
In May of 2007 a task group of the American Iron and Steel Institute – Committee on Framing Standards (AISI-COFS) developed the outline for a study to assess the impact of global (sweep) imperfections on cold-formed steel columns. Essentially, the idea for their study was to model columns in MASTAN (Ziemian 2007) with explicit geometric imperfections and vary the length of columns in order to generate column capacities as a function of the size of geometric imperfection. This paper was written in response to this study, but goes beyond the specific requests of this study to explore column curve sensitivity to global imperfections using both MASTAN and a more straightforward closed-formed solution.

### **NUMERICALLY GENERATED COLUMN CURVE VIA MASTAN**

#### **Column strength for different imperfections**

Material and geometric nonlinear MASTAN analysis (simple step using  $\sim 1000$  steps to failure) of simply supported columns with an initial circular out-of-straightness  $\delta_o$  of  $L/960$ ,  $L/768$ , and  $L/384$  was completed on a 350S162-33 (SSMA nomenclature) stud with  $f_y = 33\text{ksi}$  and  $KL/r_y$  varying from 62 to 122. The predicted column capacity from these MASTAN analyses is provided along with the AISI column curve in Figure 1. The MASTAN predicted column curves follow the same basic trend as the AISI column curve, indicating that the

analysis is capturing the basic column failure. The MASTAN analyses conducted here only include the impact of out-of-straightness on global weak-axis flexural buckling. Local buckling, torsional-flexural buckling, details of the material stress-strain curve, residual stresses, etc. are ignored.



**Figure 1 MASTAN predicted column curves for 350S162-33 with varying imperfection size**

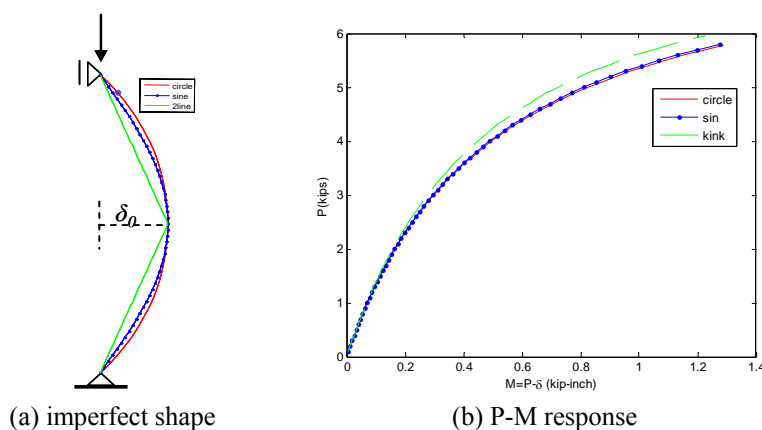
### **Influence of imperfection shape**

Due to the manufacturing process a likely out-of-straightness imperfection shape for a cold-formed steel column is a constant curvature sweep in the weak-axis direction. Typical theoretical solutions employ a sinusoidal imperfection (since the solution from the differential equation for the buckling mode is itself a sinusoid). The simplest imperfection to introduce into a model is a kink, where the column is modeled as 2 straight lines with an imperfection at midspan.

The importance of imperfection shape is studied for a 350S162-33 at  $KL/r_y$  of 97 with  $\delta_o=L/960$  in Figure 2. Figure 2 demonstrates that the magnitude of the midspan deflection ( $\delta_o$ ) is far more important than the shape. A sinusoidal imperfection delivers slightly less  $P-\delta$  moment than a constant curvature circular imperfection, but the difference is insignificant. The kink or 2-line imperfection is slightly unconservative, in that less  $P-\delta$  moment is generated at a given level of  $P$  when compared with the circular or sinusoid imperfection shape.

## CLOSED-FORM SOLUTION FOR COLUMN CURVE

For the simplified case of a pin-ended column in flexural buckling it is possible to develop a closed-form expression for the column capacity as a function of initial imperfection magnitude. The derivation relies on (i) providing the P- $\delta$  moment in a functional form, and (ii) providing the beam-column interaction equation (yield surface in MASTAN parlance) in a functional form. The intersection of the load, P, and moment, P- $\delta$ , with the beam-column interaction equation provides the column capacity.



**Figure 2 P- $\delta$  response for different out-of-straightness imperfection shapes on a 350S162-33 stud with a  $KL/r_y$  of 97.2 under increasing axial load**

### Geometric nonlinearity

For a pin-ended column with a sinusoidal initial imperfection of midspan magnitude,  $\delta_0$ , it may be shown (e.g., Chen and Lui 1987) that the midspan moment, which in the linear elastic case is simply  $P\delta_0$ , grows significantly as the axial load approaches the buckling load of the column. In particular, the midspan moment M may be expressed as

$$M = B_1 M_0 \quad (1)$$

$$M_0 = P\delta_0 \quad (2)$$

$$B_1 = 1/(1-P/P_{cr}) \quad (3)$$

$$P_{cr} = \pi^2 EI_y / L^2 \quad (4)$$

### Interaction equation

Column failure occurs when the  $P$ - $\delta$  moment,  $M$ , grows to the extent that the bending capacity of the column is exceeded. A linear beam-column interaction equation as used in AISI-S100 may be used for predicting when this occurs, via:

$$P/P_{no} + M/M_{no} \leq 1 \quad (5)$$

Where the equation is anchored by the assumed capacity in pure compression ( $P_{no}$ ) and in pure bending ( $M_{no}$ ). For the work herein:

$$P_{no} = A_g f_y = P_y \quad (6)$$

$$M_{no} = S_{effy} f_y \quad (7)$$

where the weak axis effective section modulus ( $S_{effy}$ ) is determined via AISI-S100<sup>3</sup>. The squash load  $A_g f_y$  is used instead of the effective axial load  $A_{eff} f_y$  only to provide more convenient comparison between AISI and the generated closed-formed curves. (If  $A_{eff} f_y$  is used for  $P_{no}$  the closed-form solution of this section is unchanged, but the AISI column curve determines  $A_{eff}$  at stress  $f_n$ , where  $f_n$  varies from  $f_y$  down to  $f_{cr}$  for global buckling as a function of the column global slenderness. To avoid calculation of  $A_{eff}$  for any global column slenderness in generation of the AISI column curve,  $A_{eff}$  is set to  $A_g$  herein.)

### Column strength as a function of imperfection size

Substituting Eq. (2) and (3) into Eq. (1) and the resulting expression into Eq. (5) one finds:

$$P/P_{no} + [P\delta_o(1/(1-P/P_{cr}))]/M_{no} \leq 1 \quad (8)$$

Setting the interaction equation equal to 1.0 and solving for the axial load,  $P$ , results in a quadratic equation in terms of  $P$ . The solution to Eq. (8) provides a column capacity,  $P$ , which is a function of  $P_{cr}$ ,  $P_{no}$ ,  $M_{no}$ , and  $\delta_o$ , where the typical column curve can be shown to be a function of only  $P_{cr}$  and  $P_{no}$ , but independent of  $M_{no}$  and  $\delta_o$ . Solving Eq. (8) for  $P$ , the column capacity, results in:

$$M_{no} P^2 + (-M_{no} P_{cr} - \delta_o P_{cr} P_{no} - P_{no} M_{no}) P + P_{no} M_{no} P_{cr} = 0 \quad (9)$$

The solution to which is readily found as:

$$P = \frac{-b - \sqrt{b^2 - 4ac}}{2a} \quad (10)$$

$$\text{where: } a = M_{no} \quad (11)$$

$$b = -M_{no} P_{cr} - \delta_o P_{cr} P_{no} - P_{no} M_{no} \quad (12)$$

$$c = P_{no} M_{no} P_{cr} \quad (13)$$

---

<sup>3</sup> AISIWIN v7.0 (Madsen 2007) was used for determining  $S_{effy}$ .



### Example column curves using closed-form solution

Using Eq. (10) column curves were generated for a 362S162-68 (50 ksi) and a 800S200-97 (50 ksi) as given in Figure 3 and Figure 4. The generated column curves using the closed-formed solution agree well with the AISI column curve in trend and magnitude and also shed further light on the regimes where sensitivity to out-of-straightness imperfection are the greatest. The results confirm that the existing AISI column curve inherently assumes an imperfection in the neighborhood of  $L/960$  and that the closed-formed solution can accurately model this effect.

The loss in column capacity for the 362S162-68 (50 ksi) and 800S200-97 (50 ksi) as  $\delta_0$  increases above  $L/960$  is shown in Figure 5 and Figure 6. The reduction in the column capacity is greatest in the low to intermediate slenderness range. If a column is slender the initial imperfection does not have a significant impact on the capacity, this is because as  $P$  approaches  $P_{cr}$  the  $P$ - $\delta$  moments quickly amplify leading to a capacity for  $P$  that asymptotes to  $P_{cr}$  for any  $\delta_0$ . However, in the inelastic regime the  $\delta_0$  can have a significant impact, for instance a strong reduction occurs around an unbraced length of 3 ft for the 362S162-68 and 4 ft for the 800S200-97.

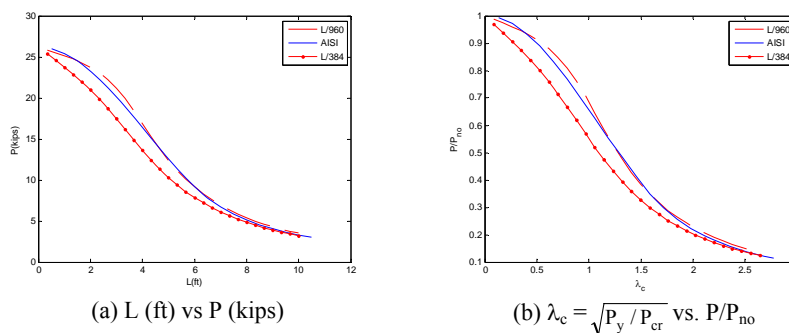
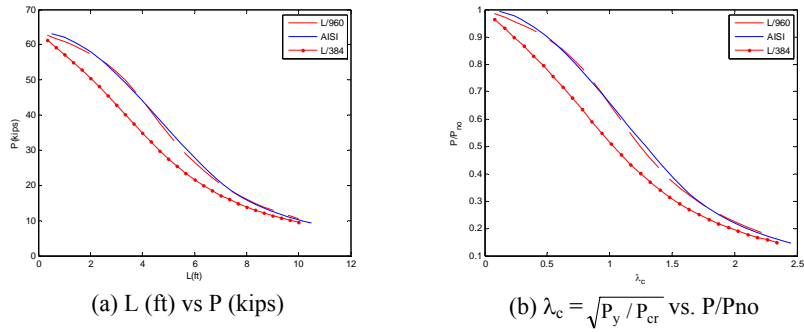
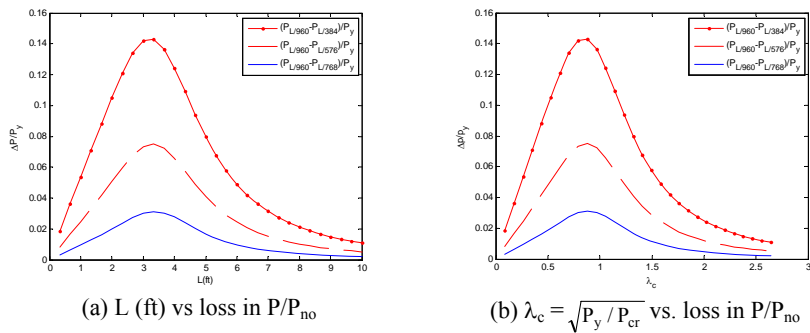


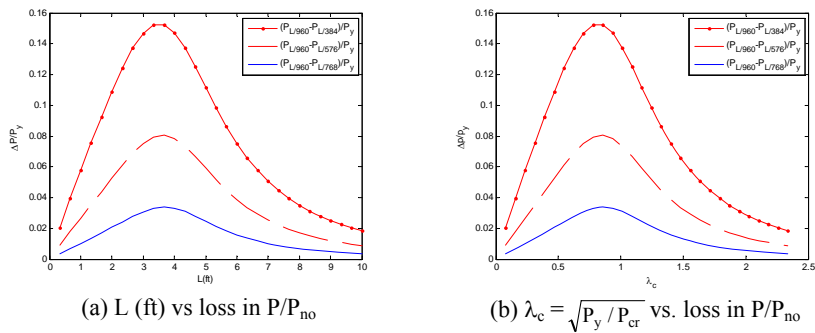
Figure 3 Predicted column curves for 362S162-68 (50 ksi) for varying imperfections



**Figure 4 Predicted column curves for 800S200-97 (50 ksi) for varying imperfections**



**Figure 5 Predicted loss in strength for 362S162-68 (50 ksi) as imperfections increase beyond L/960**



**Figure 6 Predicted loss in strength for 800S200-97 (50 ksi) as imperfections increase beyond L/960**

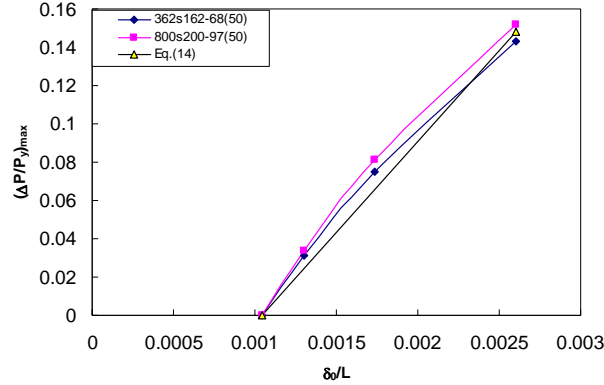


Figure 7 Maximum loss in column strength as a function of imperfection size

#### Column curve reductions for imperfections

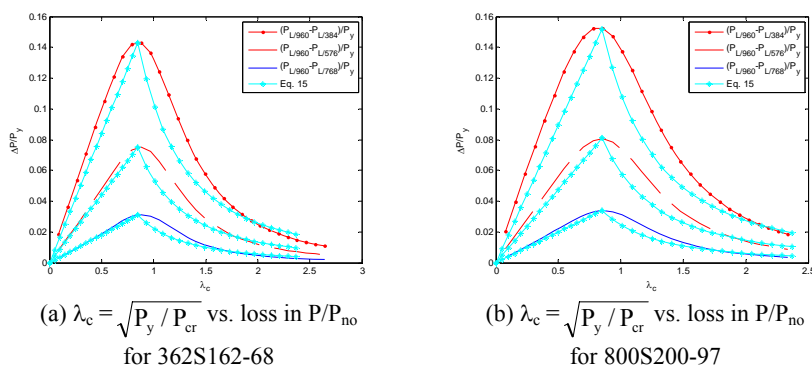
The maximum reduction in the column capacity (peak error in Figure 5 and Figure 6) is plotted as a function of imperfection size in Figure 7. Interestingly, the reduction as a function of  $P_y$  is nearly the same for the 362S162-68 and the 800S200-97, which is a bit surprising given how substantially different these sections are. Taking advantage of this fact, a simple empirical relation is found for the reduced capacity:

$$(\Delta P/P_y)_{\max} = 95(\delta_o/L - 1/960) \text{ for } \delta_o > L/960 \quad (14)$$

Use of Eq. (14) for predicting the loss in strength due to imperfections captures only the maximum loss in strength; however this loss varies as a function of length (or equivalently  $\lambda_c$ ) as shown in Figure 5 and Figure 6. With the peak loss known from Eq. (14) a simple empirical relation is found for the loss at all column slenderness:

$$\Delta P/P_y = \begin{cases} \frac{(\Delta P/P_y)_{\max} \lambda_c}{0.85} & \text{if } \lambda_c \leq 0.85 \\ \frac{(\Delta P/P_y)_{\max} 0.85^2}{\lambda_c^2} & \text{if } \lambda_c > 0.85 \end{cases} \quad (15)$$

Comparison of Eq. (15) to the closed-form solution of Eq. (10) is provided in Figure 8. The empirical relationship of Eq. (15) provides a reasonably accurate estimation to the more involved closed-form expressions.

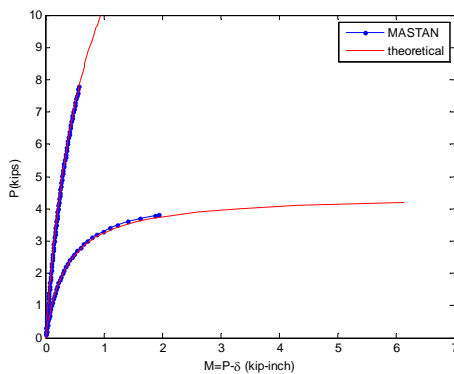


**Figure 8 Comparison of closed-form solution (Eq. 10) with empirical expressions (Eq. 15) for predicting the loss in column capacity for imperfections beyond L/960**

## COMPARISON OF MASTAN AND CLOSED-FORMED SOLUTION

### Geometric nonlinearity

The closed-form solution uses the  $B_1$  multiplier (Eq. 3) to determine the  $P$ - $\delta$  moments. To demonstrate that  $B_1$  and MASTAN provide the same solution to this geometrically nonlinear problem a 350S163-33 with  $\delta_o=L/960$  and  $KL/r = 64.8$  and 130 was analyzed in MASTAN and compared to Eq. (3) in Figure 9. MASTAN closely tracks the theoretical solution. In this simple case,  $B_1$  can replace the more involved geometrically nonlinear analysis completed in MASTAN as shown in Figure 9.



**Figure 9 Prediction of  $P$ - $\delta$  moments**

### Yield surface

In MASTAN the failure of the column is predicted to occur when the midspan P- $\delta$  moment increases to the point it reaches the yield surface<sup>4</sup>. The yield surface is anchored by the assumed capacity in pure compression ( $P_{no}$ ) and in pure bending ( $M_{no}$ ) as discussed previously. When the P- $\delta$  moments increase to such an extent that they intersect the yield surface – at this point a plastic hinge is assumed to form in the column, and for an isolated pin-ended column, this hinge formation is equivalent to axial collapse. The normalized yield surface employed in MASTAN, along with a simple linear yield surface (as used in the closed-formed solution) is shown along with the demands from two analyses in Figure 10. The two analyses are for a 350S162-33 with  $\delta_o=L/960$ ,  $f_y=33$ ksi,  $P_{no}=A_g f_y$ ,  $M_{no}=S_{eff} f_y$ , and  $KL/r_y=64.8$  and 130. The axial load ( $P$ ) at which the demand curves intersect the yield surface is the column capacity.

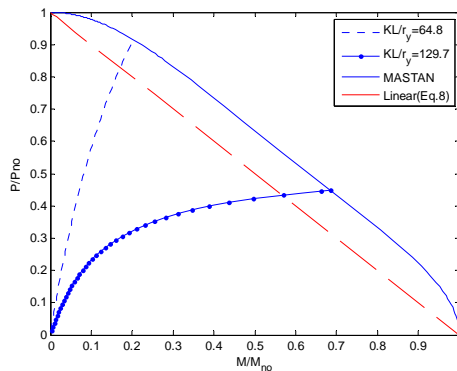


Figure 10 Comparison of yield surfaces

The MASTAN yield surface is less conservative than the simple linear yield surface (interaction equation). For low moment (little P- $\delta$  effect) the difference in axial load prediction between the two surfaces can be fairly large; however, in cases with larger P- $\delta$  moment the demand is nearly horizontal and the resulting difference in  $P$  is small. AISI-S100 conservatively assumes the linear interaction

<sup>4</sup> In conventional finite element analysis the yield surface is a function of stress, for concentrated plasticity beam elements typically the yield surface is integrated over the cross-section so that the surface is a function of forces and moments. The resulting yield-surface in force-moment space is essentially a beam-column interaction equation. In MASTAN the default yield surface follows the following equation:  $p^2+m^2+3.5p^2m^2=1$  (Eq. 10.18 McGuire et al. 2000) and is calibrated to match a typical W-section in strong-axis bending. With appropriate changes to the compression and bending anchors this function has been shown to be a reasonable (but approximate) choice for other shapes.

equation is applicable to cold-formed steel beam-columns, and this is used in the closed-formed solution provided herein.

### Column curves

The only real difference between the closed-formed solution and MASTAN is the shape of the yield surface, as described in the previous section. This difference does result in slightly different predictions for the column capacity, as shown in Figure 11 for a 350S162-33 (33ksi),  $\delta_o=L/960$ .

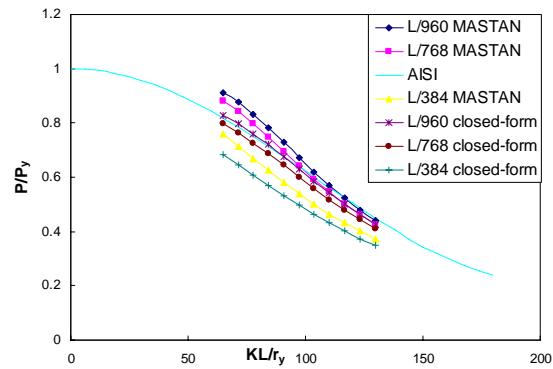
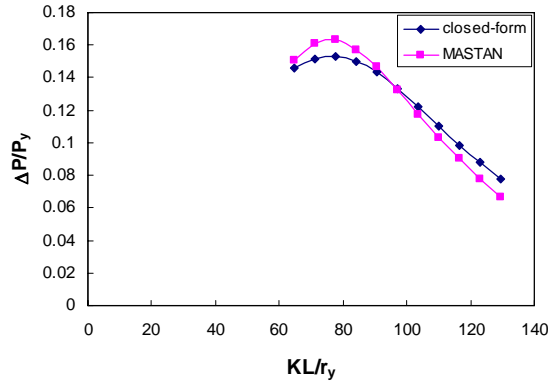


Figure 11 Comparison of MASTAN imperfect models with column curve

### Imperfection sensitivity

Although the column curves from MASTAN and the closed-formed solution are slightly different (Figure 11) the relative loss in strength between the different imperfection magnitudes is essentially the same. For the same section as Figure 11 the predicted loss in strength normalized to the squash load is shown for MASTAN and the closed-formed solution in Figure 12. Use of the closed-formed solution is recommended for all cases.



**Figure 12 Comparison of predicted strength drop between L/960 and L/384 imperfections for MASTAN and closed-form solution**

## DESIGN RECOMMENDATIONS

Based on the findings presented herein the following is recommended as a correction for the strength of cold-formed steel columns when imperfections are found to be greater than L/960. The nominal stress for a column is predicted from the existing AISI-S100 column curves as:

$$F_n^* = \begin{cases} 0.658^{\lambda_c^2} F_y & \text{if } \lambda_c \leq 1.5 \\ \frac{0.877}{\lambda_c^2} F_y & \text{if } \lambda_c > 1.5 \end{cases} \quad (16)$$

where the column slenderness is defined as

$$\lambda_c = \sqrt{F_y / F_e} , \quad (17)$$

and where  $F_y$  is the yield stress, and  $F_e$  is the global elastic buckling stress (minimum of flexural and torsional-flexural). From Eq. (14) we may define the maximum reduction in the nominal column stress due to imperfections which are greater than L/960 as:

$$(\Delta F_n)_{\max} = 95(\delta_o / L - 1/960)F_y \quad \text{for } \delta_o > L/960 \quad (18)$$

From Eq. (15) the reduction is known as a function of slenderness,  $\lambda_c$ , and may be expressed as:

$$\Delta F_n = \begin{cases} \frac{(\Delta F_n)_{\max} \lambda_c}{0.85} & \text{if } \lambda_c \leq 0.85 \\ \frac{(\Delta F_n)_{\max} 0.85^2}{\lambda_c^2} & \text{if } \lambda_c > 0.85 \end{cases} \quad (19)$$

where finally the nominal stress to be used in design is

$$F_n = F_n^* - \Delta F_n \quad (20)$$

If a simpler estimate of column nominal stress is needed  $(\Delta F_n)_{\max}$  may conservatively be used in place of  $\Delta F_n$ . The preceding recommendations conservatively extend the reductions found for flexural buckling to the case of torsional-flexural buckling.

Tabulated design examples following the equations suggested above are provided for the 362S162-68 (50 ksi) and 800S20097 (50ksi) in the Appendix.

## CONCLUSIONS

The strength of cold-formed steel columns is sensitive to imperfections. As axial load increases the imperfections lead to P- $\delta$  moments at midspan which eventually cause the bending capacity of the section to be exceeded and collapse to occur. It is possible to model both the increasing P- $\delta$  moment and the combination of axial load and moment that cause collapse using simple functions as is reported in the closed-formed solution herein. The presented closed-form solution agrees well with empirically derived cold-formed steel column design curves as well as advanced geometric and material beam finite element analysis solutions (MASTAN). Based on the closed-formed solution simple functions were determined for the appropriate reduction in the cold-formed steel column design strength when imperfections are greater than L/960. The reduced nominal column stress is recommended for use in design when out-of-straightness imperfections are known to be greater than L/960.

## ACKNOWLEDGMENTS

This work initiated in part through conversations with Tom Trestain regarding the impact of column out-of-straightness on cold-formed studs. This material presented herein is based in part upon work supported by the National Science Foundation under Grant No. 0528318. Any opinions, findings, and conclusions or recommendations expressed in this material are those of the author(s) and do not necessarily reflect the views of the National Science Foundation.



**REFERENCES**

- AISC (2005). Specification for Structural Steel Buildings. American Institute of Steel Construction, Chicago, IL. ANSI/ASIC 360-05
- AISI (2007). North American Specification for the Design of Cold-Formed Steel Structures. American Iron and Steel Institute, Washington, D.C., AISI-S100.
- Chen, W.F., Lui, E.M. (2007). Structural Stability: Theory and Implementation. Prentice-Hall.
- Galambos, T. (1998) "Guide to Stability Design Criteria for Metal Structures". 5th ed., Wiley, New York, NY, 815-822.
- Madsen (2007) AISIWIN, v7.0, Devco Software, <http://www.devcosoftware.com/aisiwin.html> last visited 11 July 2007.
- McGuire, W., Gallagher, R.H., Ziemian, R.D. (2000). Matrix Structural Analysis. 2<sup>nd</sup> Edition. Wiley.
- Ziemian (2007) MASTAN, v3.0, [www.mastan2.com](http://www.mastan2.com) last visited 11 July 2007.

**APPENDIX: TABULATED COLUMN DESIGN EXAMPLE**  
**Example column calculations for imperfection sensitivity**

BWS  
 August 2007

<b>362S162-68 (60 ksi)</b>																
E	29500 ksi															
$I_{y, gross}$	0.1858 in <sup>4</sup>															
$A_{g, gross}$	0.5237 in <sup>2</sup>															
$F_y$	50 ksi															
This example illustrates the loss in axial capacity for a 362S162-68 (50ksi) with an out-of-straightness of L/384 as the unbraced length is increased from 3 ft up to 8 ft. The nominal axial capacity is calculated by (1) ignoring the out-of-straightness using AISI 2007 and reported as $P_n^*$ below, (2) using the recommended expressions in Section "design recommendations" of the paper, reported as $P_n$ below, and (3) using the original derived strength reductions from Section "closed form solution for column curve" of the paper, $P_{n2}$ .																
<b>Design Method - stress based reduction - Section 6 of Paper</b>																
(Eq. 17) (Eq. 16) (Eq. 18) (Eq. 19) (Eq. 20) (Eq. 14) (Eq. 15)																
KL (ft)	$F_e$ (ksi)	$\square_c$	$F_n^*$ (ksi)	$A_g(F_n^*)$ (in <sup>2</sup> )	$P_n^*$ (kip)	$\square_{(L/384)}$ (in)	$(F_n)_{max}$ (ksi)	$F_n$ (ksi)	$A_g(F_n)$ (in <sup>2</sup> )	$P_n$ (kip)	$P_n^* - P_n$ (kip)	$(P_n^* - P_n) / P_n^*$ (%)	$\square_P$ (kip)	$P_{n2}$ (kip)	$(P_n^* - P_{n2}) / P_n^*$ (%)	
3	79.70	0.79	38.45	0.491	18.87	0.094	7.42	6.92	31.54	0.504	15.88	2.98	3.89	3.62	15.25	19%
4	44.83	1.06	31.35	0.504	15.80	0.125	7.42	4.81	26.54	0.515	13.66	2.14	3.89	2.52	13.29	16%
5	28.69	1.32	24.11	0.521	12.56	0.156	7.42	3.08	21.03	0.524	11.01	1.54	3.89	1.61	10.95	13%
8	11.21	2.11	9.83	0.522	5.13	0.250	7.42	1.20	8.63	0.524	4.52	0.61	3.89	0.63	4.50	12%

<b>800S200-97 (50 ksi)</b>																
E	29500 ksi															
$I_{y, gross}$	0.576 in <sup>4</sup>															
$A_{g, gross}$	1.2706 in <sup>2</sup>															
$F_y$	50 ksi															
This example illustrates the loss in axial capacity for an 800S200-97 (50ksi) with an out-of-straightness of L/384 as the unbraced length is increased from 3 ft up to 8 ft. The nominal axial capacity is calculated by (1) ignoring the out-of-straightness using AISI 2007 and reported as $P_n^*$ below, (2) using the recommended expressions in Section 6 of the paper, reported as $P_n$ below, and (3) using the original derived strength reductions from Section 4 of the paper, $P_{n2}$ .																
<b>Design Method - stress based reduction - Section 6</b>																
(Eq. 17) (Eq. 16) (Eq. 18) (Eq. 19) (Eq. 20) (Eq. 14) (Eq. 15)																
KL (ft)	$F_e$ (ksi)	$\square_c$	$F_n^*$ (ksi)	$A_g(F_n^*)$ (in <sup>2</sup> )	$P_n^*$ (kip)	$\square_{(L/384)}$ (in)	$(F_n)_{max}$ (ksi)	$F_n$ (ksi)	$A_g(F_n)$ (in <sup>2</sup> )	$P_n$ (kip)	$P_n^* - P_n$ (kip)	$(P_n^* - P_n) / P_n^*$ (%)	$\square_P$ (kip)	$P_{n2}$ (kip)	$(P_n^* - P_{n2}) / P_n^*$ (%)	
3	101.84	0.70	40.71	0.957	38.96	0.094	7.42	6.12	34.59	0.988	34.18	4.78	9.43	7.77	31.19	20%
4	57.29	0.93	34.70	0.987	34.25	0.125	7.42	6.14	28.56	1.027	29.32	4.94	9.43	7.81	26.45	23%
5	36.66	1.17	28.25	1.027	29.03	0.156	7.42	3.93	24.32	1.058	25.73	3.30	9.43	5.00	24.03	17%
8	14.32	1.87	12.56	1.200	15.07	0.250	7.42	1.54	11.02	1.225	13.50	1.56	9.43	1.95	13.11	13%



## Computed Flexural Buckling Stress for Cold-Formed Stainless Steel Columns

Shin-Hua Lin<sup>1</sup>, Chi-Ling Pan<sup>2</sup> and Chih-Peng Yu<sup>3</sup>

### Abstract

For the design of cold-formed stainless steel compression members, the ASCE Standard Specification can be used to determine the design axial strength. Due to the nonlinear stress strain behavior of the material, the design of stainless steel compression member is more complex than those of carbon steels. Instead of using the modulus of elasticity ( $E_o$ ), the non-linear tangent modulus ( $E_t$ ) were used for the design of cold-formed stainless steel columns. In this case, iterative procedures are needed to calculate the column buckling stress. Consequently, a simplified approach is developed to compute the column flexural buckling stress while without iterative process. In this simplified formulation, mathematical operation was utilized for numerical approximations. It is shown that the column strengths computed by the simplified formulas had good agreement with those determined by the ASCE Standard Specification. The simplified formulas are proposed to calculate the flexural buckling stress of cold-formed stainless steel columns. This paper presents the development of the proposed formulas for the design of stainless steel columns.

**Key Words:** Cold-Formed, Stainless Steel, Column, Specification, Tangent Modulus, Flexural Buckling, Approximation

---

<sup>1</sup> Associate Professor, Dept. of Civil Engineering, Minghsin Univ. of Science and Technology, Hsinfeng, Hsinchu, Taiwan

<sup>2</sup> Professor, Dept. of Construction Engineering, Chaoyang Univ. of Technology, Wufeng, Taichung, Taiwan

<sup>3</sup> Associate Professor, Dept. of Construction Engineering, Chaoyang Univ. of Technology, Wufeng, Taichung, Taiwan

## Introduction

Cold-Formed stainless steel compression members are widely used in architectural and structural applications, e.g., roof trusses, arched trusses and columns. These stainless steel structures are sometimes the preferred choice due to their superior corrosion resistance, attractive appearance, ease of maintenance and high strength. In the United States, ASCE Standard Specification, SEI/ASCE 8-02 (ASCE, 2002), can be used for the design of cold-formed stainless steel compression members. Because of the difference in mechanical behavior as shown in Fig. 1, the design of stainless steel columns is more complicated than those of carbon steels (ASCE, 1991). Stainless steels also have gradually yielding type of stress-strain curves with relatively low proportional limits (Johnson et al., 1969; Yu, 2000). Due to the nonlinear stress-strain behavior, the design of such compression members has long been followed by using the tangent modulus theory (Johnston, 1976; Galambos, 1968).

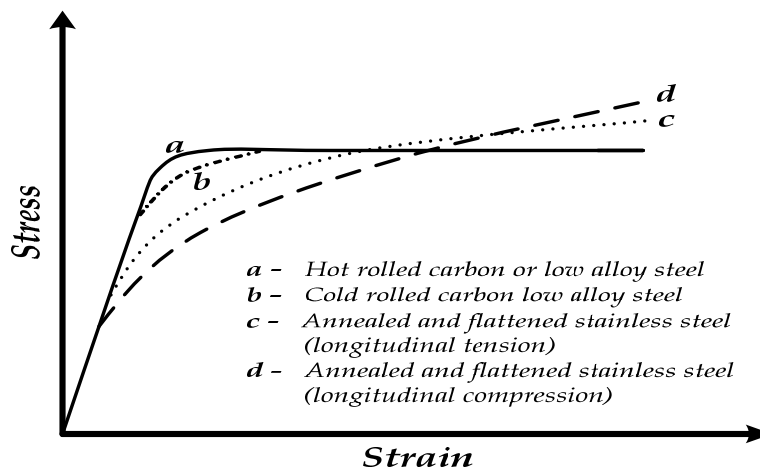


Fig. 1 Stress-Strain Curves of Carbon and Stainless Steels

Tangent modulus is used to account for the inelastic buckling of stainless steel compression components. It can be determined by using the modified Ramberg-Osgood equation (Ramberg et al., 1943; Hill, 1944) for specified types of stainless steels. Because of the nonlinear nature of tangent modulus, the column buckling stress is determined through an iterative process until the satisfied tolerance is reached. Previous research studies discussed different methods to deal with the nonlinear calculations (Rasmussen et al., 2000;

Rasmussen et al. 1997). This type of calculation is often tedious and time-consuming as compared with that of hot-rolled steel column design.

This paper presents the development of the simplified formulas for determining the flexural buckling stress of stainless steel column without successive iterations. Mathematical operations used to generate the simplified equations are discussed and the proposed design formulas are summarized herein. The proposed design formulas can be alternatively used for the design of austenitic type of cold-formed stainless steel columns subjected to flexural buckling. It is shown that the proposed design formulas can provide a quick and good solution as compared with the ASCE Standard solutions.

### Current Design Specification

The ASCE Standard Specification (ASCE 2002) provides the design requirements to determine the flexural buckling strength for concentrically loaded cold-formed stainless steel compression members. It specifies that the flexural buckling stress,  $F_n$ , shall be determined as follows:

$$F_n = \frac{\pi^2 E_t}{(KL/r)^2} \leq F_y \quad (1)$$

in which  $KL/r$  is the slenderness ratio and  $F_y$  is the specified yield strength as given in Table 1 obtained from ASCE specification for austenitic type stainless steels.

Table 1 ASCE Specified  $F_y$  for Austenitic Type Stainless Steels

Types of Stress	$F_y$ , MPa			
	Types 201, 301, 304, 316			
	Annealed	1/16Hard	1/4 Hard	1/2Hard
Longitudinal Tension	206.9	310.3	517.1	758.5
Transverse Tension	206.9	310.3	517.1	758.5
Transverse Compression	206.9	310.3	620.6	827.4
Longitudinal Compression	193.1	282.7	344.8	448.2

1 ksi = 6.895 MPa

The tangent modulus,  $E_t$ , in compression corresponding to buckling stress,  $F_n$ , can be determined by using the modified Ramberg-Osgood equation [1] as follows:

$$E_t = \frac{E_o F_y}{F_y + 0.002nE_o(F_n / F_y)^{n-1}} \quad (2)$$

in which  $E_o$  is the initial modulus of elasticity and  $n$  is the coefficient used for determining tangent modulus of specified type of stainless steel. Table 2 gives values of  $E_o$  and  $n$  for austenitic type stainless steels as specified in the ASCE Standard.

Because of the correlation between the buckling stress and tangent modulus in Eq. (2), an assumed buckling stress  $F_n$  is needed to determine the value of  $E_t$ . Then, this calculated value of  $E_t$  is substituted into Eq. (1) to determine the buckling stress,  $F_n$ . Since the calculated buckling stress is seldom equal to the first assumed buckling stress, further successive iterations are required to obtain the true buckling stress. Though the process is tedious and time-consuming, this buckling stress can be achieved when the satisfied convergence of iteration is reached.

Table 2 Specified  $E_o$  and  $n$  Values for Austenitic Type Stainless Steels

Types of Stress	Types 201, 301, 304, 316					
	Annealed and 1/16 Hard		1/4Hard		1/2Hard	
	$E_o$ (MPa)	$n$	$E_o$ (MPa)	$n$	$E_o$ (MPa)	$n$
Longitudinal Tension	193100	8.31	186200	4.58	186200	4.21
Transverse Tension	193100	7.78	193100	5.38	193100	6.71
Transverse Compression	193100	8.63	193100	4.76	193100	4.54
Longitudinal Compression	193100	4.10	186200	4.58	186200	4.22

1 ksi = 6.895 MPa

### Development of Mathematical Formulation

A simplified approach was developed to determine the flexural buckling stress without using iterative process. The tangent modulus value obtained from the modified Ramberg-Osgood equation was used to generate the simplified design equation. Numerical approximation by using Taylor series expansion is applied to simplify the calculations.

### Linearization Model

A typical flexural buckling stress curve for type 304 cold-formed stainless steel column is shown in Fig. 2. Now by applying logarithm operation to the flexural buckling stress curves, i.e.,  $\log(F_n)$ , it was found that a portion of the nonlinear buckling stress curve can be approximately expressed by a line segment between two points at A and B as shown in Fig. 3. Then this linear portion of the curve can be defined by these two specified points at  $A(C_0, \log F_y)$  and  $B(C_1, \log F_1)$  as follows:

$$\frac{\log F_1 - \log F_y}{C_1 - C_0} = \frac{\log F_n - \log F_y}{C - C_0} \quad (3)$$

in which  $C = KL/r =$  slenderness ratio, and  $C_0$  and  $C_1$  are two specified slenderness ratios with their corresponding buckling stresses at  $F_y$  and  $F_1$ , respectively.

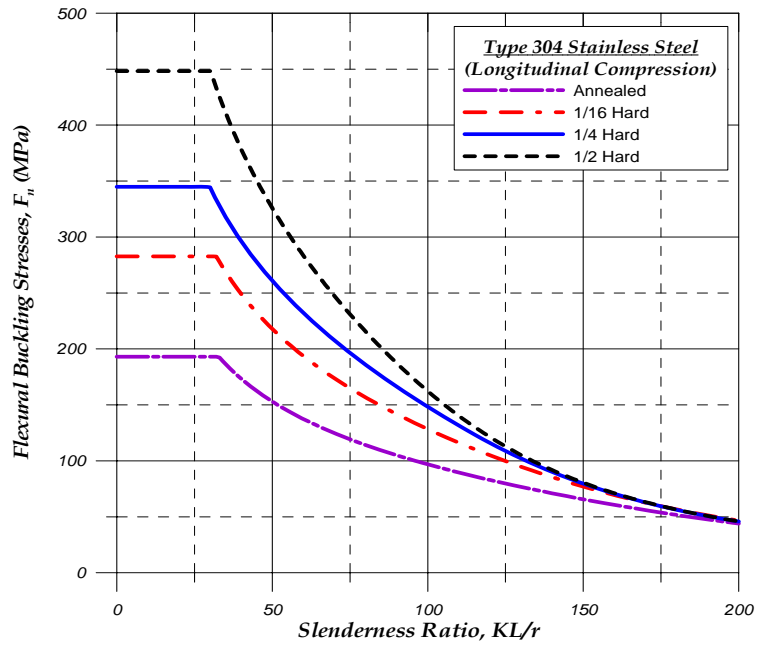


Fig. 2 Flexural Buckling Stresses For Type 304 Stainless Steel Columns



Equation (3) can be rearranged in terms of exponential expression as

$$F_n = F_1^{\frac{C-C_0}{C_1-C_0}} \times F_y^{\frac{C_1-C}{C_1-C_0}} \quad (4)$$

The slenderness ratio of  $C_0$  can be determined when  $F_n$  is equal to  $F_y$ , i.e.,

$$C_0 = KL/r = \pi \sqrt{\frac{E_y}{F_y}} \quad (5)$$

where  $E_y$  is the tangent modulus at yield strength level and is equal to

$$E_y = \frac{E_o}{1 + 0.002n \frac{E_o}{F_y}} \quad (6)$$

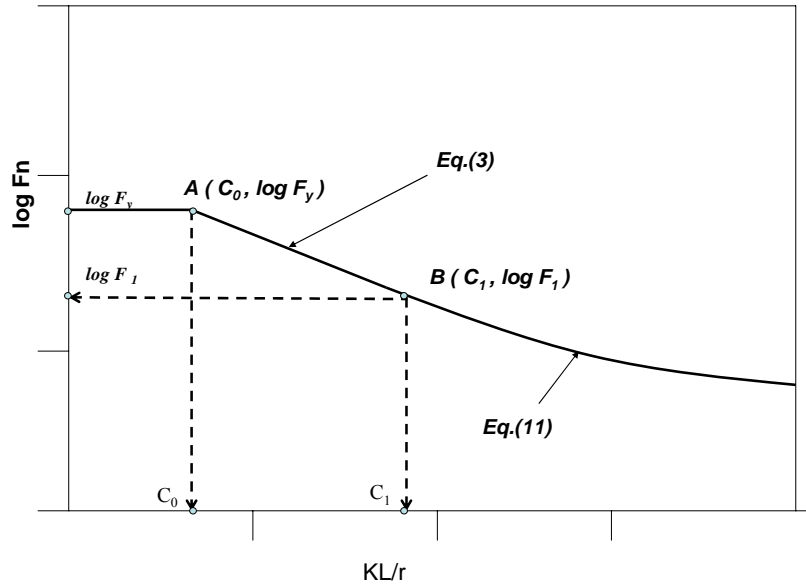


Fig. 3 Simplified Flexural Buckling Stress Curve

The buckling stress  $F_1$  defined in Fig. 3 can be obtained from Eq. (2) by rearranging  $E_t$  and  $F_n$  and replacing  $F_n$  by  $F_1$  as follows:

$$F_1 = \left[ \left( \frac{E_o - E_t}{E_t} \right) \frac{F_y}{0.002nE_o} \right]^{\frac{1}{n-1}} \times F_y \quad (7)$$

$$\text{Let } \alpha = \frac{E_o - E_t}{E_t} = \frac{E_o}{E_t} - 1 \quad (8)$$

Then, Eq. (7) becomes

$$F_1 = \left( \frac{\alpha F_y}{0.002nE_o} \right)^{\frac{1}{n-1}} \times F_y \quad (9)$$

The value of  $F_l$  can be considered as the proportional limit, which varies with respect to the type of stainless steels. The tangent modulus  $E_t$  can be expressed in terms of  $\alpha$ , i.e.,

$$E_t = \frac{E_o}{(1 + \alpha)} \quad (10)$$

Substitution of Eq. (10) into Eq. (1) yields the following general expression for  $F_n$ :

$$F_n = \frac{\pi^2 E_t}{(KL/r)^2} = \frac{\pi^2 E_o}{C^2(1 + \alpha)} \quad (11)$$

By using Eq. (11), the limiting slenderness ratio of  $C_l$  can be determined for the buckling stress at  $F_n = F_l$  as follows:

$$C_l = \pi \sqrt{\frac{E_o}{F_l(1 + \alpha)}} \quad (12)$$

### Approximation of $\alpha$

Once the  $\alpha$  value is known, the buckling stress  $F_l$  in Eq. (9) and the limiting slenderness ratio  $C_l$  in Eq. (12) can be calculated for specified type of cold-formed stainless steels. The determination of buckling stress  $F_n$  becomes easy and without iterative calculations as presented in Eq. (4). As a result, the parameter  $\alpha$  can be expressed as

$$\alpha = 0.002n \left( \frac{E_o}{F_y^n} \right) \left[ \frac{\pi^2 E_o}{C^2(1 + \alpha)} \right]^{n-1} \quad (13)$$

The above equation can also be rearranged to form a polynomial function, namely

$$f(\alpha) = \alpha(1+\alpha)^{n-1} = 0.002n \left( \frac{\pi^2}{C^2} \right)^{n-1} \left( \frac{E_o}{F_y} \right)^n \quad (14)$$

Equation (14) can be approximately expressed by using Taylor series expansion as

$$\alpha(1+\alpha)^{n-1} = \sum_{i=0}^N \frac{f^i(\alpha)}{i!} \alpha^i + \dots \quad (15)$$

in which  $f^i(\alpha)$  is the  $i^{\text{th}}$  derivative of the function  $f(\alpha)$ .

Higher degrees of derivatives in Eq. (15) are assumed to be neglected for common engineering practice. Then, for  $N = 2$ , Eq. (15) can be approximately expressed as

$$\alpha + (n-1)\alpha^2 = 0.002n \left( \frac{\pi^2}{C^2} \right)^{n-1} \left( \frac{E_o}{F_y} \right)^n \quad (16)$$

The above equation is a typical second order equation and, therefore, can be solved by the quadratic formula as follows:

$$\alpha = \frac{-1 + \sqrt{1 + 4(n-1)0.002n \left( \frac{\pi^2}{C^2} \right)^{n-1} \left( \frac{E_o}{F_y} \right)^n}}{2(n-1)} \quad (17)$$

This  $\alpha$  value is used for determining the elastic buckling stress in Eq. (11). To consider the inelastic buckling stress, the  $\alpha$  value is determined by taking  $N = 3$  in Eq. (15). To meet a satisfied convergence, the following limitation is recommended:

$$\frac{(n-1)(n-2)\alpha^3 / 2}{\alpha + (n-1)\alpha^2} \leq 5\% \quad (18)$$

Assume that the maximum value of the parameter  $\alpha$  determined from Eq. (18) is equal to  $\beta$ . It yields

$$\alpha_{\max} = \beta = \frac{1 + \sqrt{1 + \frac{2(n-2)}{0.05(n-1)}}}{n-2} \times 0.05 \quad (19)$$

in which  $\beta$  is used to determine the buckling stress of  $F_I$  in Eq. (9) and the

limiting slenderness ratio of  $C_1$  in Eq. (12) as shown in Fig. 3.

### Proposed Design Formulas

Based on the above-mentioned simplified formulations, the following design provisions were proposed herein to determine the flexural buckling stress,  $F_n$ , for austenitic types of cold-formed stainless steel compression members.

*For doubly symmetric sections, closed cross sections, and any other sections which can be shown not to be subjected to torsional or torsional-flexural buckling, the flexural buckling stress,  $F_n$ , shall be determined as follows:*

For  $KL/r \leq C_1$ :

$$F_n = F_y^{\lambda_o} F_1^{\lambda_1} \leq F_y \quad (20)$$

For  $KL/r > C_1$ :

$$F_n = \frac{\pi^2 E_o}{\left(\frac{KL}{r}\right)^2 (1 + \alpha)} \quad (21)$$

where:

$$\lambda_o = \frac{C_1 - KL/r}{C_1 - C_o} \quad (22)$$

$$\lambda_1 = 1 - \lambda_o \quad (23)$$

$$C_o = \pi \sqrt{\frac{E_y}{F_y}} \quad (24)$$

$$C_1 = \pi \sqrt{\frac{E_o}{F_1(1 + \beta)}} \quad (25)$$

$$E_y = \frac{E_o}{1 + 0.002n \frac{E_o}{F_y}} \quad (26)$$

$$F_1 = F_y \left( \frac{\beta F_y}{0.002n E_o} \right)^{\frac{1}{n-1}} \quad (27)$$

$$\alpha = \frac{-1 + \sqrt{1 + 4(n-1)0.002n \left[ \frac{\pi^2}{(KL/r)^2} \right]^{n-1} \left( \frac{E_o}{F_y} \right)^n}}{2(n-1)} \quad (28)$$

$$\beta = \frac{0.05 + \sqrt{0.0025 + \frac{0.1(n-2)}{(n-1)}}}{n-2} \quad (29)$$

### Comparisons of Results

Comparisons are made between the predicted buckling stresses computed from the ASCE Standard design equations and the proposed design formulas. This paper summarizes the result of comparison. Type 304 stainless steel columns are used to compare the predicted flexural buckling stresses. The specified material properties used to determine the buckling stress for ASCE Standard are given in Table 2. The design parameters for the same materials determined from the proposed design equations are listed in Table 3. For this type of stainless steel, the computed buckling stresses,  $F_{n,ASCE}$  and  $F_{n,prop}$ , and the ratios of  $F_{n,prop}/F_{n,ASCE}$  with respect to the slenderness ratios,  $KL/r$ , in longitudinal compression are given in Table 4. In this table,  $F_{n,ASCE}$  and  $F_{n,prop}$  are predicted flexural buckling stresses determined from the ASCE Standard and proposed design equations, respectively. This comparison is also illustrated in Fig. 4. It is shown that the proposed design equations, without having iterative calculations, can predict good results as compared with the ASCE Standard results.

### Conclusions

The buckling stress of cold-formed stainless steel compression members is determined on the basis of the tangent modulus theory because of the nonlinear stress strain behavior of the materials. The determination of flexural buckling stress needs iterative process which is often tedious and time-consuming for a typical column design. In order to simplify the design calculation, mathematical approximations are utilized to calculate flexural buckling stress which needs non-iterative process. This paper discusses the reasoning behind for the development of the simplified formulas. Comparisons are made between the predicted column flexural buckling stresses determined from the ASCE design formulas and the proposed design equations. It is shown that the flexural

buckling stresses determined by the proposed design equations are in good agreement with those calculated by the ASCE design formulas.

Table 3 Computed Parameters Used in the Proposed Design Formulas

Type of Stress(304S.S.)		$\beta$	$C_0$	$C_1$	$F_1$ (MPa)
Longitudinal Compression	Annealed	0.1500	32.8	176.6	53.12
	1/16 Hard	0.1500	32.0	137.3	87.94
	1/4 Hard	0.1252	29.9	115.0	123.48
	1/2 Hard	0.1429	30.2	98.4	165.91
Transverse Compression	Annealed	0.0526	23.2	136.1	97.72
	1/16 Hard	0.0526	22.9	108.2	154.55
	1/4 Hard	0.1179	27.8	80.5	259.62
	1/2 Hard	0.1270	27.2	67.3	373.58

1 ksi = 6.895 MPa

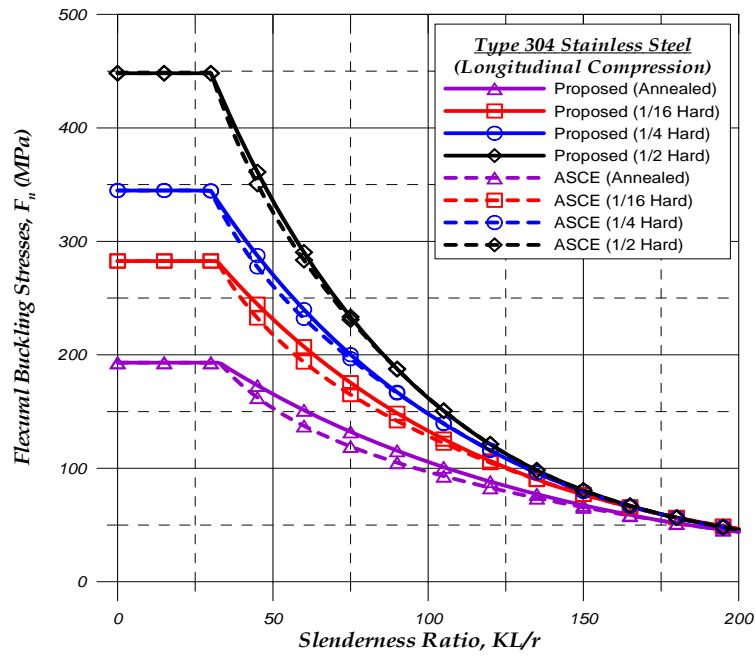


Fig. 4 Comparisons of Computed Buckling Stress Curve

Table 4 Comparisons of Computed Buckling Stresses for Type 304 Stainless Steel Columns in Longitudinal Compression

KL/r	Annealed			1/16 Hard			1/4 Hard			1/2 Hard		
	$F_{n,ASCE}$ (MPa)	$F_{n,prop}$ (MPa)	$\frac{F_{n,prop}}{F_{n,ASCE}}$	$F_{n,ASCE}$ (MPa)	$F_{n,prop}$ (MPa)	$\frac{F_{n,prop}}{F_{n,ASCE}}$	$F_{n,ASCE}$ (MPa)	$F_{n,prop}$ (MPa)	$\frac{F_{n,prop}}{F_{n,ASCE}}$	$F_{n,ASCE}$ (MPa)	$F_{n,prop}$ (MPa)	$\frac{F_{n,prop}}{F_{n,ASCE}}$
20	193.1	193.1	1.00	282.7	282.7	1.00	344.4	344.5	1.00	448.2	448.2	1.00
40	173.4	181.0	1.04	249.1	258.6	1.04	296.3	305.4	1.03	378.5	388.4	1.03
60	137.4	151.2	1.10	193.7	207.2	1.07	232.1	239.9	1.03	283.4	290.3	1.02
80	114.2	126.4	1.11	156.7	166.0	1.06	186.0	188.4	1.01	215.6	217.0	1.01
100	96.9	105.6	1.09	128.4	133.0	1.04	148.2	148.0	1.00	162.2	161.5	1.00
120	82.9	88.3	1.07	105.0	106.5	1.01	116.0	115.7	1.00	121.3	121.3	1.00
140	71.0	73.8	1.04	85.5	85.1	1.00	90.1	90.1	1.00	91.8	91.8	1.00
160	60.7	61.7	1.02	69.4	69.4	1.00	70.6	70.6	1.00	71.1	71.1	1.00
180	51.7	51.5	1.00	56.7	56.6	1.00	56.3	56.3	1.00	56.5	56.5	1.00
200	44.0	43.9	1.00	46.7	46.7	1.00	45.8	45.8	1.00	45.8	45.8	1.00
			AVG = 1.05				1.02			1.01		
			COV = 0.041				0.027			0.013		
												0.011

1 ksi = 6.895 MPa

### Appendix. – References

- American Society of Civil Engineers (ASCE), 2002, Specification for the Design of Cold-Formed Stainless Steel Structural Members (SEI/ASCE 8-02), Reston, VA.
- American Society of Civil Engineers (ASCE), 1991, Specification for the Design of Cold-Formed Stainless Steel Structural Members (ANSI/ASCE 8-90), New York.
- Galambos, T. V., 1968, Structural Members and Frames, Prentice-Hall, Englewood Cliffs, NJ.
- Hill, H. N., Feb. 1944, Determination of stress-strain relations from offset yield strength values, NACA Tech. Note, No. 927.
- Johnson, A. L., and G. A. Kelsen, Aug. 1969, Stainless Steel in Structural Applications, Stainless Steel for Architecture, American Society for Testing and Materials, STP 454.
- Johnston, B. G., Ed., 1976, Guide to Stability Design Criteria for Metal Structures, 3<sup>rd</sup> ed., John Wiley and Sons, New York.
- Ramberg, W. and Osgood, W. R., July, 1943, Description of Stress-Strain Curves by Three Parameters, NACA Technical Note, No. 902.
- Rasmussen, K. J. R. and Rondal, J., 2000, Column Curves for Stainless Steel Alloys, Journal of Constructional Steel research, 54, 89-107.
- Rasmussen, K. J. R. and Rondal, J., 1997, Explicit Approach to Design of Stainless Steel Columns, Journal of Structural Engineering, American Society of Civil Engineers, Vol. 123(7), 857-863.
- Yu, W. W., 2000, Cold-Formed Steel Design, Wiley-Interscience, New York, NY.

### Appendix. - Notation

The following symbols are used in this paper.

- $C$  = Slenderness ratio,  $KL/r$
- $C_o$  = Specified slenderness ratio at  $F_n = F_y$
- $C_l$  = Limiting slenderness ratio at  $F_n = F_l$
- $E_o$  = Initial modulus of elasticity
- $E_t$  = Tangent modulus
- $E_y$  = The tangent modulus at yield strength level
- $F_y$  = Specified yield strength
- $F_l$  = Specified buckling stress with respect to  $C_l$
- $F_n$  = Nominal buckling stress
- $F_{n,ASCE}$  = Nominal buckling stress determined from ASCE Standard Specification
- $F_{n,prop}$  = Nominal buckling stress determined from the proposed design formulas



- $K$  = Effective length factor  
 $L$  = Unbraced length of member  
 $n$  = Coefficient used for determining the tangent modulus  
 $r$  = Radius of gyration  
 $\alpha = \frac{E_o}{E_t} - 1$   
 $\beta$  = Constant  
 $\lambda_o$  = Parameter used for determining buckling stress  
 $\lambda_l = 1 - \lambda_o$

## **STABILITY OF COLD-FORMED STEEL SIMPLE AND LIPPED ANGLES UNDER COMPRESSION**

W. F. Maia<sup>1</sup>, J. Munaiar Neto<sup>1</sup>, and M. Malite<sup>1</sup>

### **Abstract**

The structural analysis of a simple angle under axial compression appears to be an elementary and therefore well known problem. However, cold-formed angles, especially those with slender legs, present two critical modes: (i) global flexural mode, in the case of long members, and (ii) a coincident local-plate/global-torsional mode (herein dubbed L/T), which is critical for shorter members. Recent works indicate that considering the L/T mode as a global mode is too conservative, while other works indicate the need for this approach. The present work involves an in-depth investigation of the structural response of simple and lipped angles subjected to centered and eccentric compression, by means of experimental and nonlinear numerical analysis via finite elements. An evaluation is made of the initial geometric imperfections, and of the results of the following standard procedures: (i) the classical effective width method, and (ii) the direct strength method (DSM), in which the angles are not considered pre-qualified sections. The results of the experimental analysis and the nonlinear numerical analysis with initial geometric imperfections indicate the need to consider the L/T mode as both a local mode and a global mode.

---

<sup>1</sup> Department of Structural Engineering  
School of Engineering of Sao Carlos – University of Sao Paulo  
Av. Trabalhador Sao-Carlense, 400 – CEP 13566-590 – Sao Carlos, SP, Brazil  
Tel.: +55 16 3373 9468; e-mail: mamalite@sc.usp.br

## 1. Introduction

Major advances in fabrication processes have led to the widespread use of steels having high mechanical strength and, hence, low thickness. This has given rise to various previously unknown modes of buckling that require special attention. Theoretical and experimental research has been dedicated to characterizing and describing the structural behavior of these elements, seeking economical and safe design methods.

Brazil has seen a growing demand for cold-formed steel angles, particularly in view of the plentiful supply of thin steel plates and the possibility of obtaining a wide variety of dimensions, including angles with unequal legs and lipped angles.

Although there are simplified calculation procedures recommended by specifications, researchers are not unanimous in considering the coincident local/torsional mode as a global mode. Rasmussen (2003) and Young (2004) believe the calculation procedures are excessively conservative in this case, because they consider the same phenomenon twice: by considering the global buckling mode by flexural-torsion, and in calculating the effective width of the section.

The local/torsional mode does not occur in lipped angles, which present better structural performance, especially insofar as local buckling is concerned. However, some authors consider that the standards for the sections are too conservative.

In this paper, we present a study of the behavior of simple and lipped angles subjected to centered and eccentric compression in order to confirm the need to consider the local/torsional mode as a global mode. Options are presented for the application of the Direct Strength Method (DSM) incorporated in the North American Specification (NAS 2004) as an alternative design method. At this point, it is opportune and relevant to evaluate the applicability of the DSM, since angles to date are not listed as pre-qualified sections for the method. A nonlinear numerical analysis via finite elements is also presented, seeking to evaluate the structural response of simple and lipped angles with respect to their sensitivity to initial geometric imperfections.

## 2. Experimental analysis

A series of analyses of cold-formed simple and lipped angles were carried out at the University of Sao Paulo at Sao Carlos Campus. The simple angle tests were

conducted with the same section as that studied by Chodraui & Malite (2006), L 60x2.38. The lipped angle tests involved two sections, Le 60x15x2.06 and Le 100x15x1.50.

Type I, II, III and IV tests corresponded to simple angles, while types V and VI involved lipped angles. The mechanical and geometric properties of the tested sections are presented in Table 1.

**Table 1 – Geometric and material properties**

Section	Flange (mm)	Lip (mm)	Thickness (mm)	$F_y$ (MPa)	$F_u$ (MPa)	E (MPa)
L 60x2.38	60	-	2.38	358	500	205,000
Le 60x15x2.06	60	15	2.06	273	392	205,000
Le 100x15x1.50	100	15	1.50	205	310	205,000

The supports for the type I, V and VI members allowed for rotation in relation to the minor axis, restricting rotation in relation to the major axis, as well as torsion and warping. The theoretical length ( $L_r$ ) was taken as being  $L_{member} + 135$  mm, corresponding to the distance between the axes of rotation of the lower and upper supports. The type II members were tests with fixed ends (without rotation). The type III and IV members were subjected to eccentric compression with the load applied on the flange by means of bolts, one bolt in type III members and two bolts in type IV members.

Prior to the centered compression tests, 12.5 mm thick steel plates were welded into the ends of the members to ensure contact between the section and the load application device.

The theoretical forecasts were based on the NAS (2004) calculation procedure, and involved examining the application of the effective width method on angles under centered compression. The displacement of the centroid of the gross section to the effective section was disregarded, and the strength was calculated based (i) on the general case of elastic stability that uses the minimum buckling load between flexural and torsional-flexural, and (ii) on the particular case which uses only flexural buckling, as recommended by Rasmussen (2003) and Young (2004).

Tables 2–4 and Figures 1–5 present the results of the tests, comparing them with the calculation procedures adopted here.

**Table 2 – Comparison of test strengths with design strengths for simple angle  
L 60x2.38 ( $F_y = 358$  MPa)**

Type	$L_r$ (mm)	NAS (2004)		Test		$P_{test}/P_n$
		$P_n$ (kN)	Failure mode	$P_{test}$ (kN)	Failure mode	
Type I – Pined end conditions about minor axis: $K_2 = 1.0$ and $K_1 = K_t = 0.5$						
I.1	615	26.7	FT	31.0	L/T	1.16
I.2	970	26.6	FT	29.0	L/T	1.09
I.3	1,330	26.4	FT	22.5	L/T	0.85
I.4	1,685	22.4	F	21.0	L/T	0.94
I.5	785	26.6	FT	36.1	L/T	1.36
I.6	1,135	26.5	FT	39.8	F	1.50
I.7	1,485	26.3	FT	28.5	F	1.08
Average						1.14
Standard deviation						0.21
Type II – Similar type I but with fixed end conditions about both principal axis: $K_1 = K_2 = K_t = 0.5$						
II.1	615	26.7	FT	40.9	L/T	1.53
II.2	970	26.6	FT	34.5	L/T	1.30
II.3	1,330	26.4	FT	30.6	L/T	1.16
II.4	1,685	26.2	FT	26.7	L/T	1.02
Average						1.25
Standard deviation						0.19
Type III – Eccentric load: angle connected by a single bolt (19mm diameter) usual case: $K_1 = K_2 = K_t = 1.0$						
III.1	615	26.5	FT	26.1	L/T	0.98
III.2	970	26.0	FT	22.8	L/T	0.88
III.3	1,330	25.3	FT	21.9	L/T	0.87
III.4	1,685	22.4	FT	17.7	L/T	0.79
Average						0.88
Standard deviation						0.07
Type IV – Eccentric load: angle connected by two bolts (19mm diameter) usual case: $K_1 = K_2 = K_t = 1.0$						
IV.1	970	26.0	FT	38.0	L/T	1.46
IV.2	1,330	25.3	FT	29.0	L/T	1.15
Average						1.30
Standard deviation						0.16

F = minor axis flexural; FT = torsional-flexural and L/T = local/torsional;  
 $L_r$  is the pin center to pin center distance for type I, full length of member for type II,  
center of hole to center of hole for type III and center of connection to center of  
connection for type IV.

**Table 3 – Comparison of test strengths with design strengths for lipped angle  
Le 60x15x2.06 ( $F_y = 273$  MPa)**

Type	$L_r$ (mm)	NAS (2004)		Test		$P_{test}/P_n$
		$P_n$ (kN)	Failure mode	$P_{test}$ (kN)	Failure mode	
Type V – Pined end conditions about minor axis: $K_2 = 1.0$ and $K_1 = K_t = 0.5$						
V.1	510	65.4	FT	76.3	FT	1.17
V.2	730	56.0	FT	62.5	FT	1.12
V.3	730	56.0	FT	58.9	FT	1.05
V.4	1,090	42.4	FT	43.1	FT	1.02
V.5	1,090	42.4	FT	43.8	FT	1.03
V.6	1,310	36.2	FT	40.0	F	1.10
V.7	1,310	36.2	FT	36.9	FT	1.02
V.8	1,530	31.3	FT	36.5	F	1.17
V.9	1,530	31.3	FT	32.0	FT	1.02
V.10	1,750	27.6	FT	27.3	FT	0.99
V.11	1,970	24.9	FT	25.7	F	1.03
Average						1.07
Standard deviation						0.06
F = minor axis flexural; FT = torsional-flexural and L = local; $L_r$ is the pin center to pin center distance.						

**Table 4 – Comparison of test strengths with design strengths for lipped angle  
Le 100x15x1.50 ( $F_y = 205$  MPa)**

Type	$L_r$ (mm)	NAS (2004)		Test		$P_{test}/P_n$
		$P_n$ (kN)	Failure mode	$P_{test}$ (kN)	Failure mode	
Type VI – Pined end conditions about minor axis: $K_2 = 1.0$ and $K_1 = K_t = 0.5$						
VI.1	535	42.2	FT	32.1	L	0.76
VI.2	535	42.2	FT	48.8	L	1.16
VI.3	635	40.1	FT	40.4	FT	1.01
VI.4	635	40.1	FT	43.8	FT	1.09
VI.5	735	37.8	FT	39.9	FT	1.06
VI.6	735	37.8	FT	47.5	FT	1.26
VI.7	1,135	28.1	FT	25.1	FT	0.89
VI.8	1,135	28.1	FT	24.0	FT	0.85
Average						1.01
Standard deviation						0.17
F = minor axis flexural; FT = torsional-flexural and L = local; $L_r$ is the pin center to pin center distance.						

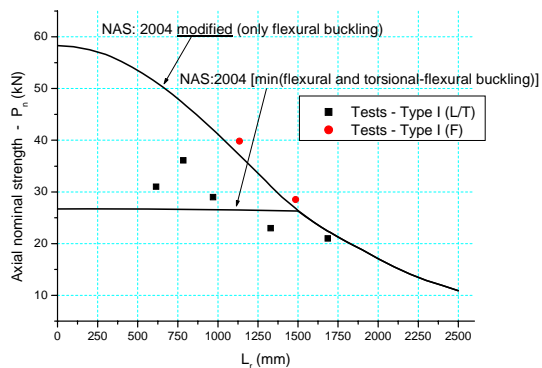


Figure 1 – Simple angle tests type I compared with NAS (2004)

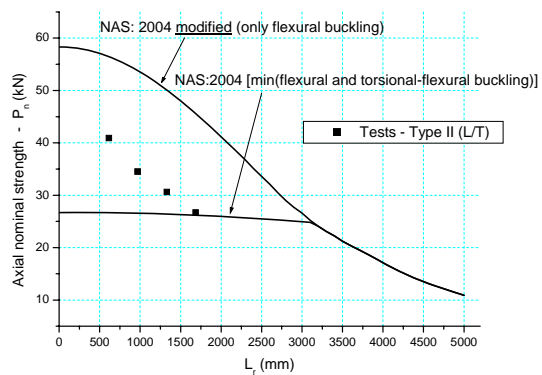


Figure 2 – Simple angle tests type II compared with NAS (2004)

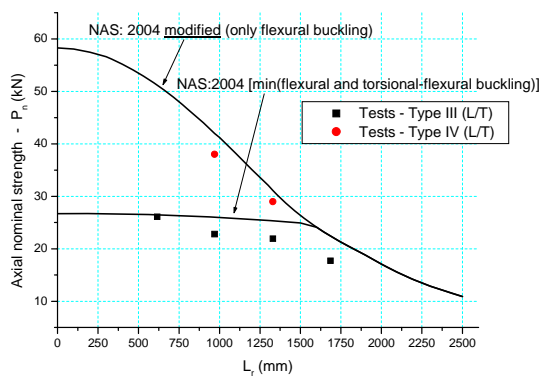


Figure 3 – Simple angle tests types III and IV compared with NAS (2004)

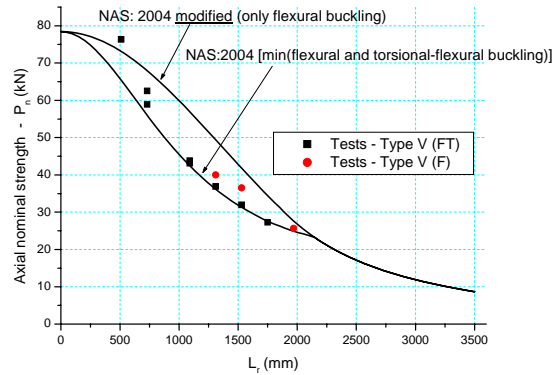


Figure 4 – Lipped angle tests type V compared with NAS (2004)

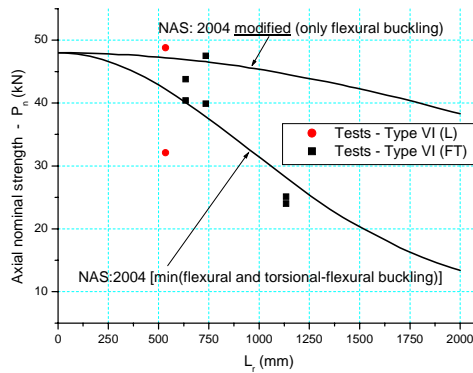


Figure 5 – Lipped angle tests type VI compared with NAS (2004)

With regard to the simple angle, most of the members were found to present torsional-flexural buckling, herein dubbed the local/torsional mode. In the type I test (Figure 1), two members presented flexural buckling, but this was not a frequent occurrence. The fact that this mode was present may be attributed to the initial geometric imperfections of the members, since different panoramas can lead to distinct buckling modes. The type II tests (Figure 2) indicated that the strength of the members was slightly higher than the strength calculated from the NAS (2004), especially that of the shorter members. However, the results were inferior to the calculated values considering only the particular case of flexural buckling. In the tests with eccentric loading, all the members displayed local/torsional buckling. Note that the members with loading applied by only one bolt showed lower results than the values calculated by NAS (Figure 3). In the case of loads applied through two bolts, there was a significant increase in



the strength, because in this case, the bolts provided some restriction to rotation of the extremities.

The lipped angles showed torsional-flexural buckling and flexural buckling modes in the type V members (Figure 4). An interesting fact was that members of the same length presented different buckling modes but very similar strengths. The experimental results were very close to the values calculated according to the NAS (2004). The type V members showed local buckling and torsional-flexural buckling modes (Figure 5). The results presented a greater variability in relation to the values calculated according to the NAS (2004), showing some unconservative results, unlike the experimental results reported by Young (2005), for which the NAS (2004) proved highly conservative.

### **3. Numerical analysis**

The numerical simulations of this work were carried out with the ANSYS program. Two elements were used: the SHELL 181 element to model the member, and the SOLID 45 element to model the end devices.

To insert the initial geometric imperfections, an eigenvalue analysis was made to identify the critical modes separately, i.e., the local/torsional and flexural global modes for the simple angle, and the local, torsional-flexural and flexural modes for the lipped angle.

Starting from the strained configuration of each of the critical modes selected for each case, a criterion was adopted to expand or reduce this amplitude, thereby obtaining a new geometry of all the nodes of the grid of finite elements of the members. It should be noted that there was overlapping of the imperfections, always seeking the most unfavorable combination.

The results of the statistical analysis presented by Schafer & Peköz (1998) were used for the localized imperfections, i.e., imperfections in stiffened elements and lip stiffened or unstiffened flange. For the simple angle, type 2 imperfections were adopted for the coincident local/torsional mode, while for the lipped angle, type 1 imperfections were adopted for the local mode and type 2 for the torsional-flexural mode. Imperfection magnitudes were selected at 25% and 75% probability of exceedance.

For the global flexural imperfection, the value of  $L/1500$  was adopted due to the great variability of results presented in the literature.

Tables 4 and 5 present the results of these analyses.

**Table 4 – Sensibility analysis of initial geometric imperfections for simple angle L 60x2.38**

Type	$L_r$ (mm)	Elastic stability: critical mode	Test		Local/torsional imperfection			
			$P_{test}$ (kN)	Failure mode	$d_2/t = 0.64^{(1)}$		$d_2/t = 1.55^{(2)}$	
					$P_{FE}$ (kN)	Failure mode	$P_{FE}$ (kN)	Failure mode
I.1	615	L/T	31.0	L/T	29.7	L/T	26.2	L/T
I.5	785	L/T	36.1	L/T	29.2	L/T	26.6	L/T
I.2	970	L/T	29.0	L/T	28.4	L/T	26.2	L/T
I.6	1135	L/T	39.8	F	27.2	L/T	25.2	L/T
I.3	1,330	L/T	22.5	L/T	25.5	L/T	23.5	L/T
I.7	1,485	L/T	28.5	F	23.9	L/T	21.9	L/T
I.4	1,685	F	21.0	L/T	21.3	L/T	19.6	L/T
II.1	615	L/T	40.9	L/T	49.7	L/T	50.5	L/T
II.2	970	L/T	34.5	L/T	41.0	L/T	42.0	L/T
II.3	1,330	L/T	30.6	L/T	37.3	L/T	38.5	L/T
II.4	1,685	L/T	26.7	L/T	34.9	L/T	36.5	L/T
III.1	615	L/T	26.1	L/T	30.1	L/T	30.3	L/T
III.2	970	L/T	22.8	L/T	27.6	L/T	27.4	L/T
III.3	1,330	L/T	21.9	L/T	24.3	L/T	23.5	L/T
III.4	1,685	L/T	17.7	L/T	19.1	L/T+F	18.6	L/T+F
IV.1	970	L/T	38.0	L/T	35.0	L/T	34.7	L/T
IV.2	1,330	L/T	29.0	L/T	28.5	L/T	28.0	L/T

<sup>(1)</sup> 75% probability of exceedance

<sup>(2)</sup> 25% probability of exceedance

F = minor axis flexural

L/T = local/torsional

In general, the results of the nonlinear numerical analysis in which imperfections of  $0.64t$  were adopted for the local/torsional mode and  $L/1500$  for the global flexural mode were very coherent with the experimental results (Table 4). A comparison of the experimental results of type I members against the values of the numerical analysis showed an average of 1.12, with  $0.88 \leq P_{test}/P_{FE} \leq 1.46$ . For the type II members, the experimental results were slightly lower than the numerical ones, presenting an average of 0.81, with  $0.76 \leq P_{test}/P_{FE} \leq 0.84$ . Moreover, the members displayed little sensitivity to initial imperfections. The experimental results of the type III members were slightly lower than the numerical values, with an average of 0.88, with  $0.83 \leq P_{test}/P_{FE} \leq 0.93$ . For the type IV members, these values were 1.09 and 1.02 for the two tested members. An interesting fact observed in the numerical analysis of the simple angle was that, upon adopting local/torsional imperfections, regardless of their amplitude,

the members consistently presented local/torsional buckling, regardless of the global flexural imperfection adopted.

**Table 5 – Sensibility analysis of initial geometric imperfections for lipped angle  
Le 60x15x2.06**

Type	$L_r$ (mm)	Elastic stability: critical mode	Test		Local and torsional-flexural imperfections			
					$d_1/t = 0.14^{(1)}$ $d_2/t = 0.64^{(1)}$		$d_1/t = 0.66^{(2)}$ $d_2/t = 1.55^{(2)}$	
			$P_{test}$ (kN)	Failure mode	$P_{FE}$ (kN)	Failure mode	$P_{FE}$ (kN)	Failure mode
V.1	510	FT	76.3	FT	59.7	FT	47.0	L+FT
V.2	730	FT	62.5	FT	52.0	FT	41.3	L+FT
V.3			58.9	FT				
V.4	1,090	FT	43.1	FT	39.3	FT	32.4	FT
V.5			43.8	FT				
V.6	1,310	FT	40.0	F	32.6	FT	27.8	FT
V.7			36.9	FT				
V.8	1,530	FT	36.5	F	27.4	FT	23.5	FT+F
V.9			32.0	FT				
V.10	1,750	FT	27.3	FT	23.3	FT	20.4	FT+F
V.11	1,970	FT	25.7	F	20.2	FT	18.0	FT+F
VI.1	535	FT	32.1	L	42.4	L	34.6	L+FT
VI.2			48.8	L				
VI.3	635	FT	40.4	FT	40.0	L+FT	30.7	L+FT
VI.4			43.8	FT				
VI.5	735	FT	39.9	FT	39.8	L+FT	31.0	L+FT
VI.6			47.5	FT				
VI.7	1,135	FT	25.1	FT	26.1	FT	21.2	FT
VI.8			24.0	FT				

<sup>(1)</sup> 75% probability of exceedance

<sup>(2)</sup> 25% probability of exceedance

F = minor axis flexural

FT = torsional-flexural

L = local

As Table 5 indicates, the results of the numerical analysis with imperfections of 0.14t, 0.64t and L/1500 for the local, global torsional-flexural and global flexural modes, respectively, were more coherent with the tests, presenting an average of 1.19, with  $1.10 \leq P_{test}/P_{FE} \leq 1.33$  for the type V members, while the type VI members showed an average of 1.01, with  $0.76 \leq P_{test}/P_{FE} \leq 1.19$ .

#### 4. Direct Strength Method (DSM)

Two options for application of the DSM are presented here. Under option 1, for the global mode, the minimum between flexural and torsional-flexural is considered, which is the coincident local/torsional mode for the simple angle. Under option 2, only flexural is considered for the global mode. Because the simple angle does not present a defined minimum point, the point where the L/T and F curves intersect is used for the local mode (Figure 6). This is considered a practical procedure for use in designing. The proposed options are summarized in Table 6.

**Table 6 – Options for the Direct Strength Method**

	Option 1	Option 2
	L 60x2.38	
$P_{cre}$	min (L/T, F)	F
$P_{cr1}$	L/T*	L/T*
	Le 100x15x1.50	
$P_{cre}$	min (FT, F)	F
$P_{cr1}$	L	L

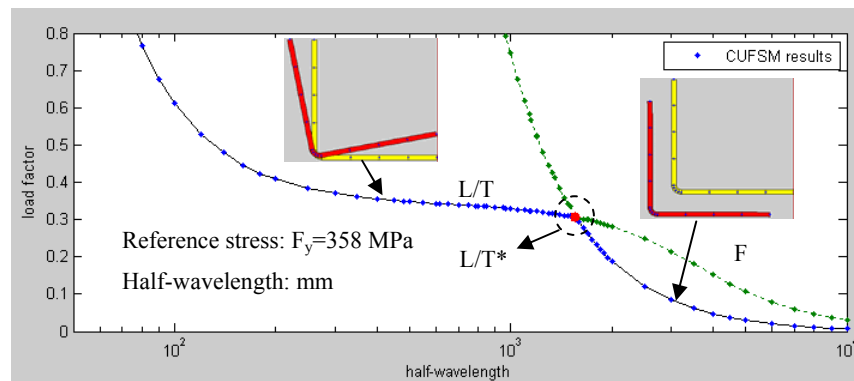
L = local mode

L/T = local/torsional mode

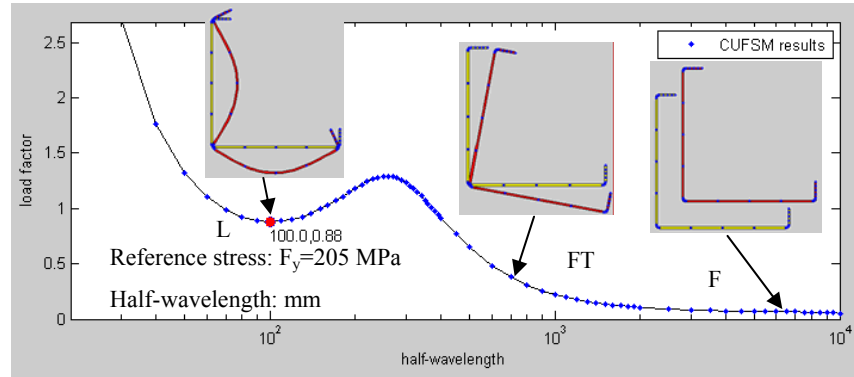
L/T\* = point where the curves L/T and F if intersect (Figure 6)

F = minor axis flexural

FT = torsional-flexural mode



**Figure 6 – Stability analysis of cold-formed steel simple angle (CUFSM) L 60x2.38**



**Figure 7 – Stability analysis of cold-formed steel lipped angle (CUFSM)  
Le 100x15x1.50**

Table 7 presents the results of the tests compared with the proposed options for application of the DSM.

For the simple angle (L 60x2.38), option 1 was more coherent with the test results. When compared with option 2, most of the results were found to be unconservative, confirming the need to consider the local/torsional mode as a global mode.

For the lipped angles, the Le 60x15x2.06 section did not show a reduction of the strength due to the local mode. It was therefore impossible to evaluate the efficiency of the DSM. For the Le 100x15x1.50 section, option 1 approached the experimental results more closely, but most of the values were unconservative. It is important to note that this was also the case when comparing the experimental results against the values calculated by the effective width method. Because the section possesses a very slender flange, the theoretical calculations tend to lead to unconservative results, in view of the great sensitivity to geometric imperfections.

**Table 7 – DSM options compared with available tests**

Type	$P_{\text{test}}$ (kN)	Option 1		Option 2	
		$P_{\text{DSM}}$ (kN)	$P_{\text{test}}/P_{\text{DSM}}$	$P_{\text{DSM}}$ (kN)	$P_{\text{test}}/P_{\text{DSM}}$
I.1	31.0	26.5	1.17	51.2	0.61
I.2	29.0	26.4	1.10	41.8	0.69
I.3	22.5	26.2	0.86	30.9	0.73
I.4	21.0	22.5	0.93	22.5	0.93
I.5	36.1	26.4	1.37	47.0	0.77
I.6	39.8	26.3	1.51	36.9	1.08
I.7	28.5	26.1	1.09	26.6	1.07
Average			1.15		0.84
Standard deviation			0.21		0.17
II.1	40.9	26.5	1.54	56.7	0.72
II.2	34.5	26.4	1.31	53.9	0.64
II.3	30.6	26.2	1.17	50.1	0.61
II.4	26.7	26.0	1.03	45.5	0.59
Average			1.26		0.64
Standard deviation			0.19		0.05
VI.1	32.1	49.2	0.65	54.9	0.58
VI.2	48.8	49.2	0.99	54.9	0.89
VI.3	40.4	46.8	0.86	54.6	0.74
VI.4	43.8	46.8	0.94	54.6	0.80
VI.5	39.9	44.2	0.90	54.2	0.74
VI.6	47.5	44.2	1.07	54.2	0.88
VI.7	25.1	31.8	0.79	52.0	0.48
VI.8	24.0	31.8	0.75	52.0	0.46
Average			0.87		0.70
Standard deviation			0.13		0.16

## 5. Conclusions

The results of the experimental tests indicate that it may be unconservative to fail to consider the coincident local/torsional mode as a global mode.

Unlike the results reported by Young (2005), in which the NAS (2004) proved highly conservative for the lipped angle, the tests carried out in this work were very coherent with the values calculated according to that specification.

Two options were analyzed for application of the Direct Strength Method: under option 1, the minimum between flexural and torsional-flexural for the global

mode and, under option 2, only the flexural mode were considered. Moreover, since the simple angle did not present a defined minimum point, the local mode was considered the point where the L/T and F curves intercept. The results confirm the need to consider the coincident local/torsional mode as a global mode for the simple angle. The results also indicate that for the lipped angle, the torsional-flexural mode should be considered.

An analysis was made of the sensitivity to initial geometric imperfections in order to study their effect on the strength of the members. To insert the initial imperfections, the critical modes (from eigenvalue analysis) observed for each section were adopted, i.e., the local/torsional and global flexural modes for the simple angle; and the local, torsional-flexural and flexural modes for the lipped angle.

The values presented by Schafer & Peköz (1998) were used for the amplitude of the imperfections adopted for the local, local/torsional and torsional-flexural modes. Imperfection magnitudes were selected at 25% and 75% probability of exceedance. The value of  $L/1500$  was adopted for the global flexural imperfection.

About numerical analysis, the procedure adopted in the work proved to be satisfactory. The results with imperfections magnitudes of 75% probability of exceedance to the local/torsional mode, local mode, torsional-flexural mode and  $L/1500$  to the flexural mode were the most nearly results the tests.

### **Acknowledgments**

Research conducted in this paper was supported by CAPES and USIMINAS.

### **References**

- American Iron and Steel Institute (2006). Direct Strength Method (DSM) Design Guide CF06-1. American Iron and Steel Institute, Washington, DC.
- American Iron and Steel Institute (2001). North American Specification for the Design of Cold-Formed Steel Structural Members. Washington: AISI.
- ANSYS (1997). Structural nonlinearities: user's guide for revision 5.5. Houston. v.1.
- Chodraui, G.M.B. (2006). Theoretical and experimental analysis of cold-formed steel members under compression. PhD Thesis (in Portuguese). School of

- Engineering of Sao Carlos – University of Sao Paulo, Sao Carlos, SP, Brazil.
- North American Specification (2004). Supplement 2004 to the North American Specification for the Design of Cold-Formed Steel Structural Members, American Iron and Steel Institute, Washington, D.C.
- Rasmussen, K.J.R. (2003). Design of Angle Columns with Locally Unstable Legs. Department of Civil Engineering, Research Report No. R830, University of Sydney, Australia.
- Schafer, B.W. (1997). Cold-Formed Steel Behavior and Design: Analytical and Numerical Modeling of Elements and Members with Longitudinal Stiffeners. PhD. Dissertation, Cornell University, Ithaca.
- Schafer, B.W. (2001). Finite strip analysis of thin-walled members. In: CUFSM: Cornell University – Finite Strip Method.
- Schafer, B.W.; Peköz, T. (1998). Computational modeling of cold-formed steel: characterizing geometric imperfections and residual stresses. *Journal of Constructional Steel Research*, v.47, 193-210.
- Young, B. (2005). Experimental Investigation of Cold-Formed Steel Lipped Angle Concentrically Loaded Compression Members. *Journal of Structural Engineering*, 131(9), 1390-1396.
- Young, B. (2004). Tests and Design of Fixed-Ended Cold-Formed Steel Plain Angle Columns. *Journal of Structural Engineering*, 130(12), 1931-1940.





## **Structural Analysis of Scaffolding with Plank and Anchor Rod during Construction**

Jui-Lin Peng<sup>1</sup>, Chi-Ling Pan<sup>2</sup>, Kuan-Hung Chen<sup>3</sup>, and Siu-Lai Chan<sup>4</sup>

### **Abstract**

This study focuses on the critical loads of scaffolding with the anchor rods, plank and inner knee brace under concentric and eccentric loads during construction. The steel rebar is used in place of the patent anchor rod in this research. This study shows that the critical load of the scaffolding increases by 1.5 times when the anchor rods of length of 30 cm are used on two sides of every story of scaffolding. The critical load increases by 4 times when the scaffolding has both anchor rods and plank. The critical load of scaffolding with the anchor rods placed on each story is twice as large as the load with anchor rod added every two stories. In addition; the failure mode of the structure is also transformed from the in-plane direction to the out-of-plane direction. The 30 cm long anchor rod, a steel bar of grade 3, provides a good lateral restraint to the scaffolding. The setup plank can significantly increase the critical load of the scaffolding. The critical load increases by 1.5 times under the concentric load, and increases up to 2.2 times under the TL/4 eccentric load defined as the load applied a quarter distances from the end. The anchor rods and the planks are suggested to install in a scaffolding to improve stability, especially under eccentric loads during construction.

---

<sup>1</sup> Professor, Department of Construction Engineering, National Yunlin University of Science and Technology, Douliu, Yunlin, 640 Taiwan, ROC.

<sup>2</sup> Professor, Department of Construction Engineering, Chaoyang University of Technology, 168, Gifeng E. Rd., Wufeng, Taichung, Taiwan, ROC.

<sup>3</sup> Research Associate, Central Taiwan Science Park Administration, National Science Council, Executive Yuan, Taiwan, ROC.

<sup>4</sup> Professor, Department of Civil and Structural Engineering, Hong Kong Polytechnic University, Hong Kong, China.

## 1. Introduction

During the construction, scaffolds are frequently used as the working scaffolding system erected at the external circumstance of the building under construction. Door-shape steel-pipe scaffolds are widely used in construction sites. Fig. 1 shows the basic assembly of the door-shape steel-pipe scaffolding system used in construction.

The feature of scaffolding system includes the single-row assembly model with cross-brace removed at the side nearer to the façade of a building.

In construction, wall scaffolds provide a good working platform for workers for assembling and disassembling of formworks and stuccoing works, etc. According to a recent survey of construction sites, it was found that the anchor rods connecting scaffolds and façade of buildings do not have a proper installed method. The grade 3 rebar of diameter equal to 3/8 in, 0.9525 cm and nominal design strength 275 N/mm<sup>2</sup>, is substituted for the patent anchor rod in construction sites. Furthermore, during stuccoing and finishing process of buildings, anchor rods are even frequently removed for the purpose of working convenience.

The wall scaffold needs to be paved with plank for working operation. Since the wall scaffold is installed in a single row for the convenient setting of formwork or finishing works for facades so that the lateral side adjacent to the constructing building has no cross-brace in the construction stage as shown in Fig. 1. The set plank should be able to enhance the critical load of a scaffolding system and strengthen the weak point of having no cross-brace as well. This scale of its enhancement should be studied.

Previous study by Godley and Beale (1997) indicated that the behavior of system scaffolds involved the windward standard to uplift forces relative to the horizontal load. Peng et al. (2008) revealed the effect of simple eccentric loads to the scaffolding systems without considering the plank and anchor rod. Most research on scaffolds (Peng et al. 2001, Yu 2004, Weesner et al. 2001) involved the strengths of shoring systems. These studies were not related to the scaffolding systems for finishing works.

This research investigates the critical loads of scaffolding systems under concentric and eccentric loads for probing into the effect of use of the anchor rod and the plank. The type of research mainly emphasizes on the test and analysis. The outlines of this research can be classified as the following five categories: (A) the structural behavior of the basic setup scaffold, (B) the effect of anchor rod to the critical load, (C) the effect of plank to the critical load, (D) the effect of both anchor rod and plank to the critical load, (E) the effect of inner knee brace to the failure model.

The analysis presented in this study is based on a three-dimensional

second-order elastic analysis using semi-rigid joint. The analysis software adopted here is GMNAF program developed by Chan (1988). For simulating the initial imperfection of the scaffolding system, the notional lateral force is applied to the structure in the analysis. This lateral notional force is approximated as 0.1~0.5% of the factored gravitational load.

## 2. Material Properties

The type of the tested scaffold used in this research is the door-shape steel-pipe scaffold with inner diagonally reinforced bracing bars, i.e. knee braces, shown in Fig. 2. The sectional dimensions of the scaffolding structural members adopted here are mainly in compliance with the requirement of Chinese National Standard (1996). Fig. 2 indicates all the dimensions of the vertical columns, horizontal bars and cross-braces.

All members are made of carbon steel in compliance with CNS requirement with the Young modulus of elasticity  $E$  for the analysis taken as that of the standard steel material or  $20006.3 \text{ kN/cm}^2$  ( $2040 \text{ tonnes/cm}^2$ ). The joint stiffness of the scaffold obtained from the previous test is  $784.6 \text{ kN-cm/rad}$  ( $80 \text{ tonne-cm/rad}$ ) (Peng et al. 2004) and this stiffness for joints in the connecting scaffolds is applied as the basic reference data for analysis in this paper.

## 3. Setup of Test

### 3.1 Setup of Scaffold

At the assembly of the testing scaffold in Fig. 3, the adjustment base with its base-plate cut-off is placed at the bottom of the scaffold. The adjustment jack base without base-plate placed on 4 pieces of iron sheets can simplify the bottom boundary condition of scaffolding system as a “hinge” in the analysis. The conditions of top layer and the lowest layer scaffold are similar so that the top boundary conditions are also assumed as “hinge” in the analysis. The top boundary condition of the scaffolds is to prevent any lateral displacement since four horizontal restraints are fixed to prevent the top H-beam frame from horizontal movement. Thus, the scaffold can only provide vertical movement under load.

### 3.2 Scaffold with Anchor Rod and Plank under Eccentric Load

In the loading test, the scaffold is installed upside down. Two pieces of steel plates are placed at the bottom of each vertical column of scaffold. Further, between the two steel plates, 9 steel balls are installed as a cross-frame window shape; i.e. 3 balls are provided at each of the 3 rows equally spaced. This type of erection enables the part in contact with the floor which is movable when the scaffolding system is subjected to the vertical load. This installation

is mainly for simulating the movable top level of the scaffolding system.

Fig. 4(I) indicates the movable situation of the shoring system. However, the top load  $P$  of the laboratory hydraulic system is placed as shown in Fig. 4(II). Since the position of the hydraulic system is fixed, the hydraulic punch head expands freely in mono-direction. Therefore, the simulating lateral displacement of scaffolding top end is not directly available. In this research, for simulating the lateral boundary displacement, the method of erection shown in Fig. 4(III) is applied.

The letters L, R, T, B shown in Fig. 5(I) represent the locations Left, Right, Top and Bottom respectively. In Fig. 5(I), "Center" indicates the central location of the applied load with respect to the  $xy$  coordinate lying on  $(d/2, L/2)$ . T/4 is the eccentric load shown in Fig. 5(II) with the load placed at the position  $(d/2, 3L/4)$  of the  $xy$  coordinate. L/4 eccentric load is located at  $(d/4, L/2)$  of  $xy$  coordinate shown in Fig. 5(III). In TL/4 eccentric loading test, the load was applied at asymmetric location along upper & lower and left & right directions, i.e. at the location  $(d/4, 3L/4)$  of  $xy$  coordinate shown in Fig. 5 (IV). All of the 4 types of eccentric loading tests are separately processed with the two types of erection as single-side cross-brace with the removal of cross-brace at the access location.

#### **4. Discussions of Test and Analysis**

##### *4.1 Structural Behavior of Basic Setup Scaffold*

The basic setup scaffold is defined as the restrained boundary with no lateral displacement and under a concentric load. The critical load of the basic setup scaffold is considered as a basis for comparison with the other scaffolding cases. The averaged critical load of the 2-story scaffold with cross-brace at both sides is 117.7 kN. The averaged critical load for the 2-story scaffold with only one single-side cross-brace is 102.9 kN. The averaged critical load for the 3-story scaffold with cross-brace at both sides is 104.1 kN. The averaged critical load for the 3-story scaffold with cross-brace at only single side is 70.2 kN. From the aforementioned test result of basic scaffolds, it is found that the second or repeated loading test results of the four groups are reduced for more than 40%. Therefore, it is known that the effect of the variation between brand new and worst used and old scaffolds to their critical load is enormous.

##### *4.2 Effect of Anchor Rod*

The tests in this research adopt a No. 3 rebar as an anchor rod to connect scaffolds. Two types of connections are respectively 45 and 90 degrees to the scaffold. As shown in Fig. 5(I), the angle of the anchor rod is defined as 90 degrees. Due to the feature of temporary accessory, anchor rods in

construction sites are frequently connected in a slight inclination. As it is taken as 45-degree connection in this research, it is deemed as the worst connection. The 90-degree connection is the standard connection angle and is deemed to be the best connection of the anchor rod.

During the test, the applied loads are the concentric load and the TL/4 eccentric load. It is intended to check the effectiveness of anchor rod to critical load of the scaffold under the eccentric loading condition. The 2-story scaffold is tested with the cross-brace of the lowest story of scaffold removed.

#### *4.2.1 Test Result*

##### *A. Concentric Load*

###### *• Without Anchor Rod*

The test without anchor rod is carried out for comparing with the strength of scaffolding structure with anchor rod and plank. Owing to limited space of testing facilities and widely practiced fastening the anchor rod in every 2-story scaffold, the test applies 2-story scaffolding structure in two types of installation as follows: (1) the scaffolding system with removal of cross-brace at access location [Type (1)] and (2) the scaffolding system with only one single-side cross-brace [Type (2)].

Fig. 6 indicates the deformed shape of the loaded scaffolding system after the test where the cross-brace of the bottom story are removed and this arrangement is denoted as Type (1). There is no restraint at the top story, i.e. the testing bottom story, of the scaffold so that apparent displacement occurred at failure. The averaged critical load of the test is 35.7 kN.

The number of cross-brace of scaffold is more than that of Type (1) scaffold so that the critical load of Type (2) is higher than that of Type (1). The averaged critical load of Type (2) is 62.0 kN. In the tests, no restraint is applied at the top story, i.e. the bottom level of the tested scaffold, of the scaffold so that significant displacement occurred at failure. The failure style of Type (2) is similar to that of Type (1).

###### *• 90 Degree Anchor Rod [Type (1)]*

The length of anchor rod is 30 cm and it connects the scaffold by coiling twice on vertical column of the scaffold. A concentric load is applied to the scaffolding system where the cross-brace at the bottom story of the scaffold is removed as well.

As the top story (i.e. the bottom story of the tested specimen) of the scaffold is restrained by the anchor rod so that the deformation becomes small here. The critical load of the test is 56.5 kN which, compared to the unrestrained condition 35.7 kN, is observed to have greatly increased.

- 45 Degree Anchor Rod [Type (1)]

The 45 degree erection is similar to the 90 degree erection. The 45 degree is defined as anticlockwise rotation of the anchor rod from the original vertical direction as shown in Fig. 5(I). The deformation of the scaffold after the load is similar to that of 90 degree. However, the averaged critical load is reduced to 44.3 kN. The ratio of the two cases of 45 and 90 degrees is 0.78 (=44.3/56.5). This indicates that the 45 degree erection has longer length to scaffold than that of 90 degree erection in Fig. 5(I) so that this reduces the critical load of the 45 degree scaffold.

#### *B. TL/4 Eccentric Load*

- Without Anchor Rod

This test without the anchor rod is also applicable for comparison of the critical loads of scaffolding systems with the anchor rod and the plank. With the exception of TL/4 eccentric load, the setups of tests are the same as the case for concentric load. It means the test is processed by using 2-story scaffolding structure under 2 types of erection as follows: (1) the scaffolding system with removal of cross-brace at access location as Type (1), and (2) the scaffolding system with only single-side cross-brace as Type (2).

As Type (1) has its bottom story cross-brace removed, its critical load is rather low. The averaged critical load is 18.1 kN. The averaged critical load of the Type (2) scaffolding system with single-side cross-brace is 32 kN. Compared with the concentric load condition, the critical load of Type (2) is reduced by approximately half as 0.51(=18.1/35.7) and 0.52 (=32/62), respectively. It indicates that the joint of the scaffolding system under TL/4 eccentric load generates a greater extent of damage, which greatly reduces the critical load of the scaffold.

- 45 Degree Anchor Rod [Type (1)]

This research adopts TL/4 eccentric load in simulating the worst eccentric load condition of the scaffolding system in construction sites. The system is a 2-story scaffold with the removal of cross-brace at access location. The anchor rod is applied with inclination  $\theta$  equal to 45 degree connecting the scaffold as shown in Fig. 5(I). The test result indicates the critical load as 32.9 kN

The averaged critical load of the scaffolding system having 45 degree erection of anchor rod is 32.9 kN. Compared with the critical load of 44.3 kN with 45 degree anchor rod scaffold under concentric load, the critical load of 32.9 kN is rather low. The ratio of the two is about 0.74 (=32.9/44.3).

However, it is quite close to the critical load 35.7 kN of the scaffolding system without anchor rod and under concentric load. This indicates that after the scaffold is fixed with 45 degree anchor, its restraining effect drops about 25% when compared with 90 degree connection. Nevertheless, when compared with the scaffold without anchor rod and under concentric load, the boundary condition can be transformed from laterally movable to unmovable conditions making the effect of TL/4 eccentric load insignificant.

#### *4.2.2 Analysis of Anchor Rod Stiffness*

The research mainly implements a 2-story scaffolding system where the anchor rod is taken as linearly elastic spring providing elastic stiffness as  $k_s$  ( $=EA/L$ ). If the anchor rod length taken as  $L=30$  cm and the elasticity modulus as  $E = 20012.4$  kN/cm<sup>2</sup> (a nominal value of steel) are adopted for the analysis, the rebar stiffness is varied by simply changing its cross-sectional area  $A$ , i.e. changing the rebar diameter.

The analysis result is shown in Fig. 7. When the diameter is increased to No. 3 rebar diameter 0.9515 cm, the stiffness of anchor rod  $k_s = 475.1$  kN/cm and the analyzed scaffolding critical load is 89.5 kN as shown in Fig. 7. The Figure further indicates that when the anchor rods diameter is 0.2 cm, i.e. at  $k_s = 21$  kN/cm, the analyzed scaffolding critical load is close to 89.5 kN. Therefore, it is found that if 30 cm long No. 3 rebar is applied as anchor rod with wide use of this No. 3 rebar in construction sites, the bending behavior of the rebar can be neglected. This implies that if the rebar is properly fixed to the scaffold, it can provide the lateral restraint to the scaffold in prevention of the lateral displacement.

### *4.3 Effect of Plank*

#### *4.3.1 Test without Anchor Rod*

##### *A. Concentric Load*

A scaffolding system having the single-side cross-brace and with the plank placed every story is the most popular and basic practice in construction sites. Deformations of the scaffold all occur in the in-plane direction of the scaffolding system at the first or origin load in the concentric loading test. The average critical load of the scaffolding system is 94.2 kN in tests. Further, the failure of the overall scaffolding system appears to have a slight rotation. The average critical load of the scaffold with plank and single-side cross-brace is increased by a factor of 1.5 ( $=94.2/62.0$ ) times, compared with the scaffolding system without plank.



### *B. TL/4 Eccentric Load*

Under TL/4 eccentric load, the test result shows that the failure of the scaffolding system occurs in the in-plane direction and the deformation is located near the loading position. This failure style is similar to the scaffold with the same installation process under the concentric load. The average critical load of the eccentric load scaffolding system is 70.6 kN. Compared with the erection without plank, the average critical load of the scaffolding system with plank increases by 2.2 ( $=70.6/32.0$ ) times. Therefore, it is found that setup of plank has a very good effect in increasing the critical load of the scaffolding system.

#### *4.3.2 Analysis of Plank Connecting Types*

This paper analyzes the connected effect of the plank to the critical load of the scaffolding system on the basis of the test results. The analysis is based on the 4 types of loads: i.e. the concentric, L/4 eccentric, T/4 eccentric and TL/4 eccentric loads shown in Fig. 5. In the analysis, the laterally movable top layer is adopted for its similarity to the case for real construction sites. Since the bottom story of the scaffolding system is not provided with jack bases, it is deemed to be a hinged joint for the conservative design. The connections between the plank and the scaffold are considered as three cases, namely as hinged joint, rigid joint and semi-rigid joint with spiral elastic stiffness equal to 490.5 kN-cm/rad.

Fig. 8 shows the analysis results based on the planking ends, fastened by hinged joint under different eccentric loads. It is found from the various planking ends, hinged joints, rigid joint and semi-rigid joint, that the connection stiffness between the planking end and the scaffold has insignificant effect to the critical loads of overall scaffolding systems. Under the same loading conditions, the critical loads of the scaffolding systems with 2 to 12 stories vary only slightly. This is quite close to the observations in another publication that the scaffolding systems under the various eccentric loads without plank (Peng et al. 2008).

If the worst condition of the planking end connection is applied, the planking end is assumed to connect to the scaffold with the hinged joint. In this case, the analysis results are compared with the critical loads of the scaffolding systems with and without the plank. The comparison is shown in Fig. 8 using the data from reference (Peng et al. 2008). Fig. 8 reveals that the critical loads of the scaffolding systems concentrated at two regions though various eccentric loads are taken into consideration. The region is divided into areas with the plank and without the plank.

As shown in Fig. 8 and under concentric loading condition, the scaffolding

system with plank increases the critical load for 2.7 (=60.9/22.4) times. Under T/4 eccentric loading condition, the critical load is increased by 2.6 (=44.9/17.8) times. Under L/4 eccentric loading condition, the critical load is increased by 3.5 (=51.1/14.7) times. Under TL/4 eccentric load condition, the critical load is increased by 3.3 (=40.9/12.3) times. From the analysis results shown in Fig. 8, it is found that if a scaffolding system is installed with the plank, the critical load of the scaffolding system can dramatically increase twice. The added plank can make up the partially lost strength of the scaffolding system when the single-side cross-brace is removed. Therefore, the plank should not be removed from the working scaffolding system in construction sites.

#### *4.4 Effect of Both Anchor Rod and Plank*

This paper analyzes the effect of the simultaneous setup of the plank and the anchor rod in scaffolds to the critical load of the scaffolding system. In addition to installing the single-side cross-brace and the plank in every story, anchor rods are also installed on both sides of every 2-story of the scaffolding systems for analysis of scaffold from 2 to 12 stories. The boundary condition is the same as the one in construction site condition. Hinged connections are assumed between the anchor rod and the scaffold. The connections between the plank and the scaffold remain the same, respectively as hinge joint, rigid joint and semi-rigid joint. Their spiral elastic stiffness is 490.5 kN-cm/rad.

Fig. 9 shows the analysis results of hinged joint of planking ends under different eccentric loads. From the test results being very close to each other in the end stiffnesses, hinged joints, rigid joint and semi-rigid joint, it is found that the connection stiffness between the planking end and the scaffold has insignificant effect to the critical load of the scaffolding system furnished with planks and anchor rods. This is similar to the analysis results of the planked scaffolding system without the anchor rod described above.

If a weak hinged joint is used as the connection for the planking end, Fig. 10 shows the analyzed strengths of scaffolding systems with and without the plank and the anchor bar. Fig. 10 indicates several results. To illustrate this, a 12-story scaffolding system is taken as the example.

- (1) Under concentric loading condition: the critical load of the scaffolding system with both the plank and the anchor rod is approximately 1.5 (=89.0/60.9) times of that of the scaffolding system with plank but without the anchor rod. Furthermore, it increases 4 times (=89.0/22.4) when compared with the critical load of the scaffolding system with the anchor rod but without the plank.
- (2) Under TL/4 eccentric loading condition: the critical load of the scaffolding system with both the plank and the anchor rod is approximately 1.4

(=57.1/40.9) times of the scaffolding system with the plank but without anchor rod. Moreover, it increases 4.6 (=57.1/12.3) times compared with the critical load of the scaffolding system with the anchor rod but without the plank.

This paper shows that under TL/4 eccentric load, the properly fastened anchor rod can approximately increase the critical load of the scaffolding system by 1.5 times. If properly installed for both the plank and the anchor rod in the scaffolding system, the critical load can be increased by more than 4 times. Therefore, neither the plank nor the anchor rod should be removed from a working scaffold in construction site. The arbitrary removal of the plank or the anchor rod would considerably reduce the critical load of the scaffolding system.

#### *4.5 Effect of Inner Knee Brace*

##### *4.5.1 2-story scaffold with Anchor Rod and Plank*

The failure of the scaffolding system with the plank and the anchor rod is unique since the damage mostly occurs at the part of the scaffold below the first anchor rod. This paper studies the effect of inner knee brace of the scaffold on the critical load of the scaffolding system.

Fig. 11 indicates the deformation of a 6-story scaffolding system with the anchor rod and the plank before and after loading. Anchor rods are setup in every 2-story height in this system. Fig. 11 shows that the deformation occurs mostly at the 2-story scaffold measured from the ground level. This scaffolding system does not deform above the level of the first anchor rod. Additionally, the deformation merely occurs in the in-plane direction of the scaffold whereas there is almost no deformation in the out-of-plane direction. Additionally, considering the 4-story scaffold without the inner knee brace, its deformation is shown in Fig. 12. It is close to the failure model in Fig. 11.

##### *4.5.2 Stiffness Effect of Anchor Rod*

If the linear elastic stiffness of the anchor rod varies, the changes of the scaffolding system within and without inner knee brace can be studied. Fig. 13 indicates a 4-story scaffolding system, when the horizontal elastic stiffness of the anchor rod changes to 21 kN/cm, i.e. when a rebar 0.2 cm diameter is used, the critical load of the scaffolding system is 89.5 kN and that of the portal frame is 52.2 kN. Also, as shown in Fig. 13, the critical loads of the scaffold and portal frame systems do not totally increase in line with the increment of the anchor rod stiffness. The critical loads of two systems respectively approach a certain fixed value.

#### 4.5.3 Scaffold with Anchor Rod and Plank in Every Story

This paper studies the effect of installing anchor rod in every story to the critical load. The analysis and comparison are made for the scaffold and the portal frame system, i.e. scaffold without inner knee brace, from 2 to 5 stories. Fig. 14 shows the analysis result of the 4-story systems with the anchor rod at every story where all analysis assumptions are the same as above, except with the installation of anchor rods. It is found in Fig. 14 that, regardless of having inner knee brace or not, the failure mode changes from the original in-plane direction to the out-of-plane direction. Since the installation of the anchor rod in every story caused a change in the failure mode so that the effective length is reduced. This makes the critical load of the scaffold systems within and without the inner knee brace unrelated to the installation height of the scaffolds. Moreover, the strengths of the two systems with the anchor rod in every story are higher than those in scaffold with anchor rod placed every 2 stories.

Fig. 15 shows the analysis result of scaffolding system within and without inner knee braces from 2 to 5 stories. It is found from Fig. 15 that the critical load of the scaffolding system within the inner knee brace with every story installed with the anchor rod is 165.5 kN. Compared with the scaffolding system having anchor rods installed in every 2-story, the critical load approximately increases by 1.8 ( $= 165.5/89.5$ ) times. It is also known from the figure that the critical load, 162.9 kN, of the scaffold not using the inner knee brace is slightly less than that of the scaffolding system with the inner knee brace. This discrepancy is not like the analysis result for the two cases where anchor rods are used in every 2-story of the scaffold.

### 5. Conclusions

- Based on this study, the critical load of the 2-story scaffolding system can increase by 1.5 times compared with that of scaffolding systems without anchor rods. The anchor rod of No. 3 rebar of 30 cm length is assumed in the studies. If both the No. 3 rebar and the plank are setup, the critical load of the scaffolding system can even increase by 4 times. While construction works is in progress, the plank and the anchor rod should not be removed.
- The plank can significantly increase the critical load of the scaffolding system when under the concentric load, the critical load increases by approximately 1.5 times, and when under TL/4 eccentric load, it is increased by 2.2 times. In addition, the failure deformation does not generate any lateral displacement in the out-of-plane direction like the scaffolding system without the plank whereas the failure shape occurs in the in-plane direction. Therefore, the installed plank in construction sites should not be removed when work is in progress.

- The critical load of the scaffolding system with the anchor rod in every story is about 2 times compared with the anchor rod installed in every 2-story height. The failure model shifts from the in-plane direction towards the out-of-plane direction. Also, since the effective length is fixed, the critical loads of different stories of scaffolding systems are rather close.
- The inner knee brace can provide additional stiffness so that if every 2-story scaffold is fastened with the anchor rod, the failure model is simply controlled by the failure of the lowest story.

## 6. Acknowledgments

The authors are grateful to the financial supports by the National Science Council of Taiwan (Project No.: NSC 94-2218-E-224-008).

## References

1. Chan SL. Geometric and material nonlinear analysis of beam-columns and frames using the minimum residual displacement method. *International Journal for Numerical Method in Engineering*, 26:2657-69, 1988.
2. Chinese National Standard, CNS-4750, No. A2067, Steel Scaffold, 1996. (In Chinese)
3. Godley MHR, Beale RG. Sway stiffness of scaffold structures. *The Structural Engineer*, 75(1):4-12, 1997.
4. Peng JL, Chen KH, Chan SL, Chen WT. Experimental and analytical studies on steel scaffolds under eccentric loads. *Journal of Constructional Steel Research*, 2008. (be accepted)
5. Peng JL, Pan ADE, Chen WF. Approximate analysis method for modular tubular falsework. *Journal of Structural Engineering ASCE*, 127(3):256-63, 2001.
6. Peng JL, Pan JL, Huang PS. Investigation of load-carrying capacity of scaffolding structures in construction. *Journal of the Chinese Institute of Civil and Hydraulic Engineering*, 16(3):425-35, 2004. (In Chinese)
7. Yu WK. An investigation into structural behaviour of modular steel scaffolds. *Steel and Composite Structures*, 4(3):211-26, 2004.
8. Weesner LB and Jones HL. Experimental and analytical capacity of frame scaffolding. *Engineering Structures*, 23:592-99, 2001.

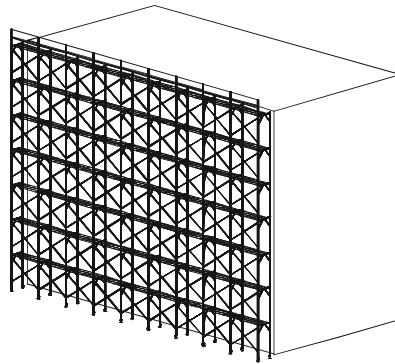


Fig. 1 Setup of steel scaffold for finishing near façade of building

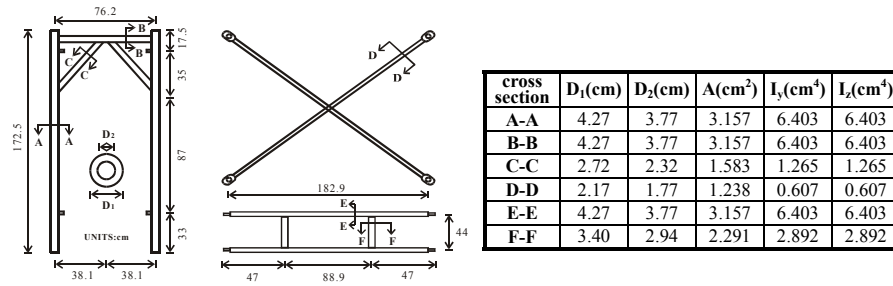


Fig. 2 Dimensions of scaffolding unit, plank and cross-brace

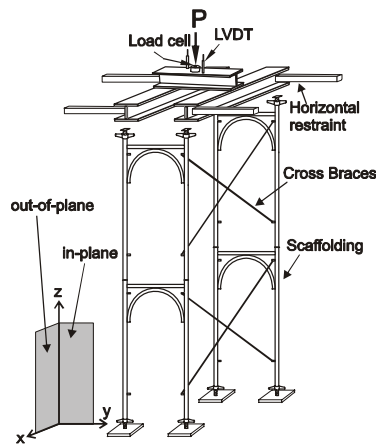


Fig. 3 Basic setup of scaffolds in loading tests

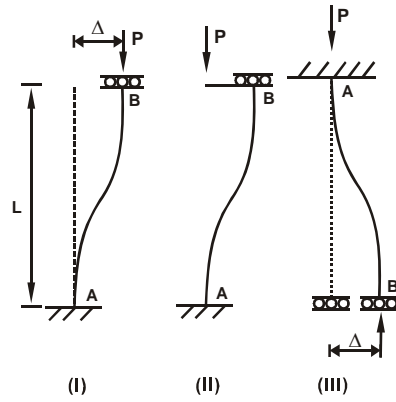


Fig. 4 Boundaries of lateral displacement of tested scaffold

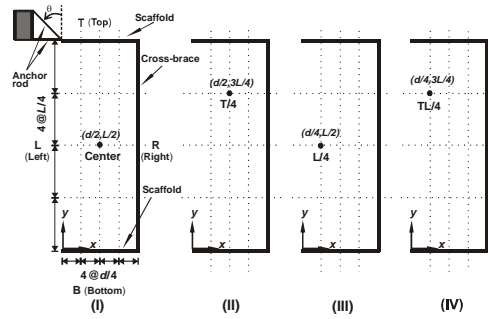


Fig. 5 Setups of loading positions and anchor rod in eccentric loading tests



Fig. 6 Test result of scaffolds with removal of cross-brace at access location under concentric loading

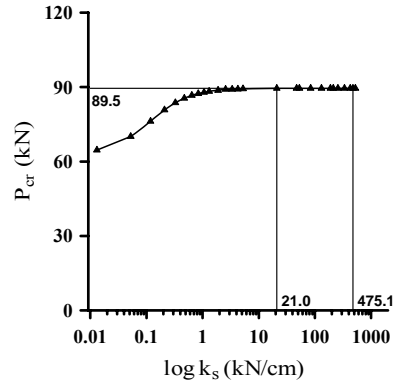


Fig. 7 Critical loads of stiffnesses of anchor rods for 2-story scaffold

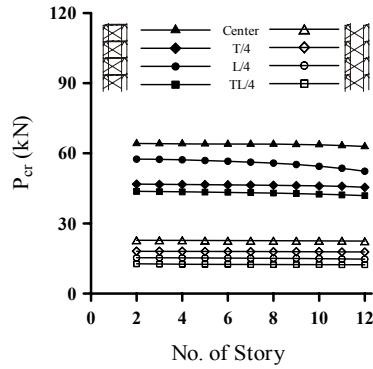


Fig. 8 Analyzed critical loads of scaffolds without and with plank using hinged connection under different eccentric loads



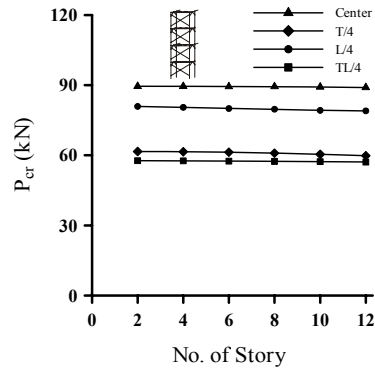


Fig. 9 Analyzed critical loads of scaffolds with anchor rod and plank using hinged connection under different eccentric loads

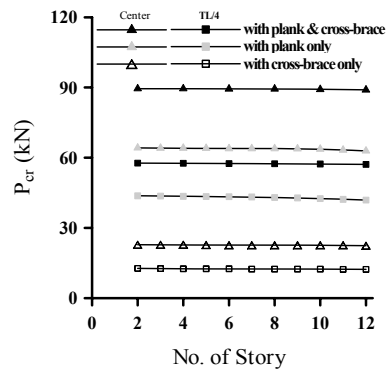


Fig. 10 Analyzed critical loads of scaffolds with and without anchor rod and plank under concentric and TL/4 eccentric loads

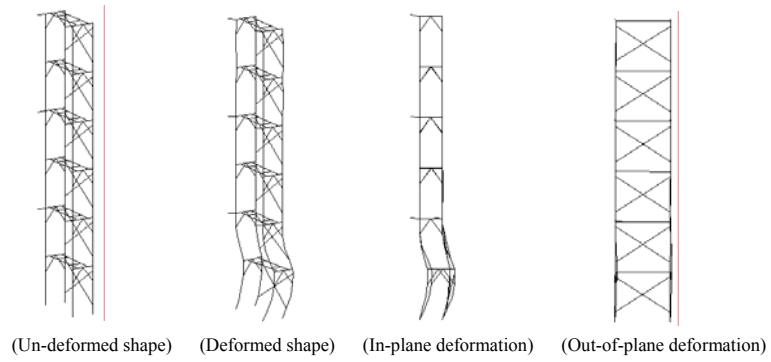


Fig. 11 Analysis results of 6-story scaffold with anchor rod and plank under concentric load ( $P_{cr}=89.4$  kN)

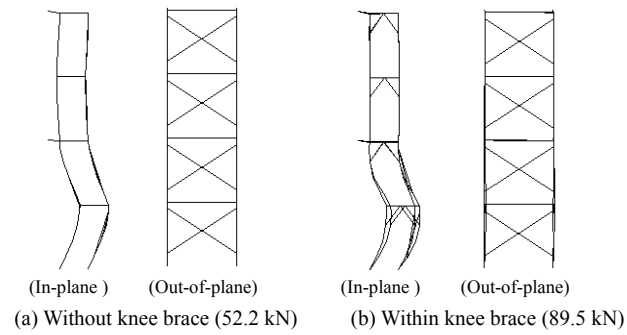


Fig. 12 Analysis results of 4-story scaffolds within and without inner knee brace after loading

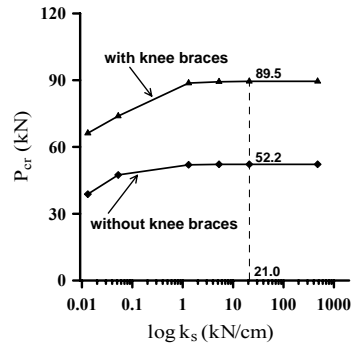


Fig. 13 Analyzed critical loads of 4-story scaffolds with stiffnesses of anchor rod every two stories and within and without inner knee brace

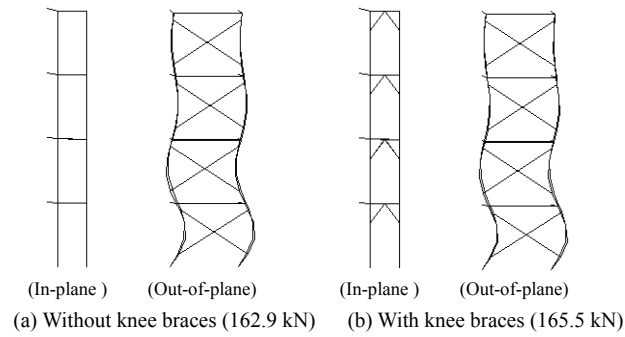


Fig. 14 Analysis results of 4-story scaffolds with anchor rod every story and within and without inner knee brace after loading

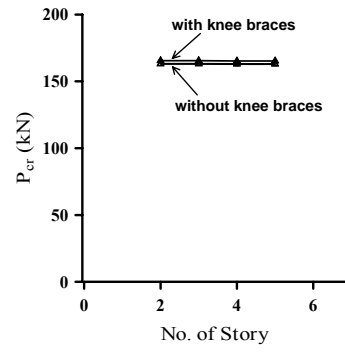


Fig. 15 Analyzed critical loads of scaffolds with anchor rod every story based on within and without inner knee brace



## **What's New in the 2007 Edition of the North American Cold-Formed Steel Specification?**

By Roger Brockenbrough<sup>1</sup>, Reinhold Schuster<sup>2</sup>,  
Roger LaBoube<sup>3</sup>, Helen Chen<sup>4</sup>, Ph.D., P.E,

### **Abstract**

The 2007 edition of the *North American Specification for the Design of Cold-Formed Steel Structural Members (Specification)* was published recently by AISI (2007a). As the name indicates, the *Specification* is intended for use throughout Canada, Mexico and the United States. The *Specification* has been approved in the United States by the American National Standards Institute as the American National Standard, in Canada by the Canadian Standards Association, and has been endorsed in Mexico by Camara Nacional de la Industria del Hierro y del Acero (CANACERO).

In the 2007 edition, many new design provisions were adopted and significant editorial and technical changes were made. This paper provides an overview of the major changes and additions.

### **Introduction**

The first edition of the *North American Specification for the Design of Cold-Formed Steel Structural Members* (AISI, 2001) was published in 2001 as the result of a joint effort of the American Iron and Steel Institute's Committee on Specifications (AISI COS), the Canadian Standard Association's Committee on Cold-Formed Steel Structural Members (CSA S136), and Mexico's Camara Nacional del la Industria del Hierro y del Acero (CANACERO). A Supplement

---

<sup>1</sup> President, R. L. Brockenbrough & Associates, PA.

<sup>2</sup> Professor, Emeritus of Structural Engineering and Director of Canadian Cold-Formed Steel Research Group, Department of Civil Engineering, University of Waterloo, Waterloo, Canada.

<sup>3</sup> Distinguished Teaching Professor, Dept. of Civil Engineering, University of Missouri-Rolla, MO.

<sup>4</sup> Senior Structural Engineer, American Iron and Steel Institute, DC.

to the 2001 edition of the *Specification* (AISI, 2004) was published in 2004. In 2007, a new edition of the *North American Specification* was published, which includes all the changes and new design provisions approved since the publication of the 2001 edition of the *Specification*.

The 2007 edition of the *North American Specification* consists of a main document, Chapters A through G and several appendices. The numbered appendices, Appendices 1 and 2 are applicable to all three countries. The lettered appendices are country specific, Appendix A for the United States and Mexico and Appendix B for Canada. To make the *Specification* more user-friendly, some contents have been reorganized according to their application. Light frame construction is covered in Section D4\*; floor, roof or wall steel diaphragm construction is covered in Section D5; and metal roof and wall systems are covered in Section D6. In addition, the definitions of commonly used terminologies are standardized as a result of a joint effort of AISI and the American Institute of Steel Construction (AISC) (AISI, 2007b).

In the following sections, an overview of the major technical changes and added provisions will be provided.

### **Technical Changes and Additions of the Design Provisions**

#### **1. Materials.**

In addition to updating all the standards for applicable steels, a new standard was added, ASTM A1039 for hot-rolled carbon steel sheet produced by the twin-roll casting process.

The North American Specification permits applications of steels that are produced to other than the listed specifications, provided that certain requirements are satisfied. In the 2007 edition, these requirements in chemical and mechanical properties, coating properties, ductility and weldability have been clarified (Appendix A, Section A2.2).

#### **2. Elements.**

Previously, the effective width of an unstiffened compression element in bending was determined assuming a uniform stress distribution. A new provision adopted in 2004 (AISI, 2004) was included in the 2007 *Specification*,

---

\* Section numbers referred to herein are those in the 2007 edition of the *North American Specification*, unless otherwise indicated.

which enables one to consider stress gradient effects. This design provision was based on research work by Bambach and Rasmussen (2002a, 2002b, and 2002c). The new design provision will result in an improved assessment of the buckling performance of an unstiffened compression element in bending (Section B3.2).

In the 2007 *Specification*, the design of uniformly compressed elements with multiple or single intermediate stiffeners was merged. This is based on the finding that the method for multiple intermediate stiffeners provides the same reliability as the previous provision for a single intermediate stiffener.

### **3. Members**

It has been recognized that cold-formed steel members may be subjected to distortional buckling, an instability that may occur in members with edge stiffened flanges, such as C- and Z-sections. Illustrated in Figures 1 and 2 are the various buckling modes for a flexural member. Distortional buckling is characterized by instability of the entire compression flange, as the flange along with the edge stiffener rotates about the junction of the compression flange and the web. However, until the 2007 edition, the *Specification* had been silent on the evaluation of the structural performance of members subject to distortional buckling. In this edition, explicit equations are provided (in Section C3.1.3 for flexural members and in Section C4.2 for compression members) for determining the distortional buckling strengths of C- and Z- shaped members. For any other shaped members, rational analysis approaches are permitted.

Since cold-formed steel members are often singly-symmetric sections, additional stresses normal to the cross section can occur if the applied forces do not pass through the shear center. As a result, unless negated by bracing, the member flexural strength can be reduced due to torsion. This reduction can now be considered by a reduction factor, which is determined by the ratio of the nominal stress due to bending alone to the combined stresses due to both bending and torsional warping at the point of maximum combined stress on the cross-section (Section C3.6).

### **4. Structural Assemblies and Systems**

As indicated previously, one of the major changes in the 2007 edition of the *Specification* was to reorganize the design provisions according to applications. These applications were divided into Light Frame Construction; Floor, Roof or Wall Diaphragm Construction; and Metal Roof and Wall Systems. The reorganized provisions and changes are outlined as follows:



- Cold-Formed Steel Light-Frame Construction (Section D4)  
 In this section, only the All Steel Design approach is included. The sheathing braced design approach for wall stud assemblies has been removed from the *Specification*. Design for sheathing braced design and other light-frame construction design is now included in a separate set of documents, the North American Standards for Cold-Formed Steel Framing - :
  - General Provisions;
  - Floor and Roof System Design;
  - Wall Stud Design;
  - Header Design;
  - Truss Design; and
  - Lateral Design (note: this standard is only applicable in the United States and Mexico).
 A detailed review of the above standards can be found in the paper, <title> by Jay Larson (2008).
  
- Floor, Roof, or Wall Steel Diaphragm Construction (Section D5)  
 The safety and resistance factors have been recalibrated based on the full-scale test data summarized in the Steel Deck Institute Diaphragm Design Manual, First edition (1987).
  
- Metal Roof and Wall Systems (Section D6)  
 This section is designated for design provisions related to metal roof and wall systems:
  - Flexural Members Having One Flange Through-Fastened to Deck or Sheathing. In these provisions, the applicable panel depth has been reduced from 1-1/4 in. (32 mm) to 1-1/8 in. (29 mm). Also, purlin systems with adjacent span lengths varying more than 20 percent are permitted to use the reduction factor, R, for the simply supported condition.
  - Flexural Members Having One Flange Fastened to a Standing Seam Roof System.
  - Compression Members Having One Flange Through-Fastened to Deck or Sheathing.
  - Strength [Resistance] of Standing Seam Roof Panel Systems.  
 In the 2007 *Specification*, a reduction factor, 0.67, is permitted to be applied to nominal wind loads for certain standing seam roof systems in Zone 2 (edge zone) or Zone 3 (corner zone) as defined in ASCE/SEI 7-05 (2005). The adoption of the reduction factor is based on research conducted by Surry et. al. (2007), which correlated the static upload capacity and the behavior of wind on a standing seam roof system.

This wind load reduction is only applicable in the United States and Mexico.

- Compression of Z-Section Members Having One Flange Fastened to a Standing Seam Roof. This new design provision is to determine the strength of strut purlins that are connected to a standing seam roof system. The provision is only applicable in the United States and Mexico.
- Anchorage of Bracing for Purlin Roof Systems Under Gravity Load with Top Flange Connected to Metal Sheathing.  
This design provision has been revised based on new research by Seek and Murray (2006, and 2007) and Sears and Murray (2007). The new provision provides better estimates for required anchorage forces and specifies the stiffness requirements for anchorage systems. A design guide, sponsored by AISI and MBMA, will be available in 2009 to assist engineers in applying this provision.
- Alternate Lateral and Stability Bracing for Purlin Roof Systems.  
As an alternate method for anchorage of purlin roof systems, torsional bracing is permitted, which prevents twist about the longitudinal axis of a member, in combination with lateral restraints that resist lateral displacement of the top flange at the frame line.

Another addition related to stability of structural assemblies is the design provision for determining the required brace strength and stiffness. The required brace strength to restrain lateral translation at a brace point for an individual compression member is given in Section D3.3 as:

$$P_{br,1} = 0.01P_n \quad (Eq. 1)$$

The required brace stiffness to restrain lateral translation at a brace point for an individual compression member is calculated from:

$$\beta_{br,1} = \frac{2[4 - (2/n)]P_n}{L_b} \quad (Eq. 2)$$

where

- $P_n$  = Axial compression strength of the member to be braced
- $P_{br,1}$  = Required nominal brace strength for a single compression member
- $P_n$  = Nominal axial compression strength of a single compression member
- $\beta_{br,1}$  = Required brace stiffness for a single compression member
- $n$  = Number of equally spaced intermediate brace locations
- $L_b$  = Distance between braces on one compression member

The above requirements for brace strength and stiffness for a single compression member were developed from a study by Green et al (2004) and are similar to the provisions for compression member nodal bracing in the AISC *Specification for Structural Steel Buildings* with the exception that in the stiffness requirement, AISC assumes  $n$  equals infinity, thus, the required brace stiffness is  $8P_n/L_b$ . For the calculation of brace strength and stiffness, the nominal axial strength of the member,  $P_n$ , is used rather than the required strength because the equations for member strength assume the brace enables the development of the full member strength.

## 5. Connections

As a new addition, a provision for determining the shear strength of sheet-to-sheet arc spot weld connections has been adopted from the Steel Deck Design Manual (SDI, 1987), which stipulates that the shear strength for a sheet-to-sheet arc spot weld connection is taken as 75% of the strength of a sheet-to-structural connection.

Since screw connections are frequently subjected to combined shear and pull-over, a new provision for checking the interaction of screw shear and pull-over was adopted. This design provision is based on the initial research at West Virginia (Luttrell, 1999) and further verification by Zwick and LaBoube (2002).

For bolted connections, the equations for determining the bolt tensile stress subjected to combined shear and tension have been consolidated for provisions applicable to the US and Mexico. The following single equation is used to determine the modified tensile strength:

$$\text{For ASD,} \quad F'_{nt} = 1.3F_{nt} - \frac{\Omega F_{nt}}{F_{nv}} f_v \leq F_{nt} \quad (\text{Eq. 3a})$$

$$\text{For LRFD,} \quad F'_{nt} = 1.3F_{nt} - \frac{F_{nt}}{\phi F_{nv}} f_v \leq F_{nt} \quad (\text{Eq. 3b})$$

where

$F'_{nt}$  = Nominal tensile stress modified to include the effects  
of required shear stress

$F_{nt}$  = Nominal tensile stress

$F_{nv}$  = Nominal shear stress

$F_v$  = Required shear stress

$\Omega$  = Safety factor

$\phi$  = Resistance factor

The equations for determining the block shear rupture strength have also been revised based on the work by Kulak and Grondin (2001) and confirmed by LaBoube and Sokol (2002).

## **6. Appendix 1, Design of Cold-Formed Steel Structural Members Using the Direct Strength Method.**

Adopted in the 2004 Supplement (AISI, 2004), the Direct Strength Method (DSM) provides an alternative approach for determining the flexural and compressive strengths and stiffness of cold-formed members. Different from the conventional “Effective Width Approach”, the DSM determines member strengths without discretizing the member cross-section into elements. This ensures that compatibility and equilibrium are maintained between junctions of the elements and the interactions between the elements are taken into consideration. In addition, the DSM provides a rational approach for determining the member strengths of cold-formed members with unconventional cross sections. To assist designers to better understand and fully utilize this method, a Direct Strength Method Design Guide (2006) has been published by AISI. The design guide can be ordered from the AISI online store at [www.steel.org](http://www.steel.org).

## **7. Appendix 2, Second-Order Analysis**

This new Appendix provides an alternative approach for frame analysis that considers both the effect of loads acting on the deflected shape of a member between joints or nodes ( $P-\delta$  effect) and the effect of loads acting on the displaced location of joints or nodes in a structure ( $P-\Delta$  effect). The analysis approach is consistent with the AISC Direct Analysis method (AISC, 2005) with differences as stipulated in the Commentary to Appendix 2.

## **8. Conclusion**

The major technical changes and additions to the *Specification* have been outlined in this paper. The *Commentary on the 2007 North American Specification for the Design of Cold-Formed Steel Structural Members* contains a more detailed discussion of the design provisions. Also, the *Commentary* provides a comprehensive bibliography for the background of the *Specification* provisions. For a more complete compilation of the changes to the 2007 *North American Specification for the Design of Cold-Formed Steel Structural Members* refer to Wei-Wen Yu Center for Cold-Formed Steel Structures' Technical Bulletin Vol. 16, No. 2, Fall 2007 ([www.mst.edu/~ccfss](http://www.mst.edu/~ccfss)).

## References

American Iron and Steel Institute (2001), *North American Specification for the Design of Cold-Formed Steel Structural Members*, Washington, DC, 2001.

American Iron and Steel Institute (2004), *Supplement 2004 to the North American Specification for the Design of Cold-Formed Steel Structural Members, 2001 Edition*, Washington, DC, 2004.

American Iron and Steel Institute (2006), *Direct Strength Method Design Guide*, Washington, DC, 2006

American Institute of Steel Construction (2005), *Specification for Structural Steel Buildings*, Chicago, IL, 2005.

American Iron and Steel Institute (2007a), *North American Specification for the Design of Cold-Formed Steel Structural Members, 2007 Edition*, Washington, DC, 2007.

American Institute of Steel Construction and American Iron and Steel Institute (2007b), *Standard Definition for Use in the Design of Steel Structures*, Washington, DC, 2007.

American Society of Civil Engineers (2005), ASCE/SEI 7-05, *Minimum Design Loads in Buildings and Other Structures*, Reston, VA, 2005.

Bambach, M. R., and K. J. R. Rasmussen (2002a), "Tests on Unstiffened Elements under Combined Bending and Compression," *Research Report R818*, Department of Civil Engineering, University of Sydney, Australia, 2002.

Bambach, M.R. and K.J.R. Rasmussen (2002b), "Elastic and Plastic Effective Width Equations for Unstiffened Elements," *Research Report R819*, Department of Civil Engineering, University of Sydney, Australia, 2002.

Bambach, M.R. and K.J.R. Rasmussen (2002c), "Design Methods for Thin-Walled Sections Containing Unstiffened Elements," *Research Report R820*, Department of Civil Engineering, University of Sydney, Australia, 2002.

Green, P.S., T. Sputo, and V. Urala (2004), "Bracing Strength and stiffness Requirements for Axially Loaded Lipped Cee Studs." *Proceeding of the Seventeenth International Specialty Conference on Cold-Formed Steel*

*Structures*, Missouri University of Science and Technology (formerly, University of Missouri-Rolla), 2004.

Jay A. Larson (2008), "An Update on AISI Standards for Cold-Formed Steel Framing", *Proceedings of the Nineteenth International Specialty Conference on Cold-Formed Steel Structures*, Missouri University of Science and Technology, Rolla, MO, 2008.

Kulak, G.L., and G.Y. Grondin, (2001), "AISC LRFD Rules for Block Shear in Bolted Connections – A Review," *Engineering Journal*, AISC, Fourth Quarter, 2001.

Luttrell, L.D. (1999), "Metal Construction Association Diaphragm Test Program," West Virginia University, WV, 1999.

Seek, M. W. and T. M. Murray (2006). "Component Stiffness Method to Predict Lateral Restraint Forces in End Restrained Single Span Z-Section Supported Roof Systems with One Flange Attached to Sheathing." *Proceedings of the Nineteenth International Specialty Conference on Cold-Formed Steel Structures*. Missouri University of Science and Technology (formerly, University of Missouri-Rolla, Rolla), MO, 2006.

Seek, M.W. and T.M. Murray (2007) "Lateral Brace Forces in Single Span Z-Section Roof Systems with Interior Restraints Using the Component Stiffness Method." *Annual Stability Conference Proceedings*, Structural Stability Research Council, 2007.

Sears, J. M. and T. M. Murray (2007), "Proposed Method for the Prediction of Lateral Restraint Forces in Metal Building Roof Systems," *Annual Stability Conference Proceedings*, Structural Stability Research Council, 2007.

Steel Deck Institute, Inc. (1987), *Steel Deck Institute Diaphragm Design Manual*, Canton, OH, 1987.

Surry, D., R. R. Sinno, B. Nail, T.C.E. Ho, S. Farquhar, and G. A. Kopp (2007), "Structurally-Effective Static Wind Loads for Roof Panels," *Journal of the Structural Engineering*, ASCE, Vol. 133, No. 6, June 2007.

Yiu, F. and T. Pekoz (2001), "Design of Cold-Formed Steel Plain Channels," Cornell University, Ithaca, NY, 2001.

Zwick, K. and R. A. LaBoube (2002), "Self-Drilling Screw Connections Subject to Combined Shear and Tension", Center for Cold-Formed Steel Structures, Missouri University of Science and Technology (formerly, University of Missouri-Rolla), 2002.

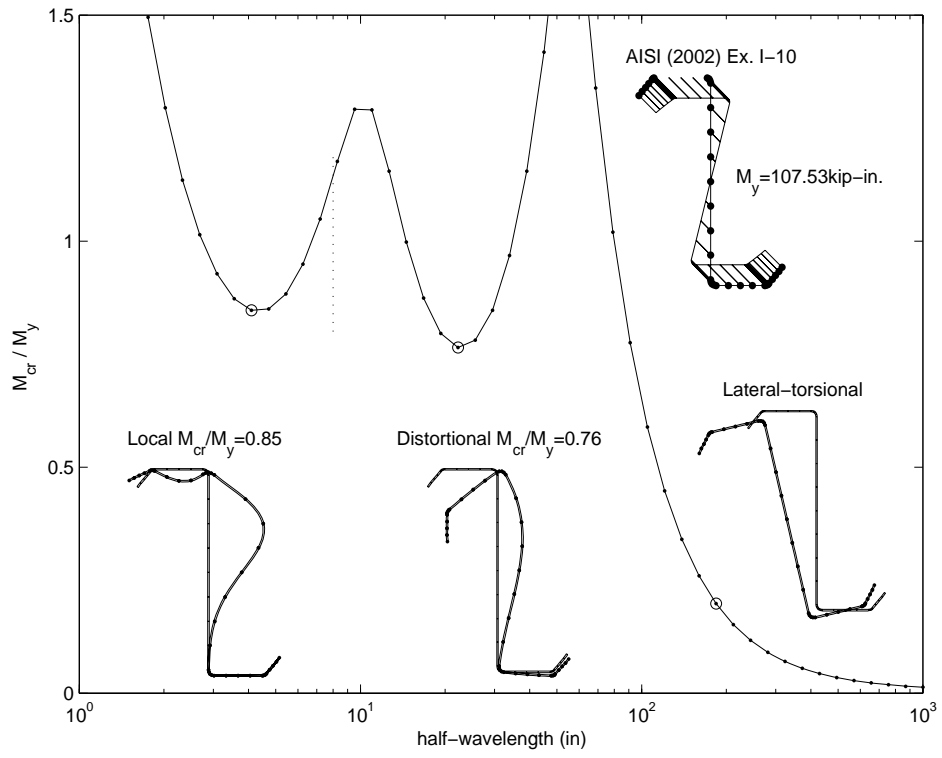


Figure 1 Buckling Modes for a Z-section



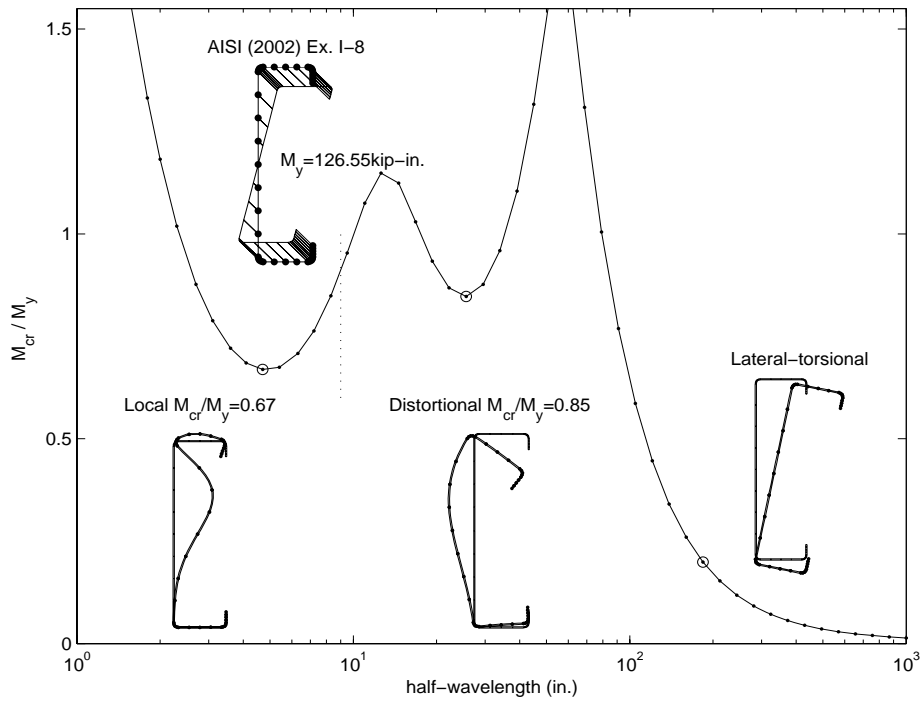


Figure 2 Buckling Modes for a C-section

## **An Update on AISI Standards for Cold-Formed Steel Framing**

Jay W. Larson, P.E., F.ASCE<sup>1</sup>

### **Abstract**

The Committee on Framing Standards of the American Iron and Steel Institute (AISI) continues its mission to eliminate regulatory barriers and increase the reliability and cost competitiveness of cold-formed steel framing through improved design and installation standards. Its suite of eight ANSI-approved, building code adopted standards and its Code of Standard Practice for Cold-Formed Steel Structural Framing build upon AISI S100, the *North American Specification for the Design of Cold-Formed Steel Structural Members*. This paper provides an overview of the significant documents that have been produced by the AISI Committee on Framing Standards and describes the ongoing work of the committee.

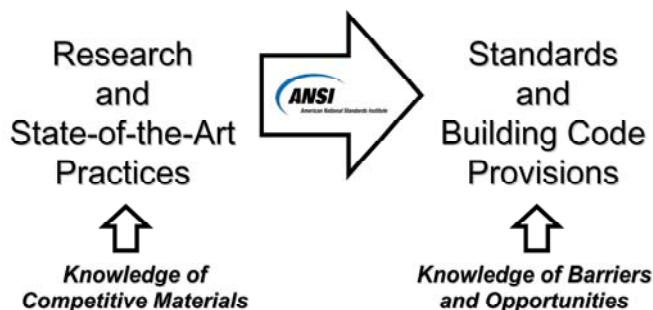
### **Introduction**

AISI has long had a role in standards development. This began with the sponsorship of research at Cornell University under Professor George Winter and the first publication of the AISI *Specification* in 1946. This initial work was started because of difficulties faced in the acceptance and the development of cold-formed steel construction because there were no provisions for it in the U.S. building codes at that time. Since those early beginnings, AISI has engaged a committed group of professionals to expand the body of knowledge and enhance the *Specification* (Yu et al., 1996). The latest edition of the *Specification* is AISI S100, the *North American Specification for the Design of Cold-Formed Steel Structural Members* (AISI, 2007a). This document is adopted in Canada as CSA S136 (CSA, 2007).

---

<sup>1</sup> Managing Director, Construction Technical, AISI.

Standards development is the process of turning research and state-of-the-art practices into standards and building code provisions (Figure 1). The *Specification* and the various design and test standards developed by AISI are different than design guides, technical notes and other non-mandatory publications. Once adopted by building codes, these standards carry the weight of law. Therefore, as a standards developer AISI has an increased obligation and is held to higher scrutiny. Consequently, the standards development activities of AISI are conducted under the auspices of ANSI, the American National Standards Institute.



**Figure 1: AISI Standards Development Process**

AISI's standards development activities operate under strict operating procedures. These procedures earned AISI the approval of ANSI as a recognized consensus standards-writing organization. Specific requirements provide for balance between producer, user and general interest categories, voting, including the resolution of negatives, public review, interpretations, and appeals.

AISI serves as Secretariat to two committees (Figure 2). The Committee on Specifications (COS), which has responsibility for the *Specification*, as well as its test procedures, design manual and design guides, and the Committee on Framing Standards (COFS), which was formed in 1997 to take on the responsibility for the new standards needed for the light framing industry. This was done due to the "increased interest in cold-formed steel for residential and light commercial framing" and the sense that "there were a number of design issues that were not adequately addressed for this emerging market. (Bielat and Larson, 2002).



**Figure 2: AISI Consensus Committees**

The COFS established as its mission: “To eliminate regulatory barriers and increase the reliability and cost competitiveness of cold-formed steel framing in residential and light commercial building construction through improved design and installation standards.” The committee also established as its primary objective: “To develop and maintain consensus standards for cold-formed steel framing, manufactured from carbon or low alloy flat rolled steel, that describe reliable and economical design and installation practices for compliance with building code requirements.” A plan was developed to supplement the *Specification* with a series of design and installation standards, which would be used for engineered or prescriptive design.

By 2001, the COFS had completed four standards for cold-formed steel framing on *General Provisions*, *Truss Design*, *Header Design*, and a *Prescriptive Method for One and Two Family Dwellings*. In 2003, a commentary on the *Prescriptive Method*, including design examples, was completed. By the end of 2004 these initial ANSI-accredited documents were updated and new standards on *Wall Stud Design* and *Lateral Design* had been introduced. AISI was well on its way towards “effectively leveraging its experience and expertise in standards development to support the growing needs of the cold-formed steel framing industry” (Larson, 2004). The COFS continued to improve the existing standards and initiated new projects to develop an industry *Code of Standard Practice* and a *Product Data* standard (Larson 2006).

### AISI Framing Standards

In early 2007, AISI gained ANSI approval of a new *North American Standard for Cold-Formed Steel Framing – Product Data*, and updated North American editions of its standards on *General Provisions*, *Header Design* and *Truss Design*. These documents completed AISI editorial and administrative review, and were published in mid-2007 by the Steel Framing Alliance (SFA) as American National Standards. A most noteworthy change is that these were North American standards, intended for adoption and use in Canada and Mexico, as well as the United States. Also, a new numeric designation system was introduced to better reference the documents in codes and specifications. Later in 2007, AISI gained ANSI approval of a new *North American Standard for Cold-Formed Steel Framing – Floor and Roof System Design*, updated North American editions of its standards on *Lateral Design* and *Wall Stud Design*, and an updated edition of its *Prescriptive Method*. Likewise, these documents completed AISI editorial and administrative review, and were published in early 2008 by SFA, completing the suite of 2007 edition ANSI-approved documents (Figure 3).

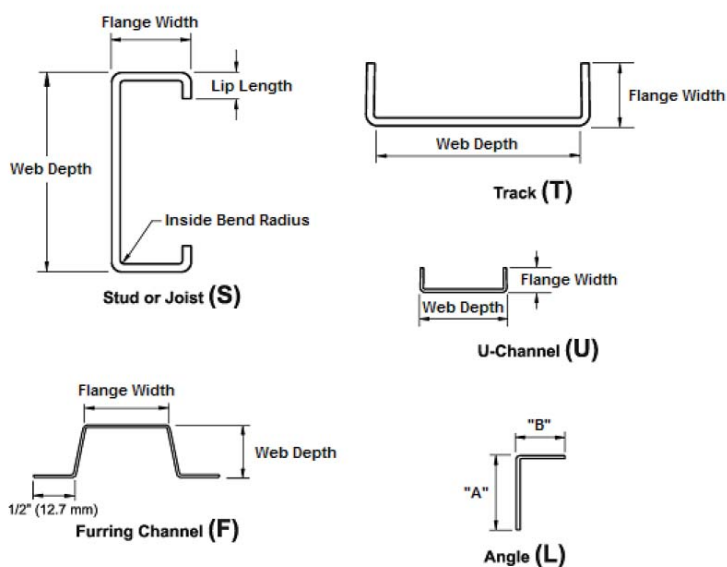


**Figure 3: 2007 Edition AISI Framing Standards**

**AISI S200-07** is the new designation for the revised *General Provisions* standard (AISI, 2007b). This standard addresses those things that are common to prescriptive and engineered design, and applies to the design, construction and installation of structural and non-structural cold-formed steel framing members where the specified minimum base metal thickness is between 18 mils (0.0179 inches) (0.457mm) and 118 mils (0.1180 inches) (3.00mm). It provides general requirements that are not addressed in the *Specification* for material, corrosion protection, products, member design, member condition, installation, and connections.

In this new North American edition, definitions for terms in all the various AISI standards for cold-formed steel framing have been centralized to assure consistency and better facilitate maintenance of the standards. Language was added to clarify that a dissimilar metal may be used in direct contact with steel framing members if approved for that application, and commentary language was added to provide guidance on when such applications might not be a problem. The minimum base metal thickness table was removed, and the thickness requirements now defer to an approved design or recognized product standard, such as the new *Product Data* standard, AISI S201 (below). A requirement was added that when specifying material for use in structural applications, the material used in design is identified on the contract documents and when ordering the material. Referenced document and product identification requirements were updated. Based on recent research, commentary language was also added to provide guidance on both the use of load bearing top track assemblies and the wall stud gap tolerance.

**AISI S201-07** is the designation for the new North American standard on *Product Data* (AISI, 2007c). This standard is intended to establish and encourage the production and use of standardized products in the United States, Canada and Mexico. It provides criteria, including material and product requirements for cold-formed steel C-shape studs, joists, track, U-channels, furring channels and angles intended to be utilized in structural and non-structural framing applications (Figure 4).



**Figure 4: Cold Formed Steel Framing Member Types**

This standard defines standard material grades and specifications, minimum base steel and design thickness, and coatings for corrosion protection. It also defines standard product designator, shapes, inside bend radius, lip length, punchouts, marking and manufacturing tolerances. This standard requires a properly documented quality control program and the proper application of quality assurance procedures.

**AISI S210-07** is the designation for the new North American standard on *Floor and Roof System Design* (AISI, 2007d). This standard is intended for the design and installation of cold-formed steel framing for floor and roof systems in buildings. The standard provides a methodology for continuously braced design; i.e., considering the structural bracing and/or composite-action contribution of attached sheathing or deck. The standard also includes provisions for clip angle bearing stiffeners, based on a recent testing program at the University of Waterloo.

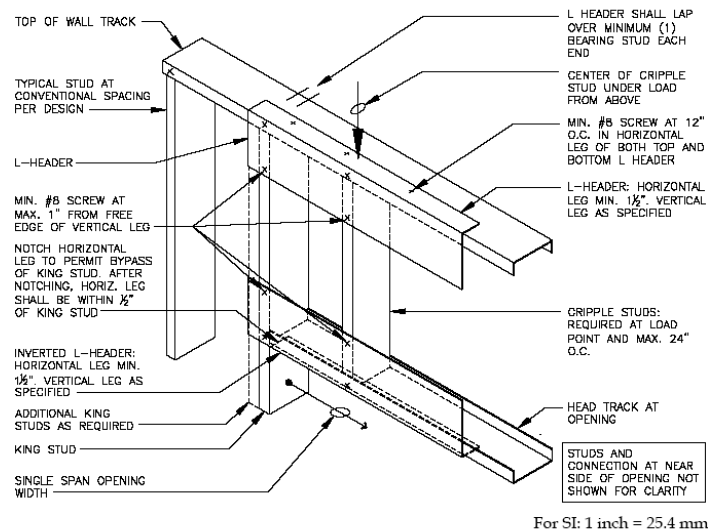
**AISI S211-07** is the new designation for the revised *Wall Stud Design* standard (AISI, 2007e). This standard provides technical information and specifications for designing wall studs made from cold-formed steel. It addresses certain items not presently covered by the *Specification*, including load combinations specific

to wall studs, a rational approach for sheathing braced design, and methodologies to evaluate stud-to-track connections and deflection track connections.

In this new North American edition, the referenced document listing was updated, and the standard and commentary were revised for consistency with other standards and research findings, as well as clarity for the users of the document. There were no substantive changes to U.S. provisions.

**AISI S212-07** is the new designation for the revised *Header Design* standard (AISI, 2007f). This standard provides design and installation requirements for headers made from cold-formed steel for use over door and window openings. The standard covers box and back-to-back headers, as well as double and single L-headers used in single-span conditions for load carrying purposes in buildings. The design methodologies are based on testing at the NAHB Research Center, the University of Missouri-Rolla and industry.

In this new North American edition, the referenced document listing was updated, requirements for evaluating shear were added for back-to-back and box headers, and provisions were included for designing inverted L-header assemblies, based on rational engineering judgment, as a means to provide improved capacity for double and single L-headers (Figure 5).



**Figure 5: Inverted L-Header Assembly**



**AISI S213-07** is the new designation for the revised *Lateral Design* standard (AISI, 2007g). This standard addresses the design of lateral force resisting systems to resist wind and seismic forces in a wide range of buildings constructed with cold-formed steel framing. It contains design requirements for shear walls, diagonal strap bracing (that is part of a structural wall) and diaphragms that provide lateral support to a building structure.

In this new North American edition, referenced documents were updated and editorial clarifications were made. Substantive changes were made to the standard and commentary, including provisions for other in-plane lateral loads, shear walls with fiberboard sheathing, and special seismic provisions for diagonal strap bracing, forces contributed by masonry and concrete walls and forces contributed by other concrete or masonry construction.

**AISI S214-07** is the new designation for the revised *Truss Design* standard (AISI, 2007h). This standard provides technical information and specifications on cold-formed steel truss construction, and applies to cold-formed steel trusses used for load carrying purposes in buildings. The standard is not just for design. It also applies to manufacture, quality criteria, installation and testing as they relate to the design of cold formed steel trusses. The requirements of the truss standard apply to both generic C-section trusses, as well as the various proprietary truss systems and were developed, in part, based on extensive research at the University of Missouri-Rolla.

In this new North American edition, the referenced document listing was updated, and the standard and commentary were revised to clarify when members are to be evaluated for axial load alone, bending alone, and combined axial load and bending, and clarify the requirements for trusses with C-shaped chord and web members. Provisions for designing gusset plates were added, based on based on a recent testing program. The required minimum number of test specimens for the full-scale structural performance load test was changed from two to three, and the special beta-factors for trusses were deleted and the user is deferred instead to AISI S100.

**AISI S230-07** is the new designation for the revised *Prescriptive Method* standard (AISI, 2007i). This standard provides prescriptive requirements for cold-formed steel-framed detached one- and two-family dwellings, townhouses, attached multi-family dwellings, and other attached single-family dwellings. It includes numerous tables and details to allow buildings complying with the limitations therein to be constructed. Alternatively such dwellings may be designed by a design professional.

In this new edition, the standard was updated to latest codes and standards, and enhanced in many ways. The allowable number of stories was increased from two to three, and provisions were added for clip angle bearing stiffeners, anchor bolt washers in high wind/seismic areas, gable endwall framing, hip roof framing, single L-headers, inverted L-header assemblies, and grade 50 headers and roof rafters

### **Other Resources**

As mentioned earlier, building code-adopted ANSI-approved standards are not the only documents needed to sustain the increased use of cold-formed steel framing. Practice guides, design guides and technical notes provide invaluable information to designers and building officials. AISI has a significant role in the development of these documents, as well.

#### Code of Standard Practice

Work towards an industry *Code of Standard Practice for the Cold-Formed Steel Structural Framing Industry* began in 2002. The latest edition (AISI, 2006), which includes Commentary, was developed by the COFS, reviewed by several peer committees within the industry, and endorsed by the Association of the Walls and Ceilings industry (AWCI), Steel Framing Alliance (SFA) and Steel Stud Manufacturers Association (SSMA). This document helps define the lines of responsibility in cold-formed steel framing design and construction, which have previously been vague and unclear. Among the many topics covered are general requirements, classification of materials, plans and specifications, installation drawings, materials, manufacture and delivery, installation requirements, quality control, and contractual relations. The document is loosely based on similar documents by the American Institute of Steel Construction (AISC) and Steel Joist Institute (SJI), and was guided by documents by the Steel truss and Component Association (STCA) and the Council of American Structural Engineers (CASE).

#### Cold-Formed Steel Framing Design Guide

In 2007, under the auspices of the COS, the *Cold-Formed Steel Framing Design Guide*, authored by Tom Trestain, was updated (AISI, 2007j). This document provides a basic introduction to design methods, loads and load combinations, design strength determination, member design as a function of bracing and design strength of connections. But the bulk of this document is devoted to the solution of four detailed design examples. Each example starts with the applied loads and illustrates how to analyze load paths, determine member and

connection forces, select members, establish proper bracing conditions, design bracing, and design connections. The detailed design examples cover wind bearing and axial load bearing stud walls and joists, and are based on the *Specification*. A number of methodologies are proposed to handle design problems not covered in the *Specification*, including a rational method to check the warping torsional stresses in channel members, an approximate method to check the bearing stresses under the bottom track of axial load bearing stud wall assemblies and a method to check the strength and stiffness of inner and outer top track assemblies for wind bearing applications. Changes from the previous edition of the design guide are numerous, including use of provisions from the updated *Specification* and COFS framing standards.

#### Steel Stud Brick Veneer Design Guide

In 2003, also under the auspices of the COS, AISI released the *Steel Stud Brick Veneer Design Guide* (AISI, 2003). This document, also authored by Tom Trestain, provides background on the key issues and industry references, provides definitions and explanations of terms, describes the function and behavior of the various components, and provides an understanding of overall system behavior and design considerations. Several design approaches are described and a clear set of recommendations is provided for the designer and installer. The recommendations in the guide are based on significant industry references, which are cited, with particular emphasis on a comprehensive long-term investigation funded by the Canada Mortgage and Housing Corporation. The recommendations include suggestions about the bracing of the stud system, the type of brick ties and what design load must be used for them, the amount of movement that is safely permitted for crack control, and insulating techniques in different climates to help prevent condensation within the wall and encourage drying of wall cavities that may experience some moisture. The document includes a very extensive bibliography. For the designer or builder preparing to install a brick veneer system over steel studs, this resource provides excellent insight into how the system should be designed, detailed and installed. Proper anticipation, mitigation and management of heat, air and moisture within the wall system can go a long way to preserving the integrity of the overall building.

#### CFSEI Technical Notes

The Cold-Formed Steel Engineers Institute (CFSEI) has as its mission; “*To enable and aid engineers in the efficient structural design of safe and cost effective cold-formed steel (CFS) framed structures.*” Of its eight key strategies, first and foremost is the production of technical documents that enable and aid engineers. The CFSEI Technical Note series is the focal point of this strategy.

These concise documents cover design, specification, installation and inspection on a broad range of design issues, including seismic, wind, fire, acoustic, bracing, fastening, deflection and durability. AISI works closely with CFSEI, through the COFS, to support and encourage the development of these Technical Notes and other design resources for the industry. Membership by design professionals in CFSEI is encouraged, as this organization offers local chapter activities, provides timely and competent response to technical inquiries, provides forums for the exchange of information and ideas, partners with aligned organizations, helps focus research spending on the needs of engineers and works to develop awareness of cold-formed steel framing through the formal education system.

### **Conclusions**

The AISI Committee on Framing Standards (COFS) has continued with earnest its mission to eliminate regulatory barriers and increase the reliability and cost competitiveness of cold-formed steel framing through improved design and installation standards.

The COFS has built on the internationally recognized AISI *Specification* and has developed and published eight ANSI-accredited consensus standards, including:

- AISI S200: General Provisions
- AISI S201: Product Data
- AISI S210: Floor and Roof System Design
- AISI S211: Wall Stud Design
- AISI S212: Header Design
- AISI S213: Lateral Design
- AISI S214: Truss Design
- AISI S230: Prescriptive Method

AISI has also facilitated the development of a much-appreciated industry code of standard practice and useful design guides for cold-formed steel framing and steel stud brick veneer construction. In addition, AISI supports and encourages the Cold Formed Steel Engineers Institute (CFSEI) in the development of technical notes on a broad range of design issues.

These documents are readily available from the Steel Framing Alliance ([www.steel framing alliance.com](http://www.steel framing alliance.com)).

### **Acknowledgements**

The members of the AISI committees, subcommittees and task groups responsible for bringing these documents to fruition are to be commended for their time and effort. It is through the participation of representatives from steel producers, fabricators, users, educators, researchers, and building code officials in this consensus process that such progress is made. The partner organizations; i.e., Steel Framing Alliance, Cold-Formed Steel Engineers Institute, Steel Stud Manufacturers Association, Canadian Sheet Steel Building Institute and Center for Cold Formed Steel Structures are to be thanked for their active participation. Particular gratitude is owed to the member companies of the American Iron and Steel Institute for their long-term vision for this market and financial support of this technical effort.

AISI's Construction Market Companies include AK Steel Corporation, ArcelorMittal Dofasco Inc., IPSCO Inc., ArcelorMittal, Nucor Corporation, Severstal North America Inc., Steelscape, Inc., Stelco Inc., United States Steel Corporation and USS-POSCO Industries.

## References

- (AISI, 2003), *Steel Stud Brick Veneer Design Guide*, CF03-1, American Iron and Steel Institute, Washington, D.C., 2003.
- (AISI, 2006), *Code of Standard Practice for Cold-Formed Steel Structural Framing*, CF-06-1, American Iron and Steel Institute, Washington, D.C., 2006.
- (AISI, 2007a), *North American Specification for the Design of Cold-Formed Steel Structural Members*, AISI S100-07, American Iron and Steel Institute, Washington, D.C., 2007.
- (AISI, 2007b), *North American Standard for Cold-Formed Steel Framing – General Provisions*, AISI S200-07, American Iron and Steel Institute Washington, D.C., 2007.
- (AISI, 2007c), *North American Standard for Cold-Formed Steel Framing – Product Data*, AISI S201-07, American Iron and Steel Institute, Washington, D.C., 2007.
- (AISI, 2007d), *North American Standard for Cold-Formed Steel Framing – Floor and Roof System Design*, AISI S210-07, American Iron and Steel Institute, Washington, D.C., 2007.
- (AISI, 2007e), *North American Standard for Cold-Formed Steel Framing – Wall Stud Design*, AISI S211-07, American Iron and Steel Institute, Washington, D.C., 2007.
- (AISI, 2007f), *North American Standard for Cold-Formed Steel Framing – Header Design*, AISI S212-07, American Iron and Steel Institute, Washington, D.C., 2007.
- (AISI, 2007g), *North American Standard for Cold-Formed Steel Framing – Lateral Design*, AISI S213-07, American Iron and Steel Institute Washington, D.C., 2007.
- (AISI, 2007h), *North American Standard for Cold-Formed Steel Framing – Truss Design*, AISI S214-07, American Iron and Steel Institute, Washington, D.C., 2007.
- (AISI, 2007i), *Standard for Cold-Formed Steel Framing – Prescriptive Method for One and Two Family Dwellings*, AISI S230-07, American Iron and Steel Institute Washington, D.C., 2007.
- (AISI, 2007j), *Cold-Formed Steel Framing Design Guide*, D110-07, American Iron and Steel Institute, Washington, D.C., 2007.

Bielat, K.R., Larson, J.W. (2002), "AISI Committee on Framing Standards – Enabling the Widespread and Economic Use of Steel Framing", *Proceedings of the 16<sup>th</sup> International Specialty Conference on Cold-Formed Steel Structures*, St. Louis, MO, 2002.

(CSA, 2007), *North American Specification for the Design of Cold-Formed Steel Structural Members*, CAN/CSA S136-07, Canadian Standards Association, Mississauga, Ontario, Canada, 2007.

Larson, J.W. (2004), "An Update on Cold-Formed Steel Framing Standards Development in the United States", *Proceedings of the 17<sup>th</sup> International Specialty Conference on Cold-Formed Steel Structures*, Orlando, FL, 2004.

Larson, J.W. (2006), "AISI Standards for Cold-Formed Steel Framing", *Proceedings of the 18<sup>th</sup> International Specialty Conference on Cold-Formed Steel Structures*, Orlando, FL, 2006.

Yu, W.W., Wolford, D.S., Johnson, A.L. (1996), "Golden Anniversary of the AISI Specification", *Proceedings of the 13<sup>th</sup> International Specialty Conference on Cold-Formed Steel Structures*, St. Louis, MO, 1996.





## **Overview of the Standard for Seismic Design of Cold-Formed Steel Structural Systems – Special Bolted Moment Frames**

by

Helen Chen<sup>1</sup>, Chia-Ming Uang<sup>2</sup>, Reidar Bjorhovde<sup>3</sup> and Bonnie Manley<sup>4</sup>

### **ABSTRACT**

Cold-formed steel has been widely used for components and main force resisting systems in commercial, industrial, and residential buildings. Cold-formed steel structural members are designed using AISI S100, *North American Specification for the Design of Cold-Formed structures Members* [AISI, 2007]. For applications in high seismic regions, additional requirements may be needed. In fact, cold-formed steel design standards have been developed for applications in high seismic regions for both rack structures [RMI, 2004] and cold-formed steel light frame construction [AISI, 2007a]. In 2003, the American Iron and Steel Institute (AISI) established a seismic design committee. Composed of suppliers, manufacturers, engineers, researchers and professors, the committee is responsible for developing design standards applicable to cold-formed steel structural systems located in seismic regions. The first edition of the *Standard for Seismic Design of Cold-Formed Steel Structural Systems – Special Bolted Moment Frames* (hereinafter referred as the *Standard*) was finished in 2007. The *Standard* has also been approved by ANSI and an American National Standard. As the title indicates, this edition of the *Standard* focuses on the design of the seismic force resisting system for special bolted moment frames, which consist of tubular columns, cold-formed channel beams and bolted moment connections. A typical connection of a cold-formed steel special bolted moment frame (CFS-SBMF) is illustrated in Figure 1. This

---

<sup>1</sup> Senior Engineer at the American Iron and Steel Institute, Washington, DC, [hchen@steel.org](mailto:hchen@steel.org)

<sup>2</sup> Professor of Civil Engineering at University of California – San Diego, La Jolla, CA, [cuang@ucsd.edu](mailto:cuang@ucsd.edu)

<sup>3</sup> President of The Bjorhovde Group, Tucson, AZ, [rbj@bjorhovde.com](mailto:rbj@bjorhovde.com)

<sup>4</sup> Regional Director at the American Iron and Steel Institute, Construction Codes and Standards, Washington, DC, [bmanley@steel.org](mailto:bmanley@steel.org)

type of special bolted moment frame is widely used in industrial platform mezzanines such as the one shown in Figure 2.

The 2007 edition of the *Standard* is based on the 2005 edition of the ANSI/AISC 341, *Seismic Provisions for Structural Steel Buildings*, [AISC, 2007] and research work [Sato and Uang, 2007] on cold-formed steel special bolted moment frame systems as a seismic force resisting system. This paper will briefly review the design provisions included in the *Standard*.

#### APPLICABILITY

This edition of the *Standard* covers the cold-formed steel special bolted moment frames (CFS-SBMF), and is mandatory in seismic design categories D, E and F. For structures in seismic design categories A, B, and C, the designer may choose one of the following options:

1. To solely use AISI S100 and the response modification coefficient,  $R$ , given in the applicable building code or ASCE/SEI 7 [ASCE, 2005], or
2. To utilize a higher value for  $R$  in a system detailed for seismic resistance and follow the requirements of this *Standard*.

#### MATERIALS

To ensure a higher level of ductility and reserve strength for inelastic seismic response, the applicable steel grades are generally required to have a ratio of  $F_u/F_y \geq 1.15$  and an elongation at fracture of not less than 12 percent in a 2 in. (50 mm) gage length, where  $F_u$  = specified minimum tensile strength and  $F_y$  = specified minimum yield stress.

To determine the expected yield stress, adjustments must be made to  $F_y$  considering not only the inelastic reserve capacity of a compact section,  $R_{re}$ , the increase in yield stress due to cold work of forming,  $R_{cf}$ , and the difference between stress level of the minimum yield stress and the expected yield stress,  $R_y$ . Taking these variables into account, the expected yield stress can be calculated as  $R_{re}R_{cf}R_yF_y$ . The expected tensile strength is calculated simply as  $R_tF_u$ , where  $R_t$  is the ratio of expected tensile strength to the specified minimum tensile strength.

The  $R_y$  and  $R_t$  values for different steels are provided in Table 1 below:

**TABLE 1,  $R_y$  AND  $R_t$  VALUES FOR VARIOUS PRODUCT TYPES**

Steel	$R_y$	$R_t$
Plates and bars: A36/A36M, A283/A283M	1.3	1.2
A242/ A242M, A529/ A529M, A572/ A572M, A588/ A588M	1.1	1.2
Hollow Structural Sections: A500 and A847	1.4	1.3
Sheet and strip (A606, A653/A653M, A792/A792M, A875, A1003/A1003M, A1008/A1008M, A1011/A1011M):		
$F_y < 37$ ksi (255 MPa)	1.5	1.2
$37$ ksi (255MPa) $\leq F_y < 40$ ksi (275 MPa)	1.4	1.1
$40$ ksi (275MPa) $\leq F_y < 50$ ksi (340 MPa)	1.3	1.1
$F_y \geq 50$ ksi (340 MPa)	1.1	1.1

#### **COLD-FORMED STEEL – SPECIAL BOLTED MOMENT FRAMES (CFS-SBMF)**

In order for CFS-SBMF to withstand the anticipated seismic forces, the CFS-SBMF is intended to dissipate seismic input energy through controlled inelastic deformation. Research work at the University of California-San Diego has revealed that the CFS-SBMF can experience substantial inelastic deformation during seismic events. Most of these deformations will take place in the bolted connections due to bolt slippage and bearing deformation as long as the beams and columns have sufficient strength when subjected to the forces resulting from the motion of the design level earthquake. This is accomplished by limiting the beam web flat width-to-thickness to a maximum of  $6.18\sqrt{E/F_y}$  and the tubular column flat width-to-thickness to  $1.58\sqrt{E/F_y}$ , where  $E$  = modulus of elasticity = 29500 ksi (203000 MPa), and  $F_y$  = specified minimum yield stress of the steel.

Based on the unique behavior of the CFS-SBMF [Sato and Uang, 2007], the *Standard* provides methods for determining both the expected moment for beam-column connections and bolt bearing plates, and the appropriate seismic design coefficients.

The expected moments,  $M_e$ , at the beam-column connection of the CFS-SBMF and the bearing plate are determined by the following equation:

$$M_e = h(V_S + R_t V_B) \quad (1)$$

where  $h$  = story height  
 $V_S$  = column shear corresponding to the slip strength of the bolt group  
 $R_t$  = ratio of expected strength to specified minimum tensile strength  
 $V_B$  = column shear corresponding to bearing strength of the bolt group

Equation (1) indicates that the column base shear due to earthquake is transferred to the beam-column connections through friction (slip strength) and bearing resistance. Based on the performance of the CFS-SBMF, the following equations are used to determine both  $V_S$  and  $V_B$ :

$$V_S = C_S k N T / h \quad (2)$$

$$\left( \frac{V_B}{V_{B,\max}} \right)^2 + \left( 1 - \frac{\Delta_B}{\Delta_{B,\max}} \right)^{1.43} = 1 \quad (3)$$

$$V_{B,\max} = C_B N R_0 / h \quad (4)$$

$$\Delta_{B,\max} = C_{B,0} C_{DB} h \quad (5)$$

$$\Delta_B = \Delta - \Delta_S - \frac{n M_e}{h K} \geq 0 \quad (6)$$

$$\Delta_S = C_{DS} h_{os} h \quad (7)$$

where  $k$  = slip coefficient = 0.33  
 $N$  = 1 for connection with a single-channel beam and 2 for connection with double-channel beams  
 $T$  = 10 kips (44.5kN) for 1-in. (25.4 mm) diameter bolts  
 $V_{B,\max}$  = column shear producing the maximum bearing strength of a bolt group

$\Delta$	=	design story drift
$\Delta_B$	=	component of design story drift causing bearing deformation in a bolt group
$\Delta_{B,max}$	=	component of design story drift corresponding to the deformation of the bolt group at maximum bearing strength
$\Delta_S$	=	component of design story drift corresponding to bolt slip deformation
$h_{OS}$	=	hole oversize
$K$	=	structural lateral stiffness
$M_e$	=	expected moment at a bolt group
$n$	=	number of columns in a frame line

Values of other variables  $C_S$ ,  $C_B$ ,  $C_{DS}$ ,  $C_{B,0}$ , and  $C_{DB}$  that are related to the geometry of the bolt configurations are tabulated and provided in the *Standard*.

To increase the bearing strength of the bolted connection, bearing plates can be welded to the beam web. The expected moment for the bearing plate is determined by Equation (8) below:

$$M_{bp} = \frac{M_e}{N} \left( \frac{t_p}{t_w + t_p} \right) \quad (8)$$

where  $t_p$  = bearing plate thickness  
 $t_w$  = beam web thickness.

Based on research [5], the response modification coefficient,  $R$ , for CFS-SBMF is 3.5, the deflection amplification factor,  $C_d$ , is 2.9, and the height limit for the system is 35 ft. The height limit is established based upon practical consideration of the system.

Once the expected moments are determined, the strengths of the members and connections are then designed in accordance with AISI S100, *North American Specification for the Design of Cold-Formed Steel Structural Members* [AISI, 2007]. For a typical CFS-SBMF, the following design procedures are recommended:

Step 1 Perform the preliminary design of the beams, columns, and bolted connections by considering all basic load combinations found in the applicable building code, and using a value of 3.5 for Response Modification Coefficient,  $R$ . In determining the earthquake load, use a rational method to determine the structural period.

- Step 2** Compute both the base shear ( $nV_S$ ) that causes the bolt groups to slip and the slip range ( $\Delta_S$ ) in terms of story drift.
- Step 3** Compute the design story drift,  $\Delta$ . Follow the applicable building code to compute the design story drift, where the Deflection Amplification Factor is taken as 2.9.
- Step 4** Determine the strength of beams and columns using AISI S100.
- Step 5** Check P- $\Delta$  effects.

### EXAMPLE

An example is provided to determine the expected moment through Equations (1) to (7). For a given one-story, two-bay CFS-SBMF, determine the expected moment of the beam-column connection at the center column. The beam and column cross-sections satisfy the flat width-to-thickness requirements for beams and columns, and are selected based on design outlined in Step 1. The beam web thickness = 0.135 in. (3.43 mm), the column wall thickness = 0.25 in. (6.35 mm), and the yield stress and tensile strength for both beam and column are 50 ksi (345 MPa) and 70 ksi (483 MPa), respectively. The bolted connection layout is shown in the elevation of Figure 1, where for bolt spacing,  $a = 3$  in. (76 mm),  $b = 6$  in. (152 mm),  $c = 4.25$  in. (108 mm), and the bolt diameter = 1 in. (25.4 mm).

The frame analysis in Step 1 also provides the stiffness of the frame system as  $K = 6.17$  kips/in. (0.175 kN/mm), and the drift corresponding to the design basis earthquake as  $\Delta_{DBE} = 2.40$  in. (61 mm). From there, the design drift is calculated as follows:

$$\Delta = C_d \Delta_{DBE} = (2.9)(2.40) = 6.96 \text{ in. (177 mm)}$$

Based on the bolt configuration, the following coefficients are obtained from the tables provided in the *Standard*:

$$C_S = 3.34 \text{ ft (1020 mm)}, C_{DS} = 3.61 \text{ ft}^{-1} (0.0118 \text{ mm}^{-1}), C_B = 5.88 \text{ ft (1790 mm)}, C_{B,0} = 0.625 \text{ in./ft. (0.0521 mm/mm)}, \text{ and } C_{DB} = 1.19.$$

The following variables are determined using Equations (2) and (4) through (7):

$$\begin{aligned} V_S &= C_S kNT/h = (3.34)(0.33)(2)(10)/(11.43) = 1.93 \text{ kips (8.59 kN)} \\ V_{B,max} &= C_B N R_0/h = (5.88)(2)(9.45)/(11.43) = 9.72 \text{ kips (43.2 kN)} \\ \Delta_{B,max} &= C_{B,0} C_{DB} h = (0.625)(1.2)(11.43) = 8.50 \text{ in. (200 mm)} \\ \Delta_S &= C_{DS} h_{os} h = (3.61)(0.0625)(11.43) = 2.58 \text{ in (65.5 mm)} \end{aligned}$$

The expected moment,  $M_e$ , and the connection bearing shear force,  $V_B$ , are obtained via iteration of Equations (1) and (3). Some of the iteration results in the vicinity of the convergence are shown in the table below:

**TABLE 2, ITERATION RESULTS**

Given $\Delta_B$ in. (mm)	$V_B$ Per Equation (3) Kips (kN)	$M_e$ Per Equation (1) Kips-ft (kN-m)	New $\Delta_B$ Per Equation (6) In (mm)	Error
1.055 (25.85)	4.043 (17.98)	77.495 (105.1)	1.085 (26.57)	2.8%
1.06 (25.97)	4.052 (18.02)	77.62 (105.2)	1.079 (26.44)	1.8%
<b>1.07</b> <b>(26.22)</b>	<b>4.071</b> <b>(18.11)</b>	<b>77.88</b> <b>(105.6)</b>	<b>1.068</b> <b>(26.18)</b>	<b>0.16%</b>
1.08 (26.46)	4.089 (18.19)	78.13 (105.9)	1.058 (25.91)	2.1%

As shown in Table 2, the converged results are:

The expected moment at the connection,  $M_e = 77.88$  kip-ft (105.6 kN-m);

The expected bearing shear force at the connection,  $V_B = 4.07$  kips (18.11 kN);

The expected bearing deformation at the bolt connection,  $\Delta_B = 1.07$  in. (26.22 mm)

The expected total base shear  $V_{total} = V_S + R_t V_B$

For Step 5, the P- $\Delta$  effect should be checked according to ASCE 7 [ASCE, 2005]. The frame members and connections should then be checked in accordance with AISI S100 to ensure the design strengths of the members and connections are greater than or equal to the expected moments and the shear forces. The design story drift of the frame should also be within the limit,  $0.05h$ , as specified in the *Standard*.



## **FUTURE WORK**

Cold-formed steel possesses higher strength and lower ductility than conventional hot-rolled steel. Since cold-formed steel members are relatively thin, they are susceptible to local, distortional and global buckling. Further research is needed to better understand the behavior of cold-formed steel members in seismic force resisting systems and to develop a more comprehensive seismic design standard for cold-formed steel. AISI will continue supporting research and partnering with interested organizations to expand the market for cold-formed steel.

## **REFERENCES**

- [1] American Iron and Steel Institute (AISI), S100-07, *North American Specification for the Design of Cold-Formed Steel Structural Members*, 2007.
- [2] Rack Manufacturers Institute (RMI), *Specification for Design, Testing, and Utilization of Industrial Steel Storage Racks*, 2004.
- [3] American Iron and Steel Institute (AISI), S213-07, *Standard for Cold-Formed Steel Framing-Lateral Design*, 2007a.
- [4] American Institute of Steel Construction (AISC), ANSI/AISC 341s1-05, *Seismic Provisions for Structural Steel Buildings*, 2005 including Supplement No. 1.
- [5] Sato, A. and Uang, C.M., "Development of a Seismic Design Procedure for Cold-Formed Steel Bolted Frames," Report No. SSRP-07/16, 2007.
- [6] American Society of Civil Engineering (ASCE), ASCE/SEI 7-05, *Minimum Design Loads for Buildings and Other Structures*, 2005 including Supplement 1.

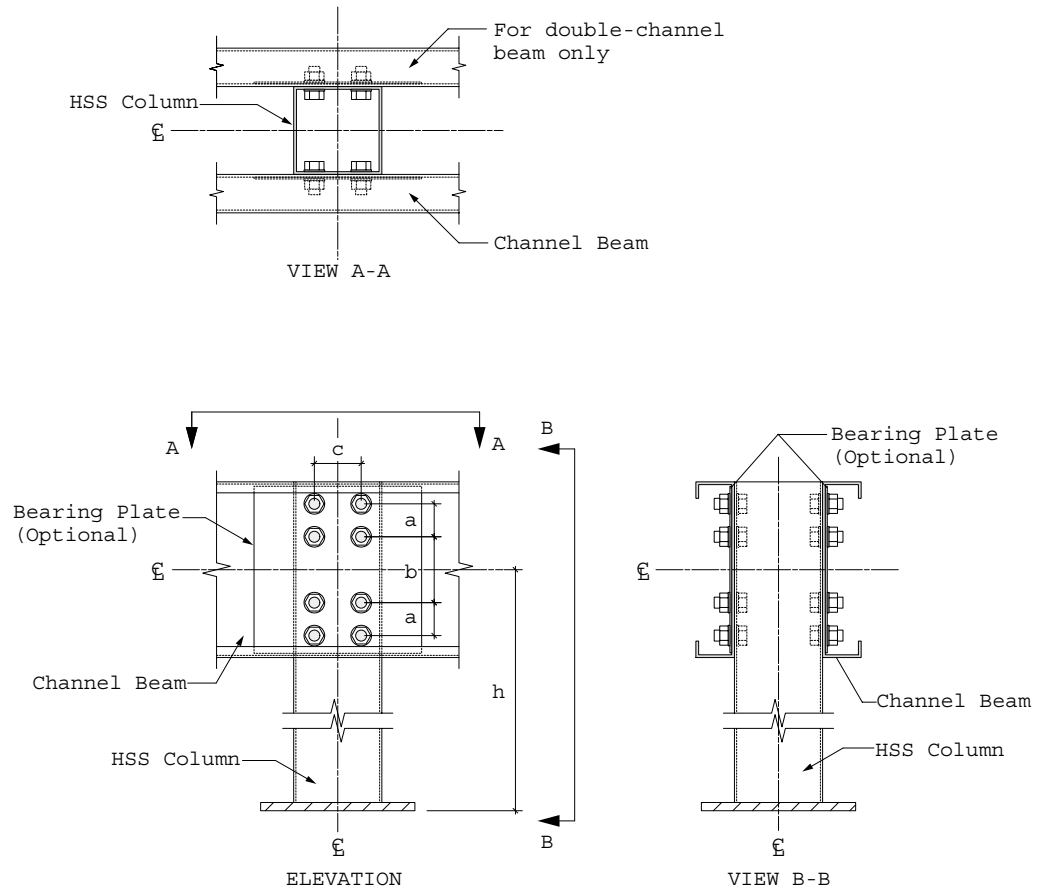


FIGURE 1 – TYPICAL CONNECTION OF CFS-SBMF

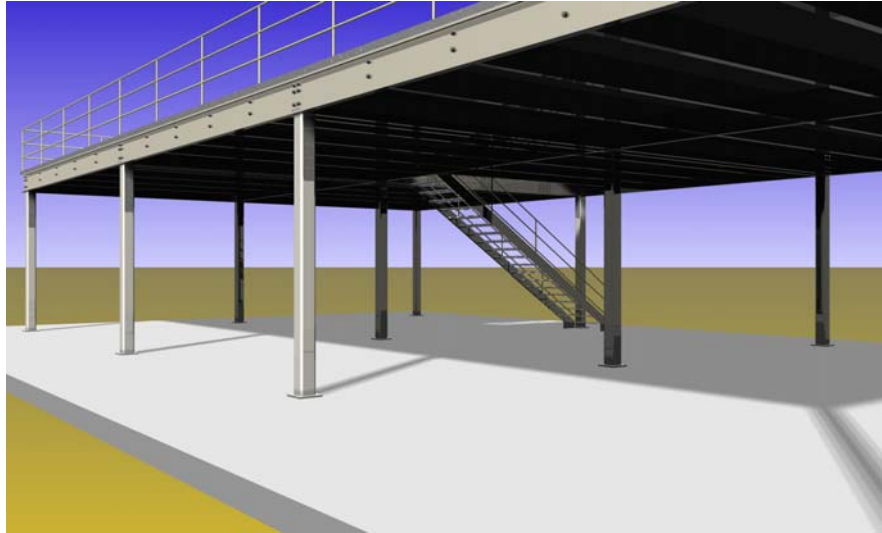


FIGURE 2 – TYPICAL CFS-SBMF USED AS INDUSTRIAL PLATFORM MEZZANINE

## **Buckling Studies of Thin-Walled Channel Sections under Combined Bending and Shear**

Cao Hung Pham<sup>1</sup> and Gregory J. Hancock<sup>2</sup>

### **Abstract**

Thin-walled section members can be subjected to axial force, bending and shear. In the cases of cantilever beams and continuous lapped purlins, where combined bending and shear occur at the purlin section just outside the end of the lap, thin-walled sections may buckle at a lower stress than if only one action was present without the other. The computational modelling of the thin-walled steel sections is implemented by means of a spline finite strip analysis to determine the elastic buckling stresses of channel sections subject to bending and shear alone and interaction relations under combined bending and shear. Both unlippped and lippped channels are studied where the main variables are the flange width, different boundary conditions and shear flow distribution. Comparisons between cases, and with classical solutions are included in this report.

### **1. Introduction**

The elastic critical stress for local buckling of flat rectangular plates has been extensively investigated and summarised by many investigators (Timoshenko and Gere, 1961; Bulson, 1970; Bleich, 1952, Allen and Bulson, 1980). For a thin flat plate simply supported along all four edges, the buckling stress of an elastic rectangular plate for local buckling in compression, bending or shear is given by Timoshenko and Gere (1961) as:

$$f_{ol} = k \frac{\pi^2 E}{12(1-\nu^2)} \left( \frac{t}{b_1} \right)^2 \quad (1)$$

---

<sup>1</sup> Doctoral Candidate, School of Civil Engineering, The University of Sydney, Sydney NSW 2006, Australia.

<sup>2</sup> Bluescope Steel Professor of Steel Structures and Dean of Engineering and Information Technologies, The University of Sydney, Sydney NSW 2006, Australia.

where  $E$  = modulus of elasticity;  $\nu$  = Poisson's ratio;  $b_1$  = width of the plate;  $t$  = thickness of the plate;  $a$  = length of the plate.  $k$  is the plate local buckling coefficient, which depends on the boundary conditions and the aspect ratio of the rectangular plate  $a/b_1$ .

For plates with all edges simply supported subjected to pure bending:  $k = 23.9$

For plates with all edges simply supported subjected to pure shear:

$k = 5.34 + \frac{4}{(a/b_1)^2}$ . As the plate is shortened, the number of local buckles is

reduced and the value of  $k$  for a plate simply supported on all four edges is increased from 5.34 for a very long plate to 9.34 for a square plate.

The traditional approach has been to investigate shear plate buckling in the web alone and to ignore the behaviour of the whole section including the flanges. There does not appear to have been any consistent investigations of the full section buckling of thin-walled sections under shear until recently Pham and Hancock (2007) provided solutions to the shear buckling of complete channel sections loaded in pure shear parallel with the web by using spline finite strip analysis (Lau and Hancock, 1986). The analysis results show that the flanges can have a significant influence on improvement of the shear buckling capacity of thin-walled channel sections. Further, it was also demonstrated that the lack of lateral restraint for sections with narrow flanges can lead to premature buckling of the section in a twisting and lateral buckling mode.

When high bending and high shear act simultaneously, the combination of shear stress and bending stress produces a further reduction in the capacity of the web. The interaction equation is a circular formula as shown in Fig 1. This interaction equation is based upon an approximation to the theoretical interaction of local buckling resulting from shear and bending as derived by Timoshenko and Gere (1961). Fig 1 shows the interaction between  $f_b/f_{cr}$  and  $\tau/\tau_{cr}$  in which  $f_b$  is the actual computed bending stress,  $f_{cr}$  is the theoretical buckling stress in pure bending,  $\tau$  is the actual computed shear stress, and  $\tau_{cr}$  is the theoretical buckling stress in pure shear. The relationship between  $f_b/f_{cr}$  and  $\tau/\tau_{cr}$  can be approximated by the following equation which is a part of the unit circle:

$$\left(\frac{f_b}{f_{cr}}\right)^2 + \left(\frac{\tau}{\tau_{cr}}\right)^2 = 1 \quad (2)$$

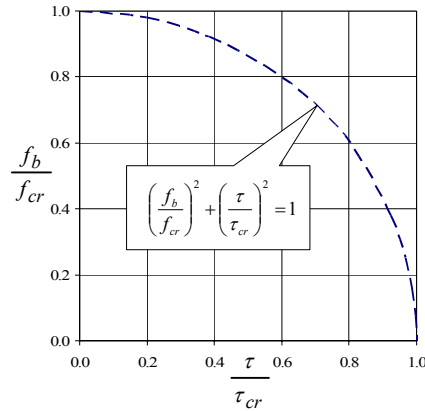


Figure 1. Interaction relation between  $f_b/f_{cr}$  and  $\tau/\tau_{cr}$  in a rectangular plate

To analyse complete channel sections under combined bending and shear, the buckling analysis is based on a spline finite strip analysis (Lau and Hancock, 1986) implemented by Gabriel Eccher in the program ISFSM Isoparametric Spline Finite Strip Method (Eccher, 2007). Both unlipped and lipped channels of varying section geometry are investigated. Three different methods, which represent different ways of incorporating the shear stresses in the thin-walled section, are used in this paper. These include pure shear in the web only, pure shear in the web and the flanges, and a shear distribution similar to that which occurs in practice allowing for section shear flow. Each method of the shear stress distributed is combined with pure bending to produce the interaction relation. A significant outcome of the study is lateral buckling under shear of sections with narrow flanges.

## 2. Modelling Sections under Combined Bending and Shear

### 2.1 Spline Finite Strip Method

The spline finite strip method is a development of the semi-analytical finite strip method originally derived by Cheung (1976). It uses spline functions in the longitudinal direction in place of the single half sine wave over the length of the section, and has been proven to be an efficient tool for analysing structures with constant geometric properties in a particular direction, generally the longitudinal one. The advantage of the spline finite strip analysis is that it allows more complex types of loading and boundary conditions other than simple supports to be easily investigated and buckling in shear is also easily accounted for. Initially, the spline finite strip method was fully developed for the linear elastic structural analysis of folded plate structures by Fan and Chueng (1982). The spline finite strip method was then extended to buckling and nonlinear analyses

of flat plates and folded-plate structures by Hancock *et al.* (1986, 1989 and 1991). The spline finite strip method involves subdividing a thin-walled member into longitudinal strips where each strip is assumed to be free to deform both in its plane (membrane displacements) and out of its plane (flexural displacements). The ends of the section under study are free to deform longitudinally but are prevented from deforming in a cross-sectional plane.

### Unlipped Channel

The geometry of the unlipped channel studied is shown in Fig 2. The channel sections consist of a web of width 200 mm, a flange of width 0.01 mm to 160 mm, both with thickness of 2 mm. The member is subdivided into 36 longitudinal strips which include 16 strips in the web and 10 strips in each flange. The length of the member studied is 1000 mm. The aspect ratio of the web rectangular plate is therefore  $a/b_1 = 5$ .

### Lipped Channel

The geometry of the lipped channel studied is shown in Fig 3. The channel section consists of a web of width 200 mm, a flange of width 0.01 mm to 160 mm, a lip size of 20 mm, all with thickness 2 mm. The member is subdivided into 40 longitudinal strips which include 16 strips in the web, 10 strips in each flange and 2 strips in each lip. The length of the member studied is 1000 mm. The aspect ratio of the web rectangular plate is therefore  $a/b_1 = 5$ .

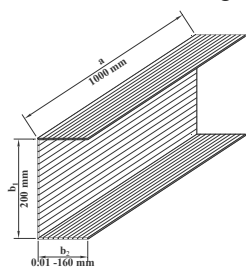


Figure 2. Unlipped Channel Geometry

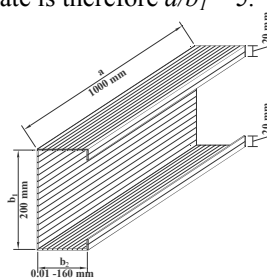


Figure 3. Lipped Channel Geometry

## 2.2 Shear Stress Distribution and Pure Bending

In order to demonstrate the different ways in which a channel member may buckle under shear stress, four cases of shear stress distribution are investigated. In *Cases A* and *B*, uniform pure shear stress is applied throughout the web panel as shown in Fig 4(a), 5(a). The only difference between *Case A* and *B* is that two longitudinal edges of the channel member in *Case A* are restrained laterally

whereas there is no restraint along the two longitudinal edges in *Case B*. In *Case C*, the pure shear stress is uniform in both the web and the flanges as shown in Fig 4(b), 5(b). Although this case is unrealistic in practice, it investigates the effect of the flanges on the buckling of the member under pure shear stress. *Case D* models the case which occurs in practice namely, a shear flow distribution as shown in Fig 4(c), 5(c) resulting from a shear force parallel with the web. To simulate the variation in shear stress, each strip in the cross-section is assumed to be subjected to a pure shear stress which varies from one strip to the other strip. The more the cross-section is subdivided into strips, the more accurately the shear stress is represented in order to match the practical shear flow distribution. Each above case is also subjected to pure bending which is shown in the following figures:

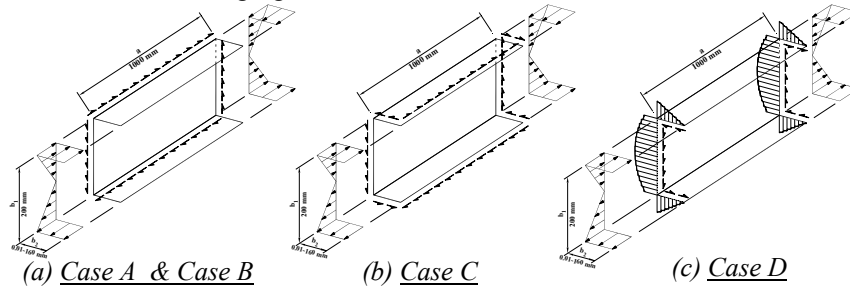


Figure 4. Stress Distribution in Unlipped Channel

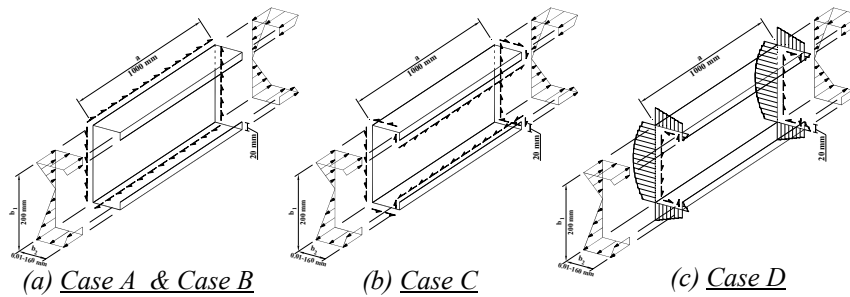


Figure 5. Stress Distribution in Lipped Channel

### 2.3 Lateral Restraints and Boundary Conditions

Two types of boundary conditions are used for the analysis of all cases in this report. A combination of lateral restraints along the two longitudinal edges of web panels and simply supported edges of the end cross-section plane is applied in *Case A*. In the remaining cases (*Cases B, C & D*), there are no lateral restraints along the two longitudinal edges of web panels. All edges of the end cross-



section are simply supported. Fig 6 and Table 1 show the lateral restraints and boundary conditions of the unlippped channel. Fig 7 and Table 2 show those for the lipped channel.

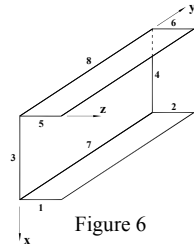


Figure 6

Cases	Edges	<i>u</i>	<i>v</i>	<i>w</i>
A	1 2 5 6	1	0	0
	3 4 7 8	0	0	1
B,C & D	1 2 5 6	1	0	0
	3 4	0	0	1
	7 8	0	0	0

Note: *u*, *v* and *w* are translations in the *x*,*y* and *z* directions respectively. 0 denotes free and 1 denotes restraint DOF

Table 1. Boundary Conditions of Unlippped Channel

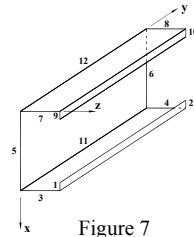


Figure 7

Cases	Edges	<i>u</i>	<i>v</i>	<i>w</i>
A	3 4 7 8	1	0	0
	1 2 5 6 9 10 11 12	0	0	1
B,C & D	3 4 7 8	1	0	0
	1 2 5 6 9 10	0	0	1
	11 12	0	0	0

Note: *u*, *v* and *w* are translations in the *x*,*y* and *z* directions respectively. 0 denotes free and 1 denotes restraint DOF

Table 2. Boundary Conditions of Lippped Channel

### 3. Results of Buckling Analyses

#### 3.1 Unlippped Channel Section – Length = 1000 mm, $a/b_1 = 5.0$ , Case A

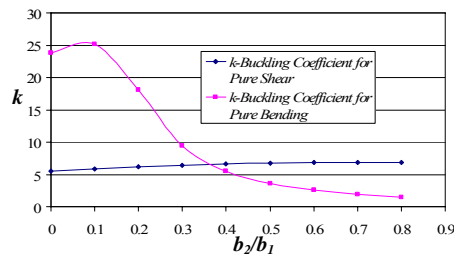


Figure 8. The Ratio of Flange and Web Widths ( $b_2/b_1$ ) and The Buckling Coefficients (*k*) of Unlippped Channel Section for Case A

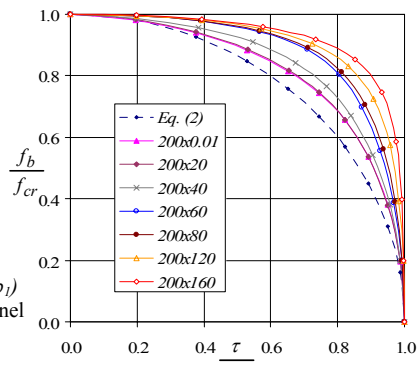


Figure 9. Interaction Relation between  $f_b/f_{cr}$  and  $\tau/\tau_{cr}$  for Case A

The results of the buckling analyses of the unlippped channel section for Case A with a length of 1000 mm and lateral restraints along the two longitudinal edges of web panel are shown in Fig 8 for the ratios of flange to web widths ( $b_2/b_1$ )

from 0.00005 to 0.8. The buckling coefficient curve ( $k$ ) of the unlippped channel section subjected to pure shear is shown as the square line ( $\square$ ), whereas the diamond line ( $\diamond$ ) represents the coefficient curve ( $k$ ) for pure bending. For pure shear, when the flange width is very small (0.01 mm), the value of  $k$  is 5.51 which is very close to the theoretical result (Timoshenko and Gere, 1961; Bulson, 1970; Bleich, 1952; Allen and Bulson, 1980). As the flange width increases to 160 mm, the value of  $k$  increases to 6.905 as a result of the elastic torsional restraint of the flange on the web. For pure bending, the buckling coefficient ( $k$ ) is 23.79 when the ratio of  $b_2/b_1$  is 0.00005. This value of  $k$  is close to the theoretical result of 23.9 (Timoshenko and Gere, 1961; Bulson, 1970; Bleich, 1952; Allen and Bulson, 1980). As the ratio of  $b_2/b_1$  increases to 0.1, the value of  $k$  improves to 25.14. The explanation for this fact is that the presence of small flange contributes to buckling capacity of channel section subjected to pure bending. The buckling mode occurs mainly in the web. However, when the ratio of  $b_2/b_1$  increases from 0.1 to 0.8, the value of  $k$  reduces dramatically due to uniform compression stress in wider flange which causes the buckling mode to occur mainly in the flange.

Fig 9 shows the interaction relation curves between  $f_b/f_{cr}$  and  $\tau/\tau_{cr}$  for *Case A* with lateral restraints along the two longitudinal edges of web panel for different flange widths. The corresponding buckling mode shapes for *Case A* under combined bending and shear are shown in Fig 10.

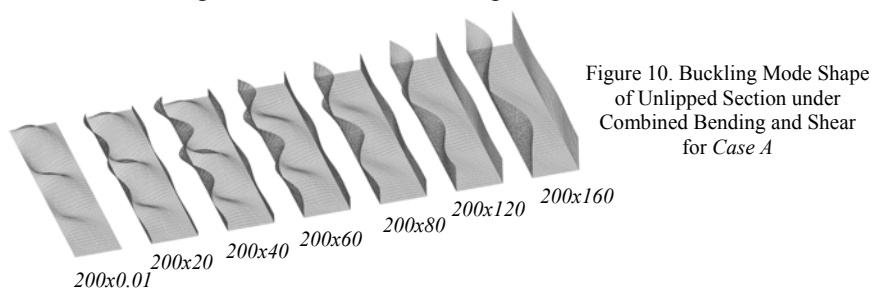


Figure 10. Buckling Mode Shape of Unlippped Section under Combined Bending and Shear for *Case A*

### 3.2 Unlippped Channel Section – Length = 1000 mm, $a/b_1 = 5.0$ , *Case B*

Fig 11 shows the results for the buckling analyses of the unlippped channel section for *Case B* with a length of 1000 mm and the ratios of flange to web width ( $b_2/b_1$ ) from 0.00005 to 0.8. In this case, there are no lateral restraints along the two longitudinal edges of web panel.

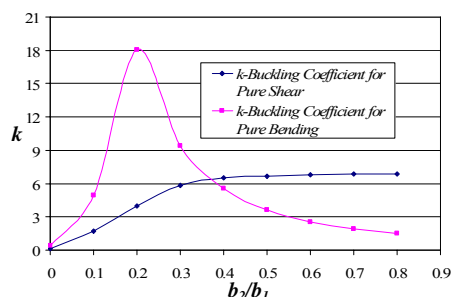


Figure 11. The Ratio of Flange and Web Widths ( $b_2/b_1$ ) And The Buckling Coefficients ( $k$ ) of Unflipped Channel Section for Case B

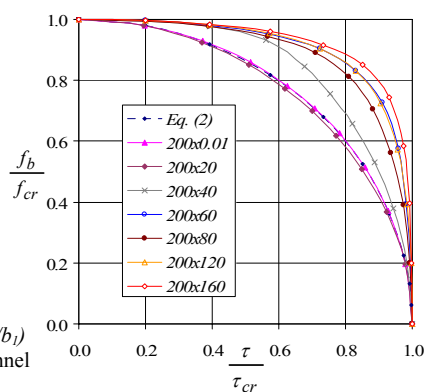


Figure 12. Interaction relation between  $f_b/f_{cr}$  and  $\tau/\tau_{cr}$  for Case B

The buckling coefficient curve ( $k$ ) of the unflipped channel section subjected to pure shear is shown as the square line (—◆—), whereas the diamond line (—■—) represents the buckling coefficient curve ( $k$ ) for pure bending. For pure shear, when the ratio of flange to web width ( $b_2/b_1$ ) is 0.00005, the value of  $k$  is very close to zero (0.109). The channel member buckles sideways as demonstrated previously (Pham and Hancock, 2007). It is interesting to note that when the ratio of  $b_2/b_1$  increases to around 0.3, the value of  $k_v$  increases dramatically to 5.853. The buckling mode shape is shown in the analysis of Pham and Hancock (2007) as a twisting mode. As the ratio of  $b_2/b_1$  keeps increasing to 0.8, the value of  $k_v$  improves to 6.889. The explanation is due to the fact that there is apparently more lateral and torsional restraint being provided by the flanges. For pure bending, the buckling coefficient ( $k$ ) is 0.436, when the ratio of  $b_2/b_1$  is 0.00005. For Case B with no lateral restraint along the two longitudinal edges of web panel, the channel member also buckles sideways. As the ratio of  $b_2/b_1$  increases to 0.2, the value of  $k$  increases dramatically to 18.064. This can be explained by the fact that the flanges minimise sideways buckling of the section although the buckling coefficient does not reach 23.9 as for a laterally restrained section. However, it should be noted that when the ratio of  $b_2/b_1$  increases further from 0.2 to 0.8, the value of  $k$  reduces dramatically from 18.064 to 1.482 due to the uniform compression in wider flange which results in the buckling mode being mainly in the flange.

Fig 12 shows the interaction relation curves for different flange widths between  $f_b/f_{cr}$  and  $\tau/\tau_{cr}$  for Case B with no lateral restraint along the two longitudinal edges of web panel. The corresponding buckling mode shapes for Case B under combined bending and shear are shown in Fig 13.

As can be seen in Fig 12, when the flange width is very small (0.01mm – 20 mm), the interaction relation curves lie slightly below the circular curve. The interaction between bending and shear is therefore significant due to the fact that the small flange width causes twisting buckling mode as shown in Fig 13. As the flange width increases, the interaction relation curves lie further above the circular curve. The interaction relation is therefore less significant. The explanation is quite similar to that of *Case A* described above. As can be seen in Fig 13, the buckling mode occurs mainly in the web due to uniform compression stress and no shear stress distribution in wider flange.

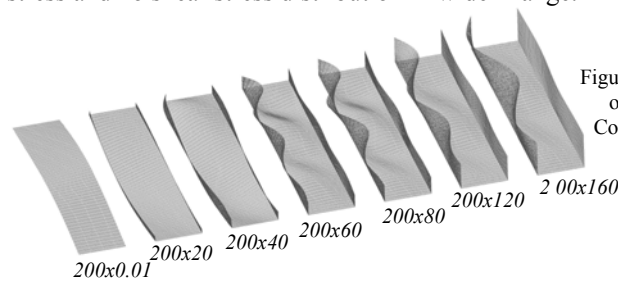


Figure 13. Buckling Mode Shape of Unlipped Section under Combined Bending and Shear for *Case B*

**3.3 Unlipped Channel Section – Length = 1000 mm,  $a/b_1 = 5.0$ , *Case C***

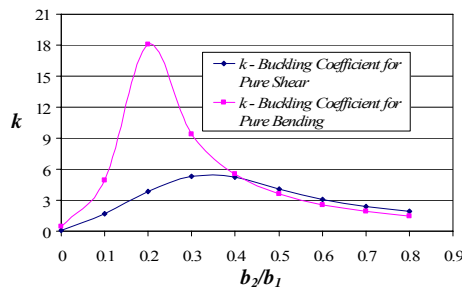


Figure 14. The Ratio of Flange and Web Widths ( $b_2/b_1$ ) and The Buckling Coefficients ( $k$ ) of Unlipped Channel Section for *Case C*

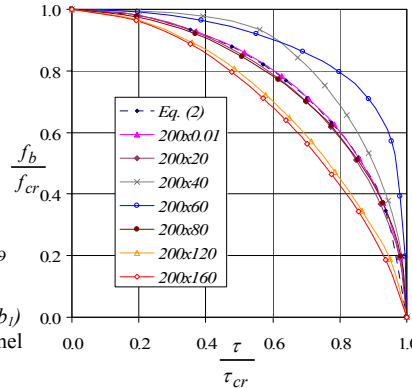


Figure 15. Interaction relation between  $f_b/f_{cr}$  and  $\tau/\tau_{cr}$  for *Case C*

The results of the buckling analyses of the unlipped channel section for *Case C* with a length of 1000 mm and pure shear flow applied in the web and the flanges are shown in Fig 14 for the ratios of flange to web widths ( $b_2/b_1$ ) from 0.00005 to 0.8. The boundary conditions are the same as those of *Case B*. The square line (—◆—) and the diamond line (—■—) represent the coefficient curves ( $k$ ) for pure shear and pure bending respectively. For pure shear, when the ratio of flange to web width ( $b_2/b_1$ ) increases from 0.00005 to 0.3, the value of  $k$  is not

significantly different from that of *Case B*. However, from the ratio of  $b_2/b_1$  of 0.4 the value of  $k$  for *Case C* reduces dramatically. The explanation is mainly a result of the effect of shear stresses in the flanges. For pure bending, the buckling coefficient curve ( $k$ ) is identical to that of *Case B* as the bending stress distribution is the same.

Fig 15 shows the interaction relation curves between  $f_b/f_{cr}$  and  $\tau/\tau_{cr}$  for different flange widths for *Case C* where pure shear flow is applied in both the web and the flanges. The corresponding buckling mode shapes for *Case C* under combined bending and shear are shown in Fig 16.

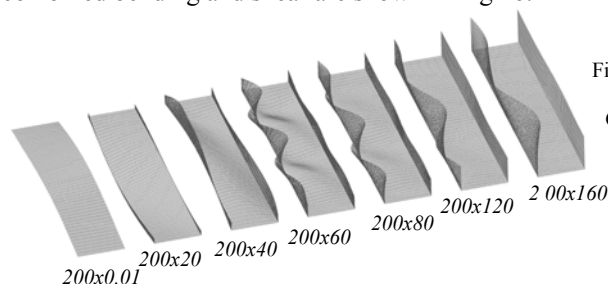


Figure 16. Buckling Mode Shape of Unlipped Section under Combined Bending and Shear for *Case C*

It can be seen in Fig 16 that when the flange width is very small (0.01mm – 20 mm), the interaction relation curves lie slightly below the circular curve as for *Case B*. The interaction is significant as the twisting buckling mode is the main reason for the interaction. As the ratio of  $b_2/b_1$  increases from 0.2 to 0.3, the relation curves make above the circular curve. The interaction relation is then less significant. However, it is interesting to note that the interaction curve is slightly below the circular curve at the ratio of  $b_2/b_1$  of 0.4. As the ratio of  $b_2/b_1$  increases to 0.8, the interaction relation curves lie further below the circular curve so that the interaction between bending and shear is very significant. The explanation for this fact is mainly due to interaction of shear buckling and compression in the flange.

### 3.4 Unlipped Channel Section – Length = 1000 mm, $a/b_1 = 5.0$ , *Case D*

Fig 17 shows the results for the buckling analyses of the unlipped channel section for *Case D* with a length of 1000 mm and the ratios of flange to web width ( $b_2/b_1$ ) from 0.00005 to 0.8. The boundary conditions are the same as those of *Case B*. The square line (—◆—) and the diamond line (—◆—) represent the coefficient curves ( $k$ ) for pure shear and pure bending respectively. For pure shear, the buckling coefficient curve ( $k$ ) is quite similar to that of *Case B* although the value of  $k$  is slightly lower due to the effect of the shear stress gradient in the flanges and the parabolic shear stress distribution in the web. For

pure bending, the buckling coefficient curve ( $k$ ) is identical to that of *Case B* as the bending stress distribution is the same.

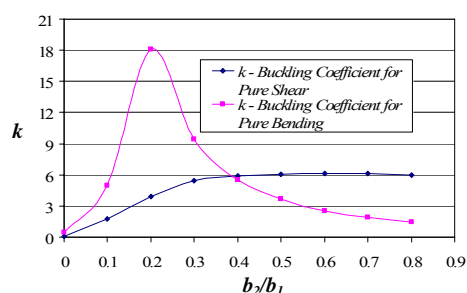


Figure 17. The Ratio of Flange and Web Widths ( $b_2/b_1$ ) and The Buckling Coefficients ( $k$ ) Of Unlipped Channel Section for *Case D*

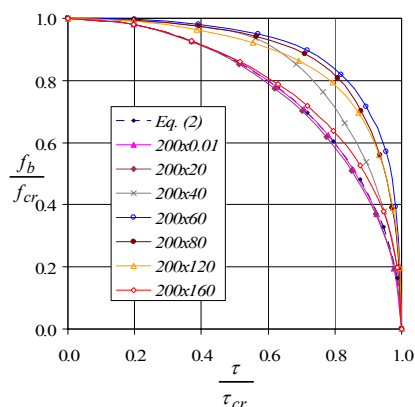


Figure 18. Interaction relation between  $f_b/f_{cr}$  and  $\tau/\tau_{cr}$  for *Case D*

Fig 18 shows the interaction relation curves between  $f_b/f_{cr}$  and  $\tau/\tau_{cr}$  for the different flange widths for *Case D*. The corresponding buckling mode shapes for *Case D* under combined bending and shear are shown in Fig 19.

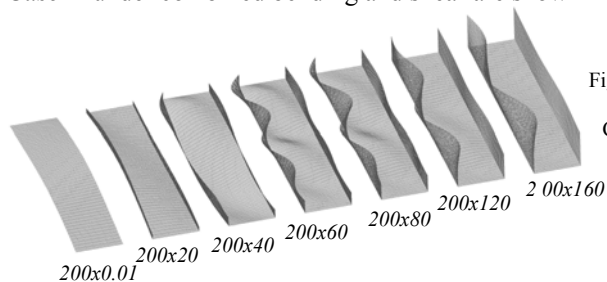


Figure 19. Buckling Mode Shape of Unlipped Section under Combined Bending and Shear for *Case D*

As can be seen in Fig 18, when the flange width is very small (0.01mm – 20 mm), the interaction relation curves are similar to those of *Cases B & C* described above. The interaction between bending and shear is significant due to the twisting buckling mode shown in Fig 19. As the ratio of  $b_2/b_1$  increases to 0.3, the interaction relation curves lie further above the circular curve. The interaction is therefore less significant. It can be noted that when the ratio of  $b_2/b_1$  increases further from 0.3 to 0.8, the interaction relation curve gets closer to the circular curve so that the interaction becomes more significant. The explanation for this fact is due to the presence of both the uniform compression stress and the actual shear stress distribution in the wider flange.

### 3.5 Lipped Channel Section – Length = 1000 mm, $a/b_1 = 5.0$ , Case A

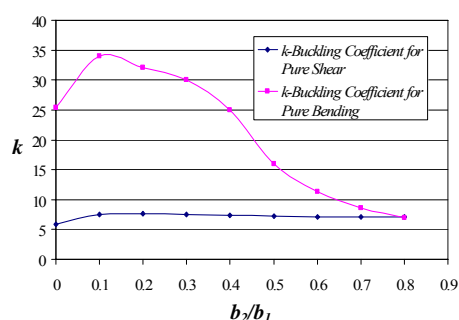


Figure 20. The Ratio of Flange and Web Widths ( $b_2/b_1$ ) and The Buckling Coefficients ( $k$ ) of Lipped Channel Section for Case A

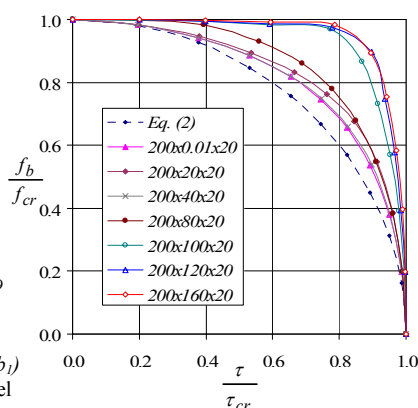
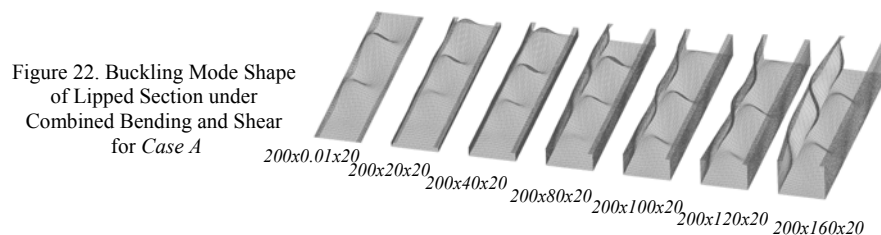


Figure 21. Interaction relation between  $f_b/f_{cr}$  and  $\tau/\tau_{cr}$  for Case A

The results of the buckling analyses of the lipped channel section for Case A with a length of 1000 mm are shown in Fig 20 for the ratios of flange to web widths ( $b_2/b_1$ ) from 0.00005 to 0.8. In this case, there are lateral restraints along the two longitudinal edges of web panel. The lip size of 20 mm is used throughout the analyses. The buckling coefficient curve ( $k$ ) of the lipped channel section subjected to pure shear is shown as the square line (—◆—), whereas the diamond line (—■—) represents the coefficient curve ( $k$ ) of pure bending. For pure shear, when the flange width is very small (0.01 mm), the value of  $k$  is 5.885 which is slightly greater than that of Case A for the unlipped channel due to the presence of the two lips which improve the shear capacity of the channel section member. As the ratio of  $b_2/b_1$  increases to 0.1, the value of  $k$  goes up rapidly. The explanation is that the small flange width with the lip contributes significantly to the shear buckling capacity of the lipped channel section. It should be noted that when the ratio of  $b_2/b_1$  increases from 0.1 to 0.2, the value of  $k$  improves slowly from 7.561 to 7.691 respectively and then reduces to 7.073 as the ratio of  $b_2/b_1$  increases to 0.8. The explanation for this fact is due to the effect of flange slenderness. As the flange width is small, there is little or no effect of flange slenderness on the shear buckling capacity. However, when flange width increases, the effect of flange slenderness is quite considerable. For pure bending, the buckling coefficient ( $k$ ) is 25.42 when the ratio of  $b_2/b_1$  is 0.00005. This value of  $k$  is slightly greater than to the theoretical result of 23.9 (Timoshenko and Gere, 1961; Bulson, 1970; Bleich, 1952; Allen and Bulson, 1980). As the ratio of  $b_2/b_1$  increases to 0.1, the value of  $k$  improves to 34.01. The explanation for this fact is that the presence of small flanges and lips

contribute to the buckling capacity of the channel section subjected to pure bending so that the buckling mode occurs mainly in the web. However, when the ratio of  $b_2/b_1$  increases from 0.1 to 0.3, the value of  $k$  reduces slightly to 25.04 due to the uniform compression stress in the wider flange. The mode of buckling is mainly local buckling mode in the flange. It is interesting to note that when the ratio of  $b_2/b_1$  increases further from 0.4 to 0.5, the value of  $k$  drops significantly from 25.04 to 15.98. The reason is that the member buckles in the distortional mode with the wider flange width. The value of  $k$  then reduces slightly to 6.94 as the ratio of  $b_2/b_1$  increases to 0.8. The buckling mode is mainly distortional buckling mode for wide flanges.

Fig 21 shows the interaction relation curves between  $f_b/f_{cr}$  and  $\tau/\tau_{cr}$  for different flange widths for *Case A* with lateral restraint along the two longitudinal edges of the web panel. The corresponding buckling mode shapes for *Case A* in the critical case of combined bending and shear are shown in Fig 22.



As can be seen in Fig 21, when the flange width is in the range from 0.01 mm – 80 mm, the interaction relation curves lie slightly above the circular curve. This shows that the interaction relation under combined bending and shear is significant. As the flange width increases from 80 mm to 160 mm, the interaction relation curves lie further above circular curve. The interaction is therefore not significant. This can be explained for *Case A* where there is no shear stress distribution in the flange, so that the uniform compression stress in the wider flange mainly causes distortional buckling as shown in Fig 22.

### 3.6 Lipped Channel Section – Length = 1000 mm, $a/b_1 = 5.0$ , *Case B*

Fig 23 shows the results of the buckling analyses of the lipped channel section for *Case B* with a length of 1000 mm and the ratios of flange to web width ( $b_2/b_1$ ) from 0.00005 to 0.8. In this case, there are no lateral restraints along the two longitudinal edges of web panel. The lip size of 20 mm is used throughout the analyses. The buckling coefficient curve ( $k$ ) of the lipped channel section subjected to pure shear is shown as the square line (—◆—), whereas the diamond line (—◆—) represents the coefficient curve ( $k$ ) for pure bending.



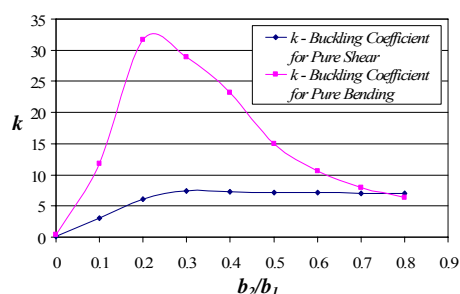


Figure 23. The Ratio of Flange and Web Widths ( $b_2/b_1$ ) and The Buckling Coefficients ( $k$ ) of Lipped Channel Section for Case B

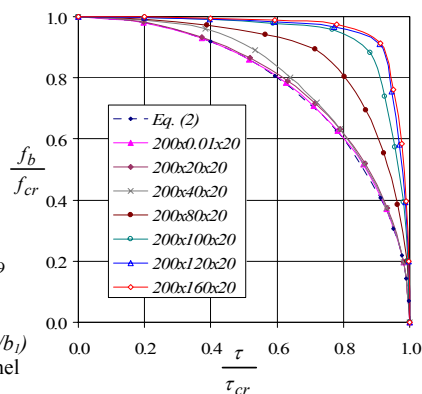
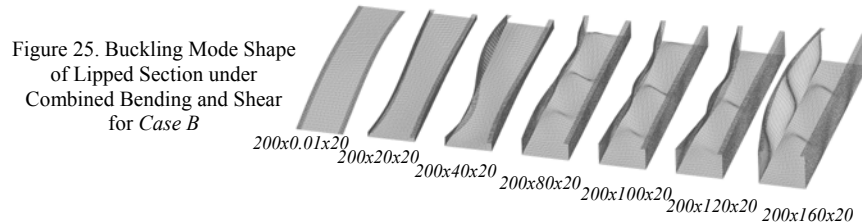


Figure 24. Interaction relation between  $f_b/f_{cr}$  and  $\tau/\tau_{cr}$  for Case B

For pure shear, when the ratio of flange to web width ( $b_2/b_1$ ) is 0.00005, the value of  $k$  is then very close to zero (0.131). The channel member buckles sideways (Pham and Hancock, 2007). It is interesting to note that when the ratio of  $b_2/b_1$  increases to 0.3, the value of  $k$  increases dramatically to 7.376. With a very small flange width, the buckling mode shown in the analyses of Pham and Hancock (2007) is twisting mode. As the ratio of  $b_2/b_1$  keeps increasing to 0.8, the value of  $k$  improves and get closer to that of Case A for the unlipped channel described above. The reason for this fact is that the flanges with lips are long enough to give full lateral restraint to the lipped channel section members. For pure bending, the buckling coefficient ( $k$ ) is 0.349, when the ratio of  $b_2/b_1$  is 0.00005. For Case B with no lateral restraint along the two longitudinal edges of web panel, the channel member also buckles sideways. As the ratio of  $b_2/b_1$  increases to 0.2, the value of  $k$  increases dramatically to 31.71. This can be explained by the fact that the flanges with lips contribute significantly to the buckling capacity of the channel section subjected to pure bending. However, it should be noted that when the ratio of  $b_2/b_1$  increases further from 0.2 to 0.4, the value of  $k$  reduces from 31.71 to 23.17 due to uniform compression in wider flange. The buckling mode is mainly local buckling. As the ratio of  $b_2/b_1$  increases from 0.4 to 0.8, the value of  $k$  drops dramatically from 23.17 to 6.42. The mode of buckling is the distortional buckling due to the uniform compression stress in wider flange.

Fig 24 shows the interaction relation curves between  $f_b/f_{cr}$  and  $\tau/\tau_{cr}$  for different flange widths for Case B with no lateral restraint along the two longitudinal edges of web panel. The corresponding buckling mode shapes for Case B under combined bending and shear are shown in Fig 25.

As can be seen in Fig 24, when the flange width is very small (0.01mm – 40 mm), the interaction relation curves lie very close to the circular curve. The interaction between bending and shear is significant. The reason for this is due to the fact that the small flange width allows the twisting buckling mode as shown in Fig 25. As the flange width increases, the interaction relation curves lie above the circular curve. The interaction relation is therefore less significant. Also can be seen in Fig 25, when the ratio of  $b_2/b_1$  increases further from 0.5 to 0.8, the interaction relation curves are further above circular curve. The interaction is therefore not significant. The explanation is similar to that for *Case A*. No shear stress in the flange and a uniform compression stress in wider flange mainly cause distortional buckling as shown in Fig 25.



**3.7 Lipped Channel Section – Length = 1000 mm,  $a/b_1 = 5.0$ , Case C**

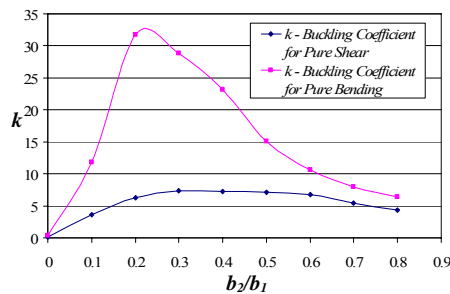


Figure 26. The Ratio of Flange and Web Widths ( $b_2/b_1$ ) and The Buckling Coefficients ( $k$ ) of Lipped Channel Section for Case C

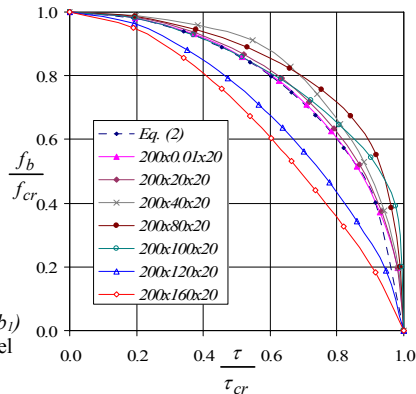
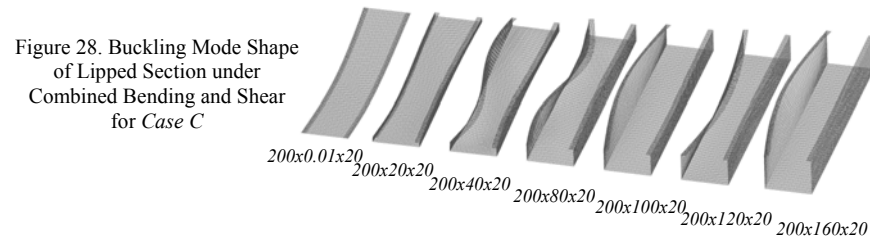


Figure 27. Interaction relation between  $f_b/f_{cr}$  and  $\tau/\tau_{cr}$  for Case C

The results of the buckling analyses of the lipped channel section for *Case C* with a length of 1000 mm are shown in Fig 26 for the ratios of flange to web widths ( $b_2/b_1$ ) from 0.00005 to 0.8. The boundary conditions are the same as those of *Case B*. The lip size of 20 mm is used throughout the analyses. The square line (—◆—) and the diamond line(—■—) represent the coefficient curves ( $k$ ) for pure shear and pure bending respectively. For pure shear, when the ratio

of the flange to web width ( $b_2/b_1$ ) increases from 0.00005 to 0.3, the value of  $k$  is not significantly different from that of *Case B*. However, when the ratio of  $b_2/b_1$  increases further from 0.4 to 0.8, the value of  $k$  for *Case C* reduces dramatically from 7.337 to 4.37. The explanation is mainly a result of the effect of shear stresses in the flanges. For pure bending, the buckling coefficient curve ( $k$ ) is identical to that of *Case B* as the bending stress distribution is the same.

Fig 27 shows the interaction relation curves between  $f_b/f_{cr}$  and  $\tau/\tau_{cr}$  for different flange widths for *Case C* where pure shear flow is applied in both web, flanges and lips. The corresponding buckling mode shapes for *Case C* under combined bending and shear are shown in Fig 28.



It can be seen in Fig 27 that when the flange width is in the range from 0.01 mm – 100 mm, the interaction relation curves lie slightly above the circular curve. The interaction is therefore significant. The explanation is mainly due to the twisting buckling mode when the flange width is small. As the ratio of  $b_2/b_1$  increases further from 0.6 to 0.8, the relation curves make below the circular curve. This shows that the interaction between bending and shear is very significant. The explanation for this fact is mainly due to the interaction of pure shear stress and uniform compression stress in the flange. As can be seen in Fig 28, the buckling mode is the twisting of the flange distortional buckling under shear and compression. There is little or no buckling in the web.

### 3.8 Lipped Channel Section – Length = 1000 mm, $a/b_1 = 5.0$ , *Case D*

Fig 29 shows the results of the buckling analyses of the lipped channel section for *Case D* with a length of 1000 mm and the ratios of flange to web width ( $b_2/b_1$ ) from 0.00005 to 0.8. The boundary conditions are the same as those of *Case B*. The square line (—◆—) and the diamond line (—◆—) represent the coefficient curves ( $k$ ) for pure shear and pure bending respectively. For pure shear, the buckling coefficient curve ( $k$ ) is quite similar to that of *Case B*. The value of  $k$  is slightly lower due to the effect of the shear stress gradient in the flange and the parabolic shear stress distribution in the web. For pure bending, the buckling coefficient curve ( $k$ ) is identical to that of *Case B* as the bending stress distribution is the same.

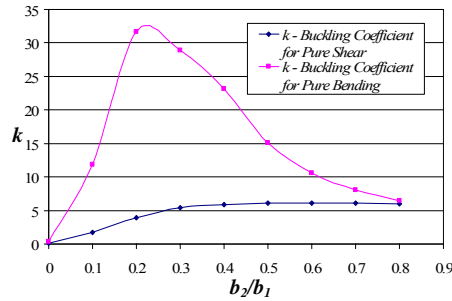


Figure 29. The Ratio of Flange and Web Widths ( $b_2/b_1$ ) and The Buckling Coefficients ( $k$ ) of Lipped Channel Section for *Case D*

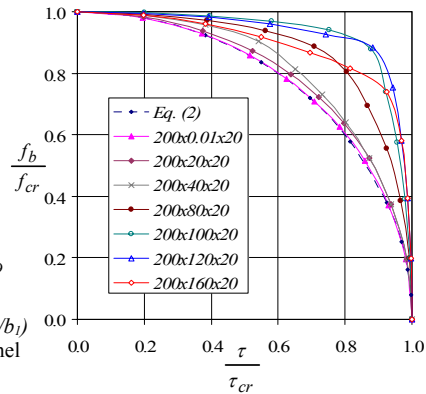


Figure 30. Interaction relation between  $f_b/f_{cr}$  and  $\tau/\tau_{cr}$  for *Case D*

Fig 30 shows the interaction relation curves between  $f_b/f_{cr}$  and  $\tau/\tau_{cr}$  for different flange widths for *Case D* where actual shear flow is applied. The corresponding buckling mode shapes for *Case D* in the critical case under combined bending and shear are shown in Fig 31.

As can be seen in Fig 30, when the flange width is in the range from 0.01mm – 80 mm, the interaction relation curves lie slightly above the circular curve. The interaction relation is quite similar to that of *Case B* for the lipped channel described above. The interaction is significant. As the ratio of  $b_2/b_1$  increases further from 0.5 to 0.8, the relation curves are more higher than the circular curve, so that the interaction between bending and shear is not significant. As the ratio of  $b_2/b_1$  increases from 0.7 to 0.8, the interaction curves get closer to the circular curve. The interaction is therefore more significant. The explanation for this fact is mainly due to interaction of the actual shear stress and uniform compression stress in the flanges. As can be seen in Fig 31, the buckling mode is similar to that of *Case C* for the lipped channel described above. The mode of buckling is distortional buckling in the flange under shear and compression. There is little or no buckling in the web.

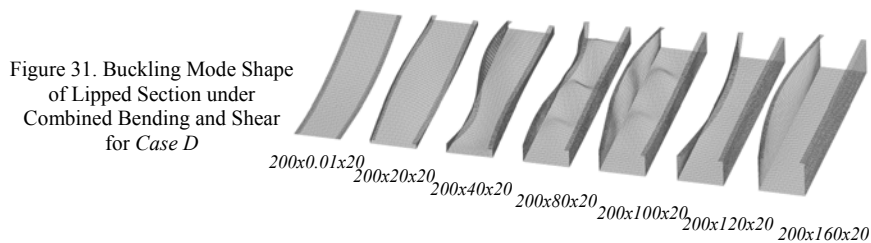


Figure 31. Buckling Mode Shape of Lipped Section under Combined Bending and Shear for *Case D*

#### 4. Conclusion

This report has outlined buckling analyses of channel section members subjected to pure shear and pure bending alone and the interaction relations under combined bending and shear. Unlipped and lipped channels were analysed by the Isoparametric Spline Finite Strip Method program. Four different shear flow distribution cases combined with pure bending were considered in this report. Two boundary conditions were used for the analyses in this study. These boundary conditions are simply supported with and without lateral restraints along two longitudinal edges of web panel. The aspect ratio of the rectangular plate  $a/b_1$  of 5.0 was chosen to investigate the interaction relation between bending and shear.

By varying the flange width, the analysis results show that the flanges can have a significant influence on the interaction relation between bending and shear. It is demonstrated that the twisting mode of sections with narrow flanges can lead to significant interaction under combined bending and shear. As the flange width increases, the interaction relation is proven to be less significant. The main reason is that the uniform compression stress in a very wide flange causes distortional buckling which does not appear to be significantly affected by shear stress.

## 5. References

- Allen, H. G and Bulson, P. 1980. "Background to Buckling", *McGraw-Hill Book*.
- Bleich, H. 1952. "Buckling Strength of Metal Structures", *McGraw-Hill Book Co. Inc*, New York, N.Y.
- Bulson, P. S. 1970. "Stability of Flat Plates", *Chatto & Windus Ltd.*, London W.C.2.
- Cheung, Y. K. 1976. "Finite Strip Method in Structural Analysis", *Pergamon Press, Inc.*, New York, N.Y.
- Eccher, G. 2007. "Isoparametric spline finite strip analysis of perforated thin-walled steel structures", *PhD Thesis, The University of Sydney, University of Trento*, Australia & Italia.
- Kwon, Y. B. and Hancock, G. J. 1991. "A Nonlinear Elastic Spline Finite Strip Analysis for Thin-Walled sections", *Thin-Walled Structures*, Vol. 12 1991, pp 295-319.
- Lau, S. C. W. and Hancock, G. J. 1986. "Buckling of Thin Flat-Walled Structures by a Spline Finite Strip Method", *Thin-Walled Structures*, Vol. 4 1986, pp 269-294.
- Lau, S. C. W. and Hancock, G. J. 1989. "Inelastic Buckling Analysis of beams, Columns and Plates using the spline finite strip method", *Thin-Walled Structures*, Vol. 7 1989, pp 213-238.
- Pham, C. H. and Hancock, G. J. 2007. "Shear Buckling of Thin-Walled Channel Sections", *Research Report No R885*, School of Civil Engineering, The University of Sydney, NSW, Australia, August, 2007.
- Timoshenko, S. P. and Gere, J. M. 1961. "Theory of Elastic Stability", *McGraw-Hill Book Co. Inc*, New York, N.Y.



## **Experimental Study on Web Crippling of Lapped Cold-Formed Steel Channels Subjected To Interior Two-Flange Loading**

Q. Rahman<sup>1</sup>; K. Sennah<sup>2</sup>; and S. Fox<sup>3</sup>

### **Abstract**

This investigation focused on the effects of lapped channels on the web crippling capacity of cold-formed steel members. The current design recommendations in North America Specifications specifies expressions for web crippling strength of different joist geometries in case of exterior end and concentrated load locations. However, it does not permit an increase in web crippling capacity when lapped cold-formed steel channels are subjected to interior two-flange loading. This may be attributed to the lack of experimental data on web crippling strength at interior support locations. Thus, the objective of the current research is to generate experimental data for CFS channels where both flanges of channel members are lapped at the interior support location and being loaded simultaneously. This paper summarizes the results of investigation. Test specimens were loaded to failure and load history and the failure pattern were recorded. Recommendations for further testing were drawn to establish design equations for web crippling strength of lapped CFS channels at interior support location when subjected to two flange loading. The test specimen used for the investigation is single web C-section.

---

<sup>1</sup>Graduate Student, Civil Engineering Dept., Ryerson University, 350 Victoria St, Toronto, ON, Canada M5B 2K3, qrahman@ryerson.ca

<sup>2</sup>Professor, Civil Engineering Dept., Ryerson University, 350 Victoria St, Toronto, ON, Canada, M5B 2K3, ksennah@ryerson.ca

<sup>3</sup>General Manager, Canadian Sheet Steel Building Institute (CSSBI), 652 Bishop St.N, Unit 2A, Cambridge, ON, Canada, N3H 4V6, Canada, sfox@cssbi.ca





### Current Design Equation

At university of waterloo in 1993 Prabakaran performed an extensive statistical analysis of the web crippling capacity of cold formed steel section. Based on his research he developed a unified equation for the web crippling capacity of cold-formed steel section. This equation (1) is used in North American Specifications for determination for web crippling resistance.

$$P_n = Ct^2F_y \sin \theta \left( 1 - C_R \sqrt{\frac{R}{t}} \right) \left( 1 + C_N \sqrt{\frac{N}{t}} \right) \left( 1 - C_h \sqrt{\frac{h}{t}} \right) \quad (1)$$

Where

$P_n$  = nominal web crippling strength

$C$  = regression analysis coefficient

$C_h$  = web slenderness coefficient

$C_N$  = bearing length coefficient

$C_R$  = inside bend radius coefficient

$F_y$  = yield strength

$h$  = flat dimension of the web measured in the plane of the web

$N$  = bearing length (lap length)

$R$  = inside bend radius

$t$  = web thickness

$\theta$  = angle between the plane of the web and the plane of the bearing surface

### Experimental Study

An experiment study performed at the Ryerson University, studied the web crippling capacity of a single web section loaded under an interior two flange condition with a variance in a lap length at support. Following is the summary of the test performed.

### Test Specimen

The specimens consisted of edge-stiffened “C” section. (Fig 2) The sections have average yield stress of 53ksi (370Mpa). A nominal depth of web ranging from 8” (203mm) to 10” (254mm), and thickness of channel ranging from 0.068” (1.7mm) to 0.045” (1.14mm). The key cross sectional parameters for each tested cross-section are summarized in Table 1.

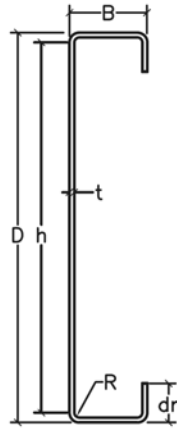


Fig. 2 Typical C-Section

### Bearing Plate

The loads were applied by means of bearing plates. All bearing plates were machined to specified dimensions. The thickness of bearing plates was 0.5" (12.7mm). The bearing plates were designed to act across the full flange width of the channels. The length of bearing plate was equal to the lap length (N). The flanges of the channel specimens were restrained by the bearing plate.

### Specimen Labelling

Total 24 specimens were tested. Each specimen was labeled such that the depth, thickness and lap length could be identified from the label. For example, the labels "10C14 250" define the following specimens.

- The first two letters shows the over all depth of the web in "inches".
- The letter "C" shows that specimen cross section is "C".
- The next two digits show the thickness of section in "gauge".
- The last three digits shows the lap length in "inches"

### Material Properties

The material properties of the test specimens were determined by tensile coupon test. For each section tested, the three coupons were taken from the center of the

Table 1. Typical "C" Section Properties

Specimen	D (in)	h (in)	t (in)	B (in)	R (in)	df (in)	Fy (ksi)	N (in)
<b>10C14</b>	10	9.52	0.067	1.62	3.38	0.787	51.80	2.5
	10	9.52	0.067	1.62	3.38	0.787	51.80	3.625
	10	9.52	0.067	1.62	3.38	0.787	51.80	6
<b>10C16</b>	10	9.68	0.056	1.62	2.77	0.708	54.70	2.5
	10	9.68	0.056	1.62	2.77	0.708	54.70	3.625
	10	9.68	0.056	1.62	2.77	0.708	54.70	6
<b>8C16</b>	8	7.63	0.055	1.62	2.77	0.708	53.16	2.5
	8	7.63	0.055	1.62	2.77	0.708	53.16	3.625
	8	7.63	0.055	1.62	2.77	0.708	53.16	6
<b>8C18</b>	8	7.75	0.047	1.62	1.78	0.708	56.50	2.5
	8	7.75	0.047	1.62	1.78	0.708	56.50	3.625
	8	7.75	0.047	1.62	1.78	0.708	56.50	6

web plate in the longitudinal direction of the undisturbed specimens. The tensile coupons were prepared and tested according to American Society of Testing and Materials (ASTM A370, 2005). To measure the actual thickness of specimen the galvanized coating was removed by hydrochloric acid solution. The averages of three coupon tests for each specimen were used in the formula. Table 2 shows the material mechanical properties of tested specimens.

**Table 2. Mechanical Properties**

Specimen	Test #	t (in)	Fy (ksi)	Fu (ksi)	% Elongation *
10C14	1	0.0678	51.90	68.50	34.5
	2	0.0676	52.20	69.00	34.5
	3	0.0677	51.40	68.50	34.0
	<b>Average</b>	<b>0.0677</b>	<b>51.80</b>	<b>68.70</b>	<b>34.3</b>
10C16	1	0.0564	54.90	69.50	32.5
	2	0.0562	54.30	70.10	33.0
	3	0.0564	54.90	70.20	32.5
	<b>Average</b>	<b>0.0563</b>	<b>54.70</b>	<b>69.90</b>	<b>32.7</b>
8C16	1	0.0555	53.20	69.70	34
	2	0.0549	53.20	70.00	34
	3	0.0552	53.10	70.00	34
	<b>Average</b>	<b>0.0552</b>	<b>53.16</b>	<b>69.90</b>	<b>34</b>
8C18	1	0.0467	56.10	73.00	22
	2	0.0476	56.80	73.20	22
	3	0.0468	56.60	73.00	22
	<b>Average</b>	<b>0.0470</b>	<b>56.50</b>	<b>73.06</b>	<b>22</b>

\* Based on 2" gauge length

### Test Procedure

The channel specimens were tested using interior two flange loading conditions (ITF) according to AISI specification. The test setup of ITF is shown in Fig 3. The channels at lapped were attached together with 4 self drilling screws size #10x1". It should be noted that the two rows of screws are located at the third point of the web depth. Two identical bearing plates of the same width were placed top and bottom of channel at lap. Length of bearing plate was equal to length of lap. Channels' sectional rotation at there ends were restrained by inserting their ends into a U-shape steel support system. In this case, the channel member is considered unbraced between this end rotational restraint and the interior support location. A 50 kip (222kN) capacity hydraulic jack was used to apply a compressive force to the test specimens over the interior support. Web lateral deflection and vertical movement of the channel top flange were recorded using LVDT's. Each specimen was loaded incrementally till complete collapse. Failure was considered at the point at which the specimens could not accept a further load. Table 3. Shows the test results of all the tested specimen.

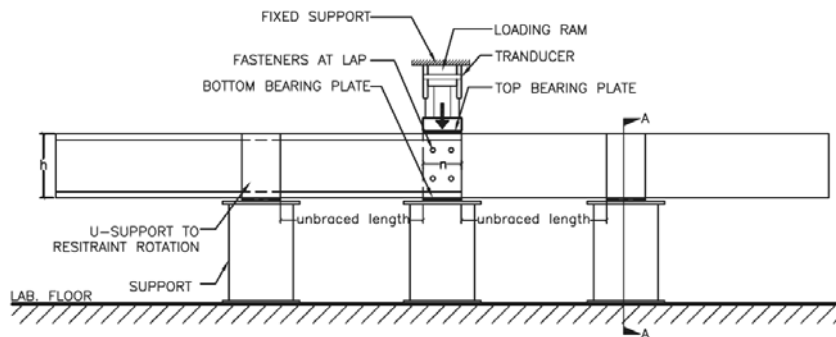


Fig 3. Schematic diagram of loading condition

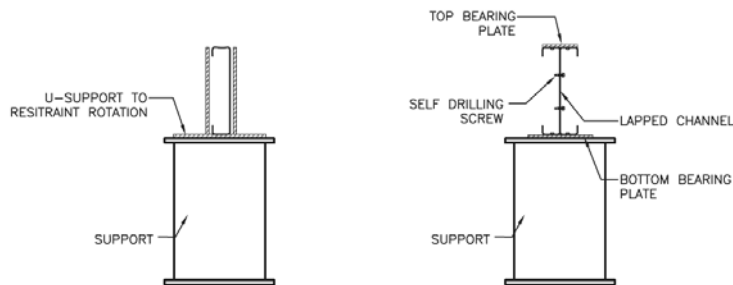


Fig 4. Section at "A-A"

Fig 5. Section at lap

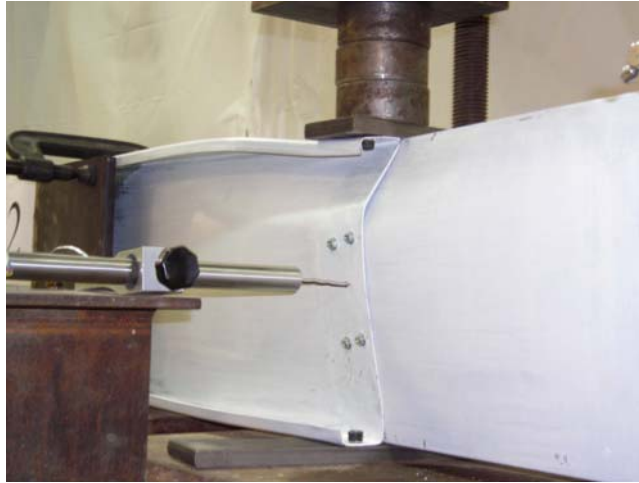


(a)



(b)

Fig 6. Specimen sample before test



(a)



(b)

Fig 7. Specimen after failure



**Table 3. Interior two flange loading Test Results**

Section	Lap Length "N" (mm)	Test #1 $P_{t1}$ (kip)	Test #2 $P_{t2}$ (kip)	Average $P_{t,avg}$ (kip)
<b>10C14</b>	2.5"	4.65	4.50	4.57
	3.625"	4.63	5.17	4.90
	6"	6.23	6.24	6.24
<b>10C16</b>	2.5"	2.84	3.20	3.02
	3.625"	3.65	3.42	3.53
	6"	5.06	5.40	5.22
<b>8C16</b>	2.5"	3.64	3.40	3.52
	3.625"	4.12	4.15	4.14
	6"	5.32	4.92	5.11
<b>8C18</b>	2.5"	2.62	2.86	2.74
	3.625"	3.00	3.57	3.30
	6"	3.60	3.94	3.76

**Development of New Coefficients**

A nonlinear regression analysis was performed by using the unified web crippling expression to update the fastened case coefficients for single web "C" section subjected to ITF loading. For the regression analysis, the results of studies were analyzed using "MinRes" computer software. New proposed correction coefficients are shown in table 4.

**Table 4. New Coefficients for Single Web Section**

Support and Flange Conditions		Load Cases		C	C <sub>R</sub>	C <sub>N</sub>	C <sub>h</sub>
Fastened To Support	Stiffened Flanges	Two Flange Loading	Interior Lap	2.5	0.02	1.01	0.001

Notes: The above coefficient apply when  $h/t \leq 172$ ,  $N/t \leq 127$ ,  $N/h \leq 0.78$ ,  $R/t \leq 1.97$  and  $\theta = 90^\circ$

### Evaluation of Test Results

For the recommendation of this study, the recorded failure load for each specimen  $P_t$  was normalized by division of the corresponding design strength  $P_n$ .  $P_n$  was calculated by using equation 1 with new coefficient calculated.  $P_t/P_n$  values greater than unity for most of the specimens, meaning that the tested web-crippling values are greater than the predicted web-crippling values. This makes the analytical approaches conservative. The  $P_t/P_n$  ratio used for analysis of the test data.

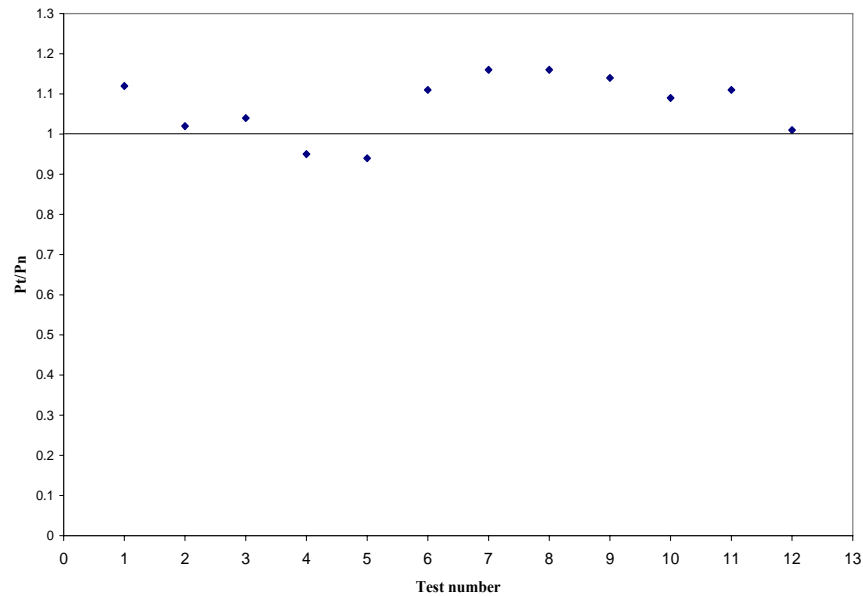


Fig 8.  $P_t/P_n$  for "C" Section

### New Safety Coefficient

The objective of structural design and construction is to produce safe, serviceable, economic, durable and aesthetic structures. Structures must be able to withstand the loads acting on them during a reasonable lifetime. For cold formed steel member design there are two different methods, Limit State Design (LSD) and Allowable Stress Design (ASD). Based on a probabilistic concept, the structural safety can be measured in terms of a reliability index,  $\beta$ . The theory of probability can be applied to both design methods to achieve the same degree of structural safety.

Procedure for calculating both the resisting factor,  $\phi$ , for load resistance factored design (LRFD), and the factor of safety,  $\Omega$ , for allowable stress design (ASD), are well described in North American Specifications. The resistance factor  $\phi$  and factor of safety  $\Omega$  can be calculated as follows. Table 5. Shows the new proposed resistance factor and factor of safety.

$$\phi = C_{\phi} (M_m F_m P_m) e^{-\beta_0 \sqrt{V_M^2 + V_F^2 + C_p V_P^2 + V_Q^2}} \quad (2)$$

$$\Omega = 1.6 / \phi \quad (3)$$

Where

$C_{\phi}$  = Calibration coefficient and is equal to 1.52 for the United States and Mexico and 1.42 for Canada

$M_m$  = Mean value of material factor, “ $M_m = 1.10$ ”

$F_m$  = Mean value of fabrication factor, “ $F_m = 1.00$ ”

$P_m$  = Mean value of professional factor, “ $P_m = 1.0$ ”

$\beta_0$  = Target reliability index and is equal to 2.5 for structural members and 3.5 for connections for the United States and Mexico, and 3.0 for structural members and 4.0 for connections for Canada

$V_M$  = Coefficient of variation of material factor “ $V_M = 0.10$ ”

$V_F$  = Coefficient of variation of fabrication factor “ $V_F = 0.05$ ”

$C_p$  = Correction factor and is equal to  $(1+1/n)m/(m-2)$  for  $n \geq 4$ , and 5.7 for  $n = 3$

$m$  = Degrees of freedom and is equal to  $(n-1)$

$n$  = Number of tests

$V_P$  = Coefficient of variation of test results, “ $V_P = 10.94\%$ ”

$V_Q$  = Coefficient of variation of load effect = 0.21

$e$  = Natural logarithmic base (2.718)

**Table 5 Resistance Factors and Factors of Safety**

Support and Flange Conditions		Load Cases		Tests No.	Mean Value	C.O.V	S136		AISI	
							$\Omega$	$\phi$	$\Omega$	$\phi$
Fastened To Support	Stiffened Flanges	Two Flange Loading	Interior Lap	24	1.045	0.109	2.30	0.70	1.90	0.85

### Conclusions

A test program on cold-formed stiffened lapped channels subjected to web crippling has been presented in this paper. Channel specimens having an average nominal yield stress of 53ksi (370Mpa) were tested. The specimens were tested using interior two flange loading condition according to American Iron and Steel Institute (AISI 2001) specification for cold-formed steel structures. The concentrated load or reaction forces were applied by means of bearing plate. New proposed correction coefficient for equation 1 is shown in this paper. New proposed resistance factor and safety factor is also shown in this paper.

### Acknowledgements

The authors are grateful to the Canadian Sheet Steel Building Institute (CSSBI) for providing all test specimens for this research. This research is part of the Master's program of the first author. The financial support from Ryerson University to the first author in the form of Ryerson Graduate Scholarship is greatly appreciated.

### Notation

C	Coefficient depending on the section type
$C_h$	Web slenderness coefficient
$C_N$	Bearing length coefficient
$C_R$	Inside bend radius coefficient
C.O.V.	Coefficient of variation
D	Total depth of the Channel
F <sub>y</sub>	Yield strength of steel
h	Flat dimension of web measured in plane of web

ITF	Interior Two Flange Loading
N	Bearing length
$P_m$	Mean
$P_n$	Computed web crippling strength
$P_t$	Web crippling strength in the test
R	Inside bend radius
t	Thickness of the web
$V_p$	Coefficient of variation
$\beta$	Reliability index
$\theta$	Angle between the plane of the web and plane of bearing surface
$\Omega$	Factor of safety
$\phi$	Resistance factor

#### References

1. American Iron and Steel Institute (AISI). (2001). "North American Specification for the Design of Cold-formed Steel Structures Members". Washington D.C.
2. Ben Young and Gregory J. Hancock. (2001). "Design of cold-formed channels subjected to web crippling" Journal of structural engineering, Vol. 127, No. 10, Oct 2001.
3. M.W. Holesapple and R.A. LaBoube. (2003). "Web crippling of cold formed steel beams at end supports". Engineering Structures 25 (2003) 1211-1216, University of Missouri-Rolla, Rolla, Mo, USA.
4. R. LaBoube, and R. Schuster. 2002. "Standard test method for determining the web crippling strength of cold-formed steel members." AISI Sponsored Report, American Iron and Steel Institute. 16p.
5. Wei-Wen Yu. "Cold formed steel design". New York: John Wiley & Sons, 2000.
6. Wei-Xin Ren; Sheng-En Fang; and Ben Young. (2006). "Finite-Element simulation and design of cold-formed steel channels subjected to web crippling". Journal of structural engineering, Vol. 132, No. 12. Dec 01, 2006.
7. W. Ren, S. Fang, and B. Young. (2006). "Finite-Element simulation and design of cold-formed steel channels subjected to web crippling." ASCE Journal of Structural Engineering, 132(12): 1967-1975.

## **Simplified models for cross-section stress demands on C-section purlins in uplift**

L.C.M. Vieira Jr.<sup>1</sup>, M. Malite<sup>2</sup> and B.W. Schafer<sup>3</sup>

### **ABSTRACT**

The objective of this paper is to provide and verify simplified models that predict the longitudinal stresses that develop in C-section purlins in uplift. The paper covers the simple case of flexural stress, where the force has to be applied at the shear center or the section braced in both flanges, up through the more complex problem of bending where movement of the tension flange alone is restricted, as commonly found in purlin-sheeting systems. Winter's model for predicting the normal stresses developed due to direct torsion is reviewed, verified, and then extended to cover the case of a bending member with tension flange restraint alone. The impact of considering the combined longitudinal stresses, in determining the elastic stability behavior is highlighted. Strength predictions of typical C-section purlins are provided for existing AISI methods and a newly proposed extension to the Direct Strength Method.

### **INTRODUCTION**

The primary concern with cold-formed steel cross-sections is that due to their thin-walled nature a host of instability phenomena must be examined, including but not limited to: local, distortional, and global buckling modes. However, due to their lack of symmetry (i.e., commonly used C- and Z-section members are singly- and point-symmetric respectively) an additional issue is that even for common applications, operating in the elastic range, the sections may develop complicated stress response, where conventional  $\sigma=My/I$  approximations are

---

<sup>1</sup> Graduate Student, Johns Hopkins University, Baltimore, MD, USA  
(formerly graduate student Universidade de São Paulo - EESC, Brazil)

<sup>2</sup> Associate Professor, Universidade de São Paulo - EESC,  
São Carlos, SP, Brazil

<sup>3</sup> Associate Professor, Johns Hopkins University, Baltimore, MD, USA

grossly inadequate. A common example of this (particularly in Brazil) is the use of C-sections as purlins in metal building roofs, as shown in Figure 1. In uplift, the twisting of the C-section results in the addition of longitudinal stresses due to partially restrained warping torsion, in addition to conventional bending stresses. This paper provides an examination of these stresses, as well as means to predict their magnitudes in design situations.

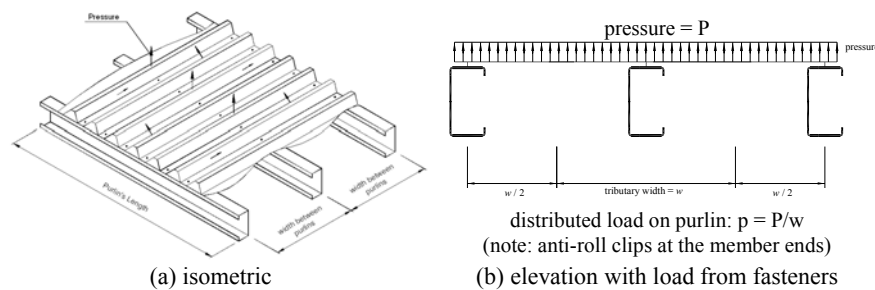


Figure 1 – Purlin-sheeting system under uplift (a – based on Basaglia 2004).

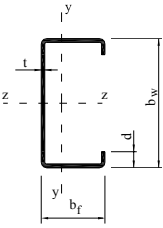
Given that longitudinal stresses are known to have a significant impact on cross-section stability and strength, in the second part of this paper we examine the application of these stresses to strength prediction. The prediction methods examined include (a) simple “R” factor reductions as found in D6.1.1 of AISI-S100-07 (AISI 2007) (b) the application of the new torsion provisions as found in C3.6 of AISI-S100-07 and (c) a novel extension to the Direct Strength Method (DSM) of Appendix 1 of AISI-S100-07 (Schafer 2008) which uses the predicted stress demands to assess the local, distortional, and global stability and strength of the section directly.

It is worthy of noting that existing research on cold-formed steel purlins and purlin-sheeting systems is extensive. Including the recent work by Tom Murray and his students on anchorage forces (Seek and Murray 2007, Sears and Murray 2007), the extensive studies by Hancock and his students and colleagues including vacuum testing and the examination of rational elastic buckling analysis in design (Clarke and Hancock 2000, Pangelis et al. 1998, Quispe and Hancock 2002, Rousch and Hancock 1996), as well as earlier theoretical and experimental work (Fisher 1986, LaBoube and Golovin 1990, Peköz and Soroushian 1982) to name but a few.

## CROSS-SECTIONS STUDIED

The basic system studied in this paper is that of Figure 1. The cross-section dimensions for the purlins are provided in Table 1. For the trapezoidal sheeting ( height = 25 mm,  $t = 0.43$  mm) shell element based finite element models were utilized to determine the rotational stiffness,  $k_{rx}$ , that the sheeting provides to the purlin, the resulting  $k_{rx}$  are provided in Table 1 (Vieira 2007). Span lengths vary depending on the cross-section (see Table 1) but in general vary from 5 m to 10 m. Additional material properties assumed include  $E = 205,000$  MPa,  $F_y = 300$  MPa, and  $\nu = 0.3$ .

Table 1 – Cross section and rotational spring stiffness.

Section	C - $b_w \times b_f \times d \times t$	$k_{rx}$ (kN.m/rad/m)
	150x60x20x1.5	0.39
	200x75x20x2	0.58
	250x85x25x2	0.68
	250x85x25x3	0.72

A typical shell element model used for determination of the stress demands is shown in Figure 2.

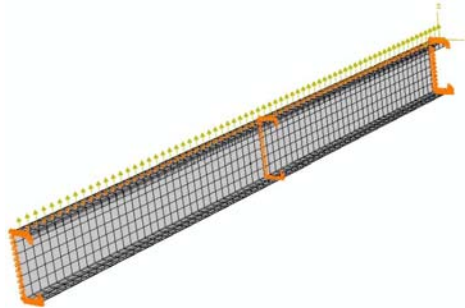


Figure 2 – Typical shell element model of bare purlin with uplift load

## FULLY BRACED: LONGITUDINAL STRESS DEMANDS

In the ideal fully braced case the behavior of a C-section purlin is well described by simple flexural stresses ( $\sigma = My/I$ ), as shown in Figure 3. For stresses to develop in this manner the section must be fully restrained from lateral



translation and twist (or be loaded at its shear center). The restraint must be provided in such a manner that the section does not distort due to the bracing forces. Some form of blocking accompanied by attachments to both flanges is known to provide such adequate restraint.

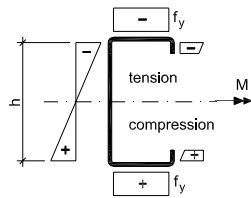
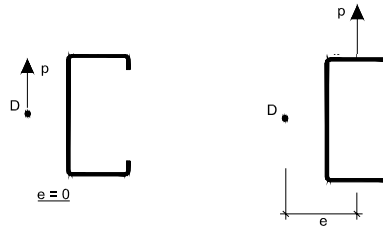


Figure 3 – Simple flexural stress



a) Load applied at shear center      b) Load applied at connection

Figure 4 – Load application points.

**UNBRACED: LONGITUDINAL STRESS DEMANDS**

For singly-symmetric sections, such as a C-section, it is well known that vertical loads must be applied at the shear center (Figure 4a) if torsion is to be avoided. However, under uplift in a purlin the load path requires that the force be transmitted through the fastener, at mid-width of the flange, considerably away from the shear center.

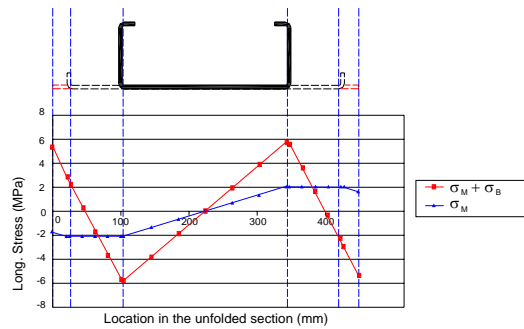


Figure 5 – Cross-section longitudinal stress distribution at mid-span (C 250x85x25x2 , uniform load (p) of 0.02N/mm, span=7524mm).

The longitudinal stresses developed in pure bending (Figure 4a) are compared with those including bending and torsion (of Figure 4b) in Figure 5, for the same load, p. In Figure 5,  $\sigma_M$  refers to the longitudinal stresses from pure bending moment “M” and  $\sigma_B$  refers to the longitudinal stresses from the warping torsion bimoment “B” from Vlasov’s theory (at mid-length). As Figure 5 indicates the introduction of warping torsion, and associated bimoment, radically alter the

applied stress distribution on the section, net compressive stresses even end up on the “tension” flange (and vice-a-versa).

### UNBRACED: WINTER’S MODEL FOR WARPING TORSION STRESS

Calculation of the longitudinal warping stresses due to torsion by Vlasov’s theory is involved; fortunately, Winter (1950) developed an accurate approximate method that is fully illustrated in AISI (2004) and summarized in Figure 6. The basic idea is similar to an approximate method long used in I-beam sections: that is, that warping torsion is resisted by lateral flange bending, thus the stresses that develop due to warping torsion may be found as simple bending stresses due to lateral flange bending. For I-beams the web’s contribution is typically ignored. For C-sections Winter recommended assuming  $\frac{1}{4}$  of the web contributed to the flange for the purposes of determining the lateral flange bending.

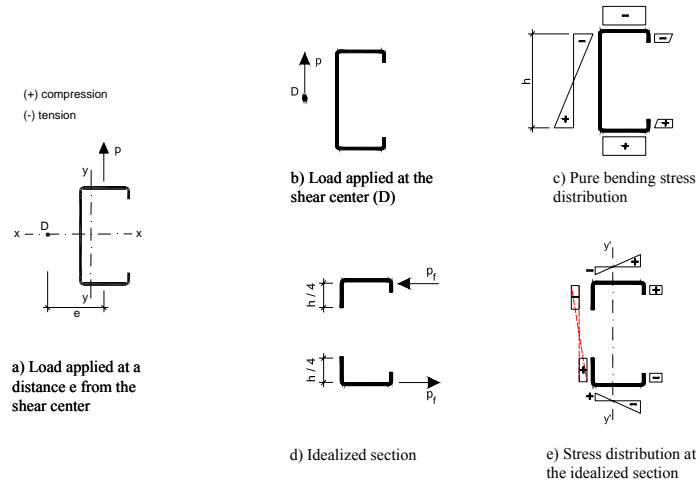


Figure 6 – Winter’s model for bending and torsion in a C-section.

As Figure 6 illustrates the stress distribution is found by summation of the pure bending stresses (Figure 6c) with the stresses developed due to torsion (Figure 6e). The stresses due to torsion are found by assuming the driving torsion moment ( $p \cdot e$ ) is restrained by a moment couple developed in the two flanges with force  $p_f = p \cdot e / h$ . Where the flange (flange, lip and  $\frac{1}{4}$  of the web actually) is assumed to carry the load  $p_f$ , through bending, i.e. at mid-span  $\sigma_B = (p_f L^2 / 8) x / I_y'$ , where  $L$  is the span length,  $I_y'$  is the moment of inertia of the flange, lip and  $\frac{1}{4}$  of the web about a  $y$ -axis through its own centroid, and  $x$  is the distance from

that centroid to any part of the flange, lip, and  $\frac{1}{4}$  of the web. One final step, consistent with Winter (1950) but not discussed in AISI (2004) is that the uniform stress gradient on the web is ignored in favor of a linear stress gradient that connects the stresses at the two flanges at their respective flange/web junctures. Comparison of Winter's approximate method with Vlasov's theory, and shell element based finite element analysis in ANSYS, for the same cross-section as Figure 5, is provided in Figure 7. Excellent agreement is observed.

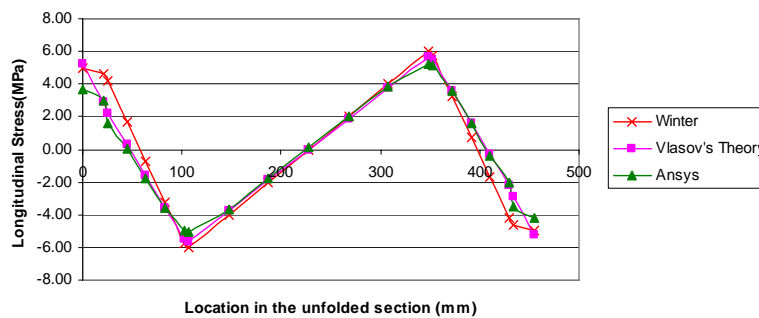


Figure 7 – Comparison of different models for torsion and bending (C 250x85x25x2 , uniform load (p) of 0.02N/mm, span=7524mm).

### TENSION FLANGE BRACED: LONGITUDINAL STRESS DEMANDS

Winter's model provides a convenient means to understand the impact of pure bending and pure warping torsion on an unbraced, in-plane rigid, cross-section. Winter's model shows that the impact of load location can be pronounced on the resulting cross-section. For the purlin of

Figure 1, the sheeting provides restraint, but only to the tension flange, and the cross-section is thin enough that distortion is possible. Using shell element based finite element models in ABAQUS (Figure 2), we examined the longitudinal stresses at midspan for four cases: (a) load through the flange but otherwise "no restriction", (b) load through the flange and the sheeting provides a "rotational spring", (c) load through the flange and the sheeting provides a "rotational spring + lateral restraint", and (d) load through the flange, but lateral restraint provided in "both flanges" as shown in Figure 8.

If both flanges are restrained, the fully braced pure bending stresses ( $\sigma=My/I$ ) results. If neither flange is restrained and the load is applied to the flange the pure bending plus pure warping torsion stresses result. If a small rotational restraint is added to the tension flange, the stresses due to warping torsion are decreased modestly. If full lateral support is also provided to the tension flange, the stresses and their distribution change dramatically. With the lateral restraint

in place the tension flange stresses follow a pure bending distribution (but elevated from  $\sigma=My/I$ ) while the compression flange stresses follows a reduced version of the bending plus torsion distribution.

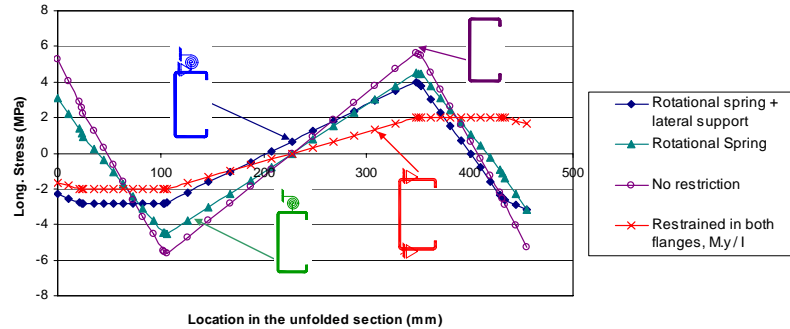


Figure 8 – Stress distribution for different kind of connections (C 250x85x25x2 uniform load ( $p$ ) of 0.02N/mm, span=2052mm).

Looking more closely at case c, where it is assumed that the sheeting can provide full lateral restraint and partial rotational restraint to the tension flange, Figure 9 provides the linear elastic displaced shape. The key feature of the deformations is that the cross-section distorts, and as shown in the stress demands, one is left with a combination primarily of bending in the tension flange and bending plus warping torsion in the compression flange. Based on this observation a modification to Winter's model to determine the stresses when tension flange restraint is present is developed.

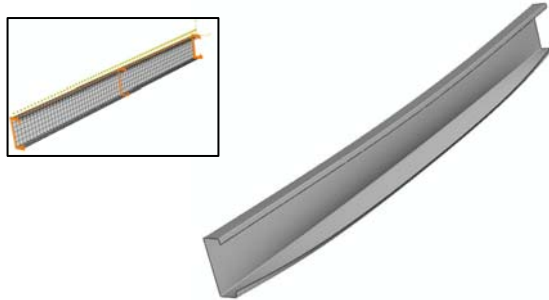


Figure 9 – Cross-section distortion associated with linear elastic deformations of a tension flange restrained purlin under uplift, ends are fully simply supported

### TENSION FLANGE BRACED: EXTENDING WINTER'S MODEL

In this section Winter's model for determining the longitudinal stresses (Figure 6) is extended to the specific case of a C-section in bending with tension flange restraints consisting of full lateral restraint and a rotational spring. The basic concept of the proposed model is provided in Figure 10. The stresses due to pure bending ( $\sigma_M$ ) are assumed as before, the stresses due to torsion ( $\sigma_B$ ) focus on the case where lateral tension flange restraint exists. In that case, warping and its associated stresses are assumed to concentrate in the compression flange; further the entire web height (as opposed to  $1/4$  of the web) are assumed to participate in resisting the lateral flange bending, as illustrated in Figure 10d-f. The rotational spring influences strongly whether  $\sigma_M$  or  $\sigma_B$  is dominant and is captured in the coefficients  $\alpha_M$  and  $\alpha_B$ .

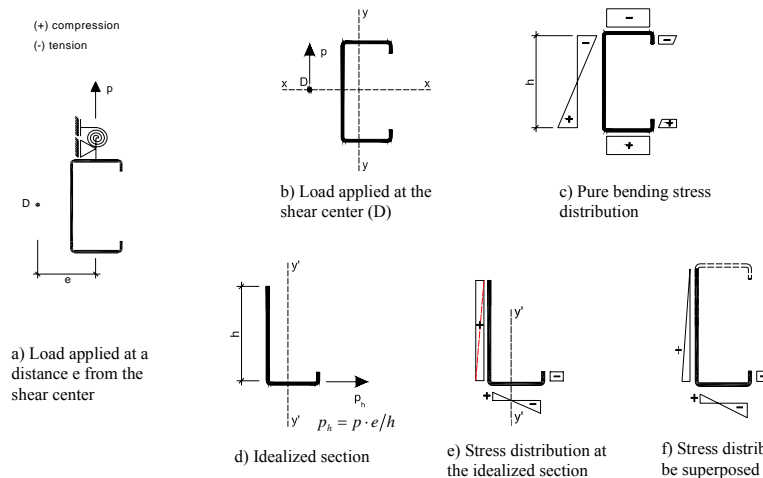


Figure 10 – Proposed model for bending & torsion with tension flange restraint.

The stresses in a C-section cross-section with tension flange restraint may be determined via:

$$\sigma = \alpha_M \sigma_M + \alpha_B \sigma_{B^*}$$

where,  $\sigma_M$  = pure bending stress as illustrated in Figure 10c,

$\sigma_{B^*}$  = warping stresses when tension-flange is laterally restrained as provided in Figure 10f,

$\alpha_M$  = factor to account for influence of tension flange rotational spring,  $k_{rx}$ , on the pure bending stress contribution, and

$\alpha_B$  = factor to account for influence of tension flange rotational spring,  $k_{rx}$ , on the stresses developed due to warping torsion.

The important feature of the above model is that it has the capability to capture stress distributions from pure bending ( $\alpha_M=1.0$ ,  $\alpha_B=0.0$ ) to partial restraint. For example, for the C 250x85x25x2 with a tension flange rotational spring of  $k_{rx}=0.68$  kN-m/rad/m, and full lateral tension flange restraint at mid-width, the appropriate  $\alpha_M$  and  $\alpha_B$  are found and the resulting stress distribution from the proposed model compared with shell element based FEM in Figure 11. The result shows excellent agreement with the overall distribution of stresses and good agreement with the peak stresses and stresses in the lips.

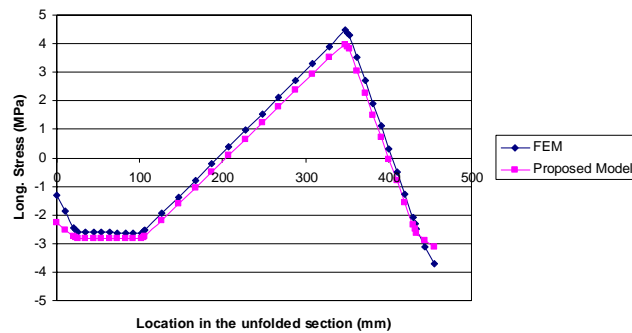


Figure 11 – Comparison between shell element FEM and proposed model (C 250x85x25x2 uniform load (p) of 0.02N/mm, span=7254).

#### Study of the coefficients $\alpha_M$ and $\alpha_B$

The proposed model for predicting the stress demands in the tension flange braced case is empirical and dependent on determination of coefficients  $\alpha_M$  and  $\alpha_B$ . For the case of Figure 11,  $\alpha_M$  was found to be 1.45 and  $\alpha_B$  to be 0.93 by minimizing the sum squared error between the model  $\sigma = \alpha_M \sigma_M + \alpha_B \sigma_B^*$  and the finite element results (at the node locations of the FE model). The fact that  $\alpha_M$  is greater than 1.0 does not imply that more “moment” M has been applied to the cross-section, but rather the amount which  $\alpha_M$  is above 1.0 reflects the impact of the torsion on this tension flange restrained section. Thus, the contribution due to bending may be recognized as  $1.0\sigma_M$  and the contribution due to the restrained torsion as  $0.45\sigma_M + 0.93\sigma_B^*$ .

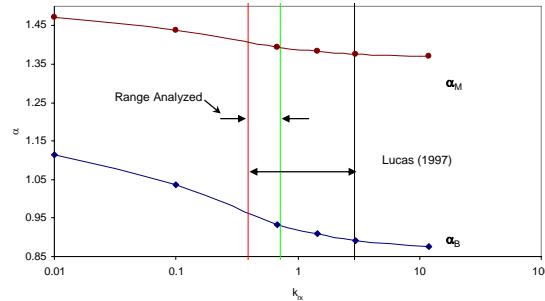


Figure 12 – Variation of  $\alpha_M$  and  $\alpha_B$  as a function of  $k_{tx}$ .  
(for C 250x85x25x2, span=7254 mm).

The tension flange braced case summarized in Figure 11 is for lateral restraint at mid-width of the flange and  $k_{tx} = 0.72 \text{ kN.m/rad/m}$ , as given in Table 1. The influence of the tension flange rotational spring ( $k_{tx}$ ) on the stress distribution is captured in Figure 12 through the  $\alpha_M$  and  $\alpha_B$  coefficients. For practical  $k_{tx}$  values the stress distribution is only modestly changed by the rotational spring. For large  $k_{tx}$   $\alpha_M$  and  $\alpha_B$  trend to constant values, but  $\alpha_M$  does not go to 1.0 and  $\alpha_B$  to 0.0, because the cross-section still distorts and the torsion cannot be fully restrained from the tension flange alone. For small  $k_{tx}$   $\alpha_M$  and  $\alpha_B$  also become constant, in this case reflecting the influence of the lateral restraint. The limiting values of  $\alpha_M$  and  $\alpha_B$  are cross-section, member length, loading, and boundary condition dependent.

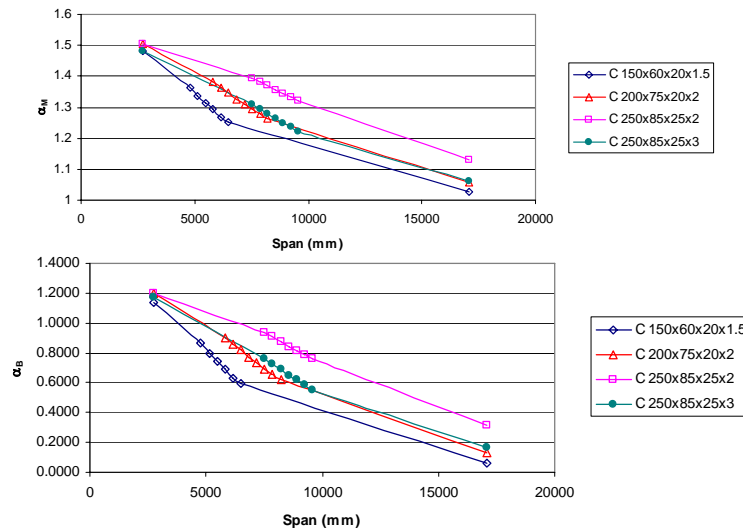


Figure 13 – Variation of  $\alpha_M$  and  $\alpha_B$  as a function of span length and section

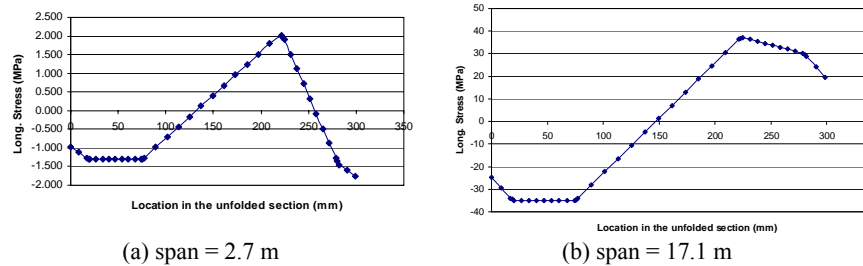


Figure 14 – Stress distribution at mid-length for C250x85x25x2

The variation of  $\alpha_M$  and  $\alpha_B$  for different cross-sections and span lengths are provided in Figure 13. Over the practical range of lengths  $\alpha_M$  and  $\alpha_B$  vary considerably, reflecting the fact that moment ( $\propto L^2$ ) and bimoment (torsion) vary differently as a function of length. However, despite this variation the limiting values of  $\alpha_M$  and  $\alpha_B$  for short span length are essentially cross-section independent; and independent of  $k_{Tx}$ . For long span lengths  $\alpha_M$  approaches 1.0 and  $\alpha_B$  approaches 0.0, but as Figure 13 shows, and Figure 14 more directly indicates, even at impractically long span lengths the pure bending case is still not quite reached.

## DESIGN METHODS: AISI SPECIFICATION

Purlins with tension flange restraint are a longstanding problem in cold-formed steel design. In AISI-S100-07 such purlins are designed per Section D6.1.1, or by testing. Section D6.1.1 defines the nominal capacity in bending,  $M_{nR}$ , as:

$$M_{nR} = R_D S_e F_y,$$

where,  $R_D$  is a reduction factor based on the depth of the beam and falls between 0.4 and 0.7,  $S_e$  is the effective section modulus (determined based on pure bending stress) and accounts for local buckling, and  $F_y$  is the yield stress.

In 2007, AISI-S100 adopted a new method, Section C3.6, to account for the influence of torsional stresses on section capacity. While the method is specifically excluded from purlins with tension flange restraint (due to the existence of Section D6.1.1) it is included here to understand better this important case. The C3.6 method uses a similar format as D6.1.1, where the nominal capacity,  $M_{nT}$ , is defined as

$$M_{nT} = R_T S_e F_y.$$

The reduction factor,  $R_T$ , is the ratio of the bending stress to the combined bending plus warping stress at the location of maximum combined stress; i.e. if



$(x^*, y^*)$  is the location in the cross-section where  $\sigma(x^*, y^*) = \max|\sigma_M + \sigma_B|$ , then for an unbraced section:

$$R_T = \sigma_M(x^*, y^*) / [\sigma_M(x^*, y^*) + \sigma_B(x^*, y^*)].$$

Further, if  $(x^*, y^*)$  is at the web/flange juncture  $R$  may be increased by up to 15%, but not to exceed 1.0.

### DESIGN METHODS: EXTENDING DIRECT STRENGTH METHOD

In the Direct Strength Method the nominal moment capacity,  $M_n$ , is defined through a series of expressions that may be summarized functionally as:

$$M_n/M_y = f(M_{cr}/M_y, M_{crd}/M_y, M_{cre}/M_y)$$

where the functions ( $f$ ) are given in Appendix 1 of AISI-S100, and  $M_{cr}/M_y$ ,  $M_{crd}/M_y$ , and  $M_{cre}/M_y$  are the elastic local, distortional, and global buckling moments normalized by the moment at first yield,  $M_y$ . If one analyzes the stability of the section assuming  $\sigma = My/I$  ( $\alpha_M = 1.0$ ,  $\alpha_B = 0.0$ ) as is common, the results for typical cross-section stability results using CUFSM (Schafer and Ádány 2006) are provided for the C 250x85x25x2 section in Figure 15. The first two minima indicate  $M_{cr}/M_y = 1.18$ , and  $M_{crd}/M_y = 1.20$ , while the third minima is an unusual feature of including the restraint in the finite strip model, and is a form of restrained lateral-torsional buckling often referred to as lateral-distortional buckling ( $M_{cre}/M_y = 0.56$ ).

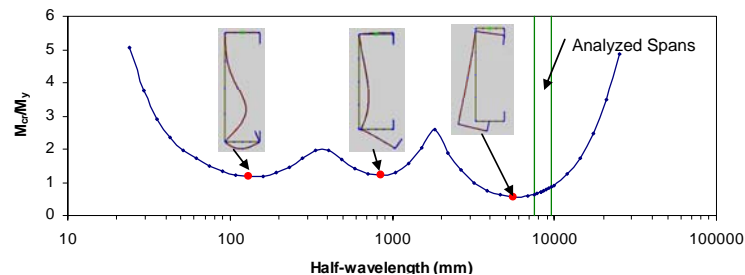


Figure 15 –Finite strip analysis for a laterally restrained C-section

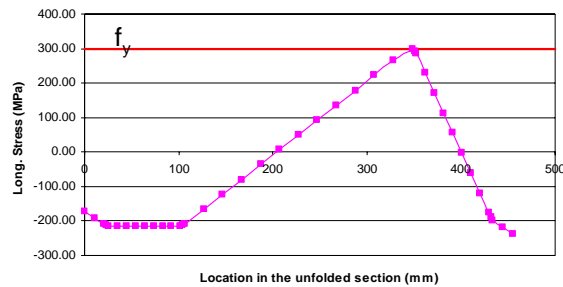
Inherent in the DSM expressions and the preceding stability analysis is the assumption that only pure bending exists in the cross-section. As previously shown herein, this is not the case, how can the DSM moment expressions be extended to cover this case? To extend DSM it is proposed that the elastic stress distribution on the section with the maximum combined stresses be employed for determination of local, distortional, and global buckling.

The first step is to determine when first yield occurs, for a given pressure,  $p$ , the stress is determined and the values scaled such that  $\sigma(x^*, y^*) = F_y$ , as shown in

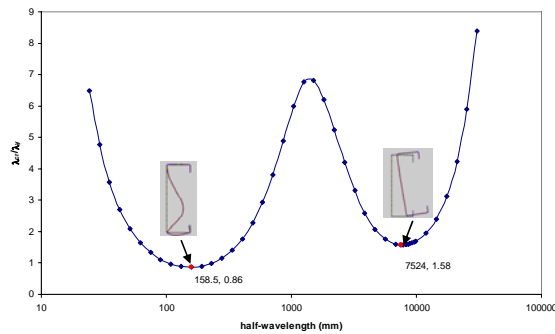
Figure 16a, for one of the C-sections studied herein. The pressure corresponding to this stress distribution is termed  $p_y$ . Next perform the cross-section stability analysis with the applied stress distribution defined by  $p_y^4$  and determine  $p_{cr}/p_y$ ,  $p_{crd}/p_y$ , and  $p_{cre}/p_y$  as shown in Figure 16b. These nondimensional ratios replace the M ratios in all of the DSM equations and provide a prediction of the capacity. For the simply supported case, and given the distributed load along the purlin,  $p$ , the distributed load  $p_n$  is converted back to moment  $M_n$  via:

$$M_n = p_n \ell^2 / 8$$

thus providing a prediction for the moment that the member will carry (in the presence of that moment plus associated bimoment from the loading).



(a) stress distribution caused by  $p$ , scaled to first yield



(b) finite strip analysis results under stress distribution of (a), note distortional buckling is indistinct, but at high enough load factors to be safely ignored

Figure 16 – Applied stress and finite strip analysis of C 250x85x25x2 at a span of 7524mm.

<sup>4</sup> In addition to including the reference applied stress  $\sigma = \alpha_M \sigma_M + \alpha_B \sigma_B^*$ , the lateral restraint and rotational spring,  $k_{rx}$ , at mid-width of the tension flange are also included. Thus, the finite strip model is an attempt to model the complete system, under its expected nonlinear stress distribution.

## COMPARISON WITH DESIGN METHODS

The design methods are compared for the sections, restraint, and span lengths of Table 1 and given in Table 2. The R-factor method of AISI D6.1.1 provides a reduction in the strength as the section depth increases. This reduction ( $R_D$ ) does not follow the same trend as the ratio of maximum bending stress to maximum combined stress ( $R_T$ ). Both of the AISI methods use local stability under the pure bending stress (i.e., that is what  $S_e F_y$  is a measure of) and ignore the actual state of stress in their attempt to empirically correct the strength.

The importance of considering stability for the actual combined stress is highlighted by the results of Figure 15 and Figure 16b, and shown to impact the strength significantly in Table 2 for the DSM solutions. Another interesting feature of including the actual combined stress is that strength is predicted to increase with span length. This counter-intuitive result occurs because the bimoment has less influence on the stress at longer lengths; a fact also reflected in  $R_T$ . To readily compare DSM under the combined stresses with the AISI methods  $M_{nDSM2}$  is divided by  $S_e F_y$  to provide an equivalent prediction for “R” in the final column of Table 2. The DSM method predicts that span length is more important than section depth, and shows smaller variation in predicted R.

Table 2 – Comparison of design methods

section	span (m)	AISI D6.1.1		AISI C3.6		Direct Strength Method		$M_{nDSM2}/S_e F_y$
		$R_D$	$M_{nR}$ (kN.m)	$R_T^*$	$M_{nT}$ (kN.m)	$\sigma=1.0\sigma_M$ $M_{nDSM1}$ (kN.m)	$\sigma=\alpha_M\sigma_M+\alpha_B\sigma_B^*$ $M_{nDSM2}$ (kN.m)	
150x60x20x1.5	4.8	0.7	4.26	0.70	4.26	4.45	2.92	0.48
	6.5			0.76	4.63		3.35	0.55
200x75x20x2	5.8	0.65	8.69	0.71	9.49	9.02	6.14	0.46
	8.2			0.77	10.29		7.33	0.55
250x85x25x2	7.5	0.4	7.86	0.71	13.95	11.70	8.14	0.41
	9.6			0.74	14.54		8.74	0.44
250x85x25x3	7.5	0.4	12.17	0.74	22.52	17.64	14.83	0.49
	9.6			0.79	24.04		15.38	0.51

\* 15% increase for max stress at web/flange juncture not applied.

## FUTURE RESEARCH

Generalization of the method ( $\alpha_M$ ,  $\alpha_B$ ) for determining stress demands with tension flange restraint is needed. In particular, partial lateral restraint needs to be accounted for, as does varying member end conditions (i.e., presence or lack of anti-roll clips). Extension of the design method comparison to a greater number of sections and comparison to experimental capacities is also needed.

## CONCLUSIONS

When singly symmetric sections are used as bending members they may be subjected to relatively complex combined longitudinal stresses due to the presence of bending and warping torsion. For the specific case of a member with bracing and loading along the tension flange, Winter's approximate method is empirically extended to predict the combined stresses. These combined stresses have a significant impact on the stability and strength of the member, as illustrated through a novel extension of the Direct Strength Method for the design of members under such combined stresses. Work remains to generalize the proposed methods and compare with available experiments.

## ACKNOWLEDGEMENTS

The authors are indebted to USIMINAS and to CNPq (Conselho Nacional de Desenvolvimento Científico e Tecnológico) (Brazil) for the grants awarded. The work reported herein was conducted by the first author as part of his master's thesis at Universidade de São Paulo under Prof. Malite's guidance and during a two months stay at Johns Hopkins University as a visiting student scholar.

## REFERENCES

- AISI-S100 (2007). North American Specification for the Design of Cold-formed Steel Structural Members. American Iron and Steel Institute Washington, D.C.
- ABAQUS (2007). "ABAQUS/Standard Version 6.7-1.", Dassault Systèmes, <http://www.simulia.com/>, Providence, RI.
- ANSYS (1997). User's guide for revision 5.5. Houston. v.1.
- Basaglia, C.D. (2004). "Sobre o comportamento estrutural de telhas de aço considerando a interação com as telhas" – in Portuguese, (Behavior of purlin-sheeting systems). Dissertation (Master), Universidade de São Paulo, São Carlos.
- Clarke, M. J.; Hancock, G. J. (2000). "Purlin design to AISI LRFD using rational buckling analysis." Proc. of the 15<sup>th</sup> Int'l. Spec. Conf. on Cold-Formed Steel Structures.

- LaBoube, R. A., Golovin, M. (1990). "Uplift behavior of purlin systems having discrete braces." Proc. of the 10<sup>th</sup> Int'l. Spec. Conf. on Cold-Formed Steel Structures.
- Lucas, R.M.; Al-Bermani, F.G.A; Kitipomchai, S. (1997). "Modelling of cold-formed purlin-sheeting systems: simplified model." *Thin Walled Structures*, 27 (4) 263-286.
- Papangelis, J.P.; Hancock, G. J.; Trahair (1998). "Computer design of cold-formed C- and Z-section purlins." *Journal of Constructional Steel Research*, 46 (1-3) 169-171.
- Pekoz, T. B., Soroushian, P. (1982). "Behavior of C- and Z- purlins under wind uplift." Proc. of the 6<sup>th</sup> Int'l. Spec. Conf. on Cold-Formed Steel Structures.
- Quispe, L.; Hancock, G. J. (2002) "Direct strength method for the design of purlins." Proc. of the 16<sup>th</sup> Int'l. Spec. Conf. on Cold-Formed Steel Structures, p 561-572.
- Rousch, C. J.; Hancock, G. J. (1996) "Determination of purlin R-factors using a non-linear analysis." Proc. of the 13<sup>th</sup> Int'l. Spec. Conf. on Cold-Formed Steel Structures.
- Schafer, B. W. (2008). "Review: The Direct Strength Method of cold-formed steel member design." *Journal of Constructional Steel Research*. In Press.
- Schafer, B. W., and Adany, S. (2006), "Buckling analysis of cold-formed steel members using CUFSM: Conventional and constrained finite strip methods." Proc. of the 18<sup>th</sup> Int'l. Spec. Conf. on Cold-Formed Steel Structures, 39-54.
- Sears, J. M.; Murray, T.M. (2007). "Proposed method for the prediction of lateral restraint forces in metal building roof systems." Annual Stability Conf. Proc., Structural Stability Research Council.
- Seek, M.W.; Murray, T.M. (2007). "Lateral brace forces in single span Z-section roof systems with interior restraints using the component stiffness method." Annual Stability Conf. Proc., Structural Stability Research Council.
- Vlasov, V. Z. (1961). "Thin-walled elastic beams." Trad. Y. Schechtman (Israel Program for Scientific Translation, Jerusalem). 2 ed. Washington: Published for the National Science Foundation.
- Vieira Jr., L. C. M. (2007). "Análise numérica do comportamento estrutural e da resistência de telhas de aço restringidas pelas telhas" – in Portuguese, (Numerical Analysis of cold-formed steel purlin-sheeting systems). Dissertation (Master), Escola de Engenharia de São Carlos – Universidade de São Paulo, São Carlos.
- Winter G.; Lansing W.; McCalley R. B. (1950). "Performance of Laterally Loaded Channel Beams." Four papers on the performance of thin walled steel structures, Cornell University, Engineering Experiment Station, Reprint No. 33.

## **Flexural Resistance of Cold-formed Steel Built-Up Box Sections Subjected to Eccentric Loading**

L. Xu<sup>1</sup> and P. Sultana<sup>2</sup>

### **Abstract**

In cold-formed steel building construction, there are several applications where built-up box sections made of a C-shape nested with a track section, with screw fastenings, are used to resist loads induced in a structural member; when a single section is not sufficient to carry the design load. The cold-formed steel box section may be subjected to eccentric loading when the web of one of the sections receives the load and transfers it through the connection to another section. There may be an unequal distribution of load in cold-formed steel built-up box assemblies loaded from one side. In the current North American Specification for the Design of Cold-Formed Steel Structural Members (CSA, 2002), there is no guideline or design equation to calculate the flexural capacity of this type of section. Cold-formed Steel Framing Design Guide (AISI, 2002) has recommended that the moment resistance and moment of inertia of the built-up sections can be taken as the sum of the two components; based on deflection compatibility of the components. However, this design approximation has yet to be justified by experimental or numerical study especially for the case of eccentric loading. Therefore, a research project involving finite element analysis was undertaken to investigate the flexural behaviour of built-up box sections assembled from cold-formed steel C-shape and track sections when subjected to eccentric loading. The proposed finite element model of the built-up box sections was validated with the tests carried out by Beshara and Lawson (2002). The ultimate moment capacities obtained from the finite element analysis were then compared with the predictions from the current design method; in order to

---

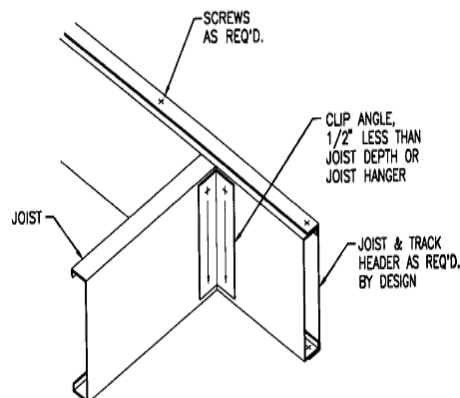
<sup>1</sup> Associate Professor, The Canadian Cold-formed Steel Research Group, Department of Civil and Environmental Engineering, University of Waterloo, Waterloo, Ontario, Canada.

<sup>2</sup> Former Research Assistant, The Canadian Cold-formed Steel Research Group, Department of Civil and Environmental Engineering, University of Waterloo, Waterloo, Ontario, Canada.

asses its suitability. Parametric studies were carried out to identify the factors affecting the flexural capacity of built up cold-formed steel box sections.

### Introduction

Cold-formed steel (CFS) sections such as C-shape and track sections are extensively used in low- and mid-rise residential and commercial building construction in North America. While single sections are not sufficient to sustain applied loads, built-up sections made of back-to-back C-shapes or a nested C-shape with a track section forming a box section, are normally used to carry heavier loads. For example, the built-up box girders or headers are commonly used for floor or wall openings as structural members to support floor joists which are connected to the web of one component of the built-up box assembly as shown in Figure 1. There may also be an unequal distribution of the load in the built-up box section and the section may also be subjected to torsional moments when loaded from one side. Unequal load distribution can potentially lead to a reduction in capacity compared to the sum of the capacities of the individual components that make up the built-up section. As a result, the resistance contributed by the component of the built-up section which is not directly connected with the floor joists, is affected the efficiency of the fasteners in transferring load and possibly other factors. The current North American Specification for the Design of Cold-Formed Steel Structural Members (CSA, 2001) does not provide any guideline on this issue. The Cold-Formed Steel Framing Design Guide (AISI, 2002) suggests that the moment of resistance and inertia of built-up sections can be approximated as the sum of that of the individual components. Addressing these problems presents an interesting challenge for the designer and more research is required to understand the flexural behaviour of CFS built-up box sections subjected to eccentric loading.



**Figure 1:** Joist to Joist-header Assembly (CSSBI, 1994)

The objective of this study is to understand the flexural behaviour of CFS built-up box sections subjected to eccentric loading, and to verify whether the current design practice for calculating the moment capacity of the of CFS built-up box section is conservative or not. The built-up box section studied herein is made from nesting a C-shape with a track section, with self-drilling screws fastened at both the top and bottom flanges. The C-shape receives the applied load first, and then transfers the load to the track section through the self-drilling screws. A finite element (FE) model is developed using the ANSYS program to determine the ultimate moment capacity of CFS built-up box sections. After that, parametric studies are conducted using FE analysis to identify the factors affecting the moment capacity of the built-up box section.

### **Previous Experimental Investigation**

A thorough literature review of previous work related to the flexural capacity of CFS built-up box sections subjected to eccentric loading was conducted. As a result, very little information was found. Serrette (2004) investigated the flexural performance of CFS built-up box rafters under eccentric loading. The built-up box sections were made with two face-to-face C-shapes, with a track section cover at the top and bottom flanges of the C-shapes respectively. The tests revealed that failure of the rafters under the eccentric loading condition ultimately resulted from twisting. The analytically computed capacities of the tested box assemblies were compared with the test values. The cumulative strength of the box members was computed based on the assumptions that there is no composite flexural action between the components and that lateral buckling is restrained. The limited test data suggests that the eccentric loading and the mechanism of load transfer from the directly loaded C-shape member to the adjacent C-shape member induces twist in the box assemblies. The edge loaded box assemblies were able to resist at most 85-90% of their calculated fully braced flexural capacity.

Beshara and Lawson (2002) conducted internal tests to evaluate the impact of varying the location of connection screws on the behaviour of built-up box sections. Two types of built-up box assemblies were tested. The first type assembly is nested a C-shape with a standard track section to form a box section while in the second assembly the standard track section is replaced with a proprietary product, named TradeReady® rim track (TD) featured with unequal flanges. The assemblies are fastened with self-drawing screws at locations of flanges and lips, respectively. All specimens tested by Beshara and Lawson were fabricated by nesting a C-Shape with either a standard or a TD track section. The cross-section dimensions and yield strengths of the specimens are



listed in Table 1. The C-shape has punched out holes spaced at 4 ft. (1219 mm), and the dimension of the hole are 1-1/2 in. (38 mm) by 4 in. (102 mm). The C-Shape and track section are fastened with #10-16 HWH T-3 self-drilling screws placed 12 in. (305 mm) on center.

The test assembly consisted of two parallel CFS built-up box specimens with span lengths of 10 ft. (3048 mm). Two 3 ft. (914) mm long cross-member beams framed into webs of the specimens through hot-rolled steel angle brackets connected the specimens. A single row of #12 self-drilling screws connected each angle bracket to the web of the C-shape specimen, defining the two vertical lines of load application along the depth of the web. The lines of loading were spaced 32 in. (813 mm) apart. The load was applied at the centre of a load distribution beam, loading each cross member equally and creating a region of constant bending moment between the two lines of load application on both specimens. The distance between the supports of specimens and the line of loading was 44 in. (1118 mm).

**Table 1 Component cross-section dimensions and yield strengths**

Section	$F_y$ (MPa) <sup>1</sup>	Thickness (mm) <sup>2</sup>	Depth (mm)	Top flange (mm)	Bottom flange (mm)	Lip (mm)
C-shape	349	1.61	254	76.2	76.2	25.4
Standard track	307	1.44	254	31.8	31.8	
TD track	417	1.39	254	31.8	63.5	

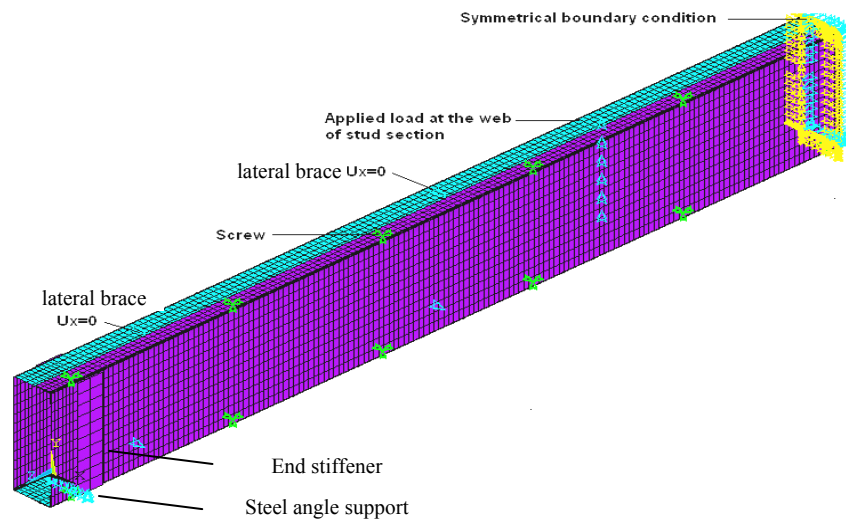
<sup>1</sup> 1 MPa = 0.145 ksi.; <sup>2</sup> 1.0 mm = 0.0394 in.

Investigation with the load applied on the C-shape side and track section side were conducted. It was found that the moment capacities of the assemblies from the tests were considerably less than the capacities calculated by adding the individual moment capacity of the C-shape and track section as suggested by CFS Framing Design Guide (AISI, 2002). Based on the results of the test series, Beshara and Lawson (2002) recommended that the nominal moment capacity of the built-up box sections should be considered equivalent to 75% of the combined nominal capacities of its components evaluated based on the Specification for the Design of Cold-Formed Steel Structural Members (AISI 1996) .

#### **Mode of Finite Element Analysis**

The FE model was developed to simulate the tests conducted by Beshara and Lawson (2002). Instead of simulating the whole test set up, initially, a half of the

specimen was modeled to take advantage of symmetry. The analysis results show that the lateral bracing between the two built-up box specimens can sufficiently be represented by setting the lateral displacement  $U_x=0$  at the location of bracing. Therefore, the model is further simplified as a quarter of the test setup as that shown in Figure 2. The Shell181 element in ANSYS was selected to model the C-shape and track sections, while the effect of screws has been accounted for by coupling translational and rotational degrees of freedom of the global x, y, and z-directions. For regions around the holes and supports, refined meshes were created to account for stress concentrations. The corner inside bend radius of CFS C-shape and track section is taken as two times of steel thickness. As CFS end stiffeners were used at support locations to prevent web crippling, the stiffeners were modeled by creating Shell181 elements that overlapped the web in the location of the stiffener, and a bond contact was defined to model the influence of the stiffener retaining the web deformation of the specimens.



**Figure 2:** Finite Element Model

The Young's modulus of the steel is taken as 29435 ksi (20300MPa), and Poisson's ratio =0.3. The yield stresses of the steel are listed in Table 1. The effects of cold work forming and residual stress were not accounted for because the ultimate moment capacities obtained from the FE analysis were compared with the nominal moment calculated according to CSA-136 (2001) without considering the cold work of forming.

In the test carried out by Beshara and Lawson (2002), the CFS built-up box specimens were placed on top of an inverted structural steel angle at one end, and a roller on the other end to create the simply supported condition. There was no bearing plate at the support. Such support condition was first investigated in this study to validate the FE model.

The flexural behaviour of thin-walled structures is sensitive to initial geometrical imperfections, especially at the ultimate load level. No measurement was taken to identify the initial geometric imperfection of the CFS built-up box specimens tested by Beshara and Lawson (2002). In this study, first eigenvalue buckling analysis was performed on the model with no initial imperfections to establish the probable collapse mode using ANSYS. Initial imperfection was incorporated in the FE model by scaling the first eigenvalue buckling mode shape, and then including it in the FE model with perfect geometry so that the maximum imperfection does not exceed the thickness of the section, as proposed by Schafer and Pekoz (Schafer and Pekoz, 1998). Then, a nonlinear analysis of the structure containing the imperfection was carried out to determine the ultimate moment capacity.

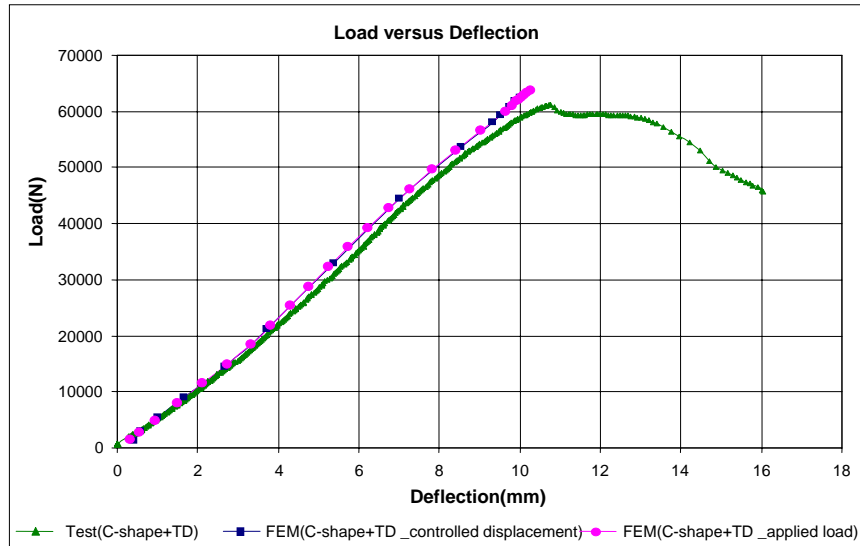
In FE analysis the loading can be applied in either one of the two ways: apply the load directly on the model, or impose displacement on the model. In order to simulate the test results, loading was applied in both ways and a comparison was made between the results in terms of the ultimate moment capacity, load-deformation behaviour, failure modes, and stress conditions. In the FE analysis while loading was the applied force, a 650 lb (2890 N) load was applied vertically downward on each node at the locations of screws attaching the built-up box assembly and cross member. The load was applied incrementally by defining the initial load as 78 lb (347 N), with a maximum and minimum load increment of 195 lb (867 N) and 0.65 lb (2.9 N), respectively. When loading was applied as the controlled displacement, a 0.7 in. (17.78 mm) vertical downward displacement was applied incrementally by defining the initial displacement as 0.014 in. (0.35 mm), with a maximum and minimum displacement increment of 0.07 in. (1.7 mm) and 0.0000145 in. (0.0003 mm), respectively. After incorporating the initial geometric imperfections, a nonlinear static analysis was performed considering both material and geometric nonlinearities. In this study, the Newton-Raphson method was used.

#### **Validation of Finite Element Model**

The nonlinear analysis was conducted with the incremental load/displacement procedure using very small increments of applied force or controlled displacement. Based on the load deflection curves shown in Figure 3, and

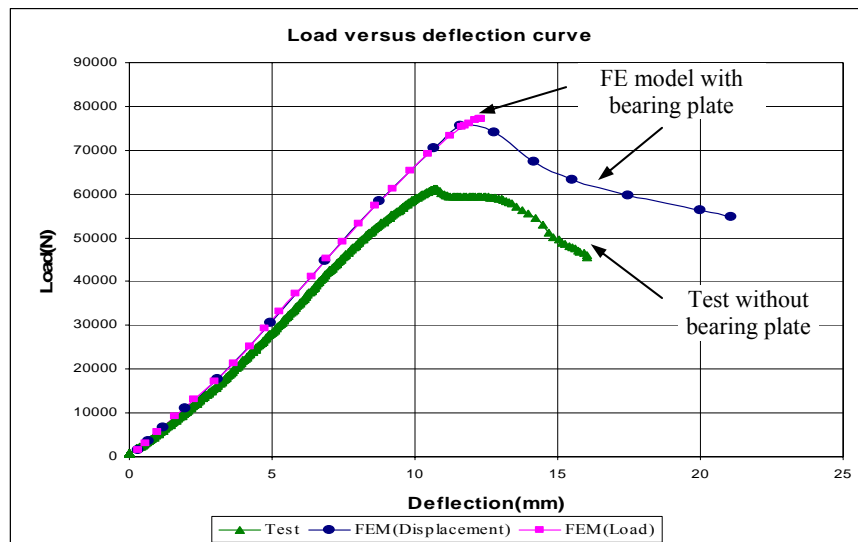
considering the difference of the ultimate moments obtained from FE analysis, and that the test are within 4%; it indicates that the FE model provides realistic simulation of the test up to the failure of the specimen. However, it was observed that the model could not predict the behaviour after reaching the ultimate load capacity; due to convergence problems even for very small increments of loading (applied force or controlled displacement). Convergence problems could not be overcome, even through the use of the Riks solution method and refining the mesh near the support. The same problem was also encountered in FE model for the built-up box section with a C-shape and a standard track section.

Upon investigating the stress and strain condition of the last converged solutions, it was found that both the von Mises stresses and strains in the C-shape at the location of the inverted steel angle support had reached the yield strength, and the percentage elongation that was reported in the material coupon test, respectively (Beshara and Lawson, 2002). To simulate the bearing support condition in practice, the inverted steel angle was replaced by a 5 mm wide steel bearing plate. The bearing plate was modeled as a 2D surface and then meshed with Shell181 elements. Bonded flexible-to-flexible contact was defined between the plate and the track section. As the C-shape comes in contact with the plate during application of load, standard flexible-to-flexible contact was also defined between the C-shape and the bearing plate at the support. The translational degree of freedom of all the nodes of the bearing plate at the support was restrained in the vertical direction.



**Figure 3:** Load-deflection curves of built-up section (inverted angle support)

Figure 4 shows the load-deflection relationship of the built-up box section with a C-shape and TD track section supported by a bearing plate at one end. It can be seen from Figure 4 that the ultimate load capacity predicted by the FE analysis with the bearing plate support is higher than that of the test with the inverted steel angle support. This is due to the local failure of the C-shape at the inverted angle support, not occurring prior to the section reaching to its ultimate load capacity in the case with the bearing plate support. Also found in Figure 4 is that when the applied load is the controlled displacement, the FE analysis is able to simulate the post-ultimate load behaviour of the specimen. Similar observations have also been perceived in the built-up box specimen formed with a C-shape and a standard track section.

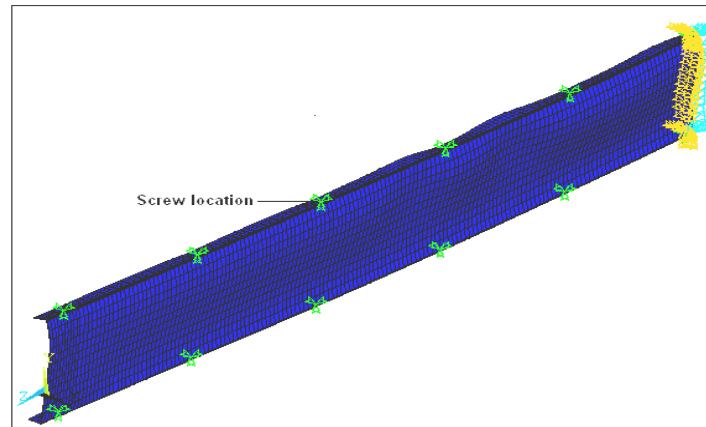


**Figure 4:** Load-deflection curves of built-up assemblies (bearing plate support)

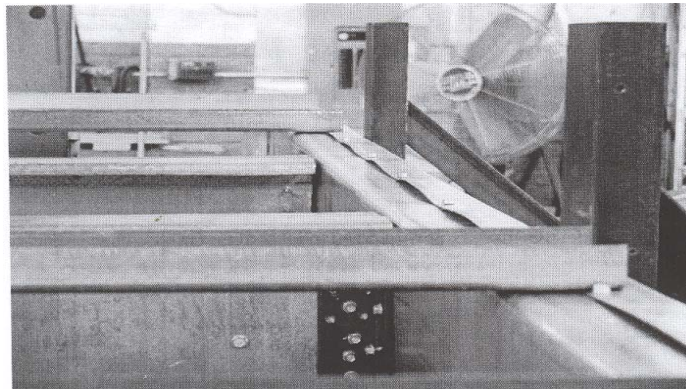
### Results Comparison

The results from the FE analysis were compared with the failure modes, load deflection curve, and ultimate moment capacity obtained from the tests (Beshara and Lawson, 2002). The failure modes shown in the FE analysis are consistent with that of the test. The top flange rippling of the track section was first observed prior to the flange buckling failure as shown in Figure 5, which was similar to that was described in the test as shown in Figure 6. The valleys of the ripples coincided with the locations of the fasteners. The load-deflection relationship obtained from the FE analysis is in good agreement as demonstrated

in Figures 3 and 4. The ultimate load capacity of the built-up section is reached when buckling occurs at the top flanges of the C-shape and track section in the constant moment region. The distortion of the built-up box section due to the eccentric loading applied to the web of the C-shape was observed in both the test and the FE analysis, as shown in Figure 7.



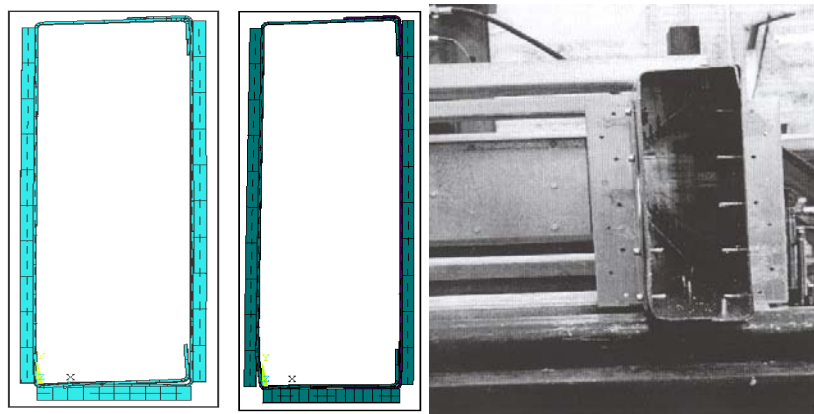
**Figure 5:** Rippled compressive flange of track section in FE analysis



**Figure 6:** Rippled compressive flange of track section in test (Beshara and Lawson, 2002)

For each type of built-up box sections, the nonlinear FE analysis was pursued with the incremental applied force and controlled displacement procedures. The ultimate moment capacities obtained from the FE analysis ( $M_{FEM}$ ) of both procedures are shown in a good agreement with each other, and with that of the

tests ( $M_{test}$ ), as illustrated in Table 2. Also presented in Table 2 are the FE analysis results of the built-up box sections supported by the bearing plate at one end of the specimens. It was found that the ultimate moment capacities of the built-up sections with the bearing plate support are 22% and 12% higher than that of the built-up sections supported by the angle support, made with TD and standard track sections, respectively. The nominal moment capacities of the built-up box sections ( $M_n$ ) listed in Table 2 are the summation of the nominal moment capacities of the corresponding C-shape and track sections as suggested by CFS Framing Design Guide (AISC, 2002). The nominal moment capacities of the C-shape and track sections are calculated in accordance with the North American Specification for Design of CFS Structural Members (CSA, 2001) and 2004 Supplement (CSA, 2004). The ratios of  $M_{test}/M_n$  and  $M_{FEM}/M_n$  are also presented in Table 2. It is clear that no matter which support condition is applied, the ultimate moment capacities obtained from either of the tests or FE analysis are lower than the nominal moment capacities calculated based on CFS Framing Design Guide (AISC, 2002). Therefore, the procedure of evaluating the flexural moment capacity of the built-up box section recommended by CFS Framing Design Guide (AISC, 2002) may not be conservative.



(a) C-shape + TD track    (b) C-shape + standard track    (c) Test: C-shape + standard track

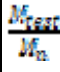

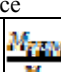
**Figure 7:** Distortion of built-up box sections

### Parametric Study

The ultimate moment capacities of CFS flexural members are highly influenced by the yield strength of the material and the width-to-thickness ratio of the flat elements in compression; assuming the members are laterally restrained

properly. For CFS built-up box sections, the capacities are affected by the effectiveness of the fasteners that connect the individual components to form the sections. Parametric studies were carried out in this study to investigate the effects of variations of web depth to thickness ratio, steel yield strength, and screw spacing, on the ultimate moment capacity of the CFS built-up box sections.

**Table 2 Comparison of ultimate moment capacity of CFS built-up box girder**

Built-up box section	Support condition	$M_{test}$ (kN-m) <sup>1</sup>	$M_n$ (kN-m)		Controlled displacement		Applied Force	
					$M_{FEM}$ (kN-m)		$M_{FEM}$ (kN-m)	
C-shape and TD tack	steel angle	17.351	22.187	0.782	17.438	0.786	17.779	0.801
C-shape and standard track	steel angle	17.458	21.194	0.824	17.984	0.848	17.194	0.811
C-shape &TD tack	bearing plate		22.187		21.103	0.951	21.557	0.971
C-shape and standard track	bearing plate		21.194		19.888	0.938	19.466	0.918

<sup>1</sup> 1 kN-m = 0.738 kip-ft

The built-up box sections in the parametric studies were formed with a C-shape and a standard track section. The length of all built-up assemblies is 126 in. (3200 mm), and the assemblies are supported on bearing plates at one ends, and rollers at other ends. The depths of sections considered in the parametric studies were 8 in. (203 mm), 10 in. (254 mm), and 12 in. (305 mm). The section thicknesses for the C-shape and track section were taken to be 0.045 in. (1.14 mm), 0.057 in. (1.44 mm) and 0.071 in. (1.81 mm). The dimensions of the flange and lip of the C-shape is 3 in. (76 mm) and 1 in. (25 mm) respectively, while the flange width of the track sections is 1.25 in (32) mm.

Initial geometric imperfections, material nonlinearity, and geometric nonlinearity were considered in the same way as stated previously. In order to predict the post-ultimate load behaviour, the loading was applied as controlled displacement in the parametric study. Shown in Figure 8 is the load versus mid-span deflection relationship associated with variation of section depth.

It is observed from Figure 8 that the FE analysis has not only successfully simulated the nonlinear load-deflection behaviour of the built-up box specimens at both prior and post ultimate load stages, but also the bilinear behaviour at the



initial loading stage. When the built-up section is initially loaded, only the bottom flange of the track section is in contact with the bearing plate at the support. As the load increases, the bottom flange of the C-shape comes into contact with the bearing plate which results in the change of the slope of the curves. The change of the slope of the load-deflection curve signifies the stiffness increase of the specimen, once the bottom flange of C-shape contacts the bearing plate.

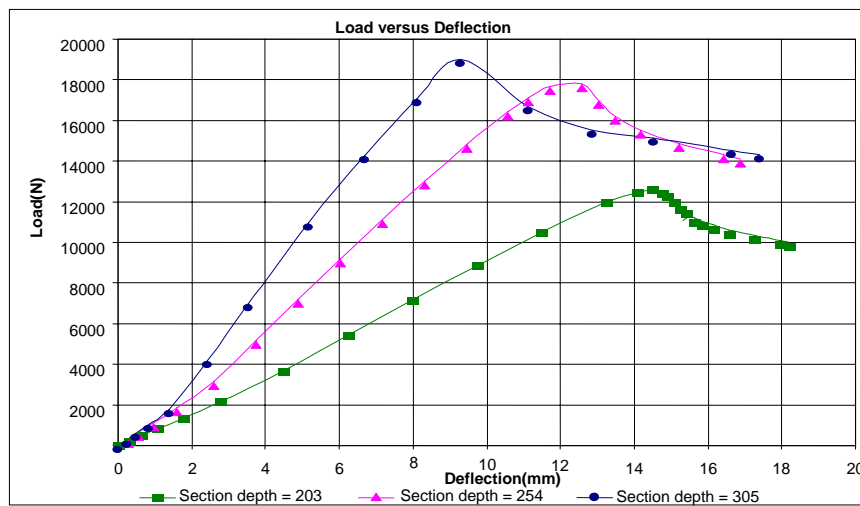


Figure 8: Load-deflection curves associated with variation of section depth

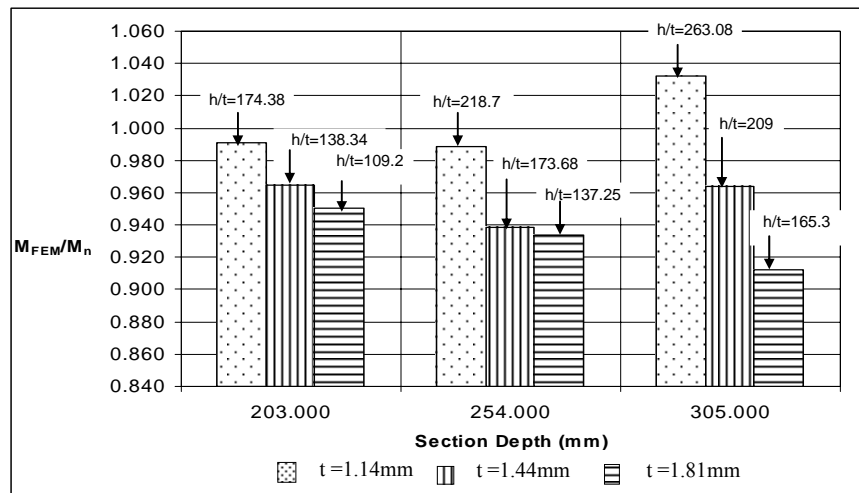
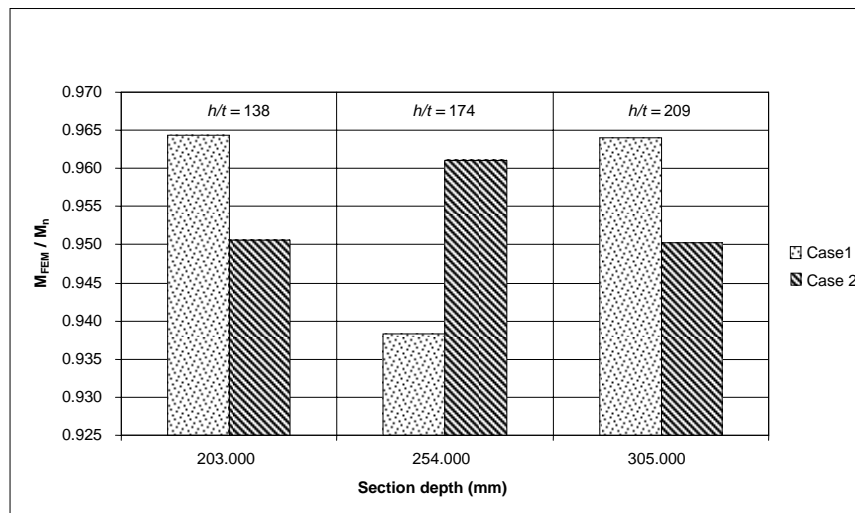


Figure 9:  $M_{FEM}/M_n$  ratio associated with variation of section thickness

The effect of section thickness on the  $M_{FEM} / M_n$  ratio is illustrated in Figure 9 for three section depths (203mm, 254mm and 305mm). It can be seen from the Figure that for a specific section depth, the  $M_{FEM} / M_n$  ratio decreases as the thickness increases, which indicates that the current practice provides better approximation of the ultimate moment capacity for the built-up sections with higher  $h/t$  ratios.

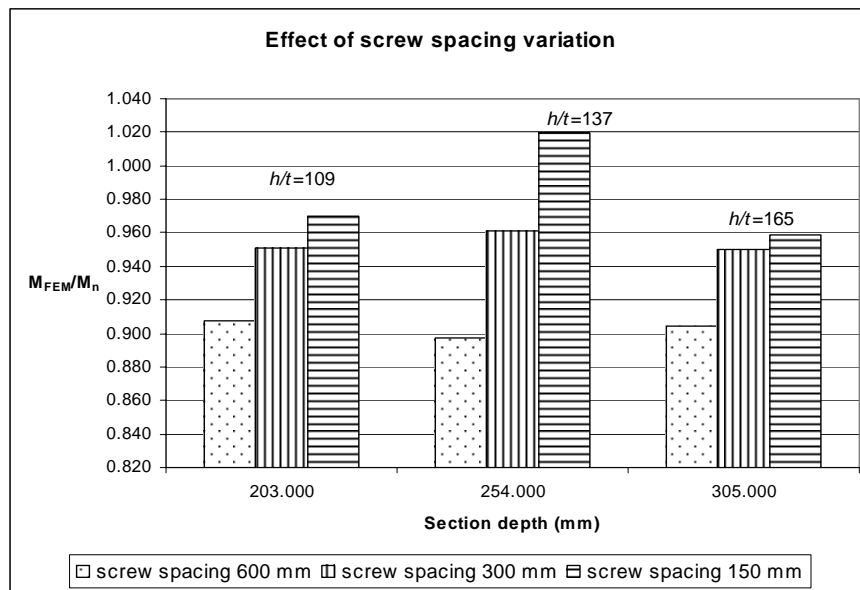
Two cases were investigated in the FE analysis on the effect of yield strength of material on the  $M_{FEM} / M_n$  ratio. In the first case, the yield strengths for the C-shape and the track section are as the same as that of the tests as 50.6 ksi(349 MPa) and 44.5 ksi (307 MPa), respectively. The yield strengths for both C-shape and the track sections are identical at 33 ksi (228 MPa) in the second case. The results for the three section depths which the section thickness  $t=0.057$  in (1.44 mm) are presented in Figure 10, and it can be seen from the Figure that the results appears to be inconclusive.



**Figure 10:**  $M_{FEM} / M_n$  ratio associated with variation of material yield stress

It is noted that the effect of screw spacing is not accounted for in the procedure of evaluation of the ultimate moment capacity of the built-up box sections suggested by the CFS Framing Design Guide (AISC, 2002). The influence of screw spacing on the ultimate moment capacity of the built-up box sections was investigated for screw spacing of 6 in. (150 mm), 12 in. (300 mm) and 24 in. (600 mm). The results of the FE analysis show that the ultimate moment capacity of the CFS built-up box sections is influenced by the screw spacing to some extent. As the screw spacing decreases, the predicted ultimate moment

capacity of the built-up section increases. The increase of the ultimate moment capacity is generally less than 6% when the screw spacing is reduced to 12 in. (300 mm) from 24 in. (600 mm) or reduced 6 in. (150 mm) from 12 in. (300 mm). The  $M_{FEM}/M_n$  ratios are also affected by the variation of screw spacing as that indicated in Figure 11. It appears that the procedure recommended by the CFS Framing Design Guide provides better estimation of the ultimate moment capacity for the built-up sections with smaller screw spacing.



**Figure 11:**  $M_{FEM}/M_n$  ratio associated with variation of screw spacing

## Conclusions

Numerical analysis was carried out with the aim of investigating the flexural behaviour of CFS built-up box sections subjected to eccentric loading, and of evaluating the appropriateness of the current design practice recommended by the CFS Framing Design Guide (AISI, 2002). A FE model was established to investigate the flexural capacity of CFS built-up box sections and validated with test results reported Beshara and Lawson (2002). Initial geometric imperfections, material nonlinearity, and geometric nonlinearity were considered in the FE analysis; and compared with the results obtained from the tests (Beshara and Lawson 2002). It was shown that the FE model could reliably predict the ultimate moment capacity as well as the prior and post

ultimate load behaviour of CFS built-up box sections. The FE analysis showed that by introducing a bearing plate at the support location, the local failure at that region can be minimized; and the ultimate moment capacity of the built-up box sections can be increased considerably compared to the inversed angle support.

A parametric study was carried out to investigate the influences of section depth, section thickness, screw spacing, and material yield stress on the ultimate moment capacities of CFS built-up box sections. From the results of the parametric studies, it was found that it is inappropriate to assume the moment capacities of CFS built-up box sections are the summation of the moment capacities of the individual components when subjected to eccentric loading. In fact, the ratio  $M_{FEM}/M_n$  was generally found to be less than one. Therefore, it is concluded that the current design practice may overestimate the moment capacities of CFS built-up box sections in the case of eccentric loading, and therefore, may not be conservative.

#### **Acknowledgements**

The authors would like to acknowledge Dietrich Design Group of Dietrich Metal Framing Inc. for providing the test report by Beshara and Lawson.

**References**

- AISI, "Specification for the Design of Cold-Formed Steel Structural Members", American Iron and Steel Institute 2002.
- AISI, "Cold-Formed Steel Framing Design Guide", American Iron and Steel Institute 2002.
- Beshara, B., and Lawson, T.J., "Built-Up Girder Screw Connection Variation Flexural Tests", Internal Report, Dietrich Design Group, 2002.
- CSSBI, "Low-Rise Residential Construction Details", Canadian Sheet Steel Building Institute, 1994.
- CSA, "North American Specification for the Design of Cold-Formed Steel Structural Members", S136, Canadian Standard Association, 2001.
- CSA, "Supplement 2004 to the North American Specification for the Design of Cold-Formed Steel Structural Members", Canadian Standard Association 2004.
- Schafer, B.W., and Pekoz, T., "Computational modelling of cold-formed steel: Characterizing geometric imperfections and residual stresses", Journal of constructional steel research, Vol.47, 1998, pp.193-210.
- Serrette, R.L., " Performance of Edge-Loaded Cold-formed Steel Built-up Box Beams", Practice Periodical on Structural Design and Construction, ASCE, Vol.9, No. 3, 2004, pp. 170-174.

## **Web Crippling Behaviour of Thin-Walled Lipped Channel Beams Subjected to EOF and ETF Loading**

Martin Macdonald<sup>1</sup>, Manoj A. Heiyantuduwa<sup>1</sup> and Jim Rhodes<sup>2</sup>

### **Abstract**

This paper presents the results of an investigation conducted to study web crippling behaviour of cold-formed thin-walled steel lipped channel beams subjected to End-One-Flange (EOF) and End-Two-Flange (ETF) loading conditions as defined by the American Iron and Steel Institute (AISI). An experimental program was designed to obtain the load-deformation characteristics of beam members with varying cross-sectional and loading parameters under the two web crippling loading conditions. The results of the experiments mainly comprised of the ultimate web crippling strength values of thirty-six specimens tested. Nonlinear finite element models were developed to simulate web crippling failure of the two loading conditions considered in the experimental program. The comparison of experimental and finite element results revealed that the nonlinear finite element models were capable of closely simulating the web crippling failure behaviour observed in the experiments. Web crippling strength predicted from the AISI Specification was also compared with the experimental results and the comparisons indicated considerable underestimations for the range of specimens under EOF and ETF loading conditions.

### **Introduction**

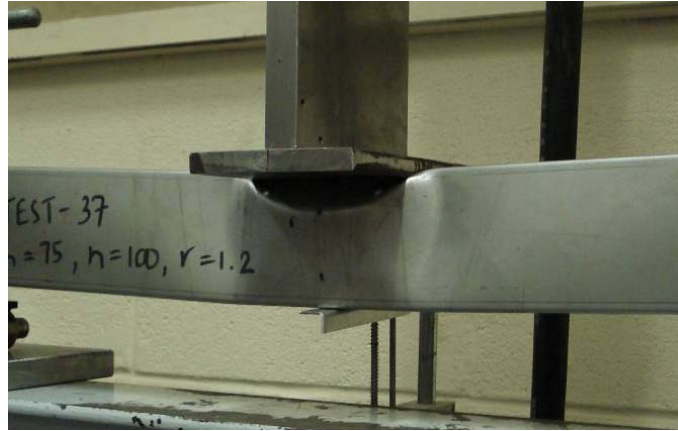
Web crippling failure may occur at places where thin-walled flexural members are subjected to high concentrated loadings or support reaction forces. Figure 1 illustrates web crippling failure at a loading point. Four different loading conditions where web crippling may take place, have been defined by the AISI

---

<sup>1</sup> School of Engineering and Computing, Glasgow Caledonian University, Glasgow, UK

<sup>2</sup> Department of Mechanical Engineering, University of Strathclyde, Glasgow, UK

based on the number of loadings involved and the location of failure initiated, namely, Interior-One-Flange (IOF), Interior-Two-Flange (ITF), End-One-Flange (EOF) and End-Two-Flange (ETF) loading conditions (Rhodes, 1991).



**Figure 1: Web crippling at loading point.**

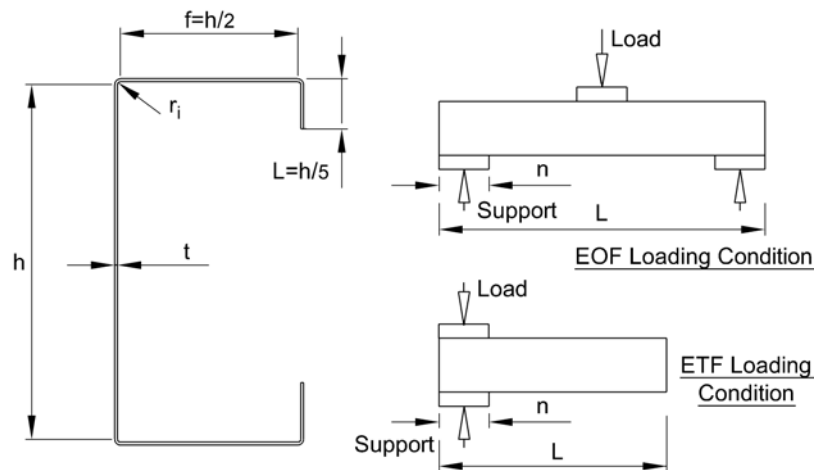
A considerable amount of research has been carried out on web crippling by numerous researchers particularly to validate various design rules for web crippling, and the majority were based on experimental investigations. The early research work conducted by Winter and Pian (1946), Ratliff (1975), Hetrakul and Yu (1979), etc. provided the basis for web crippling design rules that appeared in the early versions of the AISI Specification and consequently adopted by the other major design codes. In the recent past, a number of investigations were carried out by Young and Hancock, Prabakaran and Schuster and by Shaojie, Yu and LaBoube, and these resulted in a more unified form of design rule which was adopted by the AISI Specification - 2001 edition.

A research program was initiated to investigate web crippling behaviour of cold-formed thin-walled lipped channel beams under the four loading conditions. The results of the experimental investigations and the finite element analysis of lipped channels beams under IOF and ITF loading conditions were reported in previous publications (Heiyantuduwa, 2007 and Macdonald, 2006). The aim of this paper is to present the results of experimental investigations and finite element analysis carried out on web crippling behaviour of lipped channel sections under EOF and ETF loading conditions. The experimental results were also compared with the web crippling strength predictions from the AISI Specification.

### Experimental Investigations

Experimental investigations were designed to examine the influence of various cross-sectional and loading parameters on web crippling strength. Two separate series of tests were performed considering EOF and ETF loading conditions. The test specimens were fixed on to load bearing plates during both series of tests to prevent flange rotations and possible lateral movements of specimens during loading. Each series comprised of eighteen test specimens manufactured from 0.78mm thickness carbon steel sheets. The test specimens were designed to have three different corner radii and two different web heights, and were loaded with three different sizes of load bearing plate. Figure 2 illustrates the cross-sectional and loading parameters used in the specimen design. A separate series of tensile tests were carried out prior to specimen manufacture in order to obtain the material properties of the individual steel sheets.

During the web crippling tests, applied load, displacement at the loading point and the displacement at a number of other critical points were measured. The results of the experimental investigations were used to validate the finite element models and also to check the validity of web crippling strength predictions obtained from design codes.

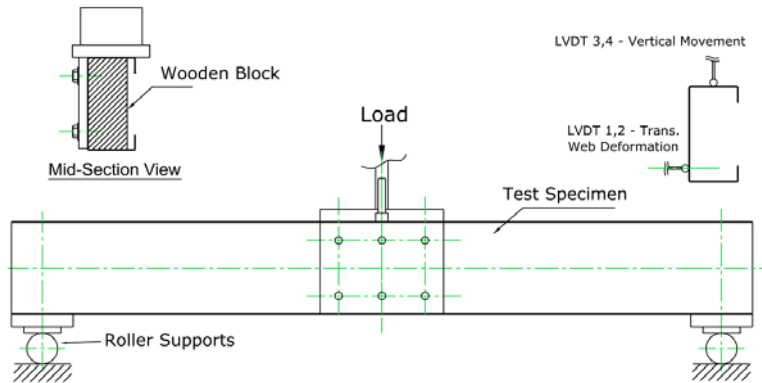


**Figure 2: Cross-sectional and loading parameters.**

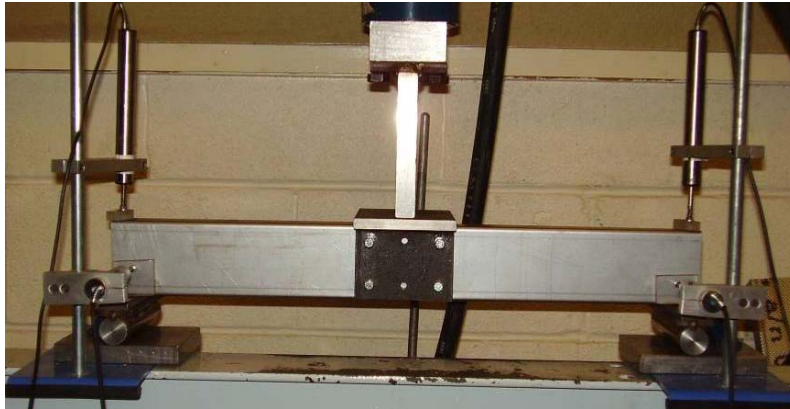


### EOF Loading Tests

EOF loading tests were performed as three point bending tests, however, the failure was intended to occur at the end of the beam (at supports) and the loading was applied to the mid-point of the beam. The load bearing plate was fully fixed at the mid-point in order to prevent failure around this area. The test rig used in the EOF loading tests is shown in Figure 3, and Figure 4 shows a photograph of the test rig with displacement transducers attached.



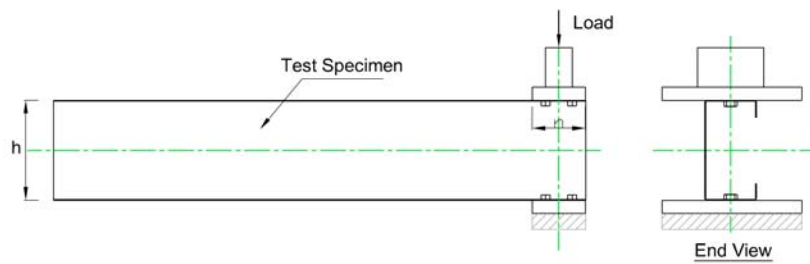
**Figure 3: Test rig for EOF loading tests.**



**Figure 4: Photograph showing EOF loading test rig with displacement transducers.**

### ETF Loading Tests

ETF loading tests were performed by applying a load which was directly above the support. Hence, the failure initiated at the end of the beam due to the heavy loading and the support reaction force. The test rig used in the ETF loading tests is shown in Figure 5, and Figure 6 shows a photograph of the test rig with displacement transducers attached.



**Figure 5: Test rig for ETF loading tests.**



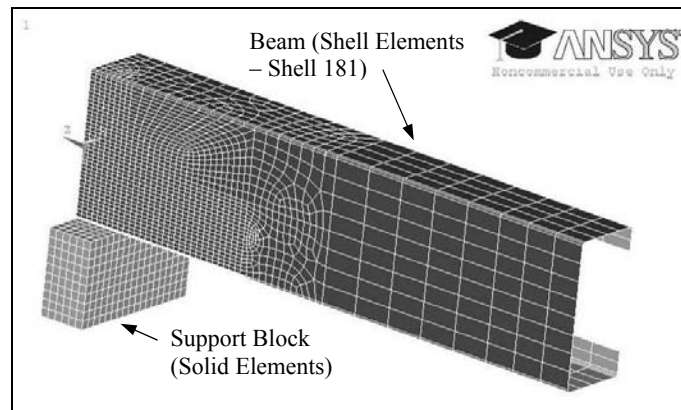
**Figure 6: Photograph showing ETF loading test rig with displacement transducer.**

### Finite Element (FE) Models

Finite element models were developed to simulate the tests conducted in the experimental investigations. Finite element analysis package ANSYS® was employed for the modelling and analysis procedure (ANSYS, 2004). Nonlinear characteristics such as material nonlinearity, geometric nonlinearity and contact situations were considered to accurately represent web crippling failure. Two different finite element models were developed to represent EOF and ETF loading tests described in the experimental investigations.

#### FE Models for EOF Loading Condition (EOF-FE Models)

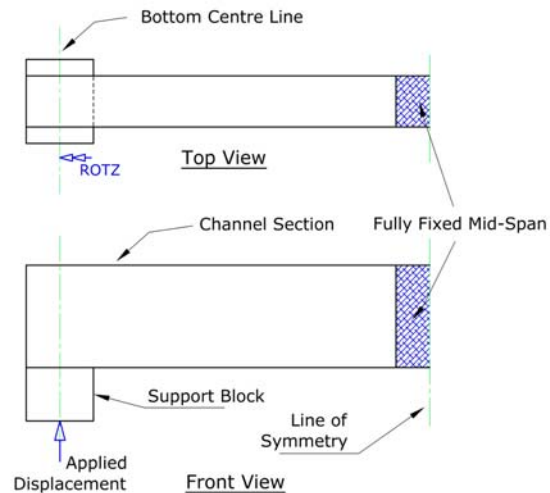
EOF-FE models were developed to simulate the EOF loading tests carried out in the experimental investigations. The geometric model for the EOF-FE models was similar to the test setup used in the EOF loading tests. However, the advantage of the vertical symmetry was used to create a half-model in this case. The geometry was initially created using the solid modelling techniques within ANSYS. Figure 7 shows the element mesh generated for EOF-FE models. In this case, web crippling failure was expected to occur at the support reaction point. Thus, the mesh was controlled to have relatively finer elements closer to the support area and coarser elements further away from the support area.



**Figure 7: Element mesh for EOF-FE models.**

The support reaction force was applied using a support block modelled with solid elements and appropriate boundary conditions were employed to simulate

the actual supports used in the experiments. Contact elements were employed in between the support block and the lipped channel beam to represent the actual loading situation. Furthermore, the flange-fixed condition was represented using a set of nodes with coupled degrees-of-freedom. The loading was applied with displacement control onto a set of nodes selected along the bottom centre line of the support block. The rotation about the Z axis was restrained along the centre line to represent the actual support conditions in the test setup. Figure 8 shows the boundary conditions used for the EOF-FE models. A set of nodes around the mid-span of the beam were fully restrained against translations and rotations in all directions.

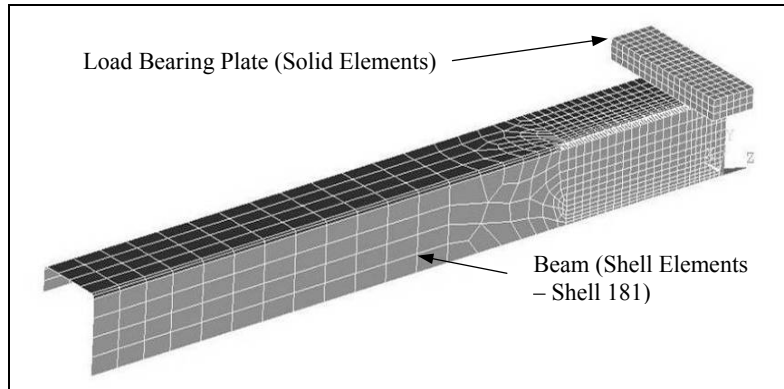


**Figure 8: Boundary conditions for EOF-FE models.**

#### FE Models for ETF Loading Condition (ETF-FE Models)

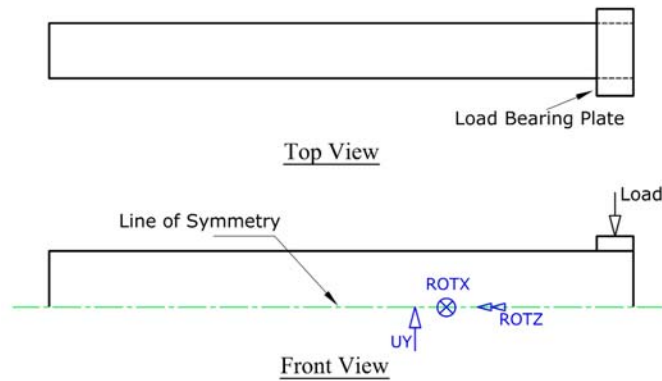
ETF-FE models were developed to simulate the ETF loading tests carried out. In this case, web crippling failure was expected to occur at the end of the beam under two opposite forces inline with each other. The geometric model for the ETF-FE models was similar to the test setup used in the ETF loading tests. The ETF loading setup was symmetrical about the horizontal plane passing through the centre line of the beam. Therefore, only one-half of the setup was modelled to use the advantage of symmetry. Figure 9 shows the element mesh generated for the ETF-FE models. Web crippling failure was identified to occur around the central area of the web under the load bearing plates. Thus, the mesh was

created to have relatively small elements around the central part of the web and coarse elements further away from the failure region.



**Figure 9: Element mesh for ETF-FE models.**

The loading was applied through a load bearing plate using the displacement control method. Contact elements were used between the load bearing plate and the top flange of the beam. Figure 10 shows the boundary conditions used in the ETF-FE models.



**Figure 10: Boundary conditions for ETF-FE models.**

### **AISI Web Crippling Strength Predictions**

The nominal web crippling strength of thirty-six specimens under EOF and ETF loading conditions was determined using the AISI Specification (AISI, 2001). The AISI Specification, 2001 edition provides a single equation to determine the nominal web crippling strength with a number of coefficients to select from the tables provided based on the type of cross-section profiles, loading condition and the flange condition where applicable.

### **Results and Comparisons**

The load-displacement graphs obtained from the tests and finite element analysis were used to determine the ultimate web crippling strength of the specimens. Tables 1 and 2 present the web crippling strength results obtained from the tests ( $P_{\text{exp.ult.}}$ ), finite element analysis ( $P_{\text{FE:ult.}}$ ) and from the AISI specification ( $P_{\text{AISI}}$ ) for EOF and ETF loading conditions respectively. Figures 11 and 12 illustrate sample load-displacement graphs obtained from tests and finite element analysis along with the corresponding AISI web crippling strength predictions. The finite element strength and the nominal web crippling strength predicted from the AISI specification were compared with the experimental web crippling strength results. Table 3 shows the mean and standard deviation of ratios between finite element strength and experimental strength ( $P_{\text{FE:ult.}} / P_{\text{exp.ult.}}$ ) as well as the AISI predictions and experimental strength ( $P_{\text{AISI}} / P_{\text{exp.ult.}}$ ).

**Table 1: Web crippling strength results for EOF loading condition.**

Test No.	h (mm)	r <sub>i</sub> (mm)	n (mm)	t (mm)	Span Length-Ls (mm)	0.2% Proof Stress (MPa)	P <sub>exp.ult.</sub> (kN)	P <sub>FE:ult.</sub> (kN)	P <sub>AISI</sub> (kN)
EOF-1	95.2	4.0	25	0.78	600	220	1.18	1.14	0.85
EOF-2	95.5	2.6	25	0.78	600	220	1.24	1.19	0.93
EOF-3	97.3	1.2	25	0.78	600	220	1.46	1.41	1.02
EOF-4	95.2	4.0	100	0.78	600	220	1.74	1.61	1.41
EOF-5	95.5	2.6	100	0.78	600	220	2.00	1.92	1.54
EOF-6	97.3	1.2	100	0.78	600	220	2.25	2.39	1.71
EOF-7	95.5	2.6	50	0.78	600	220	1.43	1.52	1.18
EOF-8	97.3	1.2	50	0.78	600	220	1.70	1.93	1.31
EOF-9	95.2	4.0	50	0.78	600	220	1.34	1.34	1.08
EOF-10	73.3	1.2	50	0.78	600	220	1.80	2.09	1.36
EOF-11	70.0	2.6	50	0.78	600	220	1.44	1.57	1.23
EOF-12	69.2	4.0	50	0.78	600	220	1.32	1.40	1.13
EOF-13	73.3	1.2	25	0.78	600	220	1.44	1.43	1.06
EOF-14	70.0	2.6	25	0.78	600	220	1.12	1.23	0.96
EOF-15	69.2	4.0	25	0.78	600	220	1.10	1.20	0.88
EOF-16	73.3	1.2	100	0.78	600	220	2.35	2.61	1.77
EOF-17	70.0	2.6	100	0.78	600	220	1.90	2.17	1.60
EOF-18	69.2	4.0	100	0.78	600	220	1.62	1.75	1.47

**Table 2: Web crippling strength results for ETF loading condition.**

Test No.	h (mm)	r <sub>i</sub> (mm)	n (mm)	t (mm)	Span Length-Ls (mm)	0.2% Proof Stress (MPa)	P <sub>exp.ult.</sub> (kN)	P <sub>FE:ult.</sub> (kN)	P <sub>AISI</sub> (kN)
ETF-1	73.0	1.6	25	0.78	400	220	0.87	0.91	0.80
ETF-2	73.4	2.4	25	0.78	400	220	0.81	0.95	0.77
ETF-3	65.2	5.0	25	0.78	400	220	0.76	0.82	0.75
ETF-4	98.2	1.6	25	0.78	400	220	1.25	0.98	0.69
ETF-5	96.2	2.4	25	0.78	400	220	0.98	0.92	0.68
ETF-6	89.8	5.0	25	0.78	400	220	0.80	0.81	0.65
ETF-7	73.0	1.6	50	0.78	400	220	1.38	1.29	0.93
ETF-8	73.4	2.4	50	0.78	400	220	0.92	1.18	0.91
ETF-9	65.2	5.0	50	0.78	400	220	1.14	0.95	0.88
ETF-10	98.2	1.6	50	0.78	400	220	1.24	1.20	0.80
ETF-11	96.2	2.4	50	0.78	400	220	1.22	1.12	0.79
ETF-12	89.8	5.0	50	0.78	400	220	0.98	0.96	0.76
ETF-13	73.0	1.6	100	0.78	400	220	1.84	1.90	1.12
ETF-14	73.4	2.4	100	0.78	400	220	1.76	1.72	1.09
ETF-15	65.2	5.0	100	0.78	400	220	1.58	1.34	1.06
ETF-16	98.2	1.6	100	0.78	400	220	1.72	1.64	0.97
ETF-17	96.2	2.4	100	0.78	400	220	1.56	1.52	0.95
ETF-18	89.8	5.0	100	0.78	400	220	1.28	1.32	0.92

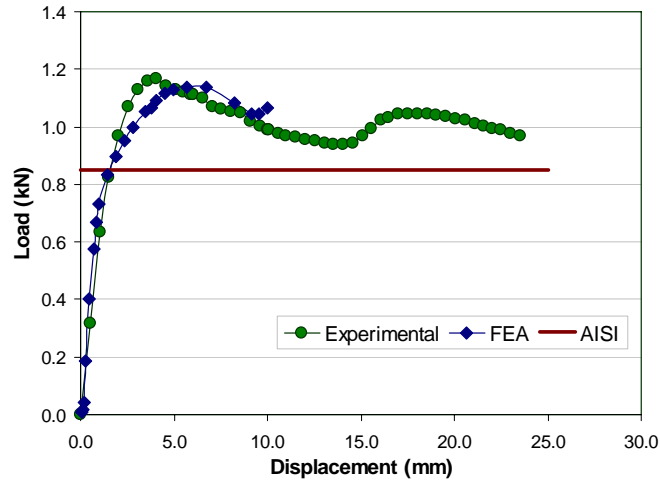


Figure 11: Experimental and FE load-displacement graphs compared with AISI web crippling strength prediction for a sample EOF test (EOF – 1).

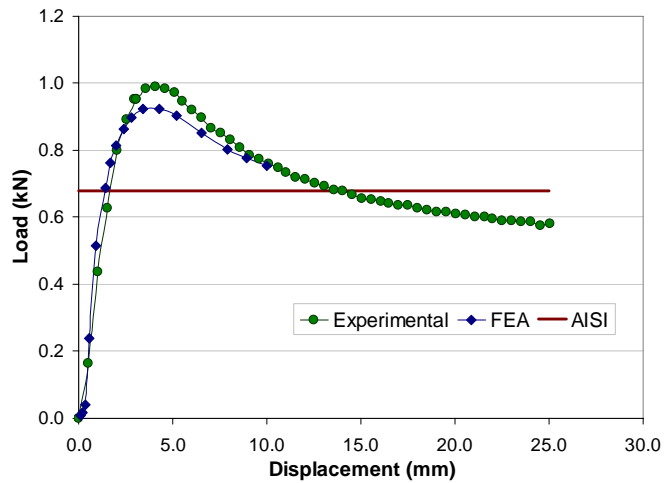


Figure 12: Experimental and FE load-displacement graphs compared with AISI web crippling strength prediction for a sample ETF test (ETF – 5).



**Table 3: Summary of comparisons.**

Loading Condition	Mean of Strength Ratios		Standard Deviation of Strength Ratios	
	$P_{FE:ult.} / P_{exp:ult.}$	$P_{AISI} / P_{exp:ult.}$	$P_{FE:ult.} / P_{exp:ult.}$	$P_{AISI} / P_{exp:ult.}$
EOF	1.01	0.77	0.13	0.05
ETF	0.98	0.73	0.11	0.12

### Conclusions

Experimental investigations were conducted to study web crippling behaviour of cold-formed steel lipped channel beams under EOF and ETF loading conditions. The tests provided results which mainly comprised of ultimate web crippling strength values of thirty-six specimens with varying cross-sectional dimensions and loaded with three separate load bearing plates having different dimensions. Finite element models were developed to simulate the tests conducted in the experimental investigations. The nonlinear characteristics such as material nonlinearity, geometric nonlinearity and contact situations were employed to represent the actual web crippling failure observed during the tests.

The results showed that the nonlinear finite elements models developed were capable of closely representing the web crippling failure of the specimens considered in this research. An average deviation of  $\pm 2\%$  of finite element strength from experimental results was observed.

The nominal web crippling strength of the thirty-six specimens was predicted using the AISI Specification and the predictions were compared with the experimental results. The comparisons indicated averages of 23% and 27% underestimations of the AISI web crippling strength predictions for EOF and ETF loading conditions respectively.

### References

- AISI, (2001) *Specification for the Design of Cold-Formed Steel Members with Commentary*, American Iron and Steel Institute, Washington DC, 2001 Edition.
- ANSYS, (2004) *Release 8.1 - User's Manuals*, ANSYS, Inc.
- Heiyantuduwa, M. A., Macdonald, M. and Rhodes, J., (2007) "Investigation of Web Crippling Behaviour of Thin-Walled Lipped Channel Beam Members", *Third International Conference on Structural Engineering, Mechanics and*

*Computation*, pp. 375-376, Cape Town, South Africa, Sept. 2007, ISBN: 978 90 5966 0540.

Hetrakul, N. and Yu, W. W., (1979) "Cold-Formed Steel I-beams Subjected to Combined Bending and Web Crippling", *Proc. International Conference on Thin-Walled Structures*, University of Strathclyde, Glasgow, April 3-6, pp413-426.

Macdonald, M., Heiyantuduwa, M. A. and Rhodes, J., (2006) "Finite Element Analysis of Web Crippling Behaviour of Cold-Formed Steel Flexural Members", *Eighteenth Specialty Conference on Cold-Formed Steel Structures*, pp. 177-190, Orlando, Florida, USA, 26-27 Oct. 2006.

Prabakaran, K. and Schuster, R.M., (1998) "Web Crippling of Cold-Formed Steel Members", *Fourteenth International Specialty Conference on Cold-Formed Steel Structures*, St. Louis, Missouri U.S.A., pp. 151-163, Oct. 15-16, 1998.

Ratliff, G. D., (1975) "Interaction of Concentrated Loads and Bending in C-Shaped Beams", *Third International Specialty Conference on Cold-Formed Steel Structures*, St. Louis, Missouri, U.S.A., pp. 337-356, Nov. 24-25.

Rhodes, J., (1991) *Design of Cold Formed Steel Members*, Elsevier Applied Science, England, ISBN 1 85166 595 1.

Winter, G. and Pian, R. H. J., (1946) *Crushing Strength of Thin Steel Webs*, Engineering Experiment Station, Cornell University, Bulletin No.35. Part 1.

Wu, S., Yu, W., and LaBoube, R. A., (1998) "Web Crippling Strength of Cold-formed Steel Structures", *Fourteenth International Specialty Conference on Cold-Formed Steel Structures*, St. Louis, Missouri U.S.A., pp. 193-207, Oct 15-16, 1998.

Young, B. and Hancock, G. J., (1998) "Web crippling behaviour of cold formed unlipped channels", *Fourteenth International Specialty Conference on Cold-Formed Steel Structures*, St. Louis, Missouri U.S.A., pp. 127-149, Oct. 15-16, 1998.

Young, B. and Hancock, G. J., (2000) "Tests and design of cold-formed unlipped channels subjected to web crippling", *Fifteenth International Specialty Conference on Cold-Formed Steel Structures*, St. Louis, Missouri U.S.A., pp. 43-69, Oct 19-20, 2000.



## **Simplified Consideration of down-aisle stability in Pallet Racking**

J Rhodes<sup>1</sup> and M. Macdonald<sup>2</sup>

### **Abstract**

The sway buckling loads predicted by the approximate equations given in European pallet racking codes are compared with those predicted by frame finite element analysis. It is found that the load capacities predicted by the approximate equations are accurate and conservative in comparison to the finite element predictions if the uprights are pin-ended and the spacing between all beam levels is constant. If the uprights have base rotational restraint, and/or the height of the first storey is less than that of the higher storeys then inaccuracy and non-conservatism can arise using the approximate equations, and the non-conservatism increases as the number of storeys increases. An attempt is made to improve the accuracy by modifying the approximate equations. The modified equations give, in general, more accurate predictions of sway buckling loads and in particular reduce the non-conservatism. The modifications also tend to ensure that for racks with properties outside the range examined in this paper the buckling loads predicted would err on the safe side.

### **Introduction**

In pallet racking systems the beams are connected to the uprights by connectors which have a degree of rotational restraint. This is generally small in comparison to full restraint, but assists the beams slightly in withstanding load and, more importantly in unbraced systems, assists the frame in resisting sway buckling.

In the design of unbraced pallet racking systems, sway buckling in the down-aisle direction is an important factor which must be taken into consideration by the designer. The evaluation of the buckling loads can be carried out using one

of many available computer packages, either general finite element programs such as ANSYS, or programs specifically directed towards racking design, for example the Pallet Program [1].

There is felt to be a need, however, for more simple design methods for use in the case of racking systems of uniform geometry and subjected to uniform loading. The latest European design codes [2], [3] are extremely comprehensive and in these codes two alternative analytical approaches to sway buckling effects are considered. These are Level 1 approach, which requires second order analysis and Level 2 approach, which allows first order analysis with the resulting moments etc subsequently increased by an amplification factor. This factor is dependent on the ratio of the design load to the sway-buckling load. In either case the sway-buckling load requires to be evaluated. In the Level 2 analysis an approach based on Ref. [4], by Horne, is described to evaluate the sway buckling load. In this approach a linear analysis of the frame is used to determine the internal forces and deflections due to notional horizontal loads. The maximum value of the sway index (change of horizontal deflection between two beam levels divided by the distance between levels) is used in a simple equation to obtain the buckling load.

To circumvent the necessity to examine the complete frame, which generally requires some form of finite element analysis, an approach due to Davies [5] is given in the European codes. This approach considers a substitute single column frame and carries out the first order analysis using the assumption that only the first two levels of the upright are flexible. This results in a set of equations for the sway buckling loads corresponding to the sway indices for the first three storeys, the least of which governs. Good accuracy is claimed for the approach. However initial perceptions suggest that since the buckling shape may be rather different than the deflected shape due to horizontal loading there will be a degree of inaccuracy. This is reinforced by the condition specified that this analysis is only valid if the design load is less than one third of the critical load.

In the UK, the Storage Equipment Manufacturer's Association, SEMA, intend to introduce a new remodelled racking design code, suitable for a limited range of 'standard' systems. This new code should be technically acceptable and should take account of behaviour such as sway buckling with greater rigour than in previous SEMA codes. The method specified in the European codes is attractive, but the limitation on applicability is somewhat disappointing, and an extension of the range of applicability would be welcome. To enable a greater range of applicability of a method such as that in the European codes, an examination of the simplified approach is required, and suitable modifications considered where possible. An attempt to achieve this has recently been made

[6] in which an energy approach obtained excellent results for frames with pinned floor connections, but could not take adequate account of the base connection stiffness without increasing the complexity of the governing equations to a substantial extent. To overcome this the investigation reported here concentrated on examining the current equations in the European (FEM/CEN) codes.

The aim of this paper is firstly to examine the approach used in the FEM/CEN codes to obtain the sway buckling load, and secondly to provide modifications to extend the range of applicability of this approach for the analysis of 'standard' frames. The beam and upright properties examined, e.g. second moment of area, connector stiffness, are rounded values typical of those used in practice

#### Approximate Sway Buckling Analysis Using the FEM code

The approximate approach used in the FEM code is outlined as follows (using somewhat different symbols).

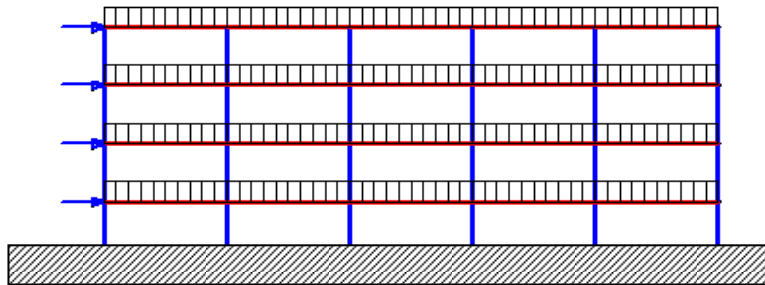


Figure 1. Fully loaded rack with 5 bays and 4 beam levels

Consider a fully loaded rack as shown in Figure 1 having in general  $m$  bays and  $n$  beam levels, with each beam having a load  $W$ , using the following notation.

$I_c$  is  $I$  for a single upright,  $I_{cc} = (m+1).I_c$  is total upright  $I$  value  
 $I_b$  is beam 2<sup>nd</sup> moment of area

$K_c$  is base stiffness for a single upright  $K_{cc} = (m+1) .K_c$  is total base stiffness

$K_b$  is beam end connector stiffness

$h$  is the height of the first beam above the floor

$H$  is the vertical spacing of subsequent beam levels

$H_T = h + (n - 1) .H$  is the total height of the rack

$L$  is the bay width

$\bar{W} = W \times m \times n$  is the total load on the rack

$\bar{W}y = \bar{W} (h + (n - 1)H/2)$  is the moment about the base of all loads if applied horizontally

Critical load factors corresponding to the sway index for first second and third levels are:-

$$V_{CR1} = \frac{K_{cc} h + E I_{cc}}{\left[ \frac{K_{cc} h}{2} + E I_{cc} \right] \theta_1 + \frac{\bar{W} h^2}{12 E I_{cc}} (K_{cc} h + 4 E I_{cc})}$$

$$V_{CR3} = -\frac{D}{G}$$

$$V_{CR2} = \frac{1}{\theta_2} \quad \text{where} \quad \theta_2 = \frac{(\bar{W} - n W) H^2}{12 E I_{cc}} + 0.5 \left[ \frac{1}{V_{CR3}} + \theta_1 \right]$$

$$\text{where} \quad F = \frac{12 m E I_b K_b}{6 E I_b + k_b L}$$

$$C = F + \frac{E I_{cc} K_{cc}}{E I_{cc} + K_{cc} h} + \frac{E I_{cc}}{H}$$

$$A = \frac{\bar{W} h}{2C} \times \frac{K_{cc} h + 2 E I_{cc}}{K_{cc} h + E I_{cc}} + \frac{(\bar{W} - m W) \times H}{2C} \quad B = \frac{E I_{cc}}{H C}$$

$$D = (n - 1 + B) \times F + \frac{E I_{cc} K_{cc} B}{E I_{cc} + K_{cc} h}$$

$$G = \frac{\bar{W} h}{2} \left[ \frac{K_{cc} h}{K_{cc} h + E I_{cc}} \right] + \frac{E I_{cc} K_{cc} A}{K_{cc} h + E I_{cc}} - \bar{W} y + F \times A$$

$$\theta_1 = A - \frac{B G}{D}$$

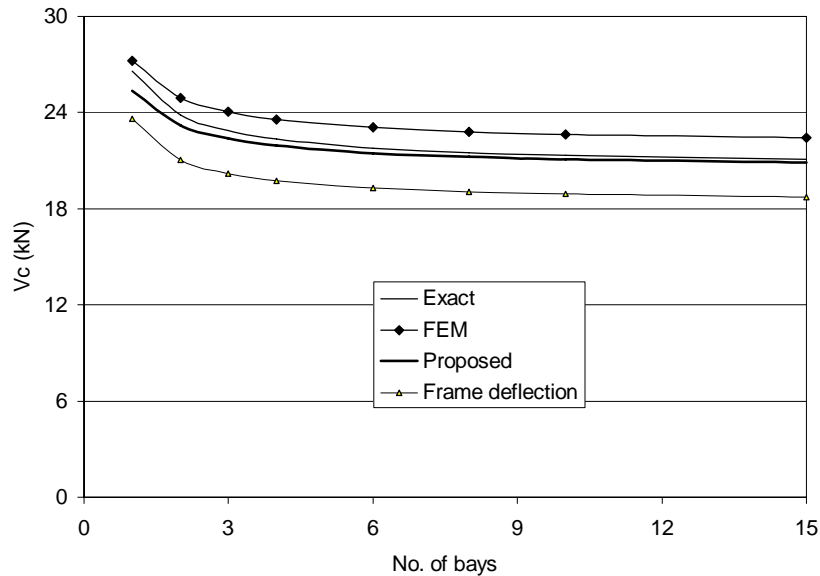
The critical load,  $V_C$ , is the smallest of  $V_{CR1}$ ,  $V_{CR2}$  and  $V_{CR3}$  multiplied by  $W$ .

### 3. Comparison of the results of different approaches

To examine the accuracy of the approximate equations a large number of evaluations of the sway buckling loads for various racks were carried out using the FEM/CEN approach and with a non-linear frame finite element analysis for comparison purposes. The frame finite element program used to carry out the Level 1 analysis was also used for linear analysis to check the validity of the basic premise that the use of the sway indices gives accurate estimations of the buckling load.

The range of parameters investigated considered base rotational stiffness from 0 to 200 kNm/radian, beam connector stiffness from 10-100 kNm/radian, number of beam levels from 2-15, beam and upright I values from 50-100 cm<sup>4</sup>. All bay widths were taken as 2.8 metres, with upper beam level spacing 1.4 metres. The lowest beam level was taken as either 1.4 metres or 0.5 metres. Parameters outwith this range were also examined to ensure that the findings were general. The number of bays investigated for most of the comparisons was set at three, but the effects of increasing the number of bays from 1 to 15 was also examined. Such an examination is shown in Figure 2 for the case of a rack with 5 beam levels.





**Figure 2. Sway Buckling Load –v- Number of Bays for 5 Beam Rack**

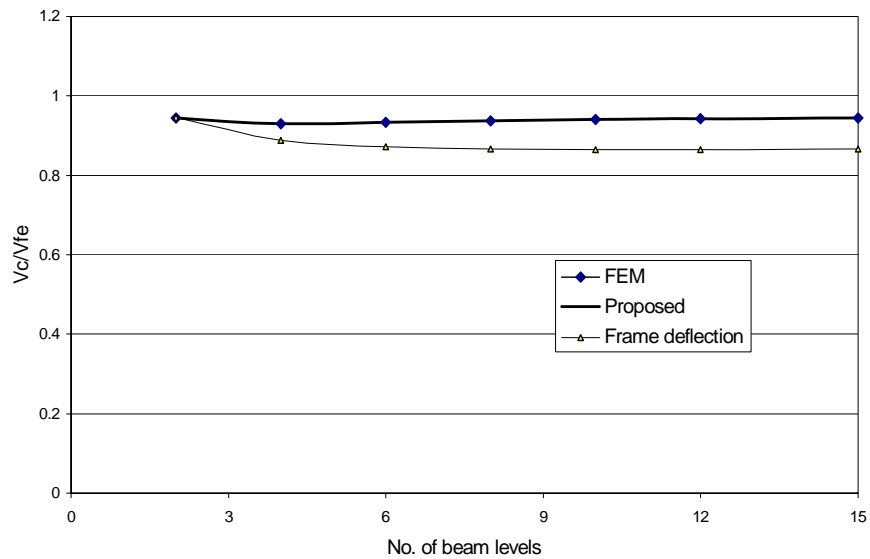
The parameters considered here are  $I_b=100 \text{ cm}^4$ ,  $I_c=50 \text{ cm}^4$ ,  $k_b = 50 \text{ kNm/rad}$  and  $k_c = 200 \text{ kNm/rad}$ . In the figure the legend “Exact” applies to the finite element results, “FEM” applies to the results obtained using the approximate equations, “Frame deflection” applies to the results obtained using the sway index together with finite element deflection results. The legend “Proposed” applies to a modification to the FEM approach which will be discussed further.

The figure suggests the values of all results relative to the “Exact” results do not vary by any significant amount with variation in the number of bays from 3 to 15. FEM results here are 5%-6% greater than exact, Frame deflection results are 11% or so below exact and ‘Proposed’ results are around 2% below exact throughout the range of bays. This gives some confidence in confining further examination to three bay racks.

Since the relative accuracy of the different methods is gauged by their comparison with the finite element results the remaining figures show the ratios of the results of each particular approach to those of the finite element analysis

### Pin-Ended racks

Figure 3 shows the comparison of buckling load ratios (i.e.  $V_c/V_{c(\text{finite element})}$ ) for 3 bay racks with  $I_b=100$ ,  $I_c=50$ ,  $k_b=100$ ,  $k_c=0$  with various beam levels from 2-15, all levels having the same spacing, including the bottom level.



**Figure 3. Sway buckling load ratios–v- No. of beam levels for 3 bay Rack**

In this case the FEM approach gives results between 5% and 7% below the exact results for all beam levels, which is accurate and safe. The frame deflection results are about 12% low. In the case of racks with pin-ended uprights which have lowest beam spacing the same as that of upper storeys the sway index for the lowest storey,  $V_{CRI}$ , always governs. In this case the FEM expression for this sway index is perfectly adequate, resulting in accurate and safe predictions of the buckling capacity. This applies through the complete range of pin-ended frames examined so long as the height from ground to the first beam was equal to the beam level spacing above the first level

### Effects of Base Stiffness

If the rack parameters examined in Figure 3 are retained, but the base stiffness is 200 kNm/rad a rather different situation arises. This is demonstrated in Figure 4 for racks with the same beam and upright properties as specified but with the specified base rotational stiffness and three different beam connector stiffnesses. For all beam connector stiffnesses the FEM approach gives results which become increasingly non-conservative as the number of levels increases and becomes greater than 20% for racks with a large number of levels.

An effect of base stiffness is to reduce the magnitude of deflections in the first storey relative to those in the upper storeys, so that  $V_{CR1}$  is greater than the critical loads obtained on the basis of second and third storey sway indices. To eliminate, or minimise, the overestimation of the buckling loads then  $V_{CR2}$  and  $V_{CR3}$  should be examined further.

The approximate equations were set up on the basis that the uprights are assumed infinitely stiff above the second beam level. For racks with a small number of beam levels this does not cause a great difference in the projected behaviour, and indeed the stiffening due to the assumed rigidity of the upper storeys has the effect of cancelling the conservatism of the basic sway index premise. However, for racks with 4 or more beam levels the assumed rigidity of an increasing number of levels induces non-conservatism in  $V_{CR1}$  and  $V_{CR2}$ . These effects increase if the distance from ground to the lowest beam level is less than the upper beam spacing.

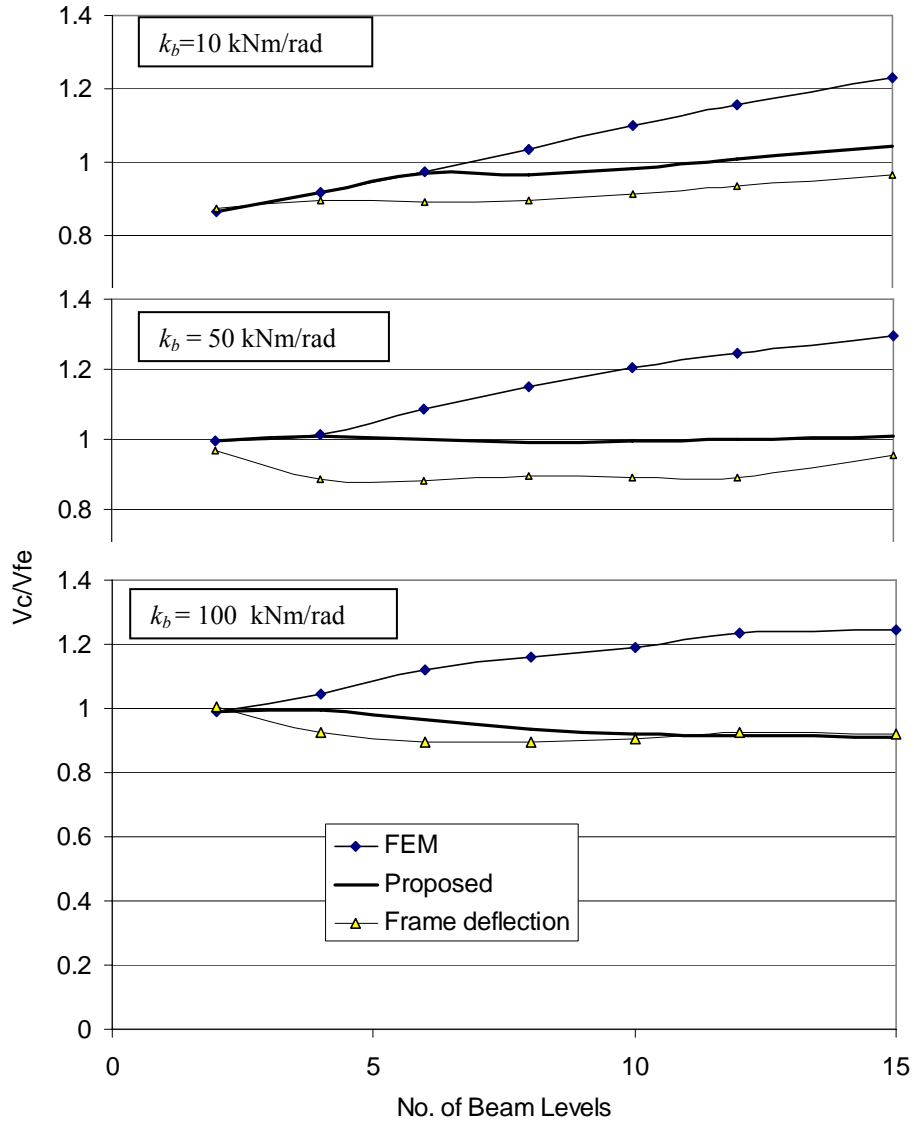


Figure 4. Buckling load ratios-v-No. of Levels -Racks with base restraint

### Modification of Approximate Equations

On the basis of a lengthy parametric investigation it was considered that the application of a multiplication factor to  $V_{CR1}$  and  $V_{CR2}$  would assist in reducing the overestimation of buckling loads. To this end a modification of the relevant equations for these indices was carried out. The relevant equations were modified to:-

$$V_{CR3} = \frac{-D}{G} \times R \quad \text{where } R = \frac{2(H_T + h + H)}{3H_T} \times \frac{\left(1.15 + 9 \frac{k_b h}{EI_b}\right)}{\left(1 + 12 \frac{k_b h}{EI_b}\right)} \quad \text{but } R \leq 1$$

$$V_{CR2} = \frac{1}{\theta_2} \times R \quad \text{where } \theta_2 = \frac{(\bar{W} - nW)H^2}{12EI_{cc}} + 0.5 \left[ \frac{R}{V_{CR3}} + \theta_1 \right]$$

The results obtained using the FEM expressions modified as described are termed 'Proposed' in the figures. Figures 2, 3 and 4 show that all of these results are close to the 'exact' results for the cases considered

### 4. Effects of Lowest Beam Height

Racking systems often have the first beam level set closer to the floor than the subsequent level spacing. This has an effect on the sway buckling capacity, and in the set up of the FEM equations this fact was noted and taken into account using a reduction factor for racks with first beam level less than subsequent spacing. The factor used in the FEM codes is as follows: -

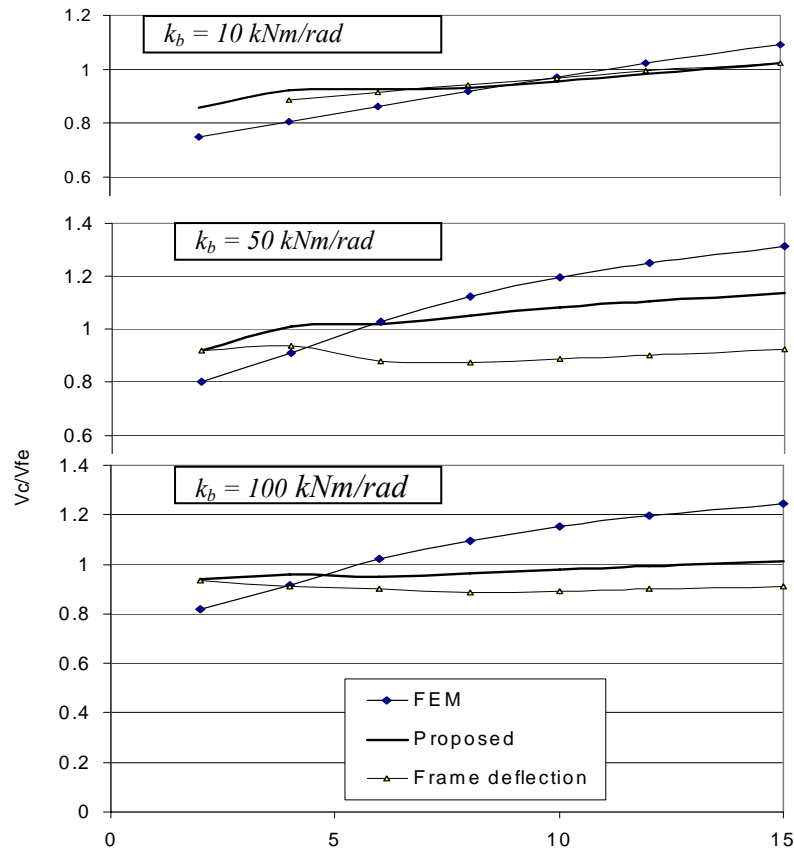
$$\text{If } h/H < 1 \text{ then } V_c \text{ as calculated previously is reduced by } (0.8 + 0.2 h/H)$$

The factor  $R$  specified in the modified equations was arrived at on the basis of examination of a widely varied set of conditions, and does not require this reduction factor.

This is evidenced by the results shown for buckling load ratios in Figure 5. The same rack parameters are examined as in Figure 4, except that the first beam level is 0.5 metres from the floor, with all subsequent levels spaced at 1.4 metres.

The results for the FEM equations take into account the reduction factor of 0.8714 while those for the 'Proposed' method do not. Figure 5 indicates that while the FEM reduction factor reduces the non-conservatism of the FEM predictions for racks with many beam levels there is still a substantial overestimation of the buckling load for high racks, and for racks with only a few beam levels the reduction is unnecessarily severe. The 'Proposed' results are in general closer to exact throughout the range tested, only those for the case  $k_b = 50$  kNm/rad exceeding a 10% overestimate for racks with over 12 beam levels.

It is also worthy of notice that the 'Frame deflection' results are almost always conservative, and quite accurate, thus proving the validity of the basic premise that sway buckling loads can be determined using linear frame analysis.



**Figure 5. Buckling load ratios–v–No. of Levels - Rack with Low First Beam**

Figure 6 shows the buckling ratios for the same racks with pinned ends. In this case all results are within acceptable limits, with the reduction factor keeping the FEM results less than 10% high apart from one case for a very tall rack. Even here, the modified FEM equations give rather better results than those from the original equations.

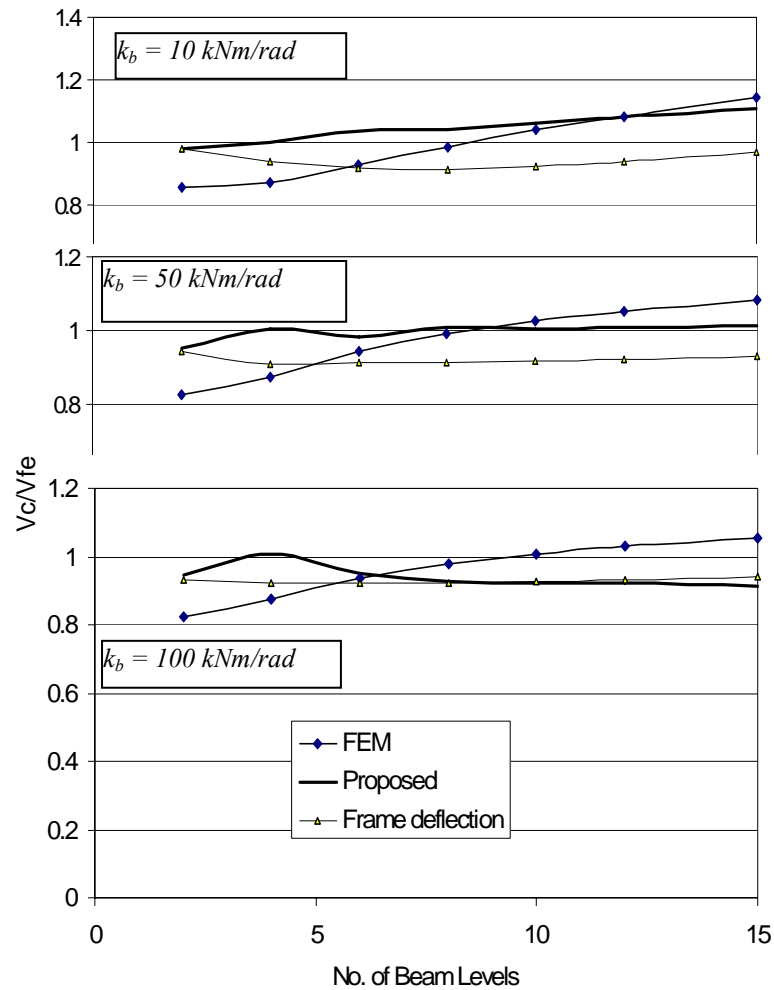


Figure 6. Buckling load ratios for Pin ended Racks with Low First Beam

### Effects of Relative Beam-Upright Rigidities

All results shown so far are for racks with beams with  $I = 100\text{cm}^4$  and uprights having  $I = 50\text{cm}^4$ . If the upright and beam  $I$  values are transposed the results are not particularly different. This is illustrated in Figure 7 for frames of the same dimensions as before but with  $I_b = 50\text{cm}^4$  and  $I_c = 100\text{cm}^4$ . This figure is directly comparable with Figure 4.

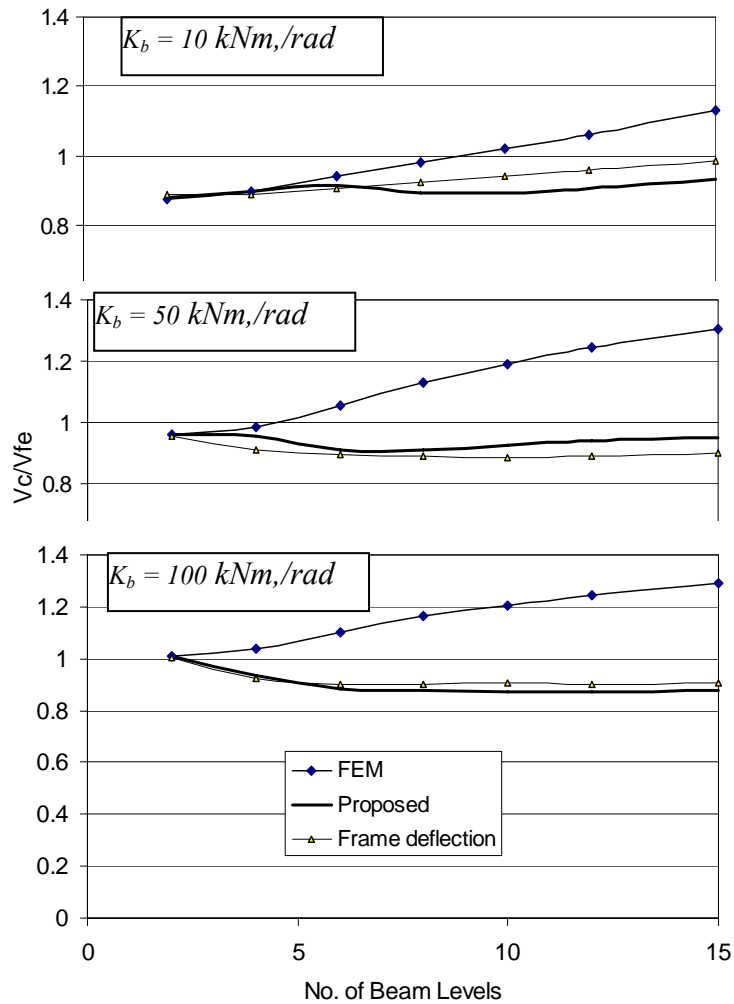


Figure 7. Buckling load ratios–v–No. of Levels–Racks with base restraint



While the results for the FEM and Frame deflection method are much the same as those of Figure 4 the modified FEM equations give a greater degree of conservatism in this case. This can be explained by examination of the modified equations which are dependant to an extent on the inverse of the beam flexural resistance. However, as one main objective of the investigation is to minimise the possibilities of overestimation of the buckling load this is not unwelcome.

## **6. Discussion and conclusions**

The modifications suggested to the FEM approximate equations are designed to (a) improve the accuracy of these equations and (b) to insure that the possibilities of overestimation of the sway-buckling load are reduced. Within the limits of the parameters investigated this is accomplished by the suggested modification to the FEM equations. The predicted buckling loads cannot be any greater than those of the FEM equations, but can be up to a maximum of 50% smaller. The results shown have suggested that the suggested modification works well within the range examined.

For frames with all level spacings equal and with pin ends the current FEM method is accurate and conservative, as the first storey promotes buckling, and the proposed modification does not alter this. If the first beam level is closer to the ground than the spacing between subsequent beam levels, or if the base has rotational stiffness, then the current FEM equations can be non-conservative, and the overestimation of the buckling capacity increases with increase in the number of beam levels. This is eliminated, or at least minimised by the modified equations.

The modified equations are valid for any base stiffness up to full fixity. This has been examined, although not reported here, and in the case of full fixity the modified equations give very good results so long as the beam end connector stiffness is within the range examined here.

The effects of high rigidities in the beam end connectors is more pronounced, and the modified equation do not always give very accurate predictions for extremely stiff beam end connectors. If the beam end connector stiffness is within the range discussed here and the base stiffness is extremely high then accurate predictions are obtained by the modified equations – much more safe and accurate than by the original equations. However if both beam connector stiffness and base stiffness are high, i.e. all connections are close to full rigidity, the modified FEM equations can underestimate the buckling capacity by up to 30%. While this is not ideal, it is at least safe, and is better than the current FEM

equations which can overestimate the buckling capacity by up to 40% when the base rigidity tends to infinity and the beam end connectors are semi-rigid. In any case, the intention here is to consider the conditions applicable to pallet rack structures, and if the equations are used to examine much more rigidly connected frames then even a 30% underestimate should be acceptable if the convenience of using a simplified approach is considered important.

Overall, the aims of improving the accuracy and applicability of the FEM approximate approach may be said to have succeeded. The modified equations improve the accuracy in general, and minimise the overestimation possibilities. These modifications can be improved, and may be “tweaked” to obtain greater accuracy, but as they stand, they do provide a more accurate and, safer, estimation of sway buckling capacity than the current FEM equations particularly for tall racks.

## References

- [1] Beale R.G. and Godley M.H.R. “The Design of the Pallet Program”. Proc. 16<sup>th</sup> Int. Speciality Conf. on Cold-Formed Steel Structures, Orlando, Florida, USA, 2002, pp 353 –368
- [2] Federation Europeene de la Manutention, FEM 10.2.02. “The Design of Static Steel Pallet Racking.” Section X of Equipement et Proceeds de Stockage, 2000
- [3] European Committee for Standardisation. “Steel static storage systems – Adjustable pallet racking systems – Principles for structural design.” Draft English Version, June 2006
- [4] Horne M. R. “An approximate method of calculating the elastic critical loads of multi-storey plane frames” Structural Engineer. Vol 53, No. 6, June 1975.
- [5] Davies J. M. “Down-Aisle Stability of Rack Structures”. Proc. 11<sup>th</sup> Int. Speciality Conf. On Cold-Formed Steel Structures, St Louis, Missouri, 1992, pp 417-435.
- [6] Rhodes, J. “Simplified Evaluation of Sway Buckling Loads in Pallet Racking”. Conference for the Retirement of Professor Jim Rhodes, Glasgow, UK , 2007



## **Response of Metal Roofs to Uniform Static and True Hurricane Wind Loads**

**By**  
**R. Ralph Sinno, Ph.D., P.E., F. ASCE\***

### **Abstract**

The primary objective of this work is two fold: (1) Development of a test method that simulates the non-uniform unsteady wind loading conditions in time and space on a roof of a low rise building. This is done using electromagnetic controlled uplift pressures, suction, on metal roofs. (2) To establish a comparative correlation between the current uniform static loading used for design and the true hurricane dynamic uplift wind loading. This is the first time ever that the wind tunnel data for the footprint of true hurricane wind loading is duplicated and applied successfully to full-scale roofs in the laboratory. The test results confirmed that the maximum anchoring reactions are almost proportional to the square of the wind speed under static and simulated true wind loading. These reactions are considerably lower under true wind loading than those from the ASCE-7-05 for uniform static loading. Deflections and deformations of end panels of the roof are noted to be excessively higher under true wind loading than those under uniform static loading. Test results and findings are applicable to any type of roof system and materials used to construct and build roofs in real life.

### **1.0 GENERAL**

The primary objective of this research is the simulation of wind tunnel loading data applied to standing seam thin sheet metal roofing. Evaluation and prediction of the clip reactions of full scale metal roofs subjected to uniform static loading and simulated wind tunnel loading is presented. Vertical legs and

---

\*Professor of Civil Engineering, P.O. Box 9546, MSU, MS 39762, Telephone 662-325-3737, E-mail [sinno@engr.msstate.edu](mailto:sinno@engr.msstate.edu)

trapezoidal standing seam roofs were used. The test results from simulated wind loading are compared to those results from uniform static loading. Uniform static loading followed the ASTM E-1592-01[2] testing procedures. The work reported here covers, in general, metal roofing commonly used by the metal building industry in the U.S.

Laboratory testing using uniform static loading conditions induced by compressed air or partial vacuum are presently used to verify the structural performance of thin metal standing seam roofs. This air pressure difference loading method for testing does not represent, or even come close to simulate, the true wind loading spectrum in the time and space. Under uniform static loading, the metal roofs usually swell to a balloon shape with severe uniform unloading pressure on the standing seamlines of the panels. Accordingly, the test results from using uniform static loading have been the center of continuous appraisals by structural engineers, wind engineering specialists, hazards mitigation experts, forensic investigators, and scientific researchers. Field surveys of wind loading on roofs in real life have confirmed the seriousness of this disparity.

## **2.0 BACKGROUND**

The most sophisticated testing device available for testing metal roofs, other than the uniform static loading, has been the BRERWULF test setup. This test was developed by Cook, Keevil, and Stobart [4]. The unsteady pressures produced in this test set-up remain spatially uniform.

Clemson University used the BRERWULF to re-create dynamic hurricane level winds in the laboratory [5]. The tests were successful in evaluating boundary effects and the variability of clip influence surfaces. However, the peak effective pressures were too small to provide insight into clip loading and roof behavior before failure.

## **3.0 THE CURRENT APPROACH FOR DESIGN OF METAL ROOFS**

The current standard design procedure for design of metal roofs for wind loading is based on statistical averages of wind tunnel data using weighted factors related to the location and terrain. To reduce the complexity of the pressure variations, the current ASCE-7 design procedure specifies that metal buildings should be designed for uniform pressures over pressure zones: interior, edge, and corner zones.

The calculated static uniform clip reactions in comparison to those caused by true wind loading remain questionable. In spite of the seriousness associated with the magnitude and steadiness of these reactions, they are used for the design of the framing and foundations that support the entire metal building.

#### **4.0 OBJECTIVE OF THE RESEARCH**

The primary objective of this research work has been two fold:

- 1) Develop a test method that simulates the non-uniform unsteady wind loading conditions in time and space on a standing seam metal roofing. Suction on metal roofing using electromagnetic controlled uplift pressures was developed in a previous MBMA research project (6). The details for loading using induce electromagnetic uplift pressures including its velocity can be found in Reference (7).
- 2) Establishing a correlation between the current uniform static testing and the dynamic electromagnetic uplift testing. This comparative study addressed also the comparative performances of the roofs under load up to failure.

#### **5.0 TESTING PROGRAM**

The testing program was basically two parts:

- 1) Test typical roofs using uniform static pressure difference as per ASTM 1592-01 protocol.
- 2) Test the same roof layout under electromagnetic uplift loading up to failure.

The testing program was executed on two roof profiles; vertical legs and trapezoidal. The tested vertical legs profile was 16 in. panel, 24 guage metal roofing, span 5' 1", and it was provided by a Houston, Texas, metal building manufacturer. Four vertical legs roofs were tested under uniform static pressure and two identical roofs were tested under electromagnetic uplift UWO wind tunnel simulation loading. The roofs were supplied and installed by corresponding metal building manufacturer duplicating all details procedures used by each in a real full scale field installation.

Two roofs made of 24 ins. wide trapezoidal panels were also tested. One roof was provided by a Houston, Texas metal building manufacturer with a metal thickness of 24 gauge, while the other roof was provided by CECO Building Systems using 22 gauge for the metal thickness. Both trapezoidal roofs were installed on 5'-1" purlin spacing. Only the test results on the vertical legs profile are reported here, and for additional coverage and test results on these tests, see References 9 and 10.

## **6.0 TEST SET-UPS**

### **6.1 Static Tests-ASTM E-1592**

The uniform static loading test set-up followed the ASTM E 1592-02 loading sequences and procedure.

Tests were also performed independently by each metal building manufacturer that supplied these roofs at their own facilities, and the findings were compared and found to confirm each other.

The main interest of running the static tests was to create a reference file on the performance of the roofs under uniform static loading that could later be used for comparison with electromagnetic uplift testing. The load deflection curves for loading and unloading and the load transfer reactions at the clips were of primary interest.

All tested roofs were made of galvalume sheet metal roofing commonly used by the metal building industry in the U.S. All roofs were made of five panels, 20'-4" long, supported on 5 purlins spaced at 5'-1".

### **6.2 Electromagnetic Uplift Test Set-Up**

Non-uniform dynamic uplift forces were produced by using intense electromagnetic suction force from suspended magnets at a gap distance from the metal roof. Extensive research on the efficiency and optimization of the induced electromagnetic uplift forces in the grid system was required to develop the electromagnets used in this study [6].

Magnetic nodal points were placed on top of the roof at variable gap distances and suspended from 8 overload beams. The layout of the 34 electromagnetic nodal points was established on the basis of the data provided by the UWO Wind Tunnel Tests.

The induced electromagnetic uplift forces were then programmed to simulate a given wind tunnel data file. University of Western Ontario boundary layer wind tunnel data were used to generate the simulated non-uniform dynamic wind loading for each electromagnet. These uplift suction forces were applied by each electromagnetic actuator at the centroid of the area as designated by the UWO wind tunnel data. Each nodal point consisted of the actuator, an electronic control board, and a load cell for verification of the force produced. The system was programmed to generate time varying forces equivalent to the forces supplied by UWO. See Figures. 1 to 5 for the electromagnetic test setup and details of related parts.

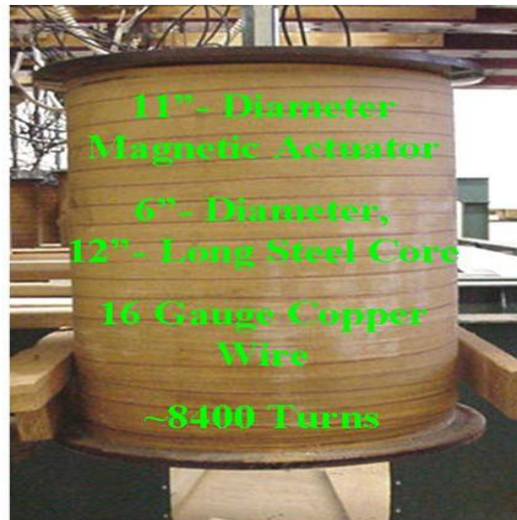


Fig 1. Electromagnetic Nodal Point - Magnet.



## Electro-Magnet Control Circuitry

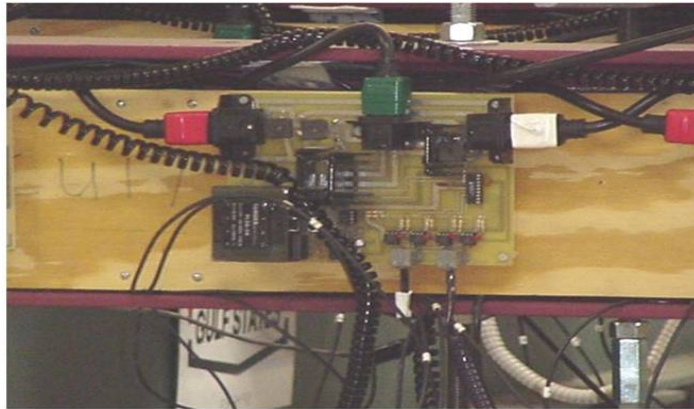


Fig 2. Electromagnetic Nodal Point - Control Panel Board Circuitry



Fig 3. Electromagnetic uplift Testing - Group of Electromagnetic Nodal Points



Fig 4. Electromagnetic uplift Testing - Front View of 34 Nodal Points Placed as per UWO Area Distribution



Fig 5. Electromagnetic uplift Testing - Back View

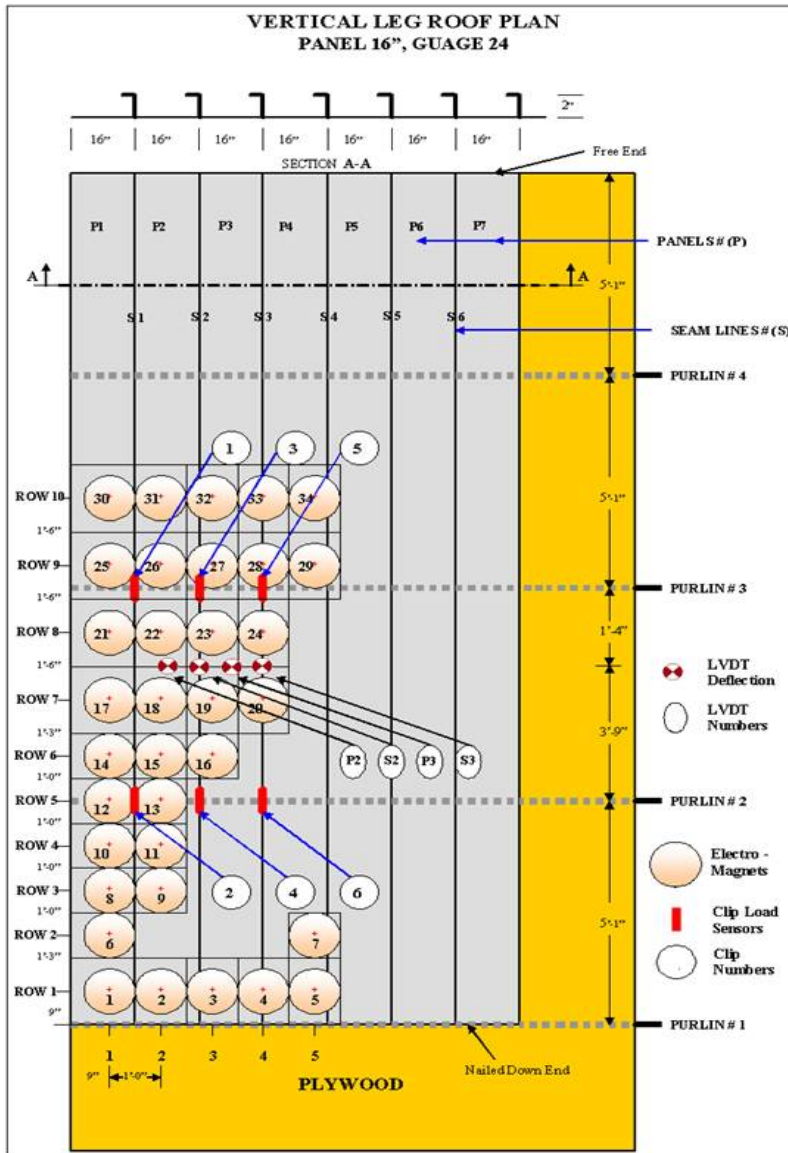


Fig 6. Electromagnetic Uplift Testing. Labeling, Instrumentation and Test Setup for Houston Vertical Legs Roofs

## 7.0 INSTRUMENTATION

The experimental setups of the roof layouts used for the static and electromagnetic uplift tests are shown in Figure 6 for the vertical legs roofs. This setup meets the requirements for a standard full scale testing as specified by the ASTM E-1592. This setup was used to acquire data for both the static and electromagnetic uplift tests so that a direct correlation could be drawn between the two sets of data. The Figure shows the labeling of all panels and seam lines, location of each of the thirty four magnets, location of LVDT's for deflection measurements and labeling of the six load cells attached to the clips for recording the reactions.

### 7.1 Static Test ASTM E-1592

Electronic data acquisition was used exclusively in this test setup. All sensors were read at 20Hz (20 readings per second) during the entire period of testing. The following electronic sensors were used:

- A pressure transducer for monitoring the uplift air pressure inside the pressure chamber. The collected data in each test was constantly checked against a pressure differential piezometer to confirm the accuracy of the electronically recorded readings.
- Linear Variable Differential Transducers (LVDT).  
Four LVDT were used for deflection measurements placed at the center of two panels and at the tip of two adjacent seam lines.

### 7.2 Electromagnetic Uplift test

The following is the description of the electronic instrumentation that was also read at 20Hz (20 readings per second) during the entire period of testing under electromagnetic uplift loading:

- A pressure transducer for monitoring the uplift air pressure inside the pressure chamber. The collected data in each test was checked against a pressure differential piezometer to confirm the accuracy of the readings.
- Load cells at each electromagnetic nodal point.  
The induced uplift suction forces created by the electromagnetic field were recorded using load cells that were secured to each magnetic

nodal point. These load cells were protected from the influence of surrounding magnetic field.

- Load cells for monitoring the clip reactions.  
A total of six load cells placed on six clips on two purlins were used. The clips on Purlin Two carried even numbers (clip #2, #4, and #6), and odd numbers (clip #1, #3, and #5) were given to the clips on Purlin Three.
- LVDT (Linear Variable Differential Transducers).  
Four LVDT were used for deflection measurements placed at the center of two panels and at the tip of two adjacent seam lines.

## **8.0 UWO TEST DATA**

The UWO data were developed using the most critical angle for loading with 110 miles per hour fastest-mile wind velocity at thirty three feet above the ground. The data were provided at 20 Hz for each area corresponding to the thirty four magnetic nodal points. The UWO area numbering, identification of wind load distribution and statistical highlights of the wind data used are shown in Figures 7 and 8, respectively.

### UWO WIND DATA FOR 110MPH

(1)	(2)	(3)	(4)	(5)	(6)	(7)	(8)	(9)
Area Number	Identification	Negative Peak Load (lbs)	99 percentile Load (lbs)	Positive Peak Load (lbs)	Mean Load (lbs)	% of time signals are suction	Backing Force (due to backing pressure over the area)	% of time signals exceeded 250 lbs
1	101 (1.5x1.5')	-274.3	-136.9	43.7	-44.8	93.9	51.5	0.02
2	104 (1'x1.5')	-124.2	-73.1	31.8	-12	69.6	34.3	0
3	106 (1'x1.5')	-123.2	-83.4	30.7	-18	75.8	34.3	0
4	108 (1'x1.5')	-125.7	-79.3	31.5	-15.9	74	34.3	0
5	110 (1'x1.5')	-129.1	-82	30.6	-16.5	74.7	34.3	0
6	401 (1.5x1')	-233.8	-139.2	31.4	-46.8	96	34.3	0
7	410 (1'x1')	-49.4	-25.9	24.7	6.2	19.2	22.9	0
8	601 (1.5x1')	-239.7	-146.6	26.8	-55.7	98.5	34.3	0
9	604 (1'x1')	-69.7	-30	26.2	6	17.3	22.9	0
10	801 (1.5x1')	-259.1	-150.7	24.6	-57.3	98.6	34.3	0.02
11	804 (1'x1')	-105.4	-51.6	24.6	-5.2	56.3	22.9	0
12	1001 (1.5x1')	-236.8	-151.8	24.2	-59.4	99	34.3	0
13	1004 (1'x1')	-132.9	-66.5	24.1	-16.5	84	22.9	0
14	1201 (1.5x1')	-209.9	-137.5	22.6	-54.2	99.2	34.3	0
15	1204 (1'x1')	-142.3	-74.7	22	-22.3	92.5	22.9	0
16	1206 (1'x1')	-79.9	-40.4	26.9	4.9	25.2	22.9	0
17	1401 (1.5x1.5')	-264.9	-182.7	36.1	-70	99	51.5	0.05
18	1404 (1'x1.5')	-206.1	-122.8	29.1	-40.2	95.7	34.3	0
19	1406 (1'x1.5')	-165.7	-78.5	40.4	-6.1	51.1	34.3	0
20	1408 (1'x1.5')	-119	-61	50.4	13.6	17.9	34.3	0
21	1701 (1.5x1.5')	-216.3	-156.6	33.6	-57.7	98.5	51.5	0
22	1704 (1'x1.5')	-180.2	-124.6	27.5	-44.8	97.9	34.3	0
23	1706 (1'x1.5')	-188.6	-98.6	37.6	-23.5	80.3	34.3	0
24	1708 (1'x1.5')	-185.2	-85.9	46.1	-3.2	44.9	34.3	0
25	2001 (1.5x1.5')	-201.4	-137.2	36.7	-48.7	97.5	51.5	0
26	2004 (1'x1.5')	-169.5	-112.4	27.6	-41.5	98.4	34.3	0
27	2006 (1'x1.5')	-166.5	-107.3	34.6	-32.1	91.1	34.3	0
28	2008 (1'x1.5')	-187.7	-101.9	41.7	-19	68.1	34.3	0
29	2010 (1'x1.5')	-121.5	-62.8	40.3	-5.8	57.4	34.3	0
30	2301 (1.5x1.5')	-183.7	-118.1	38.9	-37.9	94	51.5	0
31	2304 (1'x1.5')	-174.6	-103.3	29.4	-36	97.7	34.3	0
32	2306 (1'x1.5')	-191.4	-110.2	32.2	-35.5	94.7	34.3	0
33	2308 (1'x1.5')	-182.3	-110.7	43.4	-29.8	82.8	34.3	0
34	2310 (1'x1.5')	-177.9	-105.5	42.1	-27.4	81.3	34.3	0
35	2601 (1.5x1.5')	-157.6	-101.6	38.2	-31	90.9	51.5	0
36	2604 (1'x1.5')	-135.9	-84.5	28.2	-27.6	95.8	34.3	0
37	2606 (1'x1.5')	-149.3	-93.2	30.2	-30.6	96.6	34.3	0
38	2608 (1'x1.5')	-133.5	-80.3	33.1	-19.6	82.1	34.3	0
39	2610 (1'x1.5')	-122.2	-62.7	40.5	-0.4	45.3	34.3	0

All values are based on an applied backing pressure of 22.9 psf.

Fig 7. Statistics of Wind Load Data for the 39 Nodal Points at 10 mph –  
Provided by UWO

### UWO WIND LOAD DISTRIBUTION AT 110MPH

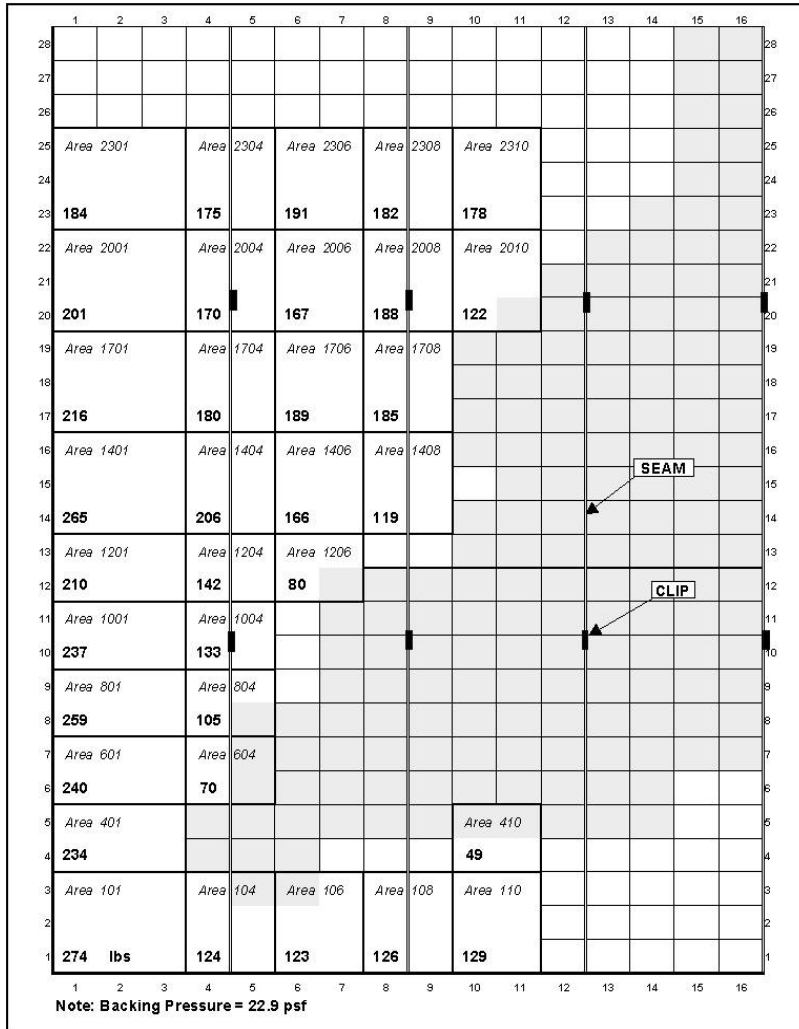


Fig 8. Wind Load Distribution at 110 mph – Mapping from UWO Wind Tunnel Data

## 9.0 UNIFORM STATIC PRESSURE TESTS – ASTM E-1592

Four full-scale vertical legs roofs were tested. The roof panel profile and layout were selected to withstand a design uplift wind load of 30-35 psf. The roofs were 16” panels, 24 gauge galvalume grade 50 ksi steel metal sheets, and placed at 5’-1” purlin spacing. The tests were carried up to the ultimate failure load of the roof. See Figures 9, 10 and 11 for selected views of the tested vertical legs roofs.

These tests provided a reference file on the performance of the roof under uniform static loading. This will be used for comparison and correlation with the dynamic simulated electromagnetic uplift wind loading. The load deflection curves for loading and unloading and the clip anchorage reactions were recorded in these tests.

Clip reactions for all 4 roofs are shown on Figures 12 and 13, respectively.

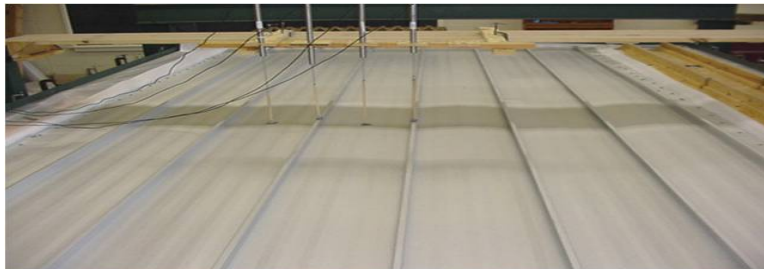


Fig 9. Uniform Static Pressure Tests- ASTM E-1592. Houston Vertical Legs Roofs – Before Loading.



Fig 10. Uniform Static Pressure Tests- ASTM E-1592. Houston Vertical Legs Roofs – During Loading.





Fig 11. Uniform Static Pressure Tests- ASTM E-1592. Houston Vertical Legs Roofs – After Failure of Seamline.

The clip reactions for the six instrumented clips are shown with the Tributary Area Line to show that the experimental collected and recorded clip reactions are within the rough estimate of the tributary area design approach. The deviation of the measured data from the tributary line can be attributed to the boundary conditions of the panels and to the roof deformation as a whole. It is interesting to note that the roof responded linearly to the uniform static pressure loading as verified by the linearity of the recorded clip reactions up and until failure. Recorded clip reactions indicated that load redistributed between clip reactions did occur at the instance of seam or clip failure.

It should be noted that roofs #1 and #2 were installed in an awkward manner by using partial pieces of a full panel for the first and last panels in the roof layout. This awkward installation was corrected in roofs #3 and #4 by using the full 16' width of the panel on all five panels of the roof. Roofs #3 and #4 will be used for comparison with electromagnetic uplift testing because they were installed identically to each others in both tests.

Figures 9 and 10 show the average clip loadings for roofs #1 and #2, and roofs #3 and #4, respectively, with the Tributary Area Lines. The average of roofs #3 and #4 compare extremely well with the expected data as shown by the plot of the Tributary Area Lines. All the roofs failed at almost exactly the expected design loads. The average of the static uniform failure pressure for these two roofs is 32 psf. It is interesting to note that clip reactions on purlin #2, (clips 2, 4 and 6), are higher than clip reactions on purlin #3, (clips 1, 3 and 5). This is to be expected because it agrees with the structural analysis.

The failure mode for all roofs under uniform static load was the same for all tests. The ultimate failure of the roof corresponded to seam line failure and loss of its integrity under load.

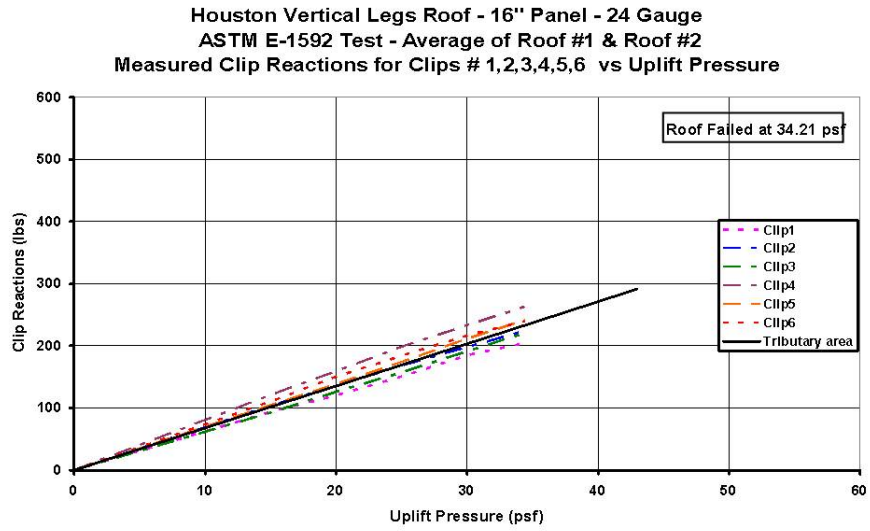


Fig 12. Uniform Static Pressure Tests-ASTM-1592. Clip Reactions - Average of Roof #1 & Roof #2

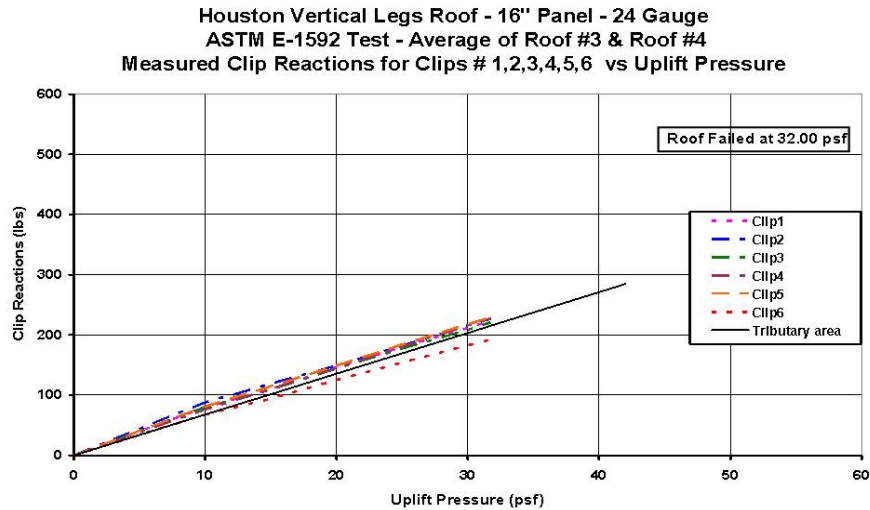


Fig 13. Uniform Static Pressure Tests-ASTM-1592. Clip Reactions - Average of Roof #3 & Roof #4

## 10.0 ELECTROMAGNETIC UPLIFT TESTS

The UWO wind tunnels loading data and the applied electromagnetic forces, after completing calibration, are shown for selected nodal points in Figures 14 and 15 for nodal points #21 and #30, respectively. These plots are shown here as typical examples. In general, all nodal points matched well with the UWO wind tunnel loading in time and space. The simulation exceeded all expectations. Detailed review and evaluation was prepared by Dr. Eric Ho of Davenport Wind Engineering Group, London, Ontario, Canada, for the accuracy of simulation, and he concluded that the correction between the wind tunnel loading and that of the electromagnetic held is accurate and exceptionally acceptable for all practical purposes.

The major difficulty in simulating the UWO wind tunnel data was in duplicating extremely high spikes in loading that lasted less than one second in time duration. Further research confirmed that the mismatch was related to the roofs not responding to less than one second duration of spikes loading effectively in time and to be reflected by measurements at the clip reaction.

Response to electromagnetic uplift testing was recorded at 20Hz for the six instrumented clips and the four LVDT deflection measurements.

The clip reactions for selected wind speeds and clips are shown in Figures 16 and 17. The clip reactions for roof #1 are superimposed on those from roof#2 to show the repetitiveness of the measured test data. As shown in Figures 16 and 17, the clip reactions from both roofs did indeed repeat themselves for the same wind speed over the entire loading period. For complete data for all instrumentations and comparative analysis of all measured data for the Houston vertical legs roofs under electromagnetic testing are included in Reference 9.

Vertical leg roofs under electromagnetic uplift testing failed at maximum clip reaction, clip #1, by slippage of the clip and final disengagement from the seam line. The clip slippage propagated into seam line failure from clip #1 to clip #2. See Figures 18 and 19. For multimedia presentation for the roof under loading up to failure see Reference 9. Roof #1 and roof #2 failed at the wind speed of 70 mph.

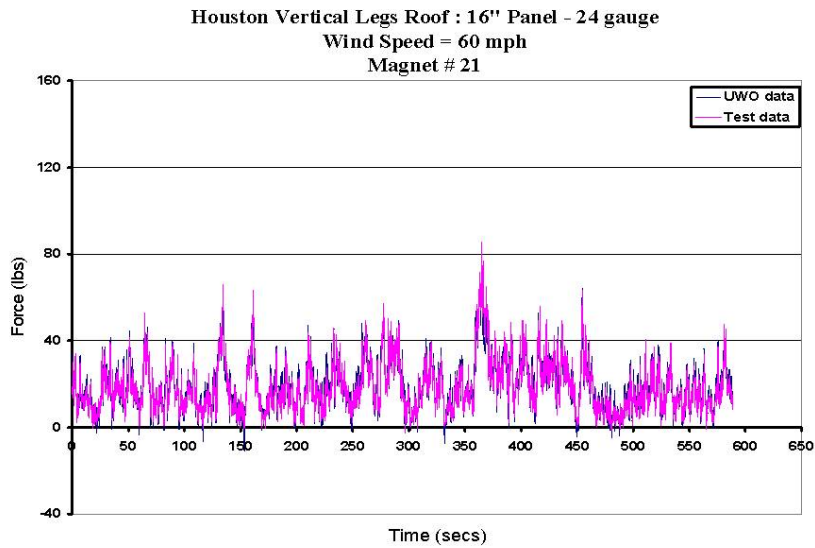


Fig 14. Electromagnetic Uplift Test Data and UWO Wind Tunnel Data Compared at 50 mph Wind - Nodal Point #21

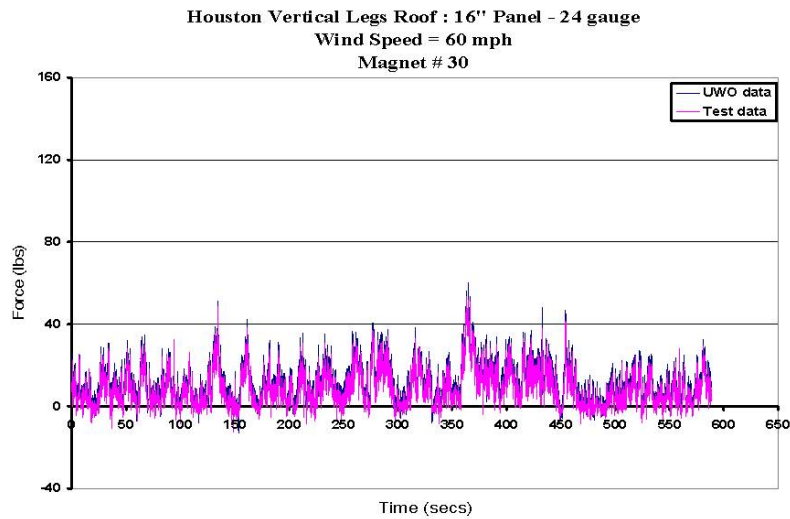


Fig 15. Electromagnetic Uplift Test Data and UWO Wind Tunnel Data Compared at 50 mph Wind - Nodal Point #30

The clip reactions for selected wind speeds for clip #1 are shown in Figures 16 and 17, roofs 1 and 2, respectively. These clip reactions for roof #1 are superimposed on those from Roof #2 to show the repetitiveness of the measured test data. As shown in Figure 18 and 19 for clips #1 and #2, respectively, the clip reaction from both roofs did indeed repeat themselves for the same wind speed over the entire loading period.

Vertical leg roofs under electromagnetic uplift testing failed at maximum clip reaction, clip #1, by slippage of the clip and final disengagement from the seam line. The clip slippage propagated into seam line failure from clip #1 to clip #2. See Figures 20 and 21.

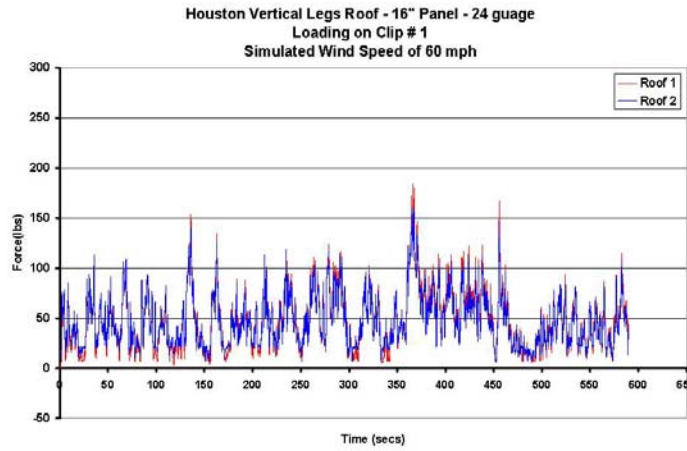


Fig 16. Comparison of Clip Reactions for Roof 1 & Roof 2 at 60 mph Wind - Clip #1

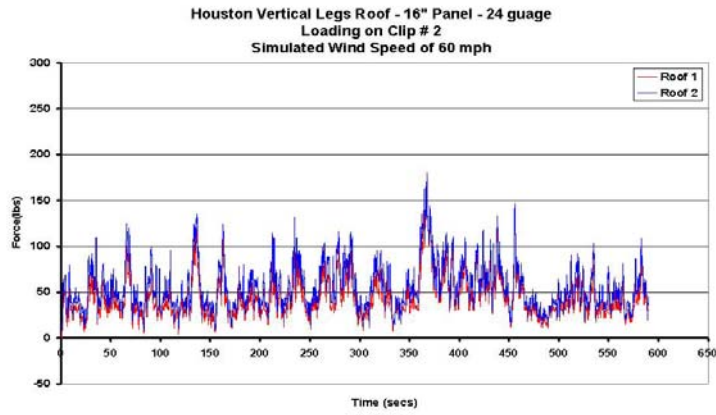


Fig 17. Comparison of Clip Reactions for Roof 1 & Roof 2 at 60 mph Wind - Clip #2

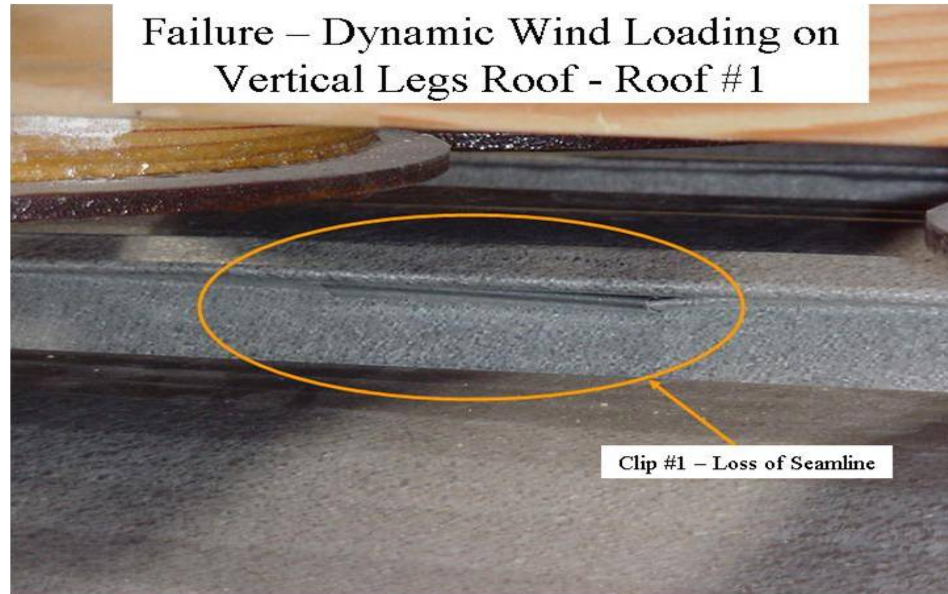


Fig 18. Failure of Clip #1 in Vertical Legs Roofs - Roof 1



Fig 19. Failure of Clip #1 in Vertical Legs Roofs - Roof 2

## 11.0 INDEX FACTOR

The index factor was created for design purposes in order to compare the uniform static pressure testing to electromagnetic uplift testing. This factor relates the maximum clip reaction in both tests. For the uniform static pressure test, ASTM 1592-02, the maximum clip reaction can be calculated from the maximum tributary area using ASCE 7-02 pressure loading under fastest mile wind speed with conversion to three second gust. The maximum recorded dynamic clip reaction using simulated UWO wind loading from the electromagnetic uplift test was then used in calculating the index factor. The magnitude of the clip reactions are also a reflection of the integrity of the adjacent seam lines. Thus, the index factor is defined as follows:

$$\text{I. F. (at any wind speed)} = \frac{\text{Clip Reaction using ASCE-7 and Tributary Area}}{\text{Maximum Recorded Dynamic Clip Reaction}} \quad (\text{Eq. 1})$$

For all practical design purposes, the above calculations for the index factor, based on its definition, are approximately equal to:

$$\text{I. F. (approx)} = \frac{(\text{Failure Wind Speed})_{\text{Dynamic}}^2}{(\text{Failure Wind Speed})_{\text{ASTM E-1592}}^2} \quad (\text{Eq. 2})$$

or

$$\text{I. F. (approx)} = \frac{\text{Dynamic Failure Pressure}}{\text{ASCE-7 Uniform Failure Pressure}} \quad (\text{Eq. 3})$$

The approximate ratios for calculating the index factor are shown only to demonstrate a simple and fast relationship between uniform static testing, ASTM 1592-02, and real world wind loading.

The calculations for the average index factor for the vertical legs roofs is shown below, and in Table 1 for intermediate loadings:



**Average of roofs 1&2 (See Table 1)**

$$I. F. \text{ (average)} = \frac{\text{Clip Reaction uniform Pressure ASCE 7 X Tributary area}}{\text{Measured Maximum Dynamic Clip Reaction}} = 1.396$$

The above compare closely using the square of equivalent failure wind speeds or wind pressures:

$$I. F. \text{ (approx)} = \frac{(\text{Failure Wind Speed})^2_{\text{Dynamic}} (70 \text{ mph})^2}{(\text{Failure Wind Speed})^2_{\text{ASTM E-1592}} (59 \text{ mph})^2} = 1.407$$

$$I. F. \text{ (approx)} = \frac{\text{Dynamic Failure Pressure } 44.05 \text{ psf}}{\text{ASCE-7 Uniform Failure Pressure } 31.31 \text{ psf}} = 1.407$$

**TABLE 1: Index Factors for Roof #1 and Roof #2**

**Average of Roof #1 & 2**

<b>Wind Speed (mph)</b>	<b>Roof #1 Index Factor (Static/Dynamic)</b>	<b>Roof #2 Index Factor (Static/Dynamic)</b>	<b>Roof #1&amp;2 Average</b>
<b>0</b>	0	0	0
<b>50</b>	1.3254	1.3784	1.351
<b>60</b>	1.3124	1.481	1.396
<b>70</b>	1.4825	1.4197	1.451
		<b>Average</b>	1.396

## 12.0 SUMMARY AND CONCLUSIONS

The electromagnetic uplift loading test based on the gap suspension of magnetic suction forces for applying in the simulated wind tunnel loading to real full scale thin metal roofs has proven its applicability and validity in this research. The applied loading data compared favorably and exceptionally well to the pre-assigned defined wind tunnel data in time and space. The success of the simulation of wind tunnel data on full scale metal roofs, built as per standard practice of the manufacturer of these roofs, was checked also against the correlation coefficients of the wind tunnel data itself. The applied simulated electromagnetic data was found to match the UWO wind tunnel data not only in time and space but also to duplicate the correlation coefficients of the wind tunnel data. Simulated loading for wind speeds from 50mph up to 160mph were applied and monitored at the rate of 20Hz. The measured clip reactions and deflections allowed for a comparison with those recorded using statistic uniform loading, ASTM E 1592 - 02.

This was the first time ever that the wind tunnel loading data was duplicated and applied successfully to a full scale thin metal roof test setup in the laboratory. The findings from this simulation allowed detailed analysis of the anchorage clip reactions for different profiles of roofs and from different manufacturers. Duplicate tests on each type of roof were conducted and measured data confirm repetitiveness of test results.

The following conclusions can be made:

1. The test results confirmed that the maximum anchoring reactions are almost proportional to the square of the wind speed under static and simulated true wind loading.
2. The anchoring reactions are considerably lower under true wind loading than those from the ASCE-7-05 for uniform static loading.
3. Failure modes of the tested roofs under simulated wind loading differ from those under static loading as they reflect the seriousness of the high intensity of wind loading at and around the roof corners.
4. Deflections and deformations of end panels of the roof are noted to be excessively higher under true wind loading than those under uniform static loading.

5. These approaches, test results, and findings presented here are applicable to any type of roof system and materials used to construct and build the roof in real life.

### **ACKNOWLEDGEMENT**

The research on electromagnetic uplift testing to simulate data generated by high wind velocity from wind tunnel testing has been sponsored for the past several years by the Metal Building Manufacturer's Association (MBMA), and the American Iron and Steel Institute (AISI). Also, partial funding was provided by Metal Construction Association (MCA), and FM Global.

The findings, conclusions, and opinions that are presented and expressed in this Report are those of the writer and are not necessarily those of the sponsors, MBMA, AISI, MCA, or FM.

### **REFERENCES**

1. Ho, E., Surry, D., and Davenport, A. (1992), "Roof Uplift Testing", MBMA Research Project, Boundary Layer Wind Tunnel Laboratory. The University of Western Ontario. London, Ontario, Canada.
2. ASTM (2001). "Standard Test Method for Structural Performance of Sheet Metal Roof and Siding Systems by Uniform Static Air Pressure Difference, ASTM E-1592-01.
3. ASCE 7-05 (2005). "Minimum Design Loads for Building and Other Structures." ASCE, Reston, VA.
4. Cook, N.J., Keevil, A.P., and Stobart, R.K. (1980). "BRERWULF- The big bad wolf." J. Wind Eng. Ind. Aerodyn., 29, 99-107.

5. Prevatt, David, and Scott Schiff (1996). Uplift Testing of Standing Seam Metal Roof Systems. Clemson University. Clemson, South Carolina.
6. Sinno, R., Nail, J., and Fowler, S. (2001). "Simulation of non-uniform unsteady wind pressures." MBMA Final Report, Civil Engineering Department, Mississippi State University, MS.
7. Shaunda L. F. (2001), "Clip reactions in standing seam roofs of metal buildings", Mississippi State University, M.S. Thesis.
8. Sinno, R., Surry, D., Flower, S., and Ho, E. (2003), "Testing of Metal Roofing Systems Under Simulated Realistic Wind Loads", Proceedings Eleventh International Conference on Wind Engineering, Lubbock, Texas, pp.1065-1071.
9. Sinno, R., "Simulation of Uplift Loading on Thin Metal Roofs (Electromagnetic Uplift Testing)," MBMA Final Report, Dec. 2005.
10. Surry, David, et. al., "Structurally Effective Static Wind Loads for Roof Panels," Journal of Structural Engineering, ASCE, June 2007, pp. 871-885.



## **State of the art report on thin-walled cold-formed profiled steel decking**

N.A.Hedaoo<sup>1</sup>, L.M. Gupta<sup>2</sup>, G.N. Ronghe<sup>3</sup>, S.K.Parikh<sup>4</sup>

### **Abstract**

Thin-walled cold-formed profiled steel decking is used extensively in the composite concrete slabs construction of modern buildings. Extensive research on cold-formed profiled steel decks has been carried out using experimental, analytical and numerical methods. In this paper, a review of the research carried out on cold-formed profiled steel decking is given with emphasis on experimental and analytical work. Experimental data has been collected and compiled in a comprehensive format listing parameters involved in the study. The review also includes research work that has been carried out to date accounting for the effects of different buckling modes and its behaviour, intermediate stiffeners, web crippling strength, embossments, ultimate moment capacity and load carrying capacity of the profiled decks

### **1. Introduction**

Two types of thin-walled cold-formed profiled steel decks i.e trapezoidal and re-entrant (Fig.1.) are currently used in composite reinforced concrete slabs as load-carrying structural members in steel frame buildings. This type of decks has many varieties, such as high strength/weight ratio, ease of transportation & construction, faster installation, a good ceiling surface, convenient ducting for routing utility services, etc. In addition the same can be easily shaped and sized to meet the design requirement. Steel decks are

<sup>1</sup> Sr.Lecturer, Department of Civil Engg, College of Engineering, Pune, INDIA

<sup>2,3</sup> Professor, Department of Applied Mechanics, VNIT, Nagpur-11, INDIA

<sup>4</sup> Ex-Professor, College of Engineering, Pune-5, INDIA

supported by steel beams. For this the decks are attached to the steel beams through shear studs. If the beam spacing is about 3 to 4 m, then no temporary propping is necessary during concreting of the slab. In this case, the construction stage controls the design of the steel decking. Due to the short slab span, the stresses in the composite slab in the final state after the concrete has hardened are very low. For such floors, trapezoidal profiled steel decks with limited horizontal shear resistance and ductility are most often used. They have the lowest steel weight per square meter of floor area.

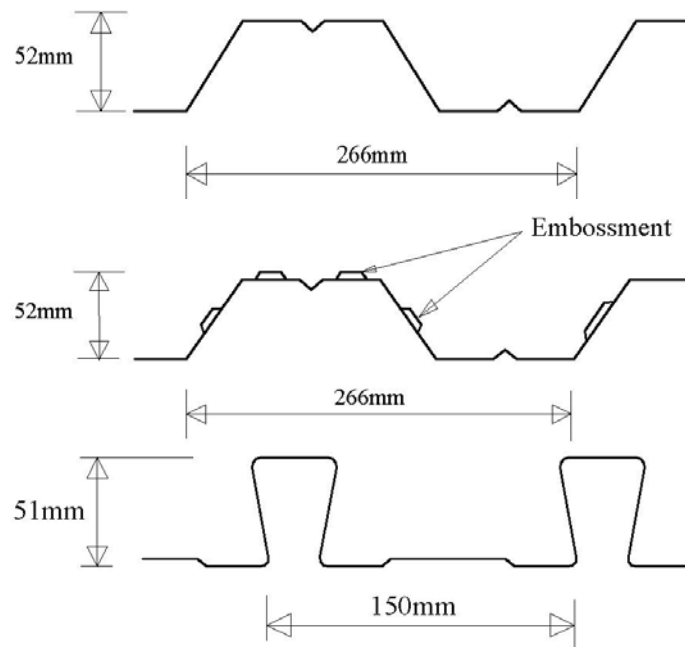


Fig. 1. Profiled Steel Decks

If the beam spacing goes up to 6 m, props are necessary to support the steel decking during concreting. Due to the longer slab span, the final composite slab is highly stressed. As a result this final state may govern the design. In this case the steel decking will require good horizontal shear bond resistance. Re-entrant profiles are often used leading to greater steel weight per square meter of floor area. However, trapezoidal decking slabs are more popular than re-entrant because of availability of more cover width and also the relative ease of casting of concrete.

The profiled steel decking is designed to behave compositely with the *in-situ* concrete, by introducing mechanical interlocks in the form of embossments in both the flanges and webs of the deck profile, so as to improve the resistance of the composite slabs in longitudinal shear. The steel decks must perform three functions, each in different phases of the construction process. First, the steel deck, after being fastened in place, serves both as a form for the fresh concrete and working platform to support workmen. The second function of the steel deck is to act as permanent shuttering for the concrete slab. Finally, it acts as sagging reinforcement for the slab.

Significant changes in the design of profiled steel decks have occurred during the past 38 years. A consequence of these changes is that the most popular structural steel for profiled steel deck construction which was ASTM A36, with a yield stress of 250 MPa, is now replaced by steel grade 345 MPa, ASTM A992 [ 2] in the United States and the higher strength steel which has a yield stress of 550 MPa is being used in Australia. The adoption of the new “North American Specification (NAS 2007) for the Design of Cold-Formed Steel Structural Members” and Direct Strength Method as an alternative to the current effective width approach may be considered as an important advancement for steel deck design when being compared to the older design procedure.

This paper presents the state of the art knowledge on thin-walled cold-formed profiled steel decking including experimental and analytical studies. The design methods and features of the specific codes for the design of steel decks are briefly described. A detailed discussion on ultimate moment capacity and load carrying capacity of the profiled decks are presented. For this the influence of; buckling modes, intermediate stiffeners, web crippling, embossments etc are considered.

## **2. Behaviour of thin-walled profiled steel decking**

Profiled steel decks are usually 38 to 200 mm high with trough spaced at 150 to 300 mm, thickness 0.6 to 1.5 mm, cover width 0.6 to 1.0 m and lengths up to 12.8 m [1, 2]. Decking is commonly fabricated from hot-dipped galvanized plate with a zinc coating of 275 g/m<sup>2</sup> on both sides, which corresponds to a mean thickness of approximately 20 µm on each side, and is normally sufficient for internal floors in a nonaggressive environment. The steel used has a yield stress in the range of 280 to 550 N/mm<sup>2</sup> [3]. V-shaped intermediate stiffener on the top side of flange tends to improve the load-carrying capacity, as also the buckling behaviour of the decks.

The steel decks are usually thin having the width-to-thickness ratios quite large. The thin elements may buckle locally at stress levels less than the yield point of steel when they are subject to compression in flexural bending, as



also, axial compression. Consequently, they are subject to more complex forms of buckling than hot-rolled section. The three basic modes of buckling [3] of steel deck members are shown in Fig. 2.

A *local buckling* is a mode involving plate flexure alone without transverse deformation of the line or lines of intersection of adjoining plates, *distortional buckling* is a mode of buckling involving change in cross-sectional shape excluding local buckling, and *flexural-torsional buckling* is a mode in which compression members can bend and twist simultaneously, without change of cross-sectional shape. This is because the sections are relatively thin and the shear center lie outside the web.

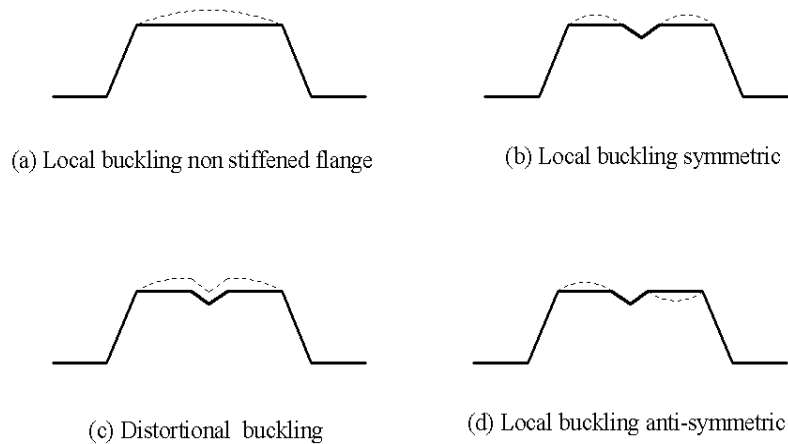


Fig. 2. Buckling modes of Profiled Steel Decks

For calculating the load carrying capacity of the decks, the bending moment using the ultimate limit state, loads arising from the weight of fresh concrete and steel deck, construction loads (i.e the weight of the operatives and concreting plant and take into account any impact or vibration that may occur during construction), ‘Ponding’ effect (increase depth of concrete due to deflection of the decking), storage loads, etc should be considered. According to Eurocode 4, in any area of 3m by 3m, in addition to the weight of fresh concrete, the characteristic construction load and weight of surplus concrete (ponding effect) should together be taken as uniform load of  $1.5 \text{ KN/m}^2$ . Over the remaining area, a characteristic loading of  $0.75 \text{ KN/m}^2$  should be added to the weight of concrete [4]. After hardening of the concrete, the steel deck cooperates with the concrete in order to undertake the additional loading on the composite slab.

### **3. State-of-the art during 1975-2008**

The studies on profiled steel decks were carried out extensively throughout the world, and were followed over the years by more experimental, analytical, and theoretical works by research workers. Experiments were conducted to obtain the information to serve as an aid to develop modeling or to formulate new design criteria. Because structural behaviour involves the interaction of steel decks with concrete, resulting into a situation, that is difficult to analyse satisfactorily; a wide range of analytical methods are formulated, to examine the suitability of decks under various loading conditions. The state-of-the art presented herein constitutes summary of various studies on profiled steel decks used in composite slabs, with specific reference to the aspects of local and distortional buckling, flexural strength, web crippling, etc. The source of information being leading international journals on steel structures.

#### **3.1 Buckling behavior**

Phenomenon local buckling of thin-walled steel decks has been known for many years, and the same been well researched. The design methods proposed in the design standards, to account for local buckling of thin-walled members in compression and bending, are based on the effective width method for stiffened and unstiffened elements. The basic concept of “effective width” is illustrated in Fig.3. In this method, it is assumed that as a consequence of top flange buckling due to high compressive stresses, the stress distribution in the top flange changes. The resulting non-uniform stress distribution over the entire width of flange is replaced by a uniform stress distribution over a width called the effective width. When the stress in the effective width reaches the yield stress; it is assumed that the decking has reached the ultimate bending moment. The effective width method is an elemental method, since it looks at the elements forming a cross-section in isolation. It was originally proposed by Von Karman (1932), and calibrated for cold-formed members by Winter (1946) [5]. Local and flexural-torsional modes of the deck members are largely covered in the design codes BS 5950: Part 6 [6], Eurocode:3 Part 1.3 [7] and AISI specifications [8]. Recently, it was observed that the distortional buckling plays an increasing role, with the use of thinner sections, made with high strength steels, in the behaviour of decking sections, and now it has been extended to stiffened elements with an intermediate stiffener of the AISI Specification (2007) [9]. It accounts for post-buckling behaviour, by using effective plate width at the design stress.

The paper by Erik Bernard, Russell Bridge and G.J.Hancock [10,11] investigated the effectiveness of size and position of single intermediate V-stiffener, flat-hat stiffener, and without stiffener in compression flange of the trapezoidal profiled steel deck section (see Fig.3.). In the first paper, a series of 30 specimens with and without V-stiffeners were tested under pure bending by applying two point loads using a plastic collapse mechanism. The intermediate stiffeners were in the middle of the compression flange and their height increased from 2 to 10 mm. The total width of the folded section was 785 mm, length of 2000 mm, and total thickness of steel 0.63 mm. Minimum yield strength was of the order 550 MPa. The experimental buckling stresses and ultimate moment for both local and distortional buckling were found to agree very well with a finite-strip elastic buckling analysis. The existing design procedure for local buckling as per AS1538-1988 (now redesignated as AS/NZS 4600:2005) [21] was conservative. It proposed a simplified design procedure for distortional buckling based on Winter formula to determine an estimate of the ultimate load-carrying capacity of deck in compression flange.

In the second paper, a series of 27 specimens with single V-stiffener, flat-hat stiffener, and without stiffener in compression flange of the steel deck section were tested to exhibit both local and distortional buckling under pure bending. The size and position of the V-stiffener and the section geometry of the profiled steel deck were similar to earlier paper. The size and position of the flat-hat stiffener were different while keeping the same section geometry of the V-stiffener. The experimental ultimate moment results were compared with design codes AISI 1991[8], Eurocode 3: Part 1.3 [7] and AS 1538-1988. The method of Eurocode 3: Part 1.3 proved to give the most consistent results. All the codes were however conservative by 20%. The prediction of the AISI 1991 Cold-formed Steel Structures Specification, and the Australian Standard AS 1538-1988 were closer to the test results, but with less consistency than Eurocode 3: Part 1.3. Proposed Modified Winter Formula method for distortional buckling that is experienced prior to ultimate failure, were however, unconservative for local buckling. The same is the case with the proposed Modified Effective Section method which accounts for the interaction of local and distortional buckling modes.

The behaviour and design of cold-formed steel deck hat sections with single and multiple intermediate stiffeners in the compression flange was investigated by B.W.Schafer and T.Pekoz [12]. Existing experimental data were used to evaluate critically the AISI specification (1991) [8], and Eurocode 3: Part 1.3 [7]. In the first experimental work, 25 sections with one and two intermediate stiffeners including the parameters such as the ratio  $w/t = 180$  &  $460$  and  $h/t = 60$  &  $90$ , were loaded by four-point bending test. In the second experimental work, 20 sections with multiple intermediate stiffeners including three material thicknesses, one to four stiffeners and  $w/t = 90$  to  $400$ , and  $h/t =$

40 to 90, were loaded uniformly by vacuum test. In the last experimental work, 22 sections with one intermediate stiffeners, by considering variety of parameters, such as the stiffener size, the slenderness of the subelement plates, the ratio  $w/t = 100$  to 300 and  $h/t = 70$  to 95 were loaded by two-point bending test. While comparing the results of the different procedures, the existing experimental data shows the AISI specification is quite unconservative and Eurocode 3: Part 1.3 often yields overly conservative results. A finite element model was developed for the parametric study using program ABAQUS for both the material and geometric nonlinearities of the specimen. Comparisons to

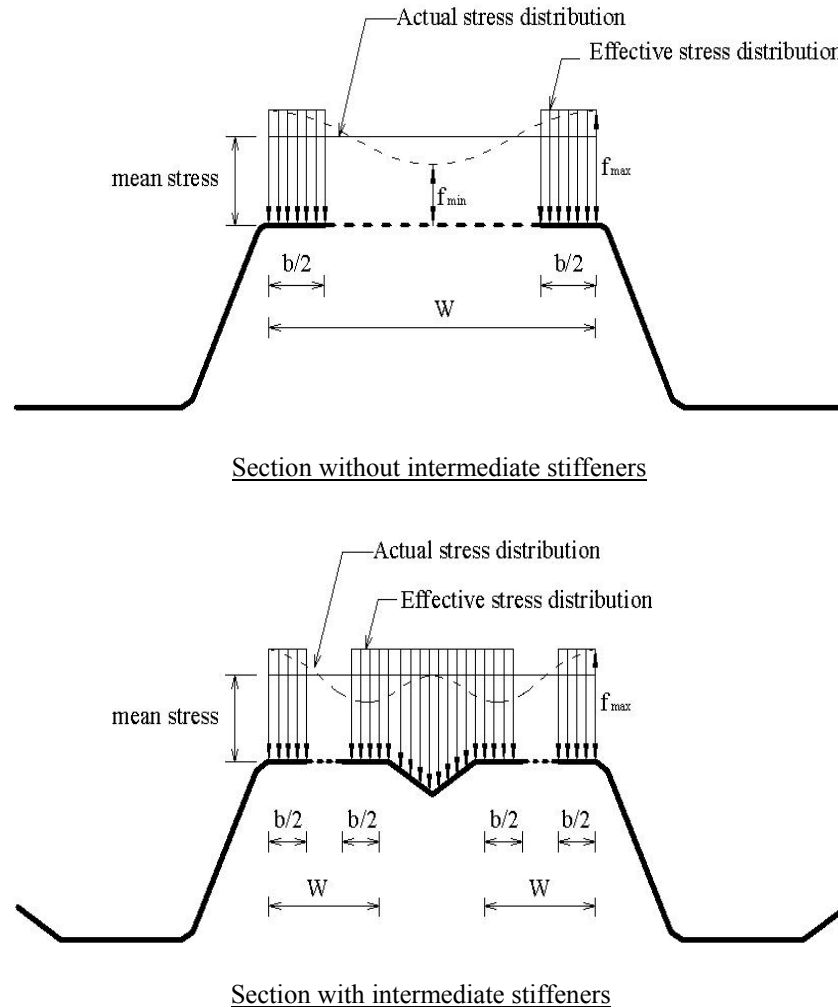


Fig.3. Effective cross section of trapezoidal profiled decks

experimental data could authentic the finite element model. An extensive parametric study was completed, which shows the importance of distortional buckling for these sections. Author's investigated two approaches, viz; Equivalent Effective Width (EQEW) and Modified Winter Equation as alternatives to the current procedures.

### 3.2 Flexural bending

Allan Bergfelt and Bo Edlund [13] have studied the behaviour of plain trapezoidal profiled steel decks under pure bending to find the load carrying capacity. 21 tests were carried out using a beam simply supported along its longitudinal edges, subjected to two line load, with the web slenderness ratio  $d/t = 110$  to 125. The author's investigated the effect of web slenderness of the decks on web buckling stress. It was found that, after the flange has buckled the theoretical critical stress of the web decreased due to the shift of the neutral axis. The results indicate that the method of the AISI (1968) web buckling stress ought to be modified for decks with slender webs.

A design of continuous decking using European Recommendation [22] is decided by considering the interaction between hogging bending moment and reaction force at an internal support. J.M.Davies and C.Jiang [14] have studied the accuracy of the European Specifications equation and compared the predicted failure conditions, where span is chosen to give the same ratio of bending moment and reaction as at the internal support in a two-span test. However, the results show a huge scatter with very poor correlation between the test results and the formula, and it requires either testing or quasi-elastic design based on the calculated moment of resistance at the internal support. This situation was improved by the author's, through investigations of a new design procedure, which is based on the formation of a pseudo-plastic collapse mechanism, which utilizes the redistribution of bending moment, following initial yielding or buckling, and to predict the moment-rotation relationship at the internal support. The two design methods combined together to produce a mathematical model for the pseudo-plastic design of continuous decking. The results of this new procedure compared well with those obtained from double span test. Author's also concluded that the influence of the web dimples was to decrease the bending strength by less than 10%, and suggested that dimples in the compression flange may affect the bending strength of composite decking and should be considered in the design for the fresh concrete stage.

Leopold Sokol [15] carried out the non-linear behaviour of continuous decking under uniformly distributed, progressively increasing loading. After the elastic-linear phase, and elastic non-linear phase, the plastic stresses and deformations appeared in the sections at and near the internal support, due to the

combined effect of bending moment and internal reaction. A plastic hinge appears over the support, and specimen enters the plastic phase (non-linear). The author studied the plastic analysis of specimens for ultimate state using the Eurocode 3: Part 1.3. The calculations are quite tedious and proposed some simplifying assumptions.

In practice sheeting fails under concentrated loads and large bending moments. The current design rules are not based on as to how sheeting fails under combined action of concentrated load and bending moment. Only global interaction between these two phenomena is described and not the real physical behaviour of the sheeting during interaction. H.Hofmeyer and J.G.M. Kerstens [16] presents a new analytical model to predict the ultimate load of sheeting under practical loading conditions. These practical conditions are defined by the ratios between bending moment and concentrated load as occurring in practice and compared with the existing Eurocode 3 design rules. For experimental works, hat-sections instead of trapezoidal sheeting have been tested because they were easier to manufacture with varying dimensions. 72 experiments were carried out for hat sections, with varying cross-sectional geometry, span length and yield stress, and tested under set-up specially made by Hofmeyer's. The first-generation sheeting failed mainly through yield arc and yield eye mechanism. The yield arc mechanism occurs for a high concentrated load, because the cross-section's of the web deforms first. For the yield arc mechanism, field lines are fixed in the web. The yield eye mechanism occurs for a high bending moment, because the top flange cripples first. In the analytical model, some part of hat-section's top flange has been considered by placing load bearing plate on that part. Due to certain load on the load bearing plate, a part of the top flange will deform, and using a bisection iteration method, the specific load at the load bearing plate, needed to reach the yield stress can be found. The deformation is modeled using predicted ultimate load of the section. In this way, a new model has been developed to predict the failure of first-generation sheeting. Without any correction, this new model functions with nearly the same quality as the Eurocode 3 interaction rule which uses three different concepts. The new model provides more insight in the structural behaviour of sheeting, subject to concentrated load and bending moment. Since the new model is based on the structural behaviour of the sheeting no interaction rules are needed. One rule is sufficient to describe two mechanisms for practically used sheeting: the yield arc; and yield eye mechanisms. The new model describes directly the relationship between the concentrated load and bending moment.

A recent paper by Euripides Mistakidis and Kyriakos Dimitriadis [17] studied the behaviour of thin-walled trapezoidal steel sheeting profile with four different embossment depth (0.5 mm, 1.0 mm, 1.5 mm and 2.5 mm) into the web, and different thicknesses of the sheeting (0.75 mm, 1.00 mm and 1.25 mm)

to determine the contribution of the embossed areas of the steel sheeting to the total strength in pure tension and in pure bending. According to Eurocode 4-Part 1-1 [4], the resistance of the composite slab in bending should be based on an effective area of the steel sheeting in which the width of embossments in the sheet is neglected, unless it is shown that a larger area is effective. The analysis is based on three-dimensional finite element (MARC Code) models of the steel sheeting, which takes into account accurately the geometry of the specific profile, where the nonlinear effects play a minor role. A parametric analysis is performed using four-point bending by applying two equal forces on the 2.0 m span in order to study the effect of the depth of the embossments to the strength and the stiffness of the steel sheeting. The study concludes that there is a strong relation between the area of the embossment region that can be considered as active, and the ratio between the depth of the embossment and the thickness of the profile.

### 3.3 Web crippling

Web crippling is also one of the failure modes of steel decks. Web crippling often occurs in steel decks because they may get loaded eccentrically from the web centerline, due to the rounded corners of the sections. Also because the webs are often slender and unstiffened.

Results of an experimental work on web crippling strength of deck profiles subjected to end one flange loading are presented by Samuel Easterling and Onur Avci [18]. A total of 78 multiweb deck specimens were tested and the results were compared with AISI (1996) [8] & NAS (2001) [23] strength prediction methods. Thirty-nine of the specimens were fastened by self-drilling screws through the tension flange to the support locations while the remaining 39 were unfastened with different support conditions. The parametric study included plain decks, embossed decks and steel sheet thickness. Test specimens laying inside and outside of certain geometric limitations were tested with both unrestrained and restrained end conditions. Fastened specimens resulted in higher web crippling strength than unfastened specimens. There were no failures of the screws connecting the decks to the supports. In the analytical study, the effect of embossments on the webs of composite decks was not taken into consideration with either method. Calculation procedure (AISI 1996 & NAS 2001) were found to be conservative for web crippling strength of deck section under EOE loading when compared with the test results. AISI (1996) values were found out to be more conservative than (NAS 2001) values for most of the specimens. New web crippling coefficients were proposed for fastened and unfastened cases based on the results.

Profiled decking of high strength *low-ductility* steel of grade G550 MPa of Australian Standard AS 1397 (Grade E of ASTM A611) is a relatively new

development in Australian building construction. None of the current international design practices include detail provisions for this kind of steel. This type of decking shows high sensitivity to distortional as well as local buckling effect. Strength of such decking under combined flexural and web crippling as well as moment-rotation capacity are of principal concern if such decking is to be design as a continuous structure to achieve better economy. A.M.Akhand and H.D.Wright [19] describes an experimental study of the behaviour of re-entrant decking of low-ductility steel under combined web crippling and flexure. There are few attempts in which analytical methods have been applied to compute combined web crippling and flexural strength of profiled steel decking, with different shapes and moderate ductility. Hofmeyer et al. [16] have presented a more complex analytical model to predict the combined strength of sheeting. Analytical provisions of various international design codes, e.g. AISI Specification [8], BS 5950: Part 6 [6] or European Recommendation [22] for estimating the inelastic moment resistances over an internal support are also known to be inadequate and overly conservative [14]. For the study, 15 specimens of re-entrant decking with 600 mm cover width 1 mm thickness and spans from 1 m to 4 m under uniformly distributed loading were tested. Because when designed as a continuous spans, the profiles have a larger scope for significant increase in strength resulting from redistribution of moments at ultimate load. Based on the experimental study, a three dimensional general second order nonlinear finite element model has been proposed for the orthotropic geometric configuration of the sheeting and for its geometric and material nonlinearities at the ultimate load range. A general purpose finite element package, LUSAS was used on the basis of the Kirchoff's theory for the study. It was found that the buckling behaviour of the sheeting is predominantly governed by distortional buckling mode in contrast to the local buckling behavior of an ordinary sheeting of medium ductility. A nonlinear finite element model has been presented which can predict the combined flexural and web crippling strength as well as the moment-rotation capacity of the sheeting with sufficient accuracy. The model can be used advantageously to derive the parameters required for the design of sheeting as continuous structures.

Ibrahim Guzelbey & Abdulkadir Cevik [20] studied the use of Neural Network using Matlab toolbox to predict the web crippling strength of trapezoidal steel decks. A closed form solution was proposed for steel decks acted upon by ultimate concentrated load. The required parameters were derived through experiments. The studies of complex web crippling behaviour of sheeting were categorized through experimental, FE modeling and mechanical models; but current design codes in this field still remain inaccurate. The experimental work on web crippling strength using different combination of concentrated load and bending moment were studied by J.M.Davies and C.Jiang [14], H.Hofmeyer and J.G.M. Kerstens [16], Samuel Easterling and Onur Avci



[18]. The proposed ANN model accurately predicts the relationship between the ultimate concentrated load and its geometric and mechanical properties. It consumes less solution time compared to that of FE modeling as well as mechanical modeling. This makes it practically more useful. The NN results are compared with the experimental results and design codes (NAS 2001) [23] and found to be considerably more accurate.

#### 4. Design codes

Based on the research efforts, inclusive of the experimental and analytical studies; various countries have proposed the codes for the design of steel decks.

##### *4.1 Code of practice for use of cold-formed light gauge steel structural members in general building construction (Indian Standard IS 801- 1975)*

In this code, only the calculation of stresses on the compression flange of the stiffened elements based on modified Winter's effective width approach, and the design using allowable design stress method is given. The calculation of the effects of distortional buckling, web crippling behaviour, bending moment & the internal reaction at the mid span support of the profiles, zinc coating and different types of loading conditions are not specified. Hence code is not of much use for steel deck design purpose. Revision of the code is thus warranted.

##### *4.2 Design of steel structures, Rules for cold formed thin gauge members and sheeting (Eurocode 3 : Part 1.3 :2001)*

This code uses ultimate limit state concepts to achieve the aims of serviceability and safety by applying partial safety factor to loads and material properties. The bending moment is calculated by elastic & partial plastic analysis with effects of local buckling, through the effective width of compression element and effective depth of web. The effective width of compression element is estimated by using reduction factor on the basis of the effective cross-section. Interaction between the flexural buckling of intermediate flange stiffeners and the web stiffeners is allowed for calculating elastic critical stress.

##### *4.3 Cold-Formed Steel Structures (AS/NZS 4600 : 2005)*

In most of the codes worldwide, the effects of plate buckling are accounted for by the concept of effective width, where the gross section is reduced to an effective section. An interaction between the elements also occurs; consequently consideration of the elements in isolation is less accurate. To overcome these problems a new method has been developed by Schafer and Pekoz called the 'Direct Strength Method' as an alternative to the current

effective width approach and the same is sufficiently accurate to predict the capacity of cross-sections correctly. It proposes a design procedure based on elastic buckling solutions for the complete cross-section rather than the individual elements. The high yield stress G550 (550 MPa) of steel sheet is proposed for design.

#### *4.4 North American Specification for the Design of Cold-Formed Steel Structural Members (NAS 2007)*

This specification supersedes the 2001 edition of the North American Cold-Formed Steel specification, and the previous edition of the Specification for the Design of Cold-Formed Steel Structural Members published by the American Iron and Steel Institute. The specification was developed by a joint effort of the American Iron and Steel Institute's and the Canadian Standards Association Committee on Cold-Formed Steel Structural Members. Since the specification is intended for use in Canada, Mexico, and the United States. This specification provides an integrated treatment of Allowable Strength Design (ASD), Load & Resistant Factor Design (LFRD), and Limit State Design (LSD). This is accomplished by including the appropriate factors ( $\Phi$ ) for use with LFRD and LSD, and the appropriate factors of safety ( $\Omega$ ) for use with ASD. The provisions for determining the effective width of uniformly compressed elements with one intermediate stiffener (previous section AISI 1989) have been replaced by the provisions provided in this new AISI 2007. Provisions for distortional buckling and effect of combined bending and torsional loading have been introduced. The equations for members subjected to combined bending and web crippling have been recalibrated.

### **5. Roll of finite element analysis in the development of the profile steel concrete composite deck.**

#### **5.1 Introduction**

The analytical approach comprising the application of finite element technique has already been established as the instrument of the dependable solution process. So much so that, unless there is a major departure from the conventional structural system, the finite element technique could be utilized for the process of the rational design of the composite deck.

#### **5.2 Element Library**

For simulating various components of the composite deck system, all the available element types, in the element library of commercial software's, such as ANSYS, ABAQUS & LUSAS etc., could be employed. In general following element types have useful application.

- a) Two noded and three noded line elements for representing the steel reinforcement rods, shear studs, etc.
- b) Shell elements with triangular domain and quadrilateral domain, for representing the steel profile segments of the composite deck system. First order or second order element could be employed as per the requirement of the situation.
- c) Solid elements for representing the concrete segment of the composite deck. Triangular prismatic and hexahedral elements could be employed. The first order or second order elements could be utilized depending upon the requirement of the situation.
- d) One dimensional and two dimensional interface elements for simulating the junction between the steel components and concrete component of the composite deck.

### 5.3 List of problems to be tackled

The conventional design for the composite deck could be undertaken through the finite element method. The structural response derived through the linear deformation analysis, in conjunction with the code recommendations would yield the required design. For deriving the ultimate response, however, non linear analysis is essential. In this connection two phase development is desirable.

**Phase 1:** It deals exclusively with the analysis of the ultimate behavior of the steel deck. The finite element analysis involves the considerations to both the geometric and material non linearities. The geometric non linearity arises due to the manifestation of the distortion of the component of the steel profile deck. The aspects, such as local buckling, curling, warping of the plate components would significantly alter the geometrical constitution of the steel profile. Both the displacements as also the strains might be of small order, but in view of the fact the geometrical changes are initiated at a level much below the yield stress of the steel, suggests that the distortions would be in conjunction with the plastic deformations. This in turn involves material non linearity. The combined influence of the geometric non linearity and the material non linearity could be analysed through a step wise elasto-plastic deformation analysis. The methods of carrying out such analysis, is well documented in the relevant literature.

**Phase 2:** In phase 1, the concrete segment of the composite deck provided only the loads on the steel deck, without the contribution to the stiffness of the system. In phase 2, the composite action of the steel profile and the concrete segment becomes active. For the analysis of the ultimate behavior, however, once again the phenomenon of the geometric non linearity, coupled with the material non linearity gets manifested. The geometric non linearity may involve features such as large displacements, global buckling, interface sliding

and or debonding between the concrete surface and steel profile. The material non linearity would arise from the phenomenon of cracking in the concrete segment due to tensile stresses and the phenomenon of softening of the concrete segment due to the compressive stresses. The constitutive laws governing this kind of behavior are sufficiently complex, and their true character would demand extensive laboratory tests over the representative samples. In phase 2 the most complex situation could arise from the thermal strains developing during the onset of fire or the dynamic loads arising from the agencies such as the blasts, earthquake shocks etc.

Many of the above mentioned aspects of non linear analysis could be undertaken with the established finite element procedures. However entire process of non linear analysis involves iterative solution technique consuming great amount of computer time. Keeping this in view the attempts are on the way to coin the special purpose finite elements, which provides the reasonable results from the analysis.

## **6. Conclusions**

Considerable progress has been made during the last three decades in the investigation pertaining to design of thin-walled cold-formed profiled steel decking as a permanent formwork, used in composite concrete slab construction. Details of the investigations on experimental, analytical and design code works is summarized in this paper. Intensive research is required on bending moment and, reaction at the internal support for continuous span, by considering its combined effects of local & distortional buckling on steel deck element, effect of embossment, etc. In this connection finite element solution technique holds bright promise. The North American Specification (NAS 2007) for the Design of Cold-Formed Steel Structural Member and Direct Strength Method as an alternative to the current effective width approach for steel deck design appears to be more rational.

## **References**

- [1] Sebastiao A.L.de Andrade, Pedro C.G.da S. Vellasco. Standardized composite slab systems for building constructions. *Journal of Constructional Steel Research* 2004; 60:493-524.
- [2] Committee Report. Construction considerations for composite steel-and-concrete floor systems. *Journal of Constructional Steel Research* 2002; 128(9): 1099-1110.
- [3] J.M.Davies. Recent research advances in cold-formed steel structures. *Journal of Constructional Steel Research* 2000; 55:267-288.

- [4] EN 1994-1-1:2003, Eurocode 4-Part 1.1. Design of composite steel and concrete structures- General rules and rules for buildings. European Committee for Standardisation, 2003.
- [5] IS 801-1975, Code of practice for use of cold-formed light gauge steel structural members in general building construction.
- [6] BS 5950: Part 6:1995, Structural use of steelwork in building: Code of practice for design of light gauge profiled steel sheeting.
- [7] EN 1993-1-3:2001, Eurocode 3-Part 1.3. Design of steel structures: supplementary rules for cold formed thin gauge members and sheeting.
- [8] AISI 1986, Specification for the design of cold-formed steel structural members.
- [9] NAS 2007, North American Specification for the design of cold-formed steel structural members.
- [10] Erik Bernard, Gregory Hancock. Tests of profiled steel decks with V-Stiffeners. *Journal of Structural Engineering*, ASCE 1993; 119(8): 2270-2293.
- [11] E. Bernard, Gregory Hancock. Design methods for profiled steel decks with intermediate stiffeners. *Journal of Constructional Steel Research* 1996; 38(1): 61-88.
- [12] B.W.Schefer, T.Pekoz. The behaviour and design of longitudinally stiffened thin-walled compression elements. *Thin Walled Structures* 1997; 27(1):65-78.
- [13] Allan Bergfelt, Bo Edlund. Experiments on trapezoidal steel sheets in bending. Third International Specialty conference on cold-formed steel structures, University of Missouri-Rolla, USA 1975:285-315.
- [14] J.M.Davies, C.Jiang. Design procedure for profiled metal sheeting and decking. *Thin Walled Structures* 1997; 27(1):43-53.
- [15] Leopold Sokol. Some specific aspects of elastic-plastic behaviour of profiled steel sheeting and decking. *Thin-Walled Structures* 1997; 29(1-4):102-112.
- [16] H.Hofmeyer, J.G.M. Kerstens. New prediction model for failure of steel sheeting subject to concentrated load (web crippling) and bending. *Thin Walled Structures* 2001; 39:773-796.
- [17] Euripides Mistakidis, Kyriakos Dimitriadis. Bending resistance of composite slabs made with thin-walled steel sheeting with indentation or embossments. *Thin Walled Structures* 2001; 46:192-206.
- [18] Easterling Samuel, Onur Avci. Web crippling strength of steel deck subjected to end one flange loading. *Journal of Structural Engineering*, ASCE 2004; 130(5):697-707.
- [19] A.M.Akhand, H.D.Wright. Combined flexure and web crippling strength of a low-ductility high strength steel decking: experimental and a finite element model. *Thin-Walled Structures* 2004; 42:1067-1082.

- [20] Ibrahim Guzelbey, Abdulkadir Cevik. Prediction of web crippling strength of cold-formed steel sheeting using neural networks. *Journal of Constructional Steel Research* 2006; 62:962-973.
- [21] AS/NZS 4600:2005, Australia/New Zealand Standard. Cold-formed steel structures.
- [22] European Recommendations for the design of profiled sheeting. European Convention for Constructional Steel work, ECCS-TC7-1983.
- [23] NAS 2001, North American Cold-Formed Steel Specification



## **Vibration Performance of Lightweight Floor Systems Supported by Cold-formed Steel Joists**

B.W. Davis<sup>1</sup>, R. Parnell<sup>1</sup> and L. Xu<sup>2</sup>

### **ABSTRACT**

A study investigating dynamic characteristics of full-scale floor systems was performed for several laboratory-constructed and in situ floors. Floors were constructed with cold-formed steel joists and designed for residential mid-rise applications. Typical construction details including span, subfloor, topping, strongback and framing condition were varied, and their influence on fundamental frequency, damping ratio and deflection at mid-span compared. Changes in construction details which significantly increased floor mass, regardless of added stiffness, were found to lower the fundamental frequency. Adding a strongback with restrained ends provided a significant increase in fundamental frequency, stiffness and damping ratio. Laboratory tested floor systems were generally found to be the worst-case scenario for natural frequency and damping ratio.

### **1. Introduction**

Over the last decade, cold-formed steel has become an increasingly popular building material for residential and commercial construction. This increased use can be attributed to the numerous advantages that cold-formed steel has over traditional residential building materials. Cold-formed steel offers resistance to

---

<sup>1</sup> Research Assistant, The Canadian Cold-formed Steel Research Group, Dept. of Civil and Environmental Engineering, University of Waterloo, Canada

<sup>2</sup> Associate Professor, The Canadian Cold-formed Steel Research Group, Dept. of Civil and Environmental Engineering, University of Waterloo, Canada



termites and moisture, design flexibility, rapid construction, and a strength to weight ratio greater than any other building material. This high strength to weight ratio is an asset in strength design, but can cause inherent vibration problems in floor systems. Cold-formed steel floor systems have larger spans than wood-supported floors while they are significantly lighter than steel joist and concrete floor systems. There is a need to characterize the performance of cold-formed floor systems built for residential applications, as there is no appropriate method in current practice for evaluating their performance. Current design methods for floor systems are applicable for use with traditional wood-framing or composite steel joist and concrete systems only. Designing a floor system to control these annoying vibrations can be challenging, and correcting inadequacies after construction is usually very costly. This is why it is imperative to find the construction and design details that will limit annoying vibrations.

Presented in this study are selected results from a recent study of vibration performance of cold-formed steel floor systems performed at the University of Waterloo. Several full-scale floor systems were tested, and their dynamic response measured. The influence of construction details and in situ floor performance was investigated.

## **2. Laboratory Floor Testing**

A laboratory testing program examining 23 unique full-scale floor systems was conducted at the University of Waterloo. Of interest to this study are the dynamic characteristics of the floor systems tested, and the influence of changes in construction details on the floor systems.

### *2.1. Test Frame*

All floor systems were tested in a large steel frame mounted on grouted beams, and reinforced with large, concrete-filled pedestals. The mass and stiffness of the frame was significantly greater than that of the floor system, and its influence was not considered. A brief description of the relevant components and capabilities will be presented. Details of the test frame can be found in previous publications (Xu, et al., 2007). The test frame accommodated floor widths of up to 16' (4.88 m), and had an adjustable length of up to 24' (7.32 m).

The floor systems examined in this study were tested with a free-support condition along the outer joists, and three different end restraints, designed to model common construction techniques. The free-support condition produced a worst-case scenario for the laboratory results. Previous experiments performed

at the University of Waterloo have shown that supporting four sides instead of two sides increased the floor stiffness slightly (Xu, 2000).

The end restraints were selected to model balloon framing, platform framing and a simple support. Balloon framed floors are attached via shear connections at each stud. To represent this condition, the webs of cold-formed steel stud members were attached to hot-rolled channels mounted on the test frame. The floor system was fastened to the flanges of the studs. Platform framed floors sit on top of the wall at each stud. To represent this condition, the floor rested on a 4" × 4" (100 mm x100 mm) wood block mounted to the test frame. A superimposed load of 130 lb/ft (1.9 kN/m) was applied at the ends to simulate the above-storey. To represent the simple support, the platform framing condition was used without the superimposed load.

## 2.2. *Materials and Construction*

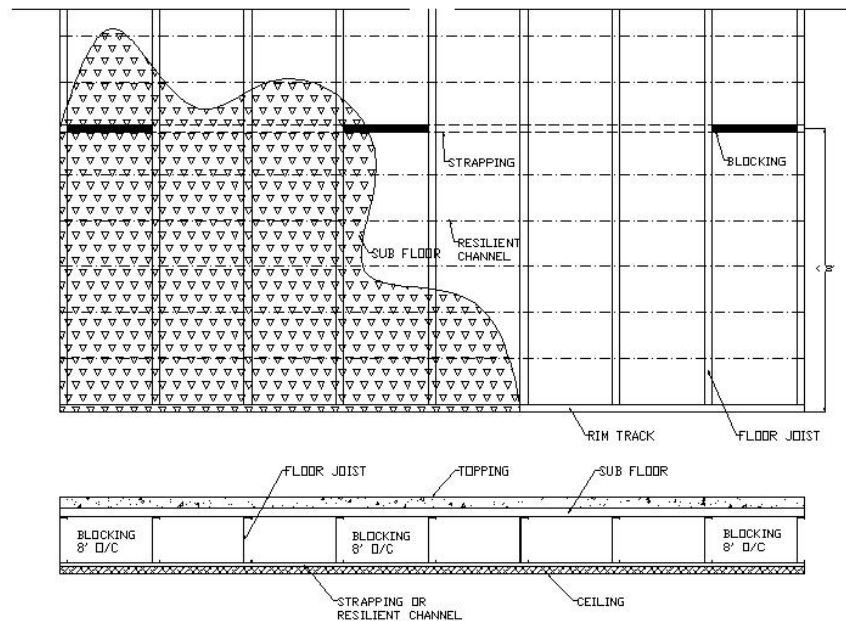
All floor systems tested in the laboratory were constructed with the same basic skeleton. Each floor system consisted of nine, 12" (305 mm), cold-formed steel joists, spaced at 24" (610 mm) on center. At the supports, the joist webs were connected to a proprietary 68 mil (1.90 mm) rim track with a punched clip-angle type tab, which also acted as a web stiffener for the joist. Traditional web stiffeners were not installed at the ends of the joists. The loads applied to the floor system during testing were not substantial enough to fail the joist web. The two joist types tested were: standard C-shape joists with 4" x 1.5" (101.6 mm x 38.1 mm) elliptical openings spaced at 4' (1.22 m) on center along the neutral axis; and proprietary TradeReady® (TDW) joists with large, circular, lip reinforced holes along the neutral axis. The holes were 8" (203 mm) in diameter and spaced at 4' (1.22 m) on center.

All floors were constructed with rows of blocking and strapping spaced every 8' (2.44 m) on center, perpendicular to the joist direction. This is a standard practice, and resulted in 1 or 2 rows, depending on floor span. The blocking pattern is not perfectly symmetric because of the odd number of joists. The center section of blocking was installed between joists 4 and 5.

Subfloor systems were fastened to the joists using the non-diaphragm screw pattern provided by the joist manufacturer. The three types of subfloor tested were: 0.75" (19 mm) oriented strand board (OSB) tongue-and-groove subfloor panels; 0.75" (19 mm) proprietary FORTACRETE® tongue-and-groove cementitious subfloor panels (FC); and 27 mil (0.76 mm), 9/16"-pattern, metal form deck (MD). The topping tested was LEVELROCK®, a gypsum-based, self leveling concrete; with a depth of 3/4" (19 mm) for FORTACRETE subfloor,

and 1.5" from the bottom flute for metal deck subfloor. The FORTACRETE subfloor was examined both with and without the LEVELROCK topping.

Floor systems were tested with and without a gypsum board ceiling, which was fastened to steel resilient channel (RC) installed perpendicular to the joist directions at 12" (305 mm) on center (when ceiling was present). Some floor systems were tested with a cold-formed steel C-section strongback at mid-span, fastened to the joists using clip angles at every joist. Ceilings with Type X and Type C fire-rated gypsum board were tested. Figure 1 shows an over head view and a cross-section of a typical floor built and tested for this study.



**Figure 1: Overhead and Cross-section View of a Typical Floor System**

### 2.3. Laboratory Testing Matrix

Table 1 lists the relevant construction details for each floor in the laboratory testing component of this study. All construction details not listed in the table were identical between all floor systems tested.

**Table 1: Floor Construction Configurations**

Name	Joist Type	Joist Thickness	Floor Span	Subfloor	Topping Thickness	Ceiling	Strongback
LF14.5A	C-shape	54 mil	14.5'	OSB	-	-	-
LF14.5B	C-shape	54 mil	14.5'	FC	-	-	-
LF14.5B <sub>i</sub>	C-shape	54 mil	14.5'	FC	-	-	-
LF14.5C	TDW	54 mil	14.5'	OSB	-	-	-
LF14.5D	TDW	54 mil	14.5'	FC	-	Type X	-
LF14.5D <sub>i</sub>	TDW	54 mil	14.5'	FC	-	-	-
LF14.5E	TDW	54 mil	14.5'	FC	3/4"	Type X	-
LF14.5F	TDW	54 mil	14.5'	MD	1.5"	Type X	-
LF17.0A	TDW	68 mil	17'	FC	3/4"	Type C	-
LF17.0C	TDW	68 mil	17'	MD	1.5"	Type C	-
LF19.5A	TDW	68 mil	19.5'	FC	3/4"	Type C	-
LF19.5A <sub>i</sub>	TDW	68 mil	19.5'	FC	3/4"	-	-
LF19.5A <sub>ii</sub>	TDW	68 mil	19.5'	FC	3/4"	-	Yes
LF19.5A <sub>iii</sub>	TDW	68 mil	19.5'	FC	3/4"	Type C	Yes
LF19.5A <sub>iv</sub>	TDW	68 mil	19.5'	FC	3/4"	Type C	-
LF19.5B	TDW	68 mil	19.5'	MD	1.5"	Type C	-
LF19.5B <sub>i</sub>	TDW	68 mil	19.5'	MD	1.5"	-	-
LF19.5B <sub>ii</sub>	TDW	68 mil	19.5'	MD	1.5"	-	Yes
LF19.5B <sub>iii</sub>	TDW	68 mil	19.5'	MD	1.5"	Type C	Yes
LF19.5B <sub>iv</sub>	TDW	68 mil	19.5'	MD	1.5"	Type C	-
LF21.8A	(2)TDW	54 mil	21.83'	MD	1.5"	Type C	-

A letter designation was used to define the construction characteristics of the floor system, with a subscript to denote that only a partial testing sequence was conducted on that floor system. For example, a floor system with the name LF14.5A was tested in the laboratory, with a span length of 14' 6" (4.42 m), and has construction details corresponding to the letter A.

### 3. In Situ Floor Testing

An in situ testing program, examining several built floor systems, was conducted at four different residential mid-rise buildings in the United States. The in situ program was designed to verify the laboratory testing results, and quantify any differences that result from field construction. Of interest to this study are the dynamic characteristics of the floor systems which correspond to the systems tested in the laboratory.

### 3.1. Materials and Construction

The in situ floor systems were selected to match the laboratory floor systems as closely as possible. The floors were located in mid-rise residential buildings with cold-formed steel for the primary structural system. At the time of testing, finished drywall was in place for the walls and ceilings, and the concrete topping had cured. Screw patterns for subfloor and blocking patterns were identical to the laboratory floors. Ceilings consisted of Type C gypsum board. All joists were 12" (305 mm) deep.

Notable variations include: all insulation, pipes, and ducting between the floor joists was in place; and floors were constructed using cold-formed steel balloon framing, and supported on all four sides. In order to make relevant comparisons, this study examines floors with ceilings fastened to the joists directly with resilient channel. Other floors tested with a drop ceiling are listed but not discussed. It was not possible to match floor width between the laboratory and the in situ floors.

### 3.2. In Situ Testing Matrix

Table 2 lists the in situ floors examined in this study, and their relevant details.

**Table 2: In Situ Construction Configurations**

Name	Joist Type	Joist Thickness	Floor Span	Floor Width	Subfloor	Topping	Ceiling
CG601	TDW	68 mil	17.5'	13.8'	FC	3/4"	RC
CG604	TDW	68 mil	14.8'	16.9'	FC	3/4"	RC
CG805	(2)TDW	68 mil	21.2'	28.0'	FC	3/4"	RC
CGMH6	TDW	68 mil	16.8'	23.8'	FC	3/4"	RC
CGMH7	TDW	68 mil	16.8'	23.8'	FC	1.5"	RC
CW708	TDW	68 mil	14.5'	28.5'	MD	1.5"	Drop
CW709	(2)TDW	54 mil	21.8'	26.3'	MD	1.5"	Drop
CW805	TDW	54 mil	19.3'	26.7'	MD	1.5"	Drop
OK401	TDW	54 mil	14.2'	34.9'	MD	1.5"	Drop
OK402	TDW	54 mil	14.2'	34.9'	MD	1.5"	Drop

## 4. Test Procedure

This test program was based on previous floor vibration tests performed at Virginia Polytechnic Institute (Kraus, et al., 1997) and at the University of Waterloo (Xu, et al., 2007). Floor tests can be grouped in two categories; dynamic and static tests. The dynamic tests performed for this study were heel

drop, sandbag, and walking tests. The static tests performed for this study were center deflection tests.

#### *4.1. Heel Drop Test*

The heel drop test was used to measure the natural frequency and the damping ratio of the floor system. The excitation was provided by a 180 lb (81.8 kg) man standing at the center of the floor system, impacting the floor with his heels. The heel drop test is considered sufficient for measuring the dynamic characteristics of a floor (Williams, et al., 2003). This procedure was first used to find the displacement of a floor system due to human activity (Ohmart, 1968).

#### *4.2. Sandbag Test*

The sandbag test was used to measure the natural frequency and the damping ratio of the floor system. It was developed to validate the measurements from the heel drop test, and examine floor system properties without the influence of an occupant. The excitation was provided by dropping a 22 lb (10 kg) sandbag from 12" (305 mm) height onto the center of the floor system.

#### *4.3. Walking Test*

The walking test was used to measure the root mean squared (RMS) acceleration response of each floor system due to walking excitation. This test was developed to provide quantitative and comparative measurements of the floor system's response to realistic occupant activity. The test was performed by a 180 lb (81.8 kg) man walking several times from one edge of the floor to the opposite; for directions both perpendicular and parallel to the joists.

#### *4.4. Deflection Test*

The deflection test was used to measure the maximum static deflection of the floor under a concentrated load of 225 lb (1 kN) at mid-span. This method was chosen so that the maximum deflection measured would correspond to the limiting deflection from several common design criteria, and a direct comparison could be made. This test was not applicable for in situ floors with drop ceilings.

## 5. Data Analysis

### 5.1. Dynamic Response

The natural frequencies, damping ratio and RMS acceleration of the floor systems were determined from acceleration response vs. time measurements. The response of each floor system was measured by three accelerometers. They were located at the center of the floor,  $\frac{1}{4}$  of the span along the center joist, and  $\frac{1}{4}$  of the width at mid-span. The heel drop and sandbag drop tests were 10s samples, while the walking test was sampled for 50s per direction. Dynamic tests were conducted three times per framing condition.

#### *Natural Frequencies*

The floor system's natural frequencies ( $f_1$  and  $f_2$ ) were determined from the frequency domain by selecting the first two dominant peaks in the power spectrum. The excitation was assumed to be an impulse load. Three accelerometers, located to measure multiple vibration modes, were used during the testing of the floor systems. The mean value of from all three accelerometers was reported.

The first peak in the power spectrum corresponds to the fundamental frequency, which is generally associated with the first flexural mode. Work done by Johnson (1994) showed that higher-order multiples, and torsional modes contribute very little to the floor response due to an impulse excitation (Johnson, 1994). Discussion in this study is limited to the fundamental frequency because it has the greatest influence on the floor system's response.

#### *Damping Ratio*

For this study two different methods were used to determine the damping ratio ( $\zeta$ ) for each floor system. The half-power bandwidth method was used to compute the damping ratio in the frequency domain, and the logarithmic decrement was used to compute the damping ratio in the time domain. Descriptions of these methods can be found in structural dynamics texts.

The half-power bandwidth method is used to find the damping ratio of a system when that system is excited by an impulse load. The sandbag drop and heel drop were assumed to be impulse excitations, so the bandwidth method is valid for both of these tests. The logarithmic decrement can be used to find the viscous damping ratio of a single-degree-of-freedom system under free vibration. The fundamental mode was isolated with a digital bandpass filter

when this method was applied, and the floor response was assumed to be free vibration.

The half-power bandwidth method cannot separate modal damping ratios for floor systems with closely spaced frequencies. When this occurred, the logarithmic decrement method was used exclusively. Otherwise, the damping ratio values reported were the means determined from both methods, which were generally in good agreement.

#### *RMS Acceleration*

The RMS value of the acceleration measured from walking tests was calculated based on the procedure described by ISO 2631 (ISO, 1997), without the frequency weighting component. The entire 50 s time history was used for the RMS calculation.

#### *5.2. Static Response*

Deflection of the center joist at mid-span was used to evaluate the static bending stiffness of the floor systems. Joist-deflection and rebound were measured at mid-span using dial gauges at the underside of the joists. The dial gauges were situated so that the sensor was directly under the web of the joist to avoid errors from flange curling, and the ceiling was cut away if necessary.

### **6. Data Summary**

#### *6.1. Laboratory Testing*

Data collected from laboratory testing is presented in the following tables, grouped by framing condition. Some floor systems were not tested in all framing conditions. Table 3 contains data from balloon framing, Table 4 contains data from platform framing, and



Table 5 contains data from the simple support. The reported frequencies were obtained from the sandbag drop test. The reported damping ratios were obtained from the heel drop test unless noted with a “\*”, which indicates values from the sandbag drop test.

**Table 3: Balloon Framing Data**

Floor Name	$f_1$ (Hz)	$f_2$ (Hz)	$\zeta$ (%)	$\Delta_{center}$ (in)
LF14.5A	25.3	32.7	4.3*	0.020
LF14.5B	22.5	25.1	3.2*	0.017
LF14.5C	26.3	33.2	2.1*	0.023
LF14.5D	19.7	24.2	4.7	0.013
LF14.5E	17.7	22.5	3.1	0.009
LF14.5F	16.1	22.5	3.8	0.007
LF17.0A	14.9	19.1	4.4	0.012
LF17.0C	14.9	19.7	3.9	0.011
LF19.5A	14.3	18.3	3.6	0.010
LF19.5A <sub>iv</sub>	13.2	24.0	4.5	0.014
LF19.5B	13.0	23.0	4.5	0.012
LF21.8A	12.5	23.4	4.0	0.010

**Table 4: Platform Framing Data**

Floor Name	$f_1$ (Hz)	$f_2$ (Hz)	$\zeta$ (%)	$\Delta_{center}$ (in)
LF14.5A	17.9	29.8	3.7*	0.026
LF14.5B	17.2	18.8	3.8*	0.019
LF14.5C	16.4	27.8	3.7*	0.024
LF14.5D	16.9	22.0	7.0	0.015
LF14.5E	16.2	22.2	5.3	0.009
LF14.5F	14.8	22.0	3.4	0.007
LF17.0A	13.6	19.4	4.0	0.013
LF17.0C	13.3	19.3	5.7	0.011
LF19.5A	13.4	18.8	4.0	0.010
LF19.5A <sub>iv</sub>	13.4	20.2	4.1	0.009
LF19.5B	11.8	17.3	3.8	0.013
LF21.8A	10.6	15.3	2.5	0.013

**Table 5: Simple Support Data**

Floor Name	$f_1$ (Hz)	$f_2$ (Hz)	$\zeta$ (%)	$\Delta_{center}$ (in)
LF14.5A	19.1	27.4	5.5*	0.022
LF14.5B	17.2	21.4	2.9*	0.021
LF14.5C	17.7	26.0	2.3*	0.028
LF14.5D	16.2	22.4	7.7	0.016
LF14.5E	15.7	21.1	5.7	0.010
LF14.5F	14.6	21.2	3.2	0.008
LF17.0A	13.5	17.9	4.8	0.013
LF17.0C	13.3	18.1	4.4	0.013
LF19.5A	12.8	18.4	3.2	0.010
LF19.5A <sub>iv</sub>	13.2	18.6	4.5	0.009
LF19.5B	11.4	16.4	4.9	0.014
LF21.8A	10.1	14.7	3.5	0.014

## 7. Influence of Construction Details

The following section will discuss the effect of construction details on the dynamic and static response of the floor systems. Comparisons were made between similar floor systems with one unique detail. The construction details analyzed were span length, joist type, subfloor material, presence of strongback, and framing condition. The dynamic and static response of the floor system was judged based on fundamental frequency, damping ratio, and center joist deflection.

### 7.1. Effect of Span Length

Two different spans were examined. Comparisons were made for each framing condition, and the observations clearly match the understood behavior of the system.

Fundamental frequency decreases with increasing span length. The decrease in frequency can be attributed to the increased mass and flexibility from the longer span. Adding mass to a system without adding stiffness will lower the fundamental frequency of a system. Center deflection increases with increasing span length. This decrease occurs because bending stiffness is inversely proportional to span length.

### 7.2. Effect of Joist Type

Two different joist types were analyzed: C-shape and TDW. Comparisons were made for each framing condition, and the results show that altering the joist type

has little impact on the vibration response of the floor systems. No trends were observed for fundamental frequency and center deflection.

The large lip-reinforced web opening reduces the TDW joist's bending stiffness by 4.6% at service load conditions, and only at discrete locations spaced 4' (1.22m) apart. It should have a minimal impact on the overall behavior of the joist. Therefore, the observed similar vibration response between joist types was expected. Small variations were likely due to construction variation. These results cannot be applied to web openings that are more closely spaced, as the web shear capacity is reduced significantly.

### *7.3. Effect of Subfloor and Topping*

The three subfloor materials compared are OSB, FORTACRETE and metal deck. Because OSB was tested without a topping, it can only be compared with FORTACRETE; similarly, metal deck was tested with a topping, and can only be compared with FORTACRETE. Comparisons were made for each framing condition.

Comparing OSB and FORTACRETE, without topping, it was observed that the floor systems with FORTACRETE had a lower fundamental frequency. This reduction is because the nominal mass of FORTACRETE is 2.05 times that of OSB. Increased stiffness did significantly reduce deflections in FORTACRETE floor systems.

FORTACRETE's increased mass dominates the effects from its increased stiffness for floor system frequencies, but the stiffness increase is observed under static loads. However, the floor systems compared had similar construction details, but different fire ratings. More mass of gypsum board ceiling may be required for OSB floor systems to achieve the same fire rating as FORTACRETE, which is non-combustible, reducing the natural frequencies of the floor system. For lightweight floor systems annoyance may be dominated by local deflections from walking, making stiffness the primary factor influencing performance.

Comparing FORTACRETE to metal deck, with topping, it was observed that the floor systems with metal deck had a lower fundamental frequency. The difference was between 3% and 5% depending on framing condition. The thicker topping gives metal deck floors a greater overall weight, reducing the fundamental frequency. However, there is a significant decrease in center deflection for floors with metal deck. This occurred because the axis of the metal deck was perpendicular to the joists, and significantly increased the transverse stiffness of the floor system, increasing the number of effective joists.

These observations are based on the tested thicknesses of topping only. Changing the relative topping thickness will change the influence of the different subfloor details.

#### *7.4. Effect of Strongback*

To determine the effect of a strongback with fixed ends, a strongback member was fastened to the web of every joist at mid-span, and the ends were fixed to a rigid pedestal using a clip angle and five screws; restricting any vertical deflection and partially restraining rotation of the strongback at its ends. This configuration was only tested in balloon framing, and required the large lip-reinforced holes provided by TDW joists for placement of the strongback within the depth of the joist web. The fundamental frequency increased by an average of 6.0%, while the center deflection decreased by an average of 7.5%. The strongback added additional constraints to the modes of vibration of the floor system by imposing a restraint on mid-span deflection at the outer joists. This reduces the influence of the first flexural mode of vibration (1/2 sine wave in joist direction), which will increase the fundamental frequency of the floor system. Addition of a strongback also increased the damping ratio.

#### *7.5. Effect of End Framing Condition*

The framing condition had an observable effect on fundamental frequency, damping ratio, and center deflection. The balloon framing condition provided the greatest increase in fundamental frequency and reduction in center deflection, while platform framing also exceeded values from the free-support condition. Because rotation at the support was restrained, bending stiffness of the floor system increased, increasing fundamental frequency and reducing center deflection. Damping ratio was greatest in the free-support condition, due to the decreased restraint at the supports.

#### *7.6. Effect of In Situ Construction*

To determine the influence of in situ construction on fundamental frequency and damping ratio, comparisons were made between floor systems built and tested in the laboratory, and similar floor systems tested on site. Typically, the width of the in situ floors was greater than the width of the laboratory floors. It is assumed that the width of the floor in the laboratory (9 joists) is sufficient to replicate the in situ conditions to a good degree. All floor systems compared were built with the balloon framing.

In almost all cases, the in situ floor systems had a greater fundamental frequency and damping ratio. It is reasonable to conclude that the laboratory floor systems

exhibit a worst-case response for fundamental frequency and damping ratio; higher frequencies and damping will reduce occupant comfort issues. Conceptually, this is supported by the following: in situ floor systems were supported on all four sides, restraining free motion of the outer joists and increasing the fundamental frequency; and, the additional components, partitions, and mechanical connections found in situ contribute to an increase in damping ratio. The comparisons between field and laboratory results presented in this paper agree well with previous research performed at the University of Waterloo (Xu, et al., 2007).

## **8. Conclusion**

Observations based on the static and dynamic response of the floor systems tested provide several conclusions for the effect of construction details on performance. As span increases, fundamental frequency decreases, and center deflection increases. The large lip-reinforced opening detail specific to the TradeReady joist does not appear to affect the static and dynamic response. Compared to OSB subfloor, FORTACRETE exhibits less center deflection and a lower fundamental frequency. From a performance perspective, this observed increase in stiffness can be beneficial for lightweight floor systems. Compared to a FORTACRETE subfloor with LEVELROCK, a metal deck subfloor with LEVELROCK exhibits less center deflection; with negligible influence on fundamental frequency. The use of a strongback with fixed ends will increase the fundamental frequency and damping ratio, while decreasing the center deflection. Balloon framing will increase fundamental frequency and decrease center deflection when compared to platform framing. Laboratory results are typically a worst-case scenario, when compared to in situ construction, producing lower fundamental frequencies and damping ratios.

## **9. Acknowledgements**

The authors would like to express thanks to Dietrich Metal Framing, United States Gypsum, and Worthington Integrated Building Systems for their support of this study.

## 10. Appendix - References

- ISO, *Mechanical Vibration and Shock - Evaluation of Human Exposure to Whole-Body Vibration*, ISO 2631-1, Geneva, 1997.
- Johnson J.R., "Vibration Acceptability of Floor Under Impact Vibration," Virginia Polytechnic Institute, Blacksburg, VA, 1994.
- Kraus C. A. and Murray T. M., "Floor Vibration Criterion for Cold-Formed C-Shaped Supported Residential Floor Systems," Virginia Polytechnic Institute, Blacksburg, VA, 1997.
- Ohmart R. D., "An Approximate Method for the Response of Stiffened Plates to a Periodic Excitation," The University of Kansas Center for Research in Engineering Science, Lawrence, KS, 1968.
- Williams M.S. and Blakeborough A., "Measurement of Floor Vibrations Using a Heel Drop Test," *Structures and Buildings 156*, Proceedings of the Institution of Civil Engineers, Issue SB4, November 2003, pp. 367-371.
- Xu L. and Tangorra F. M., "Experimental Investigation of Lightweight Residential Floors Supported by Cold-formed Steel C-shape Joists", *Journal of Constructional Steel Research*, Vol. 63, 2007, pp. 422-435.
- Xu L., "Dynamic Behaviour of Residential Floor Systems Using Cold-Formed Steel Joists: Final Report", Canadian Cold-formed Steel Research Group, University of Waterloo, Waterloo, ON, 2000.



## **Innovative Composite Cold Formed Steel Floor System**

D.M. Fox<sup>1</sup>, R.M. Schuster<sup>2</sup>, and M. Strickland<sup>3</sup>

### **Abstract**

Presented in this paper is a new, unique and innovative composite cold formed steel floor system developed by iSPAN Technologies, called the “iSPAN Composite Floor System”. The joist sections are fabricated by fastening two cold-rolled flange chord elements with cold-driven rivets to a flat web element. This makes it possible to create a section where the flange chord elements can be of a different steel thickness with respect to the web element, resulting in a most efficient structural cross section and numerous design alternatives. The joist sections have lip-reinforced web openings spaced at 4 ft o.c. along the joist length to accommodate the usual service items. The joists are typically spaced 4 ft o.c. with a 7/8 in. corrugated steel deck spanning between the joists to support the concrete during casting. Featured in this paper are the results from push-out tests that have been carried out to establish the interlocking capacity of the concrete with the top chord of the joist section. The results of a full-scale laboratory structural test are also presented to substantiate the calculated strength and stiffness characteristics. Finally, the results of a field test during construction are presented.

### **Introduction**

Composite joists have been used since the mid 1960's and early composite joists were developed based on open web steel joist architecture, using either elevated

---

<sup>1</sup> Product Development Engineer, iSPAN Technologies, Richmond Hill, Ontario, Canada

<sup>2</sup> Professor Emeritus of Structural Engineering and Director of the Canadian Cold Formed Steel Research Group, Department of Civil Engineering, University of Waterloo, Waterloo, Canada

<sup>3</sup> President, Best Joist Inc. (iSPAN Technologies), Richmond Hill, Ontario, Canada



bar web members or welded shear studs to provide the required interlocking capacity between the concrete and joists [1-2]. To date, welded shear studs, such as Nelson Studs, are commonly used as one of the popular methods of interlocking the concrete slab with joists. However, concerns over the studs acting as tripping hazards have necessitated field installation of the studs [3], which can be labour intensive and difficult to control the quality of installation.

Various alternatives to the welded stud shear connectors have been developed, such as the Hambro 'S' shaped top chord, the Vescom embossed chord, and the Tafrus perforated top chord [4]. These alternatives are all based on open web steel joist concepts, and are therefore labour intensive to fabricate. Furthermore, top chord bearing joists can be difficult to install on light steel framed walls, requiring heavy distribution members to accommodate the large end reactions.

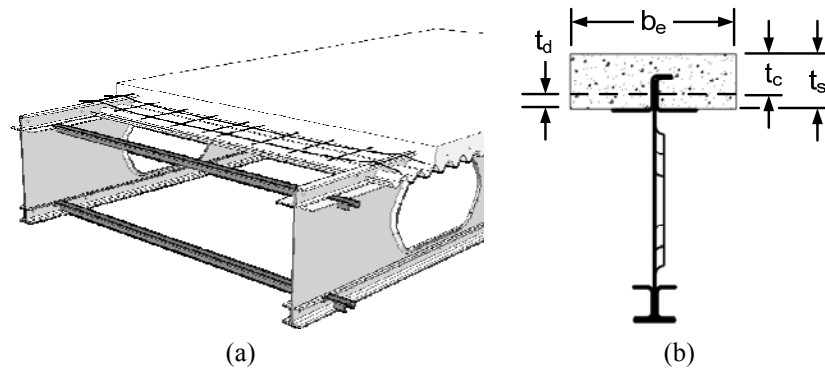
Attempts have been made to use C-sections to provide the steel component of composite joist slabs, which typically involves the installation of shear connectors to the top flanges of the joists. In some other cases, the top flanges of C-sections have been embedded into the concrete slab, which can be difficult to install the associated formwork.

iSPAN Technologies has recently introduced a fully cold-formed stay in place composite floor, called the "iSPAN Composite Floor System". The system was designed specifically for the light steel framing industry, resulting in simple fabrication and installation without the requirement of specially trained labour. Included in the system is the composite joist, where the top chord provides the required interlocking capacity with the concrete. In addition, the top chord also provides the required support for the steel deck during construction. A schematic diagram of the composite floor system and a section of the joist are illustrated in Figure 1. Presented in this paper are the results of the interlocking capacity tests of the top chord (push-out), a full scale composite flexural test, and an in-situ field deflection monitoring test during concrete placement.

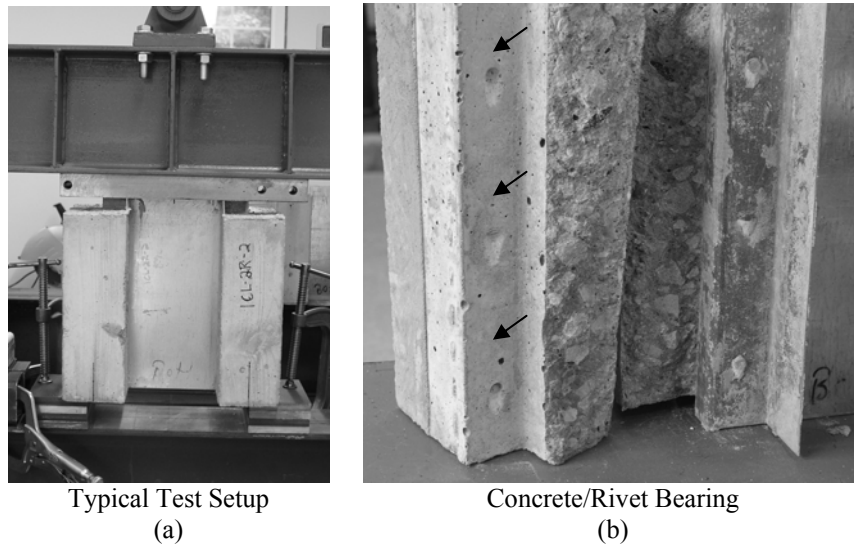
### **Top Chord Interlocking Capacity – Push-out Tests**

Push-out tests were conducted to establish the interlocking capacity of the embedded top chord with the concrete slab. Symmetrical specimens were fabricated; each specimen was comprised of two composite top chords connected to a web by rivets spaced at 8 in. o.c. The specimens were supported such that the chords were allowed to slip between the concrete elements when the load was applied. A photograph of a typical test setup is shown in Figure 2(a). A bearing plate was positioned over the exposed portion of the steel chords and the load was applied at the center of the bearing plate. Failure occurred by

slippage of the concrete along one or both chords; interlocking capacity was provided by a combination of chemical bond and rivet head interlocking. A typical bearing failure in the concrete at the location of a rivet head is shown in Figure 2(b). Two different specimen lengths were tested as summarized in Table 1, which also includes the test results.



**Figure 1 - iSPAN Composite Floor System**



**Figure 2 - Photographs of Typical Push-out Tests**

**Table 1 - Summary of Push-out Test Results**

Specimen ID	Embedment Length (in.)	No. of Rivets	Failure Load (kip)	Failure Mode <sup>1</sup>	Interface Shear, $q_u$ (lb/ft)	Average $q_u$ (lb/ft)
2R - 8"o/c - 1	12	2	-	Premature	-	16,806
2R - 8"o/c - 2	12	2	17.2	Slip 1	17,249	
2R - 8"o/c - 3	12	2	17.4	Slip 1	17,436	
3R - 8"o/c - 1	20	3	26.8	Slip 2	16,064	
3R - 8"o/c - 2	20	3	27.7	Slip 2	16,629	
3R - 8"o/c - 3	20	3	27.8	Slip 1	16,652	

**Notes:**

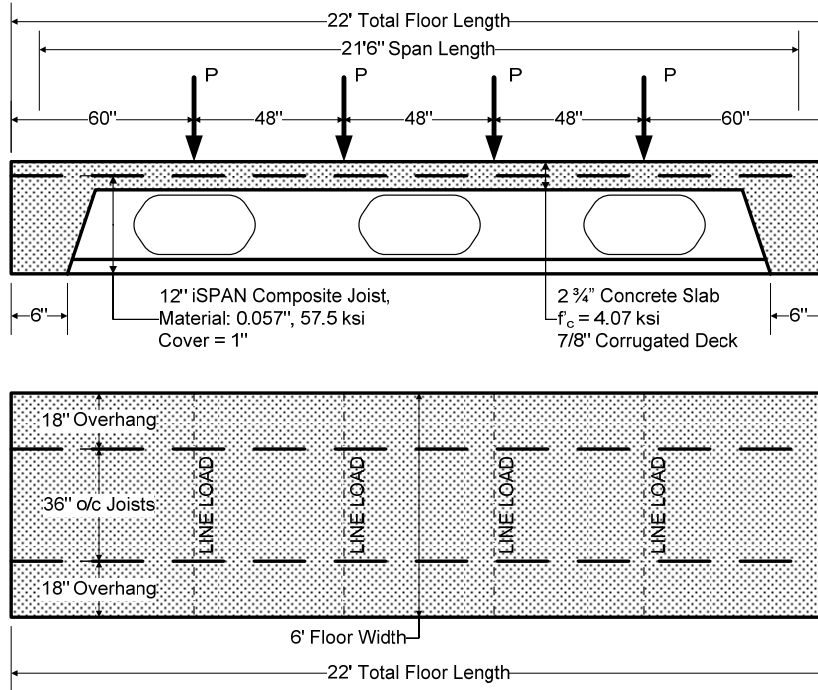
1) Failure modes describe as follows:

- (a) Slip 1: Specimen failed by slippage along one chord
- (b) Slip 2: Specimen failed by slippage along both chords

**Flexural Test**

A full scale composite floor system was tested, where the span length was 21.5 ft and two joists were spaced at 3 ft o.c. The floor joists were 12 in. in depth, and the thickness and the yield strength of the steel were 0.057 in. and 57.5 ksi, respectively. 7/8 in. deep corrugated steel decking was installed by supporting it on the wings of the top chord, and a 6x6 6/6 welded wire mesh was draped over the joists and steel deck. Concrete was placed such that a 1 in. cover was maintained over the top chord, resulting in a slab whose overall depth,  $t_s$ , measured from the bottom of the deck flute, was 2-3/4 in. The slab was cantilevered 18 in. on each side of the joist in order to provide two symmetrical composite sections. An overview of the test setup and specimen is presented in a schematic diagram in Figure 3, with a photograph of the actual test setup shown in Figure 4.

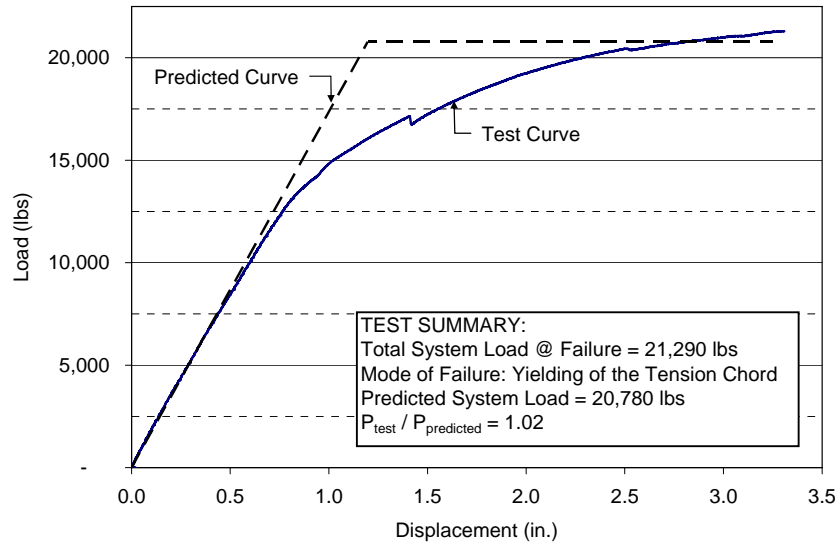
A four line load test setup was used in order to approximate a uniformly distributed load. The specimen was loaded until failure, as can be observed from the load displacement plot shown in Figure 5. Failure occurred by yielding of the bottom chord as is exhibited by the ductile load displacement curve. The test was stopped at a maximum deflection of 3.30 in. at which the recorded ultimate load was 21,290 lbs.



**Figure 3 - Schematic Full Scale Composite Flexural Test Setup**



**Figure 4 - Photograph of Full Scale Flexural Test Setup**



**Figure 5 - Load Displacement Curve of Full Scale Composite Flexural Test**

### Analytical Analysis

An analytical analysis was performed to determine the required interlocking capacity, which was accomplished by using an elastic shear flow approach and an ultimate strength approach. Both of these methods have shown to yield good correlation with test results. Finally, a comparison of calculated flexural strength and stiffness to the tested values was performed.

### Elastic Shear Flow Approach

The well known elastic shear flow expression is given in Equation (1):

$$q_{\max} = \frac{V_{\max} Q}{I_{xc}} \quad (1)$$

The first moment of area, Q, can be calculated from the following expression:

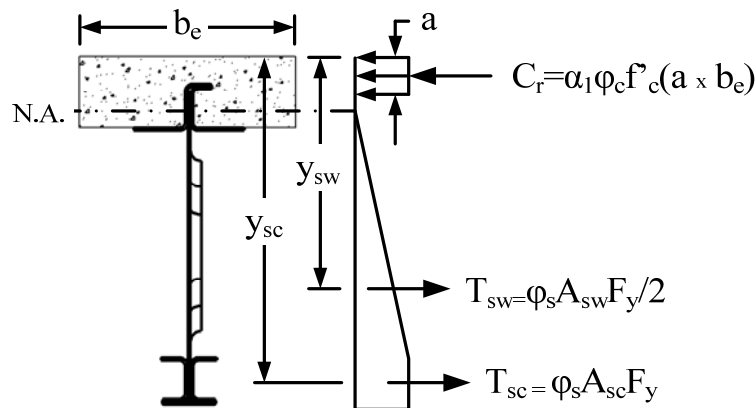
$$Q = \frac{b_e}{n} t_c \left( y_{cgc} - \frac{t_c}{2} \right) \quad (2)$$

For the purpose of calculating elastic shear flow, the effective concrete flange width,  $b_e$ , can be taken as the maximum possible width equal to the joist spacing. The effective slab depth,  $t_e$ , was taken as the overall slab depth,  $t_s$ , less the steel deck depth,  $t_d$ . It was assumed that the concrete below the deck does not contribute to the strength of the composite section.

### Ultimate Strength Approach

For most composite joist sections, such as composite trusses and open web steel joists, it is typical to consider only the bottom chord in the calculation of the flexural strength [5, 6]. These joist sections tend to have non-solid web elements which do not contribute significantly to the flexural strength of the section. However, the composite joist considered herein includes a solid web which does contribute to the flexural strength. However, the high slenderness ratio of the web does not allow the entire cross section of the web to yield. Since the web is subjected to a stress gradient (see Figure 6), the resultant tensile force can be calculated according to Equation (3):

$$T_s = T_{sc} + T_{sw} \quad (3)$$



**Figure 6 - Force Components for Composite Flexure Calculations**

Based on the assumption of full composite action, the interlocking capacity in the slab element must be greater than the tensile force in the steel. The average required interlocking shear flow between the points of minimum and maximum moments is therefore:

$$q_u = \frac{T_s}{L_q} \quad (4)$$

A traditional reinforced concrete approach was used to calculate the flexural resistance of the composite joist [7]. As per traditional reinforced concrete design:

$$M_r = T_{sc} \left( y_{sc} - \frac{a}{2} \right) + T_{sw} \left( y_{sw} - \frac{a}{2} \right) \quad (5)$$

where

$$a = \frac{T_s}{\alpha_1 \phi_c f_c' b_e}$$

As recommended by Clause 17.4.1 of CSA S16-01 [5], the effective slab width,  $b_e$ , was taken as the lesser of:

1. Joist Spacing
2. Span divided by 4

Finally, the composite moment of inertia was calculated based on traditional transformed section procedures where the effective slab width was considered to be equal to the joist spacing divided by the modular ratio:

$$I_{xc} = I_{xj} + A_j D_j^2 + \frac{b_e/n t_c^3}{12} + \left( \frac{b_e}{n} t_c \right) D_c^2 \quad (7)$$

### Test Result Comparisons

The computed flexural capacity,  $M_r$ , maximum shear flow,  $q_{\max}$ , ultimate shear flow,  $q_u$ , and composite moment of inertia,  $I_{xc}$  (expressed in equivalent steel) were computed in order to compare the calculations with the test data presented above. The parameters for the 12 in. composite joist floor system are presented in Table 2 along with the results of the calculations, where all resistance factors were set equal to 1.0.

**Table 2 - Test Result and Comparison of Flexural Test**

<b>Parameters of 12 in. Composite Joist Tested (per joist)</b>			
$\alpha_1 =$	0.81	$L_a =$	8.75 ft
$A_i =$	1.68 in.	$n =$	7.85
$A_{sc} =$	0.51 in.	$Q =$	8.68 in. <sup>3</sup>
$A_{sw} =$	0.66 in.	$t_s =$	2.75 in.
$b_e =$	36 in.	$t_c =$	1.875 in.
$D_i =$	5.17 in.	$t_d =$	0.875 in.
$D_c =$	1.00 in.	$V_{max} =$	5,323 lb
$f'_c =$	4.07 ksi	$y_{cgc} =$	1.95 in.
$F_v =$	57.5 ksi	$y_{sc} =$	12.3 in.
$I_{xi} =$	34.6 in. <sup>4</sup>	$y_{sw} =$	8.89 in.
<b>Calculated Values and Comparisons with Tested Values (per joist)</b>			
$q_{max} =$	6,099 lb/ft	$Q_r =$	16,806 lb/ft
$q_u =$	5,521 lb/ft		
$M_r =$	43.2 k-ft	$M_t =$	44.1 k-ft
$I_{xc} =$	90.9 in. <sup>4</sup>		

As shown in Table 2, the required interlocking capacity calculated either by the elastic or the ultimate approach,  $q_{max}$  and  $q_u$  respectively, are both less than the provided interlocking capacity,  $Q_r$ , determined from push-out tests as described above. This confirms that the assumption of full composite action was valid.

The calculated composite flexural strength of 43.2 k-ft compares well to the tested flexural strength of 44.1 psf; the additional moment due to dead loads (self-weight and loading apparatus) were included in the computation of the tested flexural strength. As shown in Figure 5, the predicted flexural capacity was within 2% of the tested capacity. Finally, the calculated moment of inertia for the tested joist is 90.9 in.<sup>4</sup>. From Figure 5 it can be seen that the calculated composite stiffness of the floor matched well with the test. It can be noted that an effective moment of inertia approach, similar to that recommended in codes to account for interfacial slip [5, 8] or for web deformation and joint eccentricity [4, 6], was not required to properly reflect the test data.

#### **In-situ Monitoring of Concrete Placement**

In-situ monitoring of a floor system during concrete placement was conducted to confirm the accuracy of the non-composite design method, specifically with



respect to predicting the deflection during concrete placement. The selected project was near Toronto, Ontario, and was constructed of 15 in. composite floor joists spaced at 48 in. o.c. with a clear span of 24.3 ft. The specified slab depth was 3-3/4 in. measured from the bottom of the deck flutes.

Joist strength (flexural and shear) and moment of inertia for deflection calculation were calculated according to the AISI S100 (CSA S136) [9] with modified buckling coefficients as recommended by Fox et al [10]; the moment of inertia for deflection calculation,  $I_{xd}$ , of the specified joist is 77.7 in.<sup>4</sup>. A displacement transducer was installed at midspan of a joist as shown in Figure 7. During concrete placement, the deflection was monitored and recorded; a plot of midspan deflection over the course of the pour is shown in Figure 8.

The floor system was designed for the non-composite phase as per the recommendations given in CSSBI 12M-06 [11]:

1. strength must resist the effects of system dead loads combined with either a 21 psf uniform load or a 137 lb/ft transverse line load at midspan, and
2. deflections based on system dead loads are to be limited to the smaller of  $L/180$  or  $3/4$  in. Calculated deflection is increased by a ponding factor,  $Y_p$ , of 1.10 to account for possible concrete ponding or to account for a slab thickness greater than that specified.



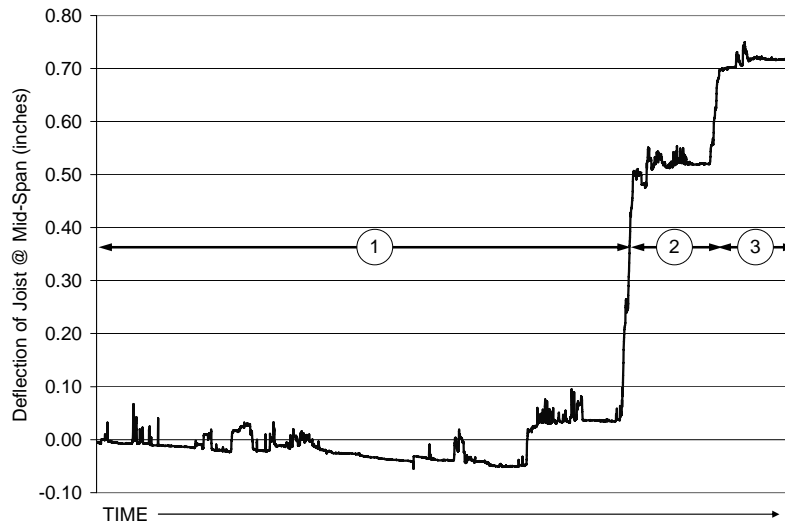
(a) Supporting Structure for Displacement Transducer



(b) Closeup of Displacement Transducer

**Figure 7 - Photographs of In-Situ Deflection Monitoring Equipment**

The dead load of the system, considering steel system self weight, metal deck, welded wire mesh, and wet concrete was estimated at 47.0 psf. Considering a ponding factor of 1.1, the expected permanent deflection due to dead loads is 0.71 in. If the ponding factor is set equal to 1.0, then the expected permanent deflection would be 0.65 in.



**Figure 8 – Mid-span Deflection During Concrete Placement**

During concrete placement, three distinct regions of deflection were experienced, as can be observed in Figure 8:

1. concrete placement away from the joist; observed deflection is a result of movement of the superstructure,
2. placement of concrete over the monitored joist's tributary area; a sustained midspan deflection of 0.52 in. is observed, and
3. placement of concrete away from the joist being monitored; deflection is a result of movement of the superstructure.

In order to confirm that the permanent deflection of the joist was 0.52 in. and also to establish the amount of concrete ponding, measurements were taken after the concrete had hardened, with the results summarized in Table 3.

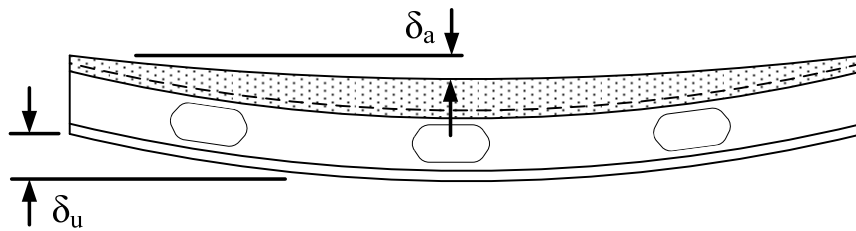
The recorded data shown in Figure 8 and the measurements taken under the joist after concrete hardening confirm that the permanent joist deflection due to self weight during concrete placement was 0.52 in. Considering a ponding factor of

1.10, the recorded deflection was 27% less than the predicted deflection. If the ponding factor is set to 1.0, the recorded deflection would be 20% less than the predicted deflection.

**Table 3 - Measurements of Monitored Joist after Concrete Hardening**

Location	Distance from datum string to joist/concrete (in.)			Maximum Deflection (in.)
	End 1	End 2	At Center Span	
Under Joist	25/32	<sup>3</sup> / <sub>4</sub>	<sup>1</sup> / <sub>2</sub>	0.52
Above Joist	1-3/8	1-9/16	1-13/16	11/32

The amount of ponding at mid-span can be determined by subtracting the deflection of the top of the slab,  $\delta_a$ , from the deflection of the bottom chord of the joist,  $\delta_u$ , (values are listed in Table 3, and locations are shown in Figure 9). It can be concluded that the maximum amount of ponding that occurred at midspan was 0.18 in. The ponding observed represents approximately a 5% increase in slab thickness at midspan with respect to the specified slab depth. The ponding factor of 1.1, which in effect assumes a 10% added weight, is a conservative estimate of the degree of ponding observed.



**Figure 9 - Determination of Ponding Through Field Measurements**

## Conclusions

A new composite floor system, named 'iSPAN Composite Floor System', specifically designed for light steel framing was introduced. The composite joist section is comprised of a unique top chord that enables simple installation and provides the required interlocking capacity for composite action. Results from push-out tests, a full scale flexural test, and in-situ deflection monitoring during concrete placement are summarized. Based on the test data, the following conclusions can be made:

1. the interlocking capacity of the top chord is more than sufficient to enable full composite action between the concrete slab and the joist,
2. the flexural capacity of the composite joists section can be predicted conservatively based on current Standards/Specifications, the flexural test indicates that the web can be considered in the flexural calculations in order to better reflect the composite behaviour,
3. the stiffness of the composite section can be accurately predicted using standard transformed section properties, and
4. the non-composite deflection calculations according to CSSBI 12M-06 [11] provide a conservative prediction of the in-situ performance.

The conclusions drawn regarding composite flexural stiffness and strength are based on one test. A test program is currently underway to carry out additional flexural tests in order to fully substantiate the conclusions presented herein.

**References**

- [1] Lembeck, Jr., H.G. Composite Design of Open Web Steel Joists, M.Sc. Thesis. Washington University, St Louis, MO., 1965.
- [2] Galambos, T.V., and Tide, R.H.R. Composite Open-Web Steel Joists. AISC Engineering Journal, January 1970.
- [3] US Department of Labor. OSHA Safety Standards for Steel Erection - 66:5317-5325. Washington, D.C., 2001.
- [4] Samuelson, D. Composite Steel Joists. AISC Engineering Journal, Third Quarter, pp 111-120, 2002.
- [5] CSA-S16-01: Limit States Design of Steel Structures. Canadian Standards Association, Mississauga, Ontario, Canada, 2001.
- [6] SJI. (2007). First Edition Standard Specifications for Composite Steel Joists. Myrtle Beach, SC., 2007.
- [7] CSA A23.3-04: Design of Concrete Structures. Canadian Standards Association, Mississauga, Ontario, Canada, 2004.
- [8] Grant, J.A., Fisher, J.W., and Slutter, R.G. Composite Beams with Formed Steel Deck. AISC Engineering Journal, First Quarter, 1977.
- [9] AISI S100 (CSA S136). North American Specification for the Design of Cold Formed Steel Structural Members. Canadian Standards Association, Mississauga, Ontario, Canada, 2007.
- [10] Fox, D.M., Schuster, R.M., and Strickland, M.R. iSPAN™, A Light Steel Floor System. Proceedings of the 18th International Specialty Conference on Cold Formed Steel Structures, Orlando, Florida, 2006.
- [11] CSSBI 12M-06: Standard for Composite Steel Deck. Canadian Sheet Steel Building Institute, Cambridge, Ontario, Canada, 2006.

**Notations**

$a$	depth of effective compressive stress block (in.)
$A_{sc}$	area of steel in bottom chord (in. <sup>2</sup> )
$A_{sw}$	area of steel in web (in. <sup>2</sup> )
$A_j$	total area of steel in joist (in. <sup>2</sup> )
$b_e$	effective width of concrete flange (in.)
$d_c$	concrete cover over top chord of joist (in.)
$\delta_a$	measured deflection of concrete along joist at midspan (in.)
$\delta_u$	measured deflection of bottom chord of joist at midspan (in.)
$D_c$	distance from composite joist to concrete flange center of gravity (in.)
$D_j$	distance from composite joist to steel joist center of gravity (in.)
$E_c$	modulus of elasticity of concrete (ksi)
$E_s$	modulus of elasticity of steel (ksi)
$F_y$	yield strength of steel (ksi)
$f'_c$	compressive strength of concrete (ksi)
$\gamma$	density of concrete (lb/ft <sup>3</sup> )
$I_{xc}$	composite moment of inertia in equivalent steel (in. <sup>4</sup> )
$I_{xd}$	Moment of inertia for deflection calculation (in. <sup>4</sup> )
$I_{xj}$	Moment of inertia of steel joist (in. <sup>4</sup> )
$L_q$	distance between points of maximum and minimum moment (ft)
$M_r$	calculated composite flexural strength (k-ft)
$M_t$	tested composite flexural strength (k-ft)
$n$	modular ratio = $E_s/E_c$
$\phi_c$	resistance factor for concrete
$\phi_s$	resistance factor for steel
$Q$	first moment of area of concrete flange in composite joist (in. <sup>3</sup> )
$Q_r$	interlocking capacity of top chord to concrete slab (lb/ft)
$q_{max}$	maximum shear flow (lb/ft)
$q_u$	ultimate interlock capacity required for full composite action
$t_c$	effective slab depth (in.)
$t_d$	steel deck depth (in.)
$t_s$	total slab depth to bottom of steel deck flute (in.)
$T_s$	total tension force (lbs)
$T_{sc}$	tension force developed in chord (lbs)
$T_{sw}$	total tension force developed in web (lbs)
$y_{egc}$	center of gravity of composite joist from top of slab (in.)
$y_{egs}$	center of gravity of steel from top of slab (in.)

$Y_p$  factor to account for concrete ponding  
 $V_{max}$  maximum shear force (lbs)

## **Flexural Behavior and Design of the New Built-up LiteSteel Beams**

Sivapathasunderam Jeyaragan<sup>1</sup> and Mahen Mahendran<sup>2</sup>

### **Abstract**

A new cold-formed steel beam, known as the LiteSteel Beam (LSB), has the potential to transform the low-rise building industry. The new beam is effectively a channel section with two rectangular hollow flanges and a slender web, and is manufactured using a simultaneous cold-forming and electric resistance welding process. Built-up LSB sections are expected to improve their flexural capacity and to increase their applications. They are also likely to mitigate the detrimental effects of lateral distortional buckling observed with single LSB members of intermediate spans. However, the behaviour of built-up beams is not well understood. Currently available design rules based on longitudinal connection spacing limits and doubling the capacity of single members were found to be inadequate. Therefore a research project based on both experimental and advanced numerical studies was undertaken to investigate the flexural behaviour of back to back LSBs with various longitudinal connection spacings under a uniform moment. This paper presents the details of the experimental and numerical studies and the results.

### **1. Introduction**

LiteSteel Beam (LSB) is a new cold-formed steel beam produced by Australian Tube Mill (ATM) and marketed by LiteSteel Technologies (LST). The new beam is effectively a channel section with two rectangular hollow flanges and a slender web, and is manufactured using a simultaneous cold-forming and electric resistance welding process. It has a unique shape with superior torsional strength properties and provides a very high strength to weight ratio. Figure 1

---

<sup>1</sup> PhD Student & <sup>2</sup> Professor, School of Urban Development, Queensland University of Technology, Brisbane, QLD 4000, Australia



illustrates the LSB cross-section and its typical use. LST is promoting the LSBs as floor bearers in residential construction, replacing hot-rolled beams (Fig. 2).

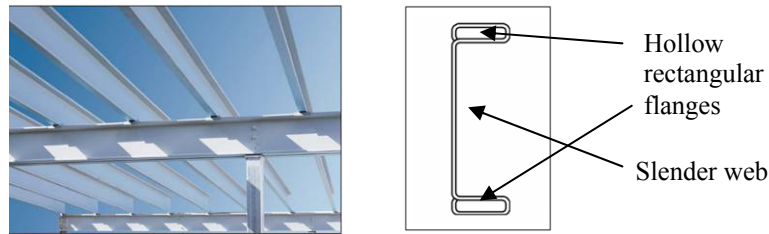


Figure 1: LiteSteel beam (LST, 2005)

Built-up LSB sections are expected to improve their flexural capacity and to expand their usage to long span applications. They can be fabricated using the traditional back to back configuration as shown in Figure 2 and can produce more than double the bending capacity of single LSBs. Mahaarachchi and Mahendran's (2005a) research on single LSB sections found the LSBs to be susceptible to Lateral Distortional Buckling (LDB). The back to back built-up LSB is likely to mitigate LDB effects to some extent by providing additional rigidity to the weakest element of the section, namely the web. However, the behaviour of built-up beams is not well understood and the current design rules are found to be inadequate in some applications. This paper presents the details of an investigation using experimental and numerical studies on back to back built-up LSB sections, the calibration of finite element models and the results.



Figure 2: Back to back built-up LSBs (LST, 2005)

## 2. Current Design Rules

AS/NZS 4600 (SA, 2005) gives limited guidance in relation to the fastener arrangements required to ensure full compatibility between the sections. Clause 4.1.1 specifies that the maximum longitudinal spacing ( $s_{max}$ ) of welds or other connectors joining two channels to form an I-section is as follows:

$$s_{\max.} = \frac{l}{6} \leq \frac{2s_g N^*}{mq} \quad (1)$$

where  $l$  = span of beam,  $N^*$  = design strength of connectors in tension,  $q$  = intensity of the design action on the beam,  $s_g$  = vertical distance between two rows of connections nearest to the top and bottom flange,  $m$  = distance from the shear centre of one channel to the mid-plane of its web.

It also gives details for determining the design load ( $q$ ) and unequal connection spacing. The American cold-formed steel code (AISI, 2001) provides identical or very similar guidelines for cold-formed built-up beams as for AS/NZS 4600.

BS 5950 Part 5 (BSI, 1998) specifies the required strength of connectors at preventing fastener failures, which is similar to AS/NZS 4600 (SA, 2005) whereas the design rules given for preventing excessive distortion between connectors differ and are given as follows:

- 1) The beam length is divided into at least three equal parts: ie.  $s_{\max} \leq \frac{l}{3}$
- 2)  $s \leq 50 r_{cy}$  where  $s$  = the longitudinal spacing of connections,  $r_{cy}$  = the minimum radius of gyration of one channel

BS 5950 Part 5 (BSI, 1998) also specifies effective lengths for compound sections in terms of fastener spacing (Clause 5.6.3). In compound sections composed of two channels back to back designed as a single integral member and connected in accordance with Clause 8.6, the effective slenderness of the compound beam ( $L_E/r_y$ ) should be calculated as follows:

$$\frac{L_E}{r_y} = \sqrt{\left(\frac{L_E}{r_l}\right)^2 + \left(\frac{s}{r_{cy}}\right)^2} > 1.4 s/r_{cy} \quad (2)$$

Where

$L_E$  - the effective length of the compound member,  $r_y$  - the radius of gyration of the compound section about the axis parallel to the webs allowing for the two elements acting as a single integral member,  $r_l$  - the radius of gyration of the compound section about the axis parallel to the webs based on normal geometric properties,  $s$  - the longitudinal spacing between adjacent fasteners or welds connecting the two sections,  $r_{cy}$  - the min. radius of gyration of one channel. The local slenderness of an individual channel section,  $s/r_{cy}$ , should not exceed 50.

### 3. Experimental Study

#### 3.1 Test specimen and test program

Based on a numerical study, Compact, Non-compact and Slender LSB sections were chosen. Test span selected was 3.5 m based on current test rig capacity and the practical range of 12 to 24 times of section depth ( $d$ ). Connector spacings (CS) selected for the specimens are the minimum spacing of span/6 as specified in AS/NZS 4600, span/4, span/3, span/2 and span/1, ie. no connections between the two end supports. For comparison purposes, single LSBs were also tested. Details of the test specimens are reported in Table 1.

#### 3.2 Test set-up and procedure

The lateral buckling tests were carried out using an overhang loading method in which a uniform moment was provided throughout the entire span ( $L$ ). Attempts were taken to reduce the level of warping restraint. Although shorter overhangs induce less restraint, they may induce shear or local buckling failure at the supports due to higher load requirements. An appropriate overhang length of 0.75 m ( $X$ ) was chosen based on preliminary finite element analyses to avoid any premature failures. The experimental arrangement of built-up LSB beams used in this research is shown in Figure 3. The test rig used by Mahaarachchi and Mahendran (2005a) for single LSB sections was modified for the built-up LSB sections. It consists of a support system and a loading system, attached to an external frame structure (Figure 4a).

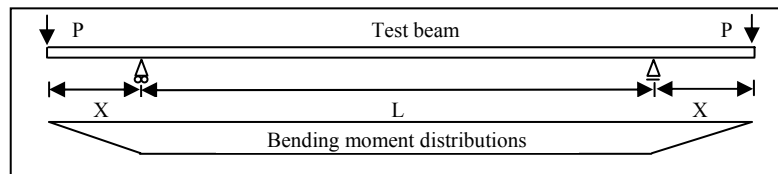


Figure 3: Overhang loading method

The support systems were designed to ensure that the test beams were simply supported in-plane and out-plane (Figure 4b). The support conditions restrained in-plane vertical deflection, out-of-plane deflections and twisting, but allowed major and minor axis rotations. One of the supports was designed as a roller. In addition, two brackets were designed to be located at the end support systems to hold back to back LSBs without any gap. Loading arms were specially designed to apply the loads through the shear centre. The loading system was designed to

prevent any restraint to the displacement and rotations of the test beam using a special wheel system. The loads were applied at the end of each overhang under displacement control method using hydraulic rams.

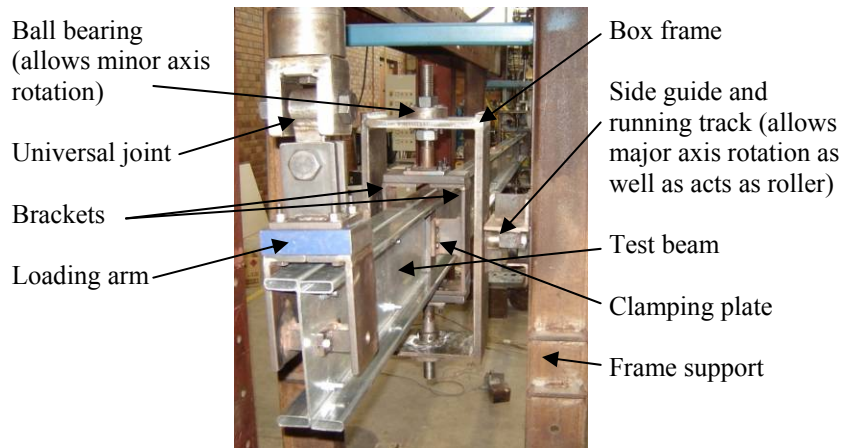
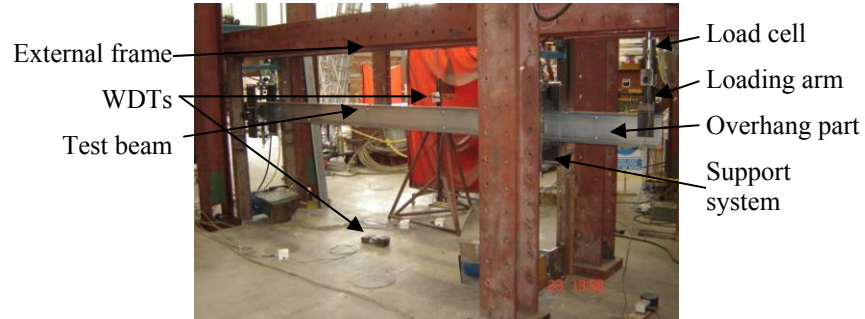


Figure 4: Test set-up

The loads were applied to the test beam until its failure while recording the measurements of the applied load, beam deformations and strains. The in-plane and out of plane deflections of top and bottom flanges at midspan, and the vertical deflection under each loading point of the overhang deformations were measured using wire potentiometer type displacement transducers (WDT). Longitudinal strains were also recorded at midspan using strain gauges.

#### 4. Experimental Results

Experimental responses of built-up beams were evaluated based on four important parameters, the moment capacity, bending deformations, failure mode and the flange separation. More details are given in Jeyaragan and Mahendran (2008a). Table 1 presents the test results and the three important parameters.

Table 1: Experimental test results and identified parameters

Test No	Specimens $d \times b_f \times t$	Span (mm)	Type	s (mm)	$M_u$ (kNm)	$\delta_v$ (mm)	Failure Mode
1	200×45×1.6 LSB	3500	B	3500	17.15	14.2	LDB
2	200×45×1.6 LSB	3500	B	1750	17.00	17.6	LDB
3	200×45×1.6 LSB	3500	B	1167	21.06	12.6	LDB
4	200×45×1.6 LSB	3500	B	875	17.93	15.7	LDB
5	200×45×1.6 LSB	3500	B	583	20.64	14.4	LDB
6	150×45×1.6 LSB	3500	B	3500	17.43	30.8	LDB
7	150×45×1.6 LSB	3500	B	1750	17.28	30.8	LDB
8	150×45×1.6 LSB	3500	B	1167	17.71	33.2	LDB
9	150×45×1.6 LSB	3500	B	875	16.68	30.4	LDB
10	150×45×1.6 LSB	3500	B	583	19.55	35.1	LDB
11	125×45×2.0 LSB	3500	B	1167	20.63	55.8	LDB
12	125×45×2.0 LSB	3500	B	583	19.84	54.4	LDB
13	150×45×1.6 LSB	3500	S	N/A	6.52	39.3	LDB
14	200×45×1.6 LSB	3500	S	N/A	7.33	13.0	LDB

Note:  $d$  – Overall depth,  $b_f$  – Flange width,  $t$  – Thickness,  $s$  – Connector spacing,  $M_u$  – Ult. Moment,  $\delta_v$  – Vertical displacement at midspan, LDB – Lateral Distortional Buckling, B – back to back built-up LSB, S – single LSB.

##### 4.1 Influence of connector spacing and comparison with single LSBs

The moment capacities of built-up 200×45×1.6 LSBs range from 17.00 kNm for connector spacing of span/2 to 21.06 kNm for connector spacing of span/3 whereas the moment capacity of corresponding single LSB is 7.33 kNm. For 150×45×1.6 LSB, the moment capacities varied from 17.28 kNm for connector spacing of span/2 to 19.55 kNm for connector spacing of span/6 while the moment capacity of corresponding single LSB is 6.52 kNm. Hence in general, test results show that the moment capacity of built-up LSBs is influenced by the connector spacing and significant increment can be noted in comparison with the corresponding single LSBs. The moment capacities of built-up LSBs were

compared with that of corresponding single LSBs and the comparisons are listed in Table 2. The beams, 200×45×1.6 LSB and 150×45×1.6 LSB, with connector spacing of span/6 had ultimate moments of 2.82 and 3.00 times the capacities of corresponding single LSBs, respectively. Thus the increment in moment capacity is about 40 – 50% for beams with AS/NZS 4600 recommended connector spacing of span/6, and is not negligible. However, the allowable capacity of back to back beams is typically determined by doubling the allowable capacity of single sections. This conservative assumption underestimates the true capacity of back to back LSB sections.

Table 2: Comparison of moment capacities

Test No	Specimens	s (mm)	$M_{ub}$ (kNm)	$M_{ub}/M_{us}$ ratio	Moment increment (%)
1	200×45×1.6 LSB	3500	17.15	2.34	17.0
2	200×45×1.6 LSB	1750	17.00	2.32	16.0
3	200×45×1.6 LSB	1167	21.06	2.87	43.5
4	200×45×1.6 LSB	875	17.93	2.45	22.5
5	200×45×1.6 LSB	583	20.64	2.82	41.0
6	150×45×1.6 LSB	3500	17.43	2.67	33.5
7	150×45×1.6 LSB	1750	17.28	2.65	32.5
8	150×45×1.6 LSB	1167	17.71	2.72	36.0
9	150×45×1.6 LSB	875	16.68	2.56	28.0
10	150×45×1.6 LSB	583	19.55	3.00	50.0

Note:  $M_{ub}$  – Ult. Moment of back to back LSB,  $M_{us}$  – Ult. Moment of single LSB

The ultimate vertical deflection at midspan for built-up 200×45×1.6 LSB varied from 12.6 to 17.6 mm. For 150×45×1.6 LSB, the deflection varied from 30.8 to 35.1 mm while they were 55.8 and 54.4 mm for 125×45×2.0 LSB. The ultimate vertical deflection at midspan for single 200×45×1.6 LSB and 150×45×1.6 LSB are 13.0 and 39.3 mm, respectively and they are in or very close to the vertical deflection range of corresponding built-up LSB sections.

#### 4.2 Failure mode

The failure mode was governed by lateral distortional buckling for all the back to back built-up specimens. The effect of cross-section distortion was governed by the depth of web. The slender section, 200×45×1.6 LSB, exhibited larger web distortion in comparison with other two sections (non-compact and compact sections). Also, the flange-web junction was distorted slightly. For 150×45×1.6

LSB, the web distortion was not as high as in the slender section. But flange rotation was very noticeable. Section  $125 \times 45 \times 2.0$  LSB exhibited very little web distortion and flange rotation. Single LSBs also exhibited lateral distortional buckling failure as shown by Mahaarachchi and Mahendran (2005a). The detrimental effects of lateral distortional buckling that occurs with single LSB sections appears to still remain with back to back LSBs, but it is not as severe as for single LSBs. Further numerical studies on both back to back and single LSB will investigate this. The deformation shape at failure for some selected built-up and single LSB specimens are shown in Figures 5 (a) and (b).

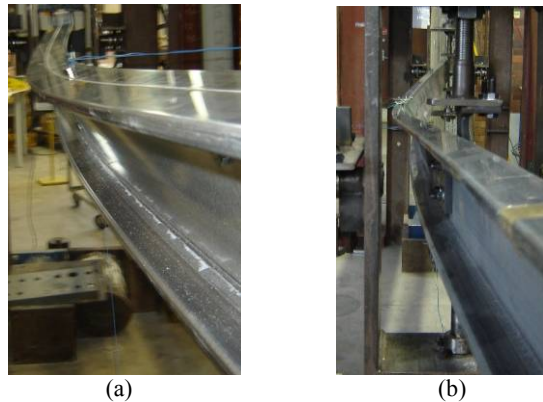


Figure 5: Deformations at failure: (a) Back to back  $150 \times 45 \times 1.6$  LSB with CS of span/4 (b) Single  $150 \times 45 \times 1.6$  LSB

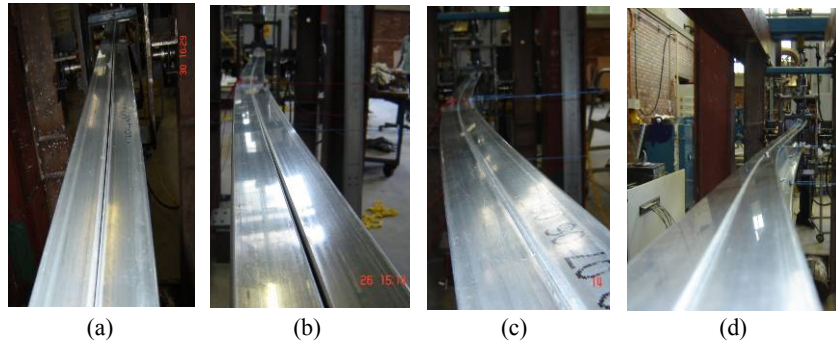


Figure 6: Flange separation (a)  $200 \times 45 \times 1.6$  LSB with CS of span/2 (b)  $150 \times 45 \times 1.6$  LSB with CS of span/3 (c)  $200 \times 45 \times 1.6$  LSB with CS of span/6 (d)  $150 \times 45 \times 1.6$  LSB with CS of span/4

### 4.3 Flange separation and a review on current design rules

The second design rule is aimed at preventing excessive distortion between connectors by separation along the flange. Tests revealed different levels of separation between connectors, depending on connector spacing. Beams with connector spacings of span/4 and span/6 exhibited very little separation ( $\leq 1$  mm) between the connectors located close to the supports (Figures 6c and d). Beams with connector spacings of span/2 and span/3 also showed smaller separations ( $\leq 3$ -4 mm) between the connectors (Figures 6a and b). Figures 6a to d show the level of separation, which is not significant from a design viewpoint.

Beams with connector spacing ratio of span/1 revealed sliding of webs on each other with a maximum value of about 5-6 mm, making the flanges not leveled. From the test results the limit of span/6 for connector spacing in AS 4600 (SA, 2005) appears to be over-conservative. In contrast, the limit given by BS 5950 Part 5 (BSI, 1998) of span/3 is an improvement. However, its second limit of not exceeding 50 times the minimum radius of gyration of the single beam makes the first limit irrelevant. For example, for all the tested specimens, the second limit is around 800 mm, which is less than the connector spacing of span/4 (875 mm). This makes the connector spacing of span/6 as the limit for the tested beams. The second rule governs the limit when the span length is increased. Hence using this second limit may also give overconservative results for long and intermediate span lengths. Thus, more suitable spacing limits are needed for the back to back LSBs with varying spans based on improved understanding.

## 5. Numerical Modelling of the Built-up LSB Section

### 5.1 General

In this research two finite element models, namely ideal and experimental models were developed using ABAQUS. Experimental models were generated to validate the finite element models in comparison with experimental results whereas ideal models were developed to conduct parametric studies and hence to develop design rules. The development of ideal models of built-up LSB beams is reported in Jeyaragan and Mahendran (2008b). The actual physical test system was simulated by experimental finite element model, which is described in the following sections.

### 5.2 Finite element mesh and material modelling

Based on convergence studies shell element, S4R5, was selected to model the LSB. This element is a thin, shear flexible, isometric quadrilateral shell with four nodes and five degree of freedom per node, utilizing reduced integration and bilinear interpolation scheme. Element widths ranging from 4.33 to 5.42 mm and a length



of 10 mm were selected as the suitable mesh size through the entire cross-section for both built-up and single LSB sections, which sufficiently represents the spread of plasticity, residual stress distribution and local buckling deformations. A simplified bi-linear stress-strain curve with no strain hardening, known as elastic-perfectly plastic model, was used in the experimental model for nonlinear analysis. This simple model was considered sufficient for modeling sections subject to a dominant failure mode of lateral buckling (Mahaarachchi and Mahendran, 2005b). Measured average yield stresses and thicknesses were adopted (Table 3).

Table 3: Measured average thicknesses and yield stresses

Section	Thickness (mm)			Yield stress (MPa)		
	$t_o$	$t_i$	$t_w$	$f_{yo}$	$f_{yi}$	$f_{yw}$
200x45x1.6 LSB	1.78	1.65	1.60	530	500	430
150x45x1.6 LSB	1.74	1.62	1.58	535	490	435

Note:  $t_o$ ,  $t_i$  and  $t_w$ , and  $f_{yo}$ ,  $f_{yi}$  and  $f_{yw}$  : Thicknesses and Yield stresses of outside flange, inside flange and web, respectively.

### 5.3 Load and boundary conditions

An idealized simply supported beam with a uniform moment within the span has generally been assumed as the worst scenario giving a lower bound solution. The following idealized simply supported (SS) boundary conditions were implemented in the ideal model:

1. SS in-plane: Both ends fixed against in-plane vertical deflection but unrestrained against in-plane rotation, and one end fixed against longitudinal horizontal displacement.
2. SS out-of-plane: Both ends fixed against out-of-plane horizontal deflection, and twist rotation, but unrestrained against minor axis rotation and warping displacements of flanges.

Simply supported boundary conditions implemented in the experimental models are slightly different from those in the ideal model and are described as follows:

1. The pin support end was modelled by restraining degree of freedom ‘234’ for the node which controls the support plate as shown in Figure 7.
2. Due to the symmetry of beam, half span modelling was permitted by restraining degree of freedom ‘156’ for all the nodes at mid span (Fig. 7).
3. Two point loads were applied on either side of the loading arm at the end of overhang (Figure 7).

The degree of freedom notations ‘1, 2 and 3’ correspond to translation in x, y and z directions while ‘4, 5 and 6’ represent the rotations about the x, y and z axes, respectively.

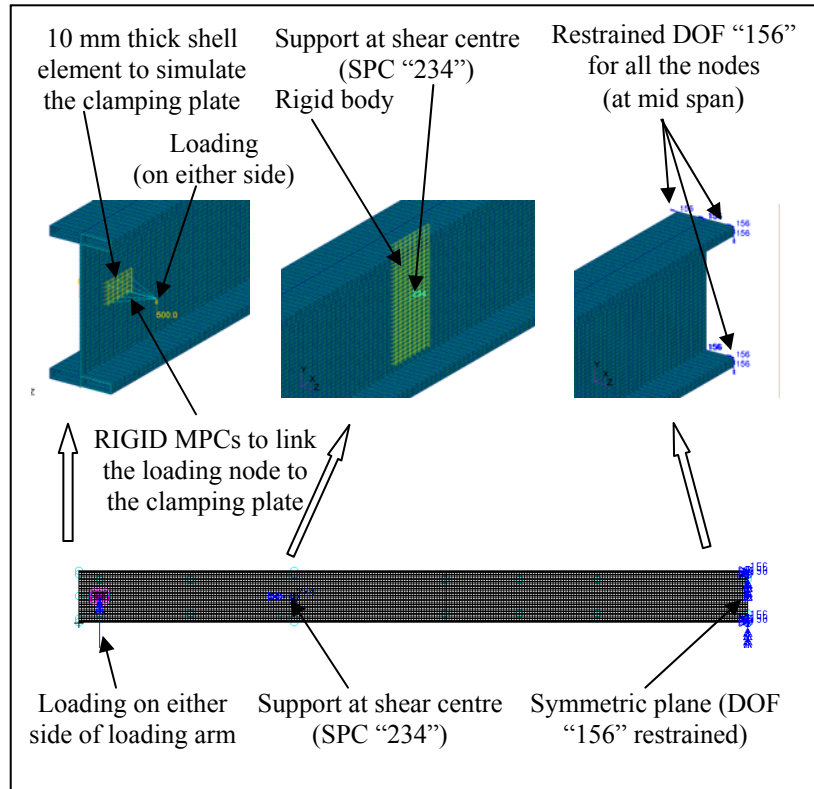


Figure 7: Load and boundary conditions for the experimental FE Model

The test members included rigid plates on either side of beam web at each support to prevent distortion and twisting of the cross-section. These stiffening plates were modelled as rigid body using R3D4 elements. The motion of the rigid body is controlled by a reference node. The control node was created at shear centre and support conditions (“234”) were applied. In the experimental set-up, a concentrated load was applied at the end of each overhang, which was transferred equally to the two beam webs. Steel plates connected to the web were modelled using thicker shell element (10 mm) with elastic properties.

#### 5.4 Fastener modelling

Fasteners play an important role in the structural response of built-up members. In this research, fasteners are designed with a greater factor of safety, and

therefore it is assumed that there will be no fastener failure. Beam element, B31, with a diameter of 10 mm, was used to model the fasteners. The material model for beam elements was elastic-perfectly plastic and a yield stress of 240 MPa was assumed. In the case of ideal model, perfect Tie MPC was simulated, which makes all active degrees of freedom equal on both sides of the connection.

### 5.5 Contact modelling

Contact modelling was implemented in order to simulate the interaction between the two LSB sections connected back to back. Surface-based contact simulation was found to be adequate to represent the contact interaction between them (Figure 8). Elements in the main web and the web of the flanges are likely to come into contact. Contact conditions were applied using symmetric “master-slave” algorithm, in which contact surface of one LSB was assigned as master surface while contact surface of other LSB was assigned as slave-surface. Small-sliding tracking approach, “hard” contact pressure-overclosure relationship, zero friction, deformable body conditions and initial gap of 0.1 mm were used in the element-based surface contact model.

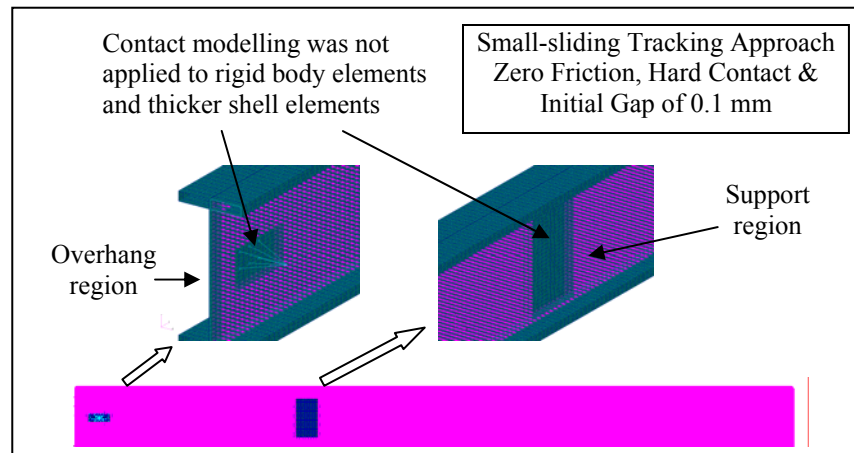


Figure 8: Contact modelling

### 5.6 Initial geometric imperfection

A geometric imperfection pattern is generally introduced for post buckling load-displacement analyses. The critical imperfection shape was introduced via ABAQUS \*IMPERFECTION option by modifying the nodal coordinates using

a vector field created by scaling the lateral buckling eigenvector obtained from an elastic buckling analysis. Measured values were used in the models.

### **5.7 Residual stresses**

The unique cold forming and dual electric resistance welding process of LSB sections introduces residual stresses, both flexural and membrane stresses. The residual stress model developed by Mahaarachchi and Mahendran (2005b) and upgraded by Seo et al. (2008) was used to introduce the initial stresses in the experimental models. The initial stresses were created using the SIGINI Fortran user subroutine and executed using ABAQUS \*INITIAL CONDITIONS option, with TYPE = STRESS. The variation of the flexural residual stress through the thickness was assumed to be linear, with zero stress at the centre fibre. Nine integration points were defined through the thickness of each element to simulate the accurate distribution of residual stresses.

## **6. Calibration of Finite Element Models**

It was necessary to validate the developed finite element models for numerical studies. For this purpose, elastic lateral buckling moments obtained using ideal finite element model were compared with the corresponding moments obtained from the established finite strip analysis program, THINWALL while the nonlinear analysis results from the experimental finite element model were compared with the experimental test results of LSBs.

### **6.1 Comparison of elastic lateral buckling moments**

Elastic buckling moments obtained for the built-up LSB sections connected continuously were compared with the predictions from THIN-WALL (Table 4). The results agree well with an average deviation of (-) 5.5%. The numerical models used are not exactly identical since in the Thin-Wall model, separate elements were used to simulate the connections whereas in the ABAQUS finite element model, Tie MPCs were used at 10 mm intervals. This might have caused the observed differences.

### **6.2 Comparison with experimental test results**

The nonlinear experimental finite element models were validated using the results from the experimental tests. Table 5 compares the ultimate moment capacity results of the nonlinear analyses using the experimental model described in Section 5 with the experimental test results. Typical bending moment versus deflection curves are provided in Figure 9.

Table 4: Comparison of elastic lateral buckling moments from finite element analysis (FEA) and Thin-Wall (TW)

Span (m)	Elastic Lateral Buckling Moment (kNm)								
	125×45×2.0 LSB			150×45×1.6 LSB			200×45×1.6 LSB		
	FEA	Thin-Wall	Dif (%)	FEA	Thin-Wall	Dif (%)	FEA	Thin-Wall	Dif (%)
2.00	40.91	43.23	5.4	31.60	33.10	4.5	32.95	34.66	4.9
3.00	28.74	30.45	5.6	22.57	23.69	4.7	22.36	23.52	4.9
4.00	22.12	23.46	5.7	17.73	18.63	4.8	17.45	18.39	5.1
5.00	17.94	19.04	5.8	14.57	15.33	5.0	14.37	15.15	5.1
6.00	15.07	16.00	5.8	12.34	12.99	5.0	12.21	12.88	5.2
7.00	12.98	13.78	5.8	10.69	11.25	5.0	10.60	11.19	5.3
8.00	11.40	12.00	5.8	9.42	9.92	5.0	9.35	9.88	5.3
9.00	10.15	10.78	5.8	8.42	8.86	5.1	8.37	8.84	5.3
10.00	9.15	9.72	5.8	7.60	8.01	5.1	7.57	7.99	5.3

Table 5: Comparison of nonlinear FEA and experimental results

Section	s (mm)	Type	Exp. results	FEA results	FEA/Exp.
200×45×1.6 LSB	1750	B	17.00	17.78	1.05
200×45×1.6 LSB	875	B	17.93	18.30	1.02
200×45×1.6 LSB	583	B	20.64	18.45	0.89
150×45×1.6 LSB	1750	B	17.28	16.43	0.95
150×45×1.6 LSB	1167	B	17.71	16.65	0.94
150×45×1.6 LSB	875	B	16.68	17.10	1.01
150×45×1.6 LSB	N/A	S	6.52	6.29	0.96
200×45×1.6 LSB	N/A	S	7.33	6.99	0.95

Note: Exp. – Experimental, FEA – Finite element analysis

Figures 10 (a) and (b) show the typical deformation of the test beams at failure and the corresponding failure predicted by FEA. Comparison of the ultimate moment capacities and the moment versus displacement curves of the tested specimens and the FEA shows a good agreement between tests and FEA.

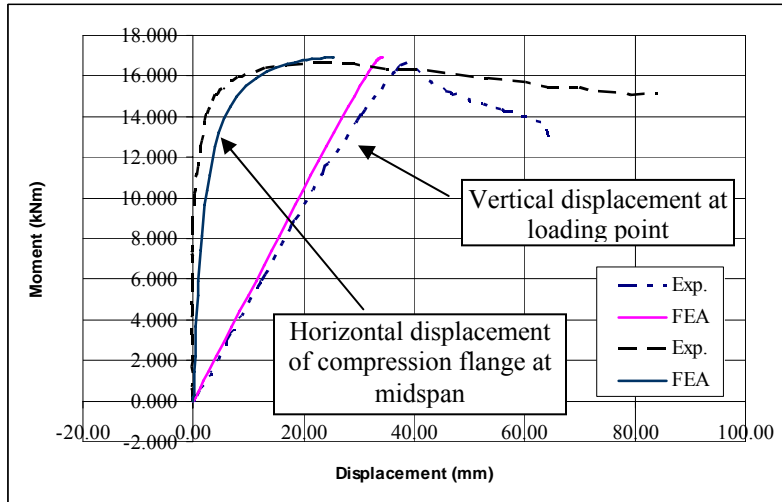


Figure 9: Moment versus displacement curve for back to back 150×45×1.6 LSB with connector spacing of span/4

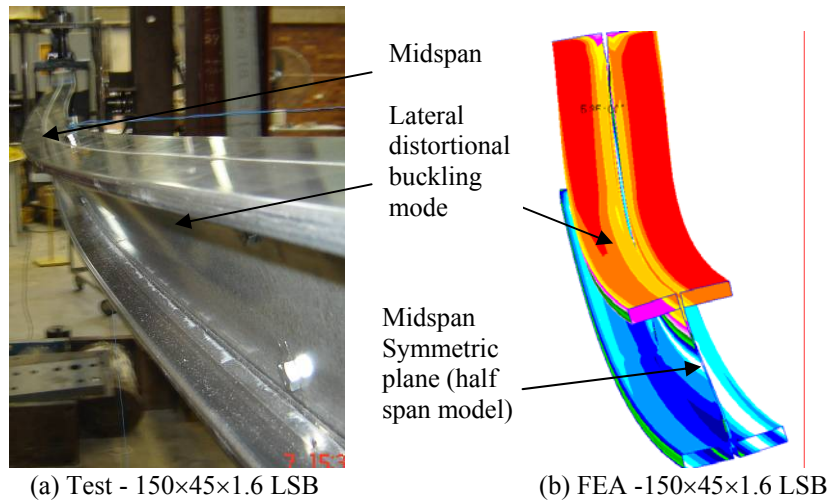


Figure 10: Typical specimen deformation at failure (a) Tested specimen (b) Experimental finite element model

## 7. Elastic Buckling Moments and Applicability of Current Rules

Elastic buckling moments of a set of built-up LSB sections obtained from the ideal finite element models are listed in Table 6. Three different LSB sections, 125×45×2.0 LSB, 150×45×1.6 LSB and 200×45×1.6 LSB, were chosen from the small and medium size LSBs. Based on AS4100 guidelines, they are classified as compact, non-compact and slender sections, respectively. Intermediate span lengths (S) of 2, 3 and 4 m in which single LSB sections exhibit lateral distortional buckling were considered. In addition, connection spacing ratio (SR) of span/6 as specified in AS/NZS 4600, span/4, span/3, span/2, span/1 and continuous connections were considered. They are shown as “1, 2, 3, 4, 6, C” in Table 6.

Table 6: Elastic buckling moments in kNm from finite element analysis

S (m)	SR	125×45×2.0 LSB	150×45×1.6 LSB	200×45×1.6 LSB
2	1	28.82	22.99	22.80
	2	35.58	27.69	29.14
	3	37.09	28.76	30.11
	4	37.97	29.39	30.69
	6	38.89	30.06	31.32
	C	40.90	31.60	32.95
3	1	20.75	16.54	16.72
	2	25.35	20.12	20.17
	3	26.48	20.91	20.83
	4	27.06	21.32	21.19
	6	27.65	21.75	21.57
	C	28.74	22.57	22.36
4	1	16.11	13.18	15.64
	2	19.68	15.93	15.90
	3	20.56	16.56	16.41
	4	21.00	16.89	16.68
	6	21.42	17.19	16.95
	C	22.12	17.73	17.45

### 7.1 Design formulae for elastic buckling moment

Elastic buckling moment ( $M_o$ ) is defined in Clause 5.6.1.1 of AS 4100 as follows:

$$M_o = \sqrt{\left[ \left( \frac{\pi^2 EI_y}{L_e^2} \right) \left[ GJ + \left( \frac{\pi^2 EI_w}{L_e^2} \right) \right] \right]} \quad (3)$$

Where  $E$  = Young's modulus,  $G$  = shear modulus,  $I_w$  = warping constant  
 $I_y$  = second moment of area about the minor principal axis  
 $J$  = torsion constant,  $L_e$  = effective length

Table 7: Comparison of elastic buckling moments obtained from Buckling formulae, Thin-wall and FEA

125×45×2.0 LSB							
$L_e$ (m)	$M_1$	$M_2$	$M_3$	$M_4$	$M_4/M_3$	$M_4/M_2$	$M_4/M_1$
2.0	69.00	39.87	43.23	40.91	0.946	1.026	0.593
3.0	44.95	30.61	30.45	28.74	0.944	0.939	0.639
4.0	33.44	22.41	23.46	22.12	0.943	0.987	0.662
5.0	26.65	18.42	19.04	17.94	0.942	0.974	0.673
6.0	22.16	15.60	16.00	15.07	0.942	0.966	0.680
8.0	16.58	11.90	12.10	11.40	0.942	0.957	0.687
10.0	13.25	9.60	9.72	9.15	0.941	0.953	0.690
150×45×1.6 LSB							
$L_e$ (m)	$M_1$	$M_2$	$M_3$	$M_4$	$M_4/M_3$	$M_4/M_2$	$M_4/M_1$
2.0	60.55	31.17	33.10	31.60	0.955	1.014	0.522
3.0	39.03	21.68	23.69	22.57	0.953	1.041	0.578
4.0	28.92	17.34	18.63	17.73	0.952	1.023	0.613
5.0	23.00	14.51	15.33	14.57	0.950	1.004	0.633
6.0	19.11	12.46	12.99	12.34	0.950	0.991	0.646
8.0	14.28	9.67	9.92	9.42	0.950	0.974	0.660
10.0	11.41	7.87	8.01	7.60	0.949	0.966	0.666
200×45×1.6 LSB							
$L_e$ (m)	$M_1$	$M_2$	$M_3$	$M_4$	$M_4/M_3$	$M_4/M_2$	$M_4/M_1$
2.0	66.85	34.43	34.66	32.95	0.951	0.957	0.493
3.0	42.40	21.73	23.52	22.36	0.951	1.029	0.527
4.0	31.22	16.97	18.39	17.45	0.949	1.029	0.559
5.0	24.75	14.17	15.15	14.37	0.949	1.014	0.581
6.0	20.53	12.20	12.88	12.21	0.948	1.000	0.595
8.0	15.32	9.53	9.88	9.35	0.947	0.982	0.611
10.0	12.23	7.79	7.99	7.57	0.947	0.971	0.619

**Note:**  $M_1$ ,  $M_2$ ,  $M_3$  and  $M_4$  are Elastic buckling moment ( $M_o$ ), Elastic lateral distortional buckling moment ( $M_{od}$ ), and Elastic buckling moments obtained using thin-wall and FEA, respectively.



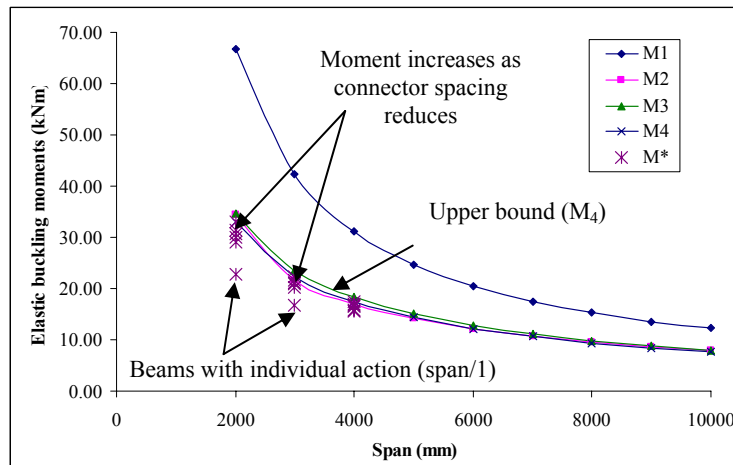
Pi and Trahair (1997) also provided equations to estimate the elastic distortional buckling moment ( $M_{od}$ ) of hollow flange beam using an approximate effective torsional rigidity ( $GJ_e$ ) as follows:

$$M_{od} = \sqrt{\frac{\pi^2 EI_y}{L^2} \left( GJ_e + \frac{\pi^2 EI_w}{L^2} \right)} \quad (4)$$

$$GJ_e = \frac{2GJ_F \frac{Et^3 L^2}{0.91\pi^2 d}}{2GJ_F + \frac{Et^3 L^2}{0.91\pi^2 d}} \quad (5)$$

Where,  $d$  = web height,  $L$  = length,  $t$  = thickness,  $J_e$  = effective torsion section constant,  $J_F$  = torsion constant of hollow flange

The beams with connector spacing of “C”, continuous connection, is the upper bound for the back to back built-up LSBs with the particular fastener locations across the depth. The elastic buckling moments obtained from FEA, Thin-Wall and design formulae for beams with connector spacing of “C” were compared and listed in Table 7.



M\* - Moment capacities of 200×45×1.6 LSBs with different fastener spacings

Figure 11: Comparison of elastic buckling moments for back to back 200×45×1.6 LSB

Elastic lateral distortional buckling moments obtained using Equation (4) agree well with FEA and Thin-wall results. But the elastic buckling moments obtained using Equation (3) did not agree with either FEA or Thin-wall. Figure 11 illustrates the comparison of elastic buckling moments for back to back 200×45×1.6 LSB section with different fastener spacings. It shows that the buckling formulae are unable to predict the elastic buckling moments of built-up LSBs as the connector spacing was increased.

## **8. Conclusion**

This paper has described the details of an experimental study into the flexural behaviour of built-up LSB members, experimental finite element model development and the calibration of finite element models. Test results show that the built-up LSB sections are likely to give higher flexural capacities. The beams with a connector spacing of span/6 increased the flexural capacity by about 40 to 50% in comparison with the corresponding single LSBs. In the back to back built-up LSB sections even with larger connector spacings of span/2, the failure mode was governed by lateral distortional buckling with very little separation between the connectors. This shows that the current limit of span/6 specified in AS/NZS 4600 (SA, 2005) in relation to excessive deformation is over-conservative for intermediate spans. Thus, more appropriate spacing limits are needed for back to back LSBs with varying spans. Numerical models were developed and validated by comparing the elastic buckling moments and the nonlinear analysis results from numerical models with the results obtained from Thin-wall and experimental tests, respectively. The elastic lateral distortional buckling moments obtained for beams with connector spacing of “C”, continuous connection, using Equation (4) agree well with the results from finite element analyses and Thin-wall. A detailed parametric study using the developed finite element model is currently under way to formulate improved design rules for built-up LSBs.

## **9. Acknowledgements**

The authors would like to thank Australian Research Council and Australian Tube Mills for their financial support and the Queensland University of Technology for providing the necessary research facilities and technical support.

## References

American Iron and Steel Institute (AISI) (2001). Specifications for the cold-formed steel structural members, Cold-formed Steel Design Manual, Washington, USA.

British Standards Institution (BSI) (1998). Structural use of steelwork in building, BS 5950, Part 5 Code of Practice for Design of Cold-formed Thin Gauge Sections, London, UK.

Jeyaragan, S. and Mahendran, M. (2008a). Experimental investigation of the new built-up LiteSteel beams, Proc. of the 5<sup>th</sup> International Conference on Thin-Walled Structures, Brisbane, Australia, (Paper accepted).

Jeyaragan, S. and Mahendran, M. (2008b). Numerical modeling and design of the new built-up LiteSteel beams, Proc. of the 5<sup>th</sup> International Conference on Coupled Instabilities in Metal Structures, Sydney, Australia, (Paper accepted).

Mahaarachchi, D. and Mahendran, M. (2005a). Lateral buckling tests of LiteSteel beam sections, Research Report, Queensland University of Technology, Brisbane, Australia.

Mahaarachchi, D. and Mahendran, M. (2005b), Finite Element Analysis of LiteSteel Beam Sections, Research Report, Queensland University of Technology, Brisbane, Australia.

Pi, Y.L. and Trahair, N.S. (1997), Lateral Distortional Buckling of Hollow Flange Beams, J. of Structural Engineering, ASCE, Vol. 123, No. 6, pp.695-702.

Seo, J.K., Anapayan, T. and Mahendran, M. (2008). Initial imperfection characteristics of mono-symmetric LiteSteel beams for numerical studies, Proc. of the 5<sup>th</sup> International Conference on Thin-Walled Structures, Brisbane, Australia, (Paper accepted).

Smorgon Steel LiteSteel Technologies (LST) (2005). Design capacity tables for LiteSteel beams, Smorgon Steel LiteSteel Technologies, Brisbane, Australia.

Standards Australia (SA) (1998), Steel Structures, AS 4100, Sydney, Australia.

Standards Australia (SA) (2005). Cold-formed steel structures, AS/NZS 4600, Sydney, Australia.

## **Experimental and Numerical Studies of the Shear Behaviour of LiteSteel Beams**

P. Keerthan<sup>1</sup> and M. Mahendran<sup>2</sup>

### **Abstract**

This paper presents the details of experimental and numerical studies on the shear behaviour of a recently developed, cold-formed steel beam known as LiteSteel Beam (LSB). The LSB section is produced by a patented manufacturing process involving simultaneous cold-forming and electric resistance welding. It has a unique shape of a channel beam with two rectangular hollow flanges, made using a unique manufacturing process. To date, no research has been undertaken on the shear behaviour of LiteSteel beams with torsionally rigid, rectangular hollow flanges. In the present investigation, a series of numerical analyses based on three-dimensional finite element modelling and an experimental study were carried out to investigate the shear behaviour of 13 different LSB sections. It was found that the current design rules in cold-formed steel structures design codes are very conservative for the shear design of LiteSteel beams. Improvements to web shear buckling occurred due to the presence of rectangular hollow flanges while considerable post-buckling strength was also observed. Experimental and numerical analysis results are presented and compared with corresponding predictions from the current design codes in this paper.

**Keywords:** *Shear behaviour, LiteSteel Beams (LSB), Cold-formed steel structures, Slender web and hollow flanges.*

### **1.0 Introduction**

In recent times cold-formed and thin-walled steel sections have been used extensively in residential, industrial and commercial buildings as primary load bearing members. The reasons for the popularity of cold-formed steel members include their wide range of applications, high strength to weight ratio, economy of transportation and handling, ease of fabrication and simple erection.

---

<sup>1</sup>PhD researcher, <sup>2</sup>Professor, School of Urban Development, Faculty of Built Environment & Engineering, Queensland University of Technology, Australia.

By taking advantage of the new material and manufacturing technologies and structurally efficient rectangular hollow flanges, Australian Tube Mills (ATM) has recently developed a new hollow flange channel section, known as the LiteSteel Beam (LSB) shown in Figure 1. Table 1 shows the nominal dimensions of LSB sections. In the large scale production of LSB sections, ATM uses the new dual electric welding and automated continuous roll-forming technologies for which it has worldwide patents. The innovative LSB sections have the beneficial characteristics of torsionally rigid closed rectangular flanges combined with economical fabrication processes from a single strip of high strength steel. They combine the stability of hot-rolled steel sections with the high strength to weight ratio of conventional cold-formed steel sections.

Flexural and shear capacities of LSBs must be known for LSBs to be used as flexural members. Flexural behaviour of LSBs has been investigated recently by Mahaarachchi and Mahendran (2005) by using experimental and numerical studies, and hence the moment capacities of LSBs are available. However, the shear behaviour of LSBs has not yet been investigated. Past research (Porter et al. 1975, Lee et al. 1995) has been restricted to plate girders and the shear buckling coefficient of the new mono-symmetric LSB sections has not been investigated. This paper presents the details of experimental and numerical studies of the shear behaviour of LSBs and the results.

Table 1: Nominal Dimensions of LSB

LSB Section	d	$b_f$	t	$d_f$
300x75x3.0	300	75	3	25
300x75x2.5	300	75	2.5	25
300x60x2.0	300	60	2	20
250x75x3.0	250	75	3	25
250x75x2.5	250	75	2.5	25
250x60x2.0	250	60	2	20
200x60x2.5	200	60	2.5	20
200x60x2.0	200	60	2	20
200x45x1.6	200	45	1.6	15
150x45x2.0	150	45	2	15
150x45x1.6	150	45	1.6	15
125x45x2.0	125	45	2	15
125x45x1.6	125	45	1.6	15

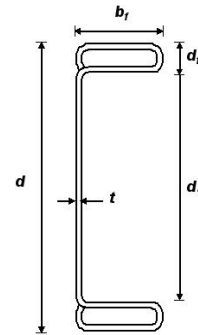


Figure 1: LiteSteel Beam

## 2.0 Experimental Study

Shear behaviour of LSBs was investigated using a series of pure shear tests of simply supported LiteSteel beams subjected to a mid-span load (see Figure 2). In order to simulate a pure shear condition, relatively short test beams of span based on aspect ratio (shear span  $a$ / clear web height  $d_1$ ) of 1 & 1.5 were selected. Two LSB sections were bolted back to back using three T-shaped

stiffeners located at the end supports and the loading point in order to eliminate any torsional loading of test beams.

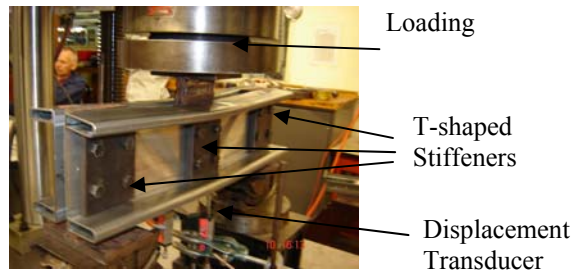


Figure 2: Experimental Set-up

The stiffeners were used to avoid eccentric loading and web crippling. A 20 mm gap (see Figure 2) was included between the sections to allow the test beams to behave independently while remaining together to resist torsional effects. Figure 2 shows the experimental set-up used in this research.

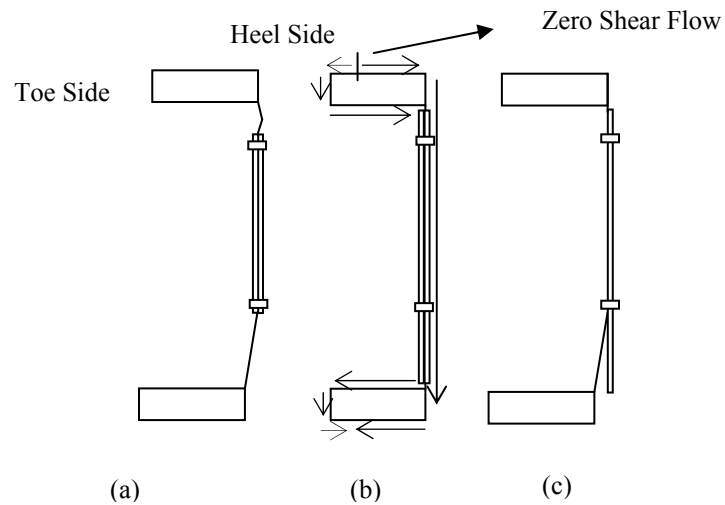


Figure 3: Effects of Web Side Plate (WSP)

Table 2: Experimental Results

Test No	LSB Section	Aspect Ratio	WSP Details	s/d <sub>1</sub> %	Ult. Load (kN)	Failure Mode
1	125x45x2.0	1.55	Both sides: 90x75	95	56.94	Shear Yielding
2	150x45x1.6	1.54	Both sides: 90x75	75	41.67	Inelastic Shear Buckling
3	150x45x1.6	1.00	Both sides: 90x75	75	43.50	Shear Yielding
4	150x45x2.0	1.00	Both sides: 90x75	75	61.22	Shear Yielding
5	150x45x2.0	1.54	Both sides: 90x75	75	53.84	Shear Yielding
6	200x45x1.6	1.50	Both sides:140x75	82	45.50	Elastic Shear Buckling
7	200x45x1.6	1.50	Both sides:156x75	92	54.19	Elastic Shear Buckling
8	250x60x2.0	1.50	One side: 206x75	98	61.12	Inelastic Shear Buckling
9	250x60x2.0	1.50	Both sides:206x75	98	>75	Inelastic Shear Buckling
10	200x60x2.0	1.50	Both sides:156x75	98	73.98	Inelastic Shear Buckling
11	300x60x2.0	1.50	Both sides:246x75	95	>75	Elastic Shear Buckling

Note: WSP sizes are given as height (s) x width;  $d_1$ = Depth of flat portion of web measured along the plane of the web.

Table 2 shows the details of the test specimens used and the results. In Tests 2 to 6, a tendency of the LSB flanges to displace laterally was observed (see Figures 3 (a) and 4). At the connection, the top flange of the LSB tended to displace laterally towards the heel side of the flange while the bottom flange would displace towards the opposite side (the toe side). This occurred when the full depth of web element of LSB was not supported by the web side plate (WSP), i.e. the WSP height (s) was less than then web height ( $d_1$ ). This led to reduced restraint to the lateral movement of flanges. When full lateral support was provided to the LSB top and bottom flanges at the connections by using WSPs with full web height as shown in Figures 3 (b) and 5, the LSB top and bottom flanges were effectively prevented from lateral displacement at the connections. The results from Tests 6 and 7 show that the shear capacity of LSB increases with increasing height of web side plate (WSP).

In Test 8, one WSP was used to investigate its effect on the shear capacity of LSB (see Figures 3(c) and 6) where LSB top flange was effectively prevented from lateral displacement at the connections by outside (Heel side) WSP while the bottom flange would displace towards the opposite side (Toe side). This

occurred because the web element was not fully supported inside by the WSP (Toe side). When the results of Test 8 (WSP on one side only) and Test 9 (WSP on both sides) are compared, there is more than 19% capacity reduction due to the lateral movement of the bottom flange. To prevent the lateral movement of bottom flange, bolts should be located near the bottom flange. More shear tests are being undertaken at present using WSPs on both sides with a height equal to that of LSB web element ( $d_f$ ).



Figure 4: Web with Two Partial WSP for 200x45x1.6 LSB



Figure 5: Web with Two Full WSP for 200x45x1.6 LSB



Figure 6: Web with by One Full WSP for 200x45x1.6 LSB

### 3. Shear Yielding Behaviour of Beam Web Panels

#### 3.1 General

A stocky web (small depth to thickness ratio) is subjected to shear yielding. The section yields, but does not buckle, as the web is compact. The stocky web



section will yield in shear at an average stress of  $f_y / \sqrt{3}$  as given by the von Mises yield criterion (Hancock, 1998). The nominal shear yielding capacity of the section is therefore given by Equation 1. Figure 7 shows the shear yielding of LiteSteel beam. The accuracy of this equation in predicting the shear capacity of LSBs will be discussed in Section 5 by comparing with experimental results.

$$V_v = 0.64 f_y d_1 t_w \quad \text{for} \quad \frac{d_1}{t_w} \leq \sqrt{\frac{E k_v}{f_y}} \quad (1)$$

where  $d_1$  = Depth of flat portion of web measured along the plane of the web,  $t_w$  = Thickness of the web  $f_y$ ,  $E$  = Yield stress used in design and Modulus of elasticity of steel;  $k_v$  = Shear buckling coefficient.



Figure 7: Shear Yielding Failure  
(125x45x2 LSB)

#### 4. Shear Buckling Behaviour of Beam Web Panels

##### 4.1 General

For a web element with a large depth to thickness ratio, its shear capacity is governed by elastic shear buckling. The elastic critical shear buckling stress can be computed by Equation 2 (Hancock, 2005). Equation 3 gives the shear capacity ( $V_v$ ) of conventional cold-formed steel beams in the case of elastic shear buckling.

$$\tau_{cr} = \frac{k_v \pi^2 E}{12(1 - \nu^2)} \left( \frac{t_w}{d_1} \right)^2 \quad (2)$$

where  $k_v$  = Shear buckling coefficient (5.34) and other symbols have been defined in Eq. (1).

$$V_v = \frac{0.905 E k_v t_w^3}{d_1} \quad \text{for} \quad 1.415 \sqrt{\frac{E k_v}{f_y}} < \frac{d_1}{t_w} \quad (3)$$

In the region where shear buckling and yielding interact, the failure stress is given by the geometric mean of the buckling stress and 0.8 times the yield stress in shear (Hancock, 1998). In the case of inelastic shear buckling the resulting equation for the nominal shear capacity ( $V_v$ ) is given by Equation 4.

$$V_{vw} = 0.64 t_w^2 \sqrt{E k_v f_y} \quad \text{for} \quad \sqrt{\frac{E k_v}{f_y}} < \frac{d_1}{t_w} \leq 1.415 \sqrt{\frac{E k_v}{f_y}} \quad (4)$$



Figure 8: Elastic Shear Buckling  
200x45x1.6 LSB



Figure 9: Inelastic Shear Buckling  
200x60x2 LSB

Figure 8 shows the elastic shear buckling of LSB while Figure 9 shows the inelastic shear buckling of LSB. The boundary condition at the juncture of the web and flange elements is somewhere between simple and fixed condition as recognized from early days. Such conservative assumption was made mainly due to the inability to evaluate it in a rational manner. For example, Basler (1961) and Porter et al. (1975) assumed that the web panel was simply supported at the juncture while Chern and Ostapenko (1969) obtained the ultimate strength by assuming that the juncture behaved like a fixed support.

The boundary condition at the flange-web juncture in practical designs is much closer to fixity for the plate girders (Lee et al. 1995). Therefore the assumption that the web panel is simply supported at the juncture sometimes leads to a considerable underestimation of the ultimate shear strength because of the underestimation of the elastic shear buckling strength of plate girders. Based on a numerical study, Lee et al. (1995) proposed simple equations to determine the shear buckling coefficients ( $k_v$ ) of plate girder web panels. A similar approach was used in this investigation for LSBs.

## 4.2 Elastic Buckling Analysis

In order to obtain the shear-buckling coefficient of LSBs, finite element analyses were carried out using ABAQUS based on the ideal model of LSB with aspect ratios (shear span  $a$ /web height  $d_1$ ) of 1 (see Figure 10). The ideal models included the nominal web and flange yield stresses of 380 and 450 MPa, respectively. These yield stresses are the minimum specified values for the range of LSB sections. Finite element model was to provide “idealized” simply supported boundary conditions. Element widths of 5 mm x 5 mm were selected as the suitable mesh size through the entire cross-section for LSB sections. The shear flow pattern loading was applied to prevent the twisting effect. These shear flow pattern loadings are calculated by using the principal shear flow equation. The boundary conditions of finite element models are given in Table 3. Figure 11 shows the shear buckling mode of LiteSteel beam.

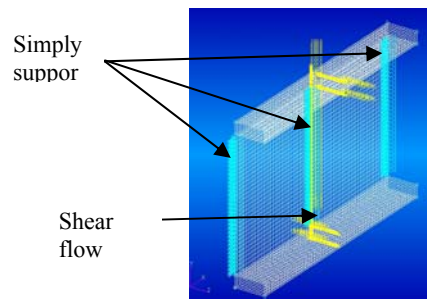


Figure 10: Ideal Finite Element Model  
(200x45x1.6 LSB)

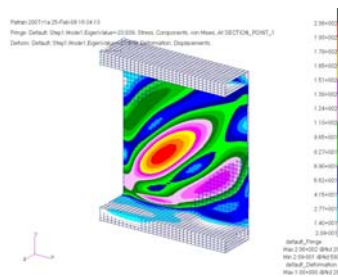


Figure 11: Shear Buckling Mode  
(200x45x1.6 LSB)

Table 3: Boundary Conditions Used in the Finite Element Model

Edges	$u$	$v$	$w$	$\theta_x$	$\theta_y$	$\theta_z$
Left and Right	0	1	1	1	0	0
Middle	1	0	1	1	0	0

Note:  $u$ ,  $v$  and  $w$  are translations and  $\theta_x$ ,  $\theta_y$  and  $\theta_z$  are rotations in the  $x$ ,  $y$  and  $z$  directions, respectively. 0 denotes free and 1 denotes restraint.



(a) 200x45x1.6 LSB  
Finite Element Model



(b) 200x45x1.6 LSB  
Experimental Model

Figure 12: Shear Buckling Deformation of LSB

Figure 12 (a) shows the deformed cross sections of the buckled LiteSteel beam. Deformed cross-section of web panels resemble the buckling mode shape of Eulerian column fixed at both ends. This observation implies that the boundary condition at the flange-web juncture of LSBs is very close to a fixed support condition. This observation was confirmed by the shear tests as shown in Figure 12 (b).

Table 4 compares the shear buckling coefficients ( $k_{LSB}$ ) determined from the eigenvalue analysis and Equation 2 for the aspect ratio of 1. Shear buckling coefficients of plate with simple-simple and simple-fixed boundaries,  $k_{ss}$  and  $k_{sf}$ , were determined by using Equations 5 and 6, respectively. Table 4 indicates that  $k_{LSB}$  is very close to  $k_{sf}$ . Therefore the realistic support condition of LSB at the web-flange juncture is closer to a fixed condition.

$$k_{ss} = 5.34 + \frac{4}{\left(\frac{a}{d_1}\right)^2} \quad \text{for} \quad \frac{a}{d_1} \geq 1 \quad (5)$$

$$k_{sf} = 8.98 + \frac{5.61}{\left(\frac{a}{d_1}\right)^2} - \frac{1.99}{\left(\frac{a}{d_1}\right)^3} \quad \text{for} \quad \frac{a}{d_1} \geq 1 \quad (6)$$

where  $a$  = Shear span of web panel and other symbols have been defined in before.

Table 4: Comparison of Shear Buckling Coefficients of LiteSteel Beams  
(Aspect Ratio =1)

LSB Section	$k_{ss}$	$k_{sf}$	$k_{LSB}$
125x45x1.6	9.34	12.6	12.58
125x45x2.0	9.34	12.6	12.59
150x45x1.6	9.34	12.6	12.57
150x45x2.0	9.34	12.6	12.58
200x45x1.6	9.34	12.6	12.19
200x60x2.0	9.34	12.6	12.57
200x60x2.5	9.34	12.6	12.58
250x60x2.0	9.34	12.6	12.45
250x75x2.5	9.34	12.6	12.58
250x75x3.0	9.34	12.6	12.59
300x60x2.0	9.34	12.6	12.41
300x75x2.5	9.34	12.6	12.43
300x75x3.0	9.34	12.6	12.45

### 4.3 Shear Buckling Coefficient

Based on the results from the finite element elastic buckling analyses the following simple equation (Equation 7) was found to determine the shear buckling coefficients of LiteSteel beams. Here the minimum shear buckling coefficient of LSB (12.19 from Table 4) was taken to propose the formula for aspect ratio  $\frac{a}{d_1} \geq 1$ . Since longer span LiteSteel beams are being used in practical

applications, the aspect ratio greater than or equal to one was considered. The values of  $k_{ss}$  and  $k_{sf}$  for a given aspect ratio were determined from Equations 5 and 6, respectively.

$$k_{LSB} = k_{ss} + 0.87(k_{sf} - k_{ss}) \quad \text{for} \quad \frac{a}{d_1} \geq 1 \quad (7)$$

This equation is similar to that proposed by Lee et al. (1995) for the shear buckling coefficient of plate girders. Proposed shear buckling coefficient equation for LiteSteel beam (Equation 7) shows that the boundary condition at flange-web juncture of LSBs is equivalent to 87% fixed condition. It is noted that the boundary condition at flange-web juncture of LSBs is almost the same as that for plate girders as Lee et al. (1995) obtained 82% fixity.

#### 4.4 New Proposed Formula for the Shear Strength of LiteSteel Beams

New design shear strength formulae were proposed for LSBs based on the design equations given in AS/NZS 4600. The increased shear buckling coefficient for LSB as given by Equation 7 is included here to allow for the additional fixity in the web-flange juncture. However, post-buckling strength was not included. Equations 8 to 10 present the relevant design equations.

$$\tau = 0.64 f_y \quad \text{for} \quad \frac{d_1}{t_w} \leq \sqrt{\frac{Ek_{LSB}}{f_y}} \quad (\text{Shear yielding}) \quad (8)$$

$$\tau = \frac{0.64 \sqrt{(Ek_{LSB} f_y)}}{\left[ \frac{d_1}{t_w} \right]} \quad \text{for} \quad \sqrt{\frac{Ek_{LSB}}{f_y}} < \frac{d_1}{t_w} < 1.415 \sqrt{\frac{Ek_{LSB}}{f_y}} \quad (\text{Inelastic shear buckling}) \quad (9)$$

$$\tau = \frac{0.905 Ek_{LSB}}{\left( \frac{d_1}{t_w} \right)^2} \quad \text{for} \quad \frac{d_1}{t_w} \geq 1.415 \sqrt{\frac{Ek_{LSB}}{f_y}} \quad (\text{Elastic shear buckling}) \quad (10)$$

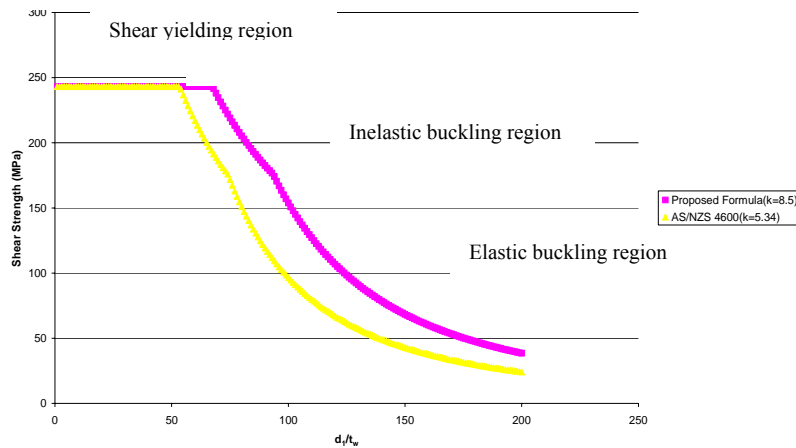


Figure 13: Shear Strength of LSB for Infinity Aspect Ratio versus Web Height to Thickness Ratio.

Longer span LiteSteel beams without transverse stiffeners are commonly used in practical applications. In order to simulate this practical application, an aspect

ratio of infinity was considered. Figure 13 shows the new design curves based on the proposed equations (8 to 10) for the aspect ratio of infinity in comparison to the original AS/NZS 4600 design equations. It shows that the shear capacities predicted by the current design rules in AS/NZS 4600 are conservative because AS/NZS 4600 (SA, 2005) assumes that the web panel is simply supported at the juncture between the flange and web elements (uses a  $k_v$  of 5.34). However in this study it was found that the realistic support condition at the web-flange juncture of LSB is closer to a fixed support condition that gives a  $k_v$  of 8.5. Therefore the assumption considered by Clause 3.3.4 of AS/NZS 4600 may result in an overly conservative shear design for LSBs.

### 5.0 Comparison of Proposed Design Formulae and Experimental Capacities

Proposed shear design formulae are valid when the WSPs are used to the full height of the web element at the supports (no lateral movements of top and bottom flanges). In Tests 1, 7, 9, 10 and 11, the WSP height was more than 90% of LSB web element height (see Table 2). Therefore these experimental results can be compared with the proposed design formulae. New shear strength formulae predictions are compared with experimental strengths in Table 5. Figure 14 shows the new design curves based on the proposed equations (8 to 10) for the aspect ratio of 1.5, and compares them with the experimental capacities and AS/NZS 4600 design equations. It shows that the shear capacities predicted by the current design rules in AS/NZS 4600 are very conservative while the proposed design formulae are also conservative as the potential post-buckling strength has not been included.

Table 5: Comparison of Ultimate Shear Strengths from Experiments and Proposed and Current Design Formulae

LSB Section	Aspect Ratio	Ultimate Shear Strength (MPa)			Failure Mode
		Experimental Results	Proposed Formula	AS/NZS 4600	
125x45x2.0	1.55	56.94	49.64	49.64	Shear yielding
200x45x1.6	1.50	54.19	46.00	31.47	Elastic Shear Buckling
200x60x2.0	1.50	73.98	72.50	59.97	Inelastic Shear Buckling
250x60x2.0	1.50	>75	72.50	59.97	Inelastic Shear Buckling
300x60x2.0	1.50	>75	57.86	39.6	Elastic Shear Buckling

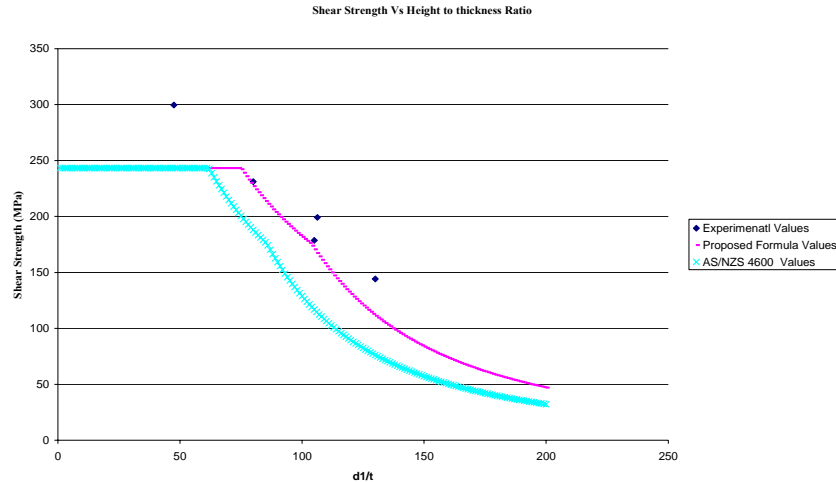


Figure 14: Shear Strength of LSB versus Web Height to Thickness Ratio ( $d_1/t_w$ ). Aspect Ratio = 1.5

Plates with a large width to thickness ratio when subjected to direct compression or shear undergo elastic buckling at a critical stress value. Analytical studies show that thin plates do not collapse when buckling stress is reached, but has considerable post-buckling strength. This has been experimentally verified for plates under axial compression and appropriate strength formulae have also been developed and included in various codes. However, this is not the case for shear loading. Presumably because of lack of experimental evidence on shear capacity of plates without stiffeners, design codes do not include the post-buckling strength in shear, and the design shear stress in webs is therefore limited by the elastic buckling capacity (Suter and Humar, 1986). This research has shown that significant reserve strength beyond elastic buckling is present and that post-buckling shear strength in LSB can be included in their design (Fig.14). Further research is currently under way using both experimental and numerical studies.

## 6. Conclusion

This paper has presented the details of an investigation into the shear behaviour of an innovative cold-formed hollow flange channel section known as LiteSteel beams. Experimental studies were performed to investigate the shear behaviour of LSBs while advanced finite element analyses were used to investigate their elastic shear buckling behaviour.



It was found that AS/NZS 4600 design equations can be used conservatively for LSBs undergoing shear yielding. The current shear capacity design rules for LSBs are based on Clause 3.3.4 of AS/NZS 4600 where the web panel is considered simply supported at the juncture between flange and web elements. However, this study has shown that the realistic support condition at the web-flange juncture of LSB is closer to a fixed support condition and therefore the assumption considered by Clause 3.3.4 of AS/NZS 4600 may result in an overly conservative shear design for LSBs. It was found that significant reserve strength beyond elastic buckling is present and that post-buckling shear strength can be included in design. Appropriate improvements have been proposed for the shear strength of LSBs based on AS/NZS 4600 design equations.

## 7. Acknowledgements

The authors would like to thank Australian Research Council and Australian Tube Mills for their financial support and the Queensland University of Technology for providing the necessary research facilities and technical support.

## References

- Basler, K. (1963). Strength of plate girders in shear. *Trans. ASCE* 128, 683–719.
- Chern, C. and Ostapenko, A. (1969). Ultimate strength of plate girders under shear. Fritz Eng. Lab. Rept. No.328.7. Bethlehem (Pa), Lehigh University, USA.
- Hancock, G.J. (2005). *Design of Cold-formed Steel Structures*. 3<sup>rd</sup> Edition, Australian Institute of Steel Construction, Sydney.
- Lee, S.C., Davidson, J.S. and Yoo, C. (1995). Shear buckling coefficients of plate girder web panels. *Journal of Computer and Structures*, 59 (5), 789-795.
- Mahaarachchi, D and Mahendran, M. (2005). Moment capacity and design of LiteSteel beam sections, Research report, QUT, Brisbane, Australia.
- Porter, D.M., Rocky K.C. and Evans H.R. (1975). The collapse behaviour of plate girders loaded in shear. *Journal of Structural Engineering*, 53(2), 313–325.
- Standards Australia/Standards New Zealand (SA) (2005). *AS/NZS4600 Cold-Formed Steel Structures*, Sydney, Australia.
- Suter, G.T. and Humar, J.L. (1986), Post-Buckling Shear Strength of a Cold-formed Steel Joist, *Proceeding of the 5<sup>th</sup> International Special Conference on Cold-formed Steel Structures*, St. Louis, Missouri, U.S.A, pp. 225-237.

## **Inelastic Performance and Design of CFS Walls Braced with Straps having Reduced Width Fuses**

K. Velchev<sup>1</sup>, G. Comeau<sup>1</sup>, N. Balh<sup>1</sup> and C.A. Rogers<sup>2</sup>

### **Abstract**

Provisions that address the seismic design of cold-formed steel frame strap braced walls are not provided in the 2005 National Building Code of Canada (NBCC) or in the Canadian Standards Association (CSA) S136 Standard for the design of cold-formed steel structures. Previous research aimed at developing appropriate seismic design provisions for these walls revealed that premature fracture of screw connected flat strap braces can lead to inadequate ductility. A subsequent research project was undertaken to evaluate the inelastic performance of screw connected single-storey braced wall configurations constructed with flat straps having a reduced width fuse. The intent of using a fuse in the brace was to reduce the extent of inelastic demand at the brace connections while confining plastic deformations to a well defined section of the brace. Test walls were specifically designed and detailed following a capacity approach. The strap braces were expected to undergo gross cross-section yielding with strain hardening along the fuse, while the other elements

---

<sup>1</sup> Graduate Student, Department of Civil Engineering & Applied Mechanics, McGill University, Montreal QC, Canada.

<sup>2</sup> Associate Professor, Department of Civil Engineering & Applied Mechanics, McGill University, Montreal QC, Canada.

in the seismic force resisting system were selected to be able to carry the probable brace capacity. A summary of the test program is provided in the paper, including failure modes and ductility measures, as well as recommendations on how proper seismic detailing may be achieved. The scope of the research also included the determination of preliminary seismic force modification factors for use with the NBCC based on the measured ductility and overstrength of the test walls.

### **Introduction**

The installation of steel strap diagonal cross bracing in a structure (Fig. 1) is an efficient and economical means to resist wind and seismic forces because the diagonals work in axial tension and therefore require only a minimum amount of material to provide adequate lateral stiffness and strength. Nevertheless, the overall lateral strength, stiffness and ductility of this bracing system depends on all the other elements in the seismic force resisting system (SFRS); i.e. strap connections, gusset plates, chord studs and tracks, as well as the anchorage including holddown and anchor rod. In order to limit inelastic deformations under seismic loading to brace yielding the strap braced walls need to be designed and detailed following a capacity approach (Al-Kharat & Rogers, 2007). In this approach an element of the SFRS is chosen to act as a fuse, while the remaining elements in the lateral load carrying path are designed and detailed for the probable capacity of the fuse element (AISI-S213, 2007). The straps are often assumed to act as a fuse element and thus should be able to reach and maintain their yield strength during the repeated displacement cycles of an earthquake. The use of screws to connect the brace ends may result in fracture of the net cross section and lead to sudden failure with a significant reduction of the ductility of the system if proper detailing and material selection are not followed (Al-Kharat & Rogers, 2008). In situations where contractors may not be able to satisfy the specific detailing and material requirements to ensure ductile braced wall performance a possible solution is to use straps having a reduced width fuse. The fuse size can be selected to reduce the inelastic demand at the brace connections and control the probable force level throughout the SFRS.



Figure 1: Example of a CFS structure with constant width strap braces

somewhat modified from that described in AISI-S213 (2007). The scope of study consisted of the monotonic and reversed cyclic testing of walls, evaluation of the performance and the determination of seismic force modification factors based on the measured ductility and overstrength.

### Test Program

Tests of ten strap braced stud wall specimens were carried out at McGill University using the loading frame illustrated in Figure 2. These ten 2440 x 2440 mm walls were divided into three configurations that can generally be referred to as light, medium and heavy CFS construction; that is, the expected factored lateral in-plane resistance in a wind and seismic loading situation was assumed to be 20, 40 and 75 kN, respectively. The dimensions of the fuse for each brace were first selected given these three lateral loads and the assumption that tension straps would be placed on both sides of each wall. The other elements in the seismic force resisting system were then designed following capacity principles; all of the components in the SFRS were expected to be able to carry the force associated with the probable ultimate capacity of the tension braces without exhibiting extensive damage.

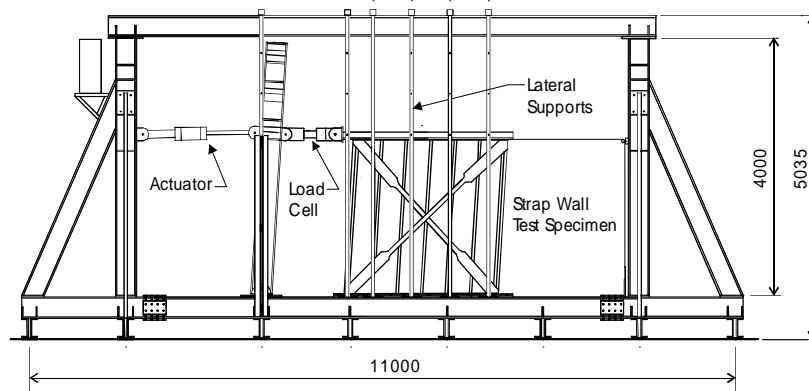


Figure 2: Schematic drawing of displaced 2440 × 2440 mm strap braced wall specimen in test frame

The components of each wall are described in Table 1. All structural members were of ASTM A653 steel (2005). In order to increase the axial capacity of the chord studs such that the vertical component of the brace force could be carried they were composed of two C-sections connected back-to-back using two No. 10 × 3/4" wafer head framing screws spaced at 305 mm o/c. The interior studs were placed at a spacing of 406 mm.

Following the details used by Al-Kharat and Rogers (2008) all walls were constructed with an extended track. Connections between the studs and tracks were made with No. 8 × 1/2" wafer head framing screws, whereas the strap braces were connected to the frame members or gusset using No. 10-3/4" wafer head self drilling screws. The gusset plates, when used, were in turn attached to the framing members using No. 10-3/4" wafer head self drilling screws. Simpson Strong-Tie S/HD10S holddown anchors were installed in all four corners of the light walls, and S/HD15S holddowns were similarly installed in the medium and heavy walls.

Table 1: Matrix of strap braced wall test specimens

Specimen Properties <sup>a</sup>	Test Specimens					
	Light		Medium		Heavy	
Test Protocol	Monotonic	CUREE Reversed Cyclic	Monotonic	CUREE Reversed Cyclic	Monotonic	CUREE Reversed Cyclic
Reduced Braces, Short Fuse	25A-M	26A-C	27A-M	28A-C	29A-M	30A-C
Reduced Braces, Long Fuse	31A-M	32A-C	-	-	33A-M	34A-C
<b>Strap Bracing (X-brace on both sides of wall)</b>						
Thickness, in (mm)	0.043 (1.09)		0.054 (1.37)		0.068 (1.73)	
Fuse Width, in (mm)	2.5 (63.5)		2.75 (69.9)		4 (101.6)	
End Width, in (mm)	3.75 (95.2)		4.25 (108)		6 (152.4)	
Grade, ksi (MPa)	33 (230)		50 (340)		50 (340)	
<b>Chord Studs (Double studs screwed together back-to-back)</b>						
Thickness, in (mm)	0.043 (1.09)		0.054 (1.37)		0.068 (1.73)	
Dimensions, in (mm)	3-5/8x1-5/8-1/2 (92.1x41x12.7)		6x1-5/8x1/2 (152x41x12.7)		6x1-5/8x1/2 (152x41x12.7)	
Grade, ksi (MPa)	33 (230)		50 (340)		50 (340)	
<b>Interior Studs</b>						
Thickness, in (mm)	0.043 (1.09)		0.043 (1.09)		0.043 (1.09)	
Dimensions, in (mm)	3-5/8x1-5/8x1/2 (92.1x41x12.7)		6x1-5/8x1/2 (152x41x12.7)		6x1-5/8x1/2 (152x41x12.7)	
Grade, ksi (MPa)	33 (230)		33 (230)		33 (230)	
<b>Tracks</b>						
Thickness, in (mm)	0.043 (1.09)		0.054 (1.37)		0.068 (1.73)	
Dimensions, in (mm)	3-5/8x1-1/4 (92.1x31.8)		6x1-1/4 (152x31.8)		6x1-1/4 (152x31.8)	
Grade, ksi (MPa)	33 (230)		50 (340)		50 (340)	
<b>Gusset Plates</b>						
Thickness, in (mm)	NA		0.054 (1.37)		0.068 (1.73)	
Dimensions, in (mm)	NA		9x7 (229x179)		10x8.5 (254x216)	
Grade, ksi (MPa)	NA		50 (340)		50 (340)	
<b>Nominal compression, tension and bearing capacity of tracks using CSA S136</b>						
Compression <sup>b</sup> (kN)	23.8		48.1		73.9	
Tension <sup>c</sup> (kN)	38.5		100.5		126.9	
Tension <sup>d</sup> (kN)	44.5		119.5		150.8	
Bearing <sup>e</sup> (kN)	14.5		30.6		116.2	
Bearing <sup>f</sup> (kN)	14.7		33.5		50.0	
<b>Nominal axial compression capacity of chord studs using CSA S136</b>						
Compression <sup>g</sup> (kN)	66.9		117.6		159.5	
Compression <sup>h</sup> (kN)	58.5		102.5		136.5	
<b>Probable forces in SFRS</b>						
$A_p R_n F_u$ Single Brace (kN)	25.7		47.4		87.0	
Total Horizontal Force <sup>i</sup> (kN)	36.3		67.0		123.0	
Total Vertical Force <sup>j</sup> (kN)	36.3		67.0		123.0	

<sup>a</sup>Nominal dimensions and material properties <sup>b</sup>Web holes not considered <sup>c</sup>Gross section yielding, web holes not considered <sup>d</sup>Net section fracture, 22.2 mm hole for shear anchor considered <sup>e</sup>Per shear anchor <sup>f</sup>Per anchor rod <sup>g</sup>Web connections at 305 mm o/c & web holes not considered <sup>h</sup>Web connections at 305 mm o/c & 36 mm web holes considered <sup>i</sup>Total force based on probable nominal capacity of two tension braces

### Wall Design

Once the fuse width and thickness had been selected (Table 1) based on the factored load level the design of other components in the SFRS was carried out following capacity principles. The approach was modified from that currently found for limited ductility walls in AISI-S213 (2007) to account for the possibility of strain hardening in the braces. The probable yield capacity of a tension brace,  $T_n$ , is defined in AISI-S213 as shown in eq. 1. However, because the fuse length was significantly shorter than the braces, it was necessary to account for strain hardening given the expected lateral drift of the wall. For this reason the probable ultimate capacity of the braces,  $T_u$ , (eq. 2) (Table 1) was used to conservatively calculate the design forces in the other SFRS components, including; the brace connections, chord studs, track, gusset plates, anchor rods, holddowns and shear anchors.

$$T_n = A_g R_y F_y \quad (1)$$

$$T_u = A_g R_t F_u \quad (2)$$

where  $A_g$  is the gross cross-sectional area of the fuse, and  $F_y$  and  $F_u$  are the minimum specified yield and ultimate strengths. The variables  $R_y$  and  $R_t$  are used with the minimum specified material strengths ( $R_y F_y$  and  $R_t F_u$ ) to obtain the probable material strength. AISI-S213 lists values for  $R_t$  of 1.2 & 1.1 and for  $R_y$  of 1.5 & 1.1 for the 230 & 340 MPa steels, respectively.

It was also necessary to define the length,  $l$ , of the fuse in each brace, which was done using eq. 3.

$$l \geq \Delta \cos \alpha / \varepsilon \quad (3)$$

where  $\Delta$  is the maximum expected lateral drift of the wall,  $\varepsilon$  is the minimum expected strain capacity of the material and  $\alpha$  is the angle of the brace with respect to horizontal. In a real design situation the maximum drift could be taken as the inelastic storey drift limit as defined in the relevant standard. However, this would likely result in a relatively short fuse and extensive strain hardening in the brace. Two fuse lengths were used for the test walls; the first of which was determined assuming that the maximum displacement was  $\Delta = 120$  mm, which corresponds to a storey drift of 5%. The minimum elongation in a 50 mm gauge length as defined in ASTM A653 (2005) for 230 MPa SS steels

could be used for the braces of the light walls (i.e.  $\varepsilon = 20\%$ ), and for 340 MPA SS Class 1 could be used for the medium and heavy wall configurations (i.e.  $\varepsilon = 12\%$ ). In order to obtain a constant fuse length for all walls a lower bound value of  $\varepsilon = 12\%$  was utilized, which resulted in a fuse length of 707 mm. This value was rounded to 30" (762 mm). Note, the 2440 x 2440 mm walls had a brace angle of  $45^\circ$ . Also, walls with a 60" (1524 mm) fuse were designed and tested to investigate the influence of fuse length. Schematic drawings of all straps, which were fabricated using a Trumpf 2D flatbed laser cutting machine, are provided in Fig. 3. Note, for each wall configuration two monotonic tests were carried out, one of which had screws attaching the strap to the interior studs. Similarly the interior straps of the cyclic tests were connected to the interior studs to identify the impact of additional screw holes in the brace.

The chord studs were designed assuming a concentrically applied compression (vertical) force (Table 1). The back-to-back C-sections were considered to have unbraced lengths of 2440 mm in the strong axis and 1220 mm in the weak axis due to the installation of bridging at mid-height of the walls. The web knock out holes as well as the fastener screw spacing were considered in the design. Chord stud tests showed that an effective length factor of  $k = 0.9$  is reasonable. Nominal capacities were used ( $\phi = 1.0$ ) because design level earthquakes are rare, having a return period of 1 in 2500 years, and due to the use of the probable strap force to obtain the chord stud load. The stud capacities were calculated in accordance with CSA S136 (2004) (Table 1).



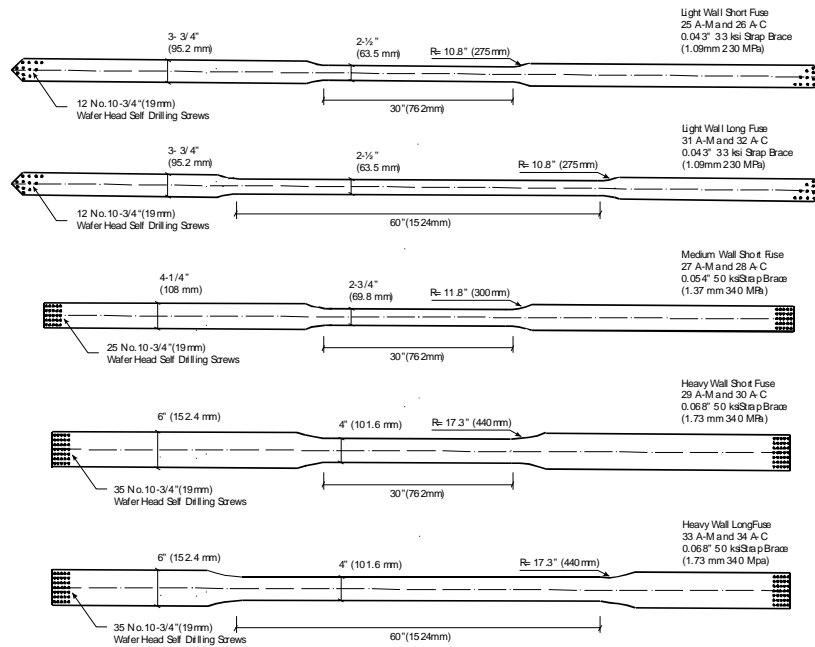


Figure 3: Schematic drawings of straps having reduced width fuse

The horizontal component of the brace force (Table 1) must be transferred through the track element to the supporting structure. The axial capacity of the track in tension, as well as the bearing capacity of the track at the anchor rod and shear anchor locations were determined. Since extended track sections (Figs. 4-5) were used the track was assumed to be placed in tension (Al-Kharat & Rogers, 2008). The horizontal brace force was directed through the extended track by means of the extra shear anchor added outside of the wall footprint. For the heavy walls the bearing capacity of the track alone was not sufficient, therefore a 2.46 mm thick 340 MPa steel plate, 80 x 100 mm, was welded to the track to increase its bearing capacity.

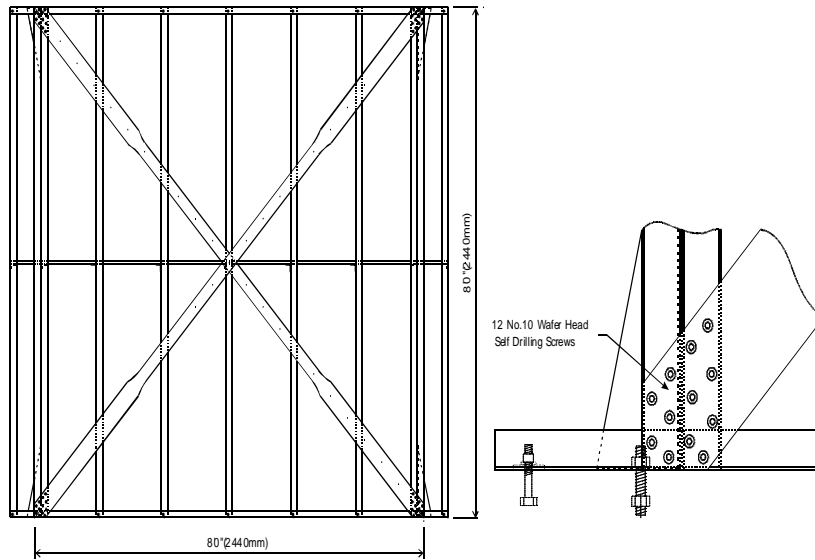


Figure 4: Schematic drawing of light test wall with long fuse

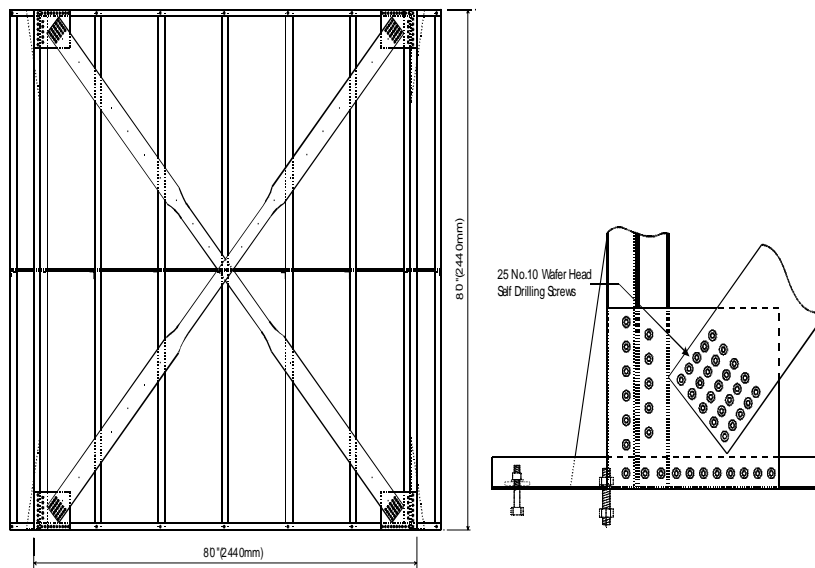


Figure 5: Schematic drawing of medium test wall short fuse

Once the chord stud and track members were selected for each specimen the brace screw connections and gusset plates were designed. The factored shear capacity of the screw connections (CSA S136, 2004) as provided by the manufacturer were compared with the probable capacity of the brace. It was also necessary to ensure that the braces did not fail by fracture at the connection; that is, the net section tension capacity at the connection must exceed the probable ultimate cross-section capacity of the fuse (eq. 4). An increase in the nominal tension resistance ( $A_n F_u$ ) by the factor  $R_t = 1.2$  (230 MPa material) or 1.1 (340 MPa material) was also considered appropriate since the yield capacity of the material had been increased in the calculation of the probable brace force. The light walls had no gusset plates and the straps were attached directly to the chord stud and track (Fig. 4). In contrast, gusset plates were used in the construction of the medium and heavy walls (Fig. 5). The size and thickness of the gusset plates were chosen considering the Whitmore section subjected to axial tension. The screw connections between the gusset plate, chord stud and track were designed to resist the vertical and horizontal components of the probable strap force.

$$A_n R_t F_u \geq A_g R_t F_u \quad (4)$$

where  $A_n$  is the reduced cross-sectional area of the brace at its end connection, and  $A_g$  is the gross cross-sectional area of the brace at the fuse. The width of the connection section of the brace was chosen so that a simple square pattern of screws could be used. Transfer of the uplift forces from the brace through to the supporting test frame was made possible by means of holddown devices from Simpson Strong-Tie and the appropriate size and grade of anchor rods selected from the manufacturer's design catalogue.

### Lateral Testing of Wall Specimens

All wall specimens were tested under lateral in-plane loading (Fig. 2) using displacement controlled monotonic and reversed cyclic protocols. Measurements consisted of strap width, in-plane wall displacements, strains in the steel straps, acceleration of the loading beam assembly, and the shear load at the wall top. A steady rate of displacement (2.5 mm/min) starting from the zero load position was applied during the monotonic load procedure. Loading continued until a drop in capacity (below 80% of ultimate) was observed or until the useable travel of the actuator was reached ( $\approx 200$  mm, 8% drift). The Consortium of Universities for Research in Earthquake Engineering (CUREE) ordinary ground motions reversed cyclic load protocol (ASTM E2126, 2005; Krawinkler et al. 2000) was adapted for the cyclic tests. Note, the maximum

displacement cycles for the reversed cyclic tests were approximately  $\pm 115$  mm (4.5% drift) due to limitations of the actuator's stroke. The yield displacement of the wall,  $\Delta_{y,y}$ , (Fig. 6) was incorporated in the calculation of the reference deformation,  $\Delta$ . It was assumed that  $\Delta = 2.667 \Delta_{y,y}$ , where  $\Delta_{y,y}$  was obtained from the nominally identical monotonic wall tests. The complete cyclic loading history for a particular wall configuration was then based upon multiples of the reference deformation. The frequency of the reversed cyclic tests was 0.5 Hz, except toward the end of the protocol where 0.25 Hz was used.

### Measured Performance and Modes of Failure

Material tests were carried out for the straps, chords, tracks and gusset plates; the results of the strap tests are reported herein (Table 2). Coupons for each strap size were tested at different speeds, 0.1 mm/min and 100 mm/min. The intent was to represent approximately the brace strain rates of the monotonic ( $0.000019 \text{ s}^{-1}$ ) and 0.5 Hz reversed cyclic ( $0.1 \text{ s}^{-1}$ ) tests, respectively. Unfortunately the strain rate for the 100 mm/min coupon tests was limited by the capability of the screw driven materials testing machine; nonetheless, the corresponding strain rate was substantially higher than the slowest coupon tests (approximately 1000 times). The measured yield strength,  $F_y$ , and tensile strength,  $F_u$ , were generally observed to increase for the steels as the strain rate increased; the ratio  $F_u / F_y$  exceeded 1.2 as per AISI-S213.

Table 2: Measured material properties of strap braces

Test Specimen	Base Metal Thickness (mm)	$F_y$ (MPa)	$F_u$ (MPa)	$F_u/F_y$	% Elong.	$F_y/F_{y,m}$	Test Speed (mm/min)	Strain Rate ( $\times 10^3 \text{ s}^{-1}$ )
25A-M, 26A-C	1.11	296	366	1.24	32.5	1.29	0.1	0.021
31A-M, 32A-C	1.11	314	377	1.20	31.7	1.36	100	20.80
27A-M, 28A-C	1.41	387	560	1.45	27.2	1.14	0.1	0.021
	1.42	406	584	1.44	28.0	1.19	100	20.80
29A-M, 30A-C	1.79	353	505	1.43	32.4	1.04	0.1	0.021
33A-M, 34A-C	1.79	373	521	1.40	31.6	1.10	100	20.80

Note:  $F_y$  = measured yield strength,  $F_u$  = measured ultimate tensile strength,  $F_{y,m}$  = minimum specified yield strength

The desirable inelastic behaviour of a cold-formed steel braced wall system is that of gross-cross section yielding of the reduced section of the straps. Ideally, the braces would be able to maintain their yield capacity, and possibly strain harden, over extended lateral displacement of the wall without failure of the other elements in the SFRS; this was the case for most of the specimens that were tested. Figure 7 provides a photograph showing how the inelastic demand was limited to the fuse section of the brace. A second photograph illustrates the different response of two monotonic tests (on the same wall) in which the inner brace was constructed with additional screws. The inner brace fractured at approximately half the storey drift measured for the wall in which the straps

were not screw connected to the interior studs (Fig. 8). The monotonic specimens without additional screws reached a  $\Delta_{max}$  value exceeding 8% drift. This level of displacement exceeds that which would typically be expected during a design level earthquake. Figures 9 and 10 provide the wall resistance vs. deformation response of representative reversed cyclic tests. None of these specimens exhibited brace fracture even when additional screws were installed; however, drifts of up to approximately 4.5% were applied whereas the monotonic tests were pushed to above 8% drift. Given these observations it is recommended that the reduced fuse section of the brace be treated as a protected zone in which additional screws and holes are not installed; however, the impact of holes on brace ductility diminished as the fuse length was increased. Note, the slight reduction of the wall resistance of test specimen 32A-C (Fig.10) was caused by a block shear failure of the connection between the braces and the flanges of the bottom track, which was not expected, nor observed during the monotonic tests (Velchev, 2008).

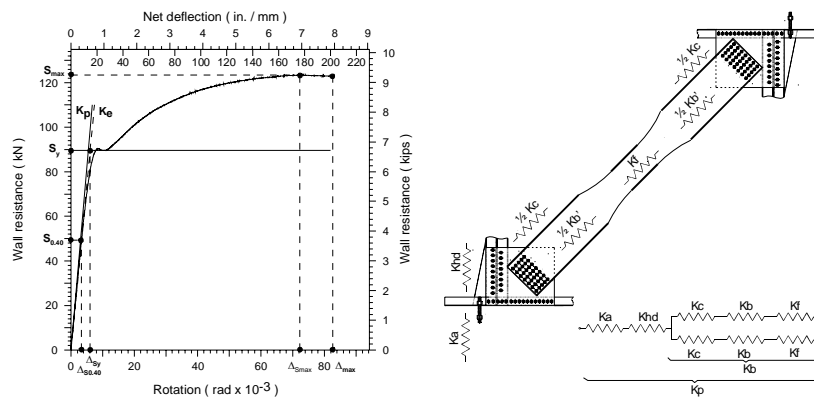


Figure 6: Definition of measured wall parameters and predicted stiffness

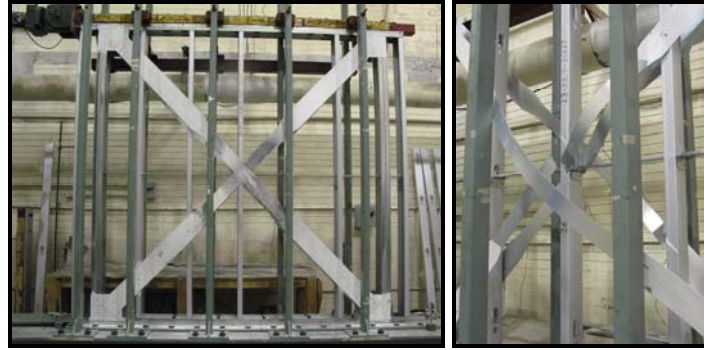


Figure 7: Test specimen photographs showing elongated fuse section

The measured yield strength,  $S_y$ , of the monotonic tests was obtained using the force level reached soon after yielding commenced (Fig. 6). The maximum lateral force,  $S_{max}$ , was higher than  $S_y$  because of strain hardening (Table 3). Due to difficulty in identifying the yield level of the cyclic tests  $S_y$  was set equal to  $S_{max}$ , and thus includes any strain hardening effects (Table 4). The measured elastic shear stiffness,  $K_e$ , was defined as the secant stiffness from the zero load level to the 40% of maximum load level,  $S_{0.40}$ , as recommended in ASTM E2126 (Tables 3-4). The predicted nominal lateral yield strength,  $S_{yn}$ , of the wall was based on the tension yield strength of the braces determined using the nominal fuse area (width  $\times$  thickness) as well as the minimum specified yield strength.  $S_{yp}$  is the predicted yield strength of the wall using the measured brace thickness and width of the fuse, as well as the material properties listed in Table 2. The predicted stiffness,  $K_p$ , incorporated the stiffness of the brace segments,

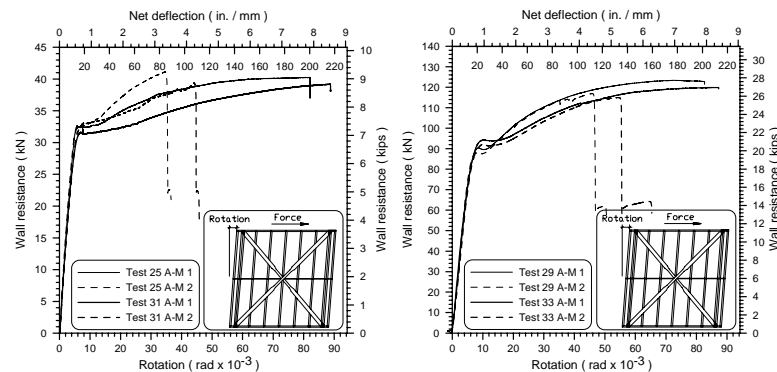


Figure 8: Monotonic resistance light & heavy strap braced walls

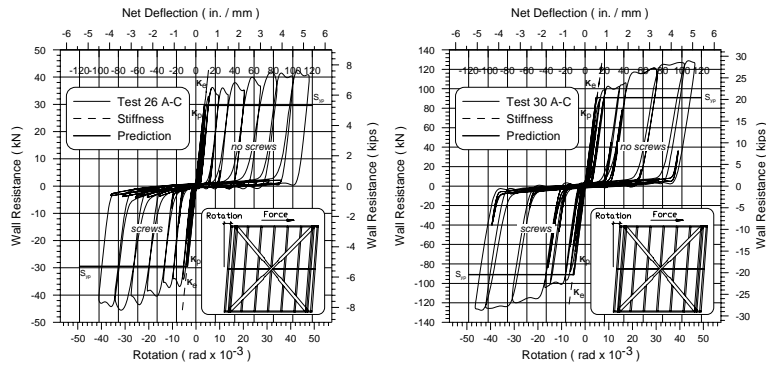


Figure 9: Cyclic resistance light & heavy short fuse strap braced walls

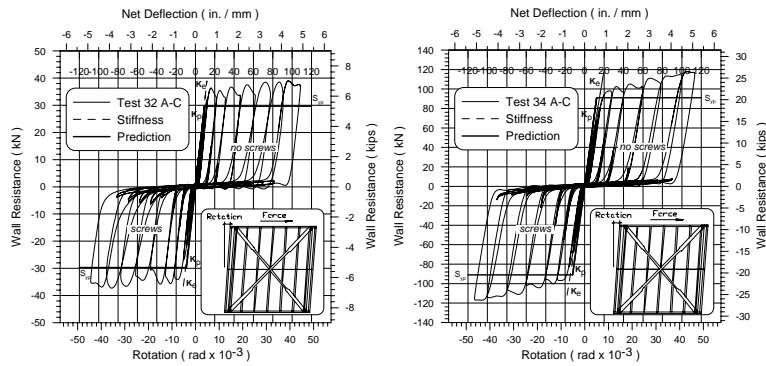


Figure 10: Cyclic resistance light & heavy long fuse strap braced walls

its connections and the holddown and its anchor rod (Fig. 6) using measured properties, whereas  $K_n$  incorporated nominal properties. The predicted lateral wall stiffness was reasonable accurate (Tables 3-4) when all of the spring segments shown in Fig. 6 were included. Calculation of  $K$  using only the axial stiffness of the braces tends to overestimate the in-plane stiffness of the wall. Predictions

Table 3: Summary of monotonic test information

Test Specimen	$K_c$ (kN/mm)	$K_p$ (kN/mm)	$K_n$ (kN/mm)	$K_c/K_p$	$K_c/K_n$	$\Delta_{max}$ (mm)	max drift (%)	Energy (Joules)
25A-M 1	2.85	3.34	3.31	0.85	0.86	210	8.62	7294
25A-M 2	3.10	3.34	3.31	0.93	0.94	89	3.66	3006
27A-M 1	4.16	5.20	5.12	0.80	0.81	211	8.64	14333
27A-M 2	4.09	5.20	5.12	0.79	0.80	88	3.59	5126
29A-M 1	6.07	7.79	7.66	0.78	0.79	202	8.27	21796
29A-M 2	6.47	7.79	7.66	0.83	0.84	114	4.66	11595
31A-M 1	2.83	3.15	3.12	0.90	0.91	217	8.88	7496
31A-M 2	2.64	3.16	3.12	0.83	0.85	109	4.48	3695
33A-M 1	6.46	7.40	7.26	0.87	0.89	213	8.73	22474
33A-M 2	5.79	7.40	7.26	0.78	0.80	135	5.54	14524

Test Specimen	$S_y$ (kN)	$S_{yp}$ (kN)	$S_{yn}$ (kN)	$S_y/S_{yp}$	$S_y/S_{yn}$	$\mu$ (mm/mm)	$R_d$	$R_o$
25A-M 1	32.4	29.6	22.5	1.09	1.44	18.5	6.00	1.89
25A-M 2	32.4	29.6	22.5	1.10	1.44	8.5	4.01	2.03
27A-M 1	57.0	53.9	46.0	1.06	1.24	15.4	5.46	1.80
27A-M 2	56.6	53.9	46.0	1.05	1.23	6.3	3.41	1.83
29A-M 1	89.6	91.0	84.5	0.98	1.06	13.7	5.13	1.53
29A-M 2	87.4	91.1	84.5	0.96	1.03	8.4	3.98	1.50
31A-M 1	31.4	29.4	22.5	1.07	1.39	19.5	6.17	1.75
31A-M 2	33.0	29.8	22.5	1.11	1.47	8.7	4.06	1.88
33A-M 1	93.8	91.2	84.5	1.03	1.11	14.7	5.32	1.46
33A-M 2	91.4	91.1	84.5	1.00	1.08	8.6	4.02	1.44

Table 4: Summary of reversed cyclic test information

Test Specimen	$K_c$ (kN/mm)	$K_p$ (kN/mm)	$K_n$ (kN/mm)	$K_c/K_p$	$K_c/K_n$	$\Delta_{max}$ (mm)	max drift (%)	Energy (Joules)	
26A-C	-ve	3.26	3.34	3.31	0.98	0.99	117	4.79	11310
	+ve	3.27	3.34	3.31	0.98	0.99	117	4.79	
28A-C	-ve	4.48	5.20	5.12	0.86	0.88	114	4.66	18837
	+ve	4.45	5.21	5.12	0.85	0.87	114	4.66	
30A-C	-ve	7.34	7.79	7.66	0.94	0.96	113	4.64	29722
	+ve	7.33	7.79	7.66	0.94	0.96	113	4.64	
32A-C	-ve	2.93	3.16	3.12	0.93	0.94	108	4.44	9885
	+ve	3.30	3.16	3.12	1.05	1.06	109	4.45	
34A-C	-ve	6.20	7.40	7.26	0.84	0.85	113	4.64	27519
	+ve	5.96	7.40	7.26	0.81	0.82	113	4.64	

Test Specimen	$S_{max}$ (kN)	$S_{yp}$ (kN)	$S_{yn}$ (kN)	$S_{max}/S_{yp}$	$S_{max}/S_{yn}$	$\mu$ (mm/mm)	$R_d$	$R_o$	
26A-C	-ve	45.5	29.5	22.5	1.55	2.02	12.9	4.98	2.24
	+ve	42.5	29.6	22.5	1.43	1.89	12.9	4.98	2.10
28A-C	-ve	77.3	53.9	46.0	1.43	1.68	9.5	4.23	1.87
	+ve	79.6	53.9	46.0	1.48	1.73	9.4	4.21	1.92
30A-C	-ve	127.6	91.0	84.5	1.40	1.51	9.1	4.16	1.68
	+ve	128.9	90.9	84.5	1.42	1.52	9.1	4.15	1.69
32A-C	-ve	37.3	29.7	22.5	1.25	1.66	10.7	4.51	1.84
	+ve	39.0	29.6	22.5	1.31	1.73	12.1	4.81	1.92
34A-C	-ve	117.1	91.1	84.5	1.29	1.39	7.7	3.80	1.54
	+ve	118.0	91.1	84.5	1.30	1.40	7.4	3.72	1.55



for tests run with a monotonic protocol utilized the material properties from coupons tested at 0.1 mm/min, whereas the tests run cyclically at 0.5 Hz were compared with resistances calculated with material properties from coupons tested at 100 mm/min.

Mitchell et al. (2003) describe the basis of the seismic force modification factors listed in the 2005 NBCC (NRCC, 2005). A similar procedure was followed using the data from the strap walls to obtain “test-based” values for  $R_d$  and  $R_o$ . The ductility related factor,  $R_d$ , (eq. 6) was calculated using the ductility,  $\mu$ , values (eq. 5) listed in Tables 3 and 4.

$$\mu = \frac{\Delta_{max}}{\Delta_{sy}} \quad (5)$$

$$R_d = \sqrt{2\mu - 1} \quad (6)$$

All test specimens showed sufficient ductility such that the calculated  $R_d$  values exceed the 2.0 currently found in AISI-S213 for limited ductility strap braced systems. The overstrength related seismic force modification factor,  $R_o$ , can be estimated by considering the product of  $R_{yield} = S_y / S_{yn}$  and the inverse of the resistance factor,  $R_\phi = 1 / \phi = 1 / 0.9 = 1.11$ . Note, the test  $R_{yield}$  also includes any strain hardening,  $R_{sh}$ , exhibited by the braces up to a drift of 4%. Note, the heavy walls 29A-M 1, 29A-M 2, 33A-M 1 and 33A-M 2 provided  $R_o$  values that were less than the other tested walls. This can be attributed to the ratio of  $F_y / F_{yn}$  of the braces which was only 1.04 (Table 2). Typically, this ratio is 1.1, as defined by  $R_y$  for 340 MPa grade steel. The material properties of the heavy braces were near the lower bound of what would normally be obtained from a mill. Furthermore, the  $R_o$  calculation approach neglected other factors that would further increase the overstrength; *i.e.* member oversize and development of a collapse mechanism. Nonetheless, the calculated  $R_o$  values for all tests exceeded 1.3, which is listed in AISI-S213.

### **Conclusions**

A series of screw connected walls braced with straps having reduced width fuses were tested to evaluate their ability to reach and maintain the yield strength (with strain hardening) in the inelastic range of deformation. Capacity principles were implemented in the design of the walls and material properties met the requirements of AISI-S213. The walls were, in general, able to achieve their assumed response. It is recommended, however, to use braces with long fuses to limit the degree of strain hardening and to reduce the possible negative effect of screws being installed along the fuse length. Tests showed that holes should not be placed in the reduced section of the brace when short fuses are used. The seismic force modification factors  $R_d = 2.0$  and  $R_o = 1.3$  currently listed in AISI-S213 for use with the NBCC are appropriate for the walls braced with straps having reduced width fuses.

### **Acknowledgements**

The authors would like to acknowledge the support provided by NSERC, CFI, the Canadian Sheet Steel Building Institute and the American Iron and Steel Institute. Materials for the test specimens were provided by Bailey Metal Products Ltd., Simpson Strong-Tie Co. Inc., ITW Buildex and Grabber Construction Products.

## References

AISI: North American standard for cold-formed steel framing – lateral design; AISI-S213 2007, American Iron and Steel Institute, Washington, DC.

Al-Kharat, M., Rogers, C.A.: Inelastic performance of screw-connected cold-formed steel strap braced walls; *Canadian Journal of Civil Engineering*, 35(1): 11-26, 2008.

Al-Kharat, M., Rogers, C.A.: Inelastic performance of cold-formed steel strap braced walls; *Journal of Constructional Steel Research*, 63(4): 460-474, 2007.

ASTM; Standard specification for steel sheet, zinc-coated (galvanized) or zinc-iron alloy-coated (galvannealed) by the hot-dip process; ASTM Standard A653 2005, American Society for Testing and Materials, West Conshohocken, Pa.

ASTM; Standard test methods for cyclic (reversed) load test for shear resistance of framed walls for buildings; ASTM standard E2126 2005, American Society for Testing and Materials, West Conshohocken, Pa.

CSA: North American specification for the design of cold-formed steel structural members; Standard CSA-S136 2004; Canadian Standards Association, Mississauga, Ont.

Krawinkler, H., Parisi, F., Ibarra, L., Ayoub, A., Medina, R.; Development of a testing protocol for woodframe structures. Report W-02 2000, Consortium of Universities for Research in Earthquake Engineering (CUREE), Richmond, CA.

Mitchell, D., Tremblay, R., Karacabeyli, E., Paultre, P., Saatcioglu, M., Anderson, D.L.; Seismic force modification factors for the proposed 2005 edition of the National Building Code of Canada, *Canadian Journal of Civil Engineering*, 30(2): 308 – 327, 2003.

NRCC: National building code of Canada. National Research Council of Canada, 2005; Ottawa, ON.

Velchev, K; Inelastic performance of screw connected CFS strap braced walls, Master's thesis, Department of Civil Engineering and Applied Mechanics, McGill University, Montreal, Canada, 2008.

## **Pilot Research on Cold-Formed Steel Framed Shear Wall Assemblies with Corrugated Sheet Steel Sheathing**

**Hitesh Vora<sup>1</sup>, Cheng Yu<sup>2</sup>**

### **Abstract**

Flat steel sheet is the common steel sheathing for cold-formed steel (CFS) framed shear walls. The current American Iron and Steel Institute Standard provides nominal shear strengths for 0.018 in. and 0.027 in. sheet steel sheathed shear wall as well as CFS walls with other sheathing materials. The CFS walls with 0.018 in. or 0.027 in. sheet steel sheathing yield relatively lower shear strength compared with the walls with 7/16 in. OSB sheathing or 15/32 in. Structural 1 sheathing (4-ply). In order to develop a high strength CFS shear wall with steel sheathing, a pilot research was conducted at University of North Texas to experimentally investigate the behavior and shear strength of CFS framed wall assemblies with 0.027 in. (20 gauge) corrugated sheet steel sheathing. The parameters considered in the test program included the framing member thickness, the fastener size and spacing, and the boundary stud configurations. Both monotonic and cyclic tests were conducted. The test results indicated that with appropriate framing members and the fastener configurations, the corrugated steel sheet can form rigid sheathing for CFS shear walls. The test results indicated that the 0.027 in. corrugated sheet steel sheathing outperformed 0.027 in. thick flat sheet steel sheathing as well as the 7/16 in. OSB sheathing. It can be alternative sheathing material for CFS walls.

---

<sup>1</sup> Graduate Student, University of North Texas, Denton, TX. (hitesh@unt.edu)

<sup>2</sup> Assistant Professor, University of North Texas, Denton, TX (cyu@unt.edu)

## Background and Motivation

The American Iron and Steel Institute (AISI) S213 (2007) “The North American Standard for Cold-Formed Steel Framing - Lateral Design” provides shear strength values for cold-formed steel framed walls with different sheathing materials including 15/32 in. Structural 1 plywood sheathing, 7/16 in. oriented strand board (OSB), and 0.018 in. and 0.027 in. flat steel sheet. Those published values were based on Serrette (1996, 1997, and 2002). Compared to the wood sheathing, the 0.027 in. and 0.018 in. sheet steel sheathing yielded relatively lower shear strength and the test results (Serrette 1997, 2002) indicated that the buckling of the steel sheet sheathing was the primary mode of failure for sheet steel shear walls.

To improve the performance of cold-formed steel shear wall with steel sheathing, the use of the corrugated sheet steel as the sheathing for CFS walls has been investigated by a few researchers. Fülöp and Dubina (2004) developed a testing program to investigate the structural characteristics of 8 ft. high  $\times$  12 ft. wide full scale CFS shear walls with different sheathing arrangements. The different sheathing arrangements included LTB20/0.5 corrugated sheet steel on one side, LTB20/0.5 corrugated sheet steel on one side and 1/2 in. gypsum boards on the other side of the wall, trap bracing on both sides, and 3/8 in. OSB on one side. The presence of a 4 ft. wide door opening was also included in the test matrix. A total of 7 monotonic tests and 8 cyclic tests were conducted. The protocol for cyclic tests adopted ECCS Recommendation (1985) with a relatively low loading frequency of either 0.00028 Hz (6 min/cycle) or 0.0056 Hz (3 min/cycle). The CFS frames used U154/1.5 tracks (6 in. web depth, 0.060 in. thickness), and C150/1.5 C-section studs (6 in. web depth, 0.060 in. thickness), the studs were placed at 24 in. on center. Double studs (back-to-back) were used at the ends of the walls and around the opening. Fülöp and Dubina (2004) concluded that the CFS walls were rigid and could effectively resist lateral loads. The failure of the seam fastener was the failure mechanism for the corrugated sheet specimens. The test results showed the 3/8 in. OSB specimens had significantly higher shear strength than the corrugated sheet specimens. However the geometries and material properties of the corrugated sheets were not reported in Fülöp and Dubina (2004).

Stojadinovic and Tipping (2007) conducted a series of 44 cyclic shear wall tests on 8 ft 2 in. high  $\times$  4 ft or 2 ft wide CFS shear walls with corrugated sheet steel sheathing on one side or both sides. Two test protocols were used in the test program, the AC154 (2005), “Acceptance Criteria for Cyclic Racing Shear Test for Metal-Sheathed Shear Walls with Steel Framing” and the AC130 (2004). “Acceptance Criteria for Prefabricated Wood Shear Panels.” The specimens

were sheathed with 0.027 in., 0.033 in., or 0.043 in. corrugated Shallow-Vercor type decking with 9/16 in. rib height. Four sizes of Steel Stud Manufacturers Association (SSMA 2001) studs with matching tracks were used for the frames: 362S162-33, 362S162-43, 362S162-54 (50 ksi), and 362S162-68 (50 ksi). No. 10, No. 12, No. 14 self-drilling screws and pins were used in the tests, and different fastener spacing was included in the test matrix. The boundary elements of all the specimens were reinforced by HSS  $6 \times 4 \times 3/8$ " which excluded failures in the boundary elements and also required no hold-down to be installed. The authors reported that in all the tests, the failure mode was the eventual pulling out of the screws due to warping in the corrugated steel sheet. Based on the test results, nominal shear strength for 0.033 in. and 0.043 in. CFS framed shear walls with 0.027 in. and 0.043 in. corrugated sheet steel sheathing were proposed by Stojadinovic and Tipping (2007).

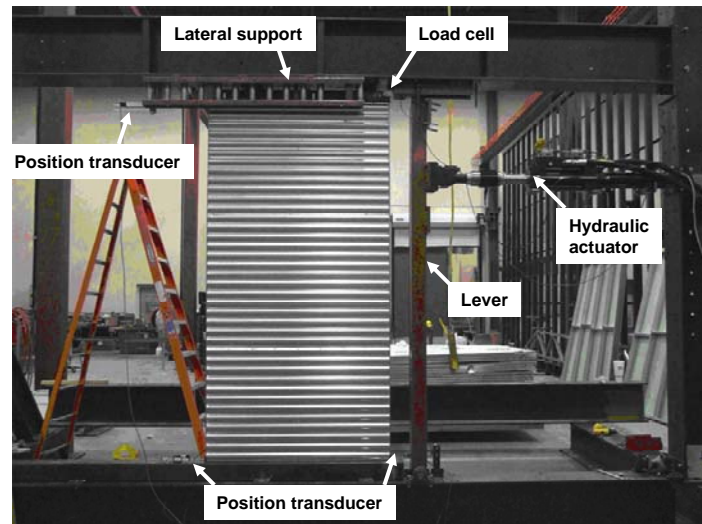
The research by Fülöp and Dubina (2004) and Stojadinovic and Tipping (2007) showed that the corrugated steel sheet steel is a feasible and strong sheathing material for CFS shear walls. Fülöp and Dubina (2004) used a different cyclic test protocol than those generally adopted in US (AC130, AC154), and the properties of the corrugated sheet were not detailed in their paper. Stojadinovic and Tipping (2007) used structural steel members to reinforce the four edges of the CFS wall specimens and no hold-down was installed. Those configurations were not the typical practice in the field. In order to investigate the performance of corrugated sheet steel shear walls by using typical framing configurations and the approved test method by International Code Council, a pilot research were conducted at University of North Texas (UNT) and presented in this paper. The UNT work included 3 monotonic and 4 cyclic tests on 0.043 in. and 0.068 in. CFS framed walls with 0.027 in. corrugated sheet sheathing. The rib height of the corrugated sheet was 9/16 in. The research object was to determine the appropriate framing and fastener configurations to achieve the ultimate shear strength of the 0.027 in. corrugated sheet steel sheathing.

## **Test Program**

### ***Test Setup***

Both the monotonic and the cyclic tests were performed on a 16 ft. span 12 ft. high adaptable testing frame at UNT. Figure 1 shows the front view of the test setup with an 8 ft.  $\times$  4 ft. CFS shear wall. Figure 2 illustrates the schematic of the test setup. All the shear wall specimens were assembled in a horizontal position and then installed vertically in the testing frame. The wall was bolted to the base beam and loaded horizontally on the top. The out-of-plane displacement of the wall was prevented by a series of steel rollers on the front side and four

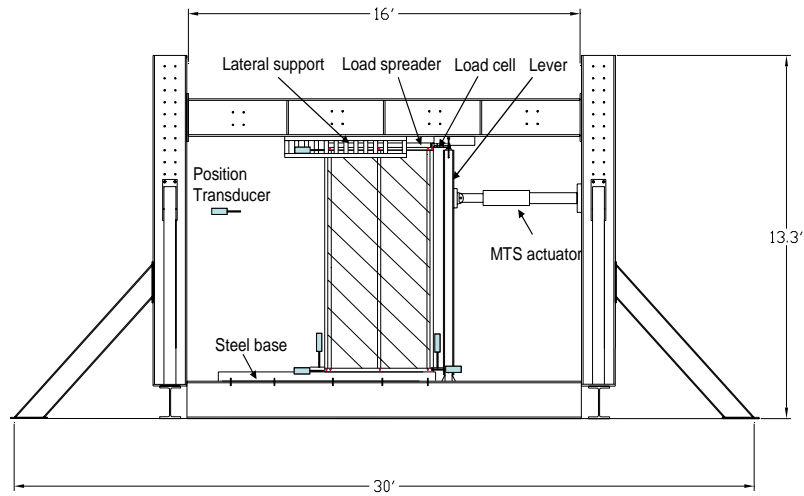
individual rollers on the back side of the wall top. The rollers also worked as a guide for the load spread T-shape as shown in Figure 3. The T-shape was attached to the top track of the wall by No. 12×1-½ in. hex washer head self-drilling screws installed one pair every 3 in. The horizontal force was applied to the T-shape by a hydraulic actuator through a lever made of structural steel tube.



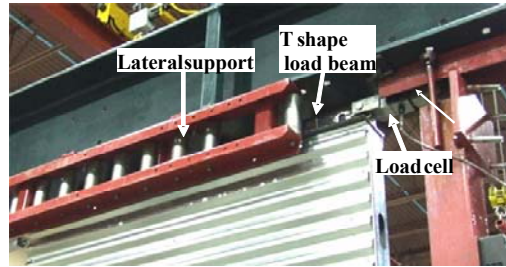
**Figure 1 Front view and back view of the test setup**

The anchorage system for monotonic tests consisted of three ½ in. or 5/8 in. dia. shear bolts with standard cut washers (ASME B18.22.1) (1998) and one Simpson Strong-Tie® S/HD10S hold-down with one 5/8 in. dia. bolt. For the cyclic tests, the anchorage system included two ½ in. or 5/8 in. dia. bolts and two Simpson Strong-Tie® S/HD10S hold-downs.

The testing frame was equipped with one 35 kip hydraulic actuator with ±5 in. stroke. A 20 kip universal compression/tension load cell was used to connect the top of lever to the T-shape for force measurement. Five position transducers were employed to measure the horizontal deflection of the wall top, the vertical deflections of the two end studs, and the horizontal deflections of the bottom of the two end studs, as shown in Figure 2. The applied force and five deflections were measured and recorded instantaneously during the test.



**Figure 2: Testing frame with a 4 ft × 8 ft wall specimen**



**Figure 3: Close up of the top of the wall specimen**

### ***Test Method***

Both the monotonic and the cyclic tests were conducted in a displacement control mode. The procedure of the monotonic tests was in accordance with ASTM E564 (2006) “Standard Practice for Static Load Test for Shear Resistance of Framed Walls for Buildings”. A preload of approximately 10% of estimated ultimate load was applied first to the specimen and held for 5 minutes to seat all connections. After the preload was removed, an incremental loading procedure started until failure; the load increment was approximately 1/3 of the estimated ultimate load.

The CUREE (Krawinkler et al. 2000) protocol, in accordance with AC130 (2004) was chosen for the cyclic tests. The CUREE basic loading history shown in Figure 4 includes 40 cycles with specific displacement amplitudes that are

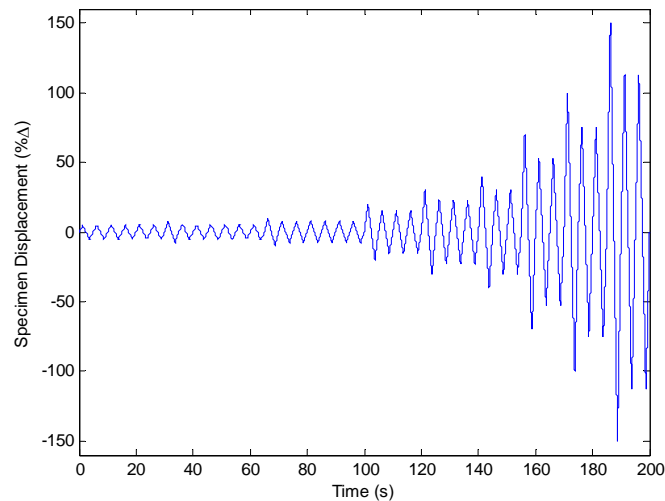


listed in Table 1. The specified displacement amplitude for this test program was chosen to be 2.5% of the wall height (2.4 in. for 8 ft. high wall). A constant cycling frequency of 0.2 Hz in the CUREE loading history was used for all the cyclic tests in this research.

**Table 1: CUREE basic loading history**

Cycle No.	% $\Delta$	Cycle No.	% $\Delta$	Cycle No.	% $\Delta$	Cycle No.	% $\Delta$	Cycle No.	% $\Delta$
1	5.0	9	5.6	17	7.5	25	30	33	53
2	5.0	10	5.6	18	7.5	26	23	34	53
3	5.0	11	5.6	19	7.5	27	23	35	100
4	5.0	12	5.6	20	7.5	28	23	36	75
5	5.0	13	5.6	21	20	29	40	37	75
6	5.0	14	10	22	15	30	30	38	150
7	7.5	15	7.5	23	15	31	30	39	113
8	5.6	16	7.5	24	15	32	70	40	113

Note:  $\Delta$  = 2.5% wall height



**Figure 4: CUREE basic loading history (0.2 Hz)**

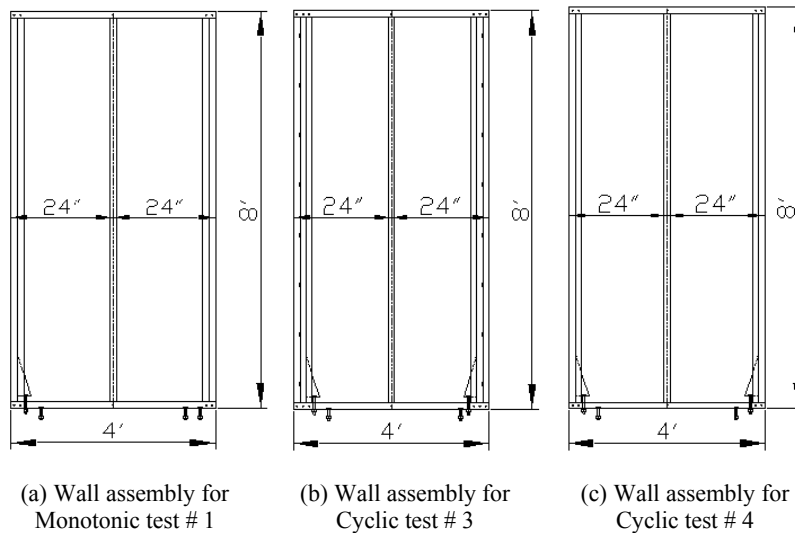
### ***Test Specimens***

This pilot research focused on developing appropriate framing details to achieve the ultimate performance for 0.027 in. corrugated steel sheet sheathing. The specimen configurations were developed accordingly as the test program progressed. Table 2 summarizes the test matrix. The various configurations considered in this test program included the thickness of the framing members (0.043 in. and 0.068 in.), the sheathing and framing fastener size (No. 8 and No. 12) and spacing, and the boundary studs details.

**Table 2: Test matrix for shear wall tests<sup>1</sup>**

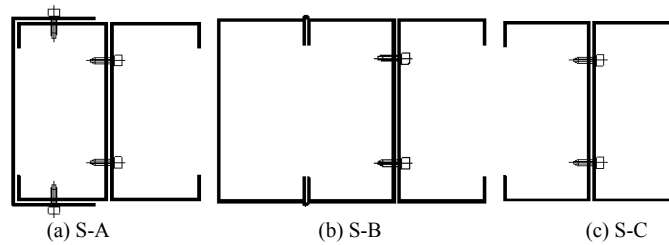
Test Label (protocol)	Nominal Framing thickness	Sheathing and Framing Fastener <sup>2</sup>	Fastener Spacing	Boundary Studs Config. <sup>3</sup>	Hold-down <sup>4</sup>
1 (monotonic)	0.043 in.	#8 × ¾ in.	5"/12 ½"	S-A	Raised
2 (monotonic)	0.043 in.	#8 × ¾ in.	5"/12 ½"	S-B	Raised
3 (cyclic)	0.043 in.	#8 × ¾ in.	5"/12 ½"	S-B	Raised
4 (monotonic)	0.068 in.	#12 × 1-¼ in.	2 ½"/5"	S-C	Raised
5 (cyclic)	0.068 in.	#12 × 1-¼ in.	2 ½"/5"	S-C	Raised, Reinforced
6 (cyclic)	0.068 in.	#12 × 1-¼ in.	2 ½"/5"	S-C	Raised, Reinforced
7 (cyclic)	0.068 in.	#12 × 1-¼ in.	2 ½"/5"	S-C	Flushed, Reinforced

Note: 1- all tests used 0.027 in corrugated sheet with rib height 9/16 in. for sheathing; 2- #8 screws were modified truss head self-drilling screws, #12 screws were hex washer head self-drilling screws; 3- stud configuration refers to Figure 6; 4- Simpson Strong Tie S/HD10S.

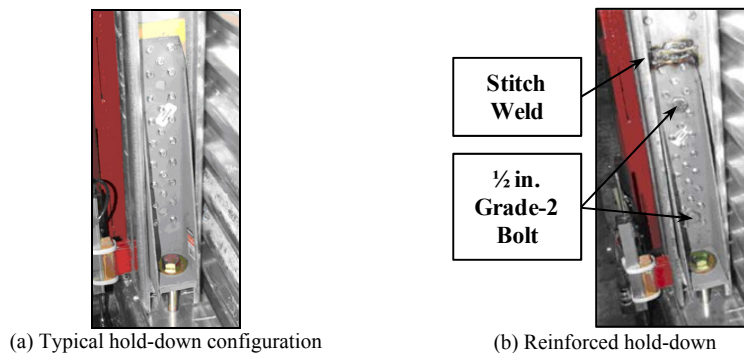
**Figure 5: Dimensions of typical 8 ft. x 4 ft. wall assembly**

All the specimens had a wall aspect ratio of 2:1 with 8 ft height and 4 ft width. The dimensions for typical wall assemblies are illustrated in Figure 5. SSMA (2001) standard tracks and studs were used. One single C-section stud was placed at the center, and two or three C-section studs were used at both ends of

the wall. Three configurations for the boundary studs were studied in this research as shown in Figure 6. The configuration S-A used two studs back-to-back connected by No. 8 screws one pair for every 6 in., the outer stud was reinforced by a matching track member fastened to the stud flanges, face-to-face, by No. 8 screws 6 in. on center. The configuration S-B used three studs, two studs were attached back-to-back, and the third stud attached to the double studs face-to-face by  $\frac{1}{2}$  in. stitch weld every 12 in. on center. The boundary stud configuration S-C used double studs, back-to-back connected by No. 12 screws one pair every 6 in. on center.



**Figure 6: Boundary stud configuration (plan view)**



**Figure 7: Hold-down configurations**

Simpson Strong-Tie® S/HD10S hold-down was used on the specimens to resist the uplift force. For the monotonic test, one hold-down was attached to the uplifted boundary studs from inside by using a total 24 of No.14 $\times$ 1 $\frac{1}{4}$  in. hex washer head self-drilling screws. For the cyclic test, two hold-downs were used, one on each side on the wall. Figure 7a shows the typical hold-down configuration. For some tests, the hold-down was reinforced by two additional  $\frac{1}{2}$  in diameter Grade 2 bolts and the top edge of the hold-down was welded to the stud, see Figure 7b. For all specimens, a 0.068 in. thick steel patch plate was used to cover the hole on the bottom of the boundary studs. The hold-downs for

Tests 1 to 6 were raised 1.5 in. above the flange of bottom track. In test 7, the hold-downs sat on the bottom track.

The details of the components of the tested CFS walls are given as follows:

Studs: 350S162-43 and 350S162-68 SSMA structural stud made of ASTM A1003 Grade 33 steel, placed in 2 ft. off center for walls.

Tracks: 350T150-43 and 350T150-68 SSMA structural track made of ASTM A1003 Grade 33 steel for walls.

Sheathing: The corrugated sheet steel (metal decking) was manufactured by Vulcraft manufacturing company. The deck type was 0.6C, 0.027 in. (22 gauge) corrugated steel sheet with 9/16 in. rib height. The sheathing was installed one side of the wall. For each wall specimen, the sheathing was made of three corrugated steel sheets which were connected by single line of screws. The screw spacing on the joint was same as that for the sheathing screws on the panel edges. Figure 8 illustrates the cross section of the corrugated sheet.

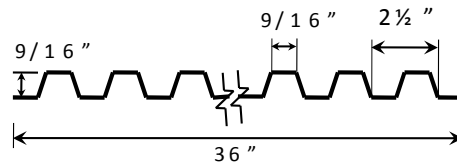


Figure 8: Corrugated steel sheet profile

## Test Results and Discussion

### *Shear Wall Tests*

Table 3 summarizes the test results. Figure 10 illustrates curves of the applied shear load in pounds per foot (plf) vs. the displacement of top of the wall. The observed failure modes were shown in Figure 11. All the specimens utilized 0.027 in. corrugated steel sheet sheathing with 9/16 in. rib height. The test program started with one 0.043 in. framed wall with S-A boundary stud configuration and No. 8  $\times$  3/4 in. sheathing screws. The fastener spacing was 5 in. on center at the panel edges and 12.5 in. on center in the field of the panel. The Test 1 failed by buckling of the boundary studs. To avoid failure in the boundary studs, three-stud configuration (S-B in Figure 6) was used for Tests 2 and 3. The fastener configuration, and the framing members in Tests 2 and 3 were same at those used in Test 1. Test 2 was monotonic and it failed by the warping of the corrugated sheet and the pull-out of the sheathing screws on the interior studs and the boundary studs. The peak load was lower than that of Test 1. In Test 1, the No. 8 sheathing screws were installed on three layers: the sheathing, the stud

and the reinforcing track, therefore the screws provided higher holding power against being pulled out than those in Tests 2 and 3 where the screws only went through two layers: the sheathing and the boundary stud. Test 3 was identical to Test 2 except that the CUREE cyclic protocol used. Due to the pull-out of a large number of screws in Test 3, a sudden drop in the shear strength was observed. The negative peak load was significantly lower than the positive peak load, and it resulted in a lower average peak load of Test 3 compared to Test 2.

**Table 3: Summary of shear wall test results**

Test Label (protocol)	Peak load (plf)		Lateral deflection at peak load (in.)		Avg. Peak Load (plf)	Avg. $\Delta$ (in.)	Failure Mode
	+P	-P	+ $\Delta$	- $\Delta$			
1 (monotonic)	1942	-	2.85	-	1942	2.85	Stud buckled
2 (monotonic)	1625	-	2.60	-	1625	2.60	Sheathing screw pullout
3 (cyclic)	1628	1150	1.75	1.39	1389	1.57	Sheathing screw pullout
4 (monotonic)	2451	-	0.81	-	2451	0.81	Hold-down screws sheared
5 (cyclic)	3717	3656	1.28	1.30	3688	1.29	Lateral support failed
6 (cyclic)	3957	3986	2.73	2.54	3972	2.64	No failure
7 (cyclic)	4113	4315	2.84	3.12	4214	2.98	Hold down failed

Tests 1, 2, and 3 indicated that the 0.027 in. corrugated sheet was rigid, and outperformed the 0.027 in. flat sheet steel, the 7/16 in. OSB, and the 15/32 in. Structural 1 sheathing. Respectively, the nominal shear strength (seismic loads) for the three other different sheathing is 1000 plf, 1235 plf, and 1330 plf for 0.043 in. framed wall with No. 8 screws placed 4 in. at panel edges and 12 in. in the field (Table C2.1-3 in AISI S213). Tests 1, 2, and 3 used No. 8 screws with 5 in./ 12 ½ in. spacing (5 in. at panel edges and 12 ½ in. in the field). Among the three tests, Test 3 gave the lowest shear strength of 1389 plf, which was still greater than the published values of the other three sheathing materials. It was also found that the test results on 0.043 in. walls in this research were comparable to the Stojadinovic and Tipping (2007) in which a 1505 plf nominal shear strength was reported for 0.043 in. walls with 0.027 in. corrugated steel sheathing. One should note that Stojadinovic and Tipping (2007) used No. 12 screws and 6 in./6 in. screw spacing in their tests.

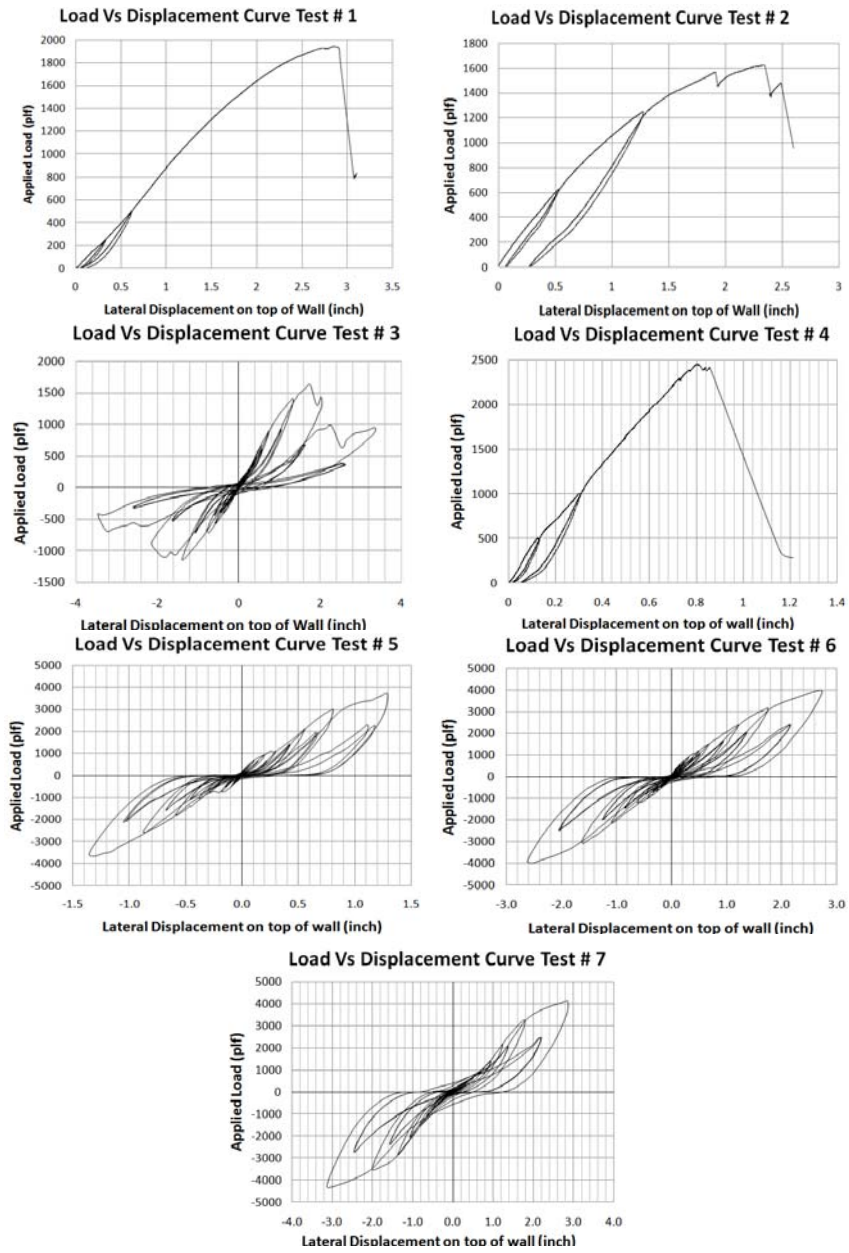


Figure 10: Load vs displacement curves

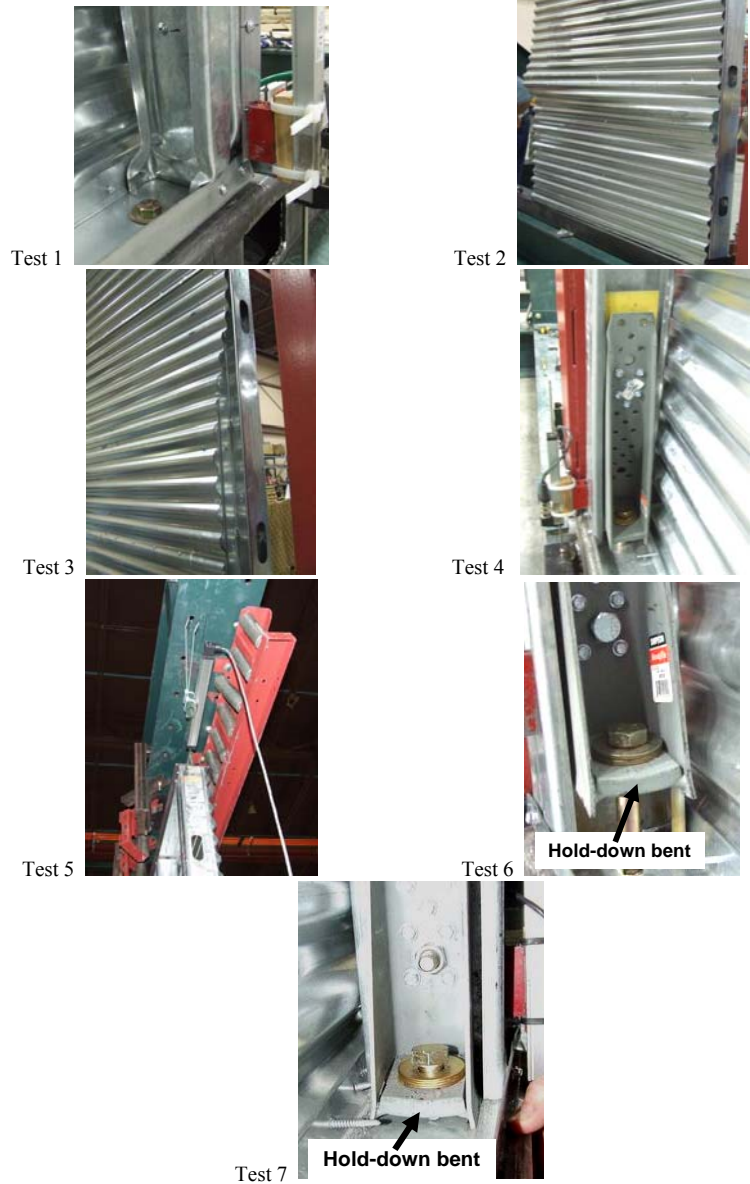


Figure 11 Observed failure modes

In terms of the failure mechanism, the first three tests showed that the warping of the sheathing generated significant force to pull out a large number of No. 8 screws and it caused sudden loss of the shear resistance of the wall specimens. Therefore larger sheathing fasteners were desired to improve the performance of the corrugated sheet specimens. The next four tests (Tests 4, 5, 6, 7) employed No. 12×1-¼ in. hex washer head self-drilling screws for both sheathing and framing. The thicker (0.068 in.) studs and tracks were used for the frames. The changes in the fasteners and the framing members greatly increased the shear strength of the wall. The Test 4 failed by the shear failure of the No. 14 screws which attached the hold-down to the studs, as shown in Figure 11. In Test 5, the lateral support was moved by large out-of-plane forces. Therefore modifications were made to reinforce the hold-down and lateral supports in Test 6 and Test 7. The specimens of Tests 6 and 7 were identical except that the hold-down was raised up in Test 6 and flushed to the bottom track in Test 7. In both tests, the sheathing behaved as a rigid body, neither the warping of the sheathing nor the pull-out of screws was observed. The connection between the screws and the corrugated sheet became loose because of the large in-plane shear force developed during the test. Further it was found that the hold-down failed in both tests, as shown in Figure 11, the flat supporting element in hold-down was bent.

The average peak load of the tests on 0.068 in. framed walls was 4093 plf which is greater than 7/16" OSB (3080 plf) and 0.027 in. flat sheet steel (1170 plf Table C2.1-3 of AISI S213). Stojadinovic and Tipping (2007) reported an average of 3290 plf for 0.068 in. framed walls with 0.027 in. corrugated sheet sheathing, 3 in. / 6 in. fastener spacing.

#### ***Material Properties***

Coupon tests were carried out according to the ASTM A370-06 (2006) "Standard Test Methods and Definitions for Mechanical Testing of Steel Products". The test results are summarized in Table 4. The coating on the steel was removed by hydrochloric acid prior to the coupon tests.

**Table 4: Material properties**

Components	Uncoated Thickness (in.)	Yield Stress $F_y$ (ksi)	Tensile Strength $F_u$ (ksi)	$F_u/F_y$ Ratio	Elongation for 2 in. Gage Length (%)
0.027 in. corrugated sheet	0.0291	90.1	93.4	1.03	4.3%
0.043 in. stud	0.0419	47.6	55.1	1.15	29.0%
0.043 in. track	0.0420	43.1	55.6	1.29	25.0%
0.068 in. stud	0.0716	46.0	57.5	1.26	14.8%
0.068 in. track	0.0706	62.2	74.2	1.19	15.2%



## Summary and Conclusions

A total of 3 Monotonic and 4 cyclic shear wall tests on cold-formed steel stud walls with 0.027 in. (22 gauge) corrugated steel sheathing on one side were conducted. 0.043 in. framed walls with No. 8 sheathing screws and 0.068 in. framed walls with No. 12 sheathing screws were investigated. It was found the 0.027 in. corrugated steel sheet was rigid and required considerable amount of fasteners to prevent from warping. The tested shear walls 0.027 in. corrugated sheet with 9/16 in. rib height demonstrated considerably higher shear resistance than the same framed walls with 7/16 in. OSB sheathing, and more than two times higher strength than the same framed walls with 0.027 in. flat sheet steel sheathing. The corrugated steel sheet is a promising sheathing material for CFS framed shear wall, 0.068 in. framing members and No. 12 self-drilling screws with tight spacing schedule are recommended to utilize the 0.027 in. corrugated sheet in the lateral resisting system of buildings.

## Acknowledgement

The sponsorship of American Iron and Steel Institute and the donation of materials by Steel Stud Manufacturers Association, Simpson Strong-Tie Company, Inc., and NuconSteel Corp. are gratefully acknowledged. The assistance and guidance provided by the AISI lateral design task group members is highly appreciated. The assistance of the UNT lab technician Bobby Grimes and Chris Matheson in setting up the facilities has been invaluable. The UNT students Pradeep Kumar and Jimmy Tucker were involved in the specimen preparation, the project could not be completed without their contributions.

## References

- AC130 (2004). "Acceptance Criteria for Prefabricated Wood Shear Panels", ICC Evaluation Service, INC., Whittier, CA.
- AC154 (2005). "Acceptance Criteria for Cyclic Racking Shear Test for Metal-Sheathed Shear Walls with Steel Framing", ICC Evaluation Service, INC., Whittier, CA.
- AISI S213 (2007). "The North American Standard for Cold-Formed Steel Framing - Lateral Design", American Iron and Steel Institute, Washington, DC.
- ASME B18.22.1 (1998). "Plan Washers", American Society of Mechanical Engineers, New York, NY.
- ASTM A370-06 (2006). "A370-06 Standard Test Methods and Definitions for Mechanical Testing of Steel Products", American Society for Testing and Materials, West Conshohocken, PA.

- ASTM E564-06 (2006). "E564-06 Standard Practice for Static Load Test for Shear Resistance of Framed Walls for Buildings", American Society for Testing and Materials, West Conshohocken, PA.
- Krawinkler, Parisi, Ibarra, Ayoub, and Medina (2000). "Development of a Testing Protocol for Woodframe Structures", Report W-02, Woodframe Project. Consortium of Universities for Research in Earthquake Engineering (CUREE), Richmond, California.
- ECCS (1985). "Recommended Testing Procedure for Assessing the Behavior of Structural Steel Elements under Cyclic Loads", European Convention for Constructional Steelwork, TWG 13 Seismic Design, Report No. 45, 1985.
- Fülöp and Dubina (2004). "Performance of wall-stud cold-formed shear panels under monotonic and cyclic loading Part I: Experimental research", *Thin-Walled Structures*, 42 (2004) 321-338.
- Serrette, R.L., Nguyen, H., Hall, G. (1996). "Shear wall values for light weight steel framing." Report No. LGSRG-3-96, Santa Clara University. Santa Clara, CA.
- Serrette, R.L. (1997). "Additional Shear Wall Values for Light Weight Steel Framing." Report No. LGSRG-1-97, Santa Clara University. Santa Clara, CA.
- Serrette, R.L. (2002). "Performance of Cold-Formed Steel-Framed Shear Walls: Alternative Configurations," Final Report: LGSRG-06-02, Santa Clara University. Santa Clara, CA.
- SSMA (2001). "Product Technical Information ICBO ER-4943P", Steel Stud Manufacturer Association, Chicago, IL.
- Stojadinovic and Tipping (2007), "Structural testing of corrugated sheet steel shear walls." Report submitted to Charles Pankow Foundation, Ontario, CA.



## **STRUCTURAL TESTING OF CORRUGATED SHEET STEEL SHEAR WALLS**

**BY**  
**BOZIDAR STOJADINOVIC<sup>1</sup>**  
**STEVEN TIPPING<sup>2</sup>**

### **Abstract**

The objective of the research is to develop an alternative lateral bracing system comprising corrugated sheet steel shear walls for use with light-framed cold-formed steel buildings. The key element of this structural system is the corrugated sheet steel shear wall: the lateral load resistance of this structural element originates with the shear strength of the corrugated sheet steel and the shear resistance of the screws connecting the sheeting to the cold-formed steel framing. To establish a design basis, a total of 44 cyclic racking tests were conducted to establish the relation between corrugated sheet steel shear wall design parameters, such as gauge of the sheet steel, gauge of the cold-formed steel framing, size and spacing of the fasteners, and the shear strength of the wall. The results of these tests are presented. Furthermore, system-level  $R$ ,  $C_d$  and  $\Omega_o$  values consistent with the test results are proposed for adoption into design codes. Finally, a design table listing the nominal shear strength values for corrugated sheet steel shear walls is provided. The primary users of the system would be practicing engineers who design light-framed cold-formed steel buildings.

- 
1. Associate Professor, University of California at Berkeley
  2. President, Tipping Mar + associates, Berkeley, CA

## Objective

The objective of the research is to provide practicing engineers with an alternative lateral bracing system which is stronger, more flexible, and less expensive than the traditional bracing systems currently available for use with light-framed cold-formed steel construction. This research project will provide the basis for developing a shear wall design table listing the nominal shear values for wind and seismic forces for shear walls framed with cold-formed steel studs and sheathed with corrugated sheet steel. In keeping with the terminology used to describe shear walls in the International Building Code, the low profile metal deck tested is referred to as “corrugated sheet steel”. The term “corrugated sheet steel shear wall” is abbreviated to “CSSSW” in the body of the paper.

## Scope

Cyclic testing was performed on 44 wall specimens. To understand the structural capabilities of the corrugated sheet steel shear wall (CSSSW) system, six design parameters were selected to vary during the tests: 1) gauge of the corrugated sheet steel, 2) gauge of the studs and tracks, 3) fastener type/size, 4) fastener spacing for attachment of corrugated sheet steel, 5) inclusion of gypsum board on one side, and 6) applying the corrugated sheet steel on one or both sides of a wall specimen. The cyclic tests provided information about the cyclic strength, stiffness, hysteretic properties, and ductility factors of the CSSSW specimens.

## Test Apparatus

The test apparatus (see Photo 1) consists of a Reaction Frame, a specimen Test Frame, and attachment plates. Because of the large number of specimens to be tested and the large variations in applied forces, it was decided to design the Test Frame with a reusable holdown system that would accommodate forces up to 100-kips (445 kN) to insure the holdowns would not fail. This approach deviates from the traditional method of having discrete holdowns and boundary elements in each specimen to simulate in-situ conditions as closely as possible. Typically, double studs with Simpson holdowns are used. Given the high shear capacity of the CSSSW system, double angle holdowns are used in the Test Frame to more accurately represent in-situ conditions of the boundary elements and the holdowns.



Photo 1

### **Test Acceptance Criteria**

The test acceptance criteria used to develop the data for this report are based in part on AC154 (March 2000 edition, editorially revised July 2005), Acceptance Criteria for Cyclic Racking Shear Tests for Metal-Sheathed Shear Walls with Steel Framing and in part on AC130, Acceptance Criteria For Prefabricated Wood Shear Panels. The AC 154 protocol was used to test the panels while the AC 130 protocol was used to establish the nominal shear values for the panels. See Acceptance Criteria Discussion section for explanation on why the two acceptance criteria were used.

The cyclic displacement protocol used is based on ATC 154. The loading sequence consists of both stabilizing cycles and decaying cycles. The loading velocity varied between 0.16 in/sec (.4 cm/sec) and 1.92 in/sec (4.9 cm/sec) during each of the tests. Each test was ended with a final 5" (12.7 cm) + and 5" (12.7 cm) – excursion which represents an inter-story drift of 5%.

The amplitudes of the displacement cycles were defined in terms of the Approximate Elastic Displacement (AED), the first significant change to occur in the applied force-displacement response of a monotonic or cyclic test of the shear wall. To estimate the AED for this research, a CSSSW specimen was subjected to the AC154 loading sequence with the AED set at 0.8 inches (2 cm) and using a constant loading velocity of 0.1 inches per second (.25 cm/sec). The new AED, which was used for all subsequent tests, was determined by noting the displacement at the first yield-point (first significant change in the applied force-displacement response).

### Instrumentation

The applied force and displacement response of each CSSSW specimen was measured with load cells and potentiometers. The AC154 testing criteria stated the minimum requirements for the quantities to be measured: lateral in-plane displacement at the top of the wall, uplift and compression at the bottom corners of the wall, base slip, and applied racking load. The instrumentation used for this research exceeds the AC154 minimum requirements.

### Specimens

A total of 44 specimens were tested between October and December of 2006 at the Davis Hall Structures Laboratory at the University of California, Berkeley. 40 of the specimens measured 4'-0" wide (1.22 m) by 8'-2" high (2.49 m) while 4 of the specimens measured 4'-0" wide (1.22 m) by 2'-0" high (.61 m)

Listed below is a summary of the parameter variables:

1. **Corrugated Sheet Steel:** The corrugated sheet steel (metal decking) was provided by Verco Manufacturing Company. The deck type used was Shallow Vercor fabricated from G90 galvanized steel conforming to ASTM A653, Grade 50. Three gauges of decking were tested: 22 gauge (.71 mm), 20 gauge (.88 mm), and 18 gauge (1.15 mm).
2. **Studs and Tracks:** Generic studs and tracks manufactured per the Steel Stud Manufactures Association (SSMA) were used. Four sizes of studs, with matching tracks, were tested: 362S162-33, 362S162-43, 362S162-54 (50 ksi), and 362S162-68 (50 ksi).
3. **Fasteners:** Three types of fasteners were tested: generic hex head self-drilling screws, a proprietary hex head self-drilling screw by Dynamic Fastener Service, Inc. called Fenderhead, and a pneumatic pin by Aerosmith

Fastening Systems. The generic hex head screws tested included #10-16 x  $\frac{3}{4}$ ", #12-14 x  $1\frac{1}{4}$ ", and #14-20 x  $1\frac{1}{2}$ ". The Fenderhead screws tested included #12-14 x  $1\frac{1}{4}$ " and #14-20 x  $1\frac{1}{2}$ ". The pin tested was a .1" diameter x  $\frac{3}{4}$ " long x  $\frac{1}{4}$ " flat T head.

4. **Fastener Spacing:** Due to the decking profile, the spacing of the fasteners was limited to a 3" (7.62 cm) module. Fastener spacing at boundaries, seams (horizontal), and field (vertical) were tested at either 3" (7.62 cm) on center or 6" (15.24 cm) on center.

5. **Gypsum Wall Board:**  $\frac{5}{8}$ " (1.59 cm) gypsum wall board was applied over the corrugated metal decking on two specimens to evaluate its affect on the strength and stiffness of the specimen. The gypsum wallboard was attached to the decking with #6 screws spaced at 6" (15.24 cm) on center at panel edges and the field.

6. **One Sided and Two Sided Panels:** Two specimens were tested with sheathing on both sides of the panel.

See Table 1 for the Group/Specimen Matrix which lists all of the parameters for each specimen tested.

### Specimen Force-Displacement Curves

Data analysis was carried out in accordance with section 3.3 of AC154 with the exception of section 3.3.5, in which case the first hysteretic loop of the last set of stable hysteretic load/displacement loops was used in accordance with AC130 rather than the second hysteretic loop. See Test Acceptance Criteria Discussion section for explanation.



Group ID	Wall ID	Double-Sided	Panel Length ft.	Metal Decking Thickness ga.	Thickness of Studs & Tracks ga.	Fastener Size (Hex Head) ga.	Fastener Spacing at Fastener Boundaries in.	Fastener Spacing at Fastener Boundaries Horiz. Spacing in.
1	3	FALSE	4	22	20	#12-14 x 1 1/4" F	6	6
1	18	FALSE	4	22	20	#12-14 x 1 1/4"	6	6
2	19	FALSE	4	22	20	#12-14 x 1 1/4"	6	6
3	4	FALSE	4	22	20	#12-14 x 1 1/4" F	3	3
3	11	FALSE	4	22	20	#12-14 x 1 1/4"	3	3
3	20	FALSE	4	22	20	#12-14 x 1 1/4"	3	3
4	12	FALSE	4	22	20	#12-14 x 1 1/4"	3	3
4	21	FALSE	4	22	20	#12-14 x 1 1/4"	3	3
5	35	TRUE	4	22	20	#12-14 x 1 1/4"	3	3
6	43	FALSE	4	22	18	#12-14 x 1 1/4"	3	3
6	44	FALSE	4	22	18	#12-14 x 1 1/4"	3	3
7	24	FALSE	4	22	16	#12-14 x 1 1/4"	6	6
7	25	FALSE	4	22	16	#12-14 x 1 1/4"	6	6
8	14	FALSE	4	22	16	#12-14 x 1 1/4" F	3	3
8	26	FALSE	4	22	16	#12-14 x 1 1/4"	3	3
9	31	FALSE	4	22	16	#12-14 x 1 1/4"	3	2
9	32	FALSE	4	22	16	#12-14 x 1 1/4"	3	2
10	37	FALSE	2	22	16	#12-14 x 1 1/4"	3	3
10	38	FALSE	2	22	16	#12-14 x 1 1/4"	3	3
11	5	FALSE	4	20	18	#12-14 x 1 1/4" F	3	3
11	8	FALSE	4	20	18	#12-14 x 1 1/4" F	3	3
11	22	FALSE	4	20	18	#12-14 x 1 1/4"	3	3
12	16	FALSE	4	20	16	#12-14 x 1 1/4" F	3	3
12	27	FALSE	4	20	16	#12-14 x 1 1/4"	3	3
13	17	FALSE	4	18	18	#12-14 x 1 1/4" F	3	3
13	28	FALSE	4	18	18	#12-14 x 1 1/4"	3	3
14	9	FALSE	4	18	16	#12-14 x 1 1/4" F	3	3
14	29	FALSE	4	18	16	#12-14 x 1 1/4"	3	3
14	30	FALSE	4	18	16	#12-14 x 1 1/4"	3	3
14	42	FALSE	4	18	16	#12-14 x 1 1/4"	3	3
15	36	TRUE	4	18	16	#12-14 x 1 1/4"	3	3
16	10	FALSE	4	18	16	#14-20 x 1 1/2" F	3	3
16	33	FALSE	4	18	16	#14-20 x 1 1/2"	3	2
16	34	FALSE	4	18	16	#14-20 x 1 1/2"	3	2
16	41	FALSE	4	18	16	#14-20 x 1 1/2"	3	3
17	39	FALSE	2	18	16	#14-20 x 1 1/2"	3	3
17	40	FALSE	2	18	16	#14-20 x 1 1/2"	3	3
18	7	FALSE	4	20	18	#12-14 x 1 1/4" F	6	6
19	1	FALSE	4	22	20	#10-16 x 3/4"	6	6
20	2	FALSE	4	22	20	#10-16 x 3/4"	3	3
21	6	FALSE	4	22	20	0.1 x 3/4" Pin	1.5	1.5
22	13	FALSE	4	22	18	#12-14 x 1 1/4" F	3	3
23	15	FALSE	4	20	20	#12-14 x 1 1/4" F	3	3

Table 1

Group Specimen Matrix

A computer program was written to process the data and plot the graphs. A force-displacement curve was plotted for each specimen. Figure 1 is representative of a typical specimen.

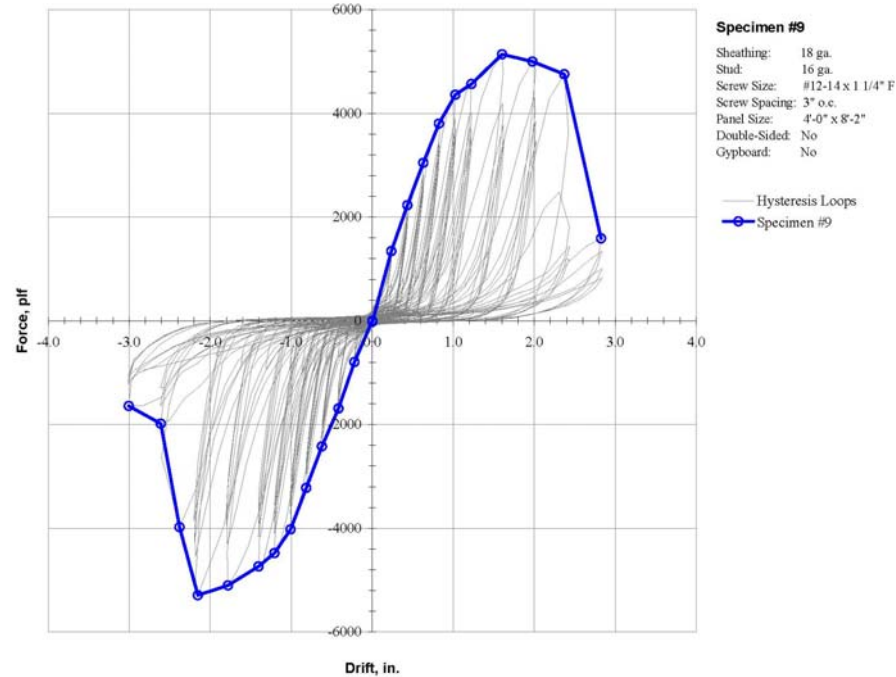


Figure 1

Specimen #9 Load/Displacement History

## Specimen Groups

The specimens were organized into groups according to construction type. A total of 24 groups were identified. In accordance with section 4.3 of AC154, a minimum of two identical wall assemblies of a given construction had to be tested. Of the 24 groups, 10 did not have a minimum of two specimens and therefore served only a limited use. Of the remaining 14 groups, the data from 7 were used to develop the final nominal shear values. The number of specimens in each group varied from 2 to 4. Groups 19, 35, and 36, which had only one specimen, were used to evaluate the affects of gypsum board and double sided panels.

### Group Backbone Curves

In accordance with sections 3.3 and 4.3 of AC154, the test data for the specimen groups was averaged. A computer program was written to analyze the data and plot the backbone curves. Backbone curves for each group were plotted. Figure 2 is representative of a typical group.

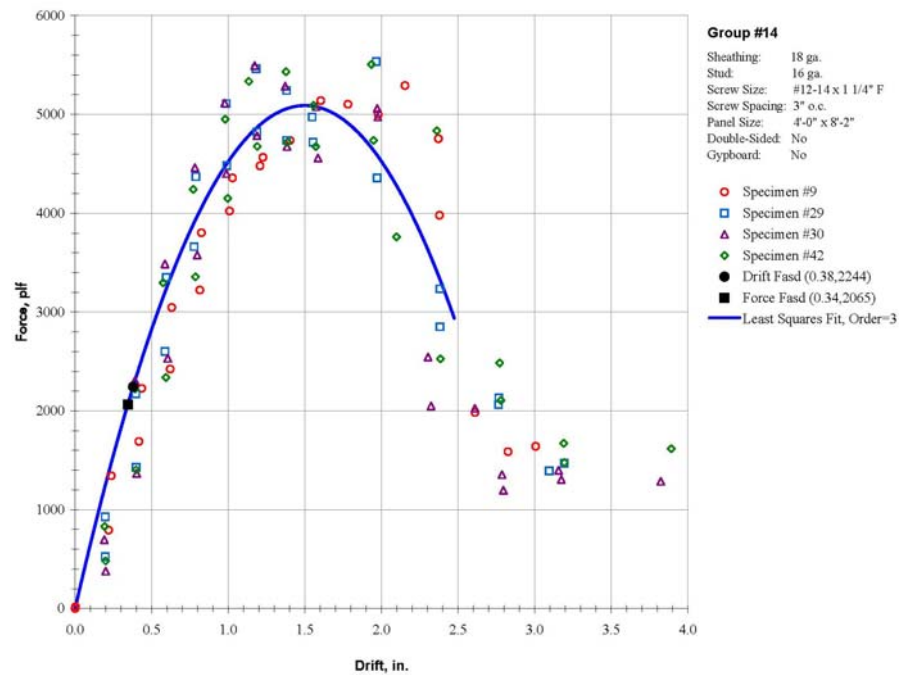


Figure 2

Specimen Group #14 Backbone Curve Fit

## **Failure Mode**

Of interest is the failure mode of the specimen panels. In all cases, the failure mode was the eventual “popping” out of the screws due to warping of the corrugated sheet steel. It was found that as the panels cyclically deformed, the screws would eventually gouge elongated holes in the metal studs and/or sheeting due to racking shear. As the inter-story drift increased, warping of the corrugated sheet steel became more pronounced and simultaneous diagonal tension and compression fields developed across the panel. As the holes in the studs enlarged, the tensile capacity of the screws was reduced and eventually the screws failed in tension due to the warping of the corrugated sheet steel and “popped” out.

It is also interesting to note the location of the screws that first “popped” out. In all cases, the first screws to “pop” out were located in the boundary members. The location of the screws that “popped” along the boundary members was random. The locations varied from top to bottom on both the left and right boundary members. The screws fastened into the top track, the bottom track, and the horizontal seams were never the first to fail.

## **Horizontal Seam Lap Splice**

The corrugated sheet steel was installed with the corrugations running horizontally. Two horizontal seams were required to construct a typical specimen. Adjacent sheets were overlapped one corrugation and fastened together with screws of the same size and spacing as the boundary condition. Based on the test results, it was concluded that no special blocking is required at horizontal lap splices.

## **Vertical Seam Splice**

Although no vertical seam splices were tested, the authors believe this is an important detail that should be discussed. The vertical seam splice can be butted at the center line of a vertical framing member, it can be lapped, or in the case of prefabricated wall panels, two panels could be joined by fastening studs together. In any case, this splice is a boundary condition and fasteners should be spaced at the same spacing as all panel edges. In discussing the splice options with a contractor, their preference was to lap the sheets between the studs rather than butt them at the stud because the lap splice would require half the number of screws. The lap splice should be sufficient length to insure development of the shear capacity of the fastener, say 1” minimum. As in the case of the horizontal lap splice, it was concluded that no special blocking is required at vertical lap splices.

## **Gypsum Board Sheathing**

Three of the specimens were sheathed with 5/8" (1.59 cm) gypsum board. The purpose of adding the gypsum board was to evaluate how it affected the strength and stiffness of the test specimen compared to a similar one without gypsum board. A comparison of the backbone curves for the three specimens compared to similarly constructed specimens without the gypsum board (Group 1 vs Group 2 and Group 3 vs Group 4) shows little difference between the groups. Based on this comparison, it appears that the addition of gypsum board to a wall sheathed with corrugated metal sheet will not materially change its behavior.

## **Miscellaneous Holes**

To represent the affect of adding electrical outlets, light switches, plumbing lines etc. to an actual wall panel, three of the test specimens had openings cut in them. Specimen 24 had a 4" (10.16 cm) diameter hole cut in the upper left hand corner of the panel. Specimen 25 had a 2" (5.1 cm) by 4" (10.16 cm) hole cut in the lower left hand corner of the panel. Specimen 42 had a 4" (10.16 cm) diameter hole cut in the upper left hand corner of the panel an To represent the affect of adding electrical outlets, light switches, plumbing lines, etc. to an actual wall d a 2" (5.1 cm) by 4" (10.16 cm) hole cut in the lower left hand corner of the panel. Field observation noted that the panels warped around the holes with no affect on the overall performance of the specimens.

## **Double Sided Walls**

To determine the affect of adding the corrugated sheet steel to both sides of a specimen, two specimens were tested. Specimen 35 (Group 5) was constructed using 20 gauge (.879 mm) studs and 22 gauge (.719 mm) corrugated sheet steel to represent a more lightly loaded wall while Specimen 36 (Group 15) was constructed with 16 gauge studs and 18 gauge corrugated sheet steel to represent a more heavily loaded wall. When comparing the results of Group 5 to Group 3, of similar one sided construction, and the results of Group 15 to Group 14, of similar one sided construction, it was found that the double sided specimens achieved allowable strengths that are basically double those of the one sided specimens. Based on these results, it was concluded that double sided walls will have double the shear strength.

### **Aspect Ratio (h/w)**

In order to determine the slenderness affects on the CSSSW system, four 24" (61 cm) wide specimens were tested. These include Specimens 37 and 38 (Group 10) and Specimens 39 and 40 (Group 17). Group 10 was constructed using 16 gauge (1.44 mm) studs and 22 gauge (.719 mm) corrugated sheet steel to represent a more lightly loaded wall while Group 17 was constructed with 16 gauge (1.44 mm) studs and 18 gauge (1.15 mm) corrugated sheet steel to represent a more heavily loaded wall. When comparing the results of Group 10 to Group 8, 48" (122 cm) wide panels of similar construction, and the results of Group 17 to Group 16, 48" (122 cm) wide panels of similar construction, it was found that the 24" (61 cm) panels are slightly stronger than the 48" (122 cm) panels from a force standpoint; however, from a deflection standpoint the allowable shear values drop substantially due to the flexibility of the panels. This is to be expected. The code addresses this issue by requiring the allowable strength of a panel to be reduced when the aspect ratio exceeds 2:1. The authors believe this is an appropriate approach for the CSSSW system.

### **Holdown System**

The CSSSW system relies heavily on the proper design of the holdown system. If the boundary members are not designed correctly, the wall panels will not be able to achieve the assumed ductility implicit in the assigned R value for the system. The design of the boundary members is addressed in Section CS, Special Seismic Requirements, Standard For Cold-Formed Steel Framing – Lateral Design – 2004. Of note to the reader is the potential magnitude of the holdown forces for the CSSSW system. The nominal shear strength of the corrugated sheet steel shear wall is two to three time higher than other conventional systems. Holdown forces in the range of 150-kips (668 kN) to 200-kips (890 kN) can be expected in a taller building.

### **Test Acceptance Criteria Discussion**

The AC154 Acceptance Criteria was developed to test metal-sheathed shear walls with cold formed steel framing. It is based in part on a document prepared by the Structural Engineers Association of Southern California entitled "Standard Method of Cyclic (Reversed) Load Test Shear Resistance of Framed Walls for Buildings" which was first published in 1996. This document established a sequential phased displacement load procedure which was carried over into AC154 as the Cyclic Load Test Protocol with only minor modifications to the last six cycles. Since each incremental step is cycled through four times, the data allows one to plot four separate backbone curves. The nominal shear strength is based on the yield strength of the second cycle backbone curve. The AC 154 acceptance criteria were chosen because the wall assemblies described in the acceptance criteria closely matched the wall assemblies being tested. During the data

processing portion of the research, the authors learned that the AC 130 protocol, which was developed for prefabricated wood shear walls, had become the consensus protocol for testing light-framed walls sheathed with either wood or sheet steel.

The AC130 Acceptance Criteria was developed as part of the CUREE/Caltech Woodframe project (Krawinkler et al., 2000) and incorporates portions of AC154. The primary difference is that the AC154 criteria define the yield load as the strength of the element bases on the second-cycle backbone curve while the AC130 criteria define the ultimate capacity as the strength of the element based on the first-cycled backbone curve. The AC 130 Cyclic Load Test Protocol was shortened from the 72 cycles required in AC 154 to 40 cycles and does not repeat cycles.

The authors chose to determine the nominal strength of the panels based on Section 5.2.4 of AC 130, which uses the first-cycle backbone curve of the cyclic load testing to establish force levels. This approach proved to be much simpler than the AC 154 method and is consistent with other research currently being done.

### **Seismic Response Parameters $R$ , $\Omega_o$ , $C_d$**

The relevant factors that determine the design strength of seismic force resisting systems consist of the Response Modification Coefficient ( $R$ ), the Deflection Amplification Factor ( $C_d$ ), and the System Over-strength Factor, ( $\Omega_o$ ). Establishing appropriate values for these parameters relies somewhat on engineering judgment to maintain a consistent and rational relationship between both actual test results and the historically accepted codified values.

To better understand the reasoning behind assigned values, the following documents were reviewed: “Ductile Design of Steel Structures”, Sections C105.2 and C105.3 from the 1999 Blue Book, including Figure C105-2, Article 4.01.010, dated September 2006 from the on line Blue Book, Chapter 5 Commentary of the 2000 edition of NEHRP Recommended Provisions For Seismic Regulations For New Buildings And Other Structures, and the Recommendations for Earthquake Resistance in the Design and Construction of Woodframe Buildings, Part 2 – Commentary from the CUREE-Caltech Woodframe Project. These documents outline the derivation of the seismic response parameters, describe the relationship between the assigned values and anticipated structural response, and highlight the inconsistencies between values assigned to different systems.

ASCE/SEI 7-05, “Minimum Design Loads for Buildings and Other Structures,” assigns light-framed bearing wall systems using wood structural panel or steel sheathing a  $R$  value of 6.5, a  $C_d$  value of 4.0, and an  $\Omega_o$  value of 3.0. Since the CSSSW system is a slight variation of the above defined bearing wall system (using corrugated metal

sheathing rather than flat metal sheathing or plywood sheathing on wood studs), an evaluation of the seismic response factors was done to see if they were appropriate for the CSSSW system. A  $R$  value of 6.5 and a  $C_d$  value of 4.0 were assigned to determine the controlling shear forces and associated drifts per the AC 130 protocol. A review of the data found that all 7 groups used to develop the Nominal Shear Strength were controlled by the drift limit. Further review of the data found the  $C_v/C_s$  values ranged from 1.84 to 2.24 versus the assumed value of 1.79 ( $2.5/1.4 = 1.79$ ).

To provide a comparison, the  $R$  value was lowered to 5.5, the  $\Omega_o$  value was lowered to 2.5, and the  $C_d$  value was lowered to 3.25 and the controlling shear forces and associated drifts were again determined per the AC 130 protocol. A review of the data found that of the 7 groups actually used to develop the Nominal Shear Strength, 6 of the groups were controlled by the ultimate load limit while only 1 was controlled by the drift limit. For the drift controlled group, the  $C_v/C_s$  value was 1.89 versus the assumed value of 1.79 ( $2.5/1.4 = 1.79$ ). It was observed that lowering the  $R$  and  $C_d$  values as noted shifts the walls from drift controlled to force controlled and more accurately predicts the over strength factor.

An alternative method to determine the seismic response parameters is being developed by the Applied Technology Council. The document, *Quantification of Building Seismic Performance Factors, ATC 63 Project Report*, is currently in 90% draft form. This methodology utilizes actual test data to determine the non-linear response of archetype buildings. Professor Greg Deierlein of Stanford University evaluated the corrugated metal shear walls per ATC 63 and compared the results with similar archetype buildings developed to evaluate wood shear walls. The evaluation found that the two systems performed similarly for the 2 story archetype building while the wood buildings performed somewhat better for the 5 story archetype building. Assuming all things equal, this suggests that the wood building has a slightly higher ductility. Professor Deierlein concluded that “neither the wood panel nor the corrugated steel panel archetypes pass the criteria to justify the  $R$ -values of 5.5 and 6 used in the designs.” He further states “Thus, strict adherence to the ATC 63 criteria would dictate that lower  $R$ -values, probably on the order of 3 to 4, should be used for design.” The ATC 63 Project Report found that when gypsum wallboard is added to the plywood shear walls, a  $R$  value of 6 could be justified per the methodology.

Based on the findings of the ATC 63 study and the observations noted above, the authors are proposing a  $R$  value of 5.5, a  $C_d$  value of 3.25, and a  $\Omega_o$  value of 2.5 be assigned to the corrugated metal shear walls. This stays in keeping with the  $R$  value of 6.5, the  $C_d$  value of 4.0, and the  $\Omega_o$  value of 3 assigned to light-framed bearing wall systems using wood structural panel or steel sheathing and acknowledges the past performance of these systems.



## Conclusion

The authors recommend that the CSSSW system be added to Table 12.2-1, Design Coefficients and Factors For Seismic Force-Resisting Systems of ASCE 7-05, classified as a Bearing Wall System utilizing light-framed cold-formed steel walls sheathed with corrugated sheet steel and have the following design parameters:

Response Modification Factor ( $R$ ) = 5.5

System Overstrength Factor ( $\Omega_o$ ) = 2.5

Deflection Amplification Factor ( $C_d$ ) = 3.25

The authors also recommend that Table 2 be added to AISI S213-07: North American Standard for Cold-Formed Steel Framing – Lateral Design.

## Appendix – Notation

Response Modification Coefficient ( $R$ ).

Deflection Amplification Factor ( $C_d$ ).

System Over-strength Factor ( $\Omega_o$ ).

Nominal Shear Strength ( $R_n$ ) for Wind and Seismic Loads for shear walls faced with corrugated sheet steel. (pounds per foot) <sup>1, 3, 4, 7</sup>

Assembly Description <sup>5, 6</sup>		20 gauge studs	18 gauge studs	16 gauge studs	
		# 12 screws	# 12 screws	# 12 screws	# 14 screws
Sheathing	Screw Spacing <sup>2</sup>	Shear (plf)	Shear (plf)	Shear (plf)	Shear (plf)
22 gauge	6" o.c.	1173	1505	1836	---
	3" o.c.	---	3050	3290	---
18 gauge	3" o.c.	---	4144	5164	5874

- 1 Nominal shear strength shall be multiplied by the resistance factor ( $\phi$ ) to determine the design strength or divided by the safety factor ( $\Omega$ ) to determine allowable shear strength as set forth in Section C2.1.
- 2 Screws in the field of the panel shall be installed 6 inches o.c. unless otherwise shown.
- 3 A shear wall height to width aspect ratio ( $h/w$ ) greater than 2:1, but not exceeding 4:1, is permitted provided the nominal shear strength is multiplied by  $2w/h$ . See Section C2.1.
- 4 See Section C2.1 for requirements for sheathing applied to both sides of wall.
- 5 Unless noted as (min.), substitution of a stud or track of a different designation thickness, per the General Provisions, is not permitted.
- 6 Wall studs and track shall be ASTM A1003 Grade 33 Type H steel for members with a designation thickness of 33 or 43 mil, and A1003 Grade 50 Type H steel for members with a designation thickness equal to or greater than 54 mils.
- 7 For SI: 1" = 25.4 mm, 1 foot = 0.305 m, 1 lb = 4.45 N

Table 2

Nominal Shear Strength for Wind and Seismic Loads



## **Shear Resistance of Cold-Formed Steel Framed Shear Wall Assemblies with 0.027-, 0.030-, 0.033-inch Sheet Steel Sheathing**

Cheng Yu<sup>1</sup>

### **Abstract**

The cold-formed steel framed wall with sheet steel sheathing is a code approved structural system to resist lateral loads such as wind loads and seismic loads. The American Iron and Steel Institute Standard for Cold-Formed Steel Framing – Lateral Design 2004 Edition provides nominal shear strength for a limited range of steel sheet sheathed shear wall configurations. This paper presents a research project developed to add values for 0.030-in. and 0.033-in. steel sheet sheathed shear walls with 2:1 and 4:1 aspect ratios and 0.027-in. sheet steel shear walls with 2:1 aspect ratio. The fastener spacing taken into account in this research was 6-in., 4-in., 3-in., and 2-in. for the panel edges, and 12-in. for the panel field. The test program consisted of two series of shear wall tests. In the first series, monotonic tests were performed to determine the nominal shear strength for wind loads. In the second series, cyclic tests were conducted to obtain the nominal shear strength for seismic loads. This paper presents the details of the test program and the test results.

---

<sup>1</sup> Assistant Professor, University of North Texas (cyu@unt.edu)

### **Background and Objectives**

The American Iron and Steel Institute (AISI) Lateral Standard (2004) provides a limited range of nominal shear strengths for both wind loads and seismic loads for sheet steel shear walls. The published shear strengths are based on the research conducted by Dr. Reynaud Serrette and his team at Santa Clara University in 1997 and 2002. In Serrette (1997), both monotonic and cyclic tests were conducted on 0.018-in. and 0.027-in. steel sheet sheathed shear walls. The test protocol used for monotonic tests in Serrette's tests was similar to ASTM E564 "Standard Practice for Static Load Test for Shear Resistance of Framed Walls for Buildings." except the incremental loading procedure in Serrette's work was based on the lateral top of wall displacement while ASTM E564 uses the estimated peak load to determine the load increments. For the cyclic tests, the sequential phase displacement protocol was used in Serrette (1997, 2002).

Serrette (2002) performed cyclic tests on 0.027-in. sheet steel shear walls with simple lap shear connections at the adjoining panel edges. The overall dimensions of the wall assemblies were 4-ft.  $\times$  8-ft. and the sheathing was made by two 4-ft.  $\times$  4-ft.  $\frac{3}{4}$ -in. sheets connected by single line of fasteners. No. 8 self-drilling screws were used to assemble the shear walls and the screws were installed at 2-in. o.c. on the edges and 12-in. o.c. in the field of the sheathing sheets. The nominal shear strength from this particular wall configuration was 787 pound per linear foot (plf). The mode of failure was pullout of the screws from the sheathing along the lap joint of the two sheets.

The AISI Lateral Standard (2004) only covers 0.018-in. and 0.027-in. sheet steel walls with a limitation of up to a 2:1 aspect ratio for the 0.018-in. steel sheet sheathing and up to a 4:1 aspect ratio for 0.027-in. steel sheet sheathing. Therefore additional tests were desired to address a wider range of options of steel sheet sheathing for cold-formed steel shear walls.

The objective of the research reported here was to develop experimental data and produce nominal shear strengths for both wind loads and seismic loads for cold-formed steel framed wall assemblies with 0.033-in., 0.030-in., or 0.027-in. steel sheathing on one side. The specific goals were to determine the nominal shear strength for:

- 0.030-in and 0.033-in. steel sheet shear walls with 2:1 and 4:1 aspect ratios (height/width) for both wind loads and seismic loads,
- 0.027-in. steel sheet shear walls with 2:1 aspect ratio for both wind loads and seismic loads.

- Fastener spacing of 6-in., 4-in., 3-in., and 2-in. at panel edges for all wall configurations of interest.

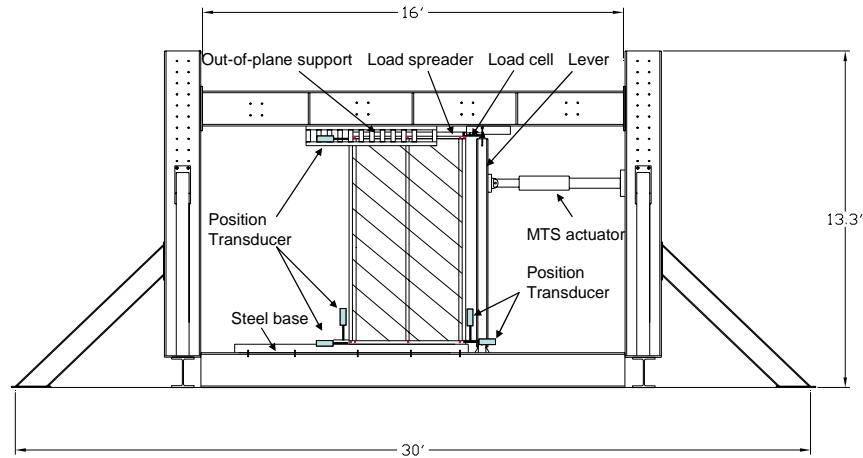
### **Test Program**

The test program was carried out during the time period from February to August 2007 in the NUCONSTEEL Structural Testing Laboratory at the University of North Texas. A total of 33 monotonic shear wall tests, 33 cyclic shear wall tests were conducted. The following sections provide the details of the test setup, testing procedure, and the test matrix.

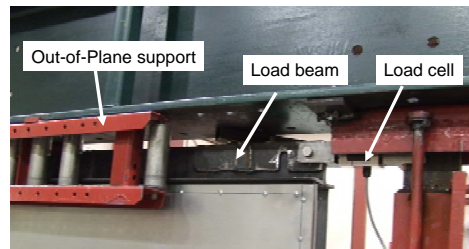
### **Test Setup**

Both the monotonic tests and the cyclic tests were performed on a 16-ft. span, 12-ft. high adaptable structural steel testing frame. Figure 1 illustrates the schematic of the testing frame with a 4-ft.  $\times$  8-ft. shear wall. All the shear wall specimens were assembled in a horizontal position and then installed vertically in the testing frame. The wall was bolted to a structural steel base beam and loaded horizontally at the top. The out-of-plane displacement of the wall was prevented by a series of steel rollers on the front side and three individual rollers on the back side of the wall top. A load beam made by structural steel “T” shape was attached to the top track member of the wall by 2 - No. 12  $\times$  1-1/2-in. hex washer head (HWH) self-drilling tapping screws placed every 3-in. on center. The “T” shape was made to be 4.5-in. wide so that it prevents the rollers from touching the test specimens during the test. Figure 2 shows the details of the top of the wall. The anchorage system for the monotonic tests used three Grade 8 1/2-in. diameter shear anchor bolts with standard cut washers (ASME B18.22.1 (1998)) and one Simpson Strong-Tie<sup>®</sup> S/HD10S hold-down with one Grade 8 1/2-in. diameter anchor bolt. For the cyclic tests, the anchorage system included two Grade 8 1/2-in. diameter shear anchor bolts and one Simpson Strong-Tie<sup>®</sup> S/HD10S hold-down with a Grade 8 1/2-in. diameter hold-down anchor bolt at each end of the shear wall.

The testing frame was equipped with one 35-kip hydraulic actuator with  $\pm 5$ -in. stroke. A 10-kip universal compression/tension load cell was placed to connect the top of lever to the “T” shape for force measuring. Five position transducers were employed to measure the horizontal displacement at the top of wall, the vertical displacement of the two boundary studs, and the horizontal displacements of the bottom of the two boundary studs, as shown in Figure 1.



**Figure 1 Testing frame with a 4-ft. x 8-ft. wall assembly**



**Figure 2 Close up of the top of the wall specimen**

### ***Test Procedure***

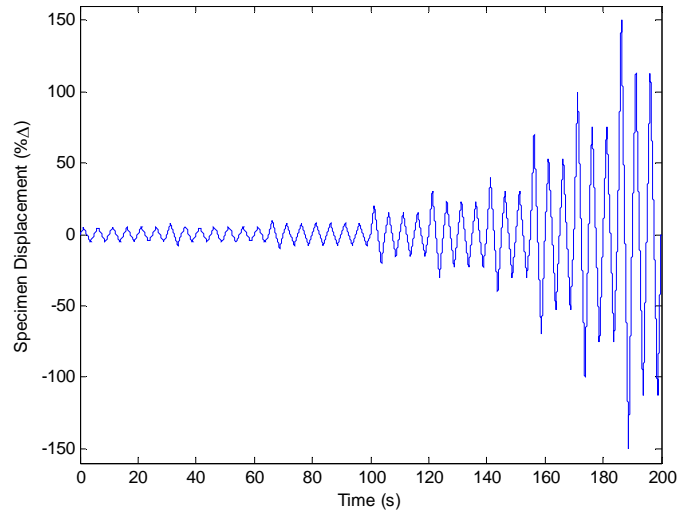
Both the monotonic tests and the cyclic tests were conducted in a displacement control mode. The procedure of the monotonic tests was in accordance with ASTM E564 (2006) “Standard Practice for Static Load Test for Shear Resistance of Framed Walls for Buildings”. A preload of approximately 10% of the estimated ultimate load was applied first to the specimen and held for 5 minutes to seat all connections. After the preload was removed, the incremental loading procedure started until failure using a load increment of 1/3 of the estimated ultimate load.

The CUREE protocol, in accordance with ICC-ES AC130 (2004), was chosen for the reversed cyclic tests. The CUREE basic loading history shown in Figure 3 includes 40 cycles with specific displacement amplitudes, which are listed in

Table 2. The specified displacement amplitudes are based on a percentage of the ultimate displacement capacity determined from the monotonic tests. The ultimate displacement capacity is defined as a portion (i.e.  $\gamma=0.60$ ) of maximum inelastic response,  $\Delta_m$ , which corresponds to the displacement at 80% peak load. However, the CUREE protocol was originally developed for wood frame structures, and it was found in this test program that using  $0.60\Delta_m$  as the reference displacement was not large enough to capture the post peak behavior of the sheet steel walls in the cyclic tests. Therefore, the lesser of 2.5% of the wall height (2.4-in. for 8 ft. high wall) and the displacement at the peak load in the monotonic tests was used as the CUREE reference displacement in this test program. A constant cycling frequency of 0.2-Hz for the CUREE loading history was adopted for all the cyclic tests in this research.

**Table 2 CUREE basic loading history**

Cycle No.	% $\Delta$	Cycle No.	% $\Delta$	Cycle No.	% $\Delta$	Cycle No.	% $\Delta$	Cycle No.	% $\Delta$
1	5.0	9	5.6	17	7.5	25	30	33	53
2	5.0	10	5.6	18	7.5	26	23	34	53
3	5.0	11	5.6	19	7.5	27	23	35	100
4	5.0	12	5.6	20	7.5	28	23	36	75
5	5.0	13	5.6	21	20	29	40	37	75
6	5.0	14	10	22	15	30	30	38	150
7	7.5	15	7.5	23	15	31	30	39	113
8	5.6	16	7.5	24	15	32	70	40	113



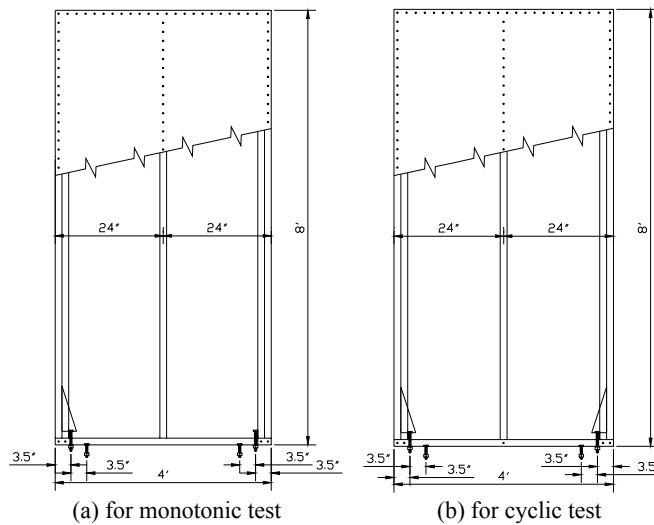
**Figure 3 CUREE basic loading history (0.2 Hz)**



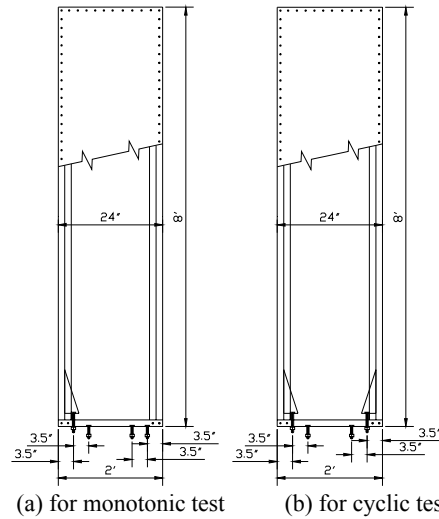
### Test Specimens

The test matrix was designed to cover two overall wall dimensions: 8-ft. (wide)  $\times$  4-ft. (high) (2:1 aspect ratio) and 8-ft.  $\times$  2-ft. (4:1 aspect ratio); three sheet steel thicknesses: 0.033-in., 0.030-in., 0.027-in.; and three fastener spacing schedules on the panel edges: 6-in., 4-in., and 2-in. The 3-in. spacing configuration was not included in the test program and the nominal shear strengths for the 3-in. fastener spacing configuration were determined by interpolating the test results of the other spacing configurations.

Figures 4 and 5 show the dimensions of the sheathed steel framed shear wall, shear anchor bolts, and the hold-downs. The framing members were assembled using No. 8 $\times$ 18-1/2" modified truss head self-drilling screws. Double C-shaped studs (back-to-back) were used for both boundary studs of the wall and the webs of the double studs were stitched together using 2 - No. 8 $\times$ 18-1/2" modified truss head self-drilling screws spaced at 6 in. o.c. 43-mil (0.043-in.) and 33-mil (0.033-in.) SSMA (Steel Stud Manufacturers Association) standard framing members were chosen for the wall assemblies. For the monotonic test, one Simpson Strong-Tie<sup>®</sup> S/HD10S hold-down was attached to the tension boundary stud from inside by using a total of 15 - No. 14 $\times$ 1" HWH self-drilling screws. For the cyclic test, one Simpson Strong-Tie<sup>®</sup> S/HD10S hold-down was used at each end of the wall, and 15 - No. 14 $\times$ 1" HWH self-drilling screws were used to attach each hold-down to the boundary studs. For all specimens, the hold-down was raised 1.5-in. above the flange of the bottom track.



**Figure 4 Dimensions of 8-ft.  $\times$  4-ft. wall assemblies**



**Figure 5 Dimensions of 8-ft. × 2-ft. wall assemblies**

The details of the components of the tested steel sheet walls are given as follows:

**Studs:**

- 350S162-33 SSMA structural stud, 0.033-in. 3-1/2-in. × 1-5/8-in. made of ASTM A1003 Grade 33 steel, placed in 2-ft. o. c. for 0.027-in. steel sheet walls.
- 350S162-43 SSMA structural stud, 0.043-in. 3-1/2-in. × 1-5/8-in. made of ASTM A1003 Grade 33 steel, placed in 2-ft. o. c. for 0.030-in. and 0.033-in. steel sheet walls.

**Tracks:**

- 350T150-33 SSMA structural track, 0.033-in. 3-1/2-in. × 1-1/2-in. made of ASTM A1003 Grade 33 steel for 0.027-in. steel sheet walls.
- 350T150-43 SSMA structural track, 0.043-in. 3-1/2-in. × 1-1/2-in. made of ASTM A1003 Grade 33 steel for 0.030-in. and 0.033-in. steel sheet walls.

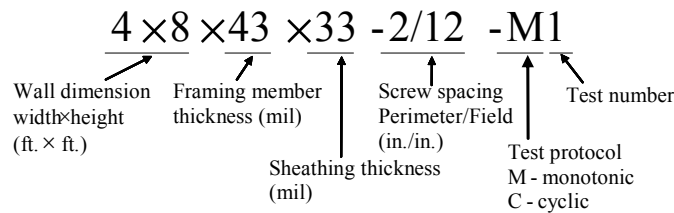
**Sheathing:**

- 0.033-in. thick ASTM A1003 Grade 33 steel.
- 0.030-in. thick ASTM A1003 Grade 33 steel.
- 0.027-in. thick ASTM A1003 Grade 33 steel.
- Steel sheet was installed on one side of the wall assembly.

### Framing and Sheathing Screws:

- No. 8×18-1/2-in. modified truss head self-drilling tapping screws. Spacing at panel edge is 6-, 4-, or 2-in. o.c. Spacing in the field of the sheathing is 12-in. for all specimen configurations. At the boundary studs, the sheathing screws were installed on the flanges of the outer stud.

For each specimen configuration, two identical tests were conducted. For the monotonic testing, a third specimen would be tested if the shear strength or stiffness of the second specimen tests is not within 15% of the result of the first specimen tested. For the cyclic testing, a third specimen would be tested if the difference between the ultimate test loads of the first two specimens is more than 10% apart. Figure 6 illustrate the definitions of the notations in the test label.



**Figure 6 Definitions of the test label**

### Material Properties

Coupon tests were conducted according to the ASTM A370-06 “Standard Test Methods and Definitions for Mechanical Testing of Steel Products”. The test results are summarized in Table 3. The coating on the steel was removed by hydrochloric acid prior to the coupon tests.

**Table 3 Material properties**

Component	Uncoated Thickness (in.)	Yield Stress $F_y$ (ksi)	Tensile Strength $F_u$ (ksi)	$F_u/F_y$ Ratio	Elongation
33 mil steel sheet	0.0358	43.4	53.8	1.24	27%
30 mil steel sheet	0.0286	48.9	55.6	1.08	24%
27 mil steel sheet	0.0240	50.3	57.8	1.15	21%
43 mil stud	0.0430	47.6	55.1	1.15	29%
33 mil stud	0.0330	47.7	55.7	1.17	24%
43 mil track	0.0420	43.1	55.6	1.29	25%
33 mil track	0.0330	57.4	67.2	1.17	28%

Note: Steel is specified as Grade 33 for all members. The specified minimum yield stress is 33 ksi and specified minimum tensile strength is 45 ksi.

## Test Results

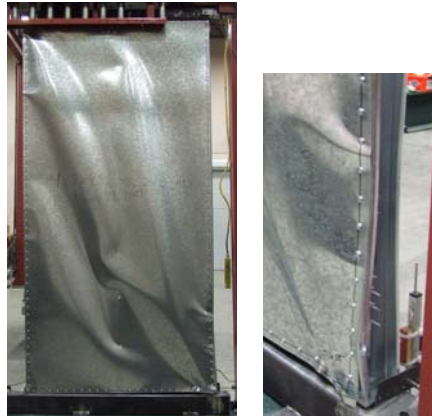
### *Shear Wall Test Results*

A total of 30 monotonic tests and 30 cyclic tests were conducted. In the 4-ft. × 8-ft. wall monotonic tests, the back-to-back double boundary studs were able to provide enough resistance against overturning forces. For the wall assemblies with 4<sup>7</sup>/<sub>12</sub>" and 6<sup>7</sup>/<sub>12</sub>" sheathing screw spacing, the failure mode was a combination of buckling of the sheathing and pullout of sheathing screws from the frame. Figure 7 shows the typical failure mode for a 0.033-in. sheet steel 4 ft. × 8 ft. wall with 6-in. screw spacing at panel edges. For the 4 ft. × 8 ft. walls with 2<sup>7</sup>/<sub>12</sub>" screw schedule, the failure mode was the buckling of the sheathing. Additionally, distortion on the outer flanges of the boundary studs in tension was also observed for shear walls with 2<sup>7</sup>/<sub>12</sub>" sheathing screw schedule. Figure 8 shows the failure mode on a 0.033-in. sheet steel wall with 2-in. screw spacing at panel edges.

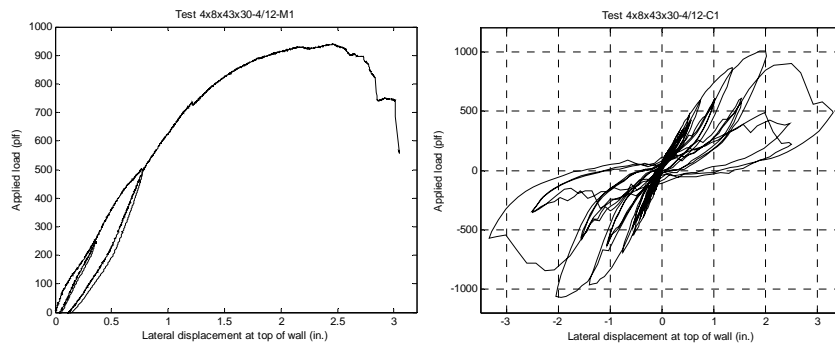


**Figure 7 Failure modes for test 4x8x43x33-6/12-M1**

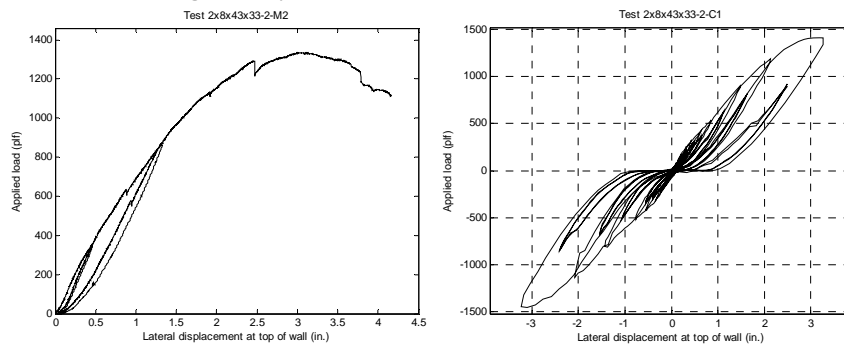
In the 2-ft. × 8-ft. wall monotonic tests, it was found that the displacement at the peak load was consistently greater than those in the 4-ft. × 8-ft. wall tests. Similar to the failure modes for the 4-ft. × 8-ft. walls, a combination of sheet buckling and screw pullout was observed for 2-ft. × 8-ft. walls with 6<sup>7</sup>/<sub>12</sub>" or 4<sup>7</sup>/<sub>12</sub>" screw spacing schedule. Similar to the finding in 4 ft. × 8 ft. wall tests, the distortion on the boundary stud in tension was observed on 2 ft. × 8 ft. walls with 2<sup>7</sup>/<sub>12</sub>" screw spacing. Figures 9 and 10 respectively show the hysteresis curves for 4-ft. × 8-ft. walls and 2-ft. × 8-ft. walls. Tables 4 and 5 summarize the test results for monotonic tests and cyclic tests respectively.



**Figure 8 Failure modes for test 4x8x43x33-2/12-M2**



**Figure 9 Hysteresis curves for test 4x8x43x30-4/12**



**Figure 10 Hysteresis curves for test 2x8x43x32-2**

**Table 4 Monotonic test results**

Test label	Peak load (plf)	Nominal shear strength (plf)	Disp. of wall top @ peak load (in.)	Avg. disp. of wall top @ peak load (in.)
4×8×43×33-6/12-M1	1023	1074	2.08	1.90
4×8×43×33-6/12-M2	1124		1.72	
4×8×43×33-4/12-M1	1173	1189	1.73	2.03
4×8×43×33-4/12-M2	1204		2.32	
4×8×43×33-2/12-M1	1317	1347	2.53	2.09
4×8×43×33-2/12-M2	1376		1.65	
4×8×43×30-6/12-M1	801	794	2.51	2.47
4×8×43×30-6/12-M2	786		2.43	
4×8×43×30-4/12-M1	940	959	2.47	2.62
4×8×43×30-4/12-M2	977		2.76	
4×8×43×30-2/12-M1	1078	1054	3.46	3.20
4×8×43×30-2/12-M2	1030		2.94	
4×8×33×27-6/12-M1	644	626	1.87	1.91
4×8×33×27-6/12-M2	607		1.95	
4×8×33×27-4/12-M1	685	684	1.90	2.11
4×8×33×27-4/12-M2	682		2.31	
4×8×33×27-2/12-M1	856	836	2.02	1.99
4×8×33×27-2/12-M2	816		1.96	
2×8×43×33-6-M1	1065	1017	3.13	2.80
2×8×43×33-6-M2	968		2.47	
2×8×43×33-4-M1	1147	1156	2.63	2.77
2×8×43×33-4-M2	1164		2.91	
2×8×43×33-2-M1	1386	1361	3.35	3.20
2×8×43×33-2-M2	1335		3.05	
2×8×43×30-6-M1	872	882	3.30	3.35
2×8×43×30-6-M2	891		3.40	
2×8×43×30-4-M1	937	950	3.32	3.29
2×8×43×30-4-M2	963		3.25	
2×8×43×30-2-M1	1096	1097	3.30	3.37
2×8×43×30-2-M2	1098		3.43	

**Table 5 Cyclic test results**

Test label	Average peak load (plf)	Nominal shear strength (plf)	Disp. of wall top @ peak load (in.)	Avg. disp. of wall top @ peak load (in.)
4×8×43×33-6/12-C1	1113	1093	1.65	1.90
4×8×43×33-6/12-C2	1072		1.61	
4×8×43×33-4/12-C1	1187	1210	1.79	2.03
4×8×43×33-4/12-C2	1232		1.67	
4×8×43×33-2/12-C1	1399	1350	1.74	2.09
4×8×43×33-2/12-C2	1301		1.80	
4×8×43×30-6/12-C1	901	911	1.92	2.47
4×8×43×30-6/12-C2	921		2.25	
4×8×43×30-4/12-C1	1041	1014	1.98	2.62
4×8×43×30-4/12-C2	987		2.03	
4×8×43×30-2/12-C1	1073	1070	1.73	3.20
4×8×43×30-2/12-C2	1066		1.77	
4×8×33×27-6/12-C1	653	647	1.54	1.91
4×8×33×27-6/12-C2	640		1.52	
4×8×33×27-4/12-C1	726	710	1.21	2.11
4×8×33×27-4/12-C2	694		1.22	
4×8×33×27-2/12-C1	802	845	1.70	1.99
4×8×33×27-2/12-C2	887		1.87	
2×8×43×33-6-C1	1132	1135	2.98	2.80
2×8×43×33-6-C2	1137		3.11	
2×8×43×33-4-C1	1252	1264	3.02	2.77
2×8×43×33-4-C2	1276		3.25	
2×8×43×33-2-C1	1429	1361	3.09	3.20
2×8×43×33-2-C2	1292		2.99	
2×8×43×30-6-C1	916	924	3.00	3.35
2×8×43×30-6-C2	931		3.26	
2×8×43×30-4-C1	1055	1053	3.22	3.29
2×8×43×30-4-C2	1051		3.09	
2×8×43×30-2-C1	1198	1203	3.09	3.37
2×8×43×30-2-C2	1208		2.96	

***Nominal Shear Strengths***

The nominal shear strength was determined as the average peak load of all the identical tests. The nominal shear strength for wind loads is based on monotonic test results and the nominal shear strength for seismic loads was obtained from

the cyclic tests. The nominal strength of the cyclic tests was taken as the average of the peak loads from the positive and negative quadrants of the hysteresis curve plot. In this test program, fastener spacing of 6-in., 4-in., and 2-in. were investigated, the nominal strengths for walls with 3 in. fastener spacing were determined by taking the average of nominal strengths for 4 in. and 2 in. fastener spacing. The same approach was also adopted by AISI Lateral Standard (2004).

The coupon tests indicate that the measured base metal (i.e., uncoated) thickness for 0.033-in. sheet steel (0.0358-in.) was greater than the design thickness (0.0346-in.), the nominal strength need to be adjusted by the ratio of  $0.0346/0.0358 = 0.966$  for 0.033-in. sheet steel shear walls. No adjustment is needed for the other shear wall configurations.

The variations between the measured tensile strength and the minimum specified value were also observed from the coupon tests. The nominal shear strengths were not adjusted according to the variation in the material tensile strength. Instead, minimum material strengths were required in order to use the nominal shear strengths resulting from this research. Future testing of shear wall assemblies with members that have close to specified strength may be completed in the future to determine what effect members with greater than the minimum specified strength have on a shear wall assembly. Most likely the shear wall component to affect the strength of the assembly the most will be the sheet steel sheathing. Based on the results of this research project, thickness-adjusted nominal shear strengths for sheet steel shear walls are summarized in Tables 6 and 7.

**Table 6 Recommended nominal shear strength for wind loads for shear walls<sup>1,2,3</sup>**  
(Pounds Per Foot)

Assembly Description	Aspect Ratio (h:w)	Fastener Spacing at Panel Edges (inches)			
		6	4	3	2
0.033" steel sheet, one side <sup>3</sup>	2:1	1037	1146	1225	1301
0.030" steel sheet, one side <sup>3</sup>	2:1	794	959	1007	1054
0.027" steel sheet, one side <sup>4</sup>	2:1	626	684	760	836
0.033" steel sheet, one side <sup>3</sup>	4:1	982	1114	1216	1315
0.030" steel sheet, one side <sup>3</sup>	4:1	882	950	1024	1097
Note: (1) Screws in the field of panel shall be installed 12 inch on center. (2) Sheet steel sheathing, wall studs, tracks, and blocking shall be of ASTM A1003 Grade 33 Type H steel with minimum yield strength, $F_y$ , of 43 ksi and a minimum tensile strength, $F_u$ , of 54 ksi. (3) Wall studs, tracks, and blocking shall be of 43 mils or thicker. (4) Wall studs, tracks, and blocking shall be of 33 mils or thicker.					



**Table 7 Recommended nominal shear strength for seismic loads for shear walls<sup>1,2,3</sup>  
(Pounds Per Foot)**

Assembly Description	Aspect Ratio (h:w)	Fastener Spacing at Panel Edges (inches)			
		6	4	3	2
0.033" steel sheet, one side <sup>3</sup>	2:1	1056	1169	1236	1304
0.030" steel sheet, one side <sup>3</sup>	2:1	911	1014	1042	1070
0.027" steel sheet, one side <sup>4</sup>	2:1	647	710	778	845
0.033" steel sheet, one side <sup>3</sup>	4:1	1097	1221	1268	1315
0.030" steel sheet, one side <sup>3</sup>	4:1	924	1053	1128	1203
Note: (1) Screws in the field of panel shall be installed 12 inch on center. (2) Sheet steel sheathing, wall studs, tracks, and blocking shall be of ASTM A1003 Grade 33 Type H steel with minimum yield strength, $F_y$ , of 43 ksi and a minimum tensile strength, $F_u$ , of 54 ksi. (3) Wall studs, tracks, and blocking shall be of 43 mils or thicker. (4) Wall studs, tracks, and blocking shall be of 33 mils or thicker.					

### Conclusions and Future Research

Monotonic and cyclic shear wall tests on cold-formed steel framed walls with steel sheet sheathing on one side were conducted. The nominal shear strengths for wind loads and seismic loads were established from the test results. The buckling of the steel sheathing and pull-out of sheathing screws were the primary failure modes for sheet steel shear walls. The flange distortion of the boundary studs in tension was also observed on the walls with 2"/12" screw spacing. It is recommended for the future research to investigate alternative sheathing fastener pattern on the boundary studs to mitigate the distortion of the stud flanges. In this research, 43-mil framing members were used for 0.030-in. and 0.033-in. sheathing, and 33-mil framing members were used for 0.027-in. sheathing. It is recommended to study the performance of the 0.030-in. and 0.033-in. sheet steel walls with 54-mil or thicker framing members, and the 0.027-in. sheet steel walls with 43-mil or thicker framing members.

### Acknowledgement

The sponsorship of American Iron and Steel Institute and the donation of materials by Steel Stud Manufacturers Association and Simpson Strong-Tie Company, Inc. are gratefully acknowledged. The assistance and guidance provided by Jeff Ellis, Jay Larson, and the other AISI COFS Lateral Design Task Group members is highly appreciated. The test specimens were prepared by UNT students Hitesh Vora, Tony Dainard, Jimmy Tucker, Pradeep Veetvkuri, the project could not be completed without their contributions.

**References**

- AISI Lateral Standard (2004). "AISI Standard for Cold-Formed Steel Framing – Lateral Design 2004 Edition", American Iron and Steel Institute, Washington, DC.
- ASTM A370-06 (2006) "A370-06 Standard Test Methods and Definitions for Mechanical Testing of Steel Products", American Society for Testing and Materials, West Conshohocken, PA.
- ASTM E564-06 (2006). "E564-06 Standard Practice for Static Load Test for Shear Resistance of Framed Walls for Buildings", American Society for Testing and Materials, West Conshohocken, PA.
- ASME B18.22.1 (1998). "Plan Washers", American Society of Mechanical Engineers, New York, NY.
- ICC-ES AC130 (2004). "Acceptance Criteria for Prefabricated Wood Shear Panels", ICC Evaluation Service, Inc., Whittier, CA.
- Serrette, R.L., Nguyen, H., Hall, G. (1996). "Shear wall values for light weight steel framing." Report No. LGSRG-3-96, Santa Clara University. Santa Clara, CA.
- Serrette, R.L. (1997). "Additional Shear Wall Values for Light Weight Steel Framing." Report No. LGSRG-1-97, Santa Clara University. Santa Clara, CA.
- Serrette, R.L. (2002). "Performance of Cold-Formed Steel-Framed Shear Walls: Alternative Configurations," Final Report:LGSRG-06-02, Santa Clara University.



## **Estimating the Effective Yield Strength of Cold-Formed Steel Light-Frame Shear Walls**

Reynaud Serrette <sup>1</sup>

### **Abstract**

Characterizing the seismic response of lateral force-resisting elements often requires an expression of the capability of these elements to sustain some portion of their peak strength at displacements well beyond their elastic limit. This paper presents an energy-based method for estimating the effective yield strength (elastic displacement limit) of cold-formed steel shear walls. The method considers the maximum usable wall displacement, the hysteretic envelope response of a wall and the expected performance of the system in which the wall is used. The resulting effective yield strength limit is shown to be consistent with interpretations of yield strength in performance-based engineering design and provides a rational basis for comparing the elastic stiffness of alternative shear wall configurations.

### **Introduction**

The seismic provisions in ASCE/SEI 7 (2005) limits the use of cold-formed steel (C-FS) light frame shear walls to bearing wall or building frame systems. For each system, seismic performance coefficients and factors (response modification coefficient,  $R$ , system overstrength coefficient,  $\Omega_o$ , and deflection amplification factor,  $C_d$ ) are specified depending on the sheathing material attached to the C-FS frame, the building height, use of the structure and the anticipated intensity of ground shaking. These coefficients and factors reflect

---

Associate Professor, Department of Civil Engineering, Santa Clara University,  
Santa Clara, CA 95053-0563, USA

the expectation that the dynamic characteristics, lateral resistance and energy dissipation capacity of the lateral-force resisting elements, when incorporated into the defined system, will result in some acceptable range of performance.

FEMA 450-2 (2004) notes that the basic objective of the current building code is the provision of “reasonable and prudent life-safety” at the code-level forces and lateral displacement limits. It is further noted that this objective “considers property damage as it relates to occupant safety for ordinary structures” and the expectation that for a major earthquake (2% chance of exceedance in 50 years) there is “some” margin of safety against collapse with associated structural damage that may not be economically repairable. Beyond the life-safety objective, however, the building code provides no explicit guidance for assessment of performance.

In response to the costly damage associated with wood light-frame construction in the 1994 Northridge earthquake (EERI 1996), a comprehensive 4-year woodframe research project was undertaken to “develop reliable and economical methods of improving woodframe building performance in earthquakes” (CUREE 2004a, 2004b). CUREE (2004a) describes the optimal performance of lateral-force resisting elements in wood light-frame construction as behavior that can “provide sufficient stiffness and high yield strength to survive a minor earthquake with minimal or no damage, and repairable structural damage and limited non-structural damage in a moderate earthquake.” Thus, at the element level, it appears CUREE associates the yield strength limit with “minimal to no damage.” Even though the term “yield strength” is used, CUREE (2004b) remarks that the notion of a defined yield strength in wood shear walls may not be appropriate due to the early onset of inelastic behavior in these elements. However, the notion of yield strength in the context of minimal to no damage of an element in an earthquake may be a useful analysis and design parameter.

SEAOC (1999) presented a set of “Tentative Guidelines for Performance-Based Seismic Engineering.” These guidelines identified five different system structural performance (SP) levels. For each SP level, two criteria, force-based and displacement-based, were proposed to define the target behavior/response at the specific level. Brief descriptions of these SP levels are presented in Table 1.

Although the SP level recommendations address system performance, SEAOC notes that until research shows otherwise, the system characteristics may serve as an acceptable surrogate for the performance requirements of elements. Adopting this approach, the yield strength limit/elastic displacement limit of a cold-formed steel frame shear wall may be interpreted as that point in the

measured wall response corresponding to minimal to zero inelastic displacement demand (that is, minimal to no damage).

Both the CUREE recommendations (2004a) and SEAOC's seismic performance level guidelines (1999) appear to support the concept of an effective yield strength limit based on minimal to no damage or minimal to zero inelastic displacement demand of the lateral element.

Table 1. SEAOC (1999) seismic performance (SP) levels

Structural Performance Level	Strength-Based	Displacement-Based
SP-1	Damage is negligible. Structural response corresponds to the effective yield limit state. Inelastic displacement capacity is substantially unused.	
	Structures designed to remain elastic. Strength design to achieve SP-1 at $R = 1.0$ .	Approximately 0% of the inelastic displacement capacity is used. $IDDR^1 \approx 0$ . System displacement ductility, $\mu_{system} = 1.0$ .
SP-2	Damage is minor to moderate. Inelastic response at $\frac{1}{2}$ the level expected for the 10% in 50-year earthquake.	
	Strength design to achieve SP-2 at $\frac{1}{2}$ the code specified $R$ .	Approximately 30% of the inelastic displacement capacity is used. $IDDR = 0.3$ . System displacement ductility, $\mu_{system} = 2.9$ .
SP-3	Damage is moderate to major. Inelastic response at the level expected for the 10% in 50-year earthquake.	
	Strength design to achieve SP-3 at the code specified $R$ (essentially the life-safety limit state addressed in the building code).	Approximately 60% of the inelastic displacement capacity is used. $IDDR = 0.6$ . System displacement ductility, $\mu_{system} = 4.8$ .
SP-4	Damage is major. Repairs may not be economically feasible. Residual strength, stiffness and margin against collapse are significantly reduced.	
	Strength design to achieve SP-4 at 1.5 times the code specified $R$ .	Approximately 80% of the inelastic displacement capacity is used. $IDDR = 0.8$ . System displacement ductility, $\mu_{system} = 6.0$ .
SP-5	Partial collapse is imminent or has occurred.	
	Should not be used as a design target.	100% of the inelastic displacement capacity is used. $IDDR = 1.0$ . This performance level should not be considered a design target.

<sup>1</sup> IDDR: Inelastic displacement demand ratio

Considering the intent of the building code as expressed in FEMA 450-2 (2004), the recommendations resulting from the CUREE studies (2004a, 2004b) and the recommendations contained in the SEAOC performance-based guidelines (1999), this paper presents a method for estimating the effective yield strength for cold-formed steel light-frame shear walls. The method is based on the concept of minimal to zero inelastic displacement demand at the effective yield strength limit state.

### ASTM E2126 Yield Strength Model

For light-frame shear walls, the most current adopted method for estimating the yield strength of the wall is described in ASTM E2126 (2007). E2126 states that the yield limit state (yield point) of a light frame shear wall may be determined as the point in the load-displacement relationship where the [secant] elastic shear stiffness of the assembly decreases 5 % or more. E2126 further suggests that for “nonlinear ductile elastic responses,” the yield point may be determined using the equivalent energy elastic-plastic (EEEE) curve to represent the envelope response of a tested shear wall (see Figure 1).

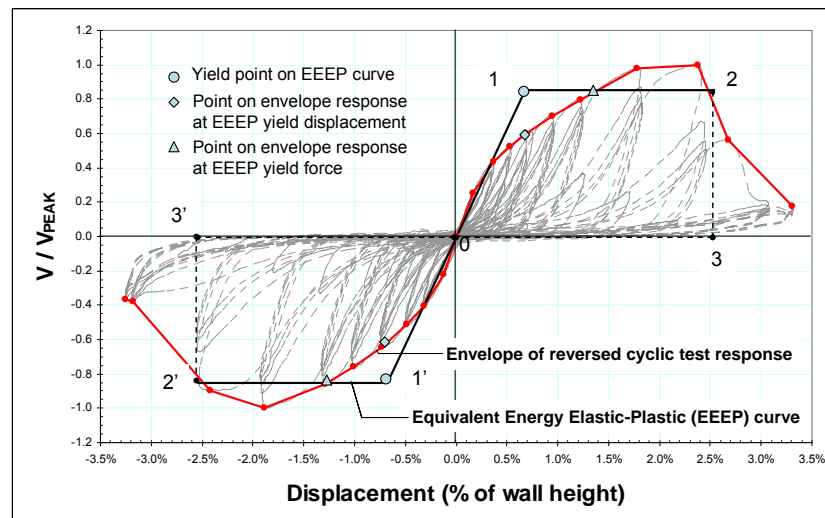


Figure 1. Yield point determination using the EEEP methodology

The 2007 North American Standard for Cold-Formed Steel Framing – Lateral Design (AISI S213) provides a commentary on the use of the EEEP methodology in the development of design values in this Standard.

Although, ASTM E2126 states when the EEEP method may be used, the Standard does not provide a basis for determining what constitutes “nonlinear ductile elastic response,” the trigger for using the EEEP method. For seismic design, ASCE/SEI 7 (2005) identifies three levels deformability (ratio of ultimate deformation to limit deformation) for elements: high-deformability elements, limited-deformability elements and low-deformability elements. These three levels are illustrated in Figure 2. If the idea that a ductile response is required to employ the EEEP method of analysis, a criterion related to element deformability may be useful for application of the EEEP method.

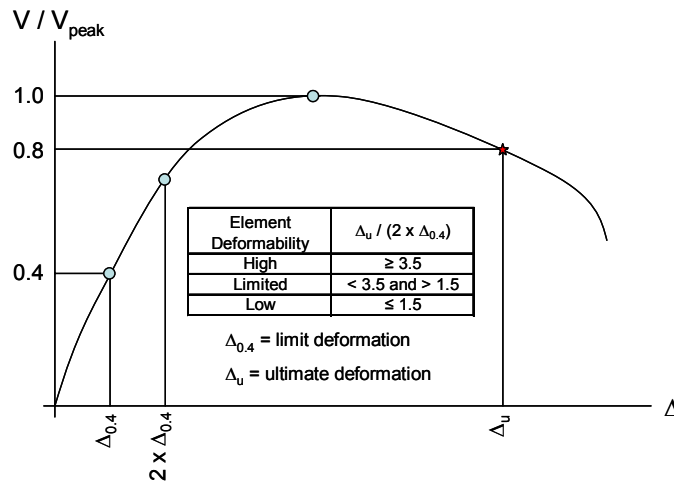


Figure 2. ASCE/SEI 7 Element deformability levels

The minimum yield strength permitted under the EEEP method is defined at 80% of the peak strength of the shear wall. Though this limit may have an historical reference, it does not appear to have a rational basis. At 80% of a cold-formed steel shear wall's peak strength, lateral displacement is likely to exceed SEAOC's (1999) structural performance level 1 (SP-1) limit, damage is likely to be beyond minimal with significant permanent displacement, and the assumption of an elastic response as defined in ASTM E2126 may not be applicable.



Application of the EEEP method alone to determine the yield strength limit does not capture the beneficial energy dissipating attributes of a more robust hysteretic response. Figure 3 illustrates, schematically, three hysteretic response envelopes for lateral-force resisting elements that may be installed in cold-formed steel light frame construction. Under the EEEP method, all three elements would be assigned the same performance characteristics, unless hysteretic energy is somehow taken into account. It is clear that the energy dissipated by the element with the robust hysteretic response should provide a superior performance, compared to the other responses, in terms of the energy dissipated within the system.

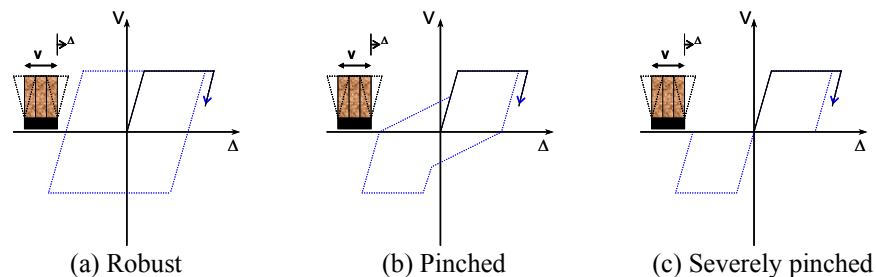


Figure 3. Schematic representation of hysteretic response envelopes

### Hysteretic Envelope Energy Balance (HEEB) Yield Strength Model

The hysteretic envelope energy balance (HEEB) methodology presented in this paper attempts to incorporate the equivalent energy elastic-plastic concept expressed in ASTM E2126 with the recommendations in CUREE and the SEAOC guidelines. The HEEB method employs a hysteretic model similar to that used for nonlinear dynamic analysis of buildings with light frame shear walls (Stewart 1987, CUREE 2002) with the exception that only the envelope response is considered.

Figure 4 shows the non-dimensionalized response of a reversed cyclically tested cold-formed steel shear wall. The envelope force-displacement response is overlaid on the hysteresis plot. To apply the HEEB method, the envelope hysteretic response is determined by considering the maximum usable displacement  $\Delta_u$ , the elastic stiffness  $K_o$  and the “pinching stiffness”  $K_p$ , as illustrated in Figure 4. To compute the energy enclosed by the envelope curve, it is assumed that at  $\Delta_u$ , the lateral element unloads with stiffness  $K_o$ . Unloading

is followed by loading in the opposite direction with an initial degraded, pinched stiffness  $K_p$  before the stiffness  $K_o$  is again achieved.

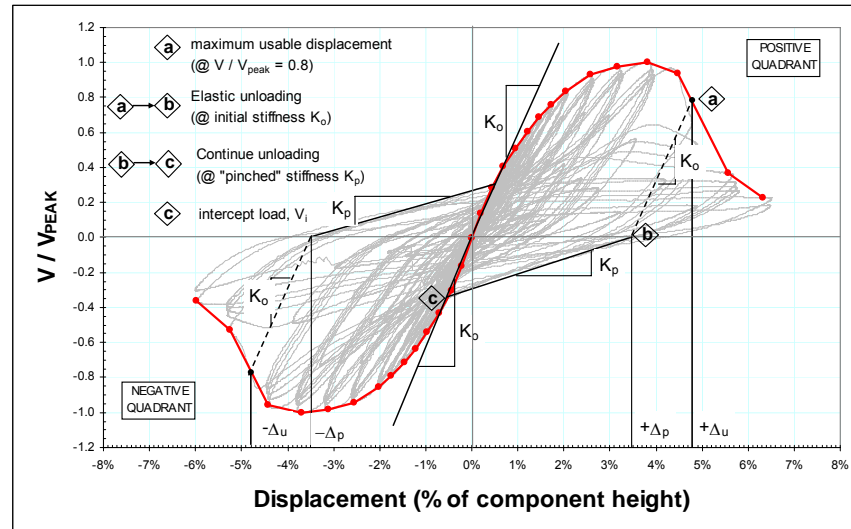


Figure 4. Development of the envelope hysteretic response envelope curve

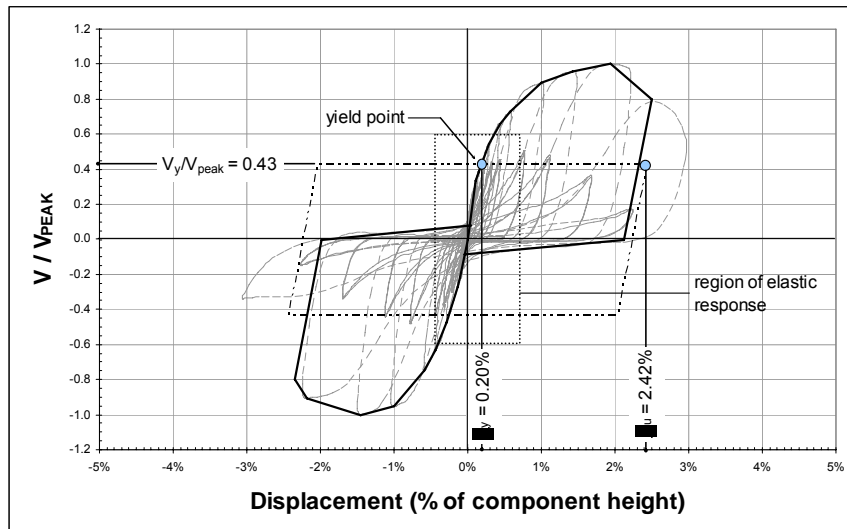
Referring to Figure 4, application of the proposed HEEB method is outlined below:

1. Develop the envelope curve for the lateral element.
2. Determine the peak lateral resistance  $V_{peak}$  and the corresponding lateral displacement  $\Delta_{V_{peak}}$  at  $V_{peak}$ .
3. Compute  $0.4V_{peak}$  and determine the lateral displacement  $\Delta_{0.4V_{peak}}$  at  $0.4V_{peak}$ .  $0.4V_{peak}$  is the limit deformation defined in ASCE/SEI 7.  $0.4V_{peak}$  also corresponds to maximum allowable stress design strength of a cold-formed steel frame shear wall based on a safety factor ( $\Omega$ ) of 2.5, as stated in the AISI Lateral Standard (AISI S213).
4. Compute the secant elastic stiffness,  $K_o$  as  $0.4V_{peak}/\Delta_{0.4V_{peak}}$ .
5. Define the maximum usable displacement  $\Delta_u$  at 80% of  $V_{peak}$  after the peak load point.  $\Delta_u$  is the ultimate deformation defined in ASCE/SEI 7.
6. Compute the permanent lateral displacement  $\Delta_p$  assuming the lateral element unloads elastically with an unload stiffness  $K_o$ .
7. From  $\Delta_p$  determine  $V_i$ , the intercept load for reload in the opposite direction using the pinched stiffness  $K_p$ .

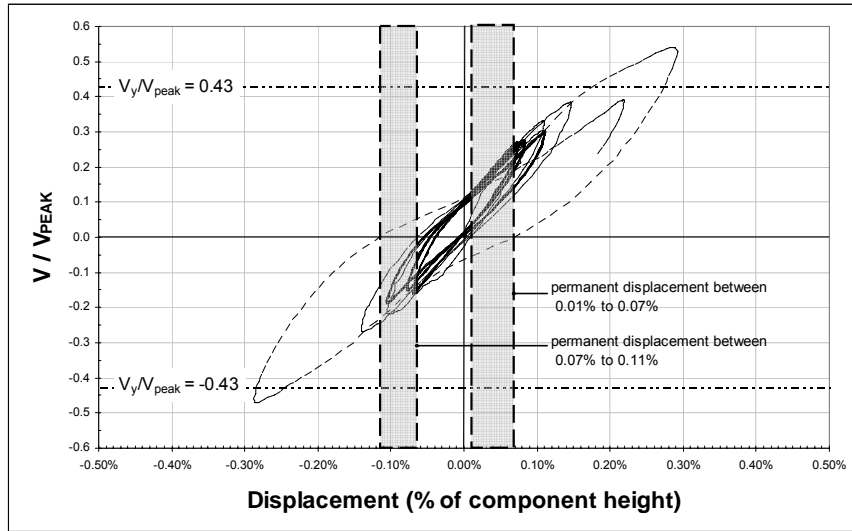
8. Repeat steps (2) through (7) for the loading in the opposite direction.
9. Compute the energy  $E_T$  enclosed by the resulting hysteretic envelope response.
10. Determine an equivalent robust elastic-plastic hysteresis response envelope defined by  $P_{yield}$  and the average (positive and negative quadrants)  $\Delta_u$ .
11. Determine the  $\Delta_y$  using  $P_{yield}$  and  $K_o$ .

### Application of the HEEB Yield Strength Model

Application of the HEEB procedure described above is illustrated in Figures 6 and 7 using data from Branston (2004) and Serrette (1996). The Branston data represents the response of a 1220 mm long by 2440 mm tall shear wall with 11 mm OSB rated sheathing attached to 43-mil framing with No. 8 screws. The screw schedule for the Branston wall was 152 mm at the panel edges and 305 mm in the panel field, and the wall was tested using the CUREE protocol (Krawinkler 2002). The Serrette data represents the response of a similar wall: 1220 mm long and 2440 mm tall with 11 mm OSB rated sheathing attached to 33-mil framing with No. 8 screws. The screw schedule was also similar to the wall in the Branston test and the wall was tested using the sequential phased displacement (SPD) protocol (SEAOSC 1997).

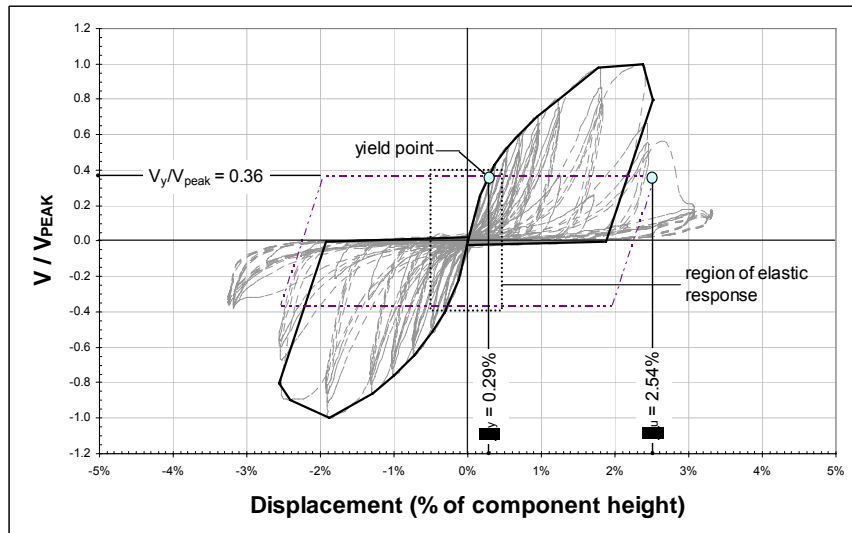


(a) Yield point

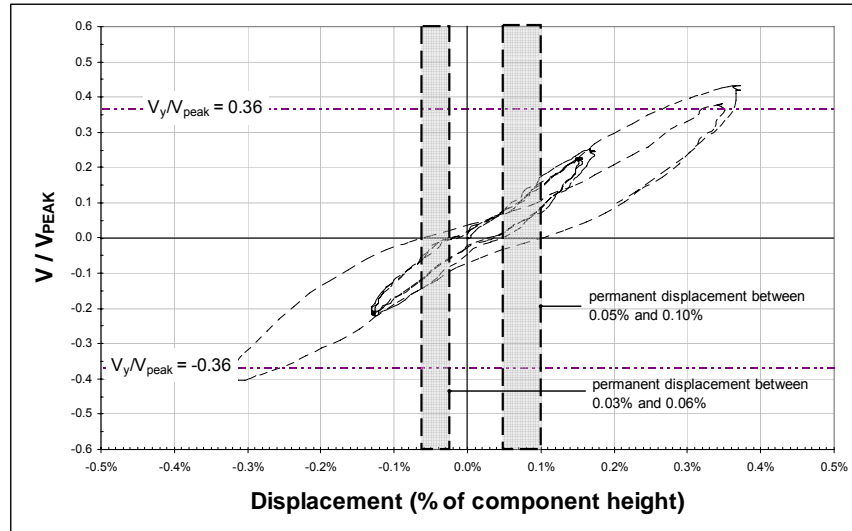


(b) Inelastic displacement demand at yield

Figure 6. HEEB analysis of Branston test data



(a) Yield point



(b) Inelastic displacement demand at yield

Figure 7. HEEB analysis of Serrette test data

As illustrated in both Figures 6(b) and 7(b), at displacements in the region on the computed yield strength/elastic limit, the permanent (unload) displacement from both tests is less than 0.11% of the wall height. At this displacement level, the behavior is essentially elastic and there is minimal demand on the inelastic displacement capacity of the walls. Thus, it appears that the HEEB model provides a result consistent with both the CUREE (2004a, 2004b) recommendations and the SEAOC performance-based guidelines (1999). Additionally, the HEEB yield point provides a relatively accurate assessment of the region in the shear wall response where a shift in the dynamic response (period shift) is likely to occur.

#### Comparison of ASTM E2126 and HEEB Yield Strength Models

Figures 8 and 9 compare the computed effective yield points for the Branston and Serrette tests, respectively, using the EEEP and the HEEB methods. As shown in these figures, the load and displacement defining the EEEP yield point occur at different positions along the envelope curve, and the yield point itself may not be in close proximity to the response envelope. Unlike the EEEP yield

point, the HEEB yield point lies on the response curve (or very close based on averaging of the positive and negative excursions).

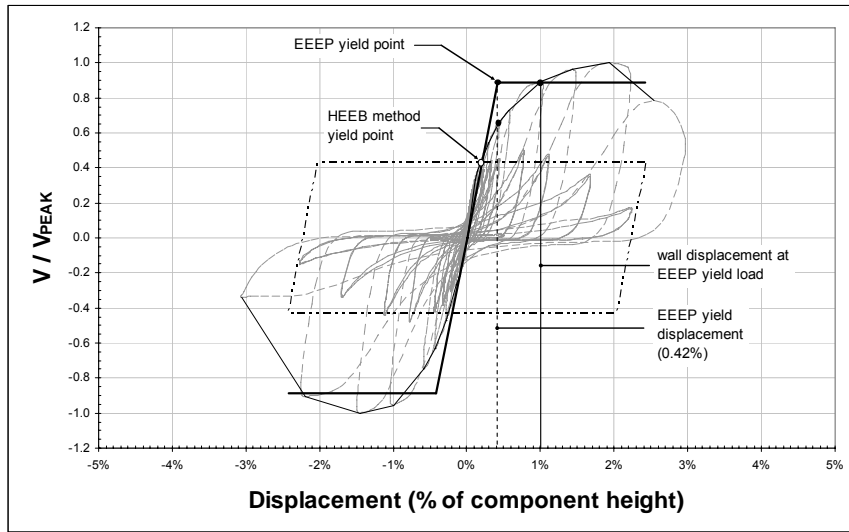


Figure 8. Comparison of EEP yield and HEEB yield—Branston's data

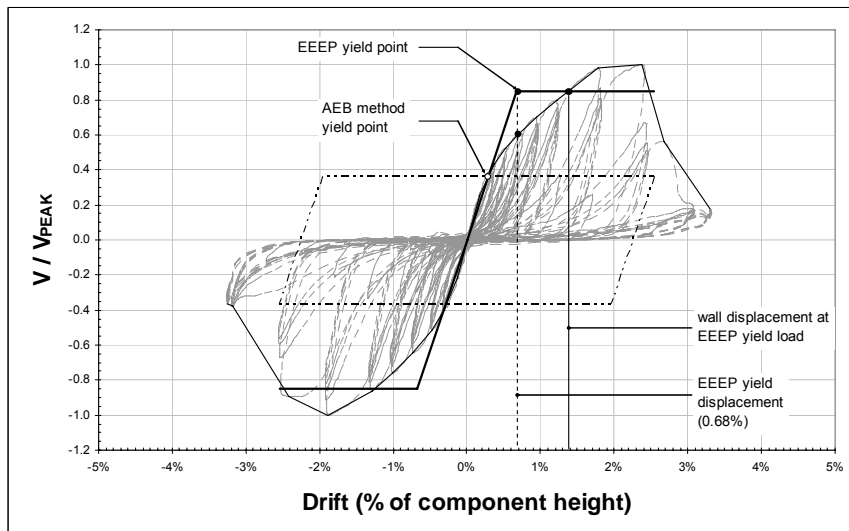


Figure 9. Comparison of EEP yield and HEEB yield—Serrette's data

Another distinctive difference between the results from EEEP and HEEB methods is the ratio of maximum usable displacement,  $\Delta_u$ , to the yield/elastic limit displacement,  $\Delta_y$ . In the examples presented, the EEEP  $\Delta_u$  to  $\Delta_y$  ratios for the Branston and Serrette tests were 5.76 and 3.73, respectively. The corresponding HEEB ratios were 12.1 and 8.76.

The SEAOC performance-based engineering guidelines recommended use of the system performance requirements for the elements in the system (pending the development of alternative requirements). Thus, for the maximum considered earthquake (MCE), equivalent to SP-4 in Table 1, the strength level displacement may be related to the maximum usable displacement by the factor 1.5R. Assuming  $R = 6.5$  (wood structural panel or sheet steel cold-formed steel frame shear walls in bearing wall buildings—ASCE/SEI 7), the ratio of the displacement at MCE to the strength level displacement would be 9.75 ( $= 1.5 \times 6.5$ ). If the yield value from the HEEB methodology is considered representative of or close to the strength level design value for the walls, the 12.1 and 8.76 values appear reasonable. Probable relationships between the yield strength and design values using the HEEB yield strength is beyond the scope of this paper.

### **Conclusion**

This paper presented an energy-based method for estimating the elastic limit displacement/effective yield strength of cold-formed steel frame shear walls. The method, referred to as the hysteretic envelope energy balance (HEEB) method, was shown to provide results consistent with the assumption of minimal to no damage or minimal demand on the inelastic displacement capacity of the wall at the effective yield strength. In addition, the derived effective yield strength provided a relatively accurate assessment of the point at which a shift in the dynamic response of the shear wall is likely to occur.

**References**

AISI S213 (2007). North American Standard for Cold-Formed Steel Framing – Lateral Design, American Iron and Steel Institute, Washington, DC.

ASCE/SEI 7 (2005). Minimum Design Loads for Buildings and Other Structures, American Society of Civil Engineers, Reston, VA.

ASTM E2126 (2007). Standard Test Methods for Cyclic (Reversed) Load Test for Shear Resistance of Vertical Elements of the Lateral Force Resisting Systems for Buildings, ASTM International, West Conshohocken, PA.

Branston, A. E. (2004). “Development of a Design Methodology for Steel Frame / Wood Panel Shear Walls,” M. Eng. Thesis, Department of Civil Engineering and Applied Mechanics, McGill University, Montréal, Québec.

CUREE (2002). A Computer Program for Seismic Analysis of Woodframe Structures, Consortium of Universities for Research in Earthquake Engineering (CUREE), CUREE Publication No. W-21, Richmond, CA.

CUREE (2004a). Recommendations for Earthquake Resistance in the Design and Construction of Woodframe Buildings – Part I: Recommendations, Consortium of Universities for Research in Earthquake Engineering (CUREE), CUREE Publication No. W-30a, Richmond, CA.

CUREE (2004b). Recommendations for Earthquake Resistance in the Design and Construction of Woodframe Buildings – Part II: Topical Discussions, Consortium of Universities for Research in Earthquake Engineering (CUREE), CUREE Publication No. W-30b, Richmond, CA.

EERI (1996). Northridge Earthquake of January 17, 1994 Reconnaissance Report - Volume 2, Earthquake Spectra, Earthquake Engineering Research Institute, Oakland, CA.

FEMA 450-2 (2004). NEHRP Recommended Provisions for Seismic Regulations for New Buildings and Other Structures – Part 2: Commentary, Building Seismic Safety Council, Washington, DC.

Krawinkler, H., et. al. (2000). “Development of a Testing Protocol for Woodframe Structures”, CUREE Publication No. W-02, Consortium of Universities for Research in Earthquake Engineering (CUREE), Richmond, CA.



SEAOC (1999). Recommended Lateral Force Requirements and Commentary – Seventh Edition, Structural Engineers Association of California, Sacramento, CA.

SEAOSC (1997). Standard Method for Cyclic (Reversed) Load Test for Shear Resistance of Framed Walls for Buildings, Structural Engineers Association of Southern California, Whittier, CA.

Serrette, R. L. et. al. (1996). “Shear Wall Values for Light Weight Steel Framing,” Report No. LGSRG-3-96, Light Gauge Steel Research Group, Department of Civil Engineering, Santa Clara University, Santa Clara, CA.

Stewart, W. G. (1987). “The Seismic Design of Plywood Sheathed Shear Walls,” Ph.D. Dissertation, University of Canterbury, New Zealand.

## **Effect of Varied Imperfections on Bracing Demand of Cold-Formed Steel Stud Walls**

Thomas Sputo<sup>1</sup>, Kevin Beery<sup>2</sup>, and Edgar Wong<sup>3</sup>

### **Abstract**

The purpose of this analytical study was to determine the effect of varied out-of-straightness imperfection on the bracing strength and stiffness demand of multiple cold-formed steel stud walls. This study is an extension of previous work performed to develop relationships between the required brace strength and stiffness for bridging of multiple stud walls and the required brace strength and stiffness of a single stud. Eight-foot tall walls with three different imperfections were analyzed using critical buckling analysis. The required cross-sectional area to prevent buckling was determined and the critical brace force and stiffness were calculated for various magnitudes of imperfection. Critical brace strength was found to accumulate directly as a multiple of the number of studs, regardless of stud out-of-straightness. Critical brace stiffness is not directly related to the number of studs, but a relationship was formulated that is independent of stud out-of-straightness. The required brace strength and stiffness of a multiple stud wall with a specified initial imperfection can thus be related to the required brace strength and stiffness of a single stud for any magnitude of imperfection.

---

<sup>1</sup> Senior Lecturer, Department of Civil and Coastal Engineering, 365 Weil Hall, University of Florida, Gainesville, FL 32611 (email: [sputo@ufl.edu](mailto:sputo@ufl.edu))

<sup>2</sup> Graduate Student, Department of Civil and Coastal Engineering, 365 Weil Hall, University of Florida, Gainesville, FL 32611

<sup>3</sup> Graduate Student, Department of Civil and Coastal Engineering, 365 Weil Hall, University of Florida, Gainesville, FL 32611

## Introduction

Previous research (Green, Sputo, Urala, 2004) was conducted to determine the required bracing strength and stiffness to provide for bracing a single stud against flexural buckling. From a series of tests, the following equations for required brace strength and stiffness were developed for a single stud:

$$\begin{aligned} \text{Required Brace Strength:} & \quad P_{br,1} = 0.01 P_n \\ \text{Required Brace Stiffness:} & \quad \beta_{br,1} = 2(4-2/n)P_n / L_b \end{aligned}$$

where:

$$\begin{aligned} P_n &= \text{nominal strength of stud} \\ L_b &= \text{unbraced length of stud} \\ n &= \text{number of brace points} \end{aligned}$$

The AISI *Specification* (2007) has incorporated these provisions in Section D3.3 (Bracing of Axially Loaded Compression Members)

In a further study (Beery and Sputo, 2006), the required brace strength and stiffness demand of a multiple stud wall was related to the number of studs and the brace strength and stiffness of a single stud. In this analytical study, walls comprised of up to 30 studs were analyzed using MASTAN2, where each of the studs was modeled with an out-of-straightness in the same direction of  $L/384$ . 8-foot walls and 12-foot walls were studied using both elastic critical load analysis and second-order elastic analysis and the following equations were recommended:

$$\begin{aligned} \text{Required Brace Strength:} & \quad P_{br,n} = n_s * P_{br,1} \\ \text{Required Brace Stiffness:} & \quad \beta_{br,n} = \beta_{br,1} & \text{for } n_s=1 \\ & \quad \beta_{br,n} = \beta_{br,1} [0.4 n_s^2 + 0.5 n_s] & \text{for } n_s>1 \end{aligned}$$

where:

$$\begin{aligned} P_{br,1} &= \text{required brace strength for a single stud} \\ \beta_{br,1} &= \text{required brace stiffness for a single stud} \\ n_s &= \text{number of studs (anchored at one end)} \\ &= \text{1/2 the number of studs (anchored at both ends)} \end{aligned}$$

The modeled out-of-straightness of  $L/384$  was derived from the ASTM C-955 maximum allowable out-of-straightness of  $L/384$ . The intent of the work reported on in this paper was to develop similar relationships for brace strength

and stiffness requirements for multiple stud walls with differing imperfections. Imperfections of L/384, L/480, and L/960 were studied. Brace strength and stiffness for these multiple stud walls were related to the number of studs in the wall and the required brace strength and stiffness of a single stud.

### **Methodology**

Models of stud walls were created in MASTAN2 (2002). The studs were eight feet tall, spaced at 24 inches on center, with a single line of horizontal bridging at mid-height. The bridging was modeled as a series of rigid links with pinned ends at the stud connection. One set of models was anchored to a fixed point at one end of the wall as shown in Figure 1. The other set of models was anchored to fixed points at both ends of the wall as shown in Figure 2. Walls comprised of 1, 5, 10, 15, 20, 25, and 30 studs were analyzed with out-of-straightness of L/384, L/480, and L/960. An axial load of 1 kip was applied to each stud, and a critical buckling analysis was performed, at which the load ratio at failure was noted. The cross sectional area of the bracing was incrementally increased until the wall failed in second mode buckling. The area and brace force were recorded and equations for critical brace strength and stiffness were then formulated. These equations are a function of the number of studs in the wall and the bracing requirements for a single stud with specified out-of-straightness.

### **Results**

The results of the analysis are tabulated in Tables 1 through 18.

Tables 1 and 2 tabulate the relationships between stiffness and brace force for one through thirty studs, anchored on one end, with an out of straightness of L/384, for the critical brace stiffness and two times the critical brace stiffness. Table 3 formulates equations for brace stiffness and brace force as functions of the number of braced studs. Likewise Tables 4 through 6 illustrate this for studs with an out-of-straightness of L/480, and Tables 7 through 9 for studs with an out-of-straightness of L/960. The stiffness ratio versus the number of braced studs for the varied out-of-straightnesses is plotted in Figure 3 and the strength ratio versus the number of braced studs for the varied out-of-straightnesses is plotted in Figure 4. It can be seen that the magnitude of the out-of-straightness plays little role in the accumulation of required brace stiffness and strength.

Tables 10 and 11 tabulate the relationships between stiffness and brace force for one through thirty studs, anchored on both ends, with an out of straightness of L/384, for the critical brace stiffness and two times the critical brace stiffness. Table 12 formulates equations for brace stiffness and brace force as functions of

the number of braced studs. Likewise Tables 13 through 15 illustrate this for studs with an out-of-straightness of  $L/480$ , and Tables 16 through 18 for studs with an out-of-straightness of  $L/960$ . The stiffness ratio versus the number of braced studs for the varied out-of-straightnesses is plotted in Figure 5 and the strength ratio versus the number of braced studs for the varied out-of-straightnesses is plotted in Figure 6. It can be seen that the magnitude of the out-of-straightness plays little role in the accumulation of required brace stiffness and strength.

As a rule, the critical brace strength of a single stud decreases as out-of-straightness is decreased. However, the critical brace strength of multiple studs also decreases, and the relationship remains the same. The critical brace stiffness does not change with different values of stud out-of-straightness. Therefore, the relationships previously derived still hold true.

For the walls anchored on both ends, half of the braces transfer force in tension, while half the braces transfer force in compression. For out-of-straightness of  $L/384$  and  $L/480$ , the compressive force in the brace exceeds the buckling capacity of a typical CRC bridging channel in walls with 15 or more studs. These results were obtained in previous research (Beery and Sputo, 2006) and were expected. However, for an out-of-straightness of  $L/960$ , the compressive brace force did not exceed the brace's capacity. This result is encouraging, since most studs are manufactured to a tighter tolerance than the ASTM C-955 tolerance of  $L/384$ .

### **Conclusions**

The results of this study indicate that the equations for the accumulation of bracing stiffness demand and brace strength are independent of the magnitude of out-of-straightness.

**Table 1.** Calculated relationships at critical stiffness, L/384, with anchor at one end

Number of Studs	30	25	20	15	10	5	1
A brace (in <sup>2</sup> )	0.2576	0.1801	0.1164	0.0666	0.0306	0.0084	0.0007
L brace (in)	720.0	600.0	480.0	360.0	240.0	120.0	24.00
$\beta_{br,n}$ (kips/in)	316.6	221.4	143.1	81.81	37.58	10.35	0.8369
$\beta_{br,n} / \beta_{br,1} * n$	12.61	10.58	8.548	6.517	4.490	2.474	1.000
$P_{br,n} / P_{br,1}$	31.51	26.24	20.97	15.70	10.43	5.167	1.000

**Table 2.** Calculated relationships at twice critical stiffness, L/384, with anchor at one end

Number of Studs	30	25	20	15	10	5	1
A brace (in <sup>2</sup> )	0.2576	0.1801	0.1164	0.0666	0.0306	0.0084	0.0007
L brace (in)	720.0	600.0	480.0	360.0	240.0	120.0	24.00
$\beta_{br,n}$ (kips/in)	316.6	221.4	143.1	81.81	37.58	10.35	0.8369
$\beta_{br,n} / \beta_{br,1} * n$	12.61	10.58	8.548	6.517	4.490	2.474	1.000
$P_{br,n} / P_{br,1}$	30.77	25.63	20.49	15.35	10.22	5.086	1.000

**Table 3.** Formulated equations, L/384 with anchor at one end

Condition	Stiffness	Brace Force
Beta	$y = 0.4056x + 0.4379$	$y = 1.0538x - 0.1061$
2Beta	$y = 0.4056x + 0.4379$	$y = 1.0273x - 0.0531$

**Table 4.** Calculated relationships at critical stiffness, L/480, anchored at one end

Number of Studs	30	25	20	15	10	5	1
A brace	0.2576	0.1801	0.1164	0.0666	0.0306	0.0084	0.0007
L brace	720.0	600.0	480.0	360.0	240.0	120.0	24.00
$\beta_{br,n}$	316.6	221.4	143.1	81.81	37.58	10.35	0.8369
$\beta_{br,n} / \beta_{br,1} * n$	12.61	10.58	8.548	6.517	4.490	2.474	1.000
$P_{br,n} / P_{br,1}$	31.50	24.95	20.96	14.77	10.43	5.169	1.000

**Table 5.** Calculated relationships at twice critical stiffness, L/480 with anchor at one end

Number of Studs	30	25	20	15	10	5	1
A brace	0.2576	0.1801	0.1164	0.0666	0.0306	0.0084	0.0007
L brace	720.0	600.0	480.0	360.0	240.0	120.0	24.00
$\beta_{br,n}$	316.6	221.4	143.1	81.81	37.58	10.35	0.8369
$\beta_{br,n} / \beta_{br,1} * n$	12.61	10.58	8.548	6.517	4.490	2.474	1.000
$P_{br,n} / P_{br,1}$	29.63	25.77	20.49	15.20	10.22	4.030	1.000

**Table 6.** Formulated equations, L/480 with anchor at one end

Condition	Stiffness	Brace Force
Beta	$y = 0.4056x + 0.4379$	$y = 1.0366x - 0.1781$
2Beta	$y = 0.4056x + 0.4379$	$y = 1.0282x - 0.4374$

**Table 7.** Calculated relationships at critical stiffness, L/960 with anchor at one end

Number of Studs	30	25	20	15	10	5	1
A brace (in <sup>2</sup> )	0.2576	0.1801	0.1164	0.0666	0.0306	0.0084	0.0007
L brace (in)	720.0	600.0	480.0	360.0	240.0	120.0	24.00
$\beta_{br,n}$ (kips/in)	316.6	221.4	143.1	81.81	37.58	10.35	0.8369
$\beta_{br,n} / \beta_{br,1} * n$	12.61	10.58	8.548	6.517	4.490	2.474	1.000
$P_{br,n} / P_{br,1}$	31.48	26.21	20.95	15.68	10.42	5.162	1.000

**Table 8.** Calculated relationships at twice critical stiffness, L/960 with anchor at one end

Number of Studs	30	25	20	15	10	5	1
A brace (in <sup>2</sup> )	0.5152	0.3602	0.2328	0.1331	0.0611	0.0169	0.0136
L brace (in)	720.0	600.0	480.0	360.0	240.0	120.0	24.00
$\beta_{br,n}$ (kips/in)	633.3	442.7	286.2	163.6	75.15	20.71	16.74
$\beta_{br,n} / \beta_{br,1} * n$	1.261	1.058	0.8548	0.6517	0.4490	0.2474	1.000
$P_{br,n} / P_{br,1}$	30.75	25.61	20.48	15.35	10.21	5.083	1.000

**Table 9.** Formulated equations, L/960 with anchor at one end

Condition	Stiffness	Brace Force
Beta	$y = 0.4056x + 0.4379$	$y = 1.0528x - 0.1065$
2Beta	$y = 0.4056x + 0.4379$	$y = 1.0265x - 0.0496$



**Table 10.** Calculated relationships at critical stiffness, L/384 with anchors at both ends

Number of Studs	15	10	5	1
A brace (in <sup>2</sup> )	0.0178	0.0084	0.0026	0.0003
L brace (in)	360.0	240.0	120.0	24.00
$\beta_{br,n}$ (kips/in)	21.85	10.36	3.134	0.4199
$\beta_{br,n} / \beta_{br,1} * n$	3.498	2.488	1.505	1.008
$P_{br,n} / P_{br,1}$	7.800	5.168	2.550	0.5009

**Table 11** Calculated relationships at twice critical stiffness, L/384 with anchors at both ends

Number of Studs	15	10	5	1
A brace (in <sup>2</sup> )	0.0356	0.0169	0.0051	0.0007
L brace (in)	360.0	240.0	120.0	24.00
$\beta_{br,n}$ (kips/in)	43.71	20.73	6.269	0.8398
$\beta_{br,n} / \beta_{br,1} * n$	3.498	2.488	1.505	1.008
$P_{br,n} / P_{br,1}$	7.6551	5.0862	2.5261	0.5006

**Table 12.** Formulated equations, L/384 with anchors at both ends

Condition	Stiffness	Brace Force
Beta	$y = 0.3615x + 0.7242$	$y = 1.0435x - 0.0388$
2Beta	$y = 0.3615x + 0.7242$	$y = 1.0224x - 0.0200$

**Table 13.** Calculated relationships at critical stiffness, L/480 with anchors at both ends

Number of Studs	15	10	5	1
A brace (in <sup>2</sup> )	0.0178	0.0084	0.0026	0.0003
L brace (in)	360.0	240.0	120.0	24.00
$\beta_{br,n}$ (kips/in)	21.85	10.36	3.134	0.4199
$\beta_{br,n}/\beta_{br,1} * n$	3.493	2.485	1.503	1.007
$P_{br,n}/P_{br,1}$	7.795	5.418	2.673	0.5251

**Table 14.** Calculated relationships at twice critical stiffness, L/480 with anchors at both ends

Number of Studs	15	10	5	1
A brace (in <sup>2</sup> )	0.0356	0.0169	0.0051	0.0007
L brace (in)	360.0	240.0	120.0	24.00
$\beta_{br,n}$ (kips/in)	43.71	20.73	6.269	0.8398
$\beta_{br,n}/\beta_{br,1} * n$	3.493	2.485	1.503	1.007
$P_{br,n}/P_{br,1}$	7.653	5.086	2.526	0.5005

**Table 15.** Formulated equations, L/480 with anchors at both ends

Condition	Stiffness	Brace Force
Beta	$y = 0.361x + 0.7232$	$y = 1.044x + 0.0572$
2Beta	$y = 0.361x + 0.7232$	$y = 1.022x - 0.0196$

**Table 16.** Calculated relationships at critical stiffness, L/960 with anchors at both ends

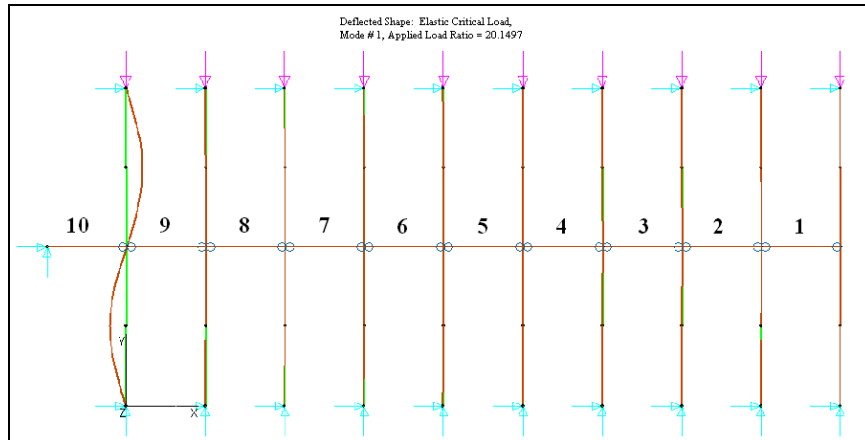
Num Studs	30	25	20	15	10	5	1
A brace (in <sup>2</sup> )	0.0666	0.0469	0.0306	0.0178	0.0084	0.0026	0.0003
L brace (in)	720.0	600.0	480.0	360.0	240.0	120.0	24.00
$\beta_{br,n}$ (kips/in)	81.83	57.59	37.59	21.85	10.36	3.13	0.4199
$\beta_{br,n}/\beta_{br,1} * n$	6.518	5.505	4.491	3.482	2.477	1.498	1.003
$P_{br,n}/P_{br,1}$	15.68	13.05	10.42	7.790	5.164	2.547	0.5004

**Table 17.** Calculated relationships at twice critical stiffness, L/960 with anchors at both ends

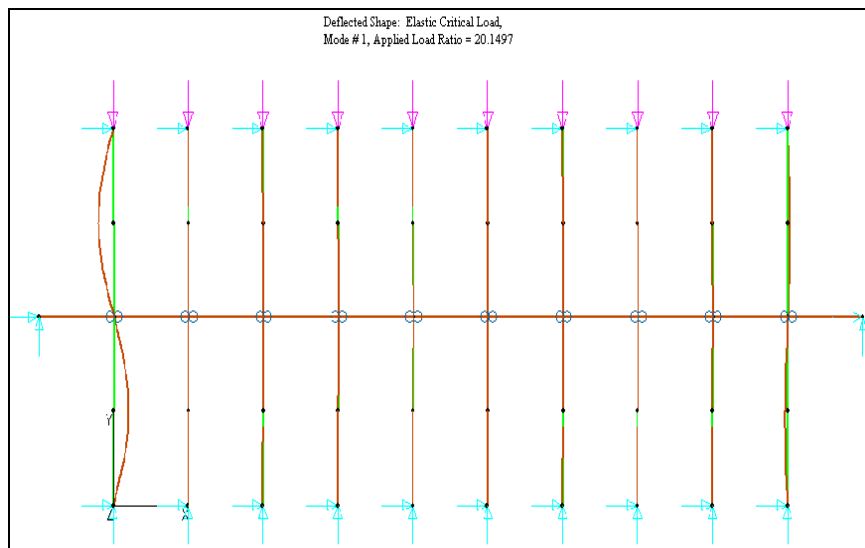
Number of Studs	30	25	20	15	10	5	1
A brace (in <sup>2</sup> )	0.1331	0.0937	0.0612	0.0356	0.0169	0.0051	0.0007
L brace (in)	720.0	600.0	480.0	360.0	240.0	120.0	24.00
$\beta_{br,n}$ (kips/in)	163.7	115.2	75.18	43.71	20.73	6.269	0.8398
$\beta_{br,n}/\beta_{br,1} * n$	6.518	5.505	4.491	3.482	2.477	1.498	1.003
$P_{br,n}/P_{br,1}$	15.35	12.78	10.21	7.649	5.083	2.524	0.5002

**Table 18.** Formulated equations, L/960 with anchors at both ends

Condition	Stiffness	Brace Force
Beta	$y = 0.3884x + 0.6267$	$y = 1.0482x - 0.0577$
2Beta	$y = 0.3884x + 0.6267$	$y = 1.0249x - 0.0307$



**Figure 1.** Model of 10-stud wall anchored on one end with 8-foot studs at 24 inches on center



**Figure 2.** Model of 10-stud wall braced on both ends with 8-foot studs at 24 inches on center.

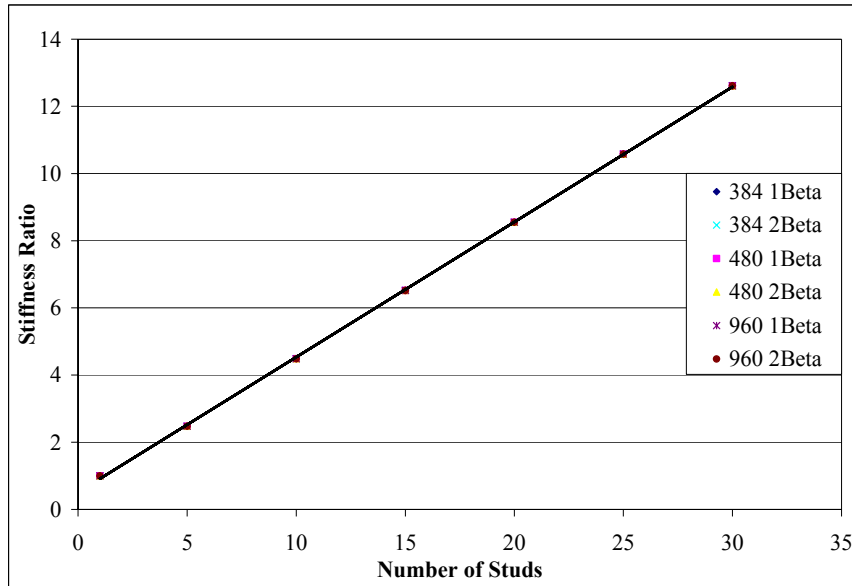


Figure 3. Stiffness ratio vs. number of studs, anchored on one end

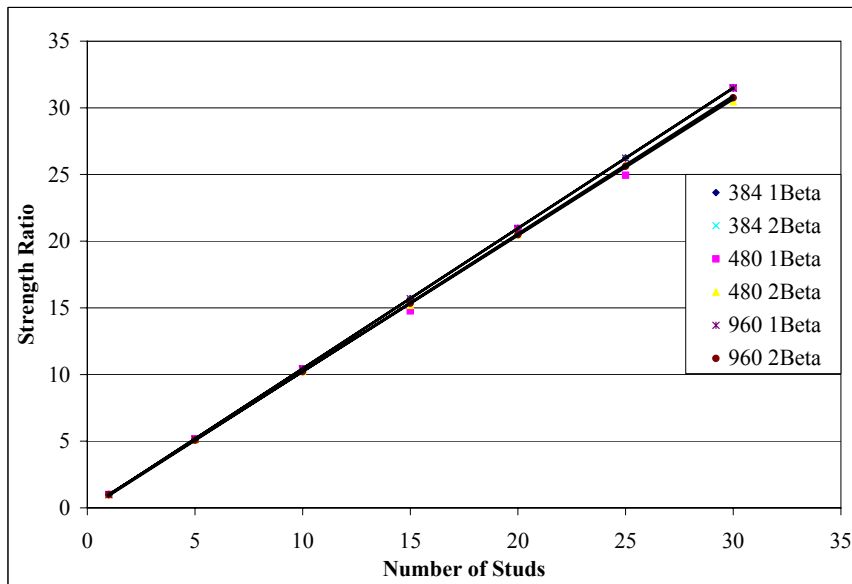


Figure 4. Strength ratio vs. number of studs, anchored at one end

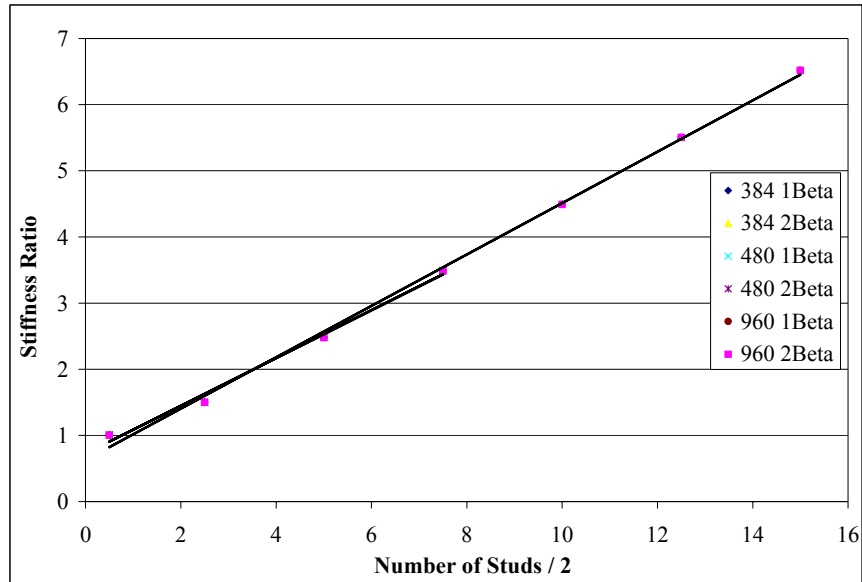


Figure 5. Stiffness ratio vs. number of studs, anchored at both ends

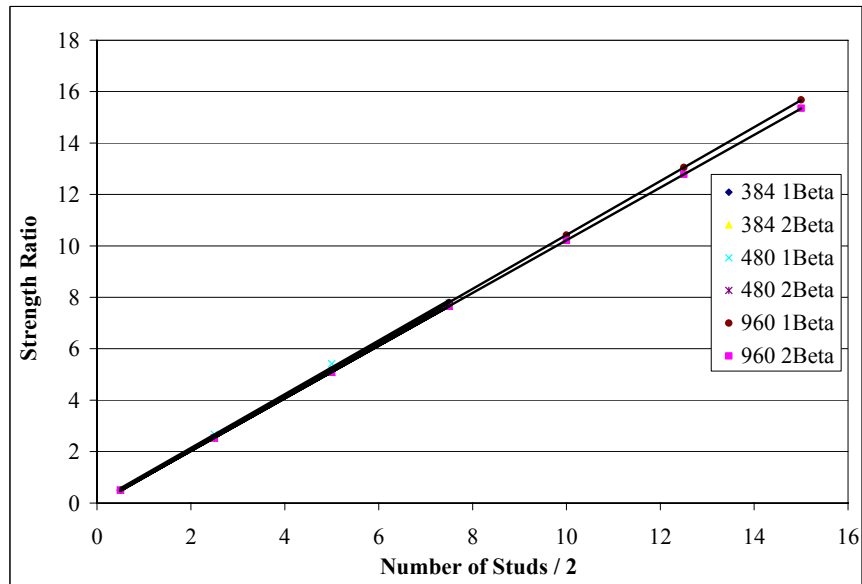


Figure 6. Strength ratio vs. number of studs, anchored at both ends

**References**

American Iron and Steel Institute (AISI) (2007). *North American Specification for the Design of Cold-Formed Steel Structural Members and Commentary*, Washington DC.

Beery, K. and Sputo, T. (2006). "Accumulation of bracing strength and stiffness demand in cold-formed steel stud walls." *Proceedings, 18th International Specialty Conference on Cold-Formed Steel*, Orlando, FL.

Green, P.S., Sputo, T. and Urala, V. (2004). "Bracing strength and stiffness requirements for axially loaded lipped cee studs." *Proceedings, 17th International Specialty Conference on Cold-Formed Steel*, Orlando, FL.

MASTAN2 (2002), Version 2.0.

## **Finite Element Analytical Investigation of Torsional Bracing Requirements for Cold-Formed Steel C-Shaped Studs**

Jennifer Tovar<sup>1</sup>, Todd Helwig<sup>2</sup>, and Thomas Sputo<sup>3</sup>

### **Abstract**

This paper provides an overview of an investigation on the torsional bracing behavior of C-shaped cold-formed steel studs. Typical bracing details for the C-shaped studs consist of a steel channel that restrains twist of the cross section. Three-dimensional finite element models were used to investigate the stiffness behavior for stability braces used to improve the torsional buckling performance of the studs. The lipped C-shaped section was modeled with pin-ended boundary conditions for the stud. Multiple models of the torsional brace were evaluated including a shell element model of a bracing channel as well as several “simpler” spring configurations. The development of these models and appropriate modeling techniques for bracing is discussed in detail. Difficulties in capturing the distortional behavior in the thin walled stud are discussed. Results from eigenvalue buckling solutions are presented. Recommendations are made for extending the use of these models to a broader range of stud sizes and analysis types to obtain recommendations for torsional bracing requirements of typical cold-formed wall studs.

---

<sup>1</sup> Structural Engineer, Schwab Structural Engineering, Inc., 555 IH 35 South, Suite 230, New Braunfels, TX 78130

<sup>2</sup> Assistant Professor, Department of Civil, Architectural and Environmental Engineering, The University of Texas at Austin, 1 University Station C1748, Austin, TX 78712-0273

<sup>3</sup> Senior Lecturer, Department of Civil and Coastal Engineering, 365 Weil Hall, University of Florida, Gainesville, FL 32611 (email: sputo@ufl.edu)



## Introduction

The capacity of cold-formed lipped-*cee* studs can be controlled by either global or local buckling modes. The possible modes consist of flexural, torsional, and torsional-flexural global modes as well as local and distortional buckling effects. Discrete bracing is often utilized to improve the global buckling behavior, and therefore increase the overall stud capacity. Discrete bracing recommendations have been provided for hot-rolled structural steel through the American Institute of Steel Construction (AISC) *Specification* since 1999. A summary of the developmental work for the AISC *Specification* (2005) provisions are provided in Yura (1995). Although the AISC *Specification* does not provide torsional bracing recommendations for columns, the basic requirements were developed and discussed by Helwig and Yura (1999). The basic principals from these previous studies have direct applications for cold-formed structures, however the thin-walled nature of these shapes increase the potential problems with distortion.

Cold-formed steel member bracing techniques have been utilized in construction practice through manufacturer specific recommendations and details, however no specific bracing requirements were provided for in American Iron and Steel Institute (AISI) *Specification* editions though 2004. Recent recommendations by Sputo and Beery (2006) for bracing of the flexural mode of buckling are included in the current AISI *Specification* (2007), however torsional bracing requirements have yet to be determined.

The objective of this research project was to continue the investigation of torsional bracing requirements for axially loaded lipped, *cee*-shaped, cold-formed wall studs using finite element analyses. This investigation was performed through (1) building a finite element model of a single, pin ended cold-formed steel stud that is loaded in axial compression; (2) determining an appropriate method of modeling a brace to resist torsion (in addition to weak-axis flexure) at the mid-height of the stud; and (3) evaluating the torsionally braced stud model analyses and results. The bracing of thin-walled members can pose a difficult problem due to local distortions on the cross-section. Several modifications of the FEA models were considered to capture an accurate model of the actual system, while also trying to keep the system computationally economical.

Wall studs are often braced using a horizontal cold-rolled channel (CRC) attached to the stud web at mid-height. Figure 1 shows a typical bracing detail used in practice which employs an unlipped channel section with a 1.5 inch deep web, 0.5 inch flanges, and 0.054 inch thickness. Braced models tested in this

study did not include the stud perforation or clip angle shown in Figure 1. While there are a number of different connection methods, those used in this study are probably most similar to the Direct Welded (DW) connection discussed in Green, Sputo, and Urala (2004) and Sputo and Beery (2006).

### **Analytical Investigation**

The three dimensional finite element program ANSYS (2005) was used to conduct the parametrical studies in this investigation. A series of single, unbraced lipped cee studs were modeled first to determine the appropriate application of boundary conditions and loading. Studs were modeled with web heights of 3.62 and 6 inches, flange widths of 1.62 and 2.50 inches, and thicknesses ranging from 0.043 to 0.097 inches. Simplified cross-sections with square corners, rather than rounded corners were used. All studs were modeled with a tensile modulus of elasticity ( $E$ ) of 29500 ksi and Poisson's ratio ( $\mu$ ) of 0.3. An 8-node shell element (SHELL93 from ANSYS) was used. Pin-ended boundary conditions were simulated at the top and bottom of the stud. This was achieved by restraining the three translational degrees of freedom at a single node in each of the flanges at the bottom of the stud. At the top of the stud, the translational degrees of freedom were restrained within the plane of the stud, but longitudinal translation was allowed. A unit load of 1 kip was distributed to the nodes at the top of the channel. To reduce the localized failures due to very high web-height to thickness ratios, the member thickness at the first row of elements (on the top and bottom of the stud) was doubled for sections with a thickness less than 0.068 inches. This adjustment was intended to reflect a more realistic distribution of load to the cross-section that would usually be achieved by loading through a track channel at the top and bottom of the wall. Buckling load predictions and mode shapes for the single unbraced stud were compared to results from a previous study (Tovar 2004) for verification.

Studs were then modeled with a discrete torsional brace at midheight. The torsional brace was modeled using a shell element representation of the CRC brace (shown in Figure 1) and a number of more simple spring configurations. The shell element model is believed to provide an accurate representation of the bracing details that are used in practice. Brace parameters were tested on a stud section that had a web height of 3.62 inches, flange width of 1.62 inches, and a lip length of 0.5 inches. Wall thicknesses of 0.043 and 0.054 inches were considered. The section with a member thickness of 0.043 inches was expected to exhibit an unbraced torsional-flexural mode of buckling and local buckling when braced at the mid-height. The section with a member thickness of 0.054 inches was expected to exhibit an unbraced torsional-flexural mode of buckling (first mode) as well as torsion flexural buckling (second mode) when braced at

the mid-height (Tovar 2004). Modeling techniques used to simulate a torsional brace and a comparison of model results for two different stud sizes are provided.

The results from these eigenvalue analyses were evaluated by relating the normalized critical buckling load to the applied brace stiffness. The normalized critical buckling load is calculated by the following relationship

$$P_{cr\_normalized} = \frac{P_{cr\_braced}}{P_{cr\_unbraced}} \quad (\text{Eq. 1})$$

Where  $P_{cr\_normalized}$  is the normalized critical buckling load;  $P_{cr\_unbraced}$  is the critical buckling load from the unbraced stud model; and  $P_{cr\_braced}$  is the critical buckling load from the braced stud model. Critical buckling loads were determined from the various braced stud model analyses. Braced stud models were used to analyze a range of brace stiffness values and therefore  $P_{cr\_braced}$  does not always correspond to a fully (or even partially) braced stud, but rather the critical buckling load prediction from the braced model analyses. Brace stiffness values correspond to the total stiffness provided by the brace type being modeled (units in kip-inches/rad).

The following notation is used to describe displacement and restraint in this paper (global directions). UX represents translations in the weak-axis direction of the stud (as well as axial deflections of the CRC brace). UY represents axial deflections in the stud and weak axis deflections in the CRC brace. UZ represents translations in the strong axis direction of the stud and brace.

### Shell Element Modeled Torsional Brace

The first braced stud model used in this study modeled the CRC bracing member (Figure 1) using shell elements. This model is probably the most accurate representation of the bracing details that are used in practice since the stiffening effects of the stud web are captured. The web of the horizontal brace was positioned at mid-height of the stud. The near end of the brace was “connected” so that it would resist twist at the mid-height of the stud through sets of coupled nodes. All four corners of the shell element brace had UX movement coupled to adjacent nodes on the stud web (Figure 2). This ensured that any twisting of the stud at mid-height would impose a coupled force (moment) at the end of the brace. UY and UZ movement at the center-web node at the edge of each brace end were coupled to the adjacent node at mid-height of the stud. This coupling provided pinned boundary conditions at the brace ends

without resisting any strong axis lateral deformations or axial shortening of the stud.

The stiffness of a member that is pinned at one end, with a moment connection to the main member at the other end is given as:

$$\beta = \frac{3E_b I_b}{L_b} \quad (\text{Eq. 2})$$

Where  $\beta$  is the member stiffness;  $E_b$  is the modulus of elasticity of the brace material;  $I_b$  is the moment of inertia of the brace about the axis of bending; and  $L_b$  is the length of the brace. The stiffness for the shell element braced model results was initially varied by changing the length,  $L$ , of the CRC brace member and holding constant values of  $E$  (29500 ksi) and  $I$ . To capture a range of brace stiffnesses that corresponded to unbraced (and transitional) stud buckling behavior, extremely long brace lengths were required. The resulting braces were unrealistically slender and susceptible to both bending and buckling (unless specifically controlled through coupling). These models also became computationally impractical (ie. brace lengths of 3,000 to 30,000 inches required for 362S162-43).  $E$  of the brace was therefore reduced by a factor of 10 to achieve a more reasonable range of brace lengths. For the studs considered in this study, channel brace lengths that were in a more practical length range than noted above provided full torsional bracing to the stud.

To ensure the brace would remain flat as it underwent deflections in the out-of-plane (UZ) direction, UY movements were coupled for all nodes at the intersection of the brace web and each flange back to a single point (along this intersection). Weak axis brace bending as well as warping (singly-symmetric CRC sections would naturally bend with a combination of torsion and strong-axis flexure) were restrained by coupling. This ensured a pure, strong axis bending of the brace to determine the torsional stiffness.

To investigate torsional buckling behavior in the stud, it was necessary to restrain weak axis flexural buckling of the full height stud. This required a UX lateral pin at midheight of the stud. If this pin was applied at the far end of the bracing channel (similar to constructed conditions), an axial force was transferred into the brace as local or longwave buckling began to develop in the stud. For the slender braces used in this study a slight axial load in the brace resulted in significant degradation of bending stiffness of the bracing channel. In some situations buckling of the bracing channel was the lowest eigenvalue for the system.

### **Analysis Results**

The 362S164-54 stud exhibited a single mode of torsional flexural buckling at brace stiffness values ranging from 0.17 to 2.86 kip-inches/rad. Figure 3 illustrates a typical buckled shape for this mode. The corresponding critical buckling load predictions reflect effectively unbraced behavior at the low end of these stiffness values, where the normalized capacity ratios begin at approximately 1.3. As the brace stiffness values increased, the buckling load predictions increased to as much as 3.36 times the unbraced stud predictions for a stiffness value of 2.86.

From stiffness values of 3.07 to 3.90, the stud transition to a higher buckling mode was marked by notable asymmetry in the torsional buckling shape. This transition continued to a more distinguishable second mode of torsional flexural buckling (partially braced behavior) that was distinguished beginning at a stiffness value of 4.29 and a normalized critical buckling value of 3.40 (Figure 4). As stiffness values increased, the torsional-flexural buckling response was “capped” by a close local buckling response exhibited from stiffness values of 5.37 and higher (Figure 5). The corresponding buckling load predictions were 3.42 times the unbraced stud capacity.

The 362S164-43 stud exhibited a single mode of torsional flexural buckling at brace stiffness values beginning at 0.17 and continuing through to 1.19 kip-inches/rad. Respective normalized critical buckling load predictions ranged from 1.39 to 4.44. The effective braced behavior for this stud was limited by local buckling at a stiffness value of 1.23. The corresponding critical buckling load predictions were only 2.45 times the predictions for the unbraced stud.

### **Spring Models for Torsional Brace**

In addition to the shell element model of the CRC bracing member, three simplified brace models were used consisting of 1) a single spring model that was attached to a single node on the stud web, 2) a multiple spring model with distributed stiffness, and 3) a single spring model that was coupled to multiple nodes. The spring element models provide a relatively simple method of modeling the torsional brace when compared to the shell element model discussed above. However, several analyses were necessary to ensure that the spring element models provided reasonable reflections of the effects of cross-sectional distortion on the bracing behavior. All three spring brace models utilized the ANSYS spring element COMBIN14, which has a single rotational DOF along the axis of the spring element. These models provided an efficient method of capturing the stud buckling response over a wide range of stiffness

values, and therefore provided valuable buckling estimates and general stiffness boundaries for the relatively time consuming shell element brace models.

The single spring brace model consisted of a spring attached to a node in the center of the stud web at mid-height (See Figure 6). The spring element is a single unit (1 inch) long and oriented so that its length runs parallel to the height of the stud. This spring orientation aligns the DOF w/ the axis for torsional rotation of the cross-section. However, it is located in line with the stud web rather than with the shear center of the section. Rotation about the Y-axis (ROTY) was restrained at the other end of the spring to engage the spring stiffness for torsional stud deformations corresponding to the rotational DOF of the spring. Rotation about the X-axis (ROTX) was also restrained to prevent “pivots” at this location, but no forces are calculated for this or other DOF’s.

Since the actual connections between the brace and the stud occur over a portion of the web depth in the stud, the distributed spring brace model spread the total brace stiffness over a larger portion of the stud web than idealized by the first single spring model. This model utilized a series of springs attached to nodes on the back of the stud web at mid-height (See Figure 7). Five springs were located at nodes that match the width of a typical CRC bracing member (1.5 inches). The total input stiffness was divided by the number of springs and applied accordingly. The orientation and boundary conditions were as described for the single spring model, except that rotation about the Z-axis (ROTZ) was also required to restrain additional “pivots” at these locations during analysis.

The actual connection between the bracing channel and the stud web is usually made at the flanges of the bracing channel and can be made with either welding or mechanical fasteners. It was not clear whether the distributed spring model appropriately captured the stiffening effect so another model was considered in which an attempt was made to model the stud web that overlapped the brace with an infinite stiffness. To simulate the stiffening that occurs due to the connection, the nodes at the four flange “corner” locations were coupled to a node at one end of a single spring (similar to Figure 6). Since this spring was not directly attached to the stud (and therefore not subject to UX, UY displacements of the stud) ROTY restraint was the only boundary condition required at the opposite end of the coupled spring.

## Observations and Comparison of Results

### Web Distortions

Localized web distortions at the brace connection were observed to influence the results for all these analyses. The high web slenderness ratios for these sections did not effectively distribute the bracing restraint to the overall cross-section of the stud. Since bracing systems follow the classic equations for springs in series, cross-sectional distortion can often render the bracing system ineffective as evidenced by the equation:

$$\frac{1}{\beta_{sys}} = \frac{1}{\beta_{brace}} + \frac{1}{\beta_{sec}} \quad (\text{Eq. 3})$$

Where  $\beta_{sys}$  is the stiffness of the bracing system,  $\beta_{brace}$  is the stiffness of the brace, and  $\beta_{sec}$  is the stiffness of the cross-section. The stiffness of the cross-section reflects the effect of cross-sectional distortion on the system. The system stiffness in Equation 3 must be less than the smallest of the brace stiffness or the cross-sectional stiffness term.

It is important to note that displacements from eigenvalue buckling analysis do not represent specific magnitudes, but are relative to a maximum eigenvector displacement of 1.0. To compare web distortions (and buckled shapes) between the spring and shell element braced models the eigenvector deformations in the stud nodes of the shell element model should be scaled to produce comparable magnitudes. The scale factor can be obtained by dividing the translational deformation of a given node by the deformation of the node that had the largest translational deformation. For example, if the maximum stud deformation occurred at a node at the tip of the flange and had a value of 0.09, each nodal deformation was modified by UY/0.09 or UX/0.09.

### Local Buckling

This study was primarily concerned with the restraint of global modes of buckling. However, in certain analyses local buckling may limit the stud capacity before a higher mode of global buckling is reached. Local buckling was observed to control some analyses due to the boundary conditions and coupling connections of the brace. When the local buckling limit was near (slightly higher) the second mode of flexural buckling it was often difficult to achieve convergence to the second mode of flexural buckling. Additionally, multiple local buckling modes often occur within a narrow range of eigenvalues. The stud results for a range of brace stiffness values therefore exhibited some variability in the critical buckling loads and mode patterns associated with this limit state.

When local buckling started to develop in the stud modeled with the shell element CRC brace, the brace coupling and attachment may have provided an unintended restraint in the development of local buckling in the stud. When local buckling starts to occur, rotation in the stud web at this location is restrained (due to UY coupling along the length of the brace) making it necessary for the buckling wave “peak” to occur at the attachment (Figure 5). This may have resulted in critical buckling results that were slightly above or below the theoretical values. The local buckling wave “peak” at the brace location also allowed some long-wave flexural deflection that was often observed in conjunction with the more symmetrical response of local buckling.

### **Spring Braced Models**

Results for the shell element CRC braced model and all three spring braced models are plotted in Figures 8 and 9 (for studs 362S162-54 and 363S162-43 respectively). Due to excessive web distortion, the single spring model did not provide enough system stiffness to achieve a second mode buckling response in the stud. Web distortion is sensitive to the length of unrestrained portion of the web. Since this model was only connected to a single node on the stud web significant web distortion resulted in inadequate system stiffness as was discussed in the presentation of Eq. 3. The single spring model results were limited at approximately 68 percent of the second mode response for the stud that buckled in torsional flexure (362S162-54) and approximately 81 percent for the stud that displayed local buckling (362S162-43).

The distributed spring model and coupled spring model both dramatically reduced the limiting effects of web distortion and results for these models achieved the expected braced stud buckling response. Overall buckling behavior for each of these spring braced models was comparable to the shell element braced model and useful for efficient determination of stud buckling behavior over a large range of stiffness values. Due to slight differences in brace attachment some localized differences were observed. The shell element model was limited with a braced local buckling mode where the spring models maintained the expected braced torsional-flexural mode of buckling. The normalized critical buckling loads for effectively braced behavior in the shell element model are approximately 1 percent less (for both stud sizes) than that of the spring models, providing the lower bound of braced (or second mode) buckling behavior for all three models.

For the range of stiffness values corresponding to unbraced stud buckling behavior and transitional stud buckling behavior, the spring element models



become nonlinear at lower load levels compared to the shell element brace model curves. This results in the achievement of effectively braced behavior at a slightly lower stiffness value than that of the distributed or coupled spring models. There was a difference in the rate at which the distributed spring model and the coupled spring model reached the effectively braced stud buckling behavior. This difference was extenuated in the 362S162-54 stud results due to a more gradual change in slope at the transition to a second mode for torsional flexural buckling (slope change for the local buckling limit of the 362S162-43 stud is more abrupt).

The observed cross-sectional rotations (Figure 10) indicate the shell element model provided the greatest torsional restraint as the results approached effectively braced stud buckling behavior. The distributed spring model allowed slightly more rotation and the coupled spring model allowed the most rotation. The coupled spring model exhibited single mode of torsional flexural buckling with a maximum UZ displacement occurring at 15.6 inches below the stud mid-height. The distributed spring model exhibited a more asymmetric single mode that transitioned to the second mode of torsional flexure, with a maximum UZ displacement occurring at 21.6 inches below mid-height. The shell element model, however displayed a somewhat asymmetric second mode of torsional flexure, with a maximum UZ deflection occurring at 23.4 inches below mid-height. This response approaches fully braced behavior where a perfectly symmetric buckled shape would contain maximum twist at the  $L/4$  or 24 inches above and below mid-height. A closer look the web distortions (Figure 11) showed similar curvature and distortion (although inverted) at the points of attachment for the coupled spring and shell element models. Due to the differences in node connectivity the distributed spring maintains relatively linear web distortions at brace attachment. However, the shell element braced model restrained overall cross-section rotations slightly better than either of the two spring braced models and is probably the most accurate representation of the problem compared to details used in practice.

One final observation from all three spring model types was that critical buckling load predictions for braced models were always higher than lipped cee stud predictions (with no brace attached). Spring models were analyzed at a stiffness value of 0.0, however normalized critical buckling loads show that predictions for both studs were approximately 1.14 times higher than model predictions when no brace applied. A small portion (about 4 percent) of this difference was attributed to small changes in the stud mesh that provided the node locations necessary for brace attachment. The majority (remaining 10 percent) of this difference was thought to be due to the pin that was applied to resist weak axis lateral deflection in the braced stud models. This restraint

forces the stud section to twist about the pin, which is located on the stud web, rather than about the section shear center.

### **Summary and Conclusions**

A number of finite element modeling techniques were used in this study to investigate the torsional bracing requirements for cold-formed lipped-tee wall studs. Eigenvalue buckling analyses were performed for two pin-ended studs (362S162-43 and 362S162-54) that were loaded in compression and braced at mid-height. Brace stiffness was applied through a shell element model of the bracing channel member, a single spring, a series of springs distributed along the web location of the bracing channel, and single spring coupled at the corner locations of the bracing channel flanges. Analyses were performed for a range of brace stiffness values to determine the stiffness range required to achieve braced stud behavior.

The shell element bracing model is believed to be the most accurate representation of details that are used in practice, but it is time consuming and susceptible to controlling local buckling effects. The spring models provide simple methods of simulating the bracing behavior; but some difference in the effects of cross-sectional distortion was observed. Overall bracing behavior and normalized critical buckling loads showed that the distributed spring and coupled spring models had reasonable agreement with the shell element braced model. All three models produced results that were close to CUFSM critical buckling predictions for braced and unbraced stud behavior (Tovar 2004).

It is recommended that a spring braced model be utilized to analyze bracing behavior of a broader range of lipped-tee stud sizes. Based on results and observations from this study the following conclusions and recommendations are provided for extending this work:

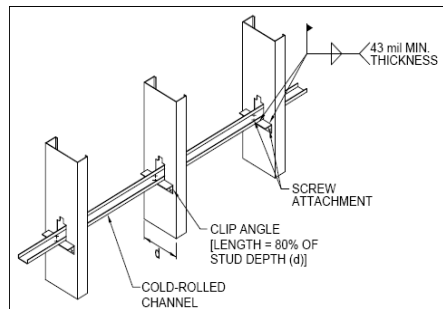
- 1) Critical buckling load predictions and mode shapes have been shown to be sensitive to specific details of CRC brace attachment to the stud, particularly in the shell element brace model.
- 2) Appropriate spring braced models provide an efficient, less sensitive alternative to obtaining results for the general range of stiffness values that correspond to the transition between unbraced buckling and braced buckling behavior for the stud.
- 3) The shell element braced model could be used to “spot check,” or make comparisons at a few stiffness values of interest, based on overall critical buckling curves developed using a spring braced model.

4) Critical buckling load predictions and mode shapes from analyses when stiffness values are equal to zero and when they provide effectively braced stud behavior should be compared to expected results from an outside source to ensure convergence on the correct mode.

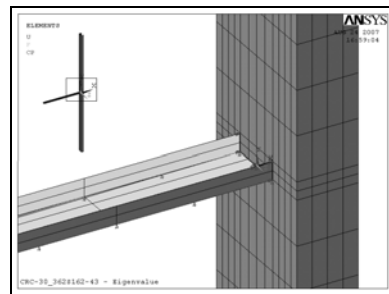
5) Results from modeling of the lipped-tee stud in this study showed good comparison for a range of stud sizes with web heights of 3.62 and 6 inch, flange widths of 1.62 inches, and member thicknesses from 0.033 to 0.097 inches. The use of these models for greater web-height-to-thickness or flange-width-to-thickness ratios may require model adjustments to avoid localized effects of loading and boundary conditions.

### Future Work

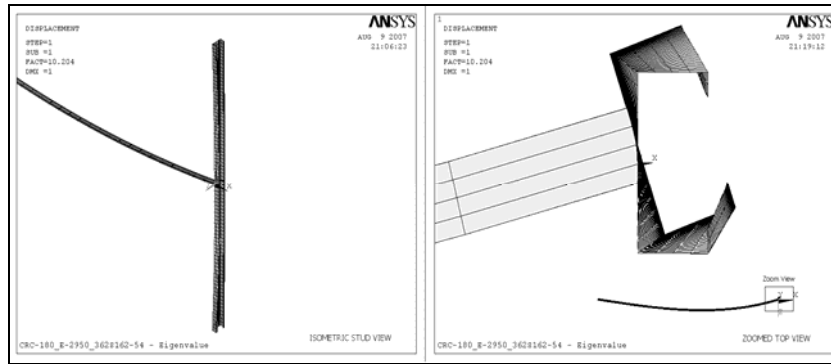
With consideration for the recommendations given above, these bracing models could be applied to a broader range of typical stud sizes to determine general torsional stiffness requirements for a single lipped-tee wall stud. Additional extensions could be made to obtain torsional brace strength requirements by performing a large displacement analysis. The ANSYS command files used in this study along with more detailed information about model development can be found in Tovar 2007.



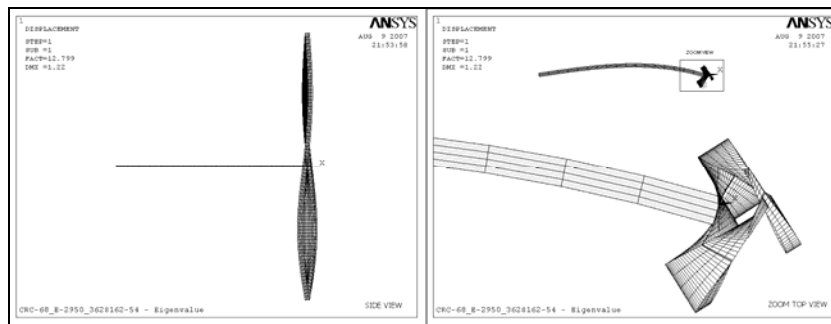
**Figure 1.** SSMA Channel Bracing Detail (SSMA, Cold-Formed Steel Details)



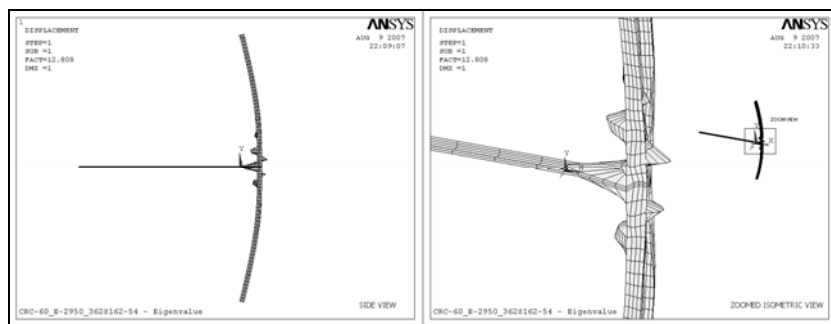
**Figure 2.** Shell Element Braced Model (ANSYS, Inc. v.10.0)



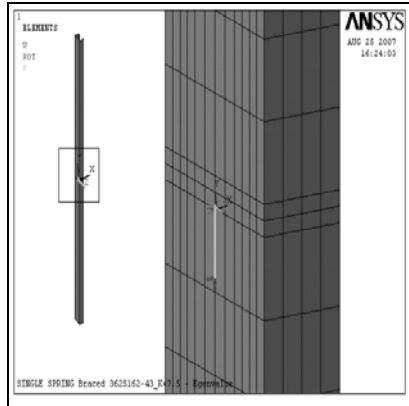
**Figure 3.** Unbraced Torsional-Flexural Buckling of 362S162-54 Stud



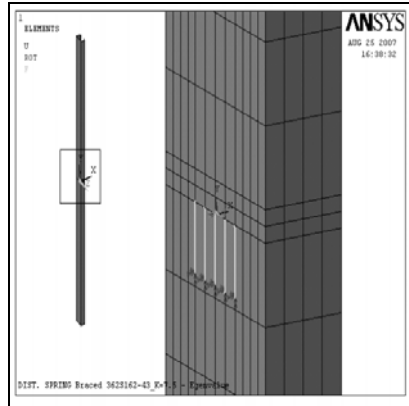
**Figure 4.** Partially Braced Second Mode Torsional-Flexural Buckling of 362S162-54 Stud



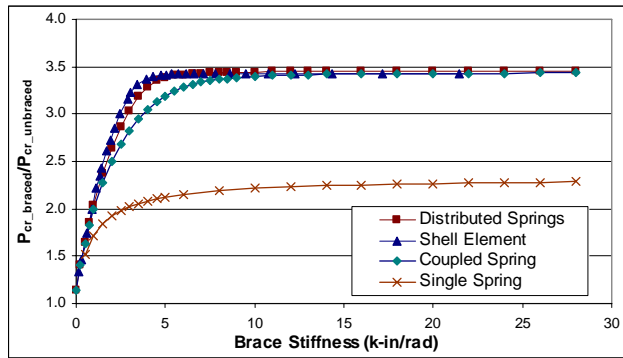
**Figure 5.** Braced Local Buckling of 362S162-54 Stud



**Figure 6.** Single Spring Braced Model (ANSYS, Inc. v.10.0)



**Figure 7.** Distributed Spring Braced Model (ANSYS, Inc. v.10.0)



**Figure 8.** Web Brace Model Comparison for the 362S162-54 Stud

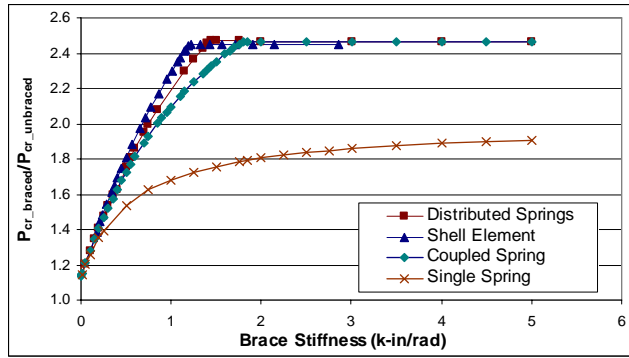


Figure 9. Brace Model Comparison for the 362S162-43 Stud

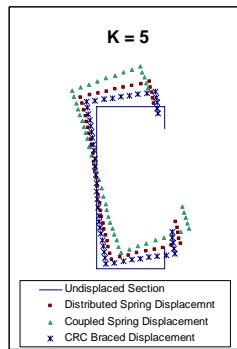


Figure 10. Cross-section of Braced Models for the 362S162-54 Stud

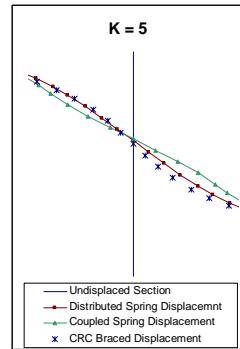


Figure 11. Web Distortion of Braced Models for the 362S162-54 Stud

**Appendix. – References**

- ANSYS. (2005) Version 10.0. SAS IP, Inc.
- American Institute of Steel Construction (AISC) (2005). *Specification for Structural Steel Buildings*, American Institute of Steel Construction, Chicago, IL.
- American Iron and Steel Institute (AISI) (2007). *North American Specification for the Design of Cold-Formed Steel Structural Members and Commentary*, Washington DC.
- CUFSM. (2004) Version 2.6.
- Green, P.S., Sputo, T. and Urala, V. (2004). “Bracing Strength and Stiffness Requirements for Axially Loaded Lipped Cee Studs.” *Proceedings, 17th International Specialty Conference on Cold-Formed Steel*, Orlando, FL.
- Helwig, T.A., Yura, J.A., (1999). “Torsional Bracing of Columns.” *Journal of Structural Engineering*, Vol. 125, No. 5, p 547-555.
- Sputo, T. and Beery, K. (2006). “Accumulation of Bracing Strength and Stiffness Demand in Cold-Formed Steel Stud Walls.” *Proceedings, 18th International Specialty Conference on Cold-Formed Steel*, Orlando, FL.
- Steel Studs Manufacturers Association (SSMA) (2001). *Cold-Formed Steel Details*, Steel Studs Manufacturers Association, Chicago, IL.
- Tovar, J. (2004). “Application of the Direct Strength Method to Axially Loaded, Perforated Cold-Formed Steel Studs”, Honors Thesis, University of Florida, Gainesville, FL.
- Tovar, J. (2007). “Finite Element Analytical Investigation of Torsional Bracing Requirements for Cold-Formed Steel C-Shaped Studs”, M.S. Thesis, University of Texas, Austin, TX.
- Yura, J.A. (1995). “Bracing for Stability – State of the Art.” *Bracing for Stability*, Structural Stability Research Council, Bethlehem, PA.

## **STRENGTH OF COLD-FORMED STEEL JAMB STUD-TO- TRACK CONNECTIONS**

A.V, Lewis<sup>1</sup>, S.R. Fox<sup>2</sup> and R.M. Schuster<sup>3</sup>

### **Abstract**

Cold-formed steel structural members are often used in building construction, with a common application being wind loadbearing steel studs. The studs frame into horizontal steel track members at the top and bottom of the wall assembly, with the stud-to-track connection typically being made with self-drilling screws. The design of the wall stud must include a check of the web crippling capacity at the end reactions, and there are design rules in place for the typical stud-to-track connection. However, at every opening in the wall assembly such as a window or door, there are jamb stud members that must also be designed for the stud-to-track connection strength. These jamb studs can occur at the termination of the bottom track or at an interior location, and can be single or multiple members. Reported in this paper are the results and analysis of a collection of end-one-flange loading tests of common jamb stud-to-track connections. Design expressions are proposed to predict the capacity of this connection for these structural members.

### **Introduction**

Cold-formed steel structural members are used extensively in building construction throughout the world due to a combination of their high strength-to-weight ratio, stiffness, recyclability, and the relatively low cost associated

---

<sup>1</sup> Operations Manager, Structural Testing and Research Inc., Cambridge, Ontario, Canada

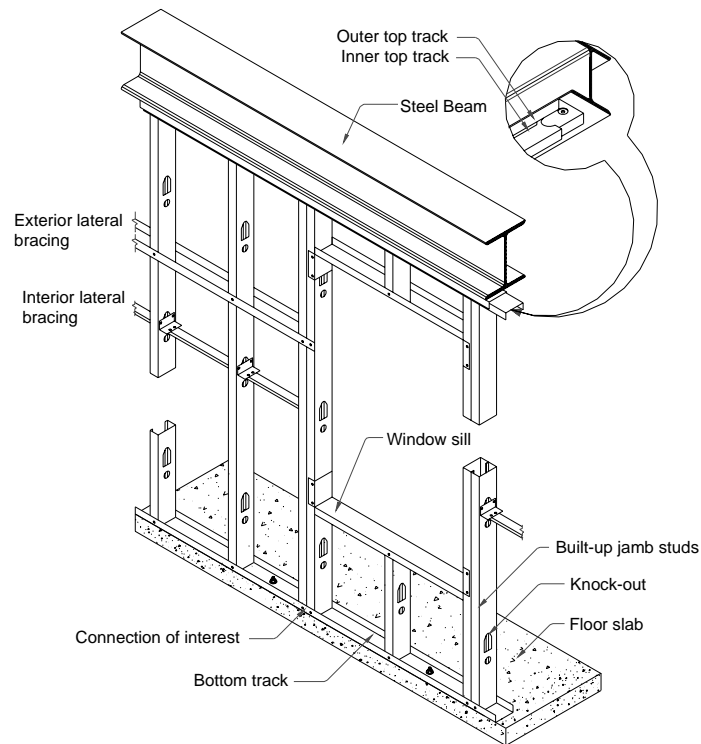
<sup>2</sup> General Manager, Canadian Sheet Steel Building Institute, Cambridge, Ontario, Canada

<sup>3</sup> Professor Emeritus of Structural Engineering and Director of the Canadian Cold-Formed Steel Research Group, Department of Civil Engineering, University of Waterloo, Waterloo, Ontario, Canada



with their supply and installation. Infill wall framing is a common application for a subset of cold-formed steel structural members referred to as ‘wind loadbearing’ studs used to support the exterior wall finish and transfer lateral loads, such as those imposed by wind pressure, to the main structure. These studs ‘infill’ the space between the main structural elements from floor-to-floor.

In wind loadbearing applications, there is some type of deflection connection at the top track to accommodate the anticipated movement of the upper floor and prevent the wall studs from being axially loaded. One type of deflection detail is illustrated in Figure 1, which uses a double top track arrangement. The behaviour of these deflection connections is not included in the scope of the experimental work reported in this paper.



**Figure 1: Typical Wind Loadbearing Wall Application**

The research presented in this paper focuses on the connection between built-up jamb members and the bottom track, both at interior locations, as shown in Figure 1 for a window opening, and at end locations, such as would be found at a doorway or building corner.

The design of cold-formed steel structural members in North America is governed by the *North American Specification for the Design of Cold-Formed Steel Structural Members*, referred to as the NASPEC [ASISI 2007a; CSA 2007]. Previous research [Fox and Schuster 2000] has studied the single stud-to-track connection strength, and a design procedure has been adopted in the *North American Standard for Cold-Formed Steel Framing – Wall Stud Design* [AISI 2007b]. However, neither the NASPEC nor the Wall Stud Design standard have design expressions for determining the strength of the built-up stud-to-track connections used as jamb studs.

### **Experimental Investigation**

An experimental study was performed at the University of Waterloo concentrating on the behaviour of jamb stud-to-track connections in curtain wall construction [Lewis 2008]. The objective of this investigation was to develop design provisions for calculating the strength of this connection. The parameters considered in the test program were as follows:

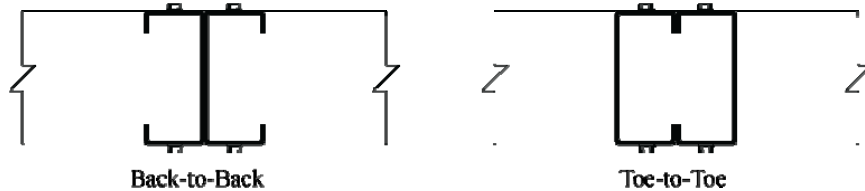
- stud and track thickness (0.8mm to 1.9mm);
- stud and track web depth (92mm and 152mm);
- configuration of jamb studs (back-to-back, toe-to-toe and single);
- location of jamb studs in the track (interior and end);
- screw size (#8, #10 and #12);
- screw location (both flanges and single flange);
- stud and track the same thickness;
- yield strengths from 300 to 450 MPa.

Test specimens were constructed of C-shaped studs with edge stiffened flanges and track sections with unstiffened flanges. For each different member type, tensile coupons were taken from the webs and tested in accordance with ASTM A370 [ASTM 2005] to determine the mechanical properties of the base steel material.

### **Test Specimen Configurations**

Framing an opening in the wall for a window usually requires leaving a solid surface at the jambs for the attachment of the window itself. To save time and

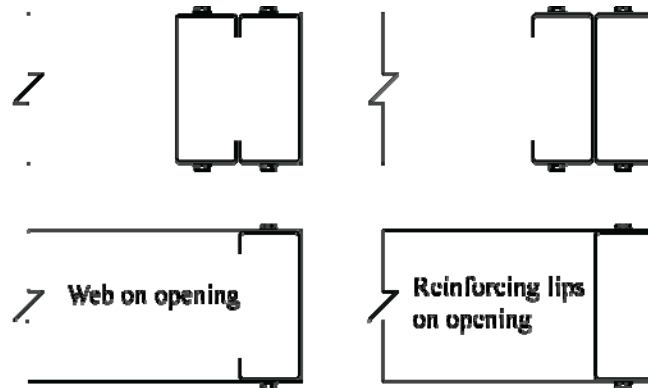
material, framers prefer using jamb studs in a toe-to-toe configuration to eliminate the need for an additional track section to close off the opening. However, in some cases due to the strength requirements or the framing methods, the jamb studs will be connected back-to-back. This configuration makes it easier to connect the members together to act as a built-up section, but does require an additional piece of track to close off the opening. Illustrated in Figure 2 are two jamb configurations at a window opening showing the studs framing into a bottom wall track that is continuous past the jamb.



**Figure 2: Jamb Studs at a Window Opening**

When the jamb is made from back-to-back members, a piece of track is added to the inside stud to provide the solid surface in the opening required for the installation of the door or window. This track may be continuous along the length of the jamb stud, but is cut short at the top and bottom since a track section cannot frame into another track section as a stud can do. Consequently, while the track adds to the flexural strength of the jamb, since it is not connected to the top and bottom wall track, the jamb track does not transfer any shear at the ends. The entire reaction at each end of the jamb is taken through the members that frame into the top and bottom wall track, specifically the studs. Even though it is very common for a built-up jamb to include track sections, these members do not contribute to the strength of the jamb stud-to-track connection and so were not included in this test program.

In a similar manner to the window framing, the built-up jambs at a doorway can also be configured in toe-to-toe or back-to-back shapes, but in a door opening the bottom wall track terminates at the jamb stud. Given that the bottom track is no longer continuous, the strength of the stud-to-track connection will be affected. Illustrated in Figure 3 are the configurations of jamb studs at a door opening that were tested. In addition to the built-up configuration, two configurations of single member were also tested.

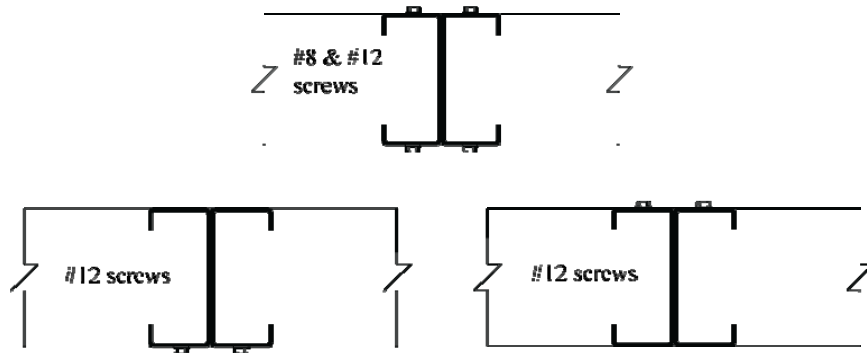


**Figure 3: Jamb Studs at a Door Opening**

#### **Screw Size and Location**

Standard practice for steel stud framing is to use a self drilling screw to connect both flanges of the stud to the track into which it frames, and the minimum size (diameter) for these screws is #8. For some of the thicker steel sections, a #8 screw is not recommended since the diameter is too small and it can shear off as it is being installed. To avoid this limitation, most of the tests in this program used #10 screws to make the connections. A series of tests were carried out with #8 and #12 screws to investigate whether the screw size does affect the strength of the connection.

In practice it may be possible to find installations where the screws had been inadvertently omitted from one side of the stud or the other. Without the screws connecting both flanges of the stud to the track, the load transfer within the connection will be different and the ultimate strength may change. A series of tests were run where screws were only installed in one flange of the stud. Illustrated in Figure 4 are the test configurations that investigated the various screw sizes and placement.



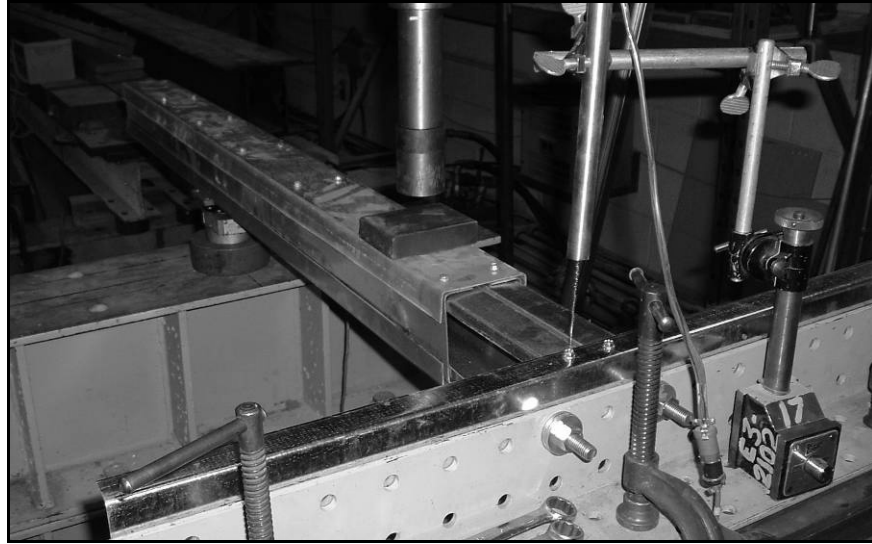
**Figure 4: Test Configurations with Varying Screw Size and Placement**

#### **Test Procedure**

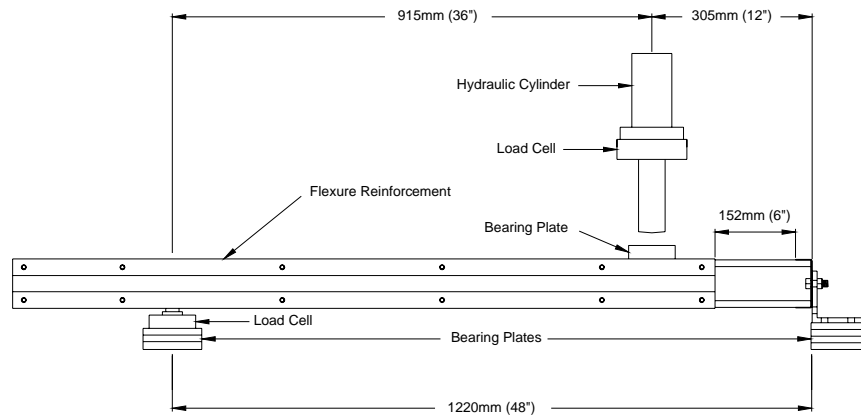
The test procedure involved conducting a series of single point loading tests on simply supported built-up jamb assemblies. The jamb studs were cut to 1220mm lengths and connected in the toe-to-toe or back-to-back configuration. For the single stud tests, the single stud was reinforced with a second stud, but the end of the reinforcing stud was kept back 152mm from the track, and the single jamb stud made the stud-to-track connection.

To prevent a flexural failure or a web crippling failure of the jamb stud at the point of applied load, the assemblies were reinforced with additional pieces of track. The track into which the jamb studs framed was bolted to an 8mm thick steel angle with two 12.7mm steel bolts and 25mm washers, spaced no more than 152mm apart, with a bolt on either side of the stud-to-track connection. Connecting the track to the supporting structure in this manner avoided potential flexural failure of the track or failure of the track-to-structure connectors.

The unconnected end of the test specimen was supported on a load cell. The readings from this load cell subtracted from the load cell measuring the total applied load gave an accurate reading of the load at the stud-to-track connection. The photograph in Figure 5 and the sketch in Figure 6 illustrate the test setup.



**Figure 5: Photograph of a Typical Test Setup**



**Figure 6: Schematic of a Typical Test Setup**

The ultimate load recorded for each test was determined when the test specimen was no longer capable of carrying an increasing load or when the deflection was considered excessive. In addition to the ultimate load, an effort was made to

record the onset of web crippling, and to record other failure modes as they occurred. For example, as some samples began to fail in web crippling, track punch-through began, and then screw failure occurred, effectively ending the test. The modes were noted, and the applied load at the onset of each mode recorded when possible.

The test fixture was not appropriate to assess the track deflection nor was that the intent of these tests; however, to qualify failure modes, it was decided to record the deflection of the connection itself—excessive deflection of the connection being considered a failure mode. The deflection data was obtained by placing a low-voltage displacement transducer (LVDT) directly above the junction of the stud and track connection (shown in Figure 5).

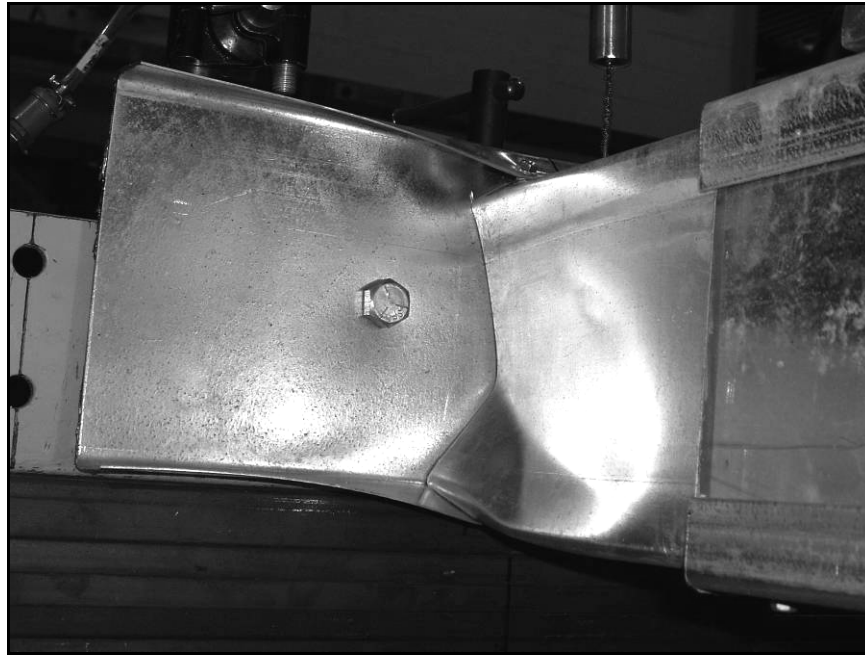
#### **Failure Modes**

The observed failure modes were:

- (a) web crippling;
- (b) track punch-through;
- (c) excessive deflection at the stud-to-track connection;
- (d) screw pull-out;
- (e) combination of screw shear and tension failure.

#### *Web crippling:*

Web crippling of the jamb stud was the most common failure mode, and occurred in all cases where studs were paired toe-to-toe, or when single stud configurations were tested. Web crippling would also occur when the studs were paired back-to-back but only with the thinner stud sections. The photograph in Figure 7 shows the web crippling failure mode.



**Figure 7: Photograph of Web Crippling Failure**

*Track Punch-through:*

Track punch-through (where the corners of the jamb stud sheared through the track flange) occurred in the back-to-back configurations, both interior and end locations, where there were fasteners in both the top and bottom flanges. With one exception, punch-through failure only occurred in material 1.52mm and 1.91mm thick. Previous research [Fox and Schuster 2000] found that for single stud connections punch-through would not occur if the track was the same thickness as the stud or greater. In all the tests being described in this paper the track thickness was the same as the stud thickness. The photograph in Figure 6 shows the back-to-back studs punching through the track without web crippling.

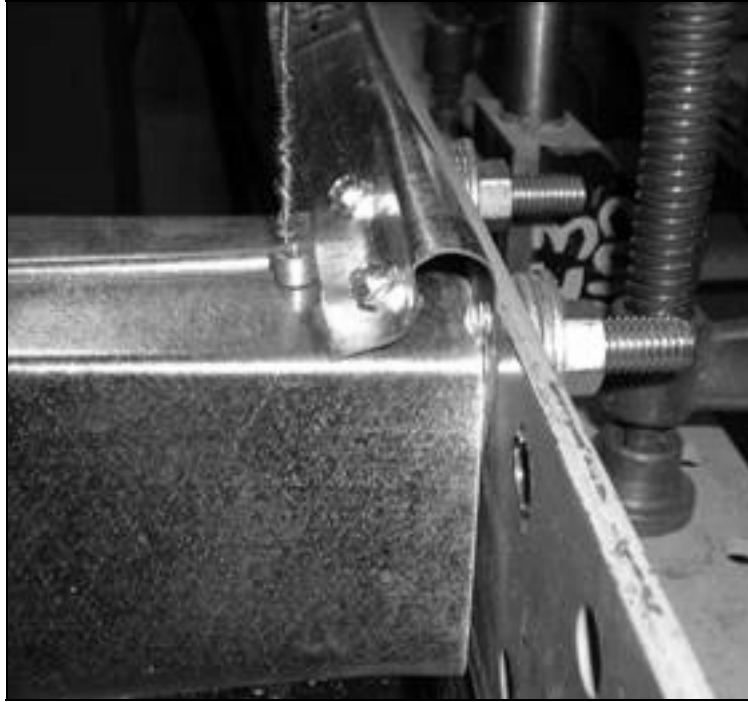




**Figure 8: Photograph of Track Punch-Through Failure**

*Deflection:*

In some cases, the test specimen was able to carry additional load after web crippling had occurred, although with increased deflection at the stud-to-track connection. In the end location tests there was no web crippling and failure was due to track deformation alone. Illustrated in the photograph in Figure 9 is an example of excessive track deflection. Deflections in excess of 12.7mm were not uncommon and would certainly be considered unacceptable from a serviceability perspective.



**Figure 8: Photograph of Excessive Track Deflection**

*Screw Failure:*

Of the three screw failure modes observed, screw pullout was the easiest to characterise, and always occurred in conjunction with web crippling and/or excessive deflection. The pull-out occurred in the screw loaded in tension connecting the top flange of the stud. With the thicker stud sections some configurations failed in a combination of screw tension and shear. Next to track punch through, screw shear was the most frequent failure mode.

**Web Crippling Predictor Equation**

The basic web crippling equation from the Wall Stud Design standard [AISI 2007b] was used with new regression coefficients determined from the test data. Web crippling coefficients are proposed for each test configuration that exhibited web crippling failure. The applicability of these design expressions should not be extended beyond the limits of the material properties and sizes of the tested specimens as shown. The web crippling predictor equation is given in

Eqn. 1 and the coefficients are provided in Table 2. Note that Eqn. 1 is non-dimensional and can be used with any consistent system of units.

$$P_n = Ct^2F_y \left( 1 - C_R \sqrt{\frac{R}{t}} \right) \left( 1 + C_N \sqrt{\frac{N}{t}} \right) \left( 1 - C_h \sqrt{\frac{h}{t}} \right) \quad \text{Eqn. 1}$$

where,

- $P_n$  = Nominal web crippling strength per stud web
- $C$  = Web crippling coefficient (see Table 2)
- $C_h$  = Web slenderness coefficient = 0.019
- $C_N$  = Bearing length coefficient = 0.74
- $C_R$  = Inside bend radius coefficient = 0.19
- $F_y$  = Yield strength of the stud material
- $h$  = Flat dimension of the stud web measured in the plane of the web
- $N$  = Bearing length = 32mm (track flange width)
- $R$  = Stud inside bend radius
- $t$  = Base steel thickness of stud
- $\Omega$  = 1.70 for ASD for single stud interior configuration  
= 1.90 for ASD for all other configurations listed in Table 2
- $\phi$  = 0.90 for LRFD for single stud interior configuration  
= 0.85 for LRFD for all other configurations listed in Table 2  
= 0.75 for LSD for single stud interior configuration  
= 0.70 for LSD for all other configurations listed in Table 2

**Table 2: Web Crippling Coefficients for Jamb Stud-to-Track Connections**

Configuration		Web crippling coefficient, C
Single stud	Interior	3.70
Single stud	Adjacent to wall opening with reinforcing lips facing opening	2.78
Single stud	Adjacent to wall opening with stud web facing opening	1.85
Double stud	Toe-to-Toe Interior	7.40
Double stud	Toe-to-Toe, Adjacent to opening	5.55
Double stud	Back-to-back, Interior	7.40
Double stud	Back-to-back, Adjacent to opening	7.40

Listed in Table 3 are averages of the tested web crippling failure loads ( $P_t$ ) divided by the predicted web crippling strength ( $P_n$ ), the coefficient of variation (COV) of these ratios, the number of tests and the geometric limits of applicability.

**Table 3: Web Crippling Prediction Results**

Test Configuration	Avg. $P_t/P_n$	COV	No. of tests	Stud Thickness (mm)	Stud Depth (mm)
Toe-to-Toe, Interior	0.980	0.058	14	0.8 – 1.9	92 - 152
Toe-to-Toe, End	0.988	0.083	16	0.8 – 1.9	92 - 152
Single, End (web on opening)	1.03	0.129	8	0.8 – 1.9	92
Single, End (reinforcing lips on opening)	0.995	0.138	8	0.8 – 1.9	92
Back-to-back, Interior	1.00	0.070	11	0.8 – 1.1	92
Back-to-back, End	1.00	0.002	3	0.8 – 1.1	92

#### Punch-Through Predictor Equation

The punch-through failure mode is a function of the material properties of the track. The Wall Stud Design standard includes a design expression for this failure mode based on determining an equivalent bearing width. A different approach is proposed here as shown in Eqn. 2.

$$P_{npt} = 15.2t_t^2 F_{ut} \quad \text{Eqn. 2}$$

where,

$P_{npt}$	=	Nominal track punch-through strength
$F_{ut}$	=	Tensile strength of the track material
$t_t$	=	Base steel thickness of track
$\Omega$	=	2.10 for ASD
$\phi$	=	0.75 for LRFD
	=	0.65 for LSD

Listed in Table 4 are averages of the tested punch-through failure loads ( $P_t$ ) divided by the predicted strength ( $P_{npt}$ ), the coefficient of variation (COV) of these ratios, the number of tests and the geometric limits of applicability.

**Table 4: Punch-Through Prediction Results**

<b>Test Configuration</b>	<b>Avg. <math>P_t/P_{npt}</math></b>	<b>COV</b>	<b>No. of tests</b>	<b>Stud Thickness (mm)</b>	<b>Stud Depth (mm)</b>
<b>Back-to-back, Interior or End</b>	1.00	0.192	19	1.1 – 1.9	92

#### **Effect of Missing Screws**

The other conditions investigated were the size and placement of the screws. The standard screw used for the majority of the tests was a #10. The failure mode varied depending on the test specimen configuration, but with a couple of exceptions, screw failure did not occur before one of the other limit states. In the test series with the #8 screws, screw shear became the failure mode for the thicker sections at a reduced load compared to the #10 screws. When the #12 screws were used (in both flanges) the failure mode and load were comparable to the same configuration with the #10 screws. When a single screw was put in the bottom flange, this was sufficient to restrain the assembly and the failure mode was punch-through. When the single screw was put in the top flange, the failure mode was excessive deflection caused by the bottom flange of the track being unrestrained and bending under load.

#### **Conclusions**

The general conclusions from this work are as follows:

- Design expressions are proposed for a range of jamb stud configurations based on a web crippling or punch-through failure mode. These design expressions should not be used beyond the limits of the material properties and sizes of the tested specimens.
- The size of screws should be selected based on the thickness of members being connected. Screws should be placed in both flanges, but some usable capacity is available when only a single screw is used.

Presented in the paper is a summary of a test program. For a complete presentation of the test data and analysis, refer to the original work [Lewis, 2008].

**References**

AISI, 2007a, *North American Specification for the Design of Cold-Formed Steel Structural Members*, AISI S100-07, American Iron and Steel Institute, Washington, DC, 2007.

AISI, 2007b, *North American Standard for Cold-Formed Steel Framing – Wall Stud Design*, AISI 211-07, American Iron and Steel Institute, Washington, DC, 2007.

ASTM, 2005, *Standard Test Methods and Definitions for Mechanical Testing of Steel Products*, ASTM A370-05. American Society for Testing and Materials, West Conshohocken, PA, 2005.

(CSA, 2007), *North American Specification for the Design of Cold-Formed Steel Structural Members*, CAN/CSA-S136-077, Canadian Standards Association, Mississauga, ON, 2007.

Fox, S.R. and Schuster, R.M. (2000), “Lateral Strength of Wind Load Bearing Wall Stud-to-Track Connections”, *Proceedings of the Fifteenth International Specialty Conference on Cold-Formed Steel Structures*, University of Missouri-Rolla, Rolla, MO, 2000.

Lewis, A.V. (2008), *Strength of Cold-Formed Steel Jamb Stud to Track Connections*, MAsc Thesis, Department of Civil Engineering, University of Waterloo, Waterloo, ON, 2008.



## Thermal Performance of Plasterboard Lined Steel Stud Walls

Prakash N. Kolarkar<sup>1</sup> and Mahen Mahendran<sup>2</sup>

**Abstract:** In response to the market demand for fire separations in the light industrial, commercial and residential buildings, a research project is currently under way to improve the thermal performance of cold-formed steel stud wall systems used in these buildings. Extensive fire testing of both non-load-bearing and load-bearing wall panels has been completed to date in the Fire Research Laboratory of Queensland University of Technology. This paper presents the details of this experimental study into the thermal performance of some small scale non-load-bearing walls lined with dual layers of plasterboard and insulation. The first two wall panels were built traditionally using lipped channels with two plasterboard linings on both sides and the cavity filled with and without glass fibre insulation. The third panel tested was built similarly, but with the insulation sandwiched between the plasterboards on either side of the steel wall frame instead of being placed in the cavity. Fire tests undertaken were based on the standard time-temperature curve recommended by AS 1530.4 (SA, 2005). Experimental results showed that the new stud wall system outperformed the traditional stud wall system giving a much higher fire rating.

**Keywords:** *Non-load-bearing walls, Gypsum Plasterboard, Cold-formed steel wall frames, Fire tests, Thermal performance, Insulation, Fire rating*

### 1. INTRODUCTION

Fire safety of light gauge cold-formed steel frame (LSF) stud wall systems is critical to the building design as their use has become increasingly popular in commercial, industrial and residential construction throughout Australia. Partition wall panels composed of a cold-formed steel frame lined with one or two plasterboards as side sheathing have been widely used in building

---

<sup>1</sup> PhD Researcher, <sup>2</sup> Professor, School of Urban Development, Faculty of Built Environment and Engineering, Queensland University of Technology, Australia.



constructions since 1940. These stud wall panels can be easily assembled to form load-bearing as well as non-load-bearing walls.

In response to a market demand for fire separations in the light industrial, commercial and residential buildings, plasterboard lining manufacturers have published fire resistance ratings for conventional stud wall systems. As part of a fire resistant construction, they satisfy three fire resistance requirements given in AS 1530.4, namely, stability, insulation and integrity (SA 2005).

- a) Load-bearing capacity (Stability): For load-bearing elements of a structure, they shall not collapse in such a way that they no longer perform the load-bearing function for which they were constructed.
- b) Insulation: For elements of a structure such as walls and floors which have a function of separating two parts of a building, the average temperature of the unexposed face of the element shall not increase above the initial temperature by more than 140°C while the maximum temperature at any point of this face shall not exceed the initial temperature by more than 180°C.
- c) Integrity: Initial integrity failure shall be deemed to have occurred when a cotton pad is ignited or when sustained flaming, having duration of at least 10s, appears on the unexposed face of the element.

The walls are required to maintain structural integrity during a fire so as to avoid structural collapse and to prevent spread of flame and smoke into adjacent areas. Ultimate integrity failure shall be deemed to have occurred when collapse of the element takes place or at an earlier time based upon integrity and insulation criteria.

In Australia, plasterboard lining manufacturers provide fire resistance ratings of non-load bearing LSF stud wall systems. They have prescribed steel stud walls with single or multiple plasterboard linings achieving fire resistance ratings ranging from 60 to 120 minutes. These systems are based on full-scale fire resistance tests using the standard fire curve recommended by ISO 834 and AS 1530.4. Adequate fire rating of these wall systems is essential for many reasons such as “to achieve sufficient fire resistance and to prevent or delay the spread of fire and smoke within the building or from one building to another and to avoid sudden collapse of building components for the safety of the people and the fire fighting personnel and assure integrity over a specific interval of time to facilitate the safe evacuation of the people and allow the fire fighters to operate safely”. Hence, with increasing demand for higher fire ratings of these walls, more than two layers of plasterboard linings are being prescribed, which not only make the construction process very laborious but also the resulting walls become very heavy.

Efforts have also been made to improve the fire ratings of the wall systems by using different types of insulations in the wall cavities, but only contradicting results were obtained. Sultan and Lougheed (1994) performed several small scale fire resistant tests on gypsum board clad steel wall assemblies (914 mm x 914 mm) and using glass fibres, rock fibres and cellulose fibres as cavity insulation. They noted that the rock and cellulose fibre cavity insulations improved fire resistance rating by approximately 30 minutes when compared with non-insulated wall assemblies, whereas only a small benefit was noted in the case of specimens using glass fibres. The cavity side of the exposed gypsum board of insulated wall assemblies heated up more rapidly reaching temperature levels of 700°C much earlier when compared to that in non-insulated wall assemblies. Following the calcination of the exposed board, the exposed side of the cavity recorded much higher temperatures when compared to that in non-insulated wall assemblies.

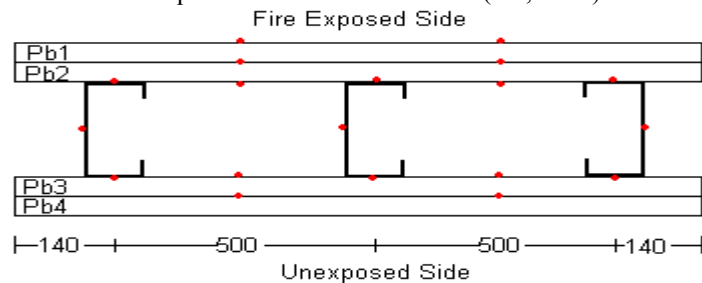
Sultan (1995) carried out full scale fire resistance tests on non-load-bearing gypsum board wall assemblies and noted that when rock fibre?? was used as cavity insulation the fire resistance rating increased by 54% over the non-insulated wall assembly. Use of glass fibre as cavity insulation did not affect the fire performance while cellulose fibre insulation reduced the fire resistance. Feng et al. (2003) conducted fire tests on non-load bearing small scale wall systems and reported that the thermal performance of wall panels improved with the use of cavity insulation.

In summary, past research has produced contradicting results about the benefits of cavity insulation to the fire rating of stud wall systems and hence further research is needed. There is also a need to develop new wall systems with increased fire rating. This research therefore proposed a new wall system that uses a thin insulation layer between two plasterboards on each side of stud wall frame instead of cavity insulation and undertook extensive fire tests of both non-load bearing and load bearing walls to increase the knowledge in this field and to improve the fire ratings of the existing wall models. This paper presents the details of fire tests of some non-load-bearing walls, examines and compares their thermal performance, and makes suitable recommendations.

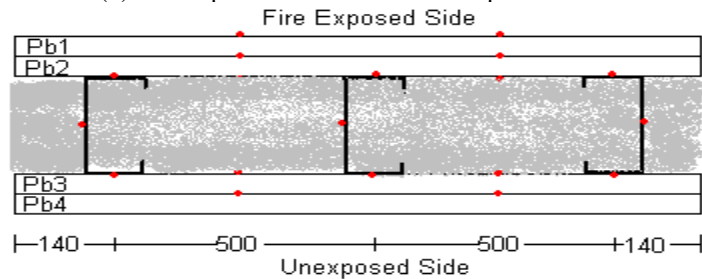
## 2. TEST SPECIMENS

Tests were conducted on three small scale wall assemblies each measuring 1280 mm in width and 1015 mm in height. The wall assemblies typically consisted of three commonly used cold-formed steel studs lipped channel sections spaced at 500 mm. The studs were fabricated from galvanized steel sheets having a

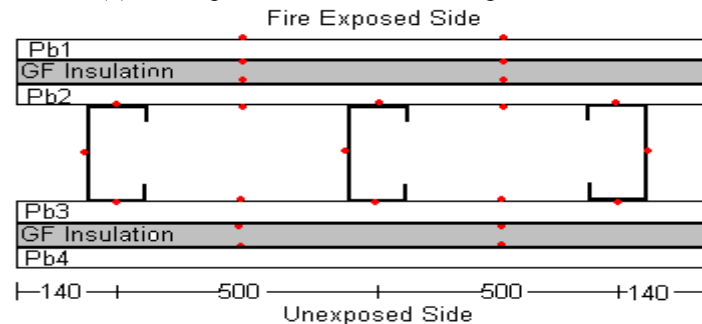
nominal base metal thickness of 1.15 mm and a minimum yield strength of 500 MPa. Test frames were made by attaching the studs to top and bottom tracks made of unflipped or plain channel sections. For Test Specimen one, the steel frames were lined on both sides by two layers of gypsum plasterboards manufactured by Boral Plasterboard under the product name FireSTOP (see Figure 1a). Test Specimen 2 was similarly built, but with the cavity filled with two of 50 mm thick glass fibre mats. Test Specimen 3 was also built like Test Specimen 1, but with a single mat of 25 mm thick glass fibre insulation sandwiched between the plasterboards thus forming composite panels on either side of the steel stud frame as shown in Figure 1c. All the plasterboards were manufactured to the requirements of AS/NZS 2588 (SA, 1998).



(a): Test Specimen 1 and thermocouple locations



(b): Test Specimen 2 and thermocouple locations

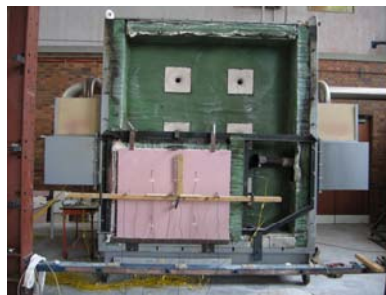


(c): Test Specimen 3 and thermocouple locations

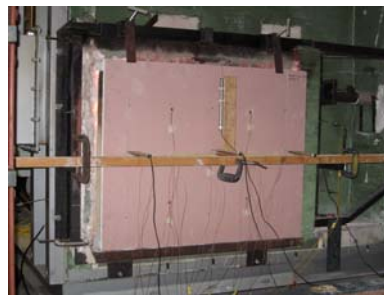
Figure 1: Details of Test Wall Specimens

### 3. TEST SET-UP

A custom built adaptor was fitted to the large furnace available at Queensland University of Technology in order to reduce the flame opening size to 1290 x 1010 mm by the use of a single burner (Figure 2a). The tests were carried out by exposing one face of the specimens to heat in this propane-fired vertical furnace (Figure 2b). The furnace temperature was measured using four type K mineral insulated and metal sheathed thermocouples symmetrically placed about the horizontal and vertical centre lines. The average temperature rise of these thermocouples served as the input to the computer controlling the furnace according to the cellulosic fire curve given in AS 1530.4 (SA, 2005). A number of type K thermocouples were placed on each test specimen as shown in Figures 1 (a) to (c) to obtain the temperature variation across the depth of the wall specimens. The specimens were allowed to expand freely during the test. The vertical edges of the specimen were kept free to allow lateral deformations. All the gaps and openings around the specimen were sealed using Isowool. The specimens were installed in the furnace as shown in Figure 2. Three Linear Variable Differential Transducers (LVDT's) were mounted on a wooden beam acting as a support bridge outside the specimen to measure the mid-height lateral deflection of the studs. Lateral deflections towards the furnace were recorded as negative. The failure of the small scale test specimens was based on the integrity and insulation criteria in AS 1530.4 (SA, 2005). The furnace and specimen temperatures were recorded using an automatic data-acquisition system at intervals of one minute.



(a) Test Specimen in the specially built adapter in the large furnace



(b) Test Specimen subjected to fire on one side

Figure 2: Fire Testing of Small Scale Wall Specimens

#### 4. OBSERVATIONS AND RESULTS

In all the wall specimens the fire side plasterboards 1 and 2 (Pb1 and Pb2 in Figures 1(a) and (b)) had partially collapsed towards the end of the fire test. They fully collapsed due to their extreme brittleness when the specimens were removed from the furnace and placed on the laboratory floor for inspection. Plasterboard 3 (base layer on ambient side) was also damaged at the centre in all the specimens. Studs of Test Specimen 1 (without insulation) were seen to be the least affected by fire whereas those of Test Specimen 2 (with cavity insulation) were the most affected.

In Test Specimen 2, the cavity insulation was burnt out completely, whereas in Test Specimen 3 the insulation on the fire side had disappeared fully but the insulation on the ambient side between the plasterboards 3 and 4 was partially intact. The unexposed wall surface of both the specimens showed no signs of damage or effect of temperature right up to the end of test. Figures 2, 3 and 4 show the photographs of Test Specimens 1, 2 and 3 after the fire test, respectively. Numerous thermocouples were installed across the width of the wall, located at mid-height of the wall as shown in Figure 3.



Figure 3: Installation of K type wire thermocouples in Test Specimens



Figure 4: Failure of Test Specimen 1 built without insulation



Figure 5: Failure of Test Specimen 2 using glass fibre as cavity insulation



Figure 6: Failure of Test Specimen 3 using glass fibre as external insulation

Figure 7 shows that the average furnace time-temperature profiles for the three tests traced very closely to the standard time-temperature curves specified by AS1530.4. This proved that the fire tests had been undertaken as per the standard fire test requirements. The furnace temperature of Test Specimen 1 showed a deviation from the standard curve, but only after 180 minutes.

Figures 8 (a) to (c) show the time-temperature profiles across Test Specimens 1, 2 and 3, respectively. From these three figures, it can be seen that the studs of Specimen 3 were much better protected due to the external layer of insulation. The stud temperatures in Test Specimen 3 remained almost constant (about 100°C) up to 85 minutes (from the start of the fire test) beyond which it rose rapidly. In Test Specimens 1 and 2 this sudden increase in stud temperatures was seen to happen much earlier (ie. after about 60 minutes), leading to earlier lateral deformations of the studs (see Figure 12). The temperature was found to be more uniform across the studs of Specimens 1 and 3 due to the faster transmission of heat by radiation in the cavity. The low conductivity of the insulation in the cavity of Specimen 2 reduced the heat flow towards the cold flanges of the studs but at the same time quickened the temperature rise of the hot flange due to the additional heat redirected from the surface of insulation. This caused the hot flange of Test Specimen 2 to heat up more rapidly than that of Test Specimens 1 and 3 and remained high over the entire test period (see Figure 9) leading to their earlier damage. The hot flange temperature of the stud in Specimen 3 surpassed that of Specimen 1 after about 150 minutes. This was probably due to the heat redirected towards the cavity by the external insulation on the ambient side.

The central studs in all the specimens showed higher temperatures at any time than the end studs, with the difference more pronounced in Specimen 2. Figure 10 shows the effect of external insulation versus cavity insulation on the temperature across the critical central stud. It can be seen that over the entire duration of the test, even the hot flange temperature of the central stud of Specimen 3 was lower than the cold flange temperature at the corresponding time in Specimen 2. In load bearing walls this would translate into much lower thermal strains and the associated thermal stresses in the steel frames. Figure 11 also shows the beneficial effect on the stud temperatures of the externally insulated wall specimen over the non-insulated wall specimen over a large initial time period (approximately 150 minutes) of fire exposure. Due to the rapid reduction in the strength and stiffness of cold-formed steel studs, large scale specimens (i.e. having two layers of plasterboard on either side of cold-formed steel frame) even with the non-load-bearing condition may not survive beyond this time due to the slenderness of the studs and the weight of the intact ambient side plasterboards.

The temperatures of fire side plasterboards of Test Specimen 2 were seen to rise more rapidly than that for Test Specimen 1 and 3. In Specimen 2, the exposed plasterboards 1 and 2 fell at around 130 and 150 minutes, respectively, whereas in Specimen 3 they fell at around 165 and 195 minutes, respectively. The fall off times of the exposed plasterboards in Test Specimen 1 could not be recorded.

Table 1 shows the unexposed surface temperatures of all the specimens at the end of 60, 120 and 180 minutes from the start of the fire test.

Table 1: Temperature of Unexposed Surface during Fire Tests

Specimen	Cavity insulation (90 mm)	External Insulation (25 mm)	Temperature in °C of unexposed surface after		
			60 min.	120 min.	180 min.
1	Nil	Nil	59	72	91
2	Glass fibre	Nil	56	71	113
3	Nil	Glass fibre	48	68	76

The unexposed surface temperature of the cavity filled specimen exceeded that of the non-insulated specimen after a period of 2 hours of heat exposure. This was probably due to the heat transmitted by thermal bridging to the ambient side from the steeply rising hot flange temperature of the studs. The external insulation layer on the ambient side of Test Specimen 3 helped the wall in achieving the best insulation properties over the entire duration of the test as seen from Table 1 and Figure 13.

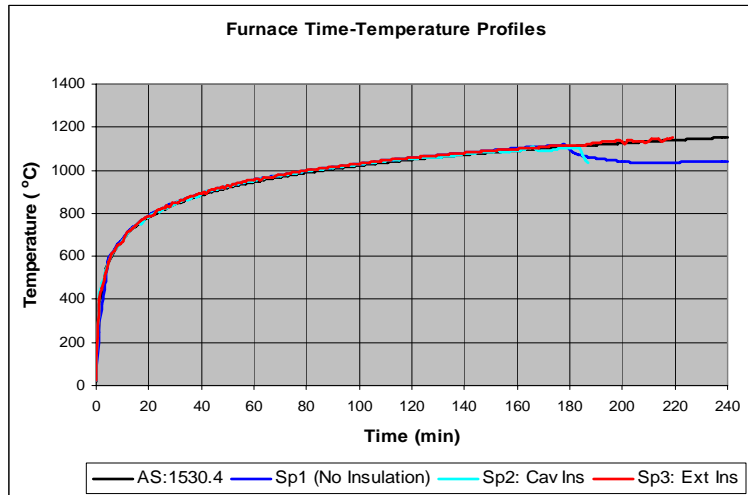
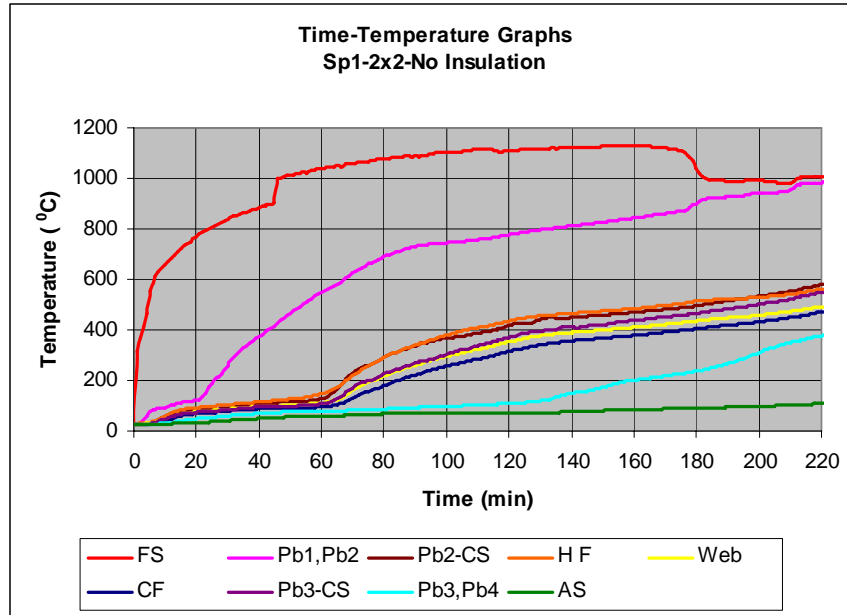
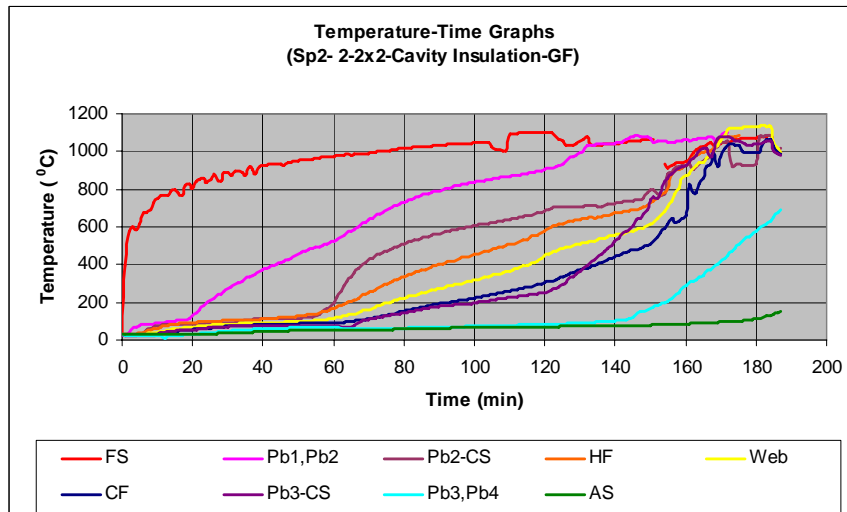


Figure 7: Furnace Time-Temperature Profiles for Test Specimens 1, 2 and 3



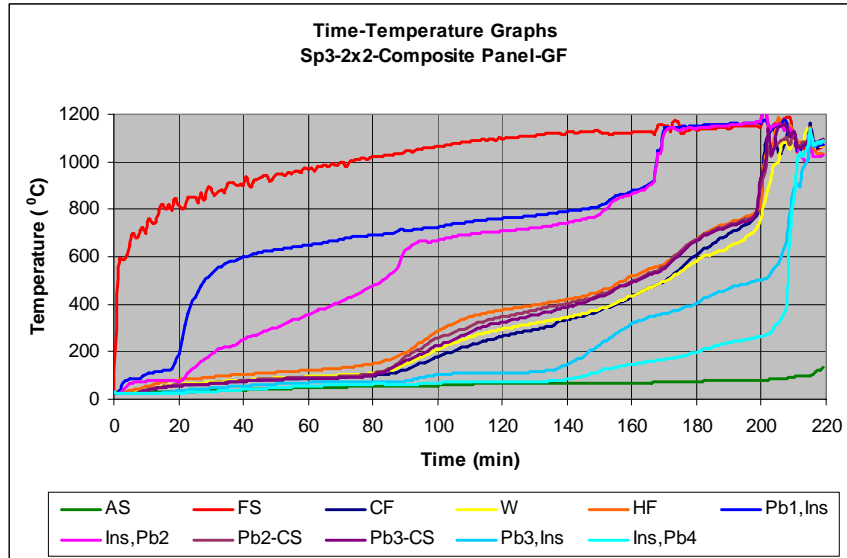
(a): Time-Temperature profiles across Test Specimen 1



(b): Time-Temperature profiles across Test Specimen 2

Figure 8: Time-Temperature Variation across the Small Scale Wall Specimens





(c): Time-Temperature profiles across Test Specimen 3

Figure 8: Time-Temperature Variation across the Small Scale Wall Specimens

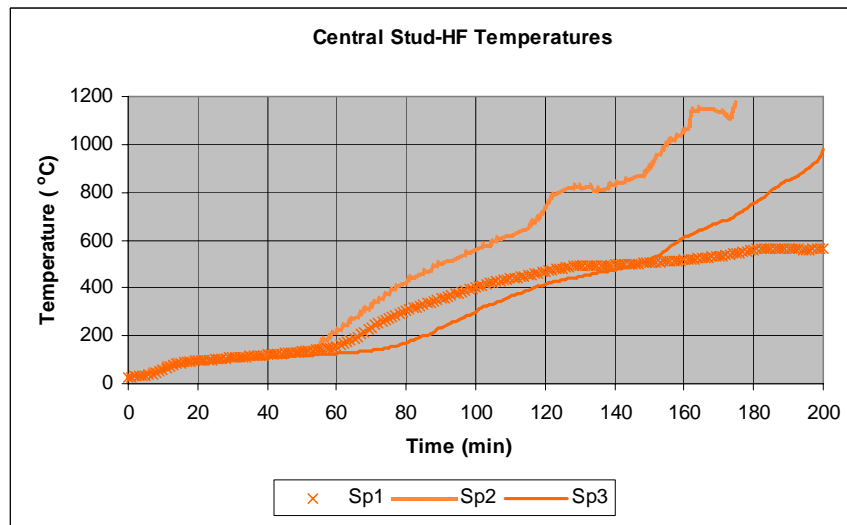


Figure 9: Time-Temperature Profiles  
(Hot flange of central stud of Test Specimens 1, 2 and 3)

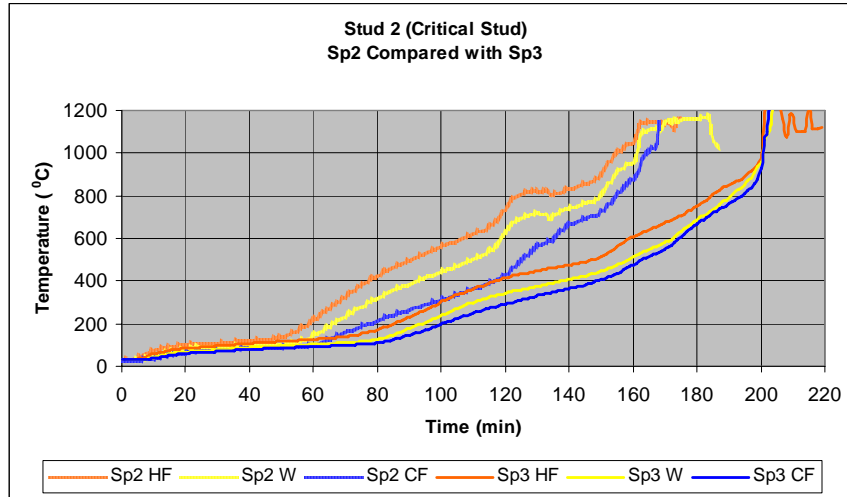


Figure 10: Time-temperature Profile for the Central Stud in Test Specimens 2 and 3

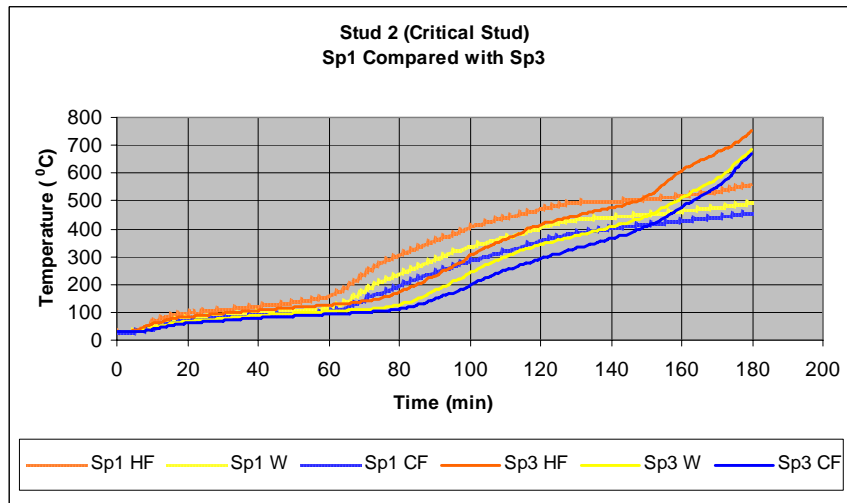


Figure 11: Time-temperature Profile for the Central Stud in Test Specimens 1 and 3

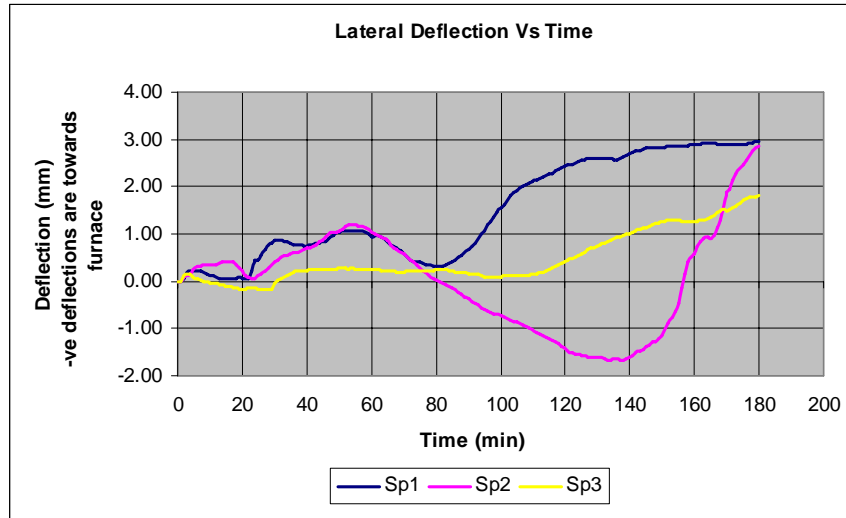


Figure 12: Lateral Deflection-Time Profile of Specimens 1, 2 and 3

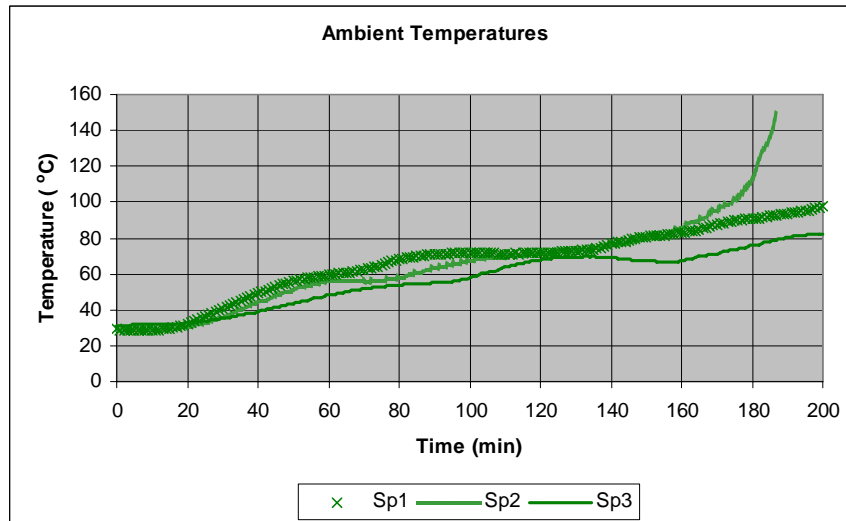


Figure 13: Ambient Side Time-Temperature Profile of Specimens 1, 2 and 3

Following symbols were used in Figures 7 to 13.

AS 1530.4: Standard Time-temperature Relationship

FS: Average temperature of the exposed face of the wall specimen.

Pb1, Pb2: Average temperature of the interface between Pb1 and Pb2.

Pb2-CS: Average temperature of the cavity facing surface of Pb2

Pb3-CS: Average temperature of the cavity facing surface of Pb3

Pb3, Pb4: Average temperature of the interface between Pb3 and Pb4.

Pb1, Ins: Average temperature of the interface between Pb1 and insulation layer.

Ins, Pb2: Average temperature of the interface between Insulation layer and Pb2

HF: Average temperature of the hot flanges of the three studs

W: Average temperature of the webs of the three studs

CF: Average temperature of the cold flanges of the three studs

Sp1/2/3 HF: Hot flange temperature of specimen 1/2/3

Sp1/2/3 W: Web temperature of specimen 1/2/3

Sp1/2/3 CF: Cold flange temperature of specimen 1/2/3

AS: Average temperature of unexposed surface (Ambient Side) of the specimen

Detailed thermal performance results for the cold-formed steel stud wall systems as discussed in this paper have shown that the use of cavity insulation is detrimental to the fire rating of walls. It has led to not only higher temperatures in the steel studs, but also a larger temperature gradient across its depth. This is expected to lead to premature failures of steel studs in load-bearing walls. In contrast, lower temperatures and a more uniform temperature distribution were present in the studs of wall systems made with external insulation. The use of external insulation offered greater thermal protection to the studs resulting in a more uniform temperature distribution across their cross-section thereby producing minimum early lateral deformation (thermal bowing). This would be of immense value in load-bearing walls, as their structural failure is usually brought about by the excessive secondary moments developed by increasing eccentricities caused by thermal bowing, which are further amplified if the walls are not allowed to expand freely in the vertical direction. Also the difference in temperature of the individual studs in the externally insulated specimen was not significant as the radiation of heat in an open cavity is very fast leading to a quick balance of temperatures in the individual studs. This helps in reducing the build up of internal stresses in the frame caused by the unequal expansions of the individual studs. The insulating properties of the new model were also found to be much better than the conventional models. These observations imply that the new wall system with external insulation is likely to provide improved performance under the three fire rating criteria of stability, integrity and insulation. Research is continuing to investigate the thermal and structural performance of stud walls using numerical modeling.

## 5. CONCLUSIONS

This paper has described an experimental study of the thermal performance of cold-formed steel stud wall systems used as non-load bearing walls. This study has shown that the use of cavity insulation led to poor thermal performance of stud walls. In contrast, the thermal performance of externally insulated steel stud walls was superior than the traditionally built stud walls with or without cavity insulation. Details of fire tests and the results are presented and discussed in this paper.

## 6. ACKNOWLEDGEMENTS

The authors wish to thank Australian Research Council for the financial support to this project through the Discovery Grants Scheme, Queensland University of Technology for providing the required experimental and computing facilities and technical support and Boral and Fletcher Insulation for providing the required plasterboard and insulation materials.

## 7. REFERENCES

- Feng, M., Wang, Y.C. and Davies, J.M., (2003), Thermal Performance of Cold-formed Thin-walled Steel Panel Systems in Fire, *Fire Safety Journal*, Vol. 38, pp. 365-394.
- ISO 834 -1 (1999), Fire Resistance Tests – Elements of Building Construction-Part 1: General Requirements, International Organization for Standardization, Geneva, Switzerland.
- Standards Australia (SA) (2005), AS 1530.4, Methods for fire tests on building materials, components and structures, Part 4: Fire-resistance tests of elements of building construction, Sydney, Australia.
- Standards Australia (SA) (1998), AS/NZS 2588, Gypsum Plasterboard, NSW, Australia.
- Sultan, M. A. (1995), Effect of Insulation in the Wall Cavity on the Fire Resistance Rating of Full-Scale Asymmetrical (1x2) Gypsum Board Protected Wall Assemblies, Proceedings of the International Conference on Fire Research and Engineering, Orlando, FL, Lund D. P. (Ed.), Society of Fire Protection Engineers, Boston, MA, pp. 545-550.
- Sultan, M. A. and Lougheed, G. D. (1994). The Effect of Insulation on the Fire Resistance of Small-scale Gypsum Board Wall Assemblies, Proceedings of the Fire and Materials Third International Conference and Exhibition, Washington, DC, Interscience Communications Limited, London, UK, pp. 11-20.

## TESTING AND EVALUATION OF CFS L-HEADERS

J. Pauls<sup>1</sup>, L. Xu<sup>2</sup>, and S. Fox<sup>3</sup>

### Abstract

Recently there has been an increased interest in cold-formed steel L-headers, in part due to their ease of installation and low material cost. Design guidance for L-headers is currently provided by the *AISI Standard for Cold-Formed Steel Framing – Header Design* in combination with the *North American Specification for Design of Cold-Formed Steel Structural Members*. The current AISI – Header Design provisions are, however, particularly limiting and lack certain design criteria for double and single L-header assemblies, primarily due to limited research.

Presented in this paper are the results from an extensive test program carried out at the University of Waterloo on both single and double cold-formed steel L-headers. A total of 48 single L-header assemblies and 56 double L-header assemblies were tested under gravity loading. The objective of the research was to develop improved design expressions for determining the flexural capacity and vertical deflections. A comparison between the flexural test data and the nominal flexural resistance calculated according to the current AISI Header Design standard is provided. The theory of semi-rigid connections is introduced to model the vertical deflections.

### Introduction

L-shaped cold-formed steel headers are becoming more common in residential construction, since they are lighter and more economical compared to conventional built-up cold-formed steel headers. However, due to limited

---

<sup>1</sup> Research Assistant, The Canadian Cold Formed Steel Research Group, Department of Civil and Environmental Engineering, University of Waterloo, Waterloo, Ontario, Canada

<sup>2</sup> Associate Professor, The Canadian Cold Formed Steel Research Group, Department of Civil and Environmental Engineering, University of Waterloo, Waterloo, Ontario, Canada

<sup>3</sup> General Manager, Canadian Sheet Steel Building Institute, Cambridge, Ontario, Canada

testing designers are still restricted to the size of L-headers that can be used. The current AISI Header Design standard (AISI 2007) is especially restrictive for single L-headers.

In 1998 the NAHB Research Center conducted 71 tests under gravity loads and 38 tests under uplift load on double L-headers (NAHB-RC 1998). In 2003 the NAHB Research Center carried out an additional 18 tests on single L-headers (NAHB-RC 2003). A paper summarizing both sets of tests was submitted to the AISI Committee on Framing Standards in 2005 by R.A. LaBoube (LaBoube 2005). Based on the analysis, LaBoube proposed a new design approach for double and single L-headers. In addition to the proposed new design methodology, LaBoube recommended additional testing to better assess the deflection performance of both single and double L-headers. LaBoube's proposed design approach has been adopted into the 2007 edition of the AISI Header Design. Currently there are no explicit design criteria for deflection determination of either single or double L-headers.

Summarized in this paper are the results obtained from the testing conducted at the University of Waterloo, and comparison of the test results to the nominal flexural capacity obtained using the current AISI Header Design. An analysis and evaluation of the vertical deflections is also presented.

### **Experimental Setup**

The experimental investigation was conducted in two phases: short span tests and long span tests. Short span tests consisted of L-header assemblies with a clear span of three feet to six feet. Long span tests consisted of spans ranging between eight feet to sixteen feet.

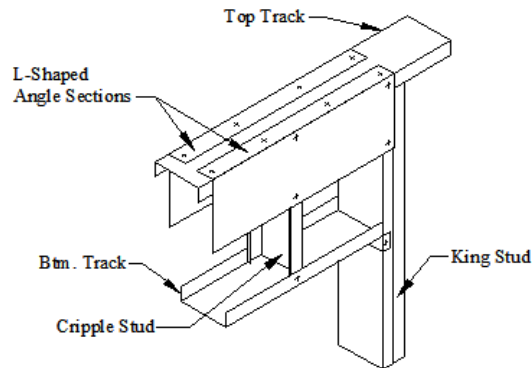
#### Test Specimen Assemblies

The header assemblies were fabricated to simulate a typical opening in a 3-5/8" (92mm) wide steel stud wall assembly. One or two L-shaped cold-formed steel sections were added over the opening with the short leg lapping over the top track section and the long leg extended down the side of the cripple stud, as shown in Figure 1. Self-drilling screws (no. 8) were used to connect the L-shapes to the track sections, cripple studs, and king studs. The track sections used (362T125-33) had a minimum thickness of 33mils (0.84mm). Back-to-back cold-formed steel studs (362S162-43) were attached to each end of the L-header, to simulate king studs. The cripple studs were also 362S162-43 sections.

Clear spans chosen for the tests were based on common spans used in construction and were the same as previous tests conducted by NAHB, for

comparison purposes. For the double L-headers five different span lengths were tested: three feet, six feet, eight feet, twelve feet, and sixteen feet. For single L-header assemblies three different span lengths were tested: four feet, six feet, and eight feet.

All assemblies were constructed based on general materials and methods appropriate for framing cold-formed steel light-commercial or residential structures. Construction and testing was entirely performed at the University of Waterloo.



**Figure 1:** Double L-header Assembly

#### Material Properties

Mechanical properties for the L-header assemblies were based on tensile coupon tests and base steel thickness measurements, conducted in accordance with ASTM A370 and ASTM A90 respectively (ASTM 2003). Three coupons were cut from the long leg of the L-shaped angle sections. Galvanized coatings were removed by dipping the coupons in a sulfuric acid solution. Table 1 summarizes the mechanical properties for all the material.

#### Section Properties

Section properties for each specimen were calculated based on the North American Specification (CSA 2004). Section properties for the header assemblies were based entirely on the L-shaped angle(s), the top track or bottom track sections were not included in the calculation. Section properties calculated for serviceability determination were based on reduced yield stress ( $0.6F_y$ ), which is commonly used for serviceability computations.



### Short Span Test Setup

All short span tests were conducted using a universal testing machine (UTM) and were loaded at a constant rate of 1/20 inch per minute until failure. The 3ft (0.91m) and 4ft (1.22m) assemblies were loaded with a single point load applied at midspan over a cripple stud. Midspan deflections were recorded using a linear variable differential transformer (LVDT). The 6ft (1.83m) assemblies were loaded by two point loads at one-third span. A spreader beam was attached to the universal testing machine and distributed the loads equally to the two cripple studs. An LVDT measured the deflection at the location of the applied load (one-third span), while the midspan deflection was recorded using a linear motion transducer (LMT) attached to the bottom track.

The king studs on either end of the assembly were positioned in fabricated base supports. The supports allowed the assembly to rotate in the plane of bending, while restraining the assembly from out of plane bending and lateral movement.

### Long Span Test Setup

The long span L-headers were tested using a Large Scale Hydraulic Truss Test Frame, which applied loads at multiple points along the L-header assembly. This frame utilized load control of the hydraulic actuators, rather than displacement control which was used for the short span tests. An equivalent rate of loading of 1.1 kip per minute was used. The king studs were positioned in the same fabricated base supports as the short span tests, and the assemblies were fully laterally braced.

The testing procedure used for the short span tests (six foot and less) was based on the procedure used at the NAHB Research Center. However, for the long span tests a different loading approach was implemented. The NAHB tests used a two-point loading at one-third span for all their long span tests, whereas the tests conducted at the University of Waterloo were loaded with multiple loads at 24 inches (610mm) on center. Applying loads at 24 inches on center is a much closer simulation of the actual loading experienced in typical residential construction.

One of the main differences between the loading configurations is that with two-point loading the maximum moment is larger than multi-point loading under the same total load. For the 12ft (3.66m) and 16ft (4.88m) assemblies under the same total load, the midspan moment is larger by 11% and 17% respectively. Furthermore, two-point loading results in a shear force of zero at midspan, while multi-point loading results in a non-zero shear force at midspan.

## Results / Data Analysis

### Gravity Loading - Ultimate Strength

Failure of both single and double short span L-header assemblies was observed to be a combination of flexure and web-crippling. For the 3ft (0.91m) and 4ft (1.22m) assemblies web-crippling was more pronounced; however, for the 6ft (1.83m) assemblies the effect of web crippling became less apparent. Assemblies longer than 6ft were observed to fail purely under flexure.

For the short span tests (3ft to 6ft) the ultimate load applied at failure of each assembly was determined directly from the data acquisition output, from which the ultimate test moment ( $M_t$ ) was computed. For the long span tests the ultimate load was determined as the sum of the individual loads applied at each cripple stud, at failure. The ultimate test moment was calculated based on the individual loads applied to each cripple stud.

The ultimate test moment was compared to the nominal gravity flexural capacity ( $M_{ng}$ ) of each header assembly as determined using the AISI Header Design standard (AISI 2007). The standard assumes the nominal gravity flexural capacity is solely based on the L-section(s) and that the track sections do not add to the capacity.

For double L-headers with a vertical leg dimension of 8" (203mm) or less the nominal flexural capacity under gravity loading is calculated according to Eq. 1.

$$M_{ng} = S_{ec} F_y \quad (\text{Eq. 1})$$

For L-header assemblies with a vertical leg dimension of greater than 8" and with a span-to-vertical leg dimension ratio equal to or greater than 10, Eq. 1 shall be used directly. However, for header assemblies with a vertical leg dimension greater than 8" and a span-to-vertical leg dimension ratio less than 10, the nominal flexural capacity calculated using Eq. 1 is multiplied by 0.9.

For single L-headers, the nominal flexural capacity under gravity loading of assemblies with a vertical leg dimension of 6" (152mm) or less is calculated according to Eq. 1. For single L-headers with a vertical leg dimension greater than 6" but not greater than 8", the nominal flexural capacity is multiplied by 0.9. Single L-headers with depths greater than 8" or spans of greater than four feet are not covered in the AISI Header Design. Tested assemblies which exceeding this criteria were calculated based on Eq. 1 with no modification factor.

The AISI Header Design uses different resistance factors based on the vertical-leg dimension of the L-shaped section when calculating the actual design moment capacity ( $M_a$ ).

Actual measured mechanical properties were used in the calculation of the nominal gravity flexural capacities. Summarized in Tables 2 and 3 are the results of the gravity tests for both double and single L-header assemblies respectively.

(a) Double L-headers

The 3ft (0.91m) header assemblies resulted in the lowest  $M_t/M_{ng}$  ratios. The nominal flexural capacity calculated as per the AISI Header Design over estimated the strength of these assemblies. Even after applying the 0.9 modification factor for short deep L-headers, the nominal flexural capacity is still over-estimated. It is probable that web-crippling and shear forces are influencing the behavior of these assemblies. The lowest  $M_t/M_{ng}$  ratios were seen for 3ft assemblies with the largest vertical leg-to-thickness ratios. As the vertical leg-to-thickness ratio of the assembly decreased the  $M_t/M_{ng}$  ratios increased closer to unity.

As the span lengths increased the  $M_t/M_{ng}$  ratios also increased. Assemblies with a span-to-vertical leg ratio of 9 had  $M_t/M_{ng}$  ratios of approximately unity. For assemblies with a span-to-vertical leg ratio of less than 9,  $M_t/M_{ng}$  ratios were consistently less than unity. Furthermore, as the span-to-vertical leg ratio increased beyond 9 the nominal flexural capacities calculated based on the AISI Header Design become conservative.

Conservative nominal flexural capacities could be due to the fact the ultimate test moment was calculated based on pinned end connections, which means the end connection rotational stiffness is zero. However, in reality the end connections would provide some rotational stiffness, therefore acting as semi-rigid connections. This added rotational stiffness would cause end moments, lowering the midspan moment and reducing the  $M_t/M_{ng}$  ratios closer to unity.

(b) Single L-headers

The results from the single L-header assemblies follow the same trends as the double L-header assemblies. The short spans had low  $M_t/M_{ng}$  ratios and as the span increased the  $M_t/M_{ng}$  ratios increased. As with the double L-headers, assemblies with a span-to-vertical leg ratio of 9 had  $M_t/M_{ng}$  ratios of approximately unity. Assemblies with a span-to-vertical leg ratio of less than 9

consistently have  $M_t/M_{ng}$  less than unity. Assemblies with span-to-vertical leg ratio greater than 9 have conservative nominal flexural capacities.

The 0.9 modification factor used in the AISI Header Design reduces the nominal flexural capacity, yet  $M_t/M_{ng}$  ratios are still less than unity.

Comparing the tested ultimate moment capacities of the single L-headers to the double L-headers, the single L-headers consistently had capacities of just over half the capacity for the same size double L-header assembly. With the nominal flexural capacity of the assemblies calculated based solely on the section modulus of the L-headers alone, doubling the section modulus for a double L-header assembly resulted in exactly double the nominal flexural capacity. However, since the track sections do somewhat influence the capacities of the assemblies, adding a second L-shaped section to the assembly did not exactly double the tested capacity. For this reason the single L-header assemblies resulted in slightly higher  $M_t/M_{ng}$  ratios compared to the same size double L-header assembly.

(c) Comparison to Previous NAHB L-header Tests

In general the results from the double L-headers tests conducted at the NAHB Research Center were similar to those conducted at the University of Waterloo. However, for the short span headers the average total load and average maximum moment at failure vary considerably between the tests conducted at the NAHB Research Center and the University of Waterloo. Nonetheless, if the differences in mechanical properties are taken into consideration the ratios of  $M_t/M_{ng}$  are fairly consistent, typically within 10% of each other. For longer span headers the average ultimate load at failure were particularly close in comparison, although the maximum moment capacities tend to be higher for the tests conducted at the NAHB Research Center (two-point loading configuration).

The single L-header tests conducted at the NAHB Research Center resulted in higher ultimate loads and maximum moments compared to those tested at the University of Waterloo. In addition, the mechanical properties of the material used for the NAHB tests were generally lower than those of the University of Waterloo tests. With lower tested capacities and higher calculated nominal flexural capacities, all tests conducted at the University of Waterloo resulted in noticeably lower  $M_t/M_{ng}$  ratios.

### Gravity Loading – Deflection

Previous testing of L-header assemblies has provided limited deflection data. As a result, the current AISI Header Design does not provide any guidance with regards to vertical deflection computations. In an effort to provide design guidance, the current L-header testing measured the vertical deflection for each of the L-header test assemblies.

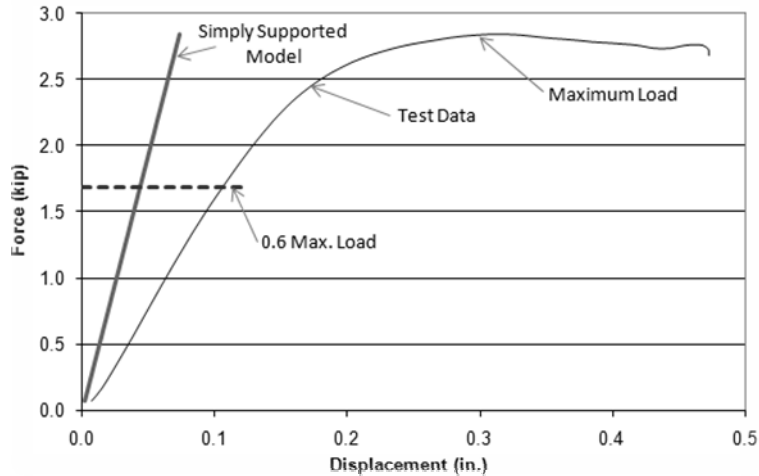
Generally headers are designed to meet a minimum deflection criterion of L/240 under service loads. Therefore, the vertical deflection results were compared to the L/240 limit at 60% of the ultimate applied load used as an approximation of the service load. Summarized in Table 4 are the deflection results for the double and single L-header assemblies.

#### (a) Deflection of Short Span L-Headers Assemblies

The maximum tested span deflection at 60% of ultimate load, for each 3ft (0.91m) and 4ft (1.22m) L-header assembly were less than L/240. The midspan load-deflection curve for each assembly was compared to a predicted curve based on a simply supported system, Eq.2.

$$\Delta_{midspan} = \frac{PL^3}{48EI_e} \quad (\text{Eq. 2})$$

The effective moment of inertia ( $I_e$ ) used in the simply supported prediction model was computed at  $f = 0.6F_y$  which is typically used for serviceability calculations. With using a constant effective moment of inertia the simply supported model produces a linear load-deflection curve. Generally, the deflections from the tested assemblies were larger than the predicted simply supported deflections. The common trend for the load-deflection curve of the L-header assemblies is as shown in Figure 2.



**Figure 2** Typical Load-Deflection Curve for Short Span Assemblies

Since the midspan deflection of the tested assemblies is consistently greater than the simply supported model, other factors than just flexural stresses are influencing the vertical deflection. It was observed that for the short spans the assemblies failed in a combination of web-crippling and flexure. Consequently, a deflection predictor equation for short span assemblies needs to incorporate web-crippling and shear deformation.

(b) Deflection of Long Span L-Headers

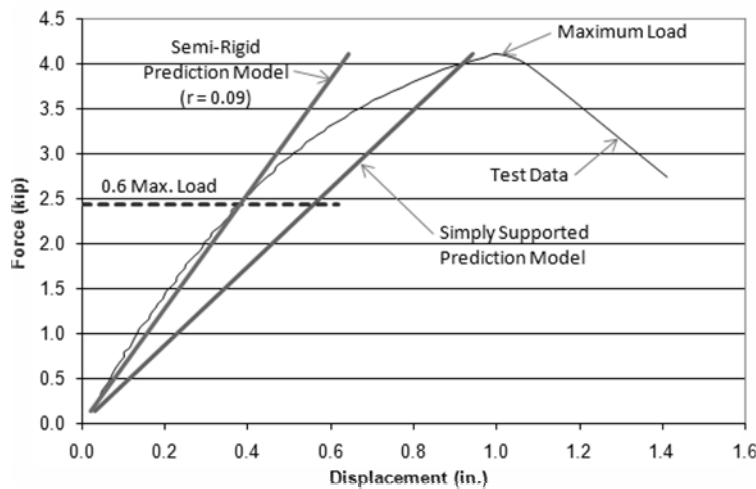
The maximum span deflections under service load for the long span L-header assemblies (single and double) were found to be typically less than  $L/240$ . As with the short span L-headers, a simply supported beam model was used to predict the midspan deflection for the long span L-headers. However, it was found that the simply supported model over-estimates the midspan deflection for these assemblies, as illustrated in Figure 3.

The simply supported model is based on pinned end connections. However, the end connections of the L-header assemblies do provide end rotational restraint to some extent, therefore behaving as semi-rigid members. For semi-rigid members the end-fixity factor as defined below reflects the relative stiffness of the end connections (Xu 2001).

$$r = \frac{1}{1 + \frac{3EI_e}{RL}} \quad (\text{Eq. 3})$$

Where  $EI_e/L$  is the effective flexural stiffness of the L-header(s) and  $R$  is the end connection rotational stiffness. For pinned connections the end-fixity factor is zero ( $r = 0$ ), while rigid end connections have an end-fixity factor of one ( $r = 1$ ). Semi-rigid members have end-fixity factors ranging between zero and one.

A semi-rigid prediction model was needed to take into consideration the rotational stiffness of the assemblies for evaluating the span deflection. An ideal model would pass through the test data curve at 60% of the ultimate load, which is typically used as the ultimate service load. Consequently, the semi-rigid prediction model was calibrated with the 60% ultimate test load as shown in Figure 3. The corresponding end-fixity factor was calculated based on deflection equations for semi-rigid members (Xu 2001).



**Figure 3** Typical Load-Deflection Curve for Long Span Assemblies

The tested header assemblies were found to have end-fixity factors ranging between 0 and 0.3 as summarized in Table 4. In general as the header assembly stiffness increased the end-fixity factor decreased. For a given header length increasing the depth or thickness results in increased assembly stiffness. As a result, the deepest and thickest 6ft (1.83m) and 8ft (2.44m) L-header assemblies

tested, had insignificant end-fixity factors. For these header assemblies the simply supported model works well at predicting the midspan deflection under service loads.

### **Conclusions**

- 1) Failure of short span single and double L-header assemblies is influenced by additional failure modes other than flexure alone. As the span increases flexural failure becomes predominate and the assembly tends to act as semi-rigid member.
- 2) The current AISI – Header Design over-estimates the nominal gravity flexural resistance for short span L-header assemblies. However, predicts conservative results for long span assemblies.
- 3) Midspan deflections for short span assemblies are larger than predicted using the simply supported beam equation alone. Shear and web-crippling deformation influence the overall displacement of these short assemblies.
- 4) Assemblies with spans greater than 6ft (1.83m) act as semi-rigid members with rotational stiffness' greater than zero, causing midspan deflections to be less than that predicted by a simply supported system.

### **Future Work**

- 1) Develop a revised ultimate limit states (ULS) design methodology for single and double L-headers, which accounts for the additional failure modes acting on short span assemblies, and takes into account the influence of the semi-rigid connections for the long spans.
- 2) Develop a new serviceability limit states (SLS) design methodology for midspan deflection determination.
- 3) Conduct uplift tests for both single and double L-header assemblies. Evaluate current AISI – Header Design uplift design approach for double L-headers.
- 4) Propose a new ultimate limit states (ULS) design approach for the flexural capacity of single L-headers under uplift loads.



### Appendix - References

AISI. *North American Standard for Cold-Formed Steel Framing - Header Design*. Washington, D.C.: American Iron and Steel Institute, 2007.

ASTM . *Standard Test Methods and Definitions for Mechanical Testing of Steel Products*. West Conshohocken, P.A.: American Society for Testing and Materials, 2003.

CSA. *North American Specification for the Design of Cold-Formed Steel Structural Members, 2001 Edition with 2004 Supplement (CAN/CSA136)*. Mississauga, Ontario: Canadian Standards Association, 2004.

LaBoube, R.A. *L-Header Testing, Evaluation and Design Methodology*. Report submitted to AISI Cold-Formed Steel Framing Committee, 2005.

NAHB-RC. *L-Shaped Header Testing, Evaluation, and Design Guidance*. Upper Marlboro, M.D.: National Association of Home Builders Research Center, 1998.

NAHB-RC. *Testing of Steel Single L-Headers*. Upper Marlboro, MD: National Association of Home Builders Research Center, 2003.

Xu, L. *Second-order Analysis for Semirigid Steel Frame Design*, Canadian Journal of Civil Engineering, Vol. 28: pp.59-76, 2001

### Appendix - Notations

$E$  = modulus of elasticity (29,000 ksi)

$F_y$  = design yield strength (ksi)

$I_e$  = effective moment of inertia, computed at  $f = 0.6F_y$  (in.<sup>4</sup>)

$L$  = clear span (in.)

$M_{ng}$  = nominal gravity flexural capacity (kip\*in.)

$P$  = load (kips)

$r$  = semi-rigid end-fixity factor

$R$  = end connection rotational stiffness (kip\*in./rad.)

$S_{ec}$  = effective section modulus calculated relative to the extreme compression fiber (in.<sup>3</sup>)

**TABLE 1 Mechanical Properties**

	<b>Material Designation<sup>1</sup></b>	<b>Base Steel Thickness (in.)</b>	<b>Yield Strength (ksi)</b>	<b>Tensile Strength (ksi)</b>	<b>Elongation (%)</b>
<b>3' / 4' / 6' Spans</b>	600L150-33	0.0334	51.8	55.7	33.7
	600L150-43	0.0437	54.5	59.5	29.4
	600L150-54	0.0541	58.5	78.0	30.1
	800L150-33	0.0341	58.5	67.2	28.2
	800L150-43	0.0434	51.2	61.4	30.3
	800L150-54	0.0541	58.5	78.0	30.1
	1000L150-33	0.0341	58.5	67.2	28.2
	1000L150-43	0.0434	51.2	61.4	30.3
	1000L150-54	0.0541	58.5	78.0	30.1
<b>8' / 12' Spans</b>	600L150-43	0.0438	50.4	55.4	30.8
	600L150-54	0.0543	55.0	71.2	31.1
	800L150-43	0.0438	50.4	55.4	30.8
	800L150-54	0.0543	55.0	71.2	31.1
	800L150-68	0.0695	55.6	72.7	30.8
	1000L150-43	0.0438	50.4	55.4	30.8
	1000L150-54	0.0543	55.0	71.2	31.1
	1000L150-68	0.0695	55.6	72.7	30.8
<b>16' Span</b>	800L150-54	0.0542	55.7	72.0	30.2
	800L150-68	0.0698	55.8	73.5	29.8
	1000L150-54	0.0542	55.7	72.0	30.2
	1000L150-68	0.0698	55.8	73.5	29.8

SI Conversion: 1 in. = 25.4 mm, 1 ksi = 47.9 kPa

<sup>1</sup>Material designated is as per the Steel Stud Manufacturers Association (SSMA). For example an 800L150-43 designation refers to an L-shaped angle with an 8" long leg (1/100 inches), 1.5" short leg (1/100 inches) and a 43 mil nominal thickness

**TABLE 2 Double L-Header Results (ULS)**

Assembly Designation <sup>1</sup>	No. of Tests <sup>2</sup>	Leg / t	L / Leg	Ultimate Load <sup>3</sup> (kip)	Moment M <sub>t</sub> (kip*in)	M <sub>n</sub> (kip*in)	M <sub>t</sub> /M <sub>n</sub>	M <sub>t</sub> /(0.9M <sub>n</sub> )
D6-33-3	2	182	6	3.61	32.5	27.5	1.18	
D6-43-3	3	140	6	4.15	37.3	40.0	0.93	
D6-54-3	2	111	6	6.00	54.0	55.7	0.97	
D6-54-6	3	111	12	5.30	63.6	55.7	1.14	
D6-43-8	2	140	16	4.05	64.2	37.5	1.52	
D6-54-8	2	111	16	5.09	81.2	53.0	1.53	
D8-33-3	3	242	4.5	4.30	38.7	52.5	0.74	
D8-43-3	3	186	4.5	5.90	53.1	61.9	0.86	
D8-43-6	2	186	9	5.88	70.5	61.9	1.14	
D8-54-6	2	148	9	7.10	85.3	91.3	0.93	
D8-43-8	2	186	12	5.47	87.1	61.8	1.41	
D8-54-8	2	148	12	6.83	108.9	86.7	1.26	
D8-54-12	2	148	18	5.21	114.1	86.7	1.32	
D8-68-12	2	118	18	7.38	161.2	118.6	1.36	
D8-54-16	2	148	24	4.32	122.2	87.6	1.40	
D8-68-16	2	118	24	5.90	165.0	119.5	1.38	
D10-33-3	2	303	3.6	4.84	43.5	78.9	0.55	0.61
D10-43-3	2	233	3.6	5.97	53.8	92.3	0.58	0.65
D10-43-6	2	233	7.2	7.18	86.1	92.3	0.93	1.04
D10-54-6	2	185	7.2	9.22	110.6	135.3	0.82	0.91
D10-43-8	2	233	9.6	6.87	109.4	92.1	1.19	1.32
D10-54-8	2	185	9.6	8.57	136.6	128.3	1.06	1.18
D10-54-12	2	185	14.4	7.40	161.9	128.3	1.26	
D10-68-12	2	147	14.4	9.14	199.3	174.2	1.14	
D10-54-16	2	185	19.2	5.17	144.5	129.7	1.11	
D10-68-16	2	147	19.2	7.19	200.7	175.6	1.14	
						Mean	1.10	0.95
						Std. Dev.	0.28	0.27
						COV	0.25	0.29

<sup>1</sup>Assembly designation is as follows: The first letter "D" or "S" represents double or single L-shape section. The first number is the vertical leg dimension (in.). The second number is the thickness of the angle (in.), followed by the clear span (ft).

<sup>2</sup>Tabulated values are based on the average of the No. of tests conducted for each assembly. A minimum of two tests were conducted for each identical assembly, if the ultimate load at failure of the two tests were not within 10% of each other further tests were performed.

<sup>3</sup>Ultimate load is the summation of the individual loads applied at 24" o.c.

**TABLE 3 Single L-Header Results (ULS)**

Assembly Designation <sup>1</sup>	No. of Tests <sup>2</sup>	Leg / t	L / Leg	Ultimate Load <sup>3</sup> (kip)	Moment M <sub>t</sub> (kip*in)	M <sub>n</sub> (kip*in)	M <sub>t</sub> /M <sub>n</sub>	M <sub>t</sub> /(0.9M <sub>n</sub> )
S6-33-4	3	182	8	1.50	18.0	13.7	1.31	
S6-43-4	4	140	8	1.80	21.6	20.0	1.08	
S6-33-6	3	182	12	1.72	20.6	13.7	1.50	
S6-43-6	3	140	12	2.48	29.7	20.0	1.49	
S6-43-8	2	140	16	2.26	35.6	18.8	1.90	
S6-54-8	2	111	16	2.68	42.3	26.5	1.60	
S8-33-4	4	242	6	1.73	20.7	26.3	0.79	0.88
S8-43-4	4	186	6	2.44	29.2	31.0	0.94	1.05
S8-54-4	2	148	6	2.81	33.8	45.6	0.74	0.82
S8-43-6	2	186	9	2.61	31.3	31.0	1.01	
S8-43-8	2	186	12	3.01	47.2	30.9	1.53	
S8-54-8	2	148	12	3.98	62.7	43.3	1.45	
S10-33-4	3	303	4.8	2.18	26.1	39.5	0.66	
S10-54-4	4	185	4.8	3.51	42.1	67.6	0.62	
S10-43-6	2	233	7.2	3.50	42.0	46.1	0.91	
S10-54-6	2	185	7.2	4.60	55.2	67.6	0.82	
S10-43-8	2	233	9.6	3.77	59.4	46.0	1.29	
S10-54-8	2	185	9.6	4.64	73.1	64.2	1.14	
						Mean	1.11	0.93
						Std. Dev.	0.37	0.11
						COV	0.33	0.12

<sup>1</sup>Assembly designation is as follows: The first letter "D" or "S" represents double or single L-shape section. The first number is the vertical leg dimension (in.). The second number is the thickness of the angle (in.), followed by the clear span (ft).

<sup>2</sup>Tabulated values are based on the average of the No. of tests conducted for each assembly. A minimum of two tests were conducted for each identical assembly, if the ultimate load at failure of the two tests were not within 10% of each other further tests were performed.

<sup>3</sup>Ultimate load is the summation of the individual loads applied at 24" o.c.

**TABLE 4 Double & Single L-Header Results (SLS)**

Assembly Designation <sup>1</sup>	No. of Tests <sup>2</sup>	Ultimate Load <sup>3</sup> (kip)	Load at L/240 (kip)	L/240 (in.)	Deflection at 60% Max Load <sup>4</sup> (in.)	Fixity Factor	End Stiffness (kip*in/rad.)
D6-33-3	2	3.61	2.92	0.15	0.12	N/A	N/A
D6-43-3	3	4.15	3.43	0.15	0.10	N/A	N/A
D6-54-3	2	6.00	3.47	0.15	0.15	N/A	N/A
D8-33-3	3	4.30	3.97	0.15	0.08	N/A	N/A
D8-43-3	3	5.90	4.79	0.15	0.10	N/A	N/A
D10-33-3	2	4.84	4.13	0.15	0.10	N/A	N/A
D10-43-3	2	5.97	4.34	0.15	0.12	N/A	N/A
D6-54-6	3	4.92	3.78	0.30	0.25	0.21	885.2
D8-43-6	2	5.88	5.19	0.30	0.18	0.16	1132.9
D8-54-6	2	7.10	5.78	0.30	0.22	0.09	739.2
D10-43-6	2	7.18	6.58	0.30	0.17	0.04	482.4
D10-54-6	2	9.22	7.76	0.30	0.20	0.00	---
D6-43-8	2	4.05	2.43	0.40	0.40	0.08	178.9
D6-54-8	2	5.09	3.02	0.40	0.40	0.07	209.4
D8-43-8	2	5.50	4.42	0.40	0.26	0.07	329.9
D8-54-8	2	6.83	4.93	0.40	0.32	0.01	73.2
D10-43-8	2	6.87	6.21	0.40	0.22	0.02	134.5
D10-54-8	2	8.57	7.48	0.40	0.23	0.00	---
D8-54-12	2	5.21	3.36	0.60	0.55	0.05	185.0
D8-68-12	2	7.38	4.27	0.60	0.63	0.04	201.0
D10-54-12	2	7.40	5.61	0.60	0.44	0.04	307.6
D10-68-12	2	9.14	6.72	0.60	0.47	0.02	230.5
D8-54-16	2	4.32	2.39	0.80	0.89	0.04	130.6
D8-68-16	2	5.90	2.88	0.80	1.03	0.04	138.8
D10-54-16	2	5.17	3.86	0.80	0.60	0.04	224.7
D10-68-16	2	7.19	4.54	0.80	0.75	0.03	197.6
S6-33-4	3	1.50	1.38	0.15	0.12	N/A	N/A
S6-43-4	4	1.80	1.42	0.15	0.15	N/A	N/A
S8-33-4	4	1.73	1.63	0.15	0.12	N/A	N/A
S8-43-4	4	2.44	2.17	0.15	0.12	N/A	N/A
S8-54-4	2	2.81	2.54	0.15	0.12	N/A	N/A
S10-33-4	3	2.18	2.07	0.15	0.11	N/A	N/A
S10-54-4	4	3.51	3.17	0.15	0.12	N/A	N/A
S6-33-6	3	1.72	1.27	0.30	0.24	0.25	327.0
S6-43-6	3	2.48	1.95	0.30	0.24	0.26	484.5
S8-43-6	2	2.61	2.42	0.30	0.16	0.17	585.0
S10-43-6	2	3.50	3.24	0.30	0.16	0.05	301.6
S10-54-6	2	4.60	3.89	0.30	0.19	0.00	---
S6-43-8	2	2.26	1.23	0.40	0.45	0.08	89.8
S6-54-8	2	2.68	1.58	0.40	0.41	0.08	118.6
S8-43-8	2	3.01	2.18	0.40	0.31	0.05	113.0
S8-54-8	2	3.98	2.58	0.40	0.36	0.02	55.5
S10-43-8	2	3.77	3.13	0.40	0.24	0.01	28.6
S10-54-8	2	4.64	3.57	0.40	0.29	0.00	---

<sup>1</sup>Assembly designation is as follows: The first letter "D" or "S" represents double or single L-shape section. The first number is the vertical leg dimension (in.). The second number is the thickness of the angle (mils), followed by the clear span (ft).

<sup>2</sup>Tabulated values are based on the average of the No. of tests conducted for each assembly. A minimum of two tests were conducted for each identical assembly, if the ultimate load at failure of the two tests were not within 10% of each other further tests were performed.

<sup>3</sup>Ultimate load is the summation of the individual loads applied at 24" o.c.

<sup>4</sup>Represents ultimate service load.

**Effects of elevated temperatures on ultimate moment capacity  
of bolted moment-connections between cold-formed steel  
members**

James B.P. Lim<sup>1</sup> and Ben Young<sup>2</sup>

**Abstract**

Experimental investigations at ambient temperature into the behaviour of bolted moment-connections between cold-formed steel members have previously been described. Full-scale joint tests have demonstrated that the channel-sections being connected are susceptible to premature failure, the result of web buckling caused by the concentration of load transfer from the bolts. The results of non-linear elasto-plastic finite element analyses have been shown to have good agreement. No consideration, however, has been given to the behaviour of such connections at elevated temperatures. This paper describes non-linear elasto-plastic finite element parametric studies into the effects of elevated temperatures on bolted moment-connections between cold-formed steel members; simple design rules are proposed that will enable designers to take into account the effects of elevated temperatures.

---

<sup>1</sup> Lecturer, Dept. of Civil Engineering, The University of Strathclyde, Glasgow, UK

<sup>2</sup> Associate Professor, Dept. of Civil Engineering, The University of Hong Kong, Hong Kong, China

## Introduction

Bolted moment-connections between cold-formed steel members, formed through brackets bolted to the webs of the cold-formed steel sections being connected (see Fig.1), are used for the joints of portal frames [Ref. 1, 2], multi-storey frames [Ref. 3, 4], and racking systems [Ref. 5]. The behaviour of such joints, however, has only been considered at ambient temperature, with no consideration being given to joint behaviour at elevated temperatures.

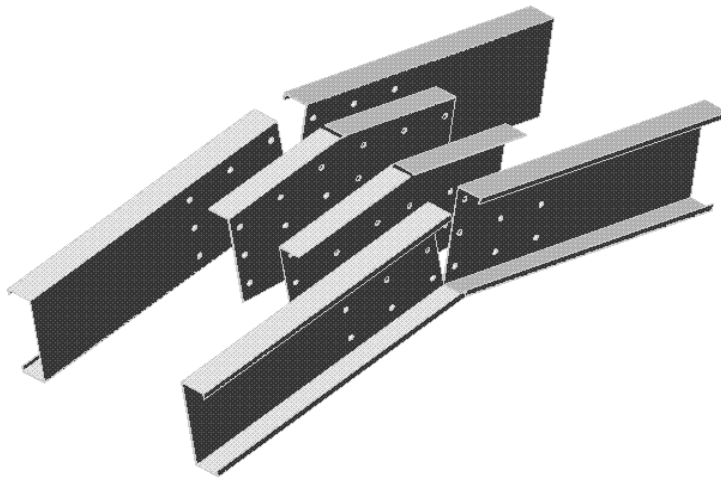


Figure 1. Details of typical bolted moment connection

The lack of design information for elevated temperatures means that it is not always possible to design safely cold-formed steel frames having such joints in fire, without resorting to the use of fire protection. Conservative design recommendations are normally based on simple modifications to the fire design rules of hot-rolled steel structures. However, in the case of hot-rolled steel, local buckling is generally not a problem. On the other hand, with cold-formed steel, both local and distortional buckling is common, making the design of these structures in fire problematic. Whilst ideally full-scale fire tests should be conducted, the cost of these tests will be prohibitive. In fact, it has only been in recent years that cold-formed steel coupon tests have been conducted at elevated temperatures.

Chen and Young recently have conducted a series of such tests [Refs 6, 7]. From the results of these tests, equations were developed that predict the stress-strain curves at elevated temperatures. In this paper, the stress-strain curves proposed by Chen and Young [Ref 6] are applied to a numerical investigation on the strength of bolted-moment connections between cold-formed steel members at elevated temperatures.

In this paper, the strength in fire of the channel-sections at the joints are investigated, which are susceptible to premature web buckling, induced by concentrated load transfer from the bolt-group. Curves are presented that illustrate how this mode of failure is affected by elevated temperatures. For cold-formed steel frames, where failure is generally non-ductile, the failure load of the joints is more important than for hot-rolled steel frames, where the frames continue to exhibit increased strength after the formation of the first plastic hinge. Simple design rules are proposed, from the results of this study, which will allow designers to take into account the effects of elevated temperatures.

### **Stress-strain curves at elevated temperatures**

Fig.2 shows stress-strain curves for cold-formed steel at eight temperatures ranging from 22°C to 700°C. In this paper, the effects of elevated temperatures at these eight temperatures will be considered. The stress-strain curves are obtained from equations proposed by Chen and Young [Ref. 6]. Table 1 summarises the Young's modulus and yield stress, calculated from equations also proposed by Chen and Young [Ref. 7].

In this paper, the general purpose finite element program ABAQUS [Ref. 8] is used for the numerical investigations. In the numerical models, non-linear stress-strain material curves are modelled. The first part of the engineering stress-strain curve represents the elastic part up to the proportional limit stress with measured elastic modulus and Poisson's ratio. In this study, the Poisson's ratio is taken as 0.3 under fire conditions. Generally, the Poisson's ratio is assumed to be independent of temperature [Refs 9, 10]. Since the analysis of post-buckling involves large in-elastic strains, the engineering stress-strain curve has been converted to a true stress and logarithmic plastic strain curve for the different temperatures. These true stress and plastic true strain curve equations are specified in ABAQUS.



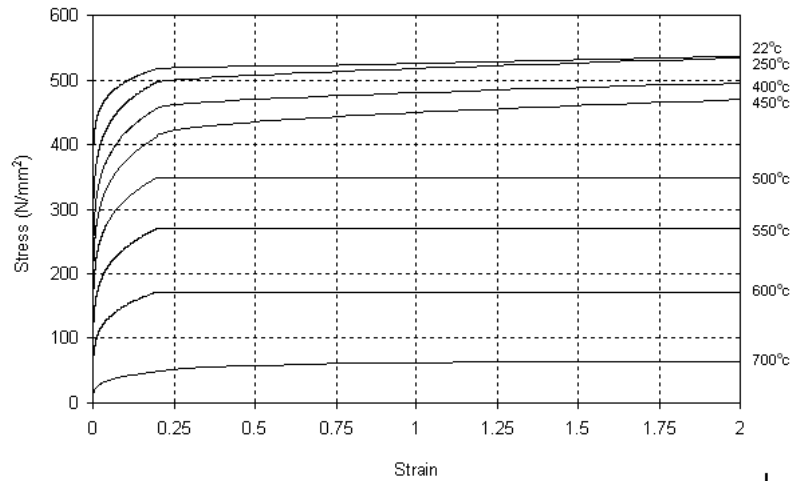


Figure 2. Stress-strain curves at different temperatures

Table 1. Summary of material properties at different temperatures

Temperature T (°C)	Young's modulus E (N/mm <sup>2</sup> )	Yield stress f <sub>y</sub> (N/mm <sup>2</sup> )
22	210000	515
250	171696	494
400	146496	454
450	138096	409
500	100609	347
550	68632	267
600	41427	170
700	16200	48.9

### Ultimate strength of bolted moment-connections

#### Phenomenon of premature web buckling

When designing bolted moment-connections, two modes of failure can easily be prevented:

- i. Overall lateral-torsional buckling of the joint. This type of buckling may be prevented through the provision of sufficient lateral restraint around the joint
- ii. Buckling of the bracket. Adopting the design recommendations of Ref. 11 would ensure that the bracket has a higher moment capacity than the channel-sections being connected.

A third mode of failure, which cannot be prevented as easily, is concerned with the reduction in strength of the channel-sections at the vicinity of the joints, caused by concentrated load transfer from the bolt-group (see Fig.3). This mode of failure, referred to as premature web buckling [Ref. 12], has been observed as the governing mode of failure in a number of laboratory tests on cold-formed steel bolted moment-connections [Refs 1, 13, 14 and 15]. A full-review of all of these tests is given in Ref. 12, in which it is demonstrated some of the joints tested failed at a moment-capacity 20% lower than the calculated moment-capacity of the channel-sections.

Fig.4 shows an example of premature web buckling induced failure. As can be seen, the mode involves buckling of the web of the channel, accompanied by sympathetic flange distortion. While the resulting failure mode shape is similar to distortional buckling, the mode of failure is initiated by premature web buckling. Premature web buckling is not covered by BS5950: Part 5 [Ref. 16], or any of the other codes of practice.

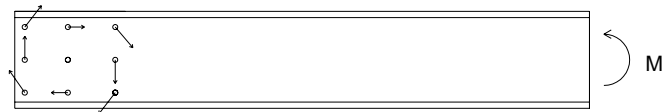


Figure 3. Free body diagram of channel-section when joint is in pure bending



Figure 4. Typical web buckling induced failure [Ref. 14]

Ref 12 describes a combination of laboratory tests and finite element analyses used to investigate this mode of failure. However, while good agreement was demonstrated between the measured ultimate moment-capacity and that predicted by using the finite element analyses, the study was only concerned with the behaviour at room temperature. In this Section, a numerical study on the influence of elevated temperatures on premature web buckling is described.

### Finite element model

Details of the finite element model used to investigate premature web buckling in Ref. 12 are shown in Fig.5. As can be seen, the model consists of only a single channel-section loaded under pure bending. The parameters used to describe the dimensions of the bolt group are shown in Fig.5. A full description of the model is given in Ref. 12.

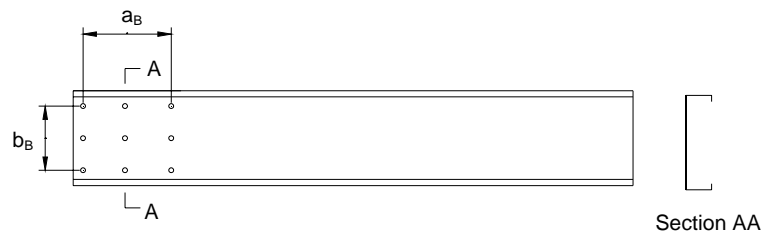


Figure 5. Details of parameters used to describe the bolt-group array

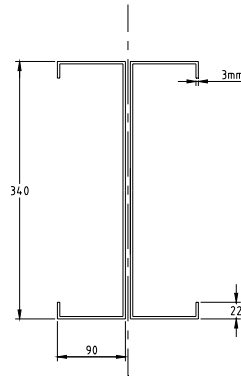


Figure 6. Dimensions of channel-section used in parametric study

### Parametric study

A parametric study was conducted to investigate the effects of elevated temperatures on premature web buckling. Fig.6 shows the dimensions of the channel-section used for the purposes of the parametric study; the same dimension of channel-section was also used in Ref. 12.

In the parametric study described in this Section, the thickness of channel-section was varied between 2 mm and 8 mm. Three bolt-group lengths ( $a_B$ ) were considered, namely, 200 mm, 500 mm and 1000 mm.

Fig.7(a) shows the reduction in moment capacity  $M_{u,T}/M_{u,normal}$  for a bolt-group length of 200 mm. For each temperature, the values of Young's modulus, yield stress and ultimate stress are also normalised their respective values at room temperature.

From Fig.7(a), it can be seen that the value of  $M_{u,T}/M_{u,normal}$  decreases with the thickness of the channel-section. This is to be expected since plate buckling is a function of the thickness cubed. For the channel-section of thickness 8 mm, the reduction in moment capacity closely follows that of the reduction in yield stress ( $f_{y,T}/f_{y,normal}$ ). However, for the channel-section of thickness 2 mm, the value of  $M_{u,T}/M_{u,normal}$  is much lower. For example, in the case of a temperature of 400°C, the reduction in strength of the 2 mm channel-section is 13% lower than that of

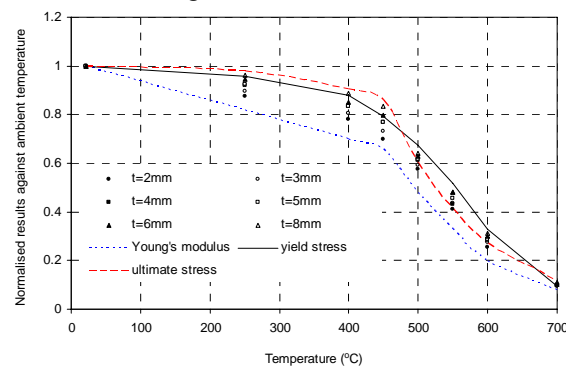
the 8 mm section. A lower bound to the reduction in strength can be seen to be  $E_T/E_{\text{normal}}$ .

It is interesting to note from Fig.7(a) that the greatest variation in  $M_{u,T}/M_{u,\text{normal}}$  between the different thicknesses of channel-section is 13% and occurs at a temperature 450°C. At this temperature, the difference between  $E_T/E_{\text{normal}}$  and  $f_{y,T}/f_{y,\text{normal}}$  is also 13%. Similarly, at a temperature of 600°C the variation in  $M_{u,T}/M_{u,\text{normal}}$  between the different thicknesses of channel-section is 6%. At this temperature, the difference between the same material properties is also 6%.

Since comparisons of the roundness of the stress-strain curves at these temperatures show no noticeable difference, it may therefore be concluded that the value of  $M_{u,T}/M_{u,\text{normal}}$  is a function of both  $E_T/E_{\text{normal}}$  and  $f_{y,T}/f_{y,\text{normal}}$ .

Fig.7(b) and Fig.7(c) show the same results for values of  $a_B = 500$  mm and 1000 mm, respectively. As can be seen, the same general trends as for Fig.7(a) can be observed, even though the value of  $a_B$  has been increased significantly from 200 mm to 1000 mm. In Ref. 12, the effect of increasing  $a_B$  from 200 mm to 1000 mm resulted in a 20% increase in moment capacity. While this increase in moment capacity has been taken into account when comparing the curves of Fig.9, owing to the fact that normalised results are presented, it is interesting to note that the results have no additional sensitivity to the value of  $a_B$ .

In general, as the value of  $a_B$  increases, the values of  $M_{u,T}/M_{u,\text{normal}}$  also increase but the range of variation between the different thicknesses of channel-sections decreases. The fact that the values of  $M_{u,T}/M_{u,\text{normal}}$  are not sensitive to the value of  $a_B$  is important for the design recommendations that follow.



(a) Bolt-group having  $a_B = 200$  mm

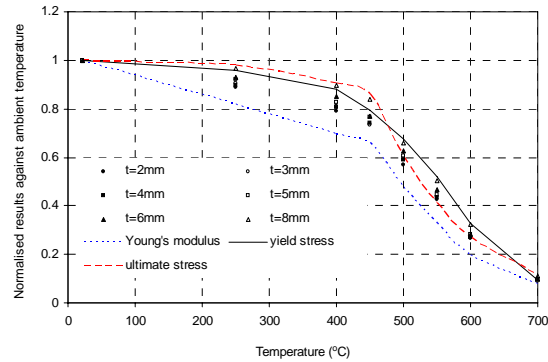
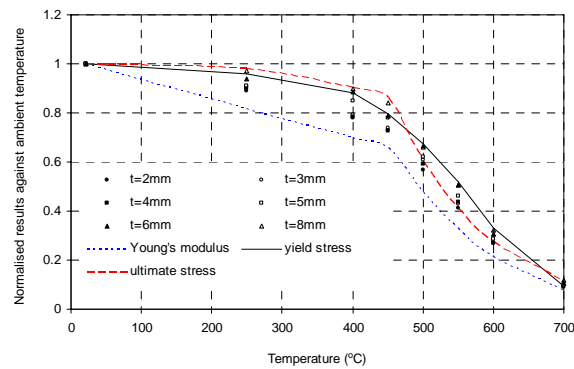
(b) Bolt-group having  $a_B = 500$  mm(c) Bolt-group having  $a_B = 1000$  mm

Figure 7. Comparison of variation of moment capacity with material properties

### Design recommendations

In the parametric study, it was observed that the reduction factor  $M_{u,T}/M_{u,normal}$  is sensitive to both  $E_T/E_{normal}$  and  $f_{y,T}/f_{y,normal}$  but not to the values of  $a_B$ . As the moment capacity of the channel-section is a function of both  $E_T$  and  $f_{y,T}$ , a design recommendation based on the reduction in moment capacity may be appropriate.

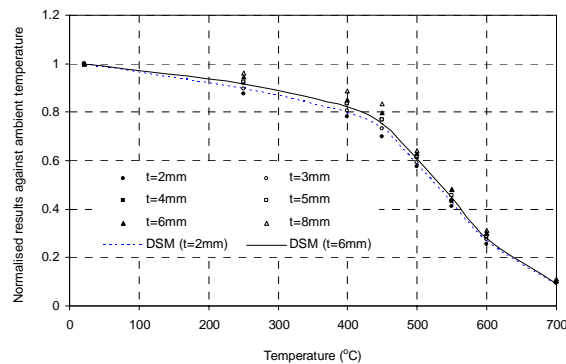
The direct strength method specified in the supplement to the North American Specification [Ref. 17] and the Australian/New Zealand Standard [Ref. 18] is

used to predict the moment capacity of the cold-formed steel channel-sections. The nominal design strengths at elevated temperatures were calculated by substituting the reduced yield stress (0.2% proof stress) and Young's modulus into the design rules. The nominal design strengths were calculated using the cross-section and the reduced material properties as those used in the parametric study of the finite element analysis.

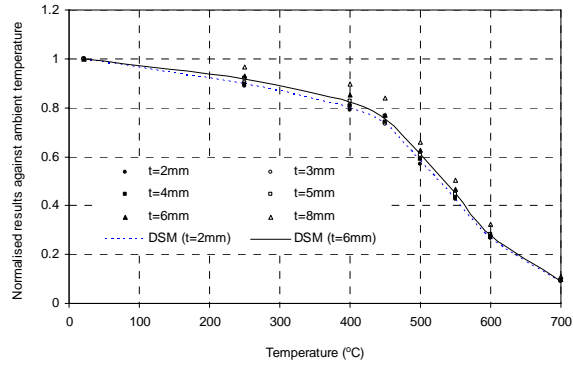
It should be noted that the current direct strength method is developed based on cold-formed steel structural members at normal room temperature by Schafer and Peköz [Ref. 19]. In this study, the direct strength method is used for cold-formed steel channel-sections subjected to bending at elevated temperatures.

Fig.8 shows the comparison of the reduction factor  $M_{u,T}/M_{u,normal}$  with the reduction factor predicted using the direct strength method ( $M_{DSM,T}/M_{DSM,normal}$ ). The value of  $M_{DSM,T}/M_{DSM,normal}$  has been calculated for values of thickness of 2 mm and 6 mm. It is shown that the values of the reduction factor  $M_{u,T}/M_{u,normal}$  plots closely to the values of  $M_{DSM,T}/M_{DSM,normal}$  within an acceptable range.

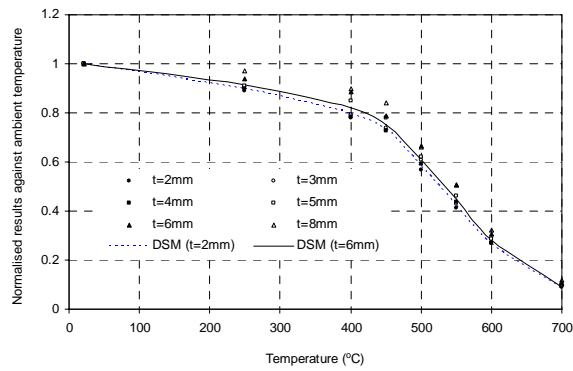
$M_{DSM,T}/M_{DSM,normal}$  is therefore appropriate for a design recommendation for the reduction in strength of a cold-formed steel channel-section undergoing premature web buckling at elevated temperatures.



(a) Bolt-group having  $a_B = 200$  mm



(b) Bolt-group having  $a_B = 500$  mm



(c) Bolt-group having  $a_B = 1000$  mm

Figure 8. Comparison of variation of moment capacity with direct strength method



**Concluding remarks**

A simple design recommendation has been proposed that will allow premature buckling to be taken into account at elevated temperatures, by applying a reduction factor to the moment capacity determined at ambient temperature. This reduction factor is based on the moment capacity of the section, calculated using the direct strength method.

**Acknowledgements**

The work described in this paper was supported by the William M.W. Mong Engineering Research Fund provided by The University of Hong Kong. The authors are also thankful to Mr Ran Feng for the assistance of this research project.

**Appendix. - References**

- 1 Kirk, P. 'Design of a cold-formed section portal frame building system', Proc. 8th International Specialty Conference on Cold-formed Steel Structures, St. Louis, University of Missouri-Rolla, 1986, p295.
- 2 Lim, J.B.P. and Nethercot, D.A. 'Design-development of a general cold-formed steel portal framing system', The Structural Engineer, 80, No. 21, 2002, p31.
- 3 Wong, M.F. and Chung, K.F. 'Experimental investigation of cold-formed steel beam-column sub-frames', Proc. 15<sup>th</sup> International Specialty Conference on Cold-formed Steel Structures, St. Louis, University of Missouri-Rolla, 2000, p607-618.
- 4 Chung, K.F. and Shi, Y.J. 'Lateral torsional buckling of gusset plates in bolted moment connections among cold-formed steel members', Jour. Constr. Steel Res., 46, Nos. 1-3, 1998, p418, Oxford, Elsevier Applied Science.
- 5 Baldassino, N. and Bernuzzi, C. 'Analysis and behaviour of steel storage pallet racks', Thin-Walled Structures, 37, No.4, 2000, p277.
- 6 Chen J and Young B. 'Experimental investigation of cold-formed steel material at elevated temperatures', Thin-Walled Struct., 2007; 45(1), p96-110.
- 7 Chen J and Young B. 'Mechanical properties of cold-formed steel at elevated temperatures', Proceedings of the 17th International Specialty Conference on Cold-Formed Steel Structures, Orlando, 2004, p437-465.
- 8 ABAQUS standard user's manual, Version 6.5. ABAQUS, Inc.; 2004.
- 9 Kaitila O. 'Finite element modeling of cold-formed steel members at high temperatures', Licentiate thesis, Helsinki University, 2002.
- 10 Zha XX. 'FE analysis of fire resistance of concrete filled CHS columns', Journal of Constructional Steel Research, 2003; 59(6), p769-779.
- 11 Lim, J.B.P. and Nethercot, D.A. 'F.E.-assisted design of the eaves bracket of a cold-formed steel portal frame', Journal of Steel and Composite Structures, 2, No. 6, 2002, p411.

- 12 Lim, J.B.P. and Nethercot, D.A. 'Ultimate strength of bolted moment-connections between cold-formed steel members' *Thin-Walled Struct.*, 41(11), 2003, p1019.
- 13 Lim, J.B.P. and Nethercot, D.A. 'Finite element idealisation of a cold-formed steel portal frame', *Journal of Structural Engineering, ASCE*, 130(1), 2004. p78-94
- 14 Chung, K.F. and Lau, L. 'Experimental investigation on bolted moment connections among cold-formed steel members', *Engng Struct*, 21, 1999, p898.
- 15 Wong, M.F. and Chung, K.F. 'Structural behaviour of bolted moment connections in cold-formed steel beam-column sub-frames', *Jour. Constr. Steel Res.*, Oxford, Elsevier Applied Science, 58, No. 2, 2002, p253.
- 16 BS5950: Part 5. Code of practice for design of cold-formed sections, London, British Standards Institution, 1998.
- 17 Supplement to the North American Specification for design of cold-formed steel structural members, American Iron and Steel Institute, Washington, D.C., 2004.
- 18 AS/NZS 4600:2005. Cold-formed steel structures, Australian/New Zealand Standard, Standards Australia, Sydney, Australian, 2005.
- 19 Schafer, B.W. Peköz, T. 'Direct strength prediction of cold-formed steel members using numerical elastic buckling solutions', *Proceedings of the 14th International Specialty Conference on Cold-Formed Steel Structures*, University of Missouri-Rolla, 1998; p69-76.

**Appendix. - Notation**

$a_B$	length of bolt-group
$b_B$	breadth of bolt-group
$D$	depth of web of channel-section
$E_{\text{normal}}$	Young's modulus at normal room temperature
$E_T$	Young's modulus at temperature $T^\circ\text{C}$
$f_y$	yield stress
$f_{y,\text{normal}}$	yield stress at normal room temperature
$f_{y,T}$	yield stress at temperature $T^\circ\text{C}$
$f_u$	ultimate stress
$f_{u,\text{normal}}$	ultimate stress at normal room temperature
$f_{u,T}$	ultimate stress at temperature $T^\circ\text{C}$
$M_{\text{DSM,normal}}$	moment capacity calculated using direct strength method at normal room temperature
$M_{\text{DSM,T}}$	moment capacity calculated using direct strength method at temperature $T^\circ\text{C}$
$M_u$	ultimate moment capacity
$M_{u,\text{normal}}$	ultimate moment capacity at normal room temperature
$M_{u,T}$	ultimate moment capacity at temperature $T^\circ\text{C}$
$t$	thickness of channel-section or plate



## **Cold-Formed Steel Special Bolted Moment Frames: Cyclic Testing and Numerical Modeling of Moment Connections**

by

Chia-Ming Uang<sup>1</sup>, Jong-Kook Hong<sup>2</sup>, Atsushi Sato<sup>3</sup> and Ken Wood<sup>4</sup>

### **ABSTRACT**

Cyclic tests on nine full-scale beam-column subassemblages were carried out in support of the development of a new lateral load-resisting system recently introduced in AISI-S110: *Standard for Seismic Design of Cold-Formed Steel Structural Systems—Special Bolted Moment Frames*. With double channel beams and HSS columns interconnected by bearing-type high-strength bolts, all specimens showed a story drift capacity significantly larger than 0.04 radian. Typical response is characterized by a linear response, a slip range, followed by a significant hardening region due to bolt bearing. Three failure modes were identified. Confining in the connection region, inelastic action through bolt slippage and bearing is ductile and desirable. Such inelastic action always occurs first, but either column or beam may also experience buckling. Beam buckling is most undesirable due to significant post-buckling strength degradation. Extending the concept of instantaneous center of rotation of an eccentrically loaded bolt group, a model that can reliably simulate the cyclic behavior of the bolted moment connection is presented.

---

<sup>1</sup> Professor of Structural Engineering, University of California, San Diego, La Jolla, CA, cmu@ucsd.edu

<sup>2</sup> Design Engineer at Myers, Houghton & Partners, Long Beach, CA, jhong@mhpse.com

<sup>3</sup> Assistant Professor of Architecture and Architectural Engineering, Kyoto University, Kyoto, JAPAN, asato@archi.kyoto-u.ac.jp

<sup>4</sup> President, KL Wood Engineering, Colorado Springs, CO, klwoodengineerin@qwest.net

## INTRODUCTION

The American Iron and Steel Institute (AISI) is in the process of developing a seismic design standard for cold-formed steel, Standard for Seismic Design of Cold-Formed Steel Structural Systems—Special Bolted Moment Frames - AISI S110 [AISI, 2007]. The first seismic force resisting system introduced in the AISI seismic standard is termed Cold-Formed Steel—Special Bolted Moment Frames (CFS—SBMF). It is common that this type of frames is composed of cold-formed Hollow Structural Section (HSS) columns and double-channel beams. Beams are connected to the column by using snug-tight high-strength bolts.

The first objective of this study was to identify through cyclic testing both the desirable limit state that can be counted on to dissipate energy in a stable manner and other limit states that should be avoided in design through the capacity design principles. The second objective of this study was to develop a mathematical model of the observed bolted connection cyclic behavior that can be used for predicting maximum forces that can be developed in moment connection for capacity design purposes [Sato and Uang, 2008].

## TEST PROGRAM

Figure 1(a) shows the test setup for the testing of beam-column subassemblies. Each specimen was composed of a column and a half-span beam on each side of the column. For testing purposes, the specimen was rotated 90 degrees. A total of nine full-scale beam-column subassemblies were tested (see Table 1). For each specimen the beam (ASTM 607 Class 1, Gr. 50 steel) was connected to the column (A500 Gr. B steel) by eight 25.4 mm (1 in.) diameter, bearing-type SAE J429 Grade 5 high-strength bolts, which were equivalent in mechanical properties to ASTM A325 bolts, in standard holes [see Figure 1(b)].

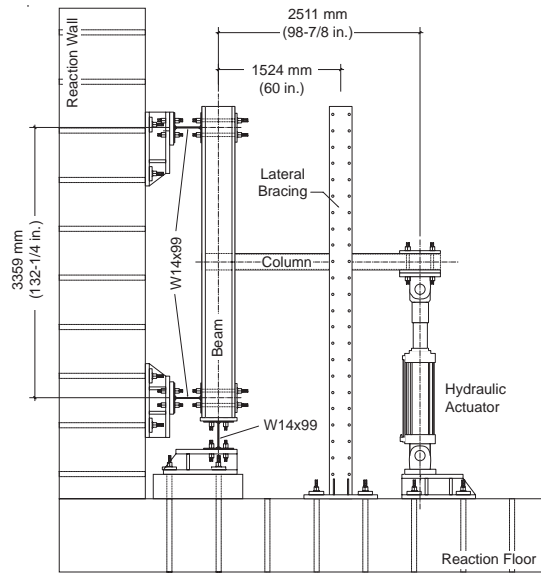


FIGURE 1(a) – TEST SETUP

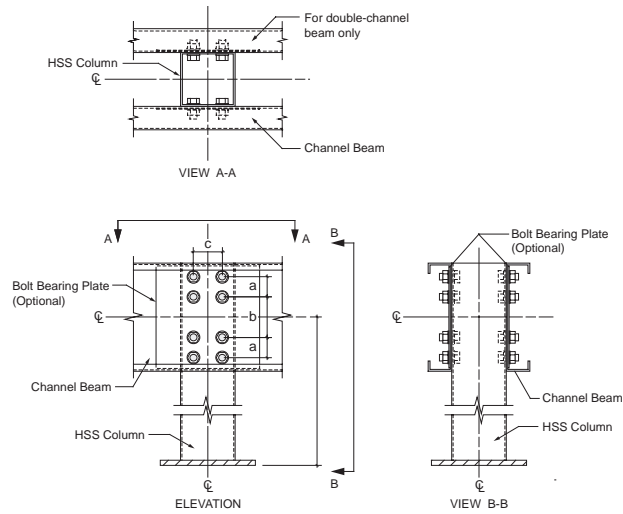


FIGURE 1(b) – BOLTED MOMENT CONNECTION



TABLE 1(a) – MEMBER SIZE

Specimen No.	Beam, mm	Column, mm	Bolt Bearing Plate, mm
1, 2	2C305×89×2.7 (2C12×3½×0.105)*	HSS203×203×6.4 (HSS8×8×¼)	3.4 (0.135)
3	2C406×89×2.7 (2C16×3½×0.105)	HSS203×203×6.4 (HSS8×8×¼)	N/A
4	2C406×89×2.7 (2C16×3½×0.105)	HSS203×203×6.4 (HSS8×8×¼)	3.4 (0.135)
5, 6, 7	2C406×89×3.4 (2C16×3½×0.135)	HSS203×203×6.4 (HSS8×8×¼)	N/A
8, 9	2C508×89×3.4 (2C20×3½×0.135)	HSS254×254×6.4 (HSS10×10×¼)	N/A

\* Dimensions in inch.

TABLE 1(b) – BOLTED CONNECTION CONFIGURATION

Specimen No.	a **, mm	b, mm	c, mm
1, 2	64 (2½)*	76 (3)	108 (4¼)
3, 4, 5, 6, 7	76 (3)	152 (6)	108 (4¼)
8, 9	76 (3)	254 (10)	159 (6¼)

\* Dimensions in inch, \*\* See Figure 1(b).

A combination of displacement transducers, inclinometers, strain gage rosettes, and uniaxial strain gages were used to measure global and local responses [Hong and Uang, 2004]. The loading sequence specified in the AISC Seismic Provisions [AISC, 2005] for steel beam-to-column moment connection test was imposed to the column tip to simulate the story drift.

### TEST RESULTS

The global response of all specimens was similar. The cyclic behavior was dominated by the slip-bearing action in the bolted connection in a story drift up to 4%. Beyond this drift level, the specimens eventually failed in either beam buckling, column buckling, or excessive bearing deformation in the bolted connection, depending on the relative strength of these structural components.

#### Connection Failure

Specimen 3 did not experience yielding or buckling in the beam and column. Instead, the specimen was able to sustain a stable hysteresis response up to a story drift of 8% [see Figure 2(a)]. Such global response, which can also

be identified in all other specimens, is characterized by three regions. Initially, the subassembly responded elastically with the bolted connection acted as a rigid joint. Once the friction resistance of the bolted connection was overcome, a plateau in the measured response due to bolt slippage resulted. The third region showed a significant hardening in strength once the bolts started to bear against the beam and column elements. Figure 2(b) shows components of the story drift due to beam, column, and connection deformations. Note that the contribution from the bolted connection (i.e., slip-bearing) was significant.

### Beam Buckling

Specimens 1, 2, and 4 experienced beam local buckling. Two beam sizes were used to study the effect of the flat depth-to-thickness ratio ( $w/t$ ) of the beam on the cyclic response.

The global response of Specimens 2 and 4 are shown in Figure 3. (The response of Specimen 1 is similar to that of Specimen 2 and is, therefore, not presented.) Beam buckling in Specimen 4 was very severe [see Figure 4(b)], which resulted in a drastic drop in strength. For Specimen 2, web local buckling (WLB) was first observed at 6% story drift. But strength degradation did not occur until flange local buckling also developed at 10% drift [see Figure 4(a)]. Although beam buckling occurred at a very large drift level, it appears prudent to limit the  $w/t$  ratio to 150, which corresponds to  $6.18\sqrt{E/F_y}$ , to control WLB.

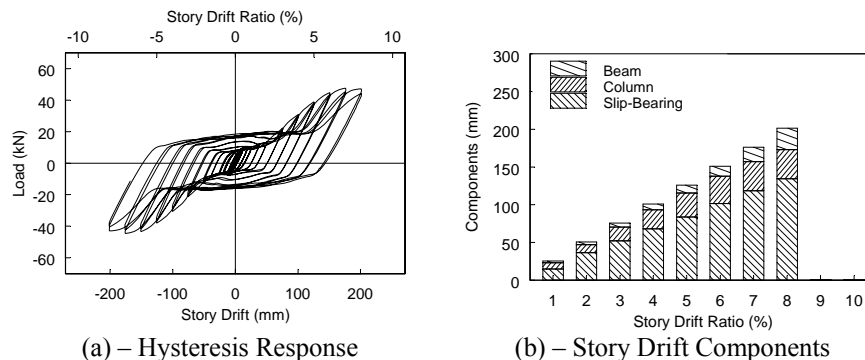


FIGURE 2 – BOLTED MOMENT CONNECTION

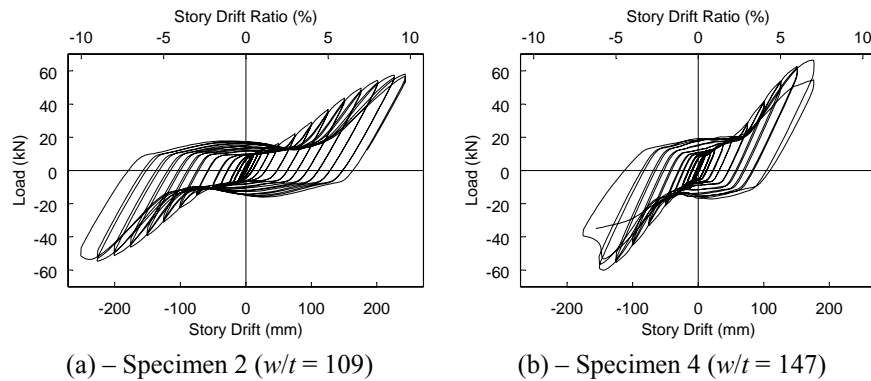


FIGURE 3 – GLOBAL RESPONSE OF SPECIMEN 2 AND 4

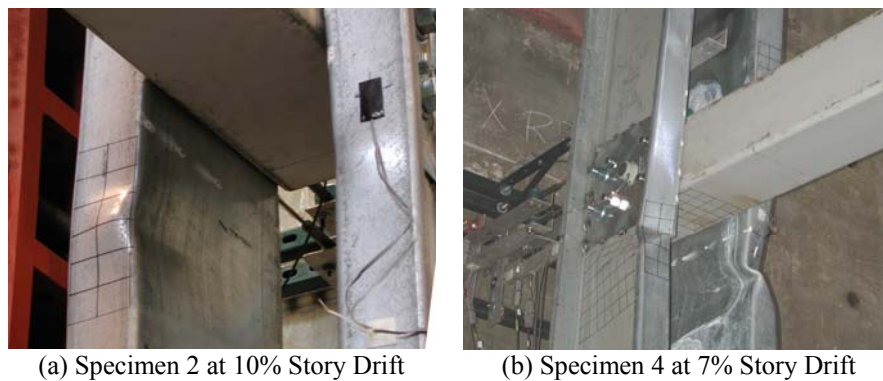


FIGURE 4 – BEAM LOCAL BUCKLING

### Column Buckling

A total of five specimens experienced column local buckling. The first group (Specimens 5, 6, and 7) had the same size column as Specimen 3, but a larger beam size was used to force column buckling. The second group (Specimens 8 and 9) had larger beams and columns.

The typical global responses from each group are presented in Figure 5. Figure 6 shows the observed column local buckling mode. Local buckling of Specimen 7 was first observed at 7% story drift. But the specimen was able to respond in a stable manner until 9% drift. Specimen 9 experienced local buckling at 4% story drift. But the higher flat width-to-thickness ratio ( $w/t = 40$ )

of the column caused the strength to degrade drastically beyond 5% story drift. To avoid significant strength degradation, however, it appears prudent to limit the  $w/t$  ratio to 40, which corresponds to  $1.58\sqrt{E/F_y}$ , to control column local buckling.

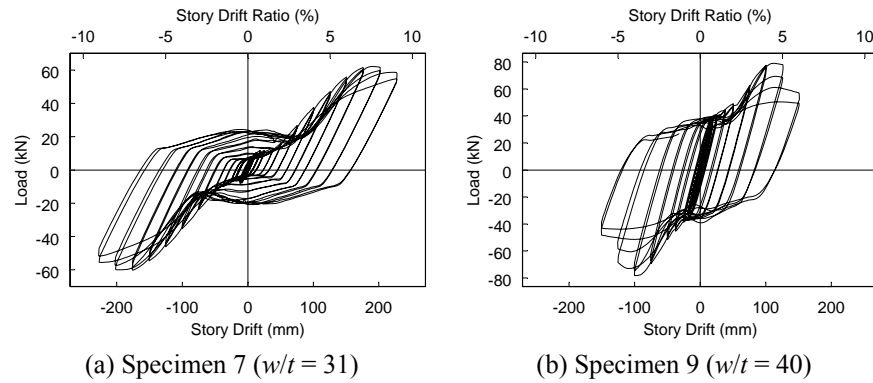


FIGURE 5 – GLOBAL RESPONSE OF SPECIMEN 7 AND 9

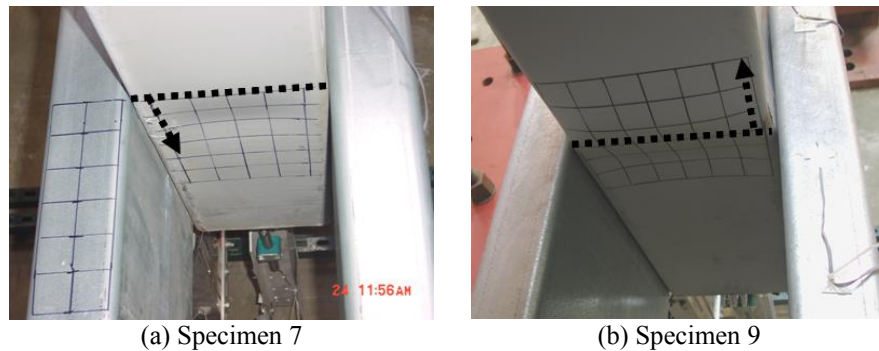


FIGURE 6 – COLUMN LOCAL BUCKLING

#### EVALUATION OF SEISMIC FORCE RESISTING MECHANISM

The global response of all specimens in the practical drift range of interest was governed by the inelastic action in the bolted moment connection. Under lateral load, the bolt group in a CFS—SBMF is subjected to an eccentric shear (Figure 7). The bolted connection first responds in the elastic range, which is

then followed by slip, hardening, and unloading in each excursion. Slip occurs when the friction resistance ( $R_S$ ) of individual bolts is overcome:

$$R_S = kT \quad (1)$$

where  $k$  = slip coefficient, and  $T$  = snug-tight bolt tension. The slip range depends on the oversize of the bolt holes. Once the bolts are in bearing, hardening would occur. The bearing resistance ( $R_B$ ) of individual bolts can be expressed by the following formula [AISC, 2005b; Fisher, 1965]:

$$R_B = R_{ult} \left[ 1 - e^{-\mu(\delta/25.4)} \right]^\lambda \quad (2)$$

where  $\delta$  = bearing deformation (mm),  $R_{ult}$  = ultimate bearing strength,  $e = 2.718$ , and  $\mu, \lambda$  = regression coefficients. In the bearing range, the resistance of individual bolts includes both friction and bearing resistances (i.e.,  $R = R_S + R_B$ ).

The coefficients and snug-tight bolt tension force assumed in this study are summarized in Table 2. Lacking data to derive coefficients [Fisher et al., 1963; Crawford and Kulak, 1968; Kulak et al., 2001], the tabulated values were shown to provide good correlation with the test results in this study.

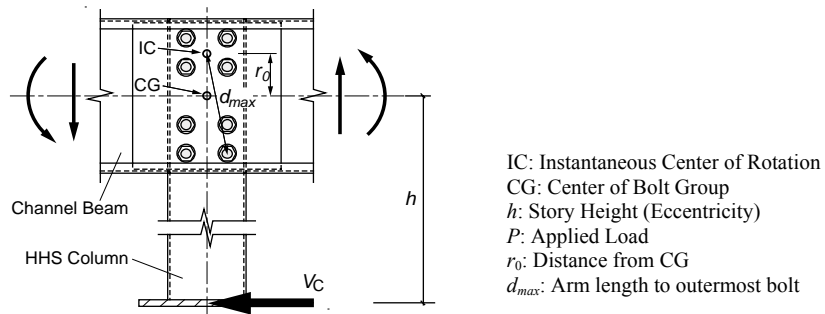


FIGURE 7 – BOLT GROUP IN ECCENTRIC SHEAR

TABLE 2 – ASSUMED COEFFICIENTS AND BOLT TENSION FORCE

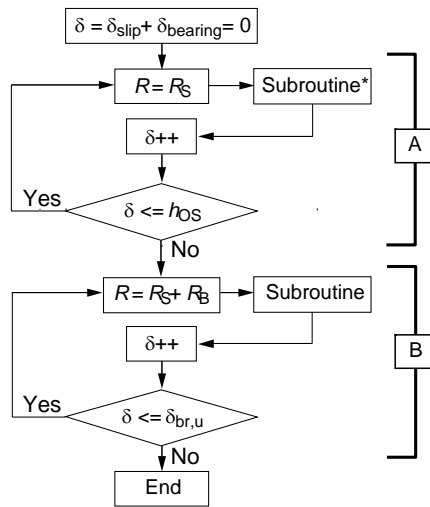
Specimen No.	$k$	$T$ , kN	$\mu$	$\lambda$
1 to 7	0.33	44.5 (10) <sup>a</sup>	5	0.55
8, 9		91.0 (21)		

<sup>a</sup> Snug-Tight Bolt Tension in kips.

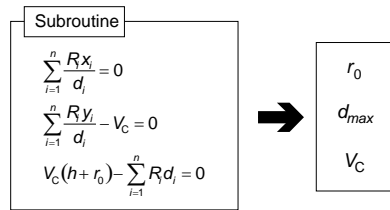
### MONOTONIC LOADING ANALYSIS

Monotonic analysis can be used to establish the response envelope as observed from cyclic testing. Referring to Figure 7 for the bolt group in eccentric shear, a strength analysis based on the instantaneous center (IC) of rotation theory was used [Crawford and Fisher, 1971; Salmon and Johnson,

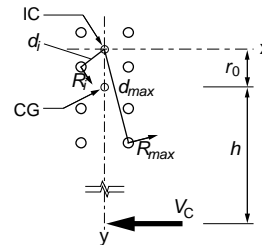
1996]. Figure 8 shows the numerical algorithm, where part A deals with the response in the slip range and part B deals with the response in the hardening range.  $h_{os}$  [= 1/16 in. (= 1.6 mm)] in the flowchart refers to the hole oversize. The typical predicted response envelopes for Specimens 2, 3, and 7 are shown in Figure 9. The predicted response envelop shows a very good agreement with the experimental results.



(a) Flow Chart



(b) Subroutine for Force Equilibrium



(c) Bolt Group Force

FIGURE 8 – NUMERICAL ALGORITHM

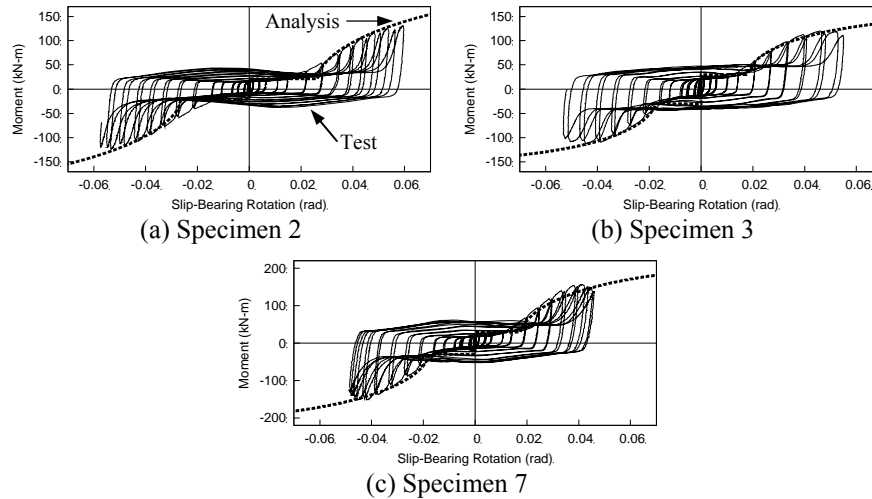


FIGURE 9 – Correlation of Response Envelope

#### CYCLIC LOADING ANALYSIS

For a given bolt configuration and story height, the slip range shown in Figure 9 under monotonic loading is a function of the bolt hole oversize. But the cyclic test results also showed that the slip range would increase with the story drift. This resulted from the elongation of the bolt hole due to prior bearing deformation. For cyclic modeling, therefore, the effect of hole ovalization needs to be considered. Referring to Figure 8, the value of hole oversize ( $h_{OS}$ ), with a proper consideration of the relative bearing strength between the beam and column webs [Sato and Uang, 2008], needs to be updated in the cyclic analysis. Rigid unloading is assumed.

Figure 10 shows the cyclic correlation for three representative specimens. Note that the growth of slip range was reasonably simulated in the proposed model.

#### SUMMARY AND CONCLUSIONS

As part of the AISI's ongoing effort to develop a standard for the seismic design of cold-formed steel structures (AISI S110), cyclic testing of nine full-scale beam-column subassemblies was conducted. These subassemblies represented a portion of the Cold-Formed Steel—Special Bolted Moment Frames (CFS—SBMF) which are commonly used in industrial platforms. This type of

frames is generally composed of cold-formed HSS columns and double-channel beams interconnected

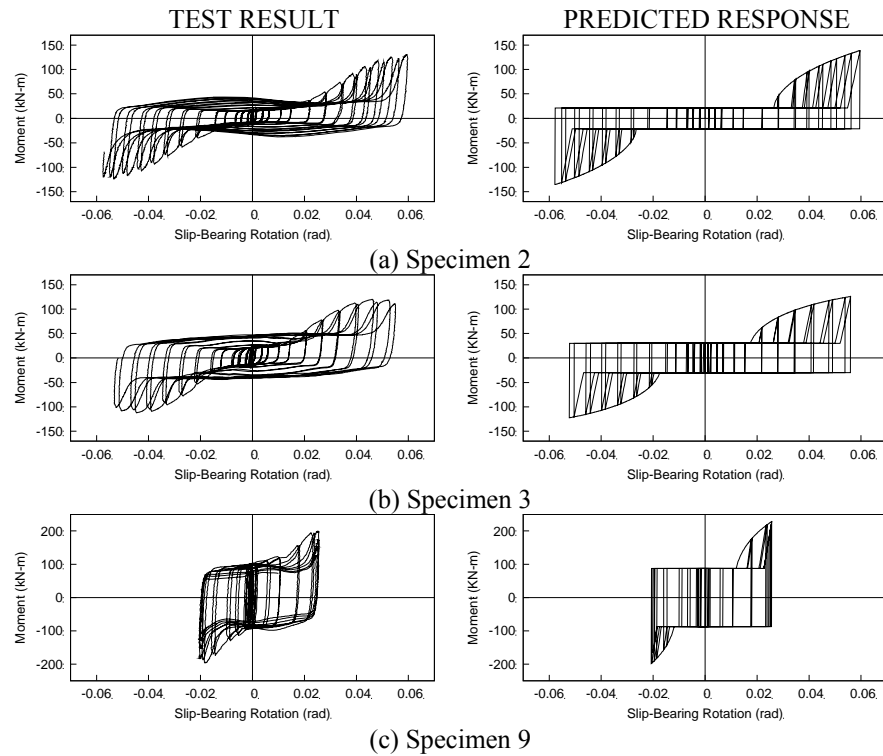


FIGURE 10 – Correlation of Cyclic Response

by snug-tight high-strength bolts. Specimens were designed such that the response of three failure modes—connection failure, beam buckling, and column buckling—could be studied. The following conclusions can be made.

- (1) All specimens were able to deform beyond 4% story drift in a ductile manner.
- (2) Typical response is characterized by three zones. Initially, these specimens responded elastically and the bolted connection acted like a rigid joint. A slip range then resulted, which corresponded to the response when the bolt friction was overcome. Bolt bearing in addition to friction then produced a region of significant hardening in strength until the specimen failed.



- (3) The bolt group in the connection region was subjected to an eccentric shear from the base of the column. All specimens showed ductile behavior due to this action; this desirable limit state involved bolt friction and bearing.
- (4) Beam local buckling was most undesirable and should be avoided by capacity design as it resulted in a significant degradation in strength. Although such local buckling occurred at a story drift beyond 4%, it is prudent to limit the flat width-to-thickness ratio of the beam web to  $6.18\sqrt{E/F_y}$  to control web local buckling.
- (5) Local buckling in HSS columns, which involved buckling of stiffened elements, could also result in a significant strength degradation. To avoid such strength degradation, test results showed that it is desirable to limit the flat width-to-thickness ratio to  $1.58\sqrt{E/F_y}$ .
- (6) A model which extends the instantaneous center of rotation concept of an eccentrically loaded bolt group for the simulation of cyclic behavior of the bolted moment connections was proposed. Considering both the friction and bearing resistance mechanisms as well as the bolt hole oversize, the simulated cyclic response correlated well with the test results.

#### ACKNOWLEDGMENT

Financial support for experimental testing was provided by FCP Inc. Dr. Paul Richards assisted in the planning of the testing. The American Iron and Steel Institute provided additional funding for the analytical study.

#### REFERENCES

- American Institute of Steel Construction (AISC), ANSI/AISC-341, *Seismic Provisions for Structural Steel Buildings*, 2005a.
- American Institute of Steel Construction (AISC), *Steel Construction Manual*, 13<sup>th</sup> Edition, 2005b.
- American Iron and Steel Institute (AISI), S110-07, *Standard for Seismic Design of Cold-Formed Steel Structural Systems—Special Bolted Moment Frames*, 2007.
- Crawford, S. F. and Fisher, J. W., “Eccentrically Loaded Bolted Connections”, *Journal of the Structural Division*, 97(ST3), 1971, 765-783.

- Fisher, J.W., Ramseier, P.O. and Beedle, L.S, “Strength of A440 Steel Joints Fastened with A325 Bolts”, *Publication. IABSE*, 23, 1963.
- Fisher, J.W., “Behavior of Fasteners and Plates with Holes”, *Journal of the Structural Division*, 91(ST6), 1965, 265-286.
- Hong, J.K. and Uang, C.M., “Cyclic Testing of A Type of Cold-Formed Steel Moment Connections for Pre-Fabricated Mezzanines”, *Report No. TR-04/03*, 2004.
- Kulak, G. L., Fisher, J. W., and Struik, J. H. A, *Guide to Design Criteria for Bolted and Riveted Joints*, 2<sup>nd</sup> Edition, American Institute of Steel Construction, 2001.
- Salmon, C. G., and Johnson, J. E., *Steel Structures Design and Behavior*, 4<sup>th</sup> Edition, HarperCollins College Publishers, 1996.
- Sato, A. and Uang, C.M., “Establishment of Capacity Design Requirements for Cold-Formed Steel—Special Bolted Moment Frames”, *Proceedings, ASCE Structural Congress*, 2008.



## **Cold-Formed Steel Special Bolted Moment Frames: Capacity Design Requirements**

by

Atsushi Sato<sup>1</sup> and Chia-Ming Uang<sup>2</sup>

### **ABSTRACT**

Design provisions of the Cold-Formed Steel—Special Bolted Moment Frame (CFS—SBMF) system in the proposed AISI Seismic Standard (AISI S110) are developed such that energy dissipation in the form of bolt slippage and bearing in the bolted beam-to-column moment connections would occur during a major seismic event. Beams and columns are then designed following the capacity design principles to remain elastic. Based on the instantaneous center of rotation concept, this paper presents background information for the design provisions in the AISI standard for calculating the expected maximum seismic force in the beams and columns at the design story drift. This requires that the resistance from both the bolt slippage and bearing actions in the moment connection be computed. Design tables are provided to facilitate the design. The recommended seismic design procedure is also provided.

### **INTRODUCTION**

The American Iron and Steel Institute (AISI) is in the process of developing a seismic design Standard for cold-formed steel, *Standard for*

---

<sup>1</sup> Assistant Professor of Architecture and Architectural Engineering at Kyoto University, Kyoto, JAPAN, asato@archi.kyoto-u.ac.jp

<sup>2</sup> Professor of Structural Engineering at University of California, San Diego, La Jolla, CA, cmu@ucsd.edu

*Seismic Design of Cold-Formed Steel Structural Systems—Special Bolted Moment Frames - AISI S110 [AISI, 2007].* The first seismic force-resisting system introduced in the AISI seismic standard is termed Cold-Formed Steel—Special Bolted Moment Frames (CFS—SBMF). It is common that this type of one-story moment frames is composed of cold-formed Hollow Structural Section (HSS) columns and double-channel beams. Beams are connected to the column by using snug-tight high-strength bolts; see Figure 1 for a typical moment connection detail.

Cyclic testing of full-scale beam-column subassemblies [Uang et al., 2008] showed that the bolted moment connection can provide a high ductility capacity through bolt slippage and bearing (Figure 2). The test results also showed that column and beam local buckling should be avoided because it would result in a strength degradation.

This paper provides the background information for the development of capacity design provisions contained in the proposed AISI Seismic Standard for CFS—SBMF. The objective of these design provisions is to ensure that inelastic action occurs in the bolted moment connections only during a design earthquake event, and that both beams and columns should remain elastic.

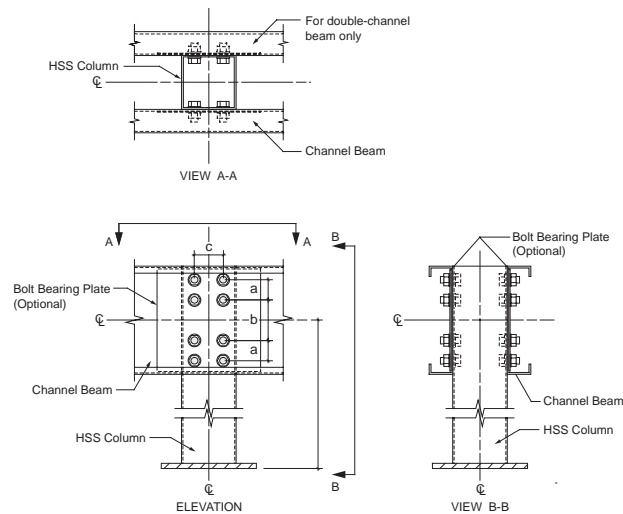


FIGURE 1 – BOLTED MOMENT CONNECTION

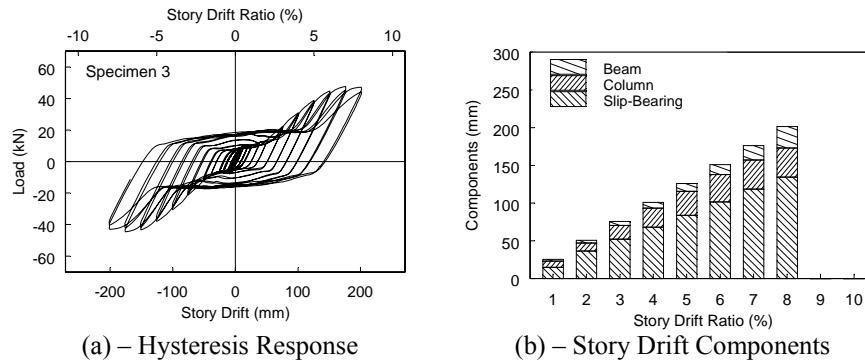


FIGURE 2 – BOLTED MOMENT CONNECTION

### EXPECTED SEISMIC RESPONSE

In accordance with the AISI Seismic Standard (AISI S110), a designer would first use a value of  $R$  (Response Modification Coefficient) of 3.5 for preliminary design. Figure 3 shows that the elastic seismic force corresponding to the Design Basis Earthquake (DBE, point ‘e’) is reduced by the  $R$  factor to point ‘d’ for sizing beams, columns, and bolted moment connections. Unlike other seismic force-resisting systems where point ‘d’ represents the first significant yielding event (e.g., formation of the plastic hinge in a moment frame), CFS–SBMF actually would ‘yield’ at a lower seismic force level (point ‘a’) due to slippage of the bolts in moment connections. A horizontal plateau (point ‘a’ to ‘b’) would result due to the oversize of the bolts. As the story drift is increased, the lateral resistance starts to increase from point ‘b’. Test results showed that such hardening in strength is very significant (see Figure 2), and it is not appropriate to assume an elastic-perfectly plastic (EPP) global response for either analysis or design.

Considering the effect of such significant hardening, a Deflection Amplification Factor,  $C_d$ , was also developed for CFS–SBMF in the AISI Seismic Standard (AISI S110). With the  $C_d$  value, the designer then can amplify the story drift at point ‘d’ to estimate the maximum inelastic story drift ( $\Delta$  at point ‘c’) that is expected to occur in a Design Earthquake event. To ensure that beams and columns will remain elastic, the challenge then is to evaluate the maximum seismic force corresponding to point ‘c’. This seismic force level represents the required seismic strength for the beams and columns.

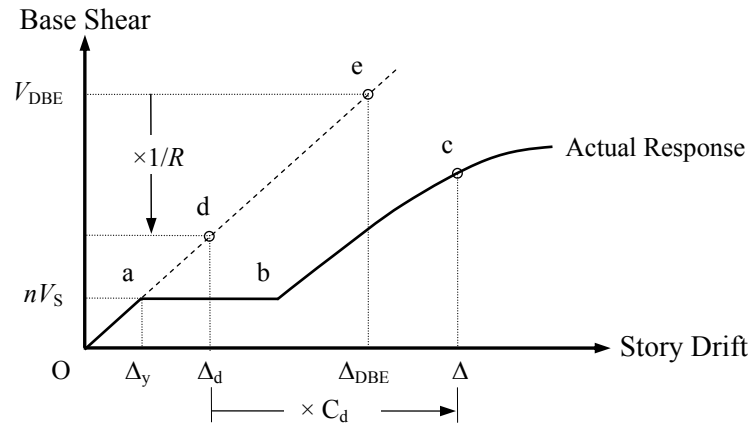


FIGURE 3 – GENERAL STRUCTURAL RESPONSE OF CFS—SBMF

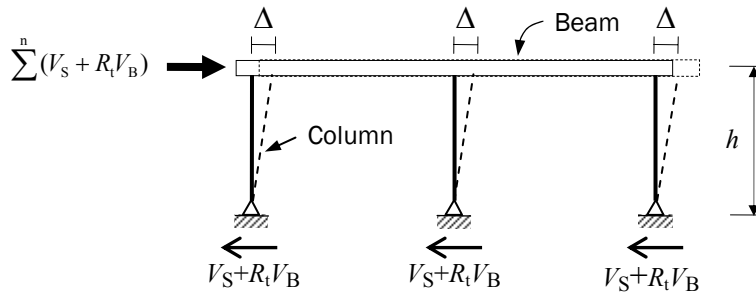


FIGURE 4 – YIELD MECHANISM AND COLUMN SHEAR DISTRIBUTION

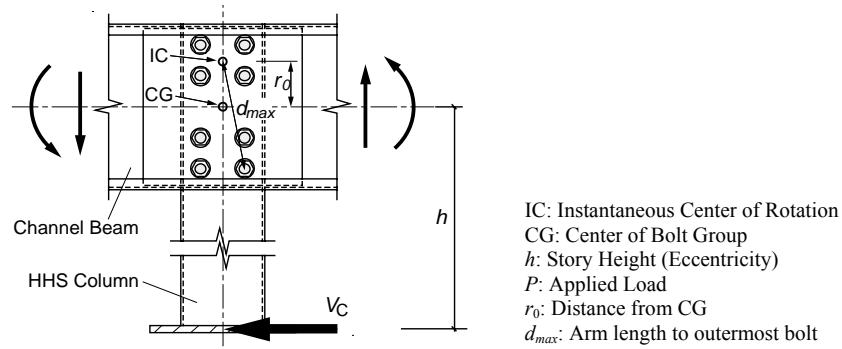


FIGURE 5 – FREEBODY OF ONE COLUMN

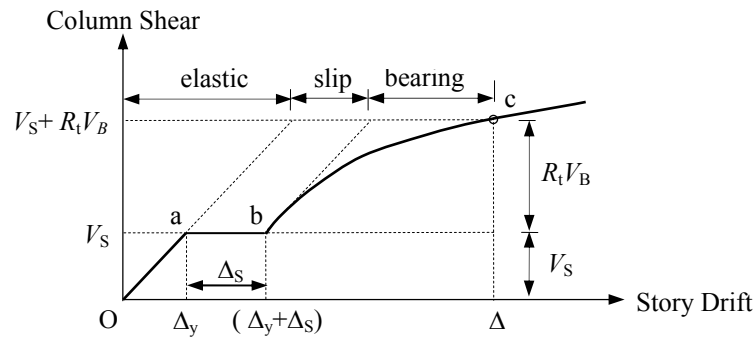


FIGURE 6 – LATERAL RESISTANCE OF ONE COLUMN

It is common that same-size beams and same-size columns are connected by high-strength bolts with the same configuration. Referring to a sample frame shown in Figure 4, interior column(s) will resist more shear than exterior columns in the elastic range. Once the frame responds in the inelastic range to point 'c' in Figure 3, however, it is reasonable to assume that column shears will equalize as shown in Figure 4. Capacity design of the beams and columns can be performed if the maximum shear force developed in the columns can be



evaluated. Specifically, the required moment for both beam and column at the connection location is

$$M_e = h(V_S + R_t V_B) \quad (1)$$

where  $h$  = story height, and  $R_t$  = the ratio of expected tensile strength to specified tensile strength.  $V_S$  and  $V_B$  represent resistance due to bolt slippage and bearing.

#### SLIP COMPONENT OF COLUMN SHEAR AND SLIP DRIFT

The freebody of one column is shown in Figure 5. With the shear at the base of the column, the bolt group is in eccentric shear. To show the components of lateral resistance of the yield mechanism in Figure 4, Figure 3 is replotted for one column only and shown as Figure 6. To calculate the maximum force developed at point 'c', it is necessary to first compute the column shear ( $V_S$ ) that causes the bolts to slip and the amount of slip, expressed in the form of story drift ( $\Delta_S$ ).

Since the bolt group is in eccentric shear, the instantaneous center of rotation concept [Crawford and Fisher, 1971; Salmon and Johnson, 1996] can be used to compute  $V_S$ . Given the bolt oversize, the slip drift ( $\Delta_S$ ) can also be computed in the analysis. These two quantities for some commonly used bolt configuration are provided in Table 1. To facilitate design, a regression analysis of the values contained in Table 1 was also conducted, which resulted in the following two expressions:

$$V_S = C_S k N T / h \quad (2)$$

$$\Delta_S = C_{DS} h_{OS} h \quad (3)$$

where  $C_S$ ,  $C_{DS}$  = regressed values from Table 2,  $k$  = slip coefficient,  $N$  = number of channels in a beam,  $T$  = snug-tight bolt tension,  $h_{OS}$  = hole oversize (= 1/16 in. for standard holes), and  $h$  = story height. A value of  $k$  equal to 0.33 and value of  $T$  equal to 10 kips were used [Uang et al., 2008].

#### BEARING COMPONENT OF COLUMN SHEAR AND BEARING DRIFT

Referring to point 'c' in Figure 6, the design story drift ( $\Delta$ ) is composed of three components: (i) the recoverable elastic component which is related to the lateral stiffness,  $K$ , of the frame, (ii) the slip component,  $\Delta_S$ , which can be computed from Eq. (3), and (iii) the bearing component computed from following equation:

$$\Delta_B = \Delta - \Delta_S - \frac{n M_e}{h K} \quad (4)$$

where  $n$  = number of column in a frame line (i.e, number of bays plus 1),  $M_e$  = expected moment at a bolt group computed from Eq. (1).

TABLE 1 – VALUES OF  $G_S$ , AND  $G_{DS}$  FOR ECCENTRICALLY LOADED BOLT GROUP

$V_S = N \times G_S \times R_S$ $\Delta_S = G_{DS} \times h_{os}$ <p><math>N = 1</math> for single-channel beams  <math>= 2</math> for double-channel beams</p>		where $V_S$ = column shear causing slip $R_S$ = slip strength per bolt (= $k \times T$ ) $k$ = slip coefficient $T$ = snug-tight bolt tension $h$ = story height, ft $a, b, \text{ and } c$ = bolt spacing, in. $\Delta_S$ = slip drift due to slip $G_S, G_{DS}$ = coefficient tabulated below $h_{os}$ = hole oversize					
		Bolt spacing $a$ and $b$ , in.					
c, in.	h, ft	a = 2-1/2, b = 3		a = 3, b = 6		a = 3, b = 10	
		$G_S$	$G_{DS}$	$G_S$	$G_{DS}$	$G_S$	$G_{DS}$
4-1/4	8	0.296	40.5	0.416	26.6	0.562	17.6
	9	0.264	45.8	0.370	30.3	0.501	20.1
	10	0.237	51.0	0.333	34.0	0.452	22.7
	11	0.216	56.3	0.303	37.7	0.411	25.3
	13	0.183	66.9	0.257	45.1	0.349	30.6
	15	0.158	77.5	0.223	52.6	0.303	35.9
	17	0.139	88.1	0.197	60.1	0.268	41.4
	19	0.125	98.7	0.176	67.6	0.240	46.9
	21	0.113	109	0.159	75.1	0.217	52.5
	23	0.103	120	0.145	82.6	0.198	58.1
	25	0.0946	130	0.134	90.2	0.182	63.7
	27	0.0879	141	0.124	97.7	0.169	69.3
	29	0.0818	152	0.115	105	0.157	75.0
	31	0.0763	162	0.108	113	0.147	80.7
33	0.0714	173	0.101	120	0.138	86.4	
35	0.0678	183	0.0955	128	0.130	92.1	
6-1/4	8	0.355	36.2	0.460	25.8	0.597	18.2
	9	0.315	40.9	0.410	29.3	0.531	20.9
	10	0.284	45.6	0.369	32.9	0.479	23.5
	11	0.259	50.4	0.335	36.4	0.436	26.2
	13	0.218	59.8	0.284	43.5	0.370	31.6
	15	0.189	69.3	0.246	50.5	0.321	37.0
	17	0.167	78.7	0.217	57.6	0.283	42.5
	19	0.150	88.2	0.194	64.7	0.253	48.0
	21	0.135	97.6	0.176	71.8	0.229	53.5
	23	0.124	107	0.161	78.9	0.210	59.0
	25	0.114	117	0.148	85.9	0.193	64.6
	27	0.105	126	0.137	93.0	0.179	70.1
	29	0.0977	135	0.127	100	0.166	75.7
	31	0.0915	145	0.119	107	0.156	81.2
33	0.0859	154	0.112	114	0.146	86.8	
35	0.0810	164	0.105	121	0.138	92.4	

TABLE 2 – VALUES OF COEFFICIENTS  $C_S$ ,  $C_{DS}$ ,  $C_B$ , AND  $C_{B,0}$ 

Bolt spacing*, in.			$C_S$ (ft)	$C_{DS}$ (1/ft)	$C_B$ (ft)	$C_{B,0}$ (in./ft)
a	b	c				
2½	3	4¼	2.37	5.22	4.20	0.887
3	6		3.34	3.61	5.88	0.625
3	10		4.53	2.55	7.80	0.475
2½	3	6¼	2.84	4.66	5.10	0.792
3	6		3.69	3.44	6.56	0.587
3	10		4.80	2.58	8.50	0.455

\* See Figure 1

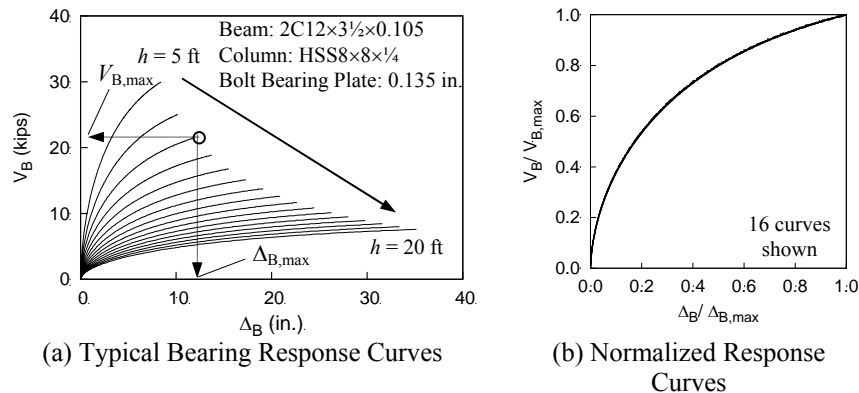


FIGURE 7 – SAMPLE RESULT OF BEARING RESPONSE

Applying the instantaneous center of rotation concept to an eccentrically loaded bolt group [Uang et al., 2008], the relationship between the bearing component of the story drift,  $\Delta_B$ , and the bearing component of the column shear,  $V_B$ , can be established. Figure 7(a) shows a sample result. For a given frame height, the last point of each curve represents the ultimate limit state when the bearing deformation of the outermost bolt reaches 0.34 in. (8.6 mm) [AISC, 2005]. Ultimate bearing shear of the column,  $V_{B,max}$ , and corresponding bearing drift deformation,  $\Delta_{B,max}$ , for some commonly used bolt configuration and story heights are computed and are tabulated in Table 3. The variable  $R_0$  refers to the governing value (or minimum value) of  $dtF_u$  of the connected components (beam and column webs).

TABLE 3 – VALUES OF  $G_B$ , AND  $G_{DB}$  FOR ECCENTRICALLY LOADED BOLT GROUP

$V_{B,max} = N \times G_B \times R_0$ $\Delta_{B,max} = C_{DB} \times \Delta_{B,0}$  $N = 1$ for single-channel beams $= 2$ for double-channel beams		where $V_{B,max}$ = column shear causing bolt maximum bearing $R_0$ = minimum values of $dF_u$ of connected beam and column webs $F_u$ = tensile strength $t$ = bearing thickness $d$ = bolt diameter $G_B$ = coefficient tabulated below $\Delta_{B,0}$ = maximum bearing drift deformation $C_{DB}$ = bearing deformation adjustment factor [Eq. (6)]					
		Bolt spacing $a$ and $b$ , in.					
c, in.	h, ft	a = 2-1/2, b = 3		a = 3, b = 6		a = 3, b = 10	
		$G_B$	$\Delta_{B,0}$ , in.	$G_B$	$\Delta_{B,0}$ , in.	$G_B$	$\Delta_{B,0}$ , in.
4-1/4	8	0.524	6.92	0.728	4.77	0.983	3.50
	9	0.466	7.81	0.649	5.40	0.878	4.00
	10	0.420	8.71	0.586	6.04	0.794	4.49
	11	0.381	9.61	0.533	6.68	0.724	4.98
	13	0.323	11.4	0.453	7.95	0.616	5.97
	15	0.281	13.2	0.393	9.23	0.536	6.96
	17	0.247	15.0	0.347	10.5	0.474	7.95
	19	0.222	16.8	0.311	11.8	0.425	8.94
	21	0.200	18.6	0.281	13.1	0.385	9.92
	23	0.183	20.4	0.257	14.3	0.352	10.9
	25	0.169	22.2	0.237	15.6	0.325	11.9
	27	0.156	24.0	0.220	16.9	0.301	12.9
	29	0.145	25.8	0.204	18.2	0.281	13.9
	31	0.136	27.6	0.191	19.5	0.262	14.9
33	0.127	29.4	0.180	20.7	0.247	15.8	
35	0.120	31.2	0.169	22.0	0.233	16.8	
6-1/4	8	0.637	6.17	0.814	4.48	1.05	3.36
	9	0.566	6.97	0.725	5.08	0.935	3.82
	10	0.510	7.77	0.654	5.68	0.845	4.29
	11	0.464	8.57	0.595	6.28	0.771	4.76
	13	0.393	10.2	0.504	7.48	0.655	5.70
	15	0.341	11.8	0.438	8.68	0.570	6.65
	17	0.302	13.4	0.387	9.88	0.504	7.59
	19	0.269	15.0	0.347	11.1	0.452	8.54
	21	0.244	16.6	0.314	12.3	0.410	9.48
	23	0.222	18.2	0.287	13.5	0.374	10.4
	25	0.205	19.8	0.264	14.7	0.345	11.4
	27	0.189	21.4	0.244	15.9	0.319	12.3
	29	0.176	23.0	0.228	17.1	0.298	13.3
	31	0.165	24.6	0.213	18.3	0.279	14.2
33	0.154	26.2	0.201	19.5	0.262	15.2	
35	0.146	27.8	0.189	20.7	0.247	16.1	

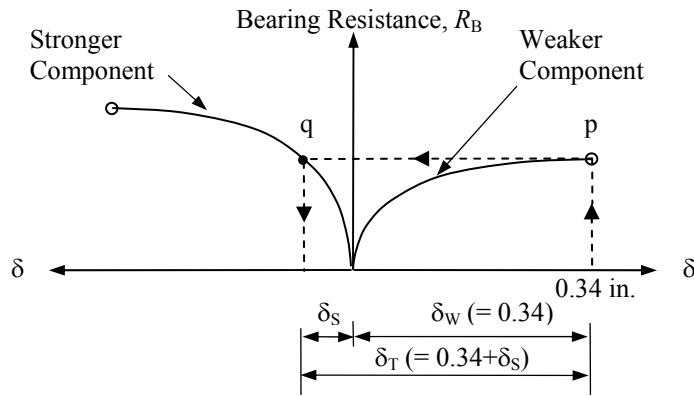


FIGURE 8 – BOLT BEARING DEFROMATION IN STRONGER AND WEAKER COMPONENTS

Each bolt in the moment connection bears against not only the column web but also the beam web. The bearing force exerted by the bolt to both components is identical. But the bearing deformation can be different between these two components, depending on the relative bearing strength,  $tF_u$ , where  $t$  = thickness of the component,  $F_u$  = tensile strength. The  $\Delta_{B,0}$  values in Table 3 correspond to the maximum drift when the bearing deformation is contributed by the weaker component (either beam or column) only. That is, it is assumed that the stronger component is rigid. The Bearing Deformation Adjustment Factor,  $C_{DB}$ , in Table 3 accounts for the additional contribution to bearing deformation from the stronger component. Refer to point 'p' in Figure 8, where the ultimate bearing deformation [= 0.34 in. (8.6 mm)] of the weaker component is reached. Since the bearing force of the bolt on both weaker and stronger components is identical, it can be shown that the corresponding bearing deformation (unit in inch) of the stronger component (i.e., point 'q') is

$$\delta_s = -\frac{1}{5} \ln \left[ 1 - 0.817 \left( \frac{(tF_u)_w}{(tF_u)_s} \right)^{1.82} \right] \quad (5)$$

The  $C_{DB}$  factor represents the ratio between the total bearing deformation and 0.34 inch.

TABLE 4 – BEARING DEFORMATION ADJUSTMENT FACTOR  $C_{DB}$ 

Relative Bearing Strength	0.0	0.4	0.5	0.6	0.7	0.8	0.9	1.0
$C_{DB}$	1.00	1.10	1.16	1.23	1.33	1.46	1.66	2.00

where  
relative bearing strength (RBS) =  $(tF_u)_{(weaker)} / (tF_u)_{(stronger)}$   
 $t$  = Thickness of beam or column component  
 $F_u$  = Tensile strength of beam or column

$$C_{DB} = \frac{0.34 + \delta_s}{0.34} = 1.0 - 0.588 \ln \left[ 1 - 0.817 \left( \frac{(tF_u)_w}{(tF_u)_s} \right)^{1.82} \right] \quad (6)$$

A regression analysis of Table 3 was conducted to derive the following design formulae, and Table 4 is provided for the bearing deformation adjustment factor,  $C_{DB}$ , to facilitate design.

$$V_{B,max} = C_B NR_0 / h \quad (7)$$

$$\Delta_{B,max} = C_{B,0} C_{DB} h \quad (8)$$

where  $C_B$ ,  $C_{B,0}$  = regressed values from Table 2.

For a given beam size, column size, and a bolt configuration, Figure 7(a) shows that the response curve is dependent on the story height. Eqs. (7) and (8) define the ultimate bearing strength point of each curve in the bearing response curve [see Figure 7(a)]. Normalizing each curve by its ultimate bearing strength point, however, Figure 7(b) shows that the normalized curves can be approximated very well by the following expression:

$$\left( \frac{V_B}{V_{B,max}} \right)^2 + \left( 1 - \frac{\Delta_B}{\Delta_{B,max}} \right)^{1.43} = 1 \quad (9)$$

Given a value of  $\Delta_B$  from Eq. (4), Eq. (9) can be used to compute the bearing component of the column shear,  $V_B$ , and, hence,  $M_e$  in Eq. (1). But since Eq. (4) also contains  $M_e$ , iteration is required to compute the expected moment,  $M_e$ . A flowchart is provided in Figure 9. The following value is suggested as the initial value for  $\Delta_B$ :

$$\Delta_B = \frac{[\Delta - (\Delta_s + \Delta_y)]K}{nV_{B,max} / \Delta_{B,max} + K} \quad (10)$$

where  $\Delta_y$  is the story drift at point 'a' in Figure 6.

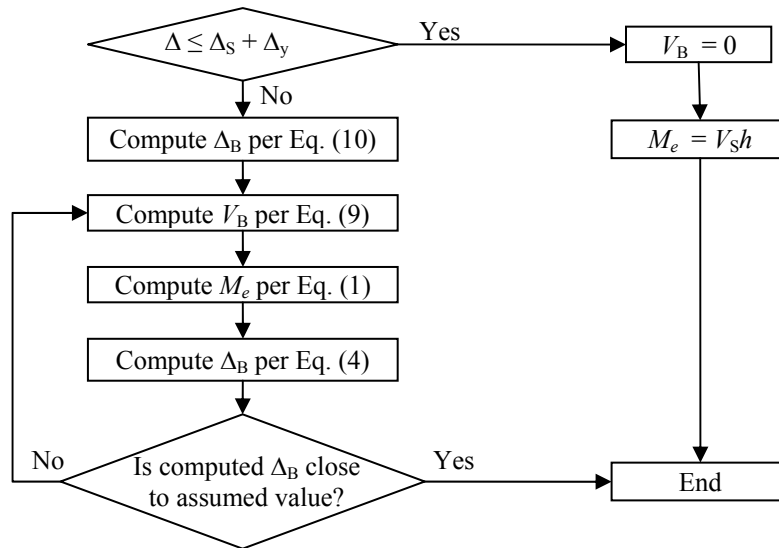


FIGURE 9 – FLOWCHART FOR COMPUTING EXPECTED MOMENT

#### DESIGN PROCEDURE FOR CFS—SBMF

The recommended seismic design procedure follows.

##### Step 1 – Preliminary design

Perform a preliminary design of the beams, columns, and bolted connections by considering all basic load combinations in the applicable building code. Use a value of  $R$  equal to 3.5. In determining the earthquake load, use a rational method to determine the structural period.

Step 2 – Compute both the base shear ( $nV_S$ ) that causes the bolt groups to slip and the slip range ( $\Delta_S$ ) in terms of story drift.

For a given configuration of the bolt group, Eqs. (2) and (3) can be used to compute both  $V_S$  and  $\Delta_S$ .  $n$  represents the number of columns in a frame line.

Step 3 – Compute the design story drift,  $\Delta$

Follow the applicable building code to compute the design story drift, where the Deflection Amplification Factor is given in the AISI Seismic Standard (AISI S110).

Step 4 – Perform capacity design of beams and columns

Beams and columns should be designed based on special seismic load combinations of the applicable building code; the seismic load effect with

overstrength,  $E_m$ , is to be replaced by the required strength in Eq. (1). The flowchart in Figure 9 can be used for this purpose.

Step 5 – Check P- $\Delta$  effects following the applicable building code.

#### ACKNOWLEDGMENT

This research was sponsored by the American Iron and Steel Institute. The authors would like to acknowledge the advice from the AISI Seismic Task Group, Chaired by Professor Reidar Bjorhovde, for the development of CFS–SBMF design provisions.

#### REFERENCES

- American Institute of Steel Construction (AISC), *Steel Construction Manual, 13th Edition*, 2005.
- American Iron and Steel Institute (AISI), S110-07, *Standard for Seismic Design of Cold-Formed Steel Structural Systems—Special Bolted Moment Frames*, 2007.
- Crawford, S. F. and Fisher, J. W., “Eccentrically Loaded Bolted Connections”, *Journal of the Structural Division*, 97(ST3), 1971, 765-783.
- Salmon, C. G., and Johnson, J. E., *Steel Structures Design and Behavior*, 4th Edition, HarperCollins College Publishers, 1996.
- Uang, C.M., Hong, J.K., Sato, A. and Wood, K., “Cyclic Testing and Modeling of Cold-Formed Steel—Special Bolted Moment Frame Connections”, *Proceedings, ASCE Structural Congress*, 2008.





## **Cold-formed steel portal frame joints: a review**

A.M. Wrzesien<sup>1</sup>, J.B.P. Lim<sup>2</sup>

### **Abstract**

This paper reviews research published on cold-formed steel portal joints, beginning with the laboratory tests of Baignent and Hancock (1982) and ending with those of Rhodes and Burns (2006). The moment-capacity of the cold-formed steel channel-sections being connected in the portal framing systems ranges from 3.6 kNm to 128.5 kNm, with each type of framing system employing a different joint detail. While in accordance with the Eurocode 3 joint classification system, the joints arrangements reported would be classified as semi-rigid, for the purpose of design the majority of the joints would be sufficiently rigid for the frames to be designed safely to the ultimate limit state using a rigid-joint assumption, with the joints capable of sustaining almost the full-moment capacity of the cold-formed steel channel-sections being connected. However, in order for the assumption of rigid joints to be valid, the number of bolts or specialist components required may, in some countries, result in the joints being uneconomical to fabricate. It is seen that of all the joints reviewed, the joint arrangement tested by Rhodes and Burns is distinctive as rigid-joints are formed inexpensively through the use of knee braces. This, however, is at the expense of losing clear height to the eaves. Using UK design practice, a parametric study of sixteen frames, having spans ranging from 8 m to 14 m, is described that compares the economy of rigid-jointed frames against that of knee-braced frames. It is shown that use of a knee-braced frame results in a 10% increase in load carrying capacity, and a 36% reduction in horizontal deflections.

---

<sup>1</sup> PhD Student, Department of Civil Engineering, University of Strathclyde, Glasgow, UK

<sup>2</sup> Lecturer, Department of Civil Engineering, University of Strathclyde, Glasgow, UK

## Introduction

In the UK, for portal frames having spans of up to 14 m (or more), the use of cold-formed steel sections for the column and rafter members can be a viable alternative to conventional hot-rolled steel sections. Some of the advantages of using cold-formed steel include a higher strength-to-weight ratio, reduced erection costs, and reduced acquisition and transportation costs (since both the primary members as well as the secondary members can be purchased from the same supplier).

However, in order for a valid comparison to be made between both types of framing system, the cost of fabrication of the joints must be taken into account. In the case of a typical hot-rolled steel portal frame, Tomà (1993) estimated that as much as 40% of the total frame cost is due to the fabrication of the joints. While it can be expected that this percentage will be lower for a typical cold-formed steel portal frame, it cannot be expected to be significantly lower.

Furthermore, with conventional hot-rolled steel portal frame joints, which are designed plastically, one of the key requirements is that the joints are designed to function as rigid. On the other hand, with cold-formed steel portal frames, which are designed elastically, the requirement of rigid joints that are expensive to fabricate may not be as important.

In this paper, research published in the literature on cold-formed steel portal joints is reviewed, beginning with the laboratory tests of Baignent and Hancock (1982) and ending with those of Rhodes and Burns (2006). The moment capacity of the joints in the review ranges from 3.6 kNm to 128.54 kNm.

The majority of the joints described attempt to form a rigid joint through the use of haunch brackets and bolts. Rhodes and Burns (2006), however, describe a haunch connection formed through knee brace member. The effect of having a knee brace is investigated further by the authors.

A parametric study is undertaken, comprising sixteen frames having spans ranging from 8 m to 14 m, comparing the economy of rigid-jointed frames to that of knee-braced frames, taking into account both ultimate and serviceability limit state design.

### Literature review

Over the past thirty years, different researchers have undertake tests on different arrangements for the eaves and apex joints of cold-formed steel portal framing systems. Table 1 summarises the joints reported in the literature by each researcher, including the moment-capacity of the cold-formed steel sections being connected, and the number of components and fasteners required to form the joint.

The earliest tests reported in the literature on cold-formed steel portal frame joints are those by Baigent and Hancock (1982). Details of this joint are given in Fig. 1. As can be seen, the joints were formed through the web of the channel-sections used for column and rafter members. The moment-capacity of the channel-sections being connected was 9.19 kNm. The thickness of the channel-sections was 1.86 mm, while the thickness of the plate used to connect the joints was 12 mm. Due to high-tensile grip bolts, the joints could be considered as being rigid.

The next set of tests reported were those by Kirk (1986) on the Swagebeam portal framing system. These tests were undertaken by Professor Bryan at Salford University. Figure 2 shows details of the joints. As can be seen, back-to-back channel sections were used for the column and rafter members. The joints were formed through back-to-back brackets bolted between the webs of the channel-sections. The moment-capacity of the back-to-back channel-sections was 32 kNm; the thickness of the channel-sections was 2.4 mm and the thickness of each bracket was 3.0 mm. The primary innovation was that the joints could formed through the swages rolled in the brackets which connected with matching swages in the webs of the channel-sections.

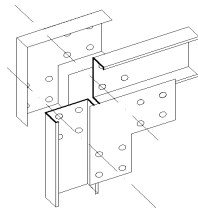


Fig.1 Eaves joint after Baigent and Hancock (1982)

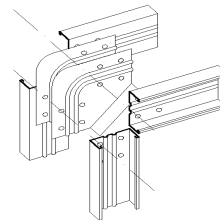


Fig.2 Swagebeam eaves joint after Kirk (1986)

Table 1. Joints reported in the literature

Author	Sections				Bracket			Fasteners	
	$d \times b \times t$ (mm)	$\sigma_y$ (N/mm <sup>2</sup> )	$M_u$ (kNm)	$l_b$ (mm)	$t_b$ (mm)	$\sigma_{yb}$ (N/mm <sup>2</sup> )	No. of brackets	Description	No. of fixings/joint
Baigent (1982)	[ 153x79x1.86	325.8	9.2	260	12	-	1	M19mm H.T. bolts	8
Kirk (1986)	[ 220x65x2.4	280*	32.0	620	3	280	2	M16 G.8.8	8
Mäkeläinen (1996)	[ 300x75**x3.0	350*	77.0	-	12	355	1	M16 G.8.8	20
Chung (1998)	[ 150x64x1.6	450*	17.9	460 <sup>b</sup> 460 <sup>ba</sup>	6 2.5	343 475	1 2	M16 G.8.8	8
Lim (2002)	[ 340x90x3	280*	82.8	746 <sup>ba</sup>	3	209	2	M16 G.8.8	16
Mills (2004)	[ 200x76x1.5	450*	10.8	End plate joint Mined joint Sections screwed back-to-back				Bolts Bolts Screws	2 2 12
Dubina (2004)	[ 350x100x3	452	117.8	940	10	235	1	M20 G.6.6	32
Danda (2005)	[ 300x75x3	468.9	51.6	Sections bolted back-to-back				M20 G.8.8 M20 G.8.8	4 8
Kwon (2006)	PRY 150x40x0.8	570*	3.6	261.6	2.3	240	1	Screws $\phi$ 4.8mm	16
Rhodes (2006)	342x97x2.5 rafter 402x97x3.2 column	343 352	76.7 128.5	Connection angles C 202x69x2 knee brace			2 2	M16 G.8.8	32

\* design yield strength, \*\* dimension not reported but assumed following standard size, <sup>b</sup> haunch, <sup>ba</sup> haunch with stiffener

Mäkeläinen (1996) described tests on a portal framing system constructed from back-to-back sigma sections connected through the web via brackets. To provide additional stiffness to the frame, a tie bar (double angle 50 x 50 x 2.5 mm) was bolted to both eaves brackets (Fig. 3a). The depth of the sections used for the tests were 250 mm, 300 mm, and 400 mm; thicknesses of 2.5 mm and 3.0 mm were considered. Figure 3 shows details of the joint brackets. These included a single plate of thicknesses of 8 mm, 10 mm and 12 mm (see Fig. 3a), four cold-formed plates thickness of 2.5mm each (see Fig. 3b), and four cold-formed plates with two outer plates outwardly lipped (see Fig. 3c). Although the moment capacities of the sections were not provided, similar compound member made from back-to-back standard sigma section 300 mm deep, 75 mm wide, and 3.0 mm were calculated to have a moment capacity of 77 kNm.

Chung (1998) and Lim and Nethercot (2002) independently reported tests on an arrangement where the joint was formed through back-to-back brackets bolted between the webs of the channel-sections being connected. In the tests described by Chung, the moment-capacity of the sections was 17.88 kNm, while that of Lim and Nethercot was 82.8 kNm. Figures 4a to 4d shows the different shape of the brackets studied by Chung. In the case of the joint details shown in Fig. 4c and 4d, the joints were tested twice. In the first stage, the joints were formed through a hot-rolled steel single gusset plates of thickness 6mm. In the second phase, the joints were formed through two back-to-back cold-formed steel brackets, each 2.5mm thick and with lip stiffeners along the catheti and hypotenuse of the bracket respectively (Fig. 4c and 4d). Unlike Chung, the joints tested by Lim and Nethercot isolated failure of the brackets from that of the channel-sections. Having ensured that the brackets themselves would not fail, research was focused on the strength and stiffness of the channel-sections, as influenced by the bolt-group size.

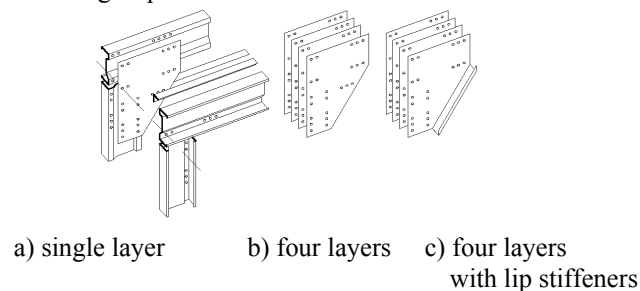


Fig.3 Eaves joint having different brackets configuration after Mäkeläinen and Kankaanpää (1996)

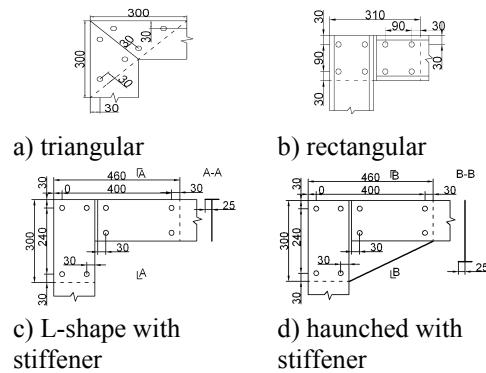


Fig.4 Eaves joint brackets after Chung and Lau (1998)

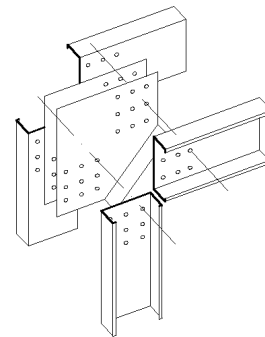


Fig.5 Eaves joint after Lim and Nethercot (2002)

Mills and LaBoube (2004) conducted experimental studies on joints currently used in Australia for cold-formed steel portal frame sheds. The joints were constructed from single channel-sections with a moment capacity of 10.84 kNm. Popular joints included an end plate connection bolted to the column and welded to the rafter (Fig. 6a), and a mitred joint (Fig. 6b). Self-drilling screws were used as an alternative to conventional bolting. A similar arrangement for the apex joint was also studied, in which double lipped channel-sections were used as the gusset plate and screwed back-to-back to the rafters.

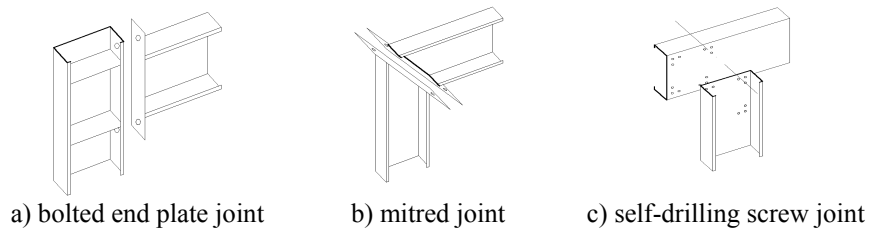


Fig.6 Eaves joints after Mills and LaBoube (2004)

Dubina *et al* (2004) described the three different type of joints. As can be seen in Figure 7a and 7c, the channel-sections were bolted only through the web of welded I-section brackets (KIS, KIP) and spaced gussets bracket (KSG). In second variant, bolts were located both on the web and on the flange (Fig. 7b) of I-section bracket (KIS) and I-section bracket with plate bisector (KIP). The moment-capacity of the channel-sections being connected was 117.8 kNm.

It should be noted that unlike Chung (1998), the joint was formed through hot-rolled steel sections instead of back-to-back brackets. However, as the strength of the hot-rolled steel sections is much greater than that of the channel-sections, the behaviour of the joints is dominated by that of the channel-sections.

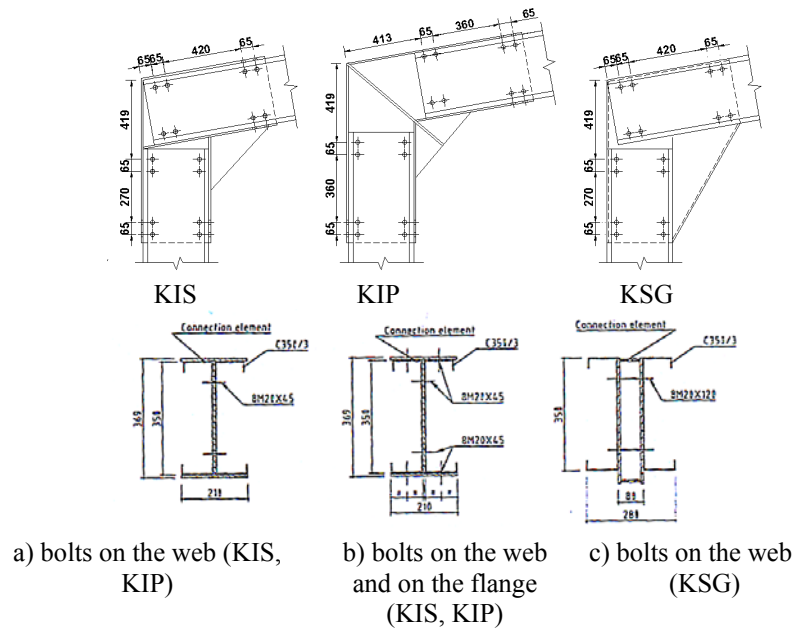


Fig.7 Eaves joints after Dubina *et al* (2004), p.382: KIS- welded I section, KIP- welded I section with plate bisector, KSG-spaced gussets,

Dundu and Kemp (2006) conducted research on single channels connected back-to-back (Fig. 8). Such an arrangement is similar to that of Mills and LaBoube (2004). Dundu and Kemp were concerned with the development of a plastic hinge, and so concentrated on the ductility of the joints. A novel method for providing lateral restraint was introduced through an angle connection between the web of the rafter and purlin. It was demonstrated that this arrangement eliminated the lateral-torsional buckling failure mode, since both the top and bottom flanges were effectively restrained, reducing torsional instability.

Kwon *et al* (2006) reported research on applications of closed sections produced by a combination of cold-rolling and clinching techniques. The sections used for the tests were 150 mm deep, 40 mm wide and 0.8 mm thick. The local buckling





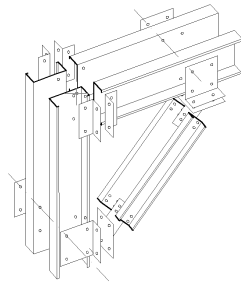


Fig. 10 Eaves joint after Rhodes and Burns (2006)

### Parametric study

The joint arrangement tested by Rhodes and Burns removed the necessity of constructing expensive rigid joints by introducing knee brace. This arrangement allowed the joint to possess as much strength as the one described by Dubina and also significantly improved the overall sway of the frame.

In this Section, a parametric study of sixteen frames is described, comparing a rigid-jointed frame to that of a knee-braced frame. The parametric study considers frames having spans between 8 m to 14 m and height to eaves between 3 m to 6 m. Table 3 shows the spans and heights of the analysed frames. The pitch of all frames is  $10^\circ$ . The distance between adjacent bays is 4 m. The column base of all frames is pinned.

For each frame geometry considered, three types of joints are analysed: Joint A, Joint B, and Joint C. Figure 11 shows details of the three types of joint. As can be seen, in the case of Joint A, the eaves and apex joints are rigid. In the case of Joint B, the eaves and apex joints are pinned. Instead, the eaves joint is formed through a knee brace pinned to the column and rafter members, respectively, at a distance of  $H/4$  from the top of the column, and a similar distance along the rafter. Similarly, the apex joint is formed through a knee brace pinned to the rafter members. The length of the apex knee-brace is a quarter of the span. Joint C is identical to Joint B except that the eaves and apex joints are rigid.

Table 3 also shows, for each frame geometry considered, the section sizes used in the frame design. A six digit designation is used to denote the section size of the channel-sections, which are used back-to-back. For the frame having a span of 8 m and height to eaves of 3 m, the back-to-back channel-sections used for the columns and rafter have a depth of 200 mm and a thickness of 2.5 mm.

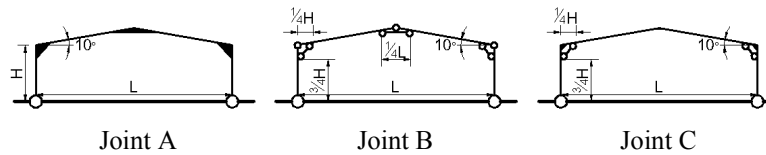


Fig. 11 Different joints arrangements

The unfactored vertical loads applied to the frames are as follows:

$$\begin{aligned} \text{Dead load (DL)} &= 0.2 \text{ kN/m}^2 \\ \text{Live load (LL)} &= 0.6 \text{ kN/m}^2 \end{aligned}$$

The unfactored wind loads are calculated in accordance to BS 6399-2 for a site located in the country, assuming a wind speed of 24 m/s, and 10 km from the sea. For the frame having a span of 8 m and height to eaves of 3 m, this corresponds to a value of  $q_s$  of 0.77 kN/m<sup>2</sup>. As  $q_s$  depends on the height and span of the frame, each frame is designed using a different value of  $q_s$ . This value of  $q_s$  is also shown in Table 3.

The frames are designed to the Ultimate Limit State (ULS) using the following load combinations:

$$\begin{aligned} \text{LC1: } &1.4 \text{ DL} + 1.6 \text{ LL} + \text{NHL} \\ \text{LC2: } &1.2 \text{ DL} + 1.2 \text{ LL} + (1.2 \times 0.85) \text{ WT}_{\text{ULS}} \\ \text{LC3: } &1.4 \text{ DL} + (1.4 \times 0.85) \text{ WT}_{\text{ULS}} \\ \text{LC4: } &1.0 \text{ DL} + (1.4 \times 0.85) \text{ WT}_{\text{ULS}} \end{aligned}$$

The  $\text{WT}_{\text{ULS}}$  loads are calculated in accordance to BS 6399-2, assuming an internal pressure coefficient,  $C_{pi}$ , of -0.3 and pressure on the windward rafter.

For the ULS design, the frame is analysed using first-order frame analysis and designed in accordance with BS 5950-5 using a combined bending and axial force check. Out-of-plane member instability is assumed to be prevented by sufficient purlins and side rails. Second-order effects are ignored.

The frames are also designed to the Serviceability Limit State (SLS) using the following load combinations:

$$\begin{aligned} \text{LC5: } &1.0 \text{ LL} \\ \text{LC6: } &1.0 \text{ WT}_{\text{SLS}} \end{aligned}$$

The  $\text{WT}_{\text{SLS}}$  loads are calculated using an internal pressure coefficient,  $C_{pi}$ , of 0 and pressure on the windward rafter.

For each frame geometry, the frame is designed three times, one for each type of Joint. The unity factors for ULS design are compared for each type of Joint and

expressed as a percentage difference. In the case of vertical SLS design, the vertical deflections of the apex (from LC5) are compared for each type of Joint and again expressed as a percentage difference. Similarly, in the case of horizontal SLS design, the horizontal deflections at the eaves (from LC6) are compared for each type of Joint and expressed as a percentage difference. The results for each frame geometry are shown in Table 3.

From Table 3 it can be seen that the effect of changing from Joint A (rigid-jointed) to Joint B (knee-brace) is an average of 10% increase in load carrying capacity. In general, the benefit of having the knee-brace increases as the height decreases. With respect to vertical deflections, there is an average of 30% reduction in deflection for frames having a height of 3 m, as a result of changing from Joint A to Joint B. However, as the frame height increases, this reduction decreases and for some frames Joint A has smaller vertical deflections than Joint B. Vertical deflections, however, rarely control design.

Of more importance is the horizontal deflections. There is an average of 36% reduction in deflections as a result of changing from Joint A to Joint B.

For the case of comparing Joint A (rigid-jointed) to Joint C (rigid-jointed with knee-brace), the average benefit of introducing the knee-brace is 14%, 37% and 38% for ULS design, vertical deflections, and horizontal deflections, respectively. This compares with 10%, 5% and 36%, respectively for the case of comparing Joint A (rigid-jointed) to Joint B (knee-brace). Since vertical deflections rarely control design, taking into account the potential semi-rigidity of the eaves and apex joint in frames having knee braces would appear to offer little benefit.

The same conclusion can be drawn from the comparison of Joint B (knee-brace) to Joint C (rigid-jointed with knee-brace).

Table 3. Portal frame comparison study

L x H (m x m)	q <sub>s</sub> (kN/m <sup>2</sup> )	Column section	Rafter section	Eaves/apex brace	Percentage load increase Joint A - Joint B			Percentage load increase Joint B - Joint C			Percentage load increase Joint A - Joint C		
					ULS <sub>cr</sub>	SLS <sub>v</sub>	SLS <sub>h</sub>	ULS <sub>cr</sub>	SLS <sub>v</sub>	SLS <sub>h</sub>	ULS <sub>cr</sub>	SLS <sub>v</sub>	SLS <sub>h</sub>
8 x 3	0.77	C20025	C20025	C15014	13	26	39	0	17	0	13	47	39
8 x 4	0.85	C30025	C30025	C15014	8	-16	40	9	58	2	18	33	43
8 x 5	0.89	C30030	C30030	C15016	8	-17	52	2	64	2	10	36	55
8 x 6	0.93	C40025	C40025	C15018	0	-29	55	3	75	0	3	25	55
10 x 3	0.78	C25020	C25020	C15018	13	38	32	-1	4	0	12	43	32
10 x 4	0.86	C30025	C30025	C15018	10	6	37	4	32	0	14	40	37
10 x 5	0.9	C40025	C40025	C15018	9	-17	37	9	64	2	19	36	40
10 x 6	0.94	C40030	C40030	C15020	6	-14	47	4	62	2	10	38	50
12 x 3	0.79	C25030	C25025	C20016	17	38	23	-1	0	0	16	38	23
12 x 4	0.87	C30025	C30025	C20016	11	19	32	3	17	2	14	39	34
12 x 5	0.91	C40025	C40025	C20016	9	-5	34	7	42	2	17	35	37
12 x 6	0.95	C40030	C40030	C20018	12	-3	45	4	48	2	16	43	48
14 x 3	0.81	C30025	C30025	C20018	13	20	8	1	6	9	15	27	17
14 x 4	0.87	C30030	C30030	C20018	11	26	28	1	9	0	13	38	28
14 x 5	0.91	C40030	C40030	C20018	9	2	31	7	32	0	17	35	31
14 x 6	0.95	C40030	C40030	C20020	13	12	43	2	28	0	15	44	43
Average					10	5	36	3	35	1	14	37	38

## Conclusions

A number of different arrangements for the eaves and apex joint of cold-formed steel portal frames have been reviewed. Whilst cold-formed steel joints that function close to rigid can be fabricated, this is often at great expense. On the other hand, while joints that function as semi-rigid can be cheaper to be fabricated, but will result in larger frame deflections.

A knee-braced joint arrangement, tested by Rhodes and Burns, has been shown to be distinctive from other joint arrangements described in the literature, as rigid-joints are formed inexpensively through the use of knee braces.

A parametric study comparing the design of portal frames in accordance with the British Standards, has led to conclusions pertaining to the most efficient joints for different geometries of the frame with and without knee braces. It has been seen that use of a knee-braced frame results in a 10% increase in load carrying capacity, and a 36% reduction in horizontal deflections. This, however, is at the expense of losing clear height to the eaves, which can be problematic, when large openings in the gable are required.

**Appendix. – References**

Baigent, A. H. and Hancock, G. J., 1982. The strength of cold-formed portal frame. *Recent Research and Development in Cold-Formed Steel Design and Construction, St. Louis, University of Missouri-Rolla*, pp.321-347.

BS5950: Part 5, 1998. *Code of practice for design of cold-formed sections*, London, British Standards Institution.

BS6399: Part 1, 1996. *Code of practice for dead and imposed loads*, London, British Standards Institution.

BS6399: Part 2, 1997. *Code of practice for wind loads*, London, British Standards Institution.

BS6399: Part 3, 1988. *Code of practice for imposed roof loads*, London, British Standards Institution.

Chung, K. F. and Lau, L., 1999. Experimental investigation on bolted moment connections among cold formed steel members. *Engineering Structures*, Vol. 21, pp. 898-911.

Dubina, D., Stratan, A., Ciutina, A., Fulop, L. and Zsolt, N. 2004. Monotonic and cyclic performance of joints of cold formed steel portal frames. *Fourth International Conference on Thin-Walled Structures*, pp.381-38.

Dundu, M. and Kemp, A. R., 2006. Plastic and lateral-torsional buckling behaviour of single cold-formed channels connected back-to-back. *Journal of Structural Engineering*, pp. 1223-1233b.

Eurocode 3 (1996): Design of steel structures: Part 1 - General rules and rules for buildings, Brussels, Committee European de Normalization.

Kirk, P., 1986. Design of a cold formed section portal frame building system. *Proc. 8th International Speciality Conference on Cold-formed Steel Structures*, St. Louis, University of Missouri-Rolla, pp. 295-310.

Kwon, Y. B. Chung, H.S. and Kim, G., 2006. Experiments of cold-formed steel connections and portal frames. *Journal of Structural Engineering*, Vol. 132, No. 4, April 1, p.600-607.

Lim, J.B.P. and Nethercot, D.A., 2002. F.E.-assisted design of the eaves bracket of a cold-formed steel portal frame. *Journal of Steel and Composite Structures*, 2, No. 6, pp. 411.

Lim, J.B.P. and Nethercot, D. A., 2004. Stiffness prediction for bolted moment-connections between cold-formed steel members. *Journal of Constructional Steel Research*, Vol. 60, pp. 85-107.

Lim, J.B.P. and Nethercot, D.A., 2003. Ultimate strength of bolted moment-connections between cold-formed steel members. *Thin-Walled Structures*, 41(11), pp. 1019.

Mäkeläinen, P. and Kankaanpää, J., 1996. Structural design study on a light-gauge steel portal frame with cold-formed sigma sections. *Proc. 13th International Specialty Conference on Cold-Formed Steel Structures*, St. Louis, University of Missouri-Rolla, pp. 349-371.

Mills, J. and LaBoube, R., 2004. Self-Drilling Screw Joints for Cold-Formed Channel Portal Frames. *Journal of Structural Engineering*, ASCE, pp. 1799-1806.

Rhodes, J. and Burns, R., 2006. Development of a portal frame system on the basis of component testing. *Proc. 18th International Specialty Conference on Cold-Formed Steel Structures*, St. Louis, University of Missouri-Rolla, pp. 367-385.

Tomà, A., Sedlacek, G. and Weynand, K., 1993. Connections in cold-formed steel. *Thin-Walled Structures*, vol.16, pp. 219-237.

Yu, W. K., Chung, K. F. and Wong, M. F., 2005. Analysis of bolted moment connections in cold-formed steel beam-column sub-frames. *Journal of Constructional Steel Research*, Vol. 61, pp. 1332-1352.

Zadanfarrokh, F and Bryan, E. R., 1992. Testing and design of bolted connections in cold formed steel sections. *Proc. 11th International Specialty Conference on Cold-Formed Steel Structures*, St. Louis, Missouri, U.S.A., pp.625-662.



**Appendix. – Notation**

b	width of the flange
d	depth of the section
H	height to the eaves of portal frame
L	span of the portal frame
$l_e$	length of the eaves bracket
$M_c$	section moment capacity reported in the literature
$q_s$	dynamic wind pressure calculated to BS 6399-2
$SLS_h$	comparison factor according to serviceability limited state criterion for horizontal deflection of the frame
$SLS_v$	comparison factor according to serviceability limited state criterion for vertical deflection of the frame
t	thickness of the section
$t_b$	thickness of the bracket
$ULS_{c,r}$	comparison factor according to ultimate limited state criterion for column or rafter design
$\sigma_y$	yield strength of the steel used for members
$\sigma_{yb}$	yield strength of the steel used for brackets

## **Strength of Arc Spot Welds made in Single and Multiple Steel Sheets**

Gregory L. Snow<sup>1</sup> and W. Samuel Easterling<sup>2</sup>

### **Abstract**

The primary focus of this research was to investigate how arc spot welding is affected by arc time (flash time). Weld sizes of 3/4 in. and 5/8 in. nominal diameter were formed using three different arc times (full-time, 2/3-time and 1/3-time). Each weld was formed in a single-, double-, or quadruple-layer of sheet steel ranging from 16 gauge (0.057 in.) to 22 gauge (0.028 in.) in thickness. Test results include weld dimensions determined from weld sectioning, weld shear strengths and comparisons made with the 2001 AISI Specification.

### **1. Introduction**

There are several methods for attaching cold-formed steel roof deck to structural steel in use today. Perhaps the most common means of attachment is through the use of arc spot welding. Arc spot welds are produced by striking an arc on the upper sheet, forcing a hole to form, while the lower unit is raised to fusion temperature. With the attainment of proper temperature, the electrode is moved in a circular pattern until the hole is filled and fusion attained on the arc-puddle perimeter (Luttrell, 2004).

Arc spot weld shear strength equations currently in use by the 2001 AISI Specification are based on research conducted at Cornell University by Teoman Pekoz and William McGuire (1980) and by Omer Blodgett (1978) of the Lincoln Electric Co. The research showed that as long as adequate end and edge distances are provided, arc spot welds will fail under either weld shear failure or sheet tear failure. Of the 126 arc spot welds tested by Pekoz and McGuire, 31

---

<sup>1</sup>Graduate Student, Virginia Tech, Blacksburg, Virginia

<sup>2</sup>Professor, Virginia Tech, Blacksburg, Virginia

failed in weld shear failure. Many of these 31 failures contained substantial pitting and porosity (Pekoz & McGuire, 1980). The area of weld remaining after each failure was determined and equations used to predict the effective diameter and shear strength of the weld were developed. These equations are both used by the 2001 AISI Specification and are listed in this document as Equations 1 and 2.

$$d_e = 0.7d - 1.5t \quad (\text{Eq 1})$$

$$Pu = \left( \frac{\pi \cdot d_e^2}{4} \right) \cdot \left( \frac{3 \cdot F_{xx}}{4} \right) \quad (\text{Eq 2})$$

Where:  
 d = The visual diameter  
 t = The total sheet steel thickness  
 F<sub>xx</sub> = The weld tensile strength

The equations used to predict the sheet tear failure mode were first developed analytically by Blodgett (1978) and then later verified through the testing performed by Pekoz and McGuire (1980). Blodgett pointed out that the stress in the material is a tensile stress at the leading edge, becoming a shear stress along the sides, and eventually becoming a compressive stress at the trailing edge of the weld (Yu, 2000). Blodgett also observed that when the average diameter to sheet steel ratio was large, the sheet would buckle behind the compression side of the weld during failure, providing little resistance to any sort of movement. Using this information, Blodgett developed Equations 3 and 4. Pekoz and McGuire (1980) later developed a transition equation, Equation 5, based on their research. All of these equations are used by the 2001 AISI Specification for estimating the ability of arc spot welds to resist sheet tear failure.

$$\text{For } \frac{d_a}{t} < 0.815 \sqrt{\frac{E}{F_u}}$$

$$Pu = 2.20t \cdot d_a \cdot F_u \quad (\text{Eq 3})$$

$$\text{For } \frac{d_a}{t} \geq 1.397 \sqrt{\frac{E}{F_u}}$$

$$Pu = 1.40t \cdot d_a \cdot F_u \quad (\text{Eq 4})$$

$$\text{For } 0.815 \sqrt{\frac{E}{F_u}} \leq \frac{d_a}{t} \leq 1.397 \sqrt{\frac{E}{F_u}}$$

$$Pu = 0.28 \left( 1 + \frac{960t}{d_a \sqrt{F_u}} \right) t \cdot d_a \cdot F_u \quad (\text{Eq 5})$$

Where:  $d_a$  = the average diameter = the visual diameter minus  $t$   
 $t$  = the average net sheet steel thickness  
 $F_u$  = the ultimate strength of the sheet steel

The performance of arc spot welds subjected to shear in typical laboratory conditions is generally well documented and well understood. Time constraints imposed by the construction schedule, however, often cause welds made in the field to be produced in a fraction of the time spent in the laboratory. The primary objective of this research was to document how arc time effects weld dimensions, weld penetration and weld shear strength in an effort to better understand the behavior of arc spot welds as they are created in today's construction industry. Comparisons were made between the observed dimensions and shear strength and those estimated using the 2001 AISI Specification.

## 2. Test Setup

### 2.1 Summary of Test Matrix

A research study was established at Virginia Tech in which 155 arc spot weld specimens were tested to determine their shear strength, dimensions, and penetration. The test matrix used in the research encompassed a broad variety of weld sizes, arc times, sheet steel thicknesses and sheet steel layers, so as to gain insight into how arc spot welds behave in a wide range of welding scenarios.

Tests were performed on both 3/4 in. and 5/8 in. nominal diameter welds, all formed using a 1/8 in. diameter E6010 electrode. Current settings varied between 105 and 200 amps, depending on the thickness of the sheet steel being attached. The sheet steel used for each specimen was ASTM A653 Grade 33 galvanized sheet steel, which was arranged in single-, double-, and quadruple-layers. The thicknesses of sheet steel included 16, 18, 20, and 22 gauge material.

Every unique combination of nominal weld size, sheet steel thickness and layer arrangement included three test series, each utilizing a distinct arc time. The first series tested was always the full-time series of welds. Each full-time series was comprised of a minimum of five specimens with two arc spot welds per specimen. The time required for making each weld and the current setting (burn off rate) used were both determined by an AWS certified welder such that the weld cross sectional dimensions were consistent with those required by the 2001 AISI Specification. This arc time was then recorded using a standard stop watch and averaged for each of the minimum ten welds in every full-time series.

The second and third test series consisted of 2/3-time welds and 1/3-time welds, respectively. The time used by the welder to complete every 2/3-time weld was limited to two-thirds of the average time used to complete a full-time weld with the same combination of nominal weld size, sheet steel thickness and layer arrangement. Similarly, the time allotted for 1/3-time welds was limited to one-third of the average time used to complete a full-time weld.

## **2.2 Lap Shear Tests**

As illustrated in Figure 2-1, each lap-shear test specimen consisted of two arc spot welds, two hot-rolled steel flat bars, and either a single-, double-, or quadruple-layer of ASTM A653 Grade 33 galvanized sheet steel. The 2.5 in. end distance and 1.5 in. edge distances used comply with section E2.2.1 of the 2001 AISI Specification for preventing tear out and net section failure of the connection.

A minimum of three specimens from every test series were loaded in shear beyond their ultimate load, so as to gain an accurate representation of the arc spot weld behavior. If any of the specimen's shear strength deviated by over ten percent from the mean strength, an additional specimen was tested.

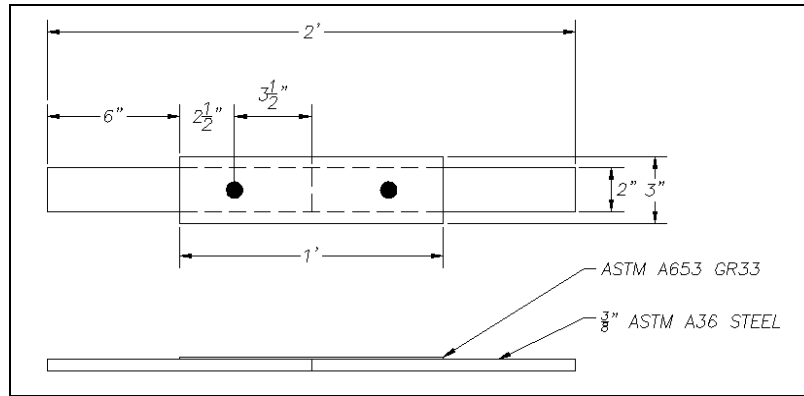


Figure 2-1: Test Specimen Configuration

### 2.3 Specimen Sectioning

Weld sectioning was performed on every test series to document weld dimensions and weld penetration. The weld dimensions that were recorded included the average diameter (the diameter of the weld at a location halfway through the sheet steel thickness) and the effective diameter (the diameter of the weld located at the top of the hot-rolled steel).

A single weld was sectioned from every full-time series and three welds were sectioned from every 2/3-time and 1/3-time series. Sectioning of the full-time series weld always occurred directly after the first full-time specimen was welded. If the specimen met the minimum dimensional requirements of the 2001 AISI Specification, the welder would continue constructing specimens using the same current setting. If the specimen did not meet the minimum AISI dimensional requirements, it would be discarded and the welder would construct another specimen after adjusting the current setting.

## 3. Results

### 3.1 Arc Time Results

Every full-time series was comprised of five specimens, each with two welds. The times spent making these ten welds were recorded and averaged. 2/3 and 1/3 of this average were then used as the time cutoffs for the 2/3-time and 1/3-time series, respectively. Figure 3-1 displays the arc times used to form both 3/4 in. and 5/8 in. diameter full-time welds. Full-time 3/4 in. welds took an average of approximately 12.8 seconds to form while full-time 5/8 in. welds took an average of approximately 8.1 seconds to form.

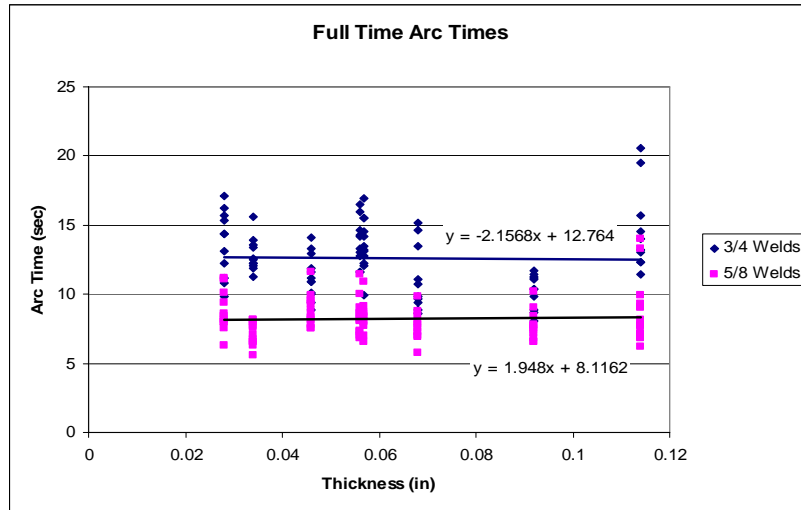


Figure 3-1: Arc Times for full-time Welds

### 3.2 Weld Sectioning Results

Every test series indicated a direct correlation between the weld dimensions and arc time regardless of the thickness of the sheet steel or the number of layers being tested. It was discovered while welding the 2/3 and 1/3-time series welds that the welder had to adjust his technique to form a visual diameter as consistent as possible with the nominal weld diameter. This adjustment was to form a smaller hole while initially burning through the sheet steel. The time saved burning a smaller hole allowed the welder to spend more time on the crown of the weld, which includes both the visual and average diameter.

The majority of 2/3-time welds tended to have visual and average diameters similar to those seen in full-time welds. However, because of the smaller initial hole in the sheet steel, they also tended to have smaller effective diameters. Full-time welds had visual diameters that were an average of 7 percent higher than those measured in the 2/3-time weld series. Effective diameters however, were an average of 22 percent higher in full-time welds. Figures 3-2 and 3-3 illustrate the difference between the full-time, 2/3-time and 1/3-time weld diameters. Note in Figure 3-2 that the diameter,  $d$ , is a nominal value (e.g. 5/8 in. or 3/4 in.), while all values of "d" ( $d$ ,  $d_a$ ,  $d_e$ ) in Figure 3-3 represent actual or measured values.

Despite saving time by starting with a smaller initial hole, most of the 1/3-time welds were found to be considerably undersized. The smaller initial hole meant that the effective diameter was undersized by an average of 36 percent when compared to full-time welds, while the visual diameter was undersized by an average of 21 percent.

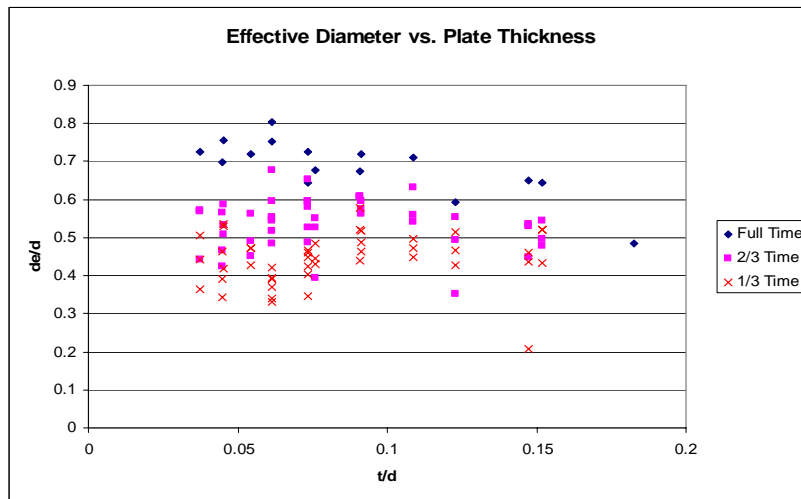


Figure 3-2: Measured Effective Weld Diameters

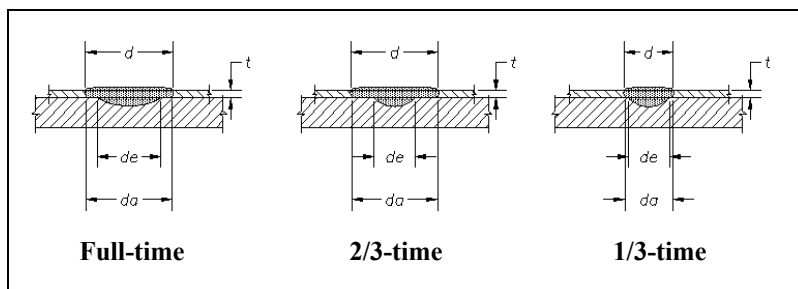


Figure 3-3: Common Weld Cross Sections

During the weld sectioning portion of the evaluations, it was found that some welds could not be satisfactorily created in certain layer configurations. When 5/8 in. welds were attempted in 16 gauge double layer conditions, three specimens had insufficient penetration and failed while sectioning. In an



attempt to remedy the situation, the current was increased. Increasing the current however, also increased the initial hole, making it impossible to create any weld smaller than 3/4 in. in diameter. For this reason only the full-time series of 5/8 in. welds were tested for the 16 gauge double-layer configuration. Similarly, none of the four-layer configurations showed sufficient penetration into the structural steel underneath. The lack of penetration was a result of too much heat being absorbed by the sheet steel and layers of air between sheets. With the current already set at 200 amps (beyond the limit for a 1/8 in. diameter electrode), it was determined that neither a 5/8 in. or 3/4 in. diameter arc spot weld could be sufficiently formed through four layers of sheet steel. It should also be noted that AWS will not certify welders to form arc spot welds through more than two layers of sheet steel.

### **3.3 Weld Sectioning Results Compared with 2001 AISI Specification**

Using the measured visual diameters and section E2.2.1 of the 2001 AISI Specification, calculated average diameters were determined. The calculated average diameters were then compared with the measured average diameters obtained during the weld sectioning tests. Figure 3-4 illustrates the ratio of measured to calculated average diameters for full-time, 2/3-time and 1/3-time welds. Full-time welds had the lowest average ratio at 0.91 followed by 2/3-time welds at 0.92 and then by 1/3-time welds at 0.94. Standard deviation values for full-time, 2/3-time and 1/3-time welds were 0.08, 0.06 and 0.10, respectively. The relatively low standard deviation and ratios close to 1.0 suggest that the 2001 AISI Specification adequately predicts average diameters for both full-time and reduced time welds, given the known value of the visible diameter.

The effective diameters of all welds were evaluated using a process similar to the one used for average diameters. Using measured visual diameters and E2.2.1 of the 2001 AISI Specification, calculated effective diameters were determined for each sectioned specimen. Next, effective diameters measured during the weld sectioning procedure were compared to the calculated values. Figure 3-5 illustrates the differences between the measured and calculated values for full-time, 2/3-time and 1/3-time weld effective diameters. The measured to calculated effective diameter ratio for full-time welds averaged 1.3 for both 3/4 in. and 5/8 in. welds with a standard deviation of 0.11, indicating that the calculated values were slightly conservative. The effective diameter ratios for 2/3-time welds averaged approximately 1.0 with a standard deviation of 0.13 for both 3/4 in. and 5/8 in. welds. The value of 1.0 indicates that the measured effective diameters are consistent with those calculated using the 2001 AISI Specification, and are also slightly less than the ratio observed in full-time

welds. The effective diameter ratio varied substantially more for 1/3-time welds than it did for either the full-time or 2/3-time welds. Although the average ratio was close to even at 1.1, the standard deviation increased to 0.26.

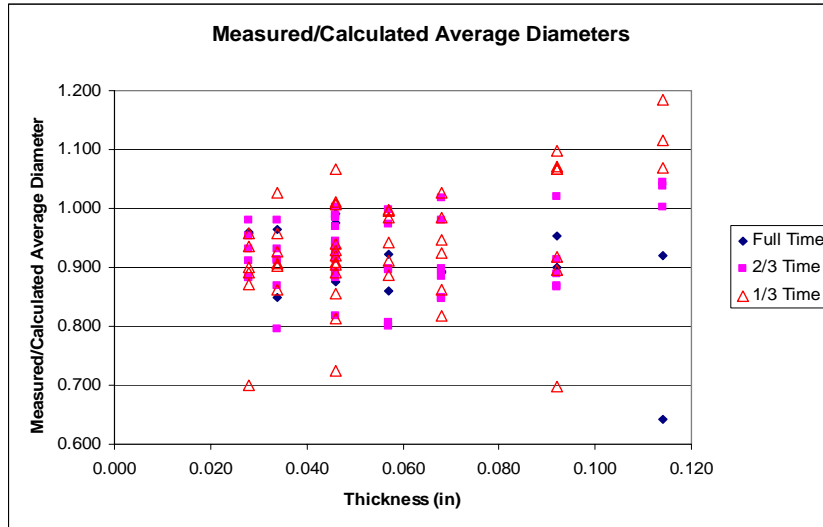


Figure 3-4: Measured/Calculated Average Diameters

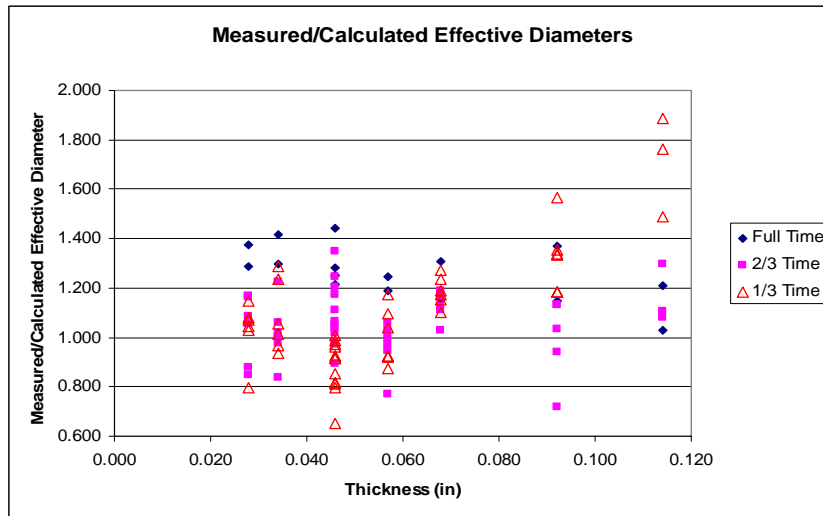


Figure 3-5: Measured/Calculated Effective Diameters

### 3.4 Weld Shear Strength Results

Along with impacting arc spot weld dimensions, arc time also had a significant influence on weld shear strength. As Figures 3-6 through 3-9 indicate, full-time welds were consistently stronger than both 2/3-time and 1/3-time welds, regardless of the thickness of the sheet steel or the nominal weld size. Overall, full-time welds were an average of 11 percent stronger than 2/3-time welds and 44 percent stronger than 1/3-time welds.

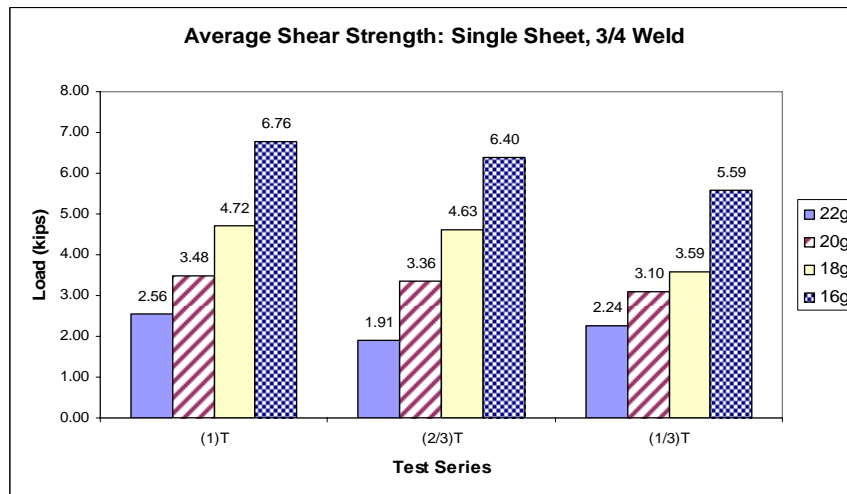


Figure 3-6: Average Shear Strength of 3/4 in. Welds in Single Sheets

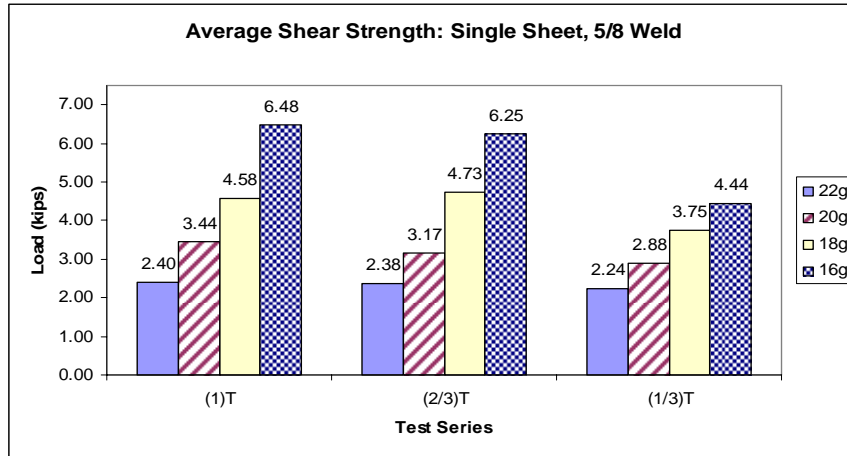


Figure 3-7: Average Shear Strength of 5/8 in. Welds in Single Sheets

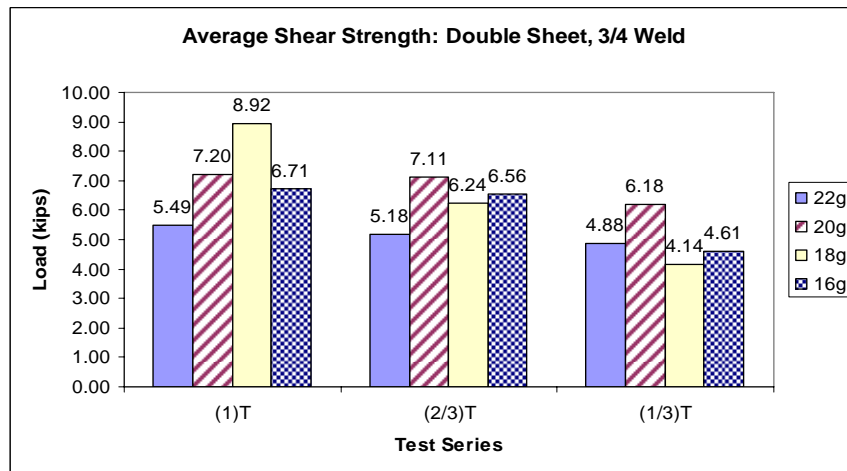
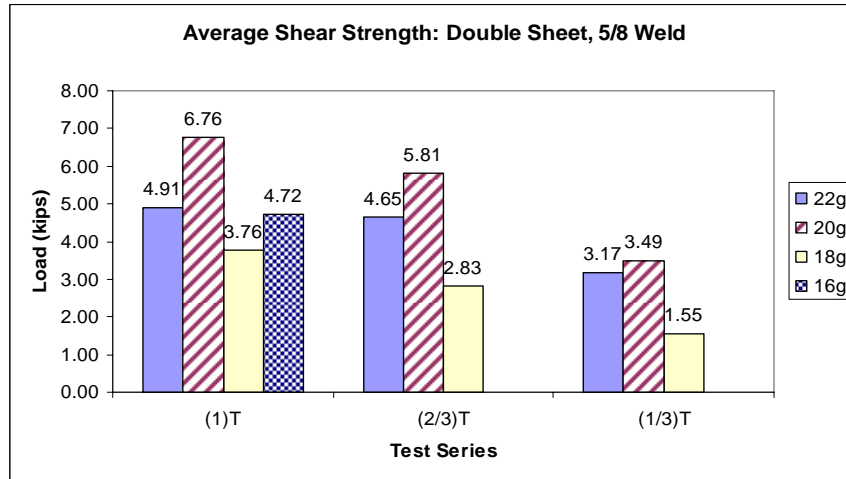


Figure 3-8: Average Shear Strength of 3/4 in. Welds in Double Sheets



*Figure 3-9: Average Shear Strength of 5/8 in. Welds in Double Sheets*

### 3.5 Weld Shear Strength Comparisons with the 2001 AISI Specification

Although considerable shear strength differences were observed between full-time, 2/3-time and 1/3-time welds, each difference was proportional to the overall weld size. Full-time welds were the strongest because they were consistently larger in diameter than either the 2/3-time or 1/3-time welds. This reduced strength was sufficiently predicted by the equations given in section E2.2.1 of the 2001 AISI Specification, provided that the measured visual diameter of the reduced-time welds was used in the equations. Conversely, if the nominal visual diameter were to be used, the equations would have over estimated the shear strength of each reduced-time arc spot weld. For full-time welds, the average ratio of measured to calculated shear strength was 1.31 with a standard deviation of 0.26. The 2/3-time welds had an average ratio and a standard deviation of 1.25 and 0.26, respectively, and 1/3-time welds had an average ratio of 1.39 and a standard deviation of 1.56.

## 4. Conclusions

### 4.1 Weld Arc Time

- The three variables having the greatest influence on weld arc time were sheet steel thickness, current setting and weld size. A greater thickness of sheet steel requires more arc time than a thinner sheet for a given current setting and weld size. Higher current settings form larger welds

in a smaller amount of time. And smaller weld sizes generally take less time to form than larger weld sizes.

- Tests show that the time required to form full-time arc spot welds varies little with respect to the sheet steel thickness. This near constant behavior can be attributed to higher currents being used in thicker steel sheets. Because thicker sheets increase required arc time and higher current settings decrease it, the two essentially offset each other, leaving weld size as the only variable to have an affect on the required arc time.
- Tests indicate that the average time required to form a 3/4 in. weld is 12.8 seconds and that the average time required to form a 5/8 in. weld is 8.1 seconds.

#### **4.2 Weld Size and Penetration**

- Arc time has a significant impact on the overall size of a given weld. When the current setting and the electrode type are held constant, a reduction in arc time will always result in a smaller weld being formed, often far less than the intended nominal size. Measured visual diameters were an average of 7 percent smaller in 2/3-time welds and 21 percent smaller in 1/3-time welds than those seen in full-time welds.
- Specimen sectioning indicated that penetration is not directly affected by weld arc time. If the current setting is properly set for the amount of sheet steel being attached, proper penetration can be achieved.
- Every quadruple-layer specimen had unsatisfactory penetration into the supporting hot rolled steel. The sum thicknesses of the sheet steel together with the added layers of air and galvanized coatings all drew too much current away from the electrode to adequately fuse with the hot rolled steel.

#### **4.3 Comparisons between Measured Dimensions and the 2001 AISI Specification**

- Although reducing the weld arc time significantly reduces the overall weld size, it has very little effect on the basic weld shape. Both 2/3-time and 1/3-time welds have approximately the same visual diameter to average diameter and visual diameter to effective diameter ratios as

those observed in full-time welds. Using the measured visual diameter, comparisons were made between the measured average and effective diameters and those calculated using the 2001 AISI specification. The comparisons prove that the specification adequately estimates average and effective weld diameters regardless of arc time, given a known visual diameter.

#### **4.4 Weld Shear Strength**

- Arc time had a significant impact on weld strength. Full-time welds were an average of 11 percent stronger than 2/3-time welds and 44 percent stronger than 1/3-time welds.
- Differences between the strength of full-time welds and reduced time welds increase as the sheet steel thickness is increased. This can be attributed to the slightly smaller effective diameter noticed in reduced time welds.

#### **4.5 Comparisons between Observed Shear Strength and the 2001 AISI Specification**

- The lower shear strength observed in reduced time welds is directly proportional to the decreased size of the welds. Using the measured visual diameter and not the nominal diameter, the 2001 AISI specification satisfactorily estimates the strength of full-time welds, 2/3-time welds, and 1/3-time welds.

### **5. Recommendations**

#### **5.1 Requirements for Weld Arc Time**

This research has proven that arc time has a tremendous influence on arc spot weld shear strength. It is therefore imperative that measures be taken to insure welds formed in the field are completed using the proper arc time.

Currently, welders must be certified at the beginning of each project they undertake that involves deck welding. The welder must form the weld using the same exact electrode and current setting that he/she will be using on the remainder of the project. This weld is then inspected by an AWS certified professional who deems the quality of the weld to be sufficient or insufficient. Provided the weld is sufficient, the welder is allowed to proceed with welding arc spot welds for the project. The chief recommendation concerning the certification process is that it be modified to include arc time. This would give

the welder three items to hold constant; the electrode, the current setting and the arc time (within a certain tolerance). Holding these three items constant would ensure that welds consistent in quality with the initially inspected weld are formed throughout the project.

### **5.2 Welds formed in Quadruple-Layered Sheet Steel**

The 2001 AISI Specification states that arc spot welds should not be formed in sheet steel totaling more than 0.15 in. in thickness. This research suggests that while single and double layered sheets may be satisfactorily welded up to 0.15 in. in thickness, quadruple layers can not be. Insufficient penetration was observed from welds made in quadruple layer sheets as thin as 0.112 in. (4-layers of 22 gauge). The additional layers of air and surface coatings draw too much heat from the electrode, preventing it from fusing with the supporting hot rolled steel. Due to lack of penetration, it is recommended that arc spot welding not be attempted in situations involving four or more layers of sheet steel.

## **6. References**

1. American Iron and Steel Institute, AISI (2001). "North American Specification for the Design of Cold-Formed Steel Structural Members," 2001 Edition, With 2004 Supplement, Washington D.C.
2. Blodgett, O.W. (1978). "Report on Proposed Standards for Sheet Steel Structural Welding," Proceedings, Fourth International Specialty conference on Cold formed Steel Structures, University of Missouri – Rolla.
3. Luttrell, L.D. (2004). "Diaphragm Design Manual." Third Edition. Steel Deck Institute. Fox River Grove, IL.
4. Pekoz, T. and McGuire, W. (1980). "Welding of Sheet Steel," Proceedings, Fifth International Specialty Conference on Cold-Formed Steel Structures, St. Louis, Missouri.
5. Yu, Wei-Wen (2000). Cold-Formed Steel Design. Third Edition. New York, New York: John Wiley and Sons, Inc.





## **Cold-Formed Steel Bolted Connections without Washers on Oversized Holes: Shear and Bearing Failures in Sheets**

Cheng Yu<sup>1</sup>, Ibraheem Sheerah<sup>2</sup>

### **Abstract**

In cold-formed steel (CFS) construction, the bolted connections without washers on oversized holes may expedite the building process and lower the cost, at the same time provides satisfied strength. The current design specifications do not stipulate provisions for such connections, and washers are required to be installed on oversized holes. In order to investigate the behavior and determine the strength of CFS bolted connections without washers on oversized holes, a test program was developed and conducted at University of North Texas. This research was focused on the shear failure and the bearing failure of the connected sheets. No washer was used for the test specimens. The studied parameters included the steel sheet thickness: from 118 mil to 33 mil; the connection type: single shear and double shear; the number of bolts: one and two; the bolt type: ASTM A307, A325; the bolt diameter: 1/4 in. and 1/2 in.; and the ductility in the sheet steel: low and high. Based on the test results, new design method for bearing strength was proposed. The paper presents the test program, test specimens, and the proposed design for CFS bolted connections without washers on oversized holes.

---

<sup>1</sup> Assistant Professor, University of North Texas, Denton, TX (cyu@unt.edu)

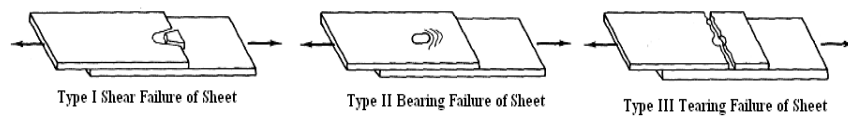
<sup>2</sup> Graduate Student, University of North Texas, Denton, TX  
(isheerah@gmail.com)

## Introduction

The cold-formed steel becomes an important alternative construction material for low-rise residential and commercial buildings. Light weight, high durability, high strength, and high material consistency are some of the reasons given for the increasing applications cold-formed steel structures in construction. The bolted connection is one important method of joining cold-formed steel members, and the subject has been studied by a number of researchers in the past [Gilchrist & Chong (1979), Yu (1982), Zadanfarrokh & Bryan (1992), LaBoube & Yu (1995), Wallace & Schuster (2002)]. However, the bolted connections using oversized holes and short slots without washers have not been fully studied yet. And the current North American Specification for the Design of Cold-Formed Steel Structures (NAS 2007) requires washers to be installed on oversized holes or short slots. The configurations of combining oversized holes or short slots and non-washers may significantly expedite the construction process and lower the cost. Therefore a research project funded by the American Iron and Steel Institute (AISI) was developed to investigate the bolted CFS connections with oversized holes and short slots without using washers. The research is still currently undergoing at the University of North Texas as of May 2008. This paper focuses on the completed tests on bolted connections with oversized holes. Bearing failure and shear failure in the sheets are of interest in this paper.

## Background

The cold-formed steel bolted connections usually fail in three modes: shear of the sheet, bearing or piling up of material in front of the bolt, and tearing of the sheet in the net section, as shown in Figure 1.



**Figure 1 Typical failures of bolted connections**

Experiments on bolted connections without washers for standard holes were conducted by a number of researchers [Yu 1982, Zadanfarrokh & Bryan 1992, LaBoube & Yu 1995, Wallace & Schuster 2002]. It was found that the shear strength of the sheet, type (I) failure, depends on the thinnest sheet thickness ( $t$ ), the tensile strength of connected sheet ( $F_u$ ), and the distance from the center of hole to the nearest edge of adjacent hole or to the end of the connected sheet

parallel to the direction of applied force (e). The nominal shear strength per bolt ( $P_n$ ) can be expressed as Equation 1 (Eq. E3.1-1 in NAS 2007).

$$P_n = t e F_u \quad (1)$$

It was also found that the Type (I) failure is likely to occur when the connections have small e/d ratios ( $e/d < 2.5$ ), where (d) is the bolt diameter. NAS (2007) Eq E3.1-1 implies that the influence of the presence of washers to the strength of Type (I) failure can be ignored in design.

When the edge distance in the bolted connections is considerably large ( $e/d > 2.5$ ), the bearing failure may occur. The previously conducted tests indicate that the bearing strength primarily depends on the tensile strength of sheet, the thickness of thinnest connected sheet, the ratio of bolt diameter to the sheet thickness (d/t) and the type of bearing connection (single or double shear, with or without washers, etc) [Yu 1982, Zadanfarrokh & Bryan 1992, LaBoube & Yu 1995, Wallace & Schuster 2002]. The presence of washers has significant impact on the bearing strength. The NAS (2007) takes into account the use of washers by using a modification factor ( $m_f$ ) (Table E3.3.1-2 in NAS) in the equation. The nominal bearing strength, therefore, is expressed as Equation 2 (Eq. E3.3.1-1 in NAS 2007).

$$P_n = m_f C d t F_u \quad (2)$$

Where: C = bearing factor (refers to Table 1)

d = nominal bolt diameter

t = uncoated sheet thickness

$F_u$  = tensile strength of sheet

$m_f$  = modification factor (0.75 for single shear and 1.33 for double shear)

One should note that the bearing equation in NAS (2007) is only applicable to the connections with standard holes.

**Table 1 Bearing factor, C, for bolted connections**

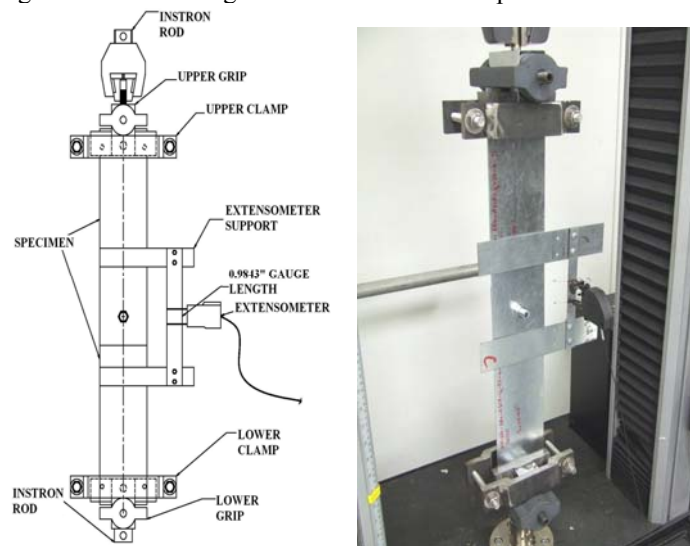
Ratio of fastener diameter to member thickness, d/t	C
$d/t < 10$	3
$10 \leq d/t \leq 22$	$4 - 0.1(d/t)$
$d/t > 22$	1.8

The main objective of the research presented here were to experimentally investigate the bearing strength and shear strength of cold-formed steel bolted

connections without washers on oversized holes; and to examine the validity of current NAS (2007) equations applied to those connection configurations.

### Test Setup

The tensile tests were conducted in a 20 kip universal testing machine. The deformation of the bolted connection was measured by an extensometer with a gauge length of 0.9843 in. Figure 2 shows the test setup.



**Figure 2 Setup for testing bolted connections**

The tensile tests were performed in a displacement control mode. The bottom grip was fixed to the base of the machine. The top grip, connected to the crosshead of the machine, moved upwards at a constant speed of 0.1 in. per minute. The applied force, the displacement of the top grip, and the deformation of the connection were measured and recorded simultaneously. All bolts were installed and tightened manually. A torque wrench was used to assure the applied torque not to exceed 40 lb-in.

### Test Specimen

#### *Specimen Configurations*

The studied the specimen configuration parameters are as follows:

- Cold-formed steel sheet thicknesses ranged from 30 mil to 118 mil.
- Single shear and double shear connections with one bolt or two bolts.

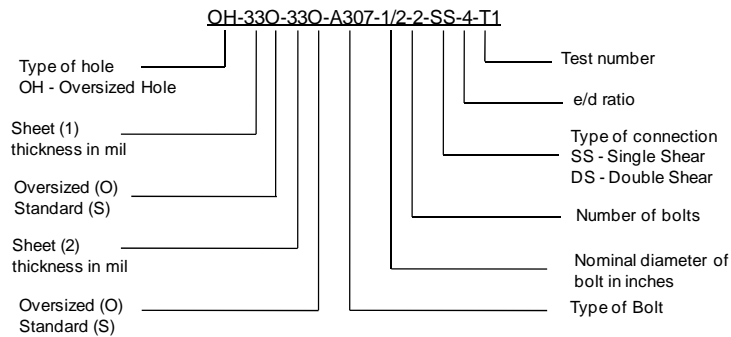
- ASTM A307 Type A bolts (0.5 in. diameter, 1.25 in. long and 0.25 in. diameter, 1 in. long) and A325 bolts (0.5 in. diameter, 1.25 in. long) were used. Washer was not installed.
- The dimensions of oversize holes refer to the maximum sizes specified in Table E3a of NAS (2007), and listed in Table 2. All the holes in the CFS sheets were punched.

**Table 2 Dimensions of oversized holes**

Nominal bolt diameter, d (in.)	Oversized hole diameter, $d_h$ (in.)
$< 1/2$	$d + 1/16$
$\geq 1/2$	$d + 1/8$

- Steel ductility in the sheets: high ductile and low ductile steel.
- For each specimen configuration, two identical tests were conducted. If the difference of the first two tests was greater than 10%, a third test was performed.

The specimens were labeled as the following.



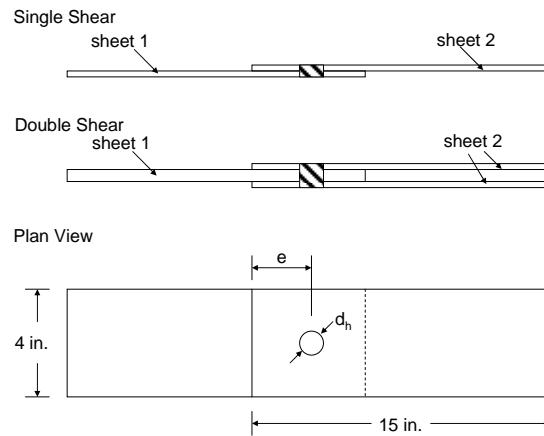
**Figure 3 Specimen labeling**

### **Sheet Dimensions**

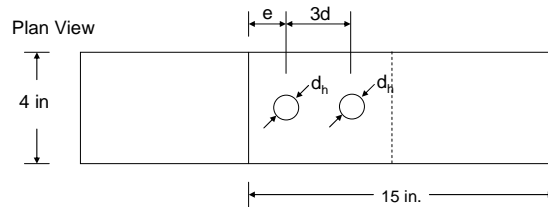
The dimensions of specimens and test matrices were designed to ensure the occurrence of the desired failure modes: Type I and II failures. The width of the connected sheets had to be sufficiently large to prevent net section fracture failure (Type III failure) from occurring. Zadanfarrokh and Bryan (1992) recommended the width of the connected sheet  $w = 6.25 d$  for bearing tests with the nominal bolt diameter  $d \geq 0.4$  in. Therefore the width of the sheets in all the tests was set to 4 in.

It was found that a small ratio of  $e/d$  would lead to shear failure in the sheet. On the other hand, a sufficiently large  $e/d$  ratio would trigger bearing failure in the sheet. Research done by Chong and Matlock (1975), Gilchrist and Chong (1979), and Yu (1982) indicated that an  $e/d = 2.5$  is approximately the transition point to distinguish between the Type I and II failures. Furthermore, the NAS (2007) requires a minimum  $e/d = 1.5$  for cold-formed steel bolted connections. Therefore in this research, the specimens for shear strength tests had  $e/d = 1.5$ , the specimens for bearing strength test had  $e/d > 3$ . The majority of bearing failure tests had  $e/d = 4$ . The overall length of all specimens was 15 in., the setup was based on the recommended by Zadanfarrokh and Bryan (1992).

The sheet dimensions for the tests are shown in Figure 4 for one-bolt connections and in Figure 5 for two bolt connections. for the two-bolt connections, the distance between centers of the bolt holes equals to three times of the nominal bolt diameter,  $d$ , which conforms to the spacing requirement in Section E3.1 of the NAS (2007).



**Figure 4 Dimensions of specimens with one bolt**



**Figure 5 Dimensions of specimens with two bolts**

### Material Properties

Coupon tests were carried out to obtain the material properties of the connected sheets following ASTM A370 Specification (ASTM 2007). The coat on the cold-formed steel sheets was removed prior to the coupon tests. For each material thickness from the same coil, three coupons were cut and tested, and the average values were used in the analysis, and reported in Table 3.

**Table 3 Materials properties**

Sheet Materials	Measured Thickness (in.)	Experimental $F_y$ (nominal) (ksi)	Experimental $F_u$ (ksi)	$F_u/F_y$	Elongation 2-in. gage length	Ductility
33 mil	0.0361	44.6 (33 ksi)	54.1	1.21	30%	High
43 mil	0.0439	51.6 (50 ksi)	70.3	1.36	20%	High
68 mil	0.0691	50.0 (50 ksi)	69.7	1.39	25%	High
118 mil	0.1305	45.3 (33 ksi)	52.2	1.15	25%	High
39 mil (1.00 mm)	0.0390	90.0	90.7	1.01	4%	Low
30 mil (0.75 mm)	0.0293	86.0	87.2	1.01	7.5%	Low

The high ductile steels used in this research (33 mil, 43 mil, 68 mil, 188 mil) met the minimum requirements for material ductility specified by NAS (2007). The current NAS requires that the ratio of tensile strength to yield stress shall not be less than 1.08, and the total elongation shall not be less than 10% measured over a two-inch gage length. The low ductile steels used in this research (30 mil, 39 mil) did not meet those minimum requirements.

### Test Results and Discussions

#### Shear Strength of Connected Sheet

Figure 6 and 7 respectively show the typical failure mode observed in shear strength tests on single shear and double shear bolted connections. In those shear strength tests, the holes were punched close to the edge of the connected sheets ( $e/d = 1.5$ ). It was founded that the bolt was tilted significantly in the single shear tests due to the eccentric loading and the oversized hole dimension. As a result, the sheet warped and piled up at the hole edge. A combined failure mode of shear and bearing were achieved in the single shear tests with  $e/d = 1.5$ . For the double shear tests, typical shear failure was observed on the inside sheet, as shown in Figure 7. The bolt was not tilted and it remained perpendicular to the sheets in the tests.

The results of the shear strength tests are summarized in Table 4 where  $P_{test}$  is the peak load,  $P_{NAS}$  is nominal strength calculated by Equation 1, and “ $\Delta$ ” is the



connection deformation (measured by extensometer) at the peak load. Figure 8 illustrates a comparison of the tested shear strengths with the NAS (2007) predictions (Eq. 1). The plot indicates that the current NAS provisions for bolted connections without washer on standard holes have a good agreement with the test results on bolted connections without washer on oversized holes. The average ratio of  $P_{test}$  to  $P_{NAS}$  for all tests is 1.03 with a standard deviation of 0.19. Therefore the current design method can be extended to the bolted connections without washers on oversized holes as specified in Table 2.

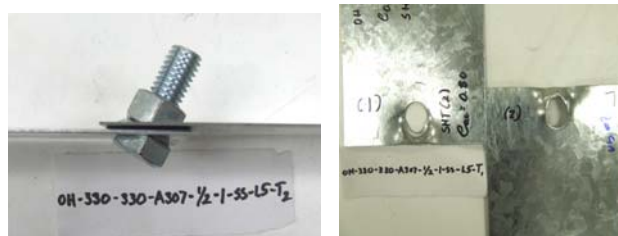


Figure 6 Failure mode of single shear connection OH-330-330-A307-1/2-1-SS-1.5-T2



Figure 7 Failure mode of double shear connection OH-330-330-A307-1/2-1-DS-1.5-T1

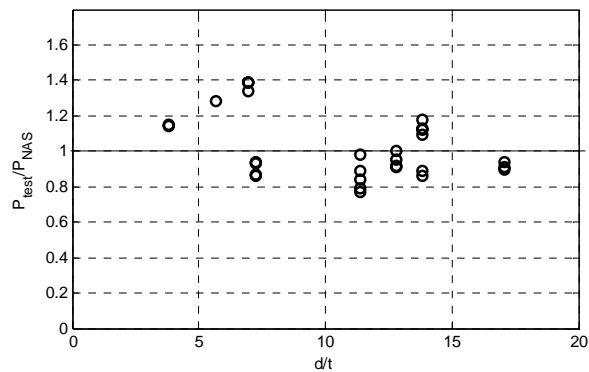


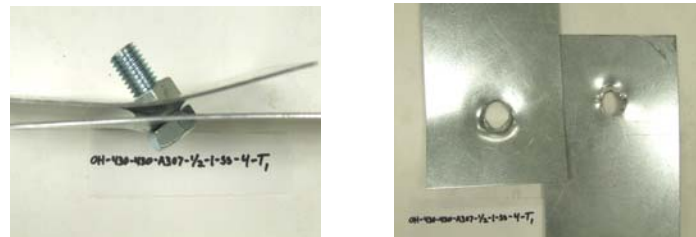
Figure 8  $P_{test}/P_{NAS}$  vs  $d/t$  plot for shear strength tests

**Table 4 Results for shear strength tests**

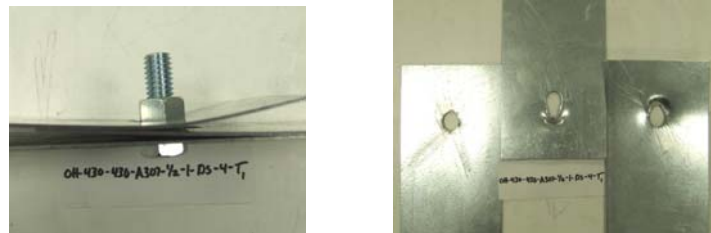
No	Specimen Label	P <sub>test</sub> (lbf)	Δ (in.)	d/t	P <sub>test</sub> / P <sub>NAS</sub>
1	OH-1180-1180-A307-1/2-1-SS-1.5-T1	5804	0.521	3.83	1.14
2	OH-1180-1180-A307-1/2-1-SS-1.5-T2	5885	0.588	3.83	1.15
3	OH-680-680-A325-1/2-1-SS-1.5-T1	3404	0.692	7.24	0.94
4	OH-680-680-A325-1/2-1-SS-1.5-T2	3363	0.680	7.24	0.93
5	OH-680-680-A307-1/2-1-SS-1.5-T1	3134	0.445	7.24	0.87
6	OH-680-680-A307-1/2-1-SS-1.5-T2	3112	0.410	7.24	0.86
7	OH-430-430-A307-1/2-1-SS-1.5-T1	2056	0.342	11.39	0.89
8	OH-430-430-A307-1/2-1-SS-1.5-T2	1951	0.171	11.39	0.84
9	OH-430-430-A307-1/4-1-SS-1.5-T1	1483	0.347	5.69	1.28
10	OH-430-430-A307-1/4-1-SS-1.5-T2	1482	0.319	5.69	1.28
11	OH-330-330-A307-1/2-1-SS-1.5-T1	1259	0.440	13.85	0.86
12	OH-330-330-A307-1/2-1-SS-1.5-T2	1303	0.400	13.85	0.89
13	OH-330-330-A307-1/4-1-SS-1.5-T1	985	0.253	6.93	1.34
14	OH-330-330-A307-1/4-1-SS-1.5-T2	1017	0.279	6.93	1.39
15	OH-330-33S-A307-1/2-1-SS-1.5-T1	1723	0.483	13.85	1.18
16	OH-330-33S-A307-1/2-1-SS-1.5-T2	1603	0.529	13.85	1.09
17	OH-300-300-A307-1/2-1-SS-1.5-T1	1727	0.197	17.06	0.90
18	OH-300-300-A307-1/2-1-SS-1.5-T2	1720	0.231	17.06	0.90
19	OH-390-390-A307-1/2-1-SS-1.5-T2	2645	0.435	12.82	1.00
20	OH-390-390-A307-1/2-1-SS-1.5-T3	2429	0.445	12.82	0.92
21	OH-430-430-A307-1/2-1-DS-1.5-T1	2266	0.218	11.39	0.98
22	OH-430-430-A307-1/2-1-DS-1.5-T2	1832	0.248	11.39	0.79
23	OH-430-430-A307-1/2-1-DS-1.5-T3	1789	0.239	11.39	0.77
24	OH-330-330-A307-1/2-1-DS-1.5-T1	1659	0.388	13.85	1.13
25	OH-330-330-A307-1/2-1-DS-1.5-T2	1637	0.447	13.85	1.12
26	OH-330-330-A307-1/4-1-DS-1.5-T1	1022	0.386	6.93	1.39
27	OH-330-330-A307-1/4-1-DS-1.5-T2	1017	0.341	6.93	1.39
28	OH-300-300-A307-1/2-1-DS-1.5-T1	1735	0.265	17.06	0.91
29	OH-300-300-A307-1/2-1-DS-1.5-T2	1810	0.325	17.06	0.94
30	OH-390-390-A307-1/2-1-DS-1.5-T1	2518	0.324	12.82	0.95
31	OH-390-390-A307-1/2-1-DS-1.5-T3	2421	0.410	12.82	0.91
Average					1.03
St. dev.					0.19

### **Bearing Strength**

Figures 9 and 10 respectively show the observed failure mode in the bearing strength tests on single shear connections and double shear connections with one bolt. Similar to the findings in the shear strength tests, the bolt in the single shear connections was tilted to a large degree. The connected sheets curled outwards as shown in Figure 9. For quite a few cases, the oversized hole was enlarged large enough during the tests to allow the tilted bolt head to go through the sheet. For the double shear connections, the bolt remained perpendicular to the loading direction during the test, and less curling deformation in the sheets was observed compared to the single shear connections.



**Figure 9 Failure mode of single shear connection OH-430-430-A307-1/2-1-SS-4-T1**



**Figure 10 Failure mode of double shear connection OH-430-430-A307-1/2-1-DS-4-T1**

Figures 11 and 12 show the failure mode for bearing strength tests on connections with two bolts. The same failure mode as that of single bolt connections was observed in the two-bolt connections. The bolts tilted in the single shear connections and remained straight in double shear connections.

The test results for the bearing strength are summarized in Tables 5 for the single shear connections and Table 6 for the double shear connections. In Tables 5 and 6,  $P_{\text{test}}$  is the tested peak load per bolt and “ $\Delta$ ” is the connection deformation at the peak load.  $P_{\text{NAS}}$  is the NAS (2007) predicted nominal strength of bolted connections with standard holes without washers. The test results

indicate that for both the single shear and double shear connections, the NAS (2007) equations for standard hole connections yield unconservative predictions for the tests on oversized hole connections. The average test-to-predicted ratio for single shear connections is 0.87, and 0.76 for double shear connections.

Based on the test results for the bearing strength, new bearing factor  $C$  and modification factor,  $m_f$ , were proposed for the oversized hole connections. The bearing strength equation (Eq. 2) will be kept unchanged. Table 7 and Table 8 respectively summarize the newly proposed factors. Figures 13 and 14 show the comparison between the test results and the two design methods for the single shear and double shear connections respectively. In the figures, the y axis is the  $P/(F_u d t)$  where  $P$  represents the nominal bearing strength for the design methods and it also stands for the peak load per bolt for the tests. Figures 13 and 14 show that the proposed design method has a good agreement with the test results for both single shear and double shear bearing connections. The average test-to-predicted ratio for the proposed method is 1.02 for single shear connections and 1.01 for double shear connections. A standard deviation of 0.13 is achieved for both types of connections.

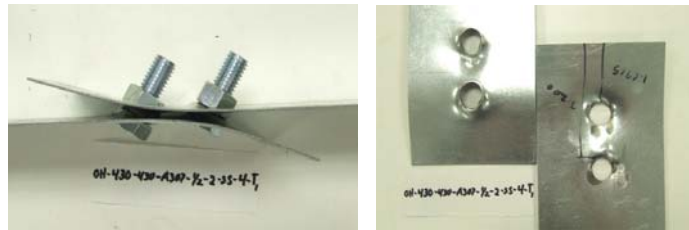


Figure 11 Failure mode of single shear connection OH-430-430-A307-1/2-2-SS-4-T1



Figure 12 Failure mode of double shear connection OH-300-300-A307-1/2-1-DS-4-T1

Table 5 Results of bearing strength tests on single shear connections

No	Specimen Label	d/t	P <sub>test</sub> (lbf)	Δ (in.)	P <sub>test</sub> / P <sub>NAS</sub>	P <sub>test</sub> / P <sub>NEW</sub>
1	OH-1180-1180-A307-1/2-1-SS-4-	3.83	8499	0.360	1.11	1.15
2	OH-1180-1180-A307-1/2-1-SS-4-	3.83	8408	0.420	1.10	1.14
3	OH-680-680-A325-1/2-1-SS-4-T1	7.24	4685	0.682	0.86	0.92
4	OH-680-680-A325-1/2-1-SS-4-T2	7.24	4945	0.691	0.91	0.97
5	OH-680-680-A307-1/2-1-SS-4-T1	7.24	3970	0.452	0.73	0.78
6	OH-680-680-A307-1/2-1-SS-4-T2	7.24	3925	0.547	0.72	0.77
7	OH-430-430-A307-1/2-1-SS-4-T1	11.39	1904	0.206	0.58	0.77
8	OH-430-430-A307-1/2-1-SS-4-T2	11.39	1929	0.237	0.58	0.78
9	OH-430-430-A307-1/2-1-SS-4-T3	11.39	1885	0.200	0.57	0.76
10	OH-430-430-A307-1/4-1-SS-4-T1	5.69	1835	0.244	1.06	1.10
11	OH-430-430-A307-1/4-1-SS-4-T2	5.69	1894	0.275	1.09	1.14
12	OH-430-430-A307-1/4-1-SS-8-T1	5.69	1825	0.244	1.05	1.10
13	OH-430-430-A307-1/4-1-SS-8-T2	5.69	1725	0.276	0.99	1.04
14	OH-430-430-A307-1/4-1-SS-3-T1	5.69	1790	0.347	1.03	1.07
15	OH-430-430-A307-1/4-1-SS-3-T2	5.69	1823	0.319	1.05	1.09
16	OH-330-330-A307-1/2-1-SS-4-T1	13.85	1451	0.352	0.76	1.03
17	OH-330-330-A307-1/2-1-SS-4-T2	13.85	1444	0.566	0.75	1.02
18	OH-330-330-A307-1/4-1-SS-4-T1	6.93	1165	0.285	1.06	1.10
19	OH-330-330-A307-1/4-1-SS-4-T2	6.93	1213	0.281	1.10	1.15
20	OH-330-330-A307-1/4-1-SS-8-T1	6.93	1145	0.355	1.04	1.09
21	OH-330-330-A307-1/4-1-SS-8-T2	6.93	1232	0.397	1.12	1.17
22	OH-330-330-A307-1/4-1-SS-3-T1	6.93	1129	0.382	1.03	1.07
23	OH-330-330-A307-1/4-1-SS-3-T2	6.93	1136	0.321	1.03	1.08
24	OH-430-330-A307-1/2-1-SS-4-T1	13.85	1672	0.421	0.87	1.18
25	OH-430-330-A307-1/2-1-SS-4-T2	13.85	1635	0.424	0.85	1.16
26	OH-330-330-A307-1/2-1-SS-4-T1	13.85	1540	0.374	0.80	1.09
27	OH-330-330-A307-1/2-1-SS-4-T3	13.85	1548	0.304	0.81	1.09
28	OH-300-300-A307-1/2-1-SS-4-T1	17.06	1620	0.319	0.74	0.97
29	OH-300-300-A307-1/2-1-SS-4-T2	17.06	1584	0.184	0.72	0.95
30	OH-390-390-A307-1/2-1-SS-4-T1	12.82	2423	0.373	0.67	0.91
31	OH-390-390-A307-1/2-1-SS-4-T2	12.82	2591	0.357	0.72	0.97
32	OH-430-430-A307-1/2-2-SS-4-T1	11.38	2100.5	0.333	0.63	0.85
33	OH-430-430-A307-1/2-2-SS-4-T2	11.38	2153	0.380	0.65	0.87
34	OH-330-330-A307-1/2-2-SS-4-T1	13.85	1306	0.400	0.68	0.92
35	OH-330-330-A307-1/2-2-SS-4-T2	13.85	1309	0.408	0.68	0.93
36	OH-330-330-A307-1/4-2-SS-4-T2	6.93	1105.5	0.263	1.01	1.05
37	OH-330-330-A307-1/4-2-SS-4-T3	6.93	1093	0.275	0.99	1.04
38	OH-330-330-A307-1/4-2-SS-8-T1	6.93	1149	0.329	1.05	1.09
39	OH-330-330-A307-1/4-2-SS-8-T2	6.93	1130.5	0.271	1.03	1.07
40	OH-330-330-A307-1/4-2-SS-3-T1	6.93	1169.5	0.381	1.06	1.11
41	OH-330-330-A307-1/4-2-SS-3-T2	6.93	1155	0.362	1.05	1.09
42	OH-430-330-A307-1/2-2-SS-4-T1	13.85	1752	0.311	0.91	1.24
43	OH-430-330-A307-1/2-2-SS-4-T2	13.85	1691.5	0.267	0.88	1.20
44	OH-300-300-A307-1/2-2-SS-4-T1	17.06	1701	0.303	0.77	1.02
45	OH-300-300-A307-1/2-2-SS-4-T2	17.06	1632.5	0.442	0.74	0.98
46	OH-390-390-A307-1/2-2-SS-4-T1	12.82	2232	0.255	0.62	0.84
47	OH-390-390-A307-1/2-2-SS-4-T2	12.82	2249.5	0.409	0.62	0.84
Average					0.87	1.02
St. dev.					0.18	0.13

**Table 6 Results of bearing strength tests on double shear connections**

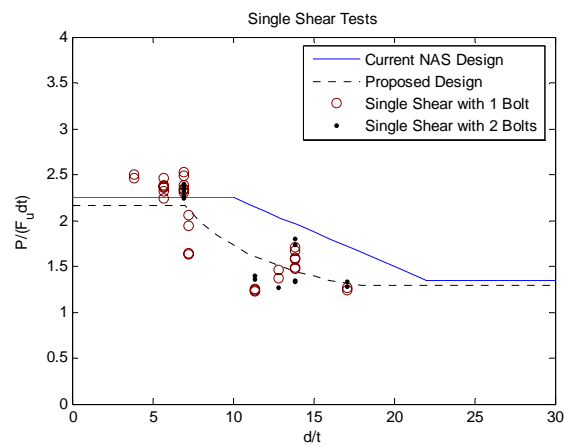
No	Specimen Label	d/t	P <sub>test</sub> (lbf)	Δ (in.)	P <sub>test</sub> / P <sub>NAS</sub>	P <sub>test</sub> / P <sub>NEW</sub>
1	OH-680-680-A325-1/2-1-DS-4-T1	7.24	6824	0.664	0.71	0.86
2	OH-680-680-A325-1/2-1-DS-4-T2	7.24	6779	0.681	0.71	0.86
3	OH-430-430-A307-1/2-1-DS-4-T2	11.39	3933	0.471	0.67	1.02
4	OH-430-430-A307-1/2-1-DS-4-T3	11.39	3677	0.595	0.63	0.95
5	OH-330-330-A307-1/2-1-DS-4-T3	13.85	2637	0.606	0.78	1.20
6	OH-330-330-A307-1/2-1-DS-4-T4	13.85	2798	0.549	0.82	1.27
7	OH-330-330-A307-1/4-1-DS-4-T1	6.93	1888	0.345	0.97	1.15
8	OH-330-330-A307-1/4-1-DS-4-T2	6.93	1997	0.428	1.02	1.22
9	OH-330-330-A307-1/4-1-DS-8-T1	6.93	1912	0.396	0.98	1.16
10	OH-330-330-A307-1/4-1-DS-8-T2	6.93	1906	0.427	0.98	1.16
11	OH-330-330-A307-1/4-1-DS-3-T1	6.93	1768	0.409	0.91	1.08
12	OH-330-330-A307-1/4-1-DS-3-T2	6.93	1618	0.346	0.83	0.99
13	OH-300-300-A307-1/2-1-DS-4-T2	17.06	2720	0.380	0.70	1.04
14	OH-300-300-A307-1/2-1-DS-4-T3	17.06	2548	0.466	0.65	0.98
15	OH-390-390-A307-1/2-1-DS-4-T1	12.82	3270	0.559	0.51	0.79
16	OH-390-390-A307-1/2-1-DS-4-T2	12.82	3335	0.675	0.52	0.81
17	OH-430-430-A307-1/2-2-DS-4-T1	11.38	3697	0.380	0.63	0.96
18	OH-430-430-A307-1/2-2-DS-4-T3	11.38	3595	0.351	0.61	0.93
19	OH-330-330-A307-1/2-2-DS-4-T1	13.85	2216	0.480	0.65	1.01
20	OH-330-330-A307-1/2-2-DS-4-T2	13.85	2004	0.464	0.59	0.91
21	OH-330-330-A307-1/4-2-DS-4-T1	6.93	1807	0.219	0.93	1.10
22	OH-330-330-A307-1/4-2-DS-4-T2	6.93	1994	0.343	1.02	1.21
23	OH-330-330-A307-1/4-2-DS-4-T3	6.93	1729	0.200	0.89	1.05
24	OH-330-330-A307-1/4-2-DS-4-T4	6.93	1675	0.366	0.86	1.02
25	OH-330-330-A307-1/4-2-DS-4-T5	6.93	1704	0.351	0.87	1.04
26	OH-330-330-A307-1/4-2-DS-8-T1	6.93	1740	0.587	0.89	1.06
27	OH-330-330-A307-1/4-2-DS-8-T2	6.93	1624	0.456	0.83	0.99
28	OH-330-330-A307-1/4-2-DS-3-T1	6.93	1594	0.474	0.82	0.97
29	OH-330-330-A307-1/4-2-DS-3-T3	6.93	1536	0.197	0.79	0.94
30	OH-330-330-A307-1/4-2-DS-3-T2	6.93	1770	0.480	0.91	1.08
31	OH-300-300-A307-1/2-2-DS-4-T1	17.06	2552	0.450	0.66	0.98
32	OH-300-300-A307-1/2-2-DS-4-T2	17.06	2681	0.287	0.69	1.03
33	OH-390-390-A307-1/2-2-DS-4-T1	12.82	3541	0.620	0.55	0.85
34	OH-390-390-A307-1/2-2-DS-4-T4	12.82	3422	0.515	0.54	0.83
35	OH-390-390-A307-1/2-2-DS-4-T2	12.82	4014	0.600	0.63	0.97
36	OH-390-390-A307-1/2-2-DS-4-T3	12.82	3116	0.483	0.49	0.75
Average					0.76	1.01
St. dev.					0.16	0.13

**Table 7 Proposed bearing factor, C, for bolted connections with oversized holes**

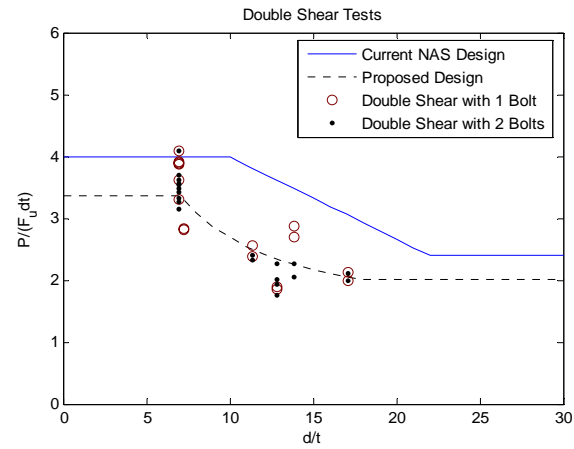
Ratio of fastener diameter to member thickness, d/t	C
$d/t < 7$	3
$7 \leq d/t \leq 18$	$1 + 14/(d/t)$
$d/t > 18$	1.8

**Table 8 Proposed modification factor,  $m_f$ , for bolted connections with oversized holes**

Type of bearing connection	$m_f$
Single shear connection without washers under both bolt head and nut on oversized hole	0.72
Inside sheet of double shear connection without washers on oversized hole	1.12



**Figure 13 Test results vs. design methods for single shear bearing connections**



**Figure 14 Test results vs. design methods for double shear bearing connections**

### **Conclusions and Continuing Research**

The tensile tests on cold-formed steel connections without washers on oversized holes were conducted to investigate both the shear strength and bearing strength. The results showed that current NAS (2007) design provisions for shear strength in connected sheets work well for the oversized hole connections. However for the bearing strength, the current design method yielded unconservative predictions. New bearing factor and modification factor were proposed herein to account for the loss in bearing strength by the oversized holes. The research is still underway to study the influence of the different bolt types and material ductility on the strength of the bolted connections without washers on oversized holes. Furthermore, the research will also investigate the behavior of bolted connections in short slots without washers.

### **Acknowledgment**

The funding provided by the AISI is gratefully acknowledged. The assistance and guidance provided by the AISI COS Oversized Hole Task Group is highly appreciated. The assistance of the UNT undergraduates George Trabazo, Stephen Mathai, and Szu-Chun Hung in preparing the test specimens has been invaluable.

### **References**

- Chong, K.P., Matlock, R. B. (1975). "Light-Gage Steel Bolted Connections without Washers," *Journal of the Structural Division, ASCE*, vol 101.
- Gilchrist, R.T., Chong, K. P. (1979). "Thin Light-Gage Bolted Connection without Washers," *Journal of the Structural Division, ASCE*, vol 105.
- LaBoube, R. A., Yu, W. W. (1995). "Tensile and Bearing Capacities of Bolted Connections," *Final Summary Report, Civil Engineering Study 95-6, Cold-Formed steel Series, Department of Civil Engineering, University of Missouri-Rolla.*
- LaBoube, R. A., Yu, W. W. (1996). "Additional Design Considerations for Bolted Connections," *Proceeding of the 13th International Specialty Conference on Cold-Formed Steel Structures, University of Missouri-Rolla.*
- NAS (2007). "North American Specification for the Design of Cold-Formed Steel Structural Members, 2007 Edition," *American Iron and Steel Institute, Washington, DC.*



Wallace, J. A., Schuster, R. M. (2002). "Testing of Bolted Cold-Formed Steel Connections in Bearing (With and Without Washers)," Proceedings of the 16th International Specialty Conference on Cold-Formed Steel Structures, Orlando, FL.

Yu, W. W. (1982). "AISI Design Criteria for Bolted Connections," Proceeding of the 6th International Specialty Conference on Cold-Formed Steel Structures, University of Missouri-Rolla.

Zadanfarrokh, F., Bryan, E. R. (1992) "Testing and Design of Bolted Connections in Cold Formed Steel Sections," Proceedings of Eleventh International Specialty Conference on Cold-Formed Steel Structures, St. Louis, Missouri.

S. Seleim & R. LaBoube. (1995). "Behavior of Low Ductility Steels in Cold-Formed Steel Connections," *Thin-Walled Structures* Vol. 25, No. 2, pp. 135-151, 1996

## **Experimental response of connections between cold-formed steel profile and cement-based panel**

Luigi Fiorino<sup>1</sup>, Ornella Iuorio<sup>2</sup>, Raffaele Landolfo<sup>2</sup>

### **ABSTRACT**

The seismic response of sheathed cold-formed steel (CFS) structures is highly influenced by the shear behaviour of panel-to-steel framing connections. Therefore, an experimental campaign aiming at characterizing the shear behaviour of different sheathing-to-CFS profiles connections has been planned. In particular, the following objectives have been selected: to compare the response of different panel typologies (cement, wood and gypsum-based panels); to examine the effect of the loaded edge distance; to investigate the outcome of different cyclic loading protocols. This paper presents and discusses the main results of this experimental investigation carried out on cement-based sheathing-to-stud connections.

### **Introduction**

The wide development of light gauge steel structures in the housing market increases the interest in searching new solutions and materials able to satisfy different market demands. Moreover, the new materials should be able to guarantee structural and environmental performance equal or higher than which provided by common materials.

<sup>1</sup>Department of Structural Engineering, University of Naples "Federico II", Naples, Italy

<sup>2</sup> Department of Constructions and Mathematical Methods in Architecture, University of Naples "Federico II", Naples, Italy

For these reasons, taking into account that in CFS studs structures the skeleton is usually sheathed with metal sheets, sandwich panels, wood-based or gypsum-based panels, the presented research has been aimed to investigate the behaviour of screw connections between CFS profiles and cement-based panels. In particular, the used panels (“Placocem” Fig. 1) are produced by BpB Italia Spa and are made of a cement core lightened with polystyrene and reinforced with a net of mineral fibers on both sides.



Figure 1: Placocem by BpB Italia Spa

When the sheathing has adequate strength and stiffness and it is effectively connected with the skeleton, then the interaction between profiles, sheathings and connections can be advantageously taken into account in the structural analysis (“sheathing-braced” design). In this case, the sheathing positively affects the structural response under vertical and horizontal loads. In particular, in case of gravity loads, the presence of sheathings can be advantageously taken into account in predicting the compression strength of vertical studs. This strength, in fact, may be significantly increased as a result of the additional resistance provided by the sheathing against global buckling modes. Hence, in current structural codes (AISI, 2002, EN 1993-1-3), it is allowed to take into account this member-to-sheathing interaction by using semi-empirical calculations based on the interpretation of test results. In the case of horizontal loads, floors, roof and walls can perform as diaphragms forming a “box system”. In particular, floors and roofs can be considered simply supported diaphragms, whereas walls can be regarded as vertical, cantilevered diaphragms. The “sheathing-braced” design approach requires the structural analysis of sheathings, connections, diaphragm edge members and tie-down connections to be carried-out. Despite the strong interrelation between the global lateral response of sheathed cold-formed “stick-built” structures and the local behaviour of sheathing-to-stud connections, few experimental programs have been carried out to study the response of sheathing to stud connections subjected

to shear loads (Filipsson, 2002, Fulop and Dubina, 2004, Okasha, 2004). For this reason, a specific experimental research has been planned, aiming to investigate both the monotonic and cyclic shear capacity of screw connections between CFS profiles and wood, gypsum or cement-based sheathings.

This paper is focused on cement-based sheathing-to-stud connections tests, and refers to Fiorino et al., 2007 for the experimental campaign on wood and gypsum-based panels. This study is part of a more comprehensive research program, devoted to analyzing the behaviour of light-gauge steel low-rise residential buildings under seismic actions (Landolfo et al., 2006)

### **The experimental program**

The experimental program was organized in two phases: in a first phase connections between studs and wood or gypsum-based panels were tested and in a second phase fasteners between studs and cement-based panels were tested. Goal of the testing program was: (1) to compare the response of different panels typologies (wood, gypsum and cement-based panels); (2) to examine the effect of the distance from the centre of the screw to the adjacent edge of the connected part in the direction parallel to the load transfer (loaded edge distance); (3) to evaluate the effect of different cyclic loading protocols; (4) to study the effect of sheathing orientation (only for the case of wood-based panels); (5) to assess the effect of the loading rate. This paper is focused on the second phase and it refers to Fiorino et al., 2007 for the first phase. Therefore, it is worth to specify that in the second phase only the first three points were tests goals, whilst orientation and effect of loading rate were not studied. Hence, 32 specimens, grouped in 8 series composed of 4 nominally identical specimens were tested. For each series, the experimental results were assumed as average values of single specimen results.

Test setup, geometry and materials properties of specimens were fixed during all the experimental campaign (Fig. 2). In particular, the generic sheathing-to-profile connection specimen consisted of two single  $200 \times 600$  mm sheathings attached to the opposite flanges of CFS profiles. Steel profiles were made of  $100 \times 50 \times 10 \times 1.0$  mm C (lipped)-sections. In particular, one single C-section was placed on the top side, whereas two back-to-back coupled C-sections were used for the bottom side. The profiles were fabricated from S350 hot dipped galvanized (zinc coated) steel (nominal yield strength  $f_y = 350$  MPa; nominal tensile strength  $f_t = 420$  MPa). The CFS profiles were bolted to hot-rolled steel (HRS) T-sections used to connect the specimens to the universal testing machine. Moreover, in order to avoid significant web deformation of the CFS profiles, a steel plate was placed at the internal side of the web of both top and

bottom studs. Three different sheathing types were selected: 9.0 mm thick type 3 oriented strand board (OSB) (EN 300, 1997), 12.5 mm thick standard gypsum wallboard (GWB, ISO-6308, 1980) and 12.5 mm thick cement based boards. In particular, taking into account that the OSB panels are composed of wood strands oriented along a principal direction, two different configurations were investigated: boards with strands in direction parallel to the applied loads (OSB//) and boards with strands in direction perpendicular to the applied loads (OSBT). Sheathings were connected using three screws (spaced at 150 mm on centre) for the top member (tested connections) and two rows of eight screws (spaced at 75 mm on centre) for the bottom members (oversized connections). Appropriate fasteners for each sheathing typology were adopted:  $4.2 \times 25$  mm (diameter  $\times$  length) flat head self drilling screws for OSB sheathings, and  $3.5 \times 25$  mm bugle head self drilling screws for CP and GWB panels. Four linear variable differential transducers (LVDTs) were used to measure the displacement between the sheathing and the profile.

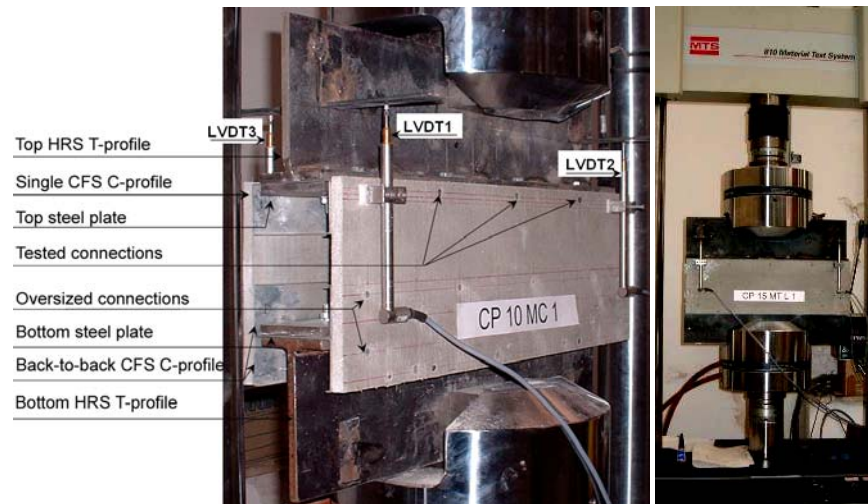


Figure 2: Generic specimen.

Three different values of the loaded edge distance ( $a$ ) were adopted ( $a = 10$  mm,  $a = 15$  mm,  $a = 20$  mm). The cyclic tests were carried out on specimens having  $a = 20$  mm. In this second phase of the experimental campaign, four displacement-controlled test procedures were adopted: monotonic tension (MT series), monotonic compression (MC series), and two types of cyclic loading history (labeled as CF and CK series). Under the monotonic loading history, specimens were subjected to progressive displacements, without unloading

phases. In the cyclic tests, two different loading protocols were adopted. In the first protocol (CF), specimens were subjected to specific loading sequences based on the results of a numerical study on the probable deformation demand from typical Italian earthquakes (Della Corte et al., 2006). In this case, specimens were tested with a constant loading rate. The second loading procedure (CK) was the CUREE protocol for ordinary ground motions (Krawinkler H, et al., 2000). It was developed to represent the seismic demand on wood framed shear walls under typical Californian earthquakes. In this case, specimens were tested with a constant cyclic frequency of  $f = 0.20$  Hz. The displacement history for each adopted loading protocol is shown in Figure 3, in which the applied displacements ( $d$ ) are normalized with respect to the reference displacement ( $\Delta$ ). The definition of the reference displacement is different for CF and CK protocols. In particular, the reference displacement is related to the yield displacement for CF procedure ( $\Delta=0.91\text{mm}$ ), while it is based on the measure of the ultimate displacement for the CK protocol ( $\Delta=4.17\text{mm}$ ). Specimens were tested with loading rate ( $v$ ) of  $0.05$  mm/s for monotonic tests,  $0.5$  mm/s for CF cyclic tests. The whole test program is summarized in Table 1, where the variables under investigation are reported for each series.

Serie Label	a (mm)	Loading protocol	Loading direction	Loading rate $v$ (mm/s)	Number of specimens
CP10MT	10	Monotonic	Tension	0.05	4
CP10MC	10	Monotonic	Compression	0.05	4
CP15MT	15	Monotonic	Tension	0.05	4
CP15MC	15	Monotonic	Compression	0.05	4
CP20MT	20	Monotonic	Tension	0.05	4
CP20MC	20	Monotonic	Compression	0.05	4
CP20CK	20	Cyclic	-	Variable	4
CP20CF	20	Cyclic	-	0.5	4

Table 1: Test program matrix

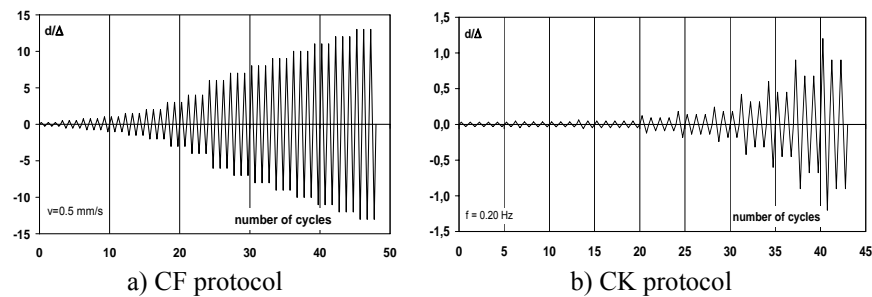


Figure 3: Loading protocols

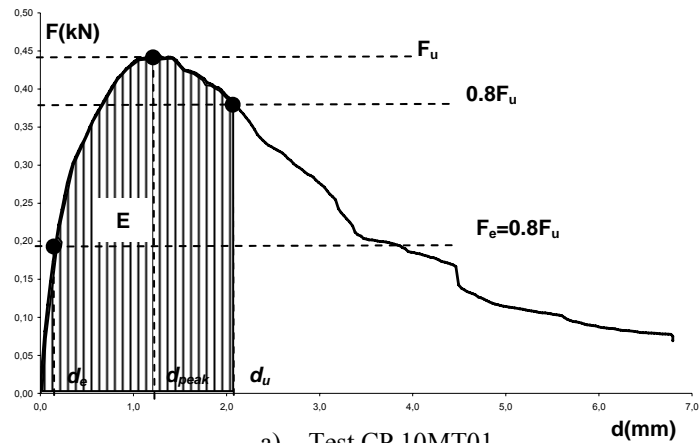
The series label defines both the specimen typology and testing procedure. Namely, the first group of characters indicates the sheathing material (CP: cement-based board); the second group of characters represents the loaded edge distance measured in millimeters (10, 15, or 20 mm); the third group describes the loading protocol (MT, MC, CF or CK). For example, the label CP 10 MT refers to a specimen made with cement-based panels, with edge distance equal to 10 mm, submitted to monotonic tension test.

### Test results

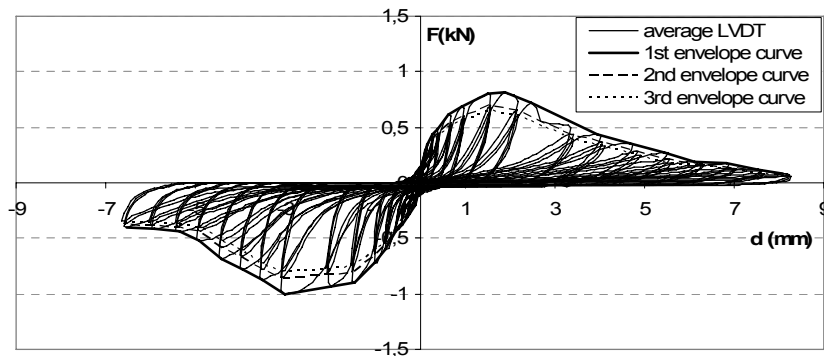
Typical experimental responses obtained in monotonic and cyclic tests are shown in Figure 4. Parameters used to describe the experimental behaviour are:

- $F = F_{tot}/6$ : average screw load ( $F_{tot}$  is the total recorded load, 6 is the total number of screws);
- $d = (d_{LVDT1} + d_{LVDT2} + d_{LVDT3} + d_{LVDT4})/4$ : average displacement ( $d_{LVDTi}$  is the displacement recorded by the  $i^{\text{th}}$  LVDT);
- $F_u$ : strength, is the maximum recorded average load;
- $d_{peak}$ : displacement corresponding to  $F_u$ ;
- $F_e = 0.4F_u$ : conventional elastic strength;
- $d_e$ : displacement corresponding to  $F_e$ ;
- $K_e = F_e/d_e$ : conventional elastic stiffness;
- $d_u$ : displacement corresponding to a load equal to  $0.80F_u$  on the post-peak branch of response;
- $\mu = d_u/d_e$ : maximum ductility;
- $E$ : absorbed energy (area under the  $F$  vs.  $d$  curve for  $d \leq d_u$ ).

In the case of cyclic tests these parameters are defined both on the positive and negative envelope curves, the latter defined considering the first hysteretic loops (Fig. 4(b)). Monotonic and cyclic test results are summarized in Table 2.



a) Test CP 10MT01



b) Test CP 20 CF 02

Figure 4: Typical experimental response

In this Table the parameters used to describe the experimental behaviour are reported together with the observed failure mode. For the cyclic tests, average values of parameters obtained on the positive and negative first envelope curves are reported.

In particular, the observed failure mechanisms during monotonic tests were (Fig. 5):

- (T) tilting of screws (Fig. 5(b));
- (P) screws pull-through the sheathing (Fig. 5(b));
- (E) breaking of sheathing edge (Fig. 5(a));

where tilting of screws was always observed in combination with the other mechanisms.



Specimen	$K_e$ (kN/mm)	$F_e$ (kN)	$d_e$ (mm)	$F_u$ (kN)	$d_{peak}$ (mm)	$d_u$ (mm)	$E$ (kN/mm)	$\mu$	Failure mode
CP 10 MT 0	2.77	0.17	0.06	0.42	1.11	2.01	0.74	33.32	E
CP 10 MT 1	1.98	0.18	0.09	0.44	1.09	2.08	0.79	23.09	E
CP 10 MT 2	4.61	1.56	0.03	0.39	0.33	1.19	0.40	35.38	E
CP 10 MT 3	2.34	0.19	0.08	0.48	0.65	2.17	0.92	26.52	E
CP 15 MT 1	2.48	0.20	0.08	0.51	0.90	2.95	1.32	36.07	E
CP 15 MT 3	3.45	0.25	0.07	0.62	1.31	1.88	1.05	26.32	E
CP 15 MT 4	2.46	0.25	0.10	0.62	1.35	2.17	1.16	21.49	E
CP 15 MT 5	3.18	0.24	0.07	0.59	1.29	1.90	1.01	25.67	E
CP 20 MT 2	2.42	0.29	0.12	0.73	1.66	3.46	2.20	28.50	T+P+E
CP 20 MT 3	3.20	0.27	0.09	0.68	1.63	2.72	1.62	31.91	T+P+E
CP 20 MT 4	3.20	0.36	0.11	0.91	1.83	2.47	1.89	21.82	E
CP 20 MT 5	2.91	0.31	0.11	0.78	2.30	3.54	2.37	32.87	E
CP 10 MC 1	1.56	0.54	0.35	1.36	1.97	3.44	3.73	9.90	T+P
CP 10 MC 2	2.22	0.37	0.17	0.92	2.46	9.33	7.52	56.44	T+P+E
CP 10 MC 3	1.59	0.37	0.23	0.93	2.08	7.45	6.02	31.80	T+E
CP 10 MC 4	0.87	0.40	0.46	0.99	2.84	9.12	7.39	20.02	T+E
CP 15 MC 1	3.47	0.54	0.16	1.35	4.52	6.61	7.73	42.41	T+P
CP 15 MC 2	0.73	0.53	0.73	1.33	6.37	6.89	6.82	9.45	T+P
CP 15 MC 3	1.31	0.52	0.39	1.29	5.50	0.52	8.84	20.14	T+P
CP 15 MC 4	1.25	0.51	0.40	1.26	5.33	6.88	7.12	17.07	T+P
CP 20 MC 1	1.93	0.57	0.30	1.43	4.10	6.09	7.22	20.57	T+P
CP 20 MC 2	0.86	0.62	0.73	1.56	6.53	8.32	10.04	11.44	T+P
CP 20 MC 3	1.29	0.64	0.50	1.60	6.54	8.18	10.34	16.52	T+P
CP 20 MC 4	1.22	0.60	0.49	1.50	4.70	5.20	5.70	10.61	T+P
CP20 CK 01	0.93	0.36	0.41	0.89	2.72	4.55	3.33	11.63	P+E
CP 20 CK 02	1.08	0.44	0.44	1.09	2.61	4.75	4.12	12.42	P+E
CP 20 CK 03	2.09	0.41	0.20	1.03	2.52	4.44	3.77	23.50	P+E
CP 20 CK 04	2.90	0.38	0.18	0.95	2.17	3.90	3.19	28.37	P+E
CP 20 CF 01	1.95	0.39	0.27	0.97	1.98	3.15	2.46	15.78	T+E
CP 20 CF 02	1.57	0.35	0.30	0.91	2.41	3.36	2.47	14.23	T+P+E
CP 20 CF 03	1.85	0.31	0.17	0.79	1.51	3.31	2.19	19.86	T+P+E
CP 20 CF 04	2.37	0.32	0.12	0.81	1.63	3.41	2.47	26.90	T+P+E

Table 2: Experimental results of monotonic and cyclic tests.

The most common mechanism observed during monotonic tension tests was the breaking of the sheathing edge ((E) failure mode), except for CP20MT2 and CP20MT3, where combination of tilting of screws, screws pull-through the sheathing and breaking of sheathing edge occurred ((T)+(P)+(E) failure mode). On the other side, in the monotonic compression tests the failure mechanism was a combination of tilting of screws and screws pull-through the sheathing ((T)+(P) failure mode), except for CP10MC3 and CP10MC4 in which the combination of tilting of screws and breaking of sheathing edge occurred ((T)+(E) failure mode). In addition, in one case the combination of three failure modes was observed: (T)+(P)+(E) for CP10MC2.

In the case of cyclic loading characterized by CK protocol, combination of screw pull-through the sheathing and breaking of sheathing edge ((P)+(E) failure mode) was the dominant mechanism. Whilst, in case of CF protocol, the combination of all the failure mechanisms (T)+(P)+(E) was observed in all the tests except for CP20CF1 when only a combination of tilting of screws and breaking of sheathing edge (T)+(E) developed.

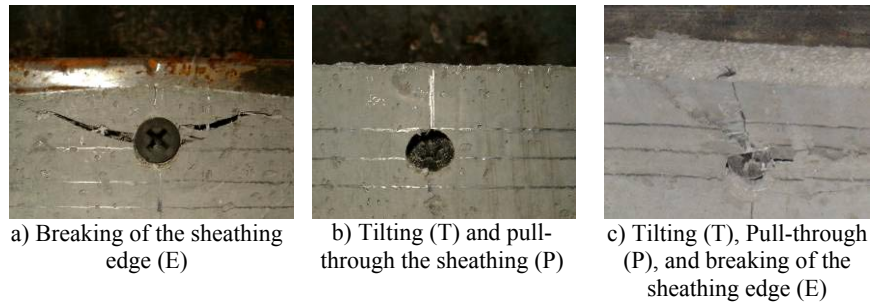


Figure 5: Test program matrix

### Effect of the sheathing type

Monotonic experimental results obtained for OSB//, OSBT, GWB and CP tests are illustrated in Figure 6. In particular, in this Figure the average values of  $K_e$  (Fig. 6(a)),  $F_u$  (Fig. 6(b)),  $\mu$  (Fig. 6(c)), and  $E$  (Fig. 6(d)) concerning to the monotonic tension (MT) and compression (MC) tests are represented as functions of the loaded edge distance ( $a$ ). Examining these figures, it can be noted that connections with CP sheathings revealed larger stiffness than any other material, with on average, values 1.6, 2.1 and 3.4 times larger than that showed by GWB, OSB// and OSBT panels, respectively. Moreover, the ductility revealed by CP was, on average 2.2 and 2.3 times larger than that showed by OSB// and OSBT panels, but 1.1 lower than that exhibited by GWB panels. On the contrary, CP panels showed less strength and absorbed energy than connections with OSB// and OSBT sheathings (on average, the strength was 2.0 and 2.3 times lower and the absorbed energy of CP panels was 3.2 and 5.8 times lower than that measured for OSB// and OSBT panels, respectively). At the same time, strength and absorbed energy were larger than that exhibited by GWB sheathings (on average, 1.5 and 1.2 times larger, respectively). Some typical load vs. displacement curves, obtained from tests under monotonic tension (Fig. 7(a)) and compression (Fig. 7(b)) loading are presented in Figure 7.

Average values of  $K_e$ ,  $F_u$ ,  $\mu$ , and  $E$  obtained in the case of cyclic tests considering CF and CK protocols are shown in Figure 6 (a)–(d). It is worth to specify that OSBT panels were not subjected to cyclic tests. The comparison about stiffness and strength among CP, OSB// and GWB sheathings results confirms the conclusions drawn in the case of monotonic tests. In fact, from cyclic loading test results it can be observed that CP sheathings have larger stiffness then OSB// and GWB (1.7 and 1.2 times, respectively) and the strength is lower then for OSB// panels (1.5 times) and higher then GWB sheathings (1.7 times). About ductility and absorbed energy, the results seem to confirm the monotonic ones for CP and GWB, in fact CP ductility is 1.7 times lower then GWB ductility while CP sheathings absorbed more energy then GWB panels. On the contrary, the comparison about ductility and absorbed energy between CP and OSB does not confirm the conclusions drawn in the case of monotonic tests. In this case, in fact, CP panels reveal lower ductility (1.2 times) and absorbed larger energy (1.2 times) then OSB// sheathings.

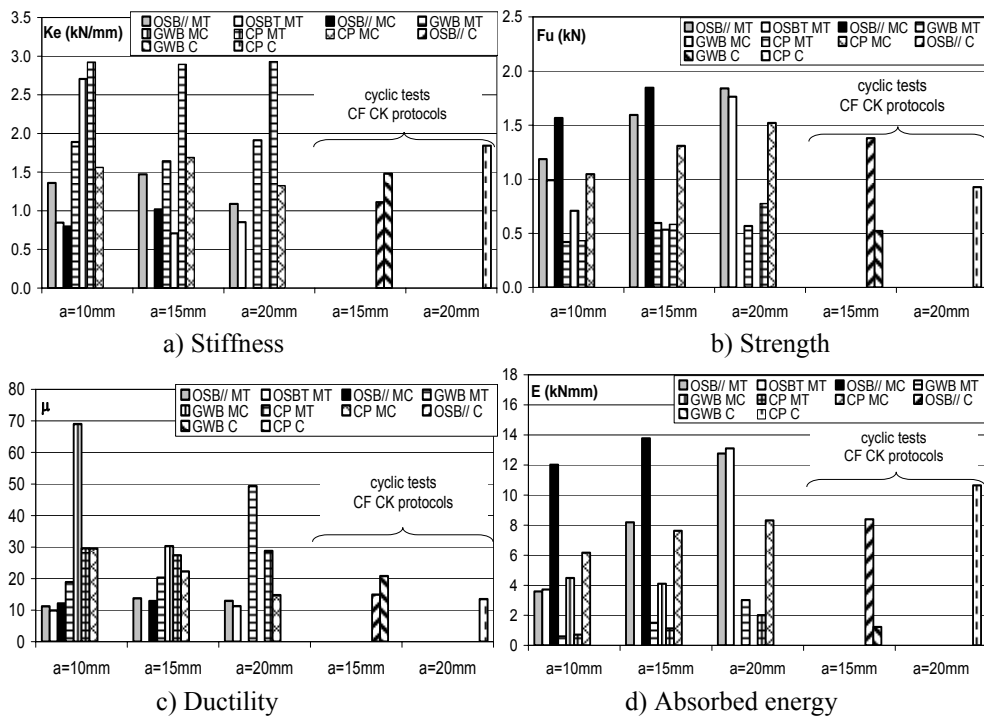


Figure 6: Average values of  $K_e$ ,  $F_u$ ,  $\mu$  and  $E$  obtained during monotonic and cyclic tests

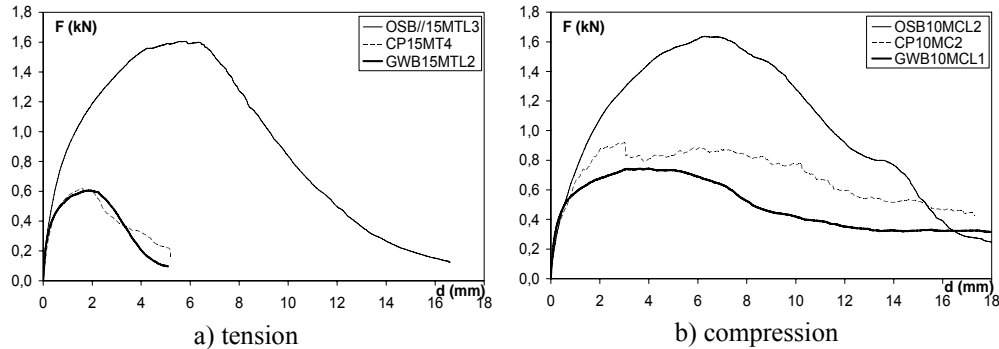


Figure 7: OSB//, GWB and CP experimental response under monotonic loads

#### Effect of the loaded edge distance

As far as the influence of the loaded edge distance ( $a$ ) is concerned, results of monotonic tests on CP sheathings represented in Figure 6 reveal that strength and absorbed energy are increasing with  $a$ . In particular, test results under monotonic tension loading show that an increase of the edge distance from 10 to 20 mm produced an increase of strength of about 1.8 times and an increase of absorbed energy of about 2.8 times. Moreover, when  $a$  was increased the strength and absorbed energy exhibited an almost linear variation. In the case of monotonic compression loading, when the edge distance was increased from 10 to 20 mm strength and absorbed energy increased about 1.5 times. The ductility did not vary significantly when  $a$  was increased in case of tension loads, while it decreases of almost 50% in case of compression loads. Finally, stiffness values varied without any noticeable trend.

Typical load vs. displacement response curves for three different values of the adopted loaded edge distance are shown in Figure 8. Examining this figure, two boundary behaviours can be individuated: (1) shear response is significantly affected by edge failure (E failure mode), for  $a = 10$  mm; (2) shear response is significantly affected by an interaction of tilting and screw pull-through the sheathing failure (T+P failure mode) for  $a = 20$  mm. In particular, the second case can be associated with a better behaviour characterized by larger strength and absorbed energy than the first one.

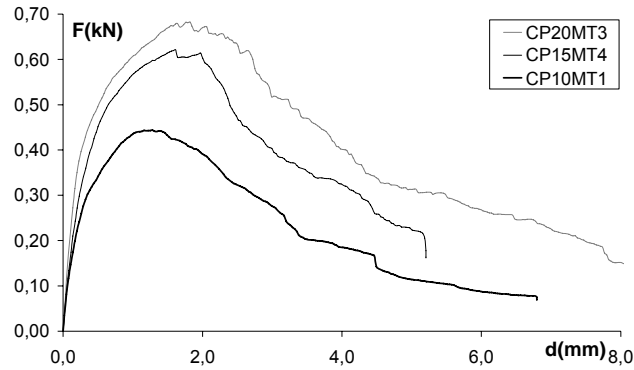


Figure 8: Experimental response of Monotonic Tension tests as function of the loaded edge distance

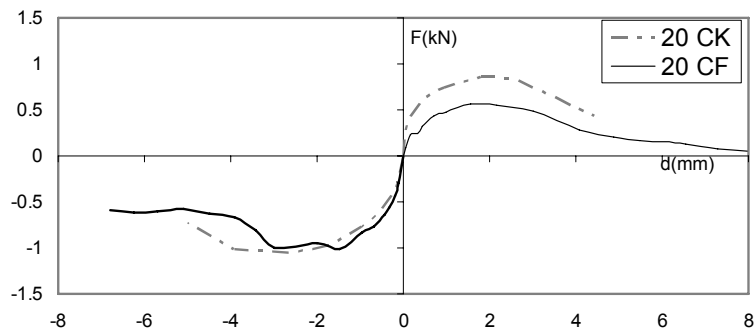


Figure 9: Average back-bone curves

The difference between these boundary behaviours justifies that in the design of shear walls based on theoretical methods, in which the global shear response is evaluated on the basis of a connection's shear response (local response), knowledge of the strength values corresponding to edge and pull-through failure modes is required. As a result of this experimental research, nominal values (experimental average values) of shear strength due to edge failure ( $F_u^{(e)}$ ) and screw pull-through the sheathing failure ( $F_u^{(p)}$ ) are suggested as follows: for 12.5mm thick standard CP sheathing fastened to 1.0 mm thick steel profiles with a  $3.5 \times 25$  mm bugle head self drilling screw:  $F_u^{(e)} = 0.43\text{kN}$  and  $F_u^{(p)} = 0.78\text{kN}$ ; standard deviations were 0.04 for  $F_u^{(e)}$  and 0.10 for  $F_u^{(p)}$ .

### Effect of different cyclic loading protocols

Figure 9 shows the average envelope curves obtained at the first hysteretic loops (envelope obtained considering the maximum value of strength measured at the first loop for each displacement amplitude) and considering the adopted loading protocols (CF, CK) for CP sheathings. For evaluating the effect of cyclic loading on the strength degradation, envelope curves obtained at the second and third hysteretic loops (envelopes obtained considering the maximum value of strength measured for each displacement amplitude at the second and third loop, respectively) have been considered together with the envelope curve obtained considering the first hysteretic loop. Figure 10 shows comparison between the monotonic and cyclic response. In this figure the values of  $K_e$ ,  $F_u$ ,  $\mu$  and  $E$  obtained applying the adopted cyclic loading protocols (CF, CS) are normalized with respect to the values that these parameters assume for the monotonic loading protocol. In particular, values of parameters assumed as representative of monotonic response have been calculated as average values of parameters obtained from monotonic tension (MT) and compression (MC) tests. Examining this figure, it can be noticed that stiffness, strength, absorbed energy and ductility obtained in cyclic tests were lower than those obtained in monotonic tests. In particular, more significant reductions were obtained for  $F_u$  (by 16% and 32% considering CK and CF protocols, respectively) and  $E$  (by 40% and 216% considering CK and CF protocols, respectively). Figure 11 shows representative curves obtained from tests (CP20MT3 vs. CP20CF2), in which monotonic and cyclic experimental response can be directly compared.

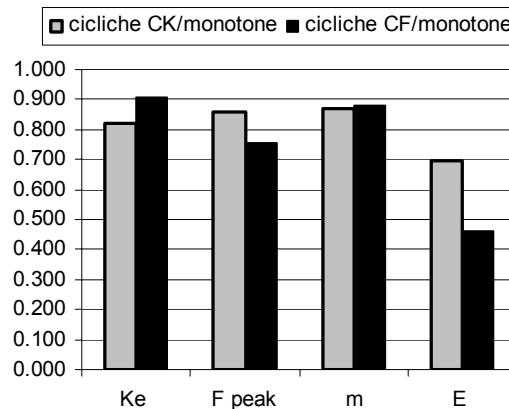


Figure 10: Monotonic vs. cyclic response

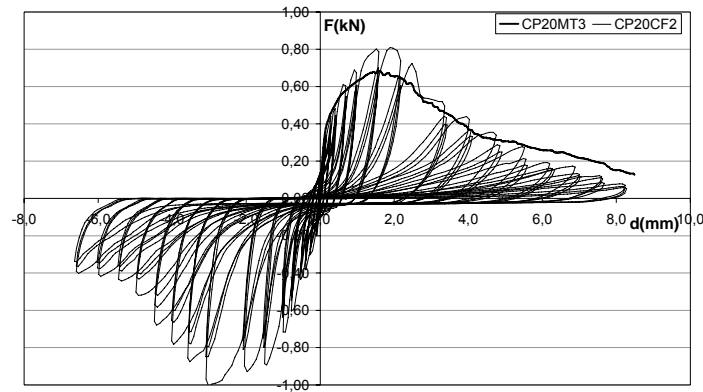


Figure 11: Monotonic vs. cyclic experimental response

## Conclusions

The sheathing strongly influences the shear response of connections. In fact, as showed in the presented paper, the CP sheathing reveals larger stiffness than OSB and GWB panels. Moreover, CP ductility is almost the same of GWB panels and it is larger than that exhibited by OSB. On the contrary, CP reveals less strength and absorbed less energy than OSB even if both are larger than that exhibited by GWB sheathing. The increment of the loaded edge distance produced an increment of strength and absorbed energy with an almost linear variation. The ductility is strongly influenced in case of compression tests, whilst ductility in tension tests and the stiffness varied without any noticeable trend. The suggested nominal strength for the tested CP screw connections (12.5 mm thick standard CP sheathing fastened to 1.0 mm thick steel profiles with a  $3.5 \times 25$  mm screw) is 0.43kN or 0.78kN in case of edge failure or pull-through the sheathing failure, respectively. Comparison between monotonic and cyclic response reveals that cyclic loading produces a reduction of all the parameters (stiffness, strength, ductility and absorbed energy), with a non-negligible reduction of absorbed energy.

## Achievements

Authors acknowledge the Italian companies BPB Italia Spa., TECFI Spa. and GUERRASIO for the furnishing of test specimen components. Specific

acknowledgments are extended to Eng. Pino Campanella for the technical support provided during the laboratory phase and to Eng. Gennaro De Crisci involved in the experimental activity during his Dissertation Thesis.

## References

- AISI. 2002. Cold-formed steel design manual. Washington (DC, USA): American Iron and Steel Institute.
- Della Corte G, Landolfo R, Fiorino L. 2006. Seismic behavior of sheathed cold formed structures: Numerical study. *Journal of Structural Engineering ASCE*; 132(4):558–69.
- EN 1993-1-3. 2005. Eurocode 3: Design of steel structures—Part 1–3: General rules — Supplementary rules for cold formed members and sheeting. Bruxelles (Belgium): European Committee for Standardization.
- EN 300. 1997. Oriented strand boards OSB-definitions, classification and specifications. Bruxelles (Belgium): European committee for standardization.
- Filipsson T. 2002. *Shear walls with double plasterboards — Evaluation of design models*. Licentiate thesis. Luleå (Sweden): Department of Civil and Mining Engineering, Division of Steel Structures, Luleå University of Technology.
- Fulop LA, Dubina D. 2004. Design criteria for seam and sheathing-to-framing connections of cold-formed steel shear panels. In *Proceedings of the 17th international specialty conference on cold-formed steel structures*. p. 743–59.
- Fiorino, L., Della Corte, G., Landolfo, R. 2007. Experimental tests on typical screw connections for cold-formed steel housing. *Engineering Structures*. Elsevier Science. Vol. 29, No. 8, pp. 1761–1773.
- ISO-6308. 1980. Gypsum plasterboard-specification. Geneva (Switzerland): International organization for standardization.
- Landolfo R, Fiorino L, Della Corte G. 2006. Seismic behavior of sheathed coldformed structures: Physical tests. *Journal of Structural Engineering ASCE*; 132(4):570–81.
- Krawinkler H, Parisi F, Ibarra L, Ayoub A, Medina R. 2000. *Development of a testing protocol for wood frame structures*. Report W-02 covering task 1.3.2, CUREE/Caltech wood frame project.
- Okasha AF. 2004. *Performance of steel frame/wood sheathing screw connections subjected to monotonic and cyclic loading*. M.Sc. Thesis. Montreal (Canada): Department of Civil Engineering and Applied Mechanics, McGill University.





## **Test Standard for Joist Connectors Attached to Cold-Formed Steel Framing**

Greg Greenlee, P.E.<sup>1</sup>

### **Abstract**

Recently the America Iron and Steel Institute (AISI) developed a new test standard for testing joist connectors attached to cold-formed steel framing. This test standard will provide designers, manufacturers, and researchers with a consistent methodology to determine load ratings for these types of commonly used connectors. Often these connectors have a composition or configuration such that calculation of their structural capacities cannot be made in accordance with the provisions of the specification. This standard has been submitted to the American National Standards Institute (ANSI) for approval as an American National Standard (ANS).

### **Introduction**

It is common in cold-formed steel construction to use a joist hanger, clip or angle to connect two structural members. The composition or configuration is commonly such that calculation of their structural capacities cannot be made in accordance with the provisions of the specification. The purpose of this test procedure is to establish test requirements for these connectors used in cold-formed steel light-framed construction. Also, it provides guidance for determining allowable stress design (ASD) and load and resistance factor design (LRFD) design loads for cold-formed steel connectors as well as deflection service limit loads for the connectors.

The scope of the document limits the application to connectors which are primarily resisting a shear reaction. Axial, bending and torsional loads, such as where the joist is unrestrained by bracing, are outside the scope of the document.

---

<sup>1</sup> Director of Engineering, USP Structural Connectors, Burnsville, MN

## **Description of the Test Standard**

The test standard developed is based on similar test standards developed for similar types of products in wood construction; specifically ASTM D1761 and ASTM D7147. Also, the International Code Council Evaluation Service (ICC-ES) has created an acceptance criteria for connectors used with cold-formed steel structural members, AC261, which is similar in content. It is anticipated that once the subject test standard is approved, it will be submitted to ICC-ES for consideration.

It should be noted that hold-down connectors are covered by the newly drafted *AISI Test Procedure for Hold-Downs Attached to Cold-Formed Steel Structural Framing*. Having different test standards recognizes and separates the important differences in performance requirements between different types of connectors

The test standard document is divided into sections to describe the test fixture, test specimens, test setup, test procedure, data evaluation, and test report.

### **1. Test Fixture**

Typically hydraulic or screw operated testing machines are used to perform these types of tests. A picture of this type of device is shown in Figure 1. The equipment needs to be capable of operating so that it is applying a controlled constant rate of loading. Load cells are used to measure the magnitude of the applied load. They are available in various sizes capable of measuring different magnitudes of load. The test equipment should also include deflection measuring devices which are capable of reading to 0.001 inch (0.025 mm). The test setup and measuring devices shall be such load and deflection characteristics of the connector are recorded during the test. This will facilitate the development of a load-deflection curve.

### **2. Test Specimen**

The test specimen includes the connector to be tested as well as the fasteners used to install the connector in making the connection. The standard requires that the fastening methods and techniques used with the connection shall be done in a manner representative of actual field conditions. Also, the steel properties, including yield strength, tensile strength, percent elongation and uncoated base steel thickness, of the tested connector used in the test assembly shall be determined. This information will be then used to adjust the results of the testing per Section F1 of AISI S100 to account for material over-strength and over-thickness.

### **3. Test Setup**

The test setup description covers the cold-formed steel joists, supporting members and connector to be investigated. The specimen shall be representative of field conditions. The standard provides guidance on how the setup shall be constructed so that unintentional load paths are avoided. It also discusses where the deflection measuring devices shall be located. Reinforcing of the joist members is permitted to prevent member failure away from the connector. Figure 2 shows a side view and top view of the test set-up. The side view is included in the test standard.

Often the greatest challenge in these tests is creating a test setup which accurately portrays field performance. For example, Figure 3 shows a test setup with a load transfer block is fastened to the side of the joist. This enables the load to be applied in the vertical shear axis of the member. Figure 4 shows the loaded joist which is loaded in the plan of the vertical shear axis and, as a result, not showing signs of torsional warping.

### **4. Test Procedures**

When testing a specimen a preload not exceeding 10 percent of the average ultimate load is permitted. This preload will effectively set the joist in the seat of the hanger. The justification for preloading the connector is that after installation there will be some initial load during the construction process that will effectively seat the joist in the hanger. If the specimen is not preloaded it is possible it will reach the established deflection limit prematurely. During testing the load shall be applied at a uniform rate between 0.03 and 0.10 in. (0.76 to 2.54 mm) per minute. As noted earlier, the load-deflection characteristics shall be recorded to create of a load-deflection curve. The standard assigns a deflection limit of 1/8 in. (3.2mm), unless justified otherwise.

### **5. Data Evaluations**

The standard does not include specific guidance to how the results shall be evaluated and the available strength of the connector determined. Rather, it refers the user to Section F1 of AISI S100.

### **6. Test Report**

The test report shall include information necessary to provide insight to the end user. This includes a description of the test specimen, steel mechanical

properties, modifications made to the joists, load rate, location of displacement information, maximum test load values, and the load-deflection curve.

### **Conclusion**

This new test standard will provide designers, manufacturers, and researchers with a consistent methodology to determine load ratings for joist hangers and similar devices attached to cold-formed steel framing. These connectors have a composition or configuration such that calculation of their structural capacities cannot be made in accordance with the provisions of the AISI NAS S100 specification. Establishing a standardized test fixture, setup, procedure, report and evaluation enables a consistent exchange of information needed to reliably communicate and understand the behavior of the connector.

### **References**

American Iron and Steel Institute (2007), *North American Specification for the Design of Cold-Formed Steel Structural Members, S100-07*, Washington D.C.

American Iron and Steel Institute (2007), *North American Standard for Cold-Formed Steel Framing – Floor and Roof System Design, S210-07*, Washington D.C.

ASTM International, D1761-88(2000), Standard Test Method for Mechanical Fasteners in Wood, West Conshohocken, PA

ASTM International, D7147-05, Standard Specification for Testing and Establishing Allowable Loads of Joist Hangers, West Conshohocken, PA

International Code Council Evaluation Service, *AC261, Acceptance Criteria for Connectors used with Cold-formed Steel Structural Members* (approved October 2004, editorially revised January 2008), Whittier, CA.

## Appendix



Figure 1: Picture of a typical testing frame

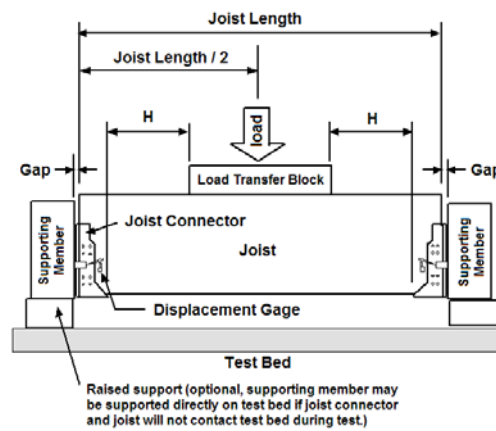
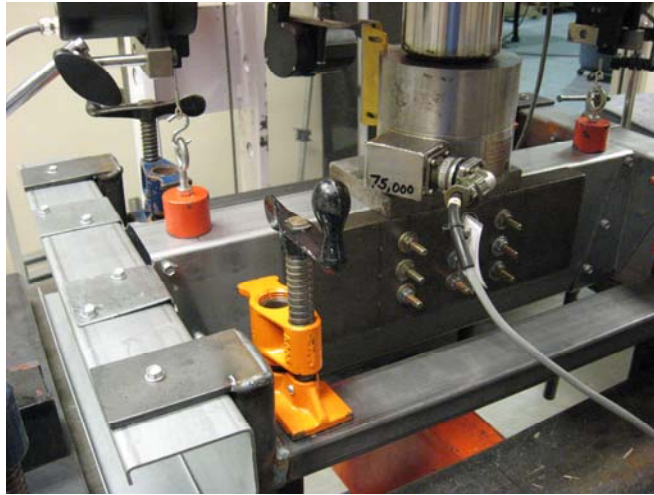
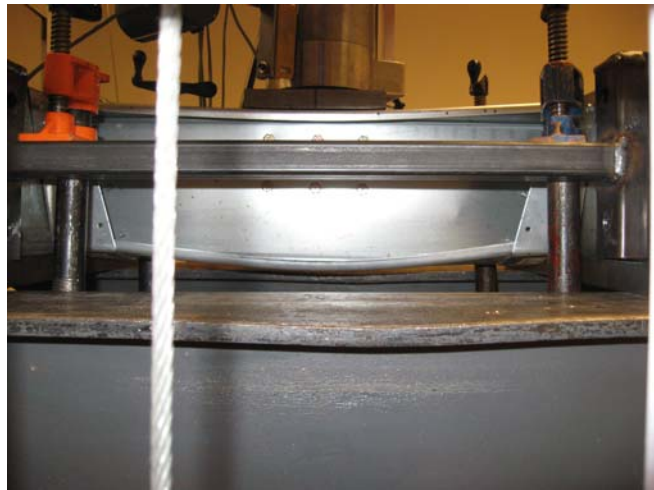


Figure 2: Test Set-up for Joist Connector



**Figure 3: Load Transfer Block Attached to Joist**



**Figure 4: Deflected Joist Loaded Through the Vertical Shear Axis**

## **New Test Standard for Hold-downs Attached to Cold-Formed Steel Structural Framing**

Jeff Ellis, P.E., S.E.<sup>1</sup>

### **Abstract**

This paper discusses the new hold-down test standard entitled “Test Standard for Hold-downs Attached to Cold-Formed Steel Structural Framing” [1] developed by the AISI Committee on Specifications for the Design of Cold-Formed Steel Structural Members. Currently, the other AISI test standards are shown in the 2002 AISI Cold-Formed Steel Design Manual [2]. Hold-downs are defined in the AISI General Provisions standard [3], which is referenced by the 2006 International Building Code [4], and have been used successfully for many years in light-frame cold-formed steel construction. The 2006 IBC Section 1604.9 requires a continuous load path to transmit forces induced to structural members and systems to the foundation. Hold-downs are commonly used as the attachment of a structural member, such as a post or joist, to the foundation or wall to complete the load path. Understanding their strength and displacement behavior is important to the proper design and detailing of cold-formed steel light-frame lateral force resisting systems. This test standard provides a standard methodology that may be used to determine and compare strength and displacement characteristics for the many types of devices used in the industry currently and that may be developed in the future.

<sup>1</sup>Senior Engineering Project Manager, Simpson Strong-Tie Co., Inc., Pleasanton, CA  
AISI COFS Lateral Design Subcommittee Chairman



## Introduction

Hold-downs are used to resist overturning forces in light-frame shear walls, or to resist uplift in vertical framing members, to resist lateral forces at wall to diaphragm connections, or to transfer lateral forces between framing members in horizontal diaphragms. These forces are typically induced by wind or seismic events. Usually, hold-downs resist tension forces, but there are some that may also be used to resist compression forces. The 2006 IBC references the 2004 AISI Lateral Design standard [5] in Section 2210.5. It is a requirement in both the 2004 [5] and 2007 [6] Lateral Design standard Section C2 that hold-downs be used in Type I and Type II cold-formed steel framed shear walls as the prescriptive shear wall values tabulated in the Lateral Design standard [5] [6] were based upon tests using hold-downs.

The building code specifies certain strength requirements for hold-downs in shear walls when the Response Modification Coefficient,  $R$ , is greater than 3 [6] and it specifies strength level (LRFD) story drift limitations - for seismic load resistance - for which the hold-down in a shear wall contributes towards [7] as shown in Figure 1. There are also specific strength and detailing requirements for hold-downs used to resist seismic forces in framing members of horizontal diaphragms [7]. These code requirements are reasons that deformation behavior is important in addition to strength determination.

Given the impact that hold-down performance has on the response of the lateral force resisting system, and thus the entire building, it was determined that a stand-alone hold-down testing standard was needed. Hold-downs have been evaluated in the past typically using Chapter F, Tests for Special Cases, from the AISI specification of which the most recent is the AISI 2007 North American Specification for the Design of Cold-Formed Steel Structural Members [8]. This has meant that a minimum of 3 tests, with no more than a 15% deviation from the average value of all the tests, were performed and then a resistance factor was determined per this chapter to determine the hold-down design strength. In some cases, hold-down device displacements were also provided.

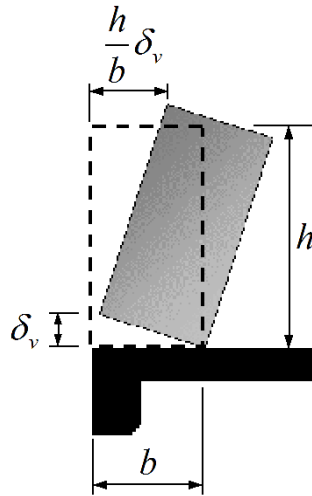


Figure 1 - S213-07 Figure C2-10 - Lateral Contribution from Anchorage/Hold-down Deformation

### Scope of Standard

The standard provides a methodology to determine both the strength as well as the deformation characteristics of the hold-down device itself (device test) as well as the overall assembly with the hold-down attached to a light-frame member(s) (assembly test). There are several hold-down types that may be evaluated using this standard as shown in Figure 2, but other types of similar hold-downs may be evaluated under this standard, as applicable.

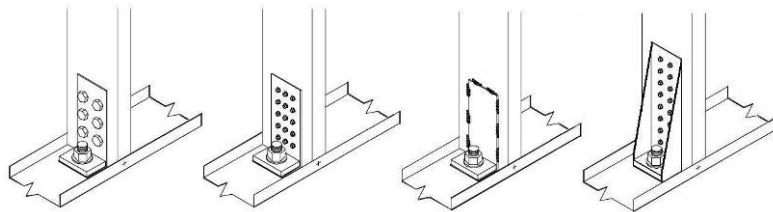


Figure 2 - Typical Hold-down Assemblies

### **Test Fixture and Specimen**

The test fixture may be either a hydraulic or screw operated testing machine that must be able to provide a constant rate of loading along with a calibrated device to measure the load. Alternatively, a hydraulic cylinder with a steel fixture and a load cell may be used.

The specimen is the hold-down device itself or the hold-down and the fasteners specified to attach it to the cold-formed steel framing member(s) when the assembly test is performed. The minimum number of test specimens and the permissible test result variation is per Chapter F [8] which requires a minimum of 3 tests and each individual test must be within 15% of the average or until at least a total of 6 tests are performed.

As is typical for any structural member test, it is required to determine the material properties of the hold-down device inclusive of yield and tensile strength and the base metal thickness. The material strength and thickness of the cold-formed steel member(s) that the hold-down is attached to in the assembly test also affect the test results and need to be determined. The fasteners used in the test are required to be sampled at random and installed as they would be in the field or if welds or other fastenings (i.e.; clinching, etc.) are used, their installation is to be the same as that performed in the field.

### **Test Setup**

It is required that the hold-down be tested individually and that the test setup represent the position and loading of the hold-down in the field. As many of these hold-down devices are eccentric, it is permitted to use low-friction material to support the steel jig or cold-formed steel members below and above the hold-down.

The anchor bolt is required to be installed to simulate field conditions as best as possible. This would include that the anchor bolt should not be longer than typically expected in the field, the anchor bolt nut should have the same bearing area as the one used in the field, and the anchor bolt nut should only be snug tightened if it is possible the hold-down might be supported by something other than a rigid structural steel or concrete or masonry base (ie; raised hold-down installation, wood sill plate, etc.). In addition, the fasteners used to attach the hold-down to the cold-formed steel members should be installed to also

represent possible field conditions. For example, this would mean that the nuts for the bolts should only be snug tight unless the installation instructions state specific tightening requirements.

### Hold-down Device Test

The hold-down device test requires the hold-down device be attached to a steel fixture, as shown in Figure 3, and this is to determine the strength of the device itself. The deformation is

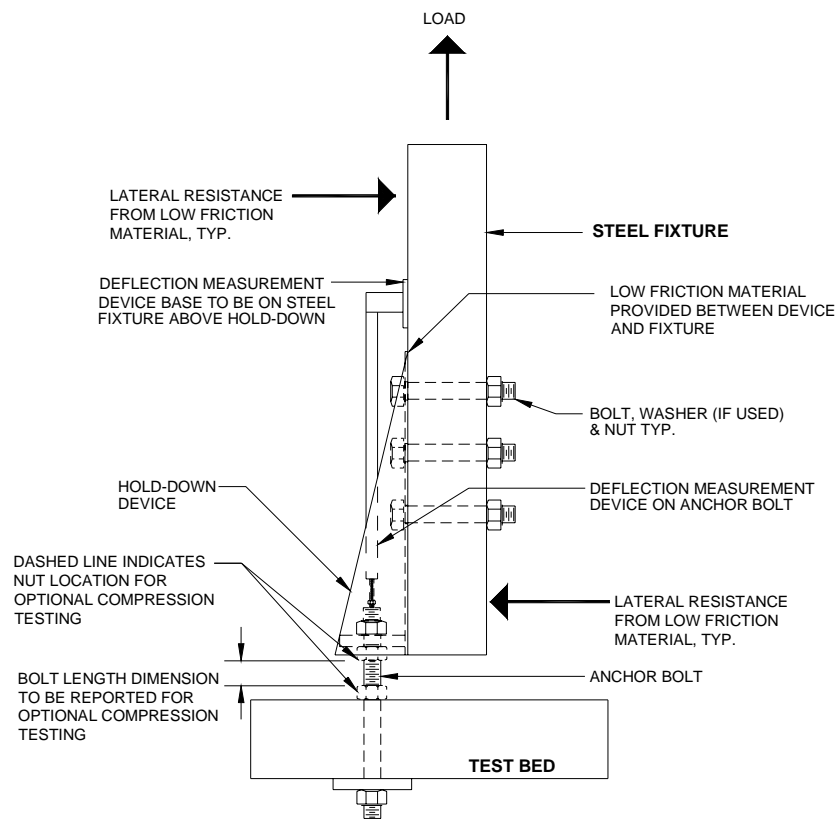


Figure 3 - Tension Load Test Set-up for a Single Hold-down Device

inclusive of the hold-down deformation, fastener slip, and anchor bolt elongation. For tension load testing, the hold-down is required to be installed a minimum of 1" above the test bed to account for raised hold-down field installations or when the hold-down may be installed on top of a non-rigid (i.e.; wood) base. It may be required to test the hold-down raised higher than 1" if the hold-down may contact the test bed, such as through seat rotation, prior to failure. It is also required that a low friction material be placed between the hold-down and the steel test jig to minimize friction or bearing resistance from the steel fixture.

If the hold-down is required to be installed in the field to a rigid structural steel or concrete base, it is permitted to test the hold-down with it installed directly on top of the test bed, similar to the test setup shown in Figure 4b. When a hold-down is tested directly on the test bed, the anchor bolt should be instrumented so that the force to the anchor bolt can be measured and compared to the applied force as some hold-downs may amplify the applied force to the anchor bolt due to prying. This anchor bolt force information is needed by the designer so that the anchorage may be properly designed and detailed.

The fasteners used to attach the device to the steel fixture and the anchor bolt, that attaches the device to the test bed, may be higher strength than specified. However, they are required to be the same diameter as specified and, if a nut and washer are used, they are to have the same bearing area as specified for the field installation. If compression testing is performed, it is also required that the bolt, nut and plate washer be of the same dimension as used in the end-use application. Also, for compression testing, it is required that the maximum unbraced length of the anchor bolt be per the manufacturer's recommendations and reported.

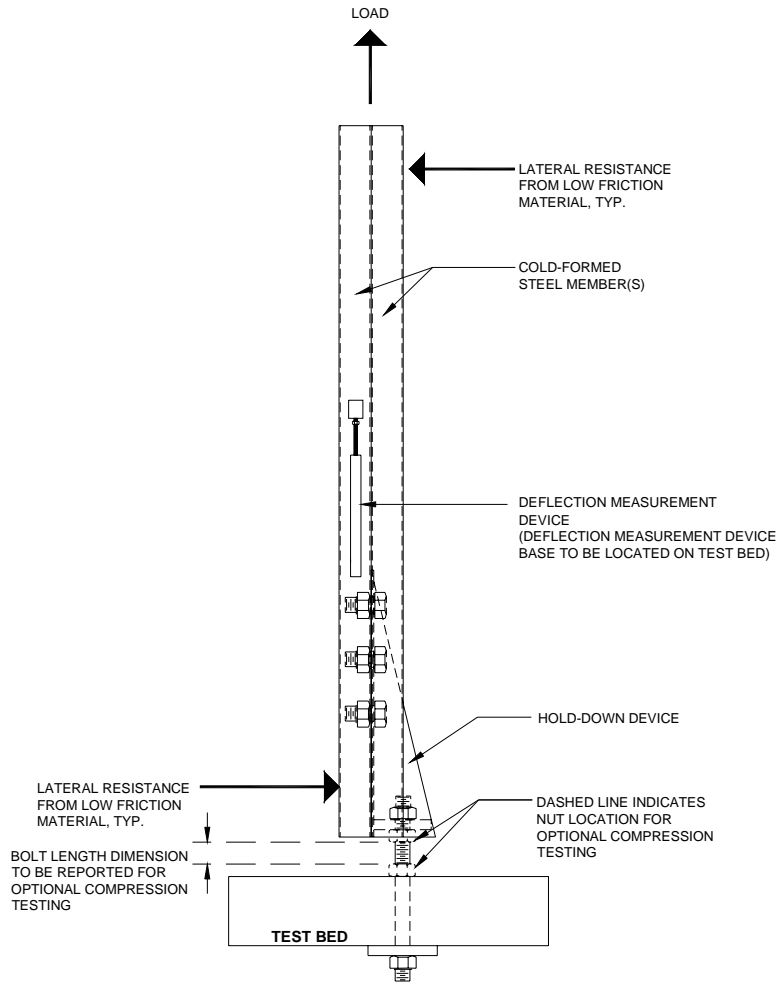
The device that is to measure the deformation is to be attached to the steel fixture above the hold-down. It is to measure the displacement that occurs between the steel fixture and the top of the anchor bolt. This will include fastener slip and hold-down deformation. An additional reference point for a displacement device could be at the top of the hold-down, such as a horizontal plate tack welded to the top of the hold-down, so as to isolate the hold-down device deformation to compare to the deformation recorded in the assembly test.

### **Hold-down Assembly Test**

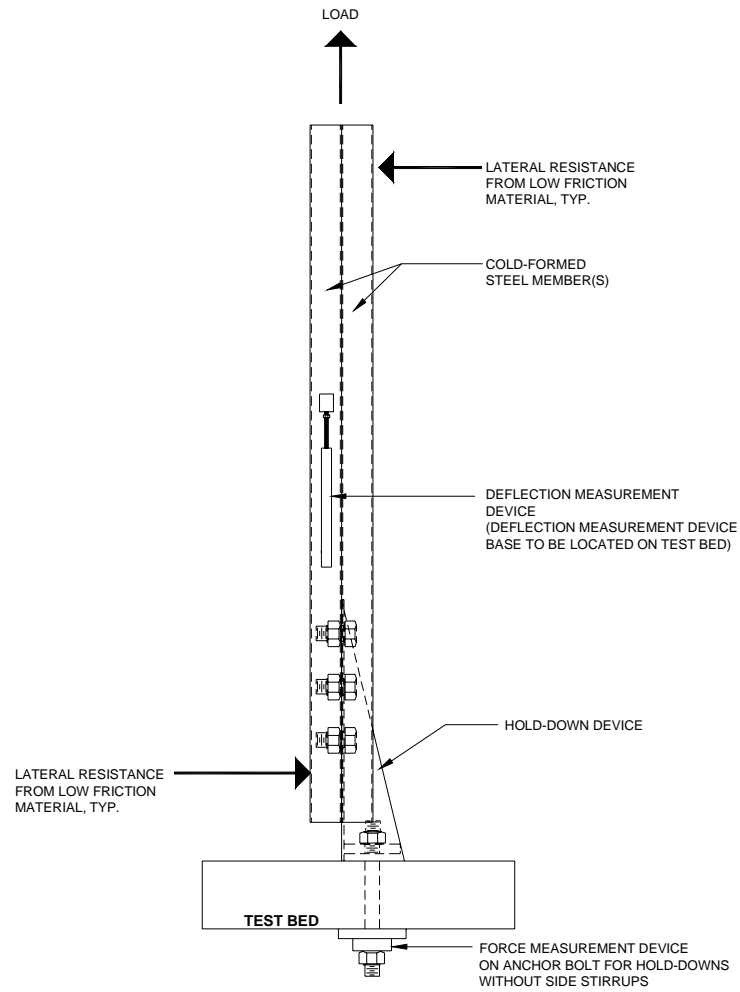
The hold-down assembly test requires the hold-down device be attached to a cold-formed steel member(s) that it will anchor to a supporting member(s), as

shown in Figure 4a, and this is to determine the strength and deformation of the entire hold-down connection assembly. Similar to the hold-down device test for tension load testing, the hold-down is required to be installed a minimum of 1" above the test bed unless it is required to be installed in the field to a rigid structural steel or concrete base, in which case it may be attached directly on top of the test bed as shown in Figure 4b. It may be required to test the hold-down raised higher than 1" if the hold-down may contact the test bed prior to failure such as through seat rotation. If a hold-down is tested directly on the test bed, the anchor bolt should be instrumented so that the force to the anchor bolt can be measured and compared to the applied force as some hold-downs may amplify the applied force to the anchor bolt due to prying. This anchor bolt force information is needed by the designer so that the anchorage may be properly designed and detailed.

The attachment of the hold-down to the cold-formed steel member(s) is to be as it will be in the end-use application. This is inclusive of the specified weld or fastener material and dimensions, the quantity of welds or fasteners, the tightness of the bolt nut, the spacing of weld or fasteners, and the end and edge distances provided for the welds or fasteners. As in the hold-down device test, the anchor bolt may be higher strength than specified, but it is to be the same diameter as specified and, if a nut and washer are used, they are to have the same bearing area as specified for the field installation. If compression testing is performed, it is also required that the bolt, nut and plate washer be of the same dimension as used in the end-use application. Also, for compression testing, it is required that the maximum unbraced length of the anchor bolt and the gap between the cold-formed steel member(s) and the test bed, if occurs, be per the manufacturer and reported. The device that is to measure the deformation is to be attached to the cold-formed steel member(s) above the hold-down. It is to measure the displacement that occurs between the cold-formed steel member(s) and the top of the test bed.



**Figure 4a - Raised Tension Load Test Set-up for a Single Hold-down Assembly**



**Figure 4b – Flush Tension Load Test Set-up  
for a Single Hold-down Assembly**

This will include fastener slip, fasteners to cold-formed steel member(s) bearing deformation, hold-down deformation, and anchor bolt elongation. In addition, the test standard requires that the cold-formed steel member(s) be a minimum of 1" above the test bed, even when the hold-down is installed flush to the test bed.



This is to ensure that the hold-down compression strength is not relying on the compression strength of the attached cold-formed steel member(s) as actual field built conditions may differ from that in the test laboratory.

### **Test Procedure**

It is not permitted to preload the test assembly as hold-downs are typically used to resist short-term loads from wind and seismic events and, therefore, seating due to long term loads may not occur prior to an event. The load is to be applied at a certain rate and in the direction that is expected in the actual condition (ie; tension, compression). The load and displacement are to be measured to produce a load-displacement curve. A minimum of eight reported displacements, spaced throughout as evenly as possible and not grouped just at the beginning or middle or end of the test, is required prior to the displacement test limit.

### **Evaluation of Data**

It is required that every test be used unless a valid reason to exclude it is given. The test data is to be analyzed and the design or available strength is the lowest of either the available strength determined using the specification Section F1 [8] or, for hold-downs in shear walls or that otherwise contribute to the story drift, the load at the deflection limit given in the test standard. If the hold-down device fails, the statistical values shown in Table F1 that are to be used in the Section F1 equation used to determine the resistance factor are to be those listed for “Structural members not listed above”.

The strength of the device is the lowest of (1) either the device or the assembly test, (2) the strength of the cold-formed steel member(s) as determined by the specification [8], (3) the strength of the fastening of the hold-down to the cold-formed steel member (connection) as determined by the specification [8], or (4) the strength of the fastener or weld itself (connector) as determined by the specification [8]. The hold-down assembly test shall be used to determine the hold-down strength when the fasteners used to attach the hold-down to the cold-formed steel members are not shown in the specification [8] or if the fastener specified is in the specification [8], but some aspect of it (i.e.; spacing, edge distance, material, etc.) does not conform to all the specification [8] fastener requirements.

The specification [8] Section F1.1(c) requires reductions when the tested material strength is greater than the specified material strength for the hold-down device or the hold-down device and the cold-formed steel members it's attached to in the assembly test. The material strength reductions are not cumulative and the larger reduction is to be used. In addition, a reduction is required when the thickness of the hold-down or the cold-formed steel members is greater than the minimum specification. These reductions are computed simply by dividing the specified value by the tested value.

The displacement of the hold-down is to be determined from the hold-down assembly test. The displacement limit for hold-downs in shear walls or that otherwise contribute to the story drift is prescribed as 0.185 inch and 0.25 inch for the hold-down device test and for the assembly test, respectively. It is a strength level displacement limit as the story drift is to be computed at strength level in accordance with ASCE7 Section 12.8.6 [7]. The load at these displacements are to be multiplied by 0.7, seismic strength to ASD conversion factor from ASCE7 load combinations, to determine the deflection limit for ASD as most light-frame design is performed using ASD. Other limits might be required by building jurisdictions or justified for other conditions.

The allowable strength design (ASD) displacement limit of 0.125 inch (0.185 inch LRFD limit) for the hold-down device itself has been used by some as a displacement limit for hold-downs in shear walls to limit the uplift of the bottom corner of the shear wall so as not to overly tax the sheathing to fastener connection. The 0.1875 inch limit (0.25 inch LRFD limit) takes into account fastener slip and bearing deformation, that might occur in typical hold-down connections, in addition to the device deflection in typical hold-down connections.

In addition, limiting the hold-down deflection is useful in that it reduces the hold-down contribution to the horizontal top of wall drift. The vertical deflection of the hold-down is one of several contributors to the horizontal top of wall drift. It is determined by multiplying the vertical hold-down displacement by the aspect ratio of the shear wall as shown in Figure 1.

For a hold-down that has a displacement of 0.125 inch at ASD in a 2:1 aspect ratio wall, this would equate to a 0.25 inch horizontal top of wall displacement just due to the hold-down device itself. This is over half of the permissible seismic story drift, in accordance with ASCE7 [7] Table 12.12-1, for an 8 foot tall shear wall. The shear wall deflection equation in AISI S213 [6] C2.1.1 is a four part equation with the horizontal top of wall displacement contribution due to the hold-down, as shown in Figure 1, as just one part.

### **Test Report Requirements**

The standard requires that the test report contain a description and drawing of the hold-down, inclusive of dimensions in both the device and assembly tests and description of the attached cold-formed steel members in the assembly tests. The tested and specified material properties for the hold-down and the welds or fasteners used must also be reported. If the cold-formed steel members were modified in some manner in the assembly tests, this information must also be provided.

Information on the attachment of the hold-down to the steel fixture and the cold-formed steel members must be given. This is inclusive of the specified weld or fastener material and dimensions, the quantity of welds or fasteners, the spacing of weld or fasteners, the end and edge distances provided for the welds or fasteners, and if the threads of the fastener were included in the shear plane between the hold-down and the steel fixture in the device test.

The report is to include a detailed drawing of the test setup indicating load direction and point of application. It is also to include the rate of loading, location of the displacement measuring devices, photographs of the test setup, and noting any deviations from any test requirements for the test fixture, for the device and assembly tests, and/or for the test procedure. It is to also include the load-displacement curves for each hold-down test.

It is required to include the load values obtained by the devices as well as a description of the failure mode(s) and its location. An example would be noting net tension fracture at the lowest bolt hole in the hold-down device. The behavior of the device during load application is also to be noted as well as including photographs of the failure.

### Hold-down Test Using New Standard

Hold-down assembly tension tests were performed using the new AISI hold-down test standard on Simpson Strong-Tie hold-downs, obtained from



**Figure 5 – Raised hold-down Assembly Tension Test Setup – Side**

production stock, attached to two 350S162-54 structural cold-formed steel studs. The hold-downs are fabricated from steel 118 mil thick and comply with ASTM A 653 GR33. The raised hold-down assembly tension test was setup in accordance with the AISI test standard as shown in Figure 4a. A picture of the test setup is shown in Figures 5 and 6. The failure was several of the hold-down screws shearing at the connection to the cold-formed steel studs. The picture of the test failure is shown in Figure 7.



Figure 6 – Raised hold-down Assembly Tension Test Setup – Front



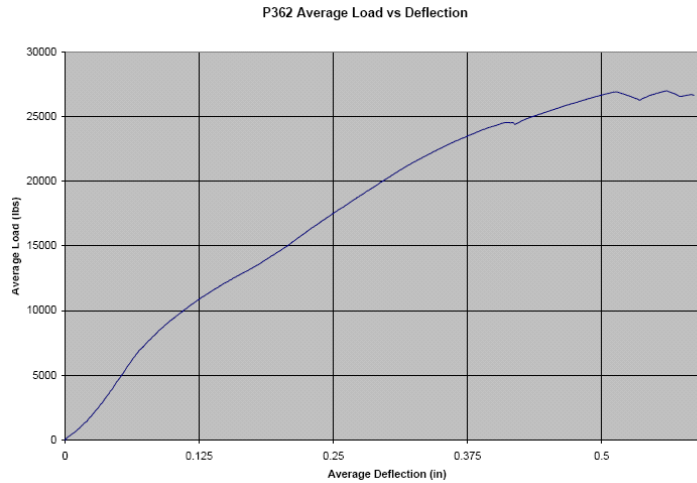
Figure 7 - Hold-down Assembly Tension Test Failure – Screw Shear

Three tests of the same setup were performed and yielded ultimate tension load values of 28,613 lbs, 27,042 lbs, and 28,358 lbs. The average ultimate value, or nominal strength, is then 28,004 lbs with a small coefficient of variation of 0.03. Based on the hold-down screw shear failure failure, the statistical values used from Table F1 to compute the resistance factor are for “Shear Strength of Screw”. Using a target reliability index,  $\beta_o$ , of 3.5 as the connection was the failure, the specification Chapter F calculation yields a resistance factor of 0.59 and an ASD safety factor,  $\Omega$ , of 2.71. Figure 8 summarizes the strength and deflection test measurements as well as the failure mode for these tests.

Description	Average	Test 1	Test 2	Test 3
Ultimate Load	<b>28004</b>	28613	27042	28358
Failure	-	Screws sheared	Screws sheared	Screws sheared
Load at 1/4"	<b>17538</b>	15989	19213	17412
Load at 1/4" / 1.4	<b>12527</b>	11421	13724	12437

**Figure 8 – Raised Hold-down Assembly Tension Test Results Summary**

The average load at the 1/4" deflection limit was 17,538 lbs and 12,527 lbs when multiplied by 0.7 to determine the ASD deflection limit load. Figure 9 shows the average load-displacement curve for these tests. The hold-down uses 18 - #14 self-tapping screws and the specification screw calculation yields a shear strength of 23,675 lbs. Therefore, available strength (ASD) is 10,334 lbs governed by the tested strength divided by the safety factor.



**Figure 9 – Raised Hold-down Assembly Tension  
Test Average Load-Displacement Curve**

Section 10.1 of the test standard requires the data be evaluated in accordance with Section F1 of the specification [8] and this section requires load reductions when the steel strength or base metal thickness of the hold-down or the attached members, in this case the structural studs, exceeds the minimum specification. The hold-down specified base metal thickness, yield strength, and tensile strength are 0.1275 inch, 33 ksi, and 45 ksi, respectively. The average base metal thickness, yield strength, and tensile strength for the hold-downs in these tests were 0.1299 inch, 47.1 ksi, and 57.2 ksi, respectively. The 350S162-54 specified base metal thickness, yield strength, and tensile strength are 0.0538 inch, 50 ksi, and 65 ksi, respectively. The average base metal thickness, yield strength, and tensile strength for the studs in these tests are 0.0545 inch, 64.7 ksi, and 71.7 ksi, respectively.

<b>Test Load Reduction for Steel Overstrength and Thickness</b>		
<b>Description</b>	<b>Hold-down</b>	<b>Stud</b>
Hold-down Ultimate (lbs)	28004	
Fy-spec,min (ksi)	33	50
Fu-spec,min (ksi)	45	65
Fy-test,avg (ksi)	47.1	64.7
Fu-test,avg (ksi)	57.2	71.7
Fy Reduction	<b>0.700</b>	0.773
Fu Reduction	0.787	0.907
t-spec,min (in.)	0.1275	0.0538
t-test,avg (in.)	0.1299	0.0545
t Reduction	<b>0.9815</b>	0.9872
Ultimate/SF (lbs)	10334	
Adjusted Ult. (lbs)	19245	
Adjusted Ult./SF (lbs)	<b>7101</b>	
Effective SF	<b>3.94</b>	

**Figure 10 – Raised Hold-down Assembly Tension Test Material Properties, Reduction Factors, and Effective Safety Factor Summary**

The hold-downs were fabricated from the same coil of steel as were the cold-formed steel studs, otherwise, material property tests would have to be performed for each test. Three tests on the steel from the hold-downs and three tests on the steel from the cold-formed steel studs were performed to determine the average yield and tensile strengths. In addition, ten thickness measurements were made for the hold-downs and ten for the studs to determine the average base metal thickness. The yield strengths, tensile strengths, base metal thicknesses, and steel strength reduction factors for the hold-down and the cold-formed steel members are summarized in Figure 10.

A strength reduction factor of 0.70, based on material strength over the minimum specification, in combination with a reduction factor of 0.98, based on thickness over the minimum specification, if applied to the design strength would result in an adjusted available strength of 7,101 lbs. A case might be made that the yield strength,  $F_y$ , reduction should only be taken if yielding is the governing failure mode rather than taking the larger of the yield or tensile strength reductions in accordance with the specification [8] Section F1.1(c). In this test the failure was shearing of the screws themselves and so, if the  $F_u$  reduction was taken instead, this would result in a 0.79 load reduction factor, in



addition to the 0.98 reduction factor for thickness, for which the adjusted available strength would be 7,984 lbs.

Another observation is that the calculated nominal shear strength determined in accordance with S100 Section E4.3.1, is 71,025 lbs and quite high compared to the test average ultimate load of 28,004 lbs. This might justify that no strength reduction factor be used as fastener bearing failure would not occur even if the studs and hold-down were fabricated from steel with strength close to the minimum specification. This has been shown to be true in tests with hold-down and cold-formed steel member strength close to specified.

When hold-down tests are performed using steel with strengths close to the minimum specifications, which is very difficult to find, the load values typically go up greater than the inverse of the conservative strength reductions using  $F_{u\text{-test}}$  divided by  $F_{u\text{-specified}}$  and  $F_{y\text{-test}}$  divided by  $F_{y\text{-specified}}$ . In this case, the safety factor required by the specification was 2.71 and, for the production hold-downs from stock tested, the approximate safety factor is 3.94 (28006/7101). So production hold-downs typically yield higher safety factors than required by the specification due to the fact that the steel supplied to fabricate these hold-downs is always stronger than the minimum specification.

## **Conclusion**

It is necessary to develop test standards to provide uniform testing procedures to better evaluate and compare the strength and displacement behavior of devices that cannot be simply calculated using the AISI specification or the COFS standards due to their complexity and the complexity of the load path through them. The AISI COS new Test Standard for Hold-downs Attached to Cold-Formed Steel Structural Framing was developed in response to this need. It was also developed in recognition of the importance these devices have in the proper functioning of cold-formed steel framing lateral force resisting systems, and thus the overall structure.

**References**

1. AISI Test Standard for Hold-downs Attached to Cold-Formed Steel Structural Framing (S913), 2008.
2. AISI Cold-Formed Steel Manual, 2002.
3. AISI North American Standard for Cold-Formed Steel Framing – General Provisions, AISI S200, 2007.
4. ICC International Building Code (IBC), 2006
5. AISI Standard for Cold-Formed Steel Framing – Lateral Design, 2004.
6. AISI North American Standard for Cold-Formed Steel Framing - Lateral Design, AISI S213, 2007.
7. ASCE7 Minimum Design Loads for Buildings and Other Structures including Supplement No. 1, 2005.
8. AISI North American Specification for the Design of Cold-Formed Steel Structural Members (S100), 2007.



## **Behavior of Arc Spot Weld Connections Subjected to Combined Shear and Tension Forces**

L. K. Stirnemann<sup>1</sup> and R. A. LaBoube<sup>2</sup>

### **Abstract**

In North America the design of arc spot weld connections is currently limited by the lack of understanding of the behavior of the welded connection when it is subject to combined shear and tension forces. An experimental investigation was conducted at the University of Missouri – Rolla to study the behavior and to develop design recommendations for the relationship (interaction) of the tension and shear forces on an arc spot weld connection. The experimental study focused on six variables that were deemed to be the key parameters that may influence the strength of the arc spot weld connection. These variables were the sheet thickness; sheet material properties to included yield strength, tensile strength and ductility of the sheet; visible diameter of the arc spot weld; and the relationship between the magnitude of the shear force and tension force. Based on an analysis of the test results, both a linear and non-linear interaction equation was developed and design recommendations were formulated based on these equations.

### **INTRODUCTION**

Since the early 1940's, cold-formed steel construction has been widely used throughout the United States and other countries. In building construction, arc spot welds, commonly known as puddle welds, are widely used for connecting roof deck to support members (Figure 1). These support members are typically hot-rolled steel beams or girders, or open web steel joists. An arc spot weld is formed by burning a hole through the decking and then filling it with weld metal, thus fusing the sheet to the structural member.

<sup>1</sup> Former graduate student, University of Missouri-Rolla, Rolla, MO

<sup>2</sup> Distinguished Teaching Professor, University of Missouri-Rolla

An arc spot weld will be subjected to different stress conditions as a result of imposed loading conditions. For example, a wind load acting on a structural system may impose both a shear and tension force on the roof when the deck is functioning as a structural diaphragm.

The use of cold-formed steel in the United States has been guided by the American Iron and Steel Institute (AISI) since it published the first edition of Light Gage Cold-Formed Steel Design Manual in 1946 (AISI, 1946). The most recent edition, published in 2007, includes specifications that extend the use of the document into Canada and Mexico (AISI, 2007). This resource for structural design only provides design information for arc spot weld connections in pure tension or pure shear.

Additional design guidance was needed for predicting the strength when the weld connection was subjected to simultaneous shear forces and tension forces. A study at the University of Missouri-Rolla focused on spot weld connections for steel deck and structural members in combined tension and shear loading.



Figure 1. Arc Spot Weld Connected Roof System

### LITERATURE REVIEW

Studies have been completed regarding a pure shear force and a pure tension force on arc spot weld connections (Pekoz and McGuire, 1979; LaBoube and Yu, 1991; LaBoube, 2001), but no test data concerning a combination load is available.

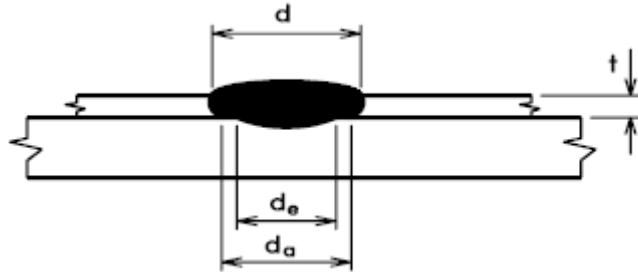


Figure 2. Definition of Parameters

The American Iron and Steel Institute's *North American Specification for the Design of Cold Formed Steel Members* (2007) provides criteria for the design of cold-formed steel members and connections. The specification includes the most updated design guidelines for the industry's use. The specification includes equations for the design arc spot weld connections subjected to either pure shear or pure tension as summarized by Yu (2000). Contained in the specification are recommendations for double sheet connections, connections with weld washers, connections that are concentrically or eccentrically loaded, side lap connections, and connections made at an edge of roof. The applicable nominal strength,  $P_n$ , equations are as follows:

For Shear Alone:

If  $(d_a/t) \leq 0.815\sqrt{(E/F_u)}$ , then

$$P_n = 2.20td_aF_u \quad (\text{Eq. 2-11})$$

If  $0.815\sqrt{(E/F_u)} < (d_a/t) < 1.397\sqrt{(E/F_u)}$ , then

$$P_n = 0.280 \left[ 1 + 5.59 \frac{\sqrt{E/F_u}}{d_a/t} \right] td_aF_u \quad (\text{Eq. 2-12})$$

If  $(d_a/t) \geq 1.397\sqrt{(E/F_u)}$ , then  $P_n = 1.40td_aF_u$  (Eq. 2-13)

For Tension Alone:

$$P_n = 0.8(F_u/F_y)^2 td_aF_u \quad (\text{Eq. 2-14})$$

$$P_n = \frac{\pi d_e^2}{4} 0.75 F_{xx} \quad (\text{Eq. 2-15})$$

For tension the following limits apply:  $td_aF_u \leq 3$  kips (13.34 kN),  $e_{\min} \geq d$ ,  $F_{xx} \geq 60$  ksi,  $F_u \geq 60$  ksi, and  $F_{xx} > F_u$ .

Where, as illustrated by Figure 2,  $P_n$  = Nominal strength (resistance) of arc spot weld,  $d$  = visible diameter of outer surface of arc spot weld,  $d_a$  = the average diameter of the arc spot weld at mid thickness of  $t$  (where  $d_a = (d-t)$  for single or multiple sheets not more than four lapped sheets over a supporting member),  $d_c = 0.7d - 1.5t \leq 0.55d$ ,  $d_c$  = effective diameter of fused area at plane of maximum shear transfer,  $t$  = total combined base steel thickness (exclusive of coatings) of sheets involved in shear transfer above plane of maximum shear transfer. Also,  $F_{xx}$  = tensile strength of electrode classification,  $F_u$  = tensile strength as specified in Section A2.1, A2.2 or A2.3.2 (AISI 2007) and  $e_{min}$  = minimum edge distance.

### EXPERIMENTAL INVESTIGATION

Six parameters were considered in the UMR test program. These parameters included the sheet thickness, yield strength, tensile strength and ductility of the sheet, diameter of the weld, and the variation in the relationship between the shear force and tension force.

Standard B deck was used for all deck that was tested. The nominal deck dimensions are shown in Figure 3.

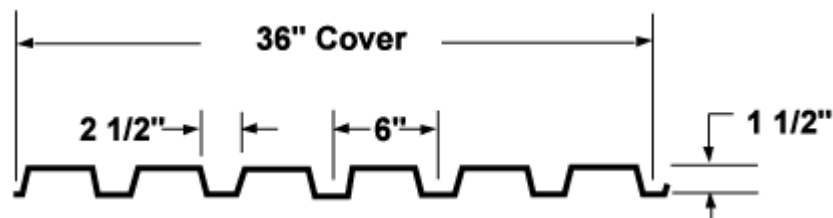


Figure 3. Typical B Deck Profile

The mechanical properties of the deck material were determined by performing standard tensile coupon tests in accordance with ASTM A370. A summary of the average results can be found in Table 3.

In addition to the thickness of the sheet, yield strength, tensile strength and ductility of the sheet, the weld diameter varied between 0.498 in. and 1.062 in.

To vary the interaction of shear and tension forces on the spot weld connection, the test setup considered three orientation angles, measuring from the vertical plane were tested: thirty degrees, sixty degrees, and seventy-five degrees (Figure 4).

Table 3. Materials Properties

Deck Type	Uncoated Thickness	Yield Point	Tensile Strength	$F_u/F_y$	Percent Elongation
	T	$F_y$	$F_u$		
	(in.)	(ksi)	(ksi)		%
B1	0.0577	97.57	99.50	1.02	0.60
B2	0.0293	100.63	104.77	1.04	0.83
B3	0.0580	48.10	59.30	1.23	20.06
B4	0.0300	42.10	52.70	1.25	20.98

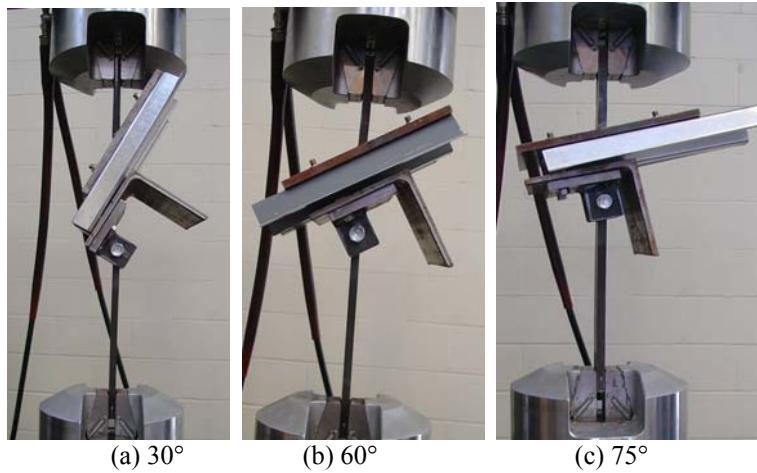


Figure 4. Orientation of Test Setup

**Test Specimen Fabrication.** Each test specimen consisted of a 12 in. x 12 in. deck section spot welded to a 6 in. x 6 in. x 3/8 in. hot-rolled angle (Figure 5). Details of the test specimen fabrication are given by Stirnemann and LaBoube (2007).



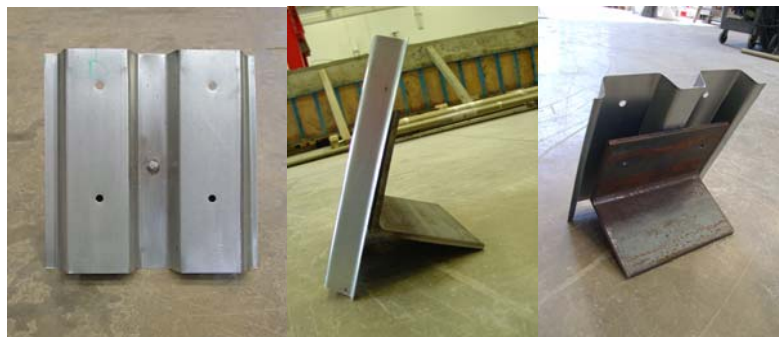


Figure 5. Test Specimen

**Test Fixture.** The test fixture consisted of an upper welded T-section (Figure 6) and a rotating arm (Figure 6). The welded T-section consisted of a flat plate 12 in. x 12 in. x 3/8 in. welded to a stem plate 2 in. x 9 in. x 3/8 in. The T-sections were fabricated at angles of 30°, 60°, and 75° the 30° and 60° T-section.

Each test specimen was attached to the test fixture. The completed test specimen attached to the test fixture and mounted in the test machine is shown by Figure 6.

**Test Procedure.** The test specimen was placed in a MTS 880 Universal Testing machine where it was loaded in tension. The test fixture's rotating arm, allowed the test specimen to be pulled through the vertical line of action of the spot weld, such that there was no out-of-plane bending forces applied to the specimen. The tension load was continuously applied until the test specimen failed.

## TEST RESULTS

A total of seventy-nine tests were performed in this test program. Thirty-five test specimens had  $F_u/F_y \leq 1.04$  (Deck Type B1 and B2) and forty-four test specimens had  $F_u/F_y \geq 1.23$  (Deck Type B3 and B4).

A typical failure mode, regardless of weld size, was a peeling, fracture and tearing of the deck around the perimeter of the weld, as shown in Figure 7.



Figure 6. Test Specimen Mounted in the Test Fixture



Figure 7. Typical Failed Test Specimen

**Deck Types B3 and B4.** For the decks with  $F_u/F_y \geq 1.23$ , two thicknesses were tested, 0.058 in. and 0.030 in. Each thickness was tested using a thirty degree T-section and a sixty degree T-section. A limited number of the Deck Type B4 were also tested using a seventy-five degree T-section.

Fracture of the deck was reached for all of the tests. In both Deck Types B3 and B4 the deck experienced large amounts of plastic deformation before the sheet failed, as depicted in Figure 8. As the deck was loaded the deck around the contour of the weld became noticeably deformed. Although the load application for the 44 test specimens was concentric with respect to the center of the weld, the distortion of the sheet during loading resulted in a non-uniform deformation around the perimeter of the weld. This can be seen in Figure 9.



Figure 8. Deformation of Deck Type B3 and B4



Figure 9. Deformed Deck Around Contour of Weld

For each test specimen the average diameter,  $d_a$ , and the effective diameter,  $d_e$ , computed per the AISI specification, the ultimate test load,  $P_u$ , and the tension and shear components of the ultimate load,  $P_{ut}$  and  $P_{uv}$  were recorded and can be found in Stirnemann and LaBoube (2007).

**Deck Types B1 and B2.** For the decks with a  $F_u/F_y \leq 1.04$  there were two thicknesses tested, 0.058 in. and 0.030 in. Each thickness was tested using a thirty degree welded T-section and a sixty degree T-section. A limited number of the Deck Type B2 were also tested using a seventy-five degree T-section.

Similar to Deck Types B3 and B4, the ultimate capacity of the deck was reached for all of the tests. However, the lower ductility steel did not show the same signs of deformation as the higher ductility steel. For the lower ductility steel typical deformations can be seen in Figure 10. The failure mode of the lower ductility deck was most often a simultaneous fracture around the entire weld instead of a tearing failure exhibited by the normal ductility deck types. Test

specimen details and test results for the low ductility specimens can be found in Stirnemann and LaBoube (2007).



Figure 10. Deformation of Deck Type B1 and B2

#### DATA ANALYSIS

The data obtained from this test program was analyzed using the current nominal tensile and shear strengths provided by AISI in the 2001 Specification, Equations 2-11 through 2-15.

#### DATA ANALYSIS USING AISI SPECIFICATION

The data obtained from this test program was analyzed with the current nominal tensile and shear strengths provided by AISI in the 2007 Specification, Equations 12 through 15. Data from LaBoube and Yu (1991) and Pekoz and McGuire (1979) is presented to define the limits of pure tension and pure shear strength.

**Nominal Strength.** For each test specimen the nominal tensile strength,  $P_{nt}$ , and nominal shear strength,  $P_{nv}$ , were computed by AISI Equations 2-11 through 2-15 and are listed in Tables 2 to 5. Also summarized in Tables 4-5 to 4.8 are the tension and shear ultimate load components,  $P_{ut}$  and  $P_{uv}$ . Ratios of  $P_{ut}/P_{nt}$  and  $P_{uv}/P_{nv}$  were computed and the values can be found for Deck Types B3, B1, B2, and B4 in Tables 2, 3, 4, and 5, respectively.

Table 2 AISI Analysis for Deck Type B3

Deck Type B3 Specimen No.	$P_u$ (lbs.)	$P_{ut}$ (lbs.)	$P_{uv}$ (lbs.)	$P_{nt}$ (lbs.)	$P_{nv}$ (lbs.)	$\frac{P_{ut}}{P_{nt}}$	$\frac{P_{uv}}{P_{nv}}$
B3-1	2817	1408	2439	2325	4207	0.606	0.580
B3-2	2803	1401	2427	2180	3944	0.643	0.616
B3-3	2335	1168	2022	2355	4260	0.496	0.475
B3-4	2288	1144	1982	2191	3964	0.522	0.500
B3-5	2731	1365	2365	2116	3829	0.645	0.618
B3-6	2772	1386	2401	2168	3923	0.639	0.612
B3-7	3379	1690	2926	2973	5380	0.568	0.544
B3-8	2602	1301	2253	2939	5318	0.443	0.424
B3-9	2803	1401	2427	2076	3757	0.675	0.646
B3-10	3387	1693	2933	2935	5311	0.577	0.552
B3-11	1703	1475	852	2189	3960	0.674	0.215
B3-12	3119	2701	1559	3037	5495	0.889	0.284
B3-13	1003	868	501	1929	3490	0.450	0.144
B3-14	2620	2269	1310	3042	5503	0.746	0.238
B3-15	2798	2423	1399	2700	4886	0.897	0.286
B3-16	3832	3318	1916	3123	5651	1.062	0.339
B3-17	2856	2474	1428	2817	5096	0.878	0.280
B3-18	1599	1385	799	2044	3699	0.677	0.216
B3-19	1228	1064	614	2179	3942	0.488	0.156
B3-20	1821	1577	910	2114	3825	0.746	0.238

**Ultimate Capacity vs. Nominal Capacity.** To assess the interaction between the tension force and shear force in an arc spot weld connection, the ratios of the ultimate capacity and the nominal capacity were evaluated. The  $P_{ut}/P_{nt}$  and  $P_{uv}/P_{nv}$  ratios are listed in Tables 2 through 5 and illustrated in Figure 11. Data from LaBoube and Yu (1991) and Pekoz and McGuire (1979) are included on Figure 11 to provide boundary conditions for pure tension and pure shear.

Table 3. AISI Analysis of Deck Type B1

Deck Type B1 Specimen No.	$P_u$ (lbs.)	$P_{ut}$ (lbs.)	$P_{sw}$ (lbs.)	$P_{nt}$ (lbs.)	$P_{nv}$ (lbs.)	$\frac{P_{ut}}{P_{nt}}$	$\frac{P_{sw}}{P_{nv}}$	$\frac{P_{nt}}{.75P_{nt}}$	$\frac{P_{nv}}{.75P_{nv}}$	$\frac{P_{ut}}{.75P_{nt}}$	$\frac{P_{sw}}{.75P_{nv}}$	$\frac{P_{nt}}{.60P_{nt}}$	$\frac{P_{nv}}{.60P_{nv}}$	$\frac{P_{ut}}{.60P_{nt}}$	$\frac{P_{sw}}{.60P_{nv}}$
B1-1	2771	1385	2399	3074	8127	0.451	0.295	2305	6095	6114	0.393	1844	4876	0.751	0.492
B1-2	2657	1329	2301	3083	8152	0.431	0.282	2312	6114	6114	0.376	1850	4891	0.718	0.470
B1-3	2545	1273	2204	2622	6933	0.485	0.318	1967	5200	6447	0.423	1573	4160	0.809	0.530
B1-4	3078	1539	2666	3109	8222	0.495	0.324	2332	6167	6660	0.432	1865	4933	0.825	0.540
B1-5	3006	1503	2604	2964	7837	0.507	0.332	2223	5878	6676	0.442	1778	4702	0.845	0.554
B1-6	2561	1280	2217	2733	7228	0.468	0.307	2050	5421	624	0.409	1640	4337	0.781	0.511
B1-7	2412	1206	2089	2385	6306	0.506	0.331	1788	4729	674	0.441	1431	3783	0.843	0.552
B1-8	2495	1248	2161	2772	7331	0.450	0.295	2079	5498	600	0.393	1663	4399	0.750	0.491
B1-9	2622	1311	2270	2812	7436	0.466	0.304	2109	5610	621	0.404	1687	4488	0.777	0.506
B1-10	1908	1652	954	2753	7280	0.600	0.131	2065	5460	800	0.174	1652	4368	1.000	0.218
B1-11	2469	2139	1235	3841	10157	0.557	0.122	2881	7618	742	0.162	2305	6094	0.928	0.203
B1-12	2836	2456	1418	3673	9712	0.669	0.146	2754	7284	891	0.194	2204	5827	1.115	0.243
B1-13	2700	2338	1350	3741	9892	0.625	0.136	2806	7419	833	0.181	2245	5935	1.042	0.227
B1-14	1806	1564	903	2557	6761	0.612	0.134	1918	5071	815	0.178	1534	4057	1.019	0.223

Table 4. AISI Analysis of Deck Type B2

Deck Type B2 Specimen No.	$P_u$ (lbs.)	$P_{ut}$ (lbs.)	$P_{lw}$ (lbs.)	$P_{nt}$ (lbs.)	$P_{nv}$ (lbs.)	$\frac{P_{ut}}{P_{nt}}$	$\frac{P_{nv}}{P_{nt}}$	$\frac{P_{nw}}{P_{nt}}$	$.75P_{nt}$	$.75P_{nv}$	$\frac{P_{ut}}{.75P_{nt}}$	$\frac{P_{nw}}{.75P_{nv}}$	$.60P_{nt}$	$.60P_{nv}$	$\frac{P_{ut}}{.60P_{nt}}$	$\frac{P_{nw}}{.60P_{nv}}$
B2-1	976	488	846	1336	2726	0.365	0.310	1002	1002	2045	0.487	0.413	801	1636	0.609	0.517
B2-2	731	366	633	1400	2747	0.261	0.230	1050	1050	2060	0.348	0.307	840	1648	0.435	0.384
B2-3	960	480	832	1307	2716	0.367	0.306	980	2037	0.489	0.408	784	1630	0.612	0.510	
B2-4	928	464	804	1234	3132	0.376	0.257	926	2349	0.501	0.342	741	1879	0.626	0.428	
B2-5	1323	662	1146	1996	3222	0.332	0.356	1497	2417	0.442	0.474	1198	1933	0.553	0.593	
B2-6	1449	724	1254	2322	3749	0.312	0.335	1742	2812	0.415	0.446	1393	2249	0.520	0.558	
B2-7	1230	615	1065	2096	3383	0.293	0.315	1572	2537	0.391	0.419	1257	2030	0.489	0.525	
B2-8	1261	631	1092	2250	3633	0.280	0.301	1688	2725	0.373	0.400	1350	2180	0.467	0.501	
B2-9	712	356	617	1386	2742	0.257	0.225	1039	2057	0.342	0.299	832	1645	0.428	0.375	
B2-10	955	477	827	1350	2730	0.354	0.303	1013	2048	0.471	0.403	810	1638	0.589	0.505	
B2-11	1002	868	501	2075	3350	0.418	0.150	1566	2513	0.557	0.199	1245	2010	0.697	0.249	
B2-12	890	771	445	2098	3387	0.368	0.131	1573	2540	0.490	0.175	1259	2032	0.613	0.219	
B2-13	695	602	347	1407	2749	0.428	0.126	1055	2062	0.570	0.168	844	1649	0.713	0.211	
B2-14	603	522	301	1361	2734	0.384	0.110	1021	2051	0.511	0.146	817	1640	0.639	0.184	
B2-15	735	636	367	1389	2743	0.458	0.134	1042	2057	0.610	0.178	833	1646	0.763	0.223	
B2-16	571	495	286	1425	2755	0.347	0.104	1069	2066	0.462	0.138	855	1653	0.578	0.173	
B2-17	971	841	486	2222	3687	0.379	0.135	1666	2690	0.505	0.180	1333	2152	0.631	0.226	
B2-18	1050	909	525	2204	3559	0.412	0.147	1653	2669	0.549	0.196	1323	2135	0.687	0.246	
B2-19	730	632	365	1483	2773	0.426	0.132	1112	2080	0.568	0.175	890	1664	0.711	0.219	
B2-20	773	670	387	1980	3197	0.338	0.121	1485	2398	0.450	0.161	1188	1918	0.563	0.202	
B2-21	745	720	193	1653	2828	0.435	0.068	1240	2121	0.580	0.090	992	1697	0.726	0.114	

Table 5 AISI Analysis for Deck Type B4

Deck Type B4 Specimen No.	$P_u$ (lbs.)	$P_{ut}$ (lbs.)	$P_{uv}$ (lbs.)	$P_{nt}$ (lbs.)	$P_{nv}$ (lbs.)	$\frac{P_{ut}}{P_{nt}}$	$\frac{P_{uv}}{P_{nv}}$
B4-1	1562	781	1353	913	1602	0.856	0.845
B4-2	1562	781	1353	1224	2015	0.638	0.671
B4-3	1562	781	1353	1511	2079	0.517	0.651
B4-4	1030	515	892	1036	1817	0.497	0.491
B4-5	985	493	853	1026	1801	0.480	0.474
B4-6	1021	510	884	868	1523	0.588	0.580
B4-7	1076	538	932	951	1669	0.566	0.558
B4-8	1236	618	1071	1963	2180	0.315	0.491
B4-9	1561	781	1352	1424	2060	0.548	0.657
B4-10	864	748	432	1148	1198	0.652	0.361
B4-11	938	812	469	1150	1998	0.706	0.235
B4-12	739	640	370	1020	1790	0.628	0.206
B4-13	877	760	439	1070	1877	0.710	0.234
B4-14	1051	911	526	1187	2007	0.767	0.262
B4-15	676	585	338	1743	2131	0.336	0.159
B4-16	738	639	369	1531	2083	0.418	0.177
B4-17	1106	958	553	2046	2285	0.468	0.242
B4-18	1125	974	563	1729	2128	0.564	0.264
B4-19	656	634	170	1048	1839	0.605	0.092
B4-20	745	720	193	1261	2023	0.571	0.095
B4-21	638	616	165	1020	1790	0.604	0.092
B4-22	931	899	241	1292	2030	0.696	0.119
B4-23	1139	1100	295	1313	2035	0.837	0.145
B4-24	600	579	155	1140	1996	0.508	0.078

**Adjustment For Low Ductility Steel.** To better align the normal and low ductility test results, the nominal strengths of Deck Type B1 and B2 were multiplied by a factor,  $L$ , equal to 0.75. Interestingly, the 0.75 factor is required by AISI Specification Section A.2.3.2 for low ductile steels. For Deck Type B3 and B4  $L$ , was taken as unity. Figure 4.4 illustrates this modified interaction relationship.



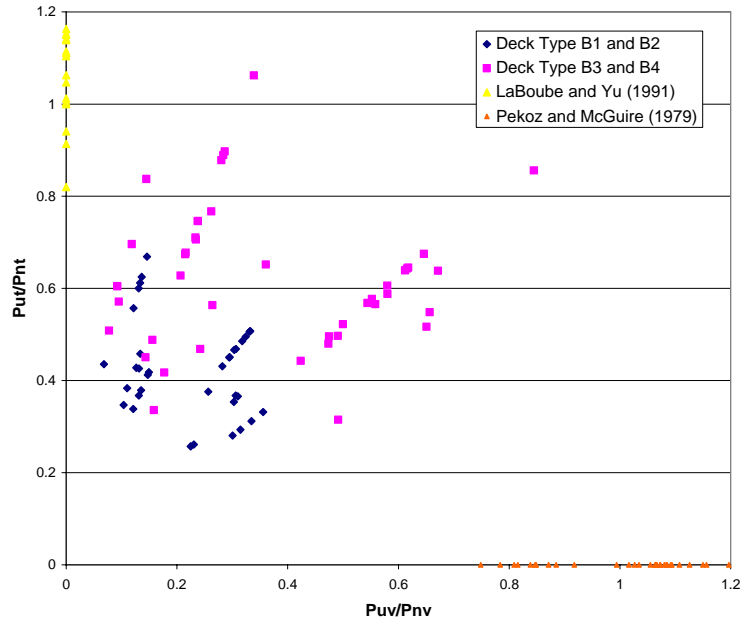


Figure 11. Interaction of Shear and Tension using AISI Equations

#### DEVELOPMENT OF INTERACTION EQUATION

Based on the data analysis, both a non-linear and linear interaction equation was developed.

**Non-linear Interaction Equation.** Using the data of Figure 11 an interaction equation was developed and can be seen graphically by Figure 12. To better align the normal and low ductility test results, the nominal strengths of Deck Type B1 and B2 were multiplied by a factor,  $L$ , equal to 0.75. Interestingly, the 0.75 factor is required by AISI Specification Section A.2.3.2 for low ductile steels. For Deck Type B3 and B4,  $L$ , was taken as unity.

The test data for Figure 11 can be found in Tables 2 through 5.

$$\left( \frac{P_{ut}}{LP_{nt}} \right)^6 + \left( \frac{P_{uv}}{LP_{nv}} \right) \leq 1.0 \quad (\text{Eq. 17})$$

where:

$$L = 1.0, \text{ for } F_u/F_y \geq 1.23$$

$$L = 0.75, \text{ for } F_u/F_y \leq 1.04$$

$P_{nv}$  = AISI Nominal Shear Strength (Eqs. 12 and 13)

$P_{nt}$  = AISI Nominal Tension Strength (Eq. 15)

**Linear Interaction Equation.** A linear equation was developed however an L value of 0.60 for Deck Types B1 and B2 was used for both  $P_{nt}$  and  $P_{nv}$ . For normal ductility decks, Deck Types B3 and B4, L was taken as unity.

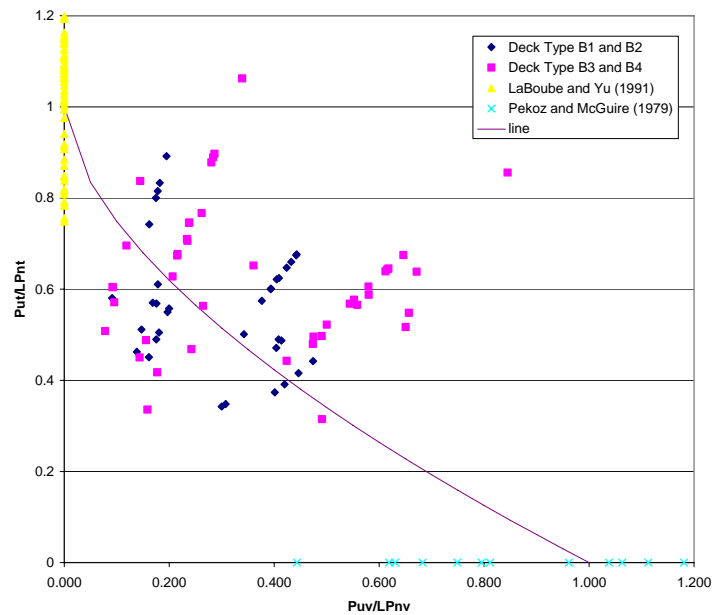


Figure 12. Non-linear Interaction Relationship

The linear interaction Equation 18 can be seen graphically by Figure 13.

$$\left( \frac{P_{ut}}{LP_{nt}} \right) + \left( \frac{P_{uv}}{LP_{nv}} \right) \leq 1.0 \quad (\text{Eq. 18})$$

where:

$$L = 1.0, \text{ for } F_u/F_y \geq 1.23$$

$L = 0.60$ , for  $F_u/F_y \leq 1.04$

$P_{nv}$  = AISI Nominal Shear Strength (Eqs. 12 and 13)

$P_{nt}$  = AISI Nominal Tension Strength (Eq. 15)

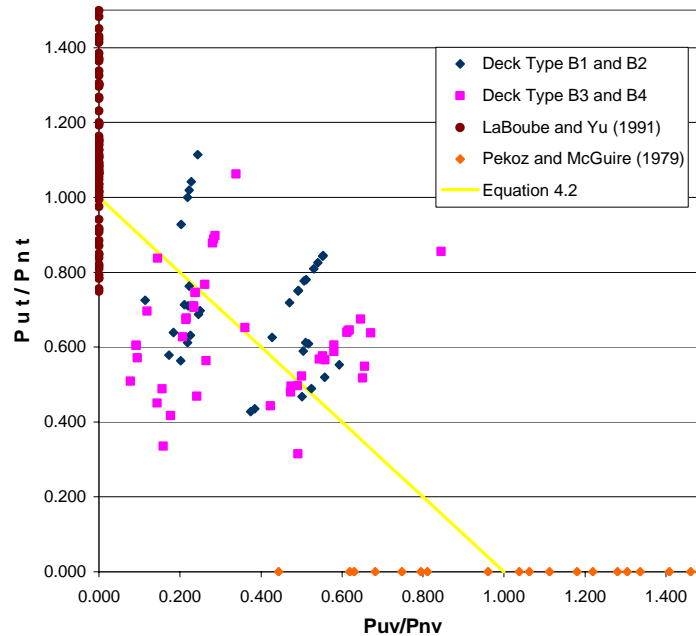


Figure 13. Linear Interaction Relationship

### CONCLUSIONS AND DESIGN RECOMMENDATIONS

A total of seventy-five specimens were tested in order to establish an understanding of the behavior of arc spot weld connections subjected to combined shear and tension and develop a design methodology. Based on an analysis of the test data, an interaction equation was derived.

### ACKNOWLEDGEMENTS

This investigation was sponsored by the American Iron and Steel Institute and their financial support is gratefully acknowledged. The AISI Subcommittee on Connections (A.J. Harrold, former chairperson) is acknowledged for providing valuable technical guidance. Special thanks are also extended to Dr. Helen Chen, Senior Structural Engineer, for the American Iron and Steel Institute and

Mr. John Mattingly of Nicholas J. Bouras for their assistance and technical guidance throughout the research study. The steel deck used for test specimens was provided by Nicholas J. Bouras and the hot-rolled angle was donated by Terry Zwick of Atlas Iron Works. The generosity of these individuals and organizations is gratefully acknowledged. Appreciation is also expressed to technical staff of the UMR Civil Engineering Department for their assistance in the preparation, fabrication, and performance of the test program.

### **BIBLIOGRAPHY**

American Iron Steel Institute, AISI. (2007). "North American Specification for the Design of Cold-Formed Steel Structural Members." 2007 Edition, Washington DC

American Iron Steel Insititute, AISI. (1946). "Light Gage Cold-Formed Steel Design Manual." 1946. New York.

LaBoube, R. A., (2001), "Tension on Arc Spot Welded Connections – AISI Section E2.2.2," University of Missouri – Rolla, Rolla, MO

LaBoube, R. A., and Yu, W. W. (1991). "Tensile Strength of Welded Connections." Civil Engineering Study 91-3 Cold Formed Steel Series. Rolla, MO., June, 1991, University of Missouri-Rolla, Center for Cold-Formed Steel Structures.

Pekoz, T., and McGuire, W. (1979). "Welding of Sheet Steel." Report SG 79-2. American Iron and Steel Institute, Washington, DC

Steel Deck Institute, SDI. (2004). "Diaphragm Design Manual." Third Edition. Fox River Grove, IL.

Stirnemann, L.K. and LaBoube, R.A. (2007). "Behavior of Arc Spot Weld Connections Subjected to Combined Shear and Tension Forces." Final Report, Cold-Formed Steel Series, Department of Civil Engineering, Wei-Wen Yu Center for Cold-Formed Steel Structures, University of Missouri-Rolla, Rolla, Missouri

Yu, W. W. (2000). "Cold-Formed Steel Design." Second Edition. John Wiley and Sons, Inc, New York, NY.